

High Resolution Prediction of Gas Injection  
Process Performance for Heterogeneous Reservoirs

Final Report

Prepared for the U.S Department of Energy  
Under Grant No. DE-FC26-00BC15319

Principal Investigator: Franklin M. Orr, Jr.  
Department of Petroleum Engineering  
Stanford University

May 2004

## **Disclaimer**

This report was prepared as an account of work sponsored by an agency of the United States Government. Neither the United States Government nor any agency thereof, nor any of their employees, makes any warranty, express or implied, or assumes any legal liability or responsibility for the accuracy, completeness, or usefulness of any information, apparatus, product, or process disclosed, or represents that its use would not infringe privately owned rights. Reference herein to any specific commercial product, process, or service by trade name, trademark, manufacturer, or otherwise does not necessarily constitute or imply its endorsement, recommendation, or favoring by the United States Government or any agency thereof. The views and opinions of authors expressed herein do not necessarily state or reflect those of the United States Government or any agency thereof.

## Acknowledgements

This report is the result of much hard work on the part of many people.

Margot Gerritsen, Assistant Professor of Petroleum Engineering, contributed in countless ways to the smooth running of the research group. Her deep knowledge of numerical techniques for solving nonlinear partial differential equations was critical to the success of the simulation effort described here, as was her constant attention to supervising the students and helping them join productively in the research effort.

Kristian Jessen, Research Associate and now Acting Assistant Professor of Petroleum Engineering, was deeply involved in many parts of the work, especially the research on analytical solutions for one-dimensional flow of two-phase, multicomponent mixtures and the development of compositional streamline methods for field-scale reservoir simulation. He worked extensively with the students, simulated experiments, and also led assembly of this report from the contributions of the other members of our research group.

PhD student Brad Mallison explored the use of higher order finite difference schemes for numerical solutions of one-dimensional flow of multicomponent mixtures. His analysis of the details of these schemes reveals much about impact of numerical error on composition paths in these systems. He also explored deeply the impact of mapping errors on overall accuracy and developed improved mapping schemes that reduce those errors.

MS and now PhD student Carolyn Seto demonstrated the power of the streamline approach with a set of example simulations for a condensate reservoir. Her work showed conclusively that streamline methods are more accurate than conventional finite difference simulations for this type of reservoir, and they are also fast enough that the variability of process performance over many realizations of estimated permeability can be explored.

Research Associate Yildiray Cinar led the extensive experimental effort to investigate the impact of low interfacial tensions between two phases in the presence of a third phase, performing and analyzing most of the experiments. Undergraduate Taku Ide assisted ably with the phase equilibrium and interfacial tension measurements. MS candidate Sharoh Marquez performed and analyzed the experiments to investigate three-phase relative permeabilities in oil-wet systems. Together they have assembled the largest available data set for three-phase displacement behavior when two phases display low interfacial tension. Yildiray Cinar also designed and performed an extensive set of crossflow experiments, which Kristian Jessen simulated.

MS student Nitin Srivastava investigated the accuracy of the assumption, always used in constructing analytical solutions to compositional problems, that phase behavior can be evaluated at a constant pressure. His results indicate that the assumption is a surprisingly good one.

MS student Linda Sam-Olibale explored the interplay of gravity segregation, capillary crossflow, and viscous crossflow in an extensive simulations. Her analysis provides useful

guidance for users of streamline methods as to when the basic streamline model needs to be augmented with representations of the effects of gravity and capillary pressure.

Roman Berenblyum, PhD student at the Technical University of Denmark, was responsible for work on streamline simulation that also includes the effect of capillary crossflow. We were fortunate to have Roman visit with our research group for six months, and we are grateful to his research adviser, Professor Erling Stenby, for continuing fruitful collaboration.

We are very fortunate to work in a department with many talented students and faculty, and all of us are grateful to them for endless discussions of the research issues considered here. In particular, we thank Ruben Juanes and Hamdi Tchelepi for contributing their time and expertise in countless ways. David DiCarlo, now at the USDA/ARS National Sedimentation Laboratory, was an important participant in the early days of the project.

All of us in the gas injection research group are indebted to Thuy Nguyen for her quiet dedication to keeping us organized. She looked after the money, organized our annual project review meetings, and kept track of the reporting requirements for the project.

This work was supported primarily by DOE contract number DE-FC26-00BC15319. In addition, the member companies of the SUPRI-C Gas Injection Industrial Affiliates Program provided substantial support. Those sources of support are gratefully acknowledged.

Lynn Orr  
May, 2004

## Abstract

This final technical report describes and summarizes results of a research effort to investigate physical mechanisms that control the performance of gas injection processes in heterogeneous reservoirs and to represent those physical effects in an efficient way in simulations of gas injection processes. The research effort included four main lines of research:

1. Efficient compositional streamline methods for 3D flow
2. Analytical methods for one-dimensional displacements
3. Physics of multiphase flow
4. Limitations of streamline methods

In the first area, results are reported that show how the streamline simulation approach can be applied to simulation of gas injection processes that include significant effects of transfer of components between phases.

In the second area, the one-dimensional theory of multicomponent gas injection processes is extended to include the effects of volume change as components change phase. In addition an automatic algorithm for solving such problems is described.

In the third area, results on an extensive experimental investigation of three-phase flow are reported. The experimental results demonstrate the impact on displacement performance of the low interfacial tensions between the gas and oil phases that can arise in multicontact miscible or near-miscible displacement processes.

In the fourth area, the limitations of the streamline approach were explored. Results of an experimental investigation of the scaling of the interplay of viscous, capillary, and gravity forces are described. In addition results of a computational investigation of the limitations of the streamline approach are reported.

The results presented in this report establish that it is possible to use the compositional streamline approach in many reservoir settings to predict performance of gas injection processes. When that approach can be used, it requires substantially less (often orders of magnitude) computation time than conventional finite difference compositional simulation.

## Executive Summary

This report describes results of research to improve the accuracy of predictions of the performance of gas injection processes. Research was conducted in four areas:

1. Development of compositional streamline simulation methods for fast, accurate prediction of the performance of gas injection processes in heterogeneous reservoirs,
2. Analytical solutions for one-dimensional flow of multicomponent mixtures,
3. Experimental investigation of the fundamentals of three-phase flow applicable to gas injection process, in particular, the impact of low interfacial tensions between two phases in the presence of a third phase, and
4. Experimental and theoretical investigation of the limitations of streamline simulation methods, especially the effects of gravity segregation and capillary crossflow.

In Chapter 2, we demonstrate the use of one-dimensional (1D) analytical solutions for two-phase, multicomponent flow in combination with streamline simulations. While this approach is limited to problems in which initial and injection compositions are constant, the simulations require orders of magnitude less computation time than conventional finite difference simulations, and they are less subject to the adverse of numerical dispersion. For calculations that involve more general injection and initial conditions, we report results of a detailed investigation of the use of numerical solutions for the 1D flow problem along each streamline. Several higher order methods for solving this problem are evaluated. They show that it is possible to design numerical methods for the 1D solution along streamlines that are more accurate and more efficient than are conventional finite difference schemes. We also describe and demonstrate an operator splitting approach to allow handling of gravity segregation in compositional streamline simulations. We show that compositional streamline simulation can be used to investigate condensate vaporization processes, and we demonstrate that the approach is sufficiently computationally efficient that the uncertainties associated with permeability variations can be evaluated with multiple simulations. Finally we show that remapping of streamlines can be a significant source of error in streamline simulations, and we describe improved methods for mapping streamlines that reduce those errors.

In Chapter 3, we extend previous research to solve the general problem of automatic generation of 1D solutions to multicomponent two-phase flow including effects of volume change on mixing. We also demonstrate how to obtain analytical solutions for displacements in which two-phases are present initially in the porous medium, and we apply that technique to obtain analytical solutions for condensate displacements.

In Chapter 4, we report results of an extensive investigation of three-phase flow. In multicontact miscible or near-miscible displacements the interfacial tension (IFT) between the oil and gas phases can be low, while at the same time the IFT for the gas/water and oil/water pairs of phases remain much higher. We report phase compositions, phase densities and viscosities and interfacial tensions for two analogue oil/water/alcohol systems used to

examine the impact of low IFT on three-phase relative permeability. Results of extensive experiments in water-wet and oil-wet unconsolidated porous media and in Berea sandstone are reported. They show that reduction of IFT by about two orders of magnitude typically causes an increase in oil relative permeability of about an order of magnitude.

In Chapter 5, we report results of experiments to investigate the scaling of the interplay of viscous, gravity and capillary forces. Results of extensive flow visualization experiments in two-layer porous media in vertical, horizontal, and vertical cross-section orientations demonstrate the transitions from capillary-dominated to flow dominated by viscous or gravity forces. In addition, the limitations of the basic approach to streamline simulation are examined in two ways. First, the impact of the assumption made in constructing analytical solutions that phase behavior can be evaluated at a constant pressure is evaluated by comparing the analytical solutions with finite-difference compositional simulations. The results show that the evaluation of phase behavior at constant pressure is a surprisingly good assumption, which suggests that there are many applications where the use of analytical solutions in streamline simulations is reasonable. In addition, two-dimensional finite-difference simulations are compared with basic streamline simulations to determine the ranges of viscous, capillary, and gravity forces for which streamline simulation can be used without representation of capillary and gravity-driven crossflow, and when the more sophisticated forms of streamline simulation or other computational techniques are required.

The results presented in this report establish that it is possible to use the compositional streamline approach in many reservoir settings to predict flow performance with high resolution and high accuracy. In many of those physical situations, the streamline approach requires substantially less computation time than conventional compositional simulation approaches. The parallel experimental investigations also establish that low interfacial tensions that arise in near-miscible gas injection processes increase local relative permeability substantially over typical gas/oil relative permeabilities even when three phases are flowing. Finally, the analysis of scaling, confirmed by experiments, delineate when the streamline approach is appropriate and when it is not.

# Contents

<b>Disclaimer</b>	<b>iii</b>
<b>Acknowledgements</b>	<b>iv</b>
<b>Abstract</b>	<b>vi</b>
<b>Executive Summary</b>	<b>vii</b>
<b>Contents</b>	<b>ix</b>
<b>List of Tables</b>	<b>1</b>
<b>List of Figures</b>	<b>3</b>
<b>1 Introduction</b>	<b>11</b>
<b>2 Efficient Compositional Streamline Methods in 3D Flow</b>	<b>14</b>
<b>2.1 Analytical 1D solutions in compositional streamline simulation.....</b>	<b>14</b>
2.1.1 Mathematical model .....	15
2.1.2 Time of flight formulation and coordinate transformation.....	16
2.1.3 Tracing streamlines.....	17
2.1.4 Mapping 1D analytical solutions to streamlines.....	18
2.1.5 Streamline simulation using an analytical 1D solver .....	18
2.1.6 Simulation examples.....	19
2.1.6.1 Two-dimensional example.....	19
2.1.6.2 Three-Dimensional Example .....	22
2.1.7 Discussion and conclusions .....	23
<b>2.2 Numerical 1D solutions in compositional streamline simulation .....</b>	<b>24</b>
2.2.1 Motivation and overview .....	25
2.2.2 Governing equations.....	27
2.2.3 Analytical theory for multicomponent flow .....	29
2.2.4 First order scheme .....	31
2.2.5 High order finite difference schemes.....	33
2.2.5.1 Total variation diminishing schemes .....	34

2.2.5.2	Essentially non-oscillatory schemes .....	35
2.2.5.3	Weighted ENO schemes .....	35
2.2.6	Extension to multicomponent systems .....	35
2.2.7	High order time stepping .....	36
2.2.8	Results .....	36
2.2.8.1	Example 1: Vaporizing drive .....	37
2.2.8.2	Example 2: Condensing drive .....	37
2.2.8.3	Summary for constant K-values.....	39
2.2.8.4	Example 3: Vaporizing N <sub>2</sub> drive.....	40
2.2.8.5	Example 4: Near-miscible CO <sub>2</sub> flood .....	42
2.2.9	Efficiency and adaptive mesh refinement .....	44
2.2.10	Discussion.....	45
2.2.11	Conclusions .....	46
2.2.12	Appendix: Iteration for total velocity .....	46
<b>2.3</b>	<b>Gravity segregation and compositional simulation .....</b>	<b>47</b>
2.3.1	Introduction .....	47
2.3.2	Mathematical formulation .....	47
2.3.3	Solution along gravity lines.....	50
2.3.4	Calculation examples.....	53
2.3.4.1	1D Displacement calculation .....	54
2.3.4.2	2D Homogeneous displacement .....	55
2.3.4.3	2D Heterogeneous displacement.....	57
2.3.4.4	3D Quarter five spot.....	58
2.3.4.5	3D Five spot.....	60
2.3.5	Results and discussion.....	62
2.3.6	Conclusions .....	63
2.3.7	Nomenclature.....	63
<b>2.4</b>	<b>Streamline simulation of enhanced condensate recovery .....</b>	<b>64</b>
2.4.1	Dominant flow mechanisms in condensate reservoirs .....	66
2.4.1.1	Capillary crossflow .....	68
2.4.1.2	Gravity-driven crossflow .....	69

2.4.1.3	Viscous cross flow .....	69
2.4.1.4	Dispersion .....	70
2.4.2	Comparative simulation study .....	70
2.4.2.1	Reservoir system .....	71
2.4.2.2	Fluid description .....	73
2.4.2.3	1D Displacement calculation .....	74
2.4.2.4	2D Displacement calculation .....	76
2.4.2.5	3D Displacement calculation .....	79
2.4.2.6	Field scale displacement .....	82
2.4.2.7	Speed-up factors.....	85
2.4.3	Compositional streamline simulation and reservoir management.....	85
2.4.3.1	Ranking geological models.....	86
2.4.3.2	Uncertainty analysis on a dynamic reservoir model.....	89
2.4.4	Field Scale Fine Reservoir Description.....	92
2.4.5	Conclusions .....	94
2.4.6	Nomenclature.....	96
<b>2.5</b>	<b>Improved accuracy of compositional streamline simulation .....</b>	<b>96</b>
2.5.1	Introduction .....	96
2.5.2	Governing equations.....	98
2.5.3	Streamline method.....	99
2.5.4	Results with standard mappings .....	102
2.5.5	Improved streamline mappings .....	104
2.5.6	Improved mapping to streamlines .....	104
2.5.7	Improved mapping to the background grid .....	105
2.5.8	Results .....	107
2.5.9	Discussion.....	110
2.5.10	Conclusions .....	111
<b>2.6</b>	<b>Summary.....</b>	<b>112</b>
<b>3</b>	<b>Analytical Solutions for One-Dimensional Flow</b>	<b>113</b>
<b>3.1</b>	<b>Analytical solutions for multicomponent gas/oil displacements.....</b>	<b>113</b>
3.1.1	Solution construction.....	115

3.1.1.1	Shocks .....	115
3.1.1.2	Continuous variation (tie-line path and nontie-line path) .....	116
3.1.2	Analytical solutions for self-sharpening systems .....	119
3.1.3	Analytical solutions for general displacements .....	126
3.1.4	Discussion.....	128
3.1.5	Conclusions .....	129
<b>3.2</b>	<b>Analytical solutions for enhanced condensate recovery.....</b>	<b>129</b>
3.2.1	Solution construction for condensate displacements.....	130
3.2.1.1	Vaporizing drives.....	130
3.2.1.2	Development of miscibility in vaporizing drives.....	134
3.2.1.3	Combined condensing and vaporizing drives .....	135
3.2.2	Multicomponent displacements.....	138
3.2.3	Discussion.....	141
3.2.4	Conclusions .....	141
3.2.5	Nomenclature.....	142
<b>3.3</b>	<b>Additional analytical solutions .....</b>	<b>142</b>
<b>3.4</b>	<b>Summary.....</b>	<b>143</b>
<b>4</b>	<b>Physics and Chemistry of Multiphase Flow</b>	<b>144</b>
<b>4.1</b>	<b>Analogue three-phase systems .....</b>	<b>144</b>
4.1.1	Experimental procedures .....	145
4.1.2	Experimental results and interpretation.....	146
4.1.2.1	Compositional data .....	146
4.1.2.2	Computational model for compositional data.....	155
4.1.2.3	Analogy to reservoir fluids based on IFT data.....	156
4.1.3	Effect of IFT variation and wettability on three-phase relative permeability in unconsolidated media .....	160
4.1.4	Experimental approach .....	161
4.1.4.1	Analysis procedure.....	161
4.1.4.2	Porous medium .....	163
4.1.4.3	Fluids.....	165
4.1.4.4	Apparatus .....	166

4.1.4.5	Experimental procedure .....	168
4.1.5	Experimental results .....	171
4.1.5.1	Analogue water-wet porous medium (PTFE powder pack) .....	171
4.1.5.2	Artificial oil-wet porous medium (glass bead packs) .....	180
4.1.6	Discussion.....	186
4.1.7	Summary.....	188
4.1.8	Effect of IFT variation and wettability on three-phase relative permeability in berea sandstone .....	189
4.1.9	Experimental design .....	191
4.1.9.1	Porous medium .....	191
4.1.9.2	Fluids.....	191
4.1.9.3	Experimental set-up .....	192
4.1.10	Displacements with C <sub>16</sub> /NBA/H <sub>2</sub> O/IPA liquid system .....	193
4.1.11	Displacements with C <sub>16</sub> /NBA/H <sub>2</sub> O/NaCl liquid system .....	197
4.1.12	Results and discussion .....	201
4.1.13	Conclusions .....	207
<b>4.2</b>	<b>Summary.....</b>	<b>207</b>
<b>5</b>	<b>Limitations of Streamline Simulation</b>	<b>209</b>
<b>5.1</b>	<b>Crossflow effects in two-phase displacements.....</b>	<b>209</b>
5.1.1	Experimental approach .....	211
5.1.1.1	Apparatus .....	211
5.1.1.2	Fluid system .....	214
5.1.1.3	Experimental procedures .....	216
5.1.1.4	Homogeneity of the flow model .....	217
5.1.2	Experimental results .....	218
5.1.2.1	Scaling groups for flow regions in displacements .....	223
5.1.2.2	Favorable displacements .....	227
5.1.2.3	Unfavorable displacements.....	254
5.1.3	Discussion: Analysis of scaling groups .....	269
5.1.4	Conclusions .....	274
5.1.5	Nomenclature.....	275

<b>5.2</b>	<b>When is the streamline approach accurate? .....</b>	<b>275</b>
5.2.1	Crossflow mechanisms .....	279
5.2.2	Simulation model.....	281
5.2.3	Quantifying effects of numerical dispersion .....	285
5.2.4	Results .....	287
5.2.4.1	Capillary effects .....	287
5.2.4.2	Gravity effects.....	295
5.2.5	Conclusions .....	297
5.2.6	Nomenclature.....	297
<b>5.3</b>	<b>Including capillary effects in streamline simulation.....</b>	<b>298</b>
<b>5.4</b>	<b>Effects of pressure gradients on displacement performance for miscible/near miscible gas floods.....</b>	<b>299</b>
5.4.1	1D displacements.....	300
5.4.2	2D displacements.....	307
5.4.3	Conclusions .....	315
<b>5.5</b>	<b>Summary.....</b>	<b>315</b>
<b>6</b>	<b>Summary</b>	<b>317</b>
<b>7</b>	<b>References</b>	<b>320</b>

## List of Tables

Table 2-1: Parameters and component properties used in example 1.....	30
Table 2-2: Parameters and component properties used in example 2.....	39
Table 2-3: Parameters and component properties used in example 3.....	40
Table 2-4: Parameters and component properties used in example 4.....	42
Table 2-5: Binary interaction coefficients used in examples 3 and 4.....	43
Table 2-6: Fluid description used in calculation examples ( $T_{res} = 387.45$ K) .....	53
Table 2-7: Compositional description used for reservoir fluid characterization. ....	54
Table 2-8: Summary of CPU requirements in seconds (2.8 GHz) .....	62
Table 2-9: Parameters used to calculate expected $N_B$ in a typical condensate reservoir. ....	68
Table 2-10: Parameters used to calculate expected $N_{gv}$ in a typical condensate reservoir. ....	69
Table 2-11: Range of values of $(N_{gv}M)/(1+M)$ in a typical condensate reservoir. ....	70
Table 2-12: Parameters used to calculate expected $Pe$ in a typical condensate reservoir. ....	70
Table 2-13: Average reservoir properties of test reservoir. ....	71
Table 2-14: Variogram parameters used to generate permeability realizations. ....	72
Table 2-15: Average fluid composition. ....	73
Table 2-16: Properties of tuned fluid characterization. ....	74
Table 2-17: $Pe_{Num}$ for finite difference slimtube simulations. ....	75
Table 2-18: Dimensions of 2D displacement model.....	77
Table 2-19: Dimensions of 3D displacement model.....	79
Table 2-20: $Pe$ calculation for sector model displacement. ....	81
Table 2-21: Dimensions of field scale displacement model. ....	82
Table 2-22: Summary of speed up factors. ....	85
Table 2-23: Variogram parameters of geological ranking application. ....	86
Table 2-24: Summary of uncertainty analysis on well deliverability. ....	91
Table 2-25: Dimensions of field scale displacement model. ....	92
Table 3-1: Oil and injection gas compositions for the 15-component displacements. ....	124
Table 3-2: CPU requirements for analytical and numerical solutions for gas displacements.....	125
Table 3-3: Comparison of CPU (sec.) requirement for the MOC and FD approaches.....	128
Table 3-4: EOS parameter for the ternary displacement. All $K_{ij} = 0$ .....	130
Table 3-5: MOC solution for ternary displacement.....	133
Table 3-6: EOS parameter for the quaternary displacement.....	135
Table 3-7: MOC solution for quaternary displacement.....	137
Table 3-8: EOS parameter for the 13 component displacement. ....	138
Table 3-9: MOC solution for near-miscible 13 component displacement.....	139
Table 4-1: Three-phase compositional data for $C_{16}/NBA/H_2O/IPA$ system. ....	149
Table 4-2: Two-phase compositional data for the base ternary system shown in Fig. 4.1...150	
Table 4-3: Two-phase compositional data for $NBA/H_2O/IPA$ ternary system.....	151
Table 4-4: Two-phase compositional data for $C_{16}/H_2O/IPA$ system. ....	151
Table 4-5: Three-phase compositional data for $C_{16}/NBA/H_2O/NaCl$ system. ....	154
Table 4-6: Fluid characterization constants. ....	155
Table 4-7: Physical properties of the phases obtained from $C_{16}/NBA/H_2O/IPA$ system. ....	157
Table 4-8: Physical properties of the phases obtained from $C_{16}/NBA/H_2O/NaCl$ system. ...	159
Table 4-9: Correspondence of analog and reservoir phases. ....	164

Table 4-10: Contact angles of analog liquids in teflon and glass tubing. ....	164
Table 4-11: Core properties. ....	167
Table 4-12: Data for the displacement experiments in water-wet system ( $q_t = 1.5 \text{ cm}^3/\text{min}$ )	171
Table 4-13: Data for the displacement experiments in oil-wet system ( $q_t = 5.2 \text{ cm}^3/\text{min}$ ). ...	180
Table 4-14: Summary of three-phase flow experiments in consolidated porous media.....	190
Table 4-15: Core properties. ....	191
Table 4-16: Data for the displacement experiments in Berea core ( $q_t = 1.1 \text{ cm}^3/\text{min}$ ). ....	194
Table 4-17: Data for the displacement experiments with Berea core ( $q_t = 1.1 \text{ cm}^3/\text{min}$ ). ....	197
Table 4-18: Data for the displacement experiments in glass bead packs ( $q_t = 2.3 \text{ cm}^3/\text{min}$ ). ...	201
Table 5-1: Conditions for flow regions (Zhou <i>et al.</i> , 1994).....	210
Table 5-2: Physical properties of the phases.....	215
Table 5-3: Summary of the displacement experiments.....	216
Table 5-4: Summary of displacement experiments. ....	220
Table 5-5: Model parameters for experimental J-function data.....	222
Table 5-6 Simulation times (Example 1: 200x1x50).....	277
Table 5-7 Simulation time (Example 2: 200x1x50) .....	278
Table 5-8: Types of Crossflow .....	280
Table 5-9: Model parameters for calculation examples.....	281
Table 5-10: Fluid properties .....	283
Table 5-11: Simulator regions for unit mobility displacements .....	295
Table 5-12: Pressure solves required to reach convergence ( $N_{cv} = 0$ ) .....	295
Table 5-13: Oil and injection gas composition for 2D heterogeneous displacements.....	313

## List of Figures

Fig. 2.1: Total oil production (OPT) and gas to oil ratio (GOR) as a function of total gas injected (GIT). (1) E300, (2) analytical 1D solution (MOC) and streamlines (SL), (3) dispersed 1D numerical solution (FD100) + SL. ....	20
Fig. 2.2: Saturation distribution after 0.4PVI: (1) E300 (top), (2) MOC+SL (middle) and (3) FD100+SL (bottom). CPU requirements: E300 404 sec, 1D+SL: 5 sec. ....	21
Fig. 2.3: Total oil production (OPT) and gas to oil ratio (GOR) vs. total gas injected (GIT). (1) E300, (2) MOC+SL, (3) FD100+SL and (4) FD50+SL. ....	22
Fig. 2.4: 3D simulation. Saturation distribution after 200 days of injection: (a) E300 and (b) FD50+SL. CPU (2 PVI): E300 = 2083 min, 1D+SL = 2.55min. ....	23
Fig. 2.5: The analytical MOC solution is shown for a three-component vaporizing drive with constant equilibrium K-values, $K_1=2.50$ , $K_2=1.50$ , $K_3=0.05$ . ....	30
Fig. 2.6: Mole fraction profiles for the first two components and the composition path are shown for the SPU scheme with 200 grid cells. ....	32
Fig. 2.7: Results for the SPU scheme with 200 grid cells starting with the MOC solution as initial data. ....	33
Fig. 2.8: Mole fraction profiles, gas saturation profiles, and composition paths in phase space are given for the following schemes applied to example 1 with 200 grid cells: a) SPU, b) TVD-F, c) ENO-3, d) WENO-3, and e) WENO-5. ....	38
Fig. 2.9: A close view of the numerical composition paths near the equal eigenvalue point is given for the four high order schemes: a) TVD-F, b) ENO-3, c) WENO-3, d) WENO-5. ....	39
Fig. 2.10: Mole fraction profiles, gas saturation profiles, and composition paths in phase space are given for the following schemes applied to example 2 with 200 grid cells: a) SPU, b) TVD-F, c) ENO-3, d) WENO-3, and e) WENO-5. ....	41
Fig. 2.11: Mole fraction profiles and gas saturation profiles are given for SPU applied to example 3 with 200 grid cells. ....	42
Fig. 2.12: Mole fraction profiles and gas saturation profiles are given for ENO-3 applied to example 3 with 200 grid cells. ....	43
Fig. 2.13: Mole fraction profiles and gas saturation profiles are given for SPU applied to example 4 with 400 grid cells. ....	43
Fig. 2.14: Mole fraction profiles and gas saturation profiles are given for ENO-3 applied to example 4 with 400 grid cells. ....	44
Fig. 2.15: AMR results are shown using ENO-3 with 50 grid cells on the coarse grid and 200 grid cells on the fine grid. ....	45
Fig. 2.16: Path dependence of compositional flows. ....	50
Fig. 2.17: Pseudo-immiscible gravity segregation. ....	51
Fig. 2.18: 1D displacement. Recovery and gas-oil ratio predicted by CSLS and E300. ....	55
Fig. 2.19: Comparison of gas saturation distribution for 2D homogeneous and anisotropic displacements (100 days = 0.5 PVI and 200 days = 1.0 PVI) ....	56
Fig. 2.20: Oil recovery and gas-oil ratio for homogeneous displacement (E300 and CSLS). ....	56
Fig. 2.21: Permeability field, $\ln(K)$ , for 2D displacement. ....	57
Fig. 2.22: Gas saturation for 2D heterogeneous displacements (0.25 PVI and 0.5 PVI) ....	57
Fig. 2.23: Comparison of recovery and gas-oil ratio for heterogeneous 2D displacement. ....	58
Fig. 2.24: Gas saturation distribution for 3D heterogeneous quarter five-spot (0.3 PV). ....	59

Fig. 2.25: Comparison of recovery and gas-oil ratio for for 3D heterogeneous quarter five-spot.....	59
Fig. 2.26: Gas saturation after 100 days of injection (0.1 PVI).....	60
Fig. 2.27: Gas saturation after 200 days of injection (0.2 PVI).....	61
Fig. 2.28: Comparison of oil recovery and gas-oil ratio for five-spot simulation. ....	61
Fig. 2.29: Thermodynamic path followed by depletion of a condensate reservoir.....	67
Fig. 2.30: Test reservoir with well locations. Injectors indicated by red dots, producers indicated by open circles. ....	72
Fig. 2.31: Cross-section of the study reservoir. ....	72
Fig. 2.32: Comparison of tuned 13 component fluid description with laboratory CVD experiment. ....	74
Fig. 2.33 Analytical solution of condensate recovery with 100% CO <sub>2</sub> .....	75
Fig. 2.34: Mobility changes as fluids propagate through reservoir. ....	76
Fig. 2.35. Permeability field of 2D displacement. ....	77
Fig. 2.36: 2D displacement - Gas saturation after 2 PVI. ....	78
Fig. 2.37: Recovery and GOR predictions for 2D displacement simulations.....	79
Fig. 2.38. Permeability field and well locations for 3D sector displacement. ....	80
Fig. 2.39. Saturation distribution of areal slices of the 3D sector displacement after 2500 days injection. ....	81
Fig. 2.40. Recovery and GOR predictions for 3D displacement simulations.....	82
Fig. 2.41. Permeability field ( <i>mD</i> ) and well locations for field scale displacement. ....	83
Fig. 2.42. Saturation distribution of field scale displacement after 1.16 PV injection. ....	84
Fig. 2.43. Recovery and GOR predictions for field scale displacement simulations. ....	84
Fig. 2.44. Top layer permeability distributions in geological ranking application.....	87
Fig. 2.45. Base case S <sub>gas</sub> distribution through reservoir after 2 PVI.....	87
Fig. 2.46. Anisotropy case S <sub>gas</sub> distribution through reservoir after 2 PVI.....	88
Fig. 2.47. Correlation length case S <sub>gas</sub> distribution though reservoir after 2 PVI.....	88
Fig. 2.48. Recovery and GOR predictions from permeability cases used in geological ranking application. ....	89
Fig. 2.49. Range of predicted recoveries and GORs for 100 equiprobable sector model displacements.....	90
Fig. 2.50. Cumulative distribution function of predicted recovery for 100 equiprobable sector model displacements. ....	91
Fig. 2.51. Fine scale permeability distribution ( <i>mD</i> ) of field scale model. ....	92
Fig. 2.52. Saturation distributions after 1 PV injected for well placement scenarios of the fine scale geological model. ....	93
Fig. 2.53. Recovery and GOR predictions for well placement scenarios of the fine scale geological model.....	94
Fig. 2.54: The standard mapping to streamlines assumes a piecewise constant representation of saturations on the background grid (a). The resulting 1D profile along streamlines is also piecewise constant (b). ....	99
Fig. 2.55: Synthetic permeability field and streamlines used in our first example. The domain is square with unit length and 60 cells in each direction. Pressure at the left boundary is fixed at one and on the right is zero. No flow boundary conditions are imposed on the top and bottom. For simplicity the porosity is constant and equal to unity. ....	102

Fig. 2.56: Saturation fields computed using the standard mappings and (a) 1, (b) 5, (c) 10 and (d) 20 time steps. As the number of time steps is increased, the numerical smearing due to the mappings to and from streamlines also increases. ....	103
Fig. 2.57: Our improved mapping to streamlines utilizes a piecewise linear representation of saturations on the background grid (a). The resulting 1D profile along streamlines is also piecewise linear (b).....	105
Fig. 2.58: Kriging utilizes both the proximity of streamlines to the background grid cell (a) and the proximity between streamlines (b). Because both of these correlations (shown as dotted lines) are included, the Kriging weights are accurate when streamlines are clustered.....	106
Fig. 2.59: Saturation profiles shown were computed with 20 time steps using (a) improved mapping to streamlines and time-of-flight weighting to map to the background grid, and (b) improved mapping to streamlines and Kriging to map to the background grid.....	107
Fig. 2.60: (a) Permeability field used in our second example was taken from layer 9 of the SPE 10 model. (b) Approximately 150 streamlines were required to cover each cell with at least one streamline. Other parameters are used in this example are the same as in the previous example. ....	108
Fig. 2.61: Example 2 was run using 5 (top), 10 (middle) and 20 (bottom) global time steps. Saturation fields (a), (c) and (e) were found using the standard mappings to and from streamlines. The cases shown in (b), (d) and (f) were computed with our improved strategies for mapping saturations to and from streamlines. ....	108
Fig. 2.62: (a) Permeability field used in our final example was taken from layer 59 of the SPE 10 model. (b) Approximately 350 streamlines were required to cross each cell at least once. Other parameters are used in this example are the same as in the previous examples. ....	109
Fig. 2.63: The final example was also run with 5 (top), 10 (middle) and 20 (bottom) global time steps. Saturation fields (a), (c) and (e) were found with the standard mappings. The results shown in (b), (d) and (f) were computed with our improved mappings to and from streamlines. ....	111
Fig. 3.1: Variation of wave speed, saturation and total velocity along a non-tie line path....	119
Fig. 3.2: Saturation profiles for displacement of a five-component oil by CO <sub>2</sub> at 109 atm (1600 psia) and 344 K (160 F). ....	122
Fig. 3.3: Analytical and numerical solutions for a five-component oil at 0.7 pore volumes injected.....	122
Fig. 3.4: Saturation profile for a displacement of a near-miscible five-component oil by CO <sub>2</sub> at 161 atm and 344 K.....	123
Fig. 3.5: Effects of volume change in displacement of Oil 1 by Gas 1 at 275 atm and 387 K.....	123
Fig. 3.6: Comparison of numerical and analytical solutions with volume change for displacement of Oil 3 by a gas containing 75% CO <sub>2</sub> and 25% CH <sub>4</sub> at 275 atm and 368 K.....	124
Fig. 3.7: Comparison of recovery curves for the displacement of Oil 2 by pure N <sub>2</sub> at 387K generated by analytical calculations and numerical simulations.....	125
Fig. 3.8: Analytical solution and FD simulations for a quaternary displacement.....	127
Fig. 3.9: Comparison of analytical solutions and FD simulations for a 15 component system.....	128

Fig. 3.10: Phase envelope of a ternary $C_1/C_2/C_5$ mixture. Near-critical retrograde behavior is observed at 325 K. ....	131
Fig. 3.11: Displacement of 3 component condensate by pure $C_1$ at 325 K and 75 atm (MMP = $P_{dew} = 100$ atm) .....	131
Fig. 3.12: Displacement of 3 component condensate by pure $C_1$ at 325 K and 75 atm (MMP = $P_{dew} = 100$ atm) .....	132
Fig. 3.13: Semi-analytical and numerical (1000 grid blocks) solution profiles for the displacement of a 3 component condensate by pure $C_1$ at 75 atm and 325 K. ....	134
Fig. 3.14: Phase envelope of 4 component mixture. Near-critical behavior at 344 K.....	135
Fig. 3.15: Near-miscible displacement of 3 component condensate by pure $CO_2$ (4 components) at 344 K and 100 atm (MMP = 106 atm).....	136
Fig. 3.16: Semi-analytical and numerical (1000 grid blocks) solution profiles for the displacement of a 4 component condensate by pure $CO_2$ at 100 atm and 344 K	137
Fig. 3.17: Phase envelope of 13 component mixture. Near-critical retrograde behavior at 335 K .....	139
Fig. 3.18: Semi-analytical and numerical solution profiles for the displacement of a 13 component condensate by pure $CO_2$ at 90 atm and 335 K (MMP = 93 atm).....	140
Fig. 3.19: Semi-analytical and numerical solution profiles for the displacement of a 13 component condensate by pure $CO_2$ at 126 atm and 375 K (MMP = 128 atm)..	141
Fig. 4.1: Ternary phase diagram for the $C_{16}/NBA/H_2O$ system at ambient conditions. ....	146
Fig. 4.2: Quaternary phase diagram for the $C_{16}/NBA/H_2O$ /IPA system.....	147
Fig. 4.3: Phase compositions for mixtures of $C_{16}/NBA/H_2O$ /IPA system.....	148
Fig. 4.4: Quaternary phase diagram for the $C_{16}/NBA/H_2O/NaCl$ system.....	152
Fig. 4.5: Phase compositions for mixtures of $C_{16}/NBA/H_2O/NaCl$ system.....	153
Fig. 4.6: Soave-Redlich-Kwong+Association (CPA) model for 3-phase compositional data of $C_{16}/NBA/H_2O/IPA$ system. ....	156
Fig. 4.7: IFT variation of $C_{16}/NBA/H_2O/IPA$ quaternary system as a function of IPA concentration at the center of each tie triangle. ....	157
Fig. 4.8: IFT between oil, gas and brine phases as a function of pressure at reservoir conditions (T=82.2 °C) [Amin and Smith (1998)]. ....	158
Fig. 4.9: IFT variation of $C_{16}/NBA/H_2O/NaCl$ quaternary system as a function of NaCl concentration at the center of each tie triangle. ....	159
Fig. 4.10: Correlation between IFT and density difference. ....	160
Fig. 4.11: The Welge method for the determination of saturations at the end of core. ....	163
Fig. 4.12: The JBN method for the determination of the pressure gradient at the end of core.	163
Fig. 4.13: Coexistence of analog liquid phases of Mix. 1 (Table 4-1) in the teflon tubing. ....	165
Fig. 4.14: Coexistence of analog liquid phases of Mix. 1 (Table 4-1) in the glass capillary. ....	165
Fig. 4.15: Three-phase compositions used in the experiments. ....	166
Fig. 4.16: Experimental equipment for displacement experiments. ....	167
Fig. 4.17: Sample saturation path for three-phase displacement experiment in an artificial water-wet porous medium. ....	169
Fig. 4.18: Sample saturation path for dynamic displacement experiments in an artificial oil-wet porous medium.....	170
Fig. 4.19: Pore volume effluents as a function of pore volumes injected. (The IFT values in the legend box represent those between the NBA-rich “oil” and $H_2O$ -rich “gas” phases). ....	173

Fig. 4.20: Pressure drops as a function of pore volumes injected. (The IFT values in the legend box represent those between the NBA-rich “oil” and H <sub>2</sub> O-rich “gas” phases). .....	173
Fig. 4.21: Saturation paths for the displacement experiments. ....	174
Fig. 4.22: The NBA-rich “oil” recovery versus capillary number. ....	175
Fig. 4.23: Relative permeability of the C <sub>16</sub> -rich (W, “water”) phase as a function of its own saturation. ....	176
Fig. 4.24: Relative permeability of NBA-rich (IW, “oil”) phase as a function of its own saturation. ....	177
Fig. 4.25: Configuration of analog liquids on teflon surface. ....	178
Fig. 4.26: Relative permeability of H <sub>2</sub> O-rich (NW, “gas”) phase as a function of its own saturation. ....	178
Fig. 4.27: Relative permeability of NBA-rich (IW, “oil”) phase as a function of IFT. ....	179
Fig. 4.28: Relative permeability of H <sub>2</sub> O-rich (NW, “gas”) phase as a function of IFT. ....	179
Fig. 4.29: Schematic illustration of using analog liquid system in the experiments. ....	181
Fig. 4.30: Recovery plots for displaced phases. ....	182
Fig. 4.31: Differential pressure across the core. ....	183
Fig. 4.32: The C <sub>16</sub> -rich “water” relative permeability as a function of its own saturation. ..	184
Fig. 4.33: The H <sub>2</sub> O-rich “oil” relative permeability as a function of its own saturation. ....	185
Fig. 4.34: The NBA-rich “gas” relative permeability as a function of its own saturation. ....	185
Fig. 4.35: Summary of relative permeabilities for artificial “oil”-wet system. (S <sub>or</sub> = 0.1). NW: Non-wetting, IW: Intermediate wetting, W: Wetting. The IFTs in the legend box represent those between the NBA-rich and H <sub>2</sub> O-rich phases. ....	187
Fig. 4.36: Summary of relative permeability for artificial “water”-wet system (S <sub>wr</sub> = 0.615). ....	187
Fig. 4.37: Experimental set-up for displacements in consolidated porous medium. ....	192
Fig. 4.38: Saturation path for three-phase displacement experiment in a water-wet Berea sandstone core. ....	193
Fig. 4.39: Recovery and differential pressure data for horizontal displacements in “oil-wet” Berea sandstone core. (The C <sub>16</sub> /NBA/H <sub>2</sub> O/IPA analog liquid system was used.) ....	195
Fig. 4.40: Relative permeabilities determined from horizontal displacements performed in “oil-wet” Berea sandstone core. (The C <sub>16</sub> /NBA/H <sub>2</sub> O/IPA analog liquid system was used.) .....	196
Fig. 4.41: Recovery and differential pressure data for horizontal displacements performed in “water-wet” Berea sandstone core. (The C <sub>16</sub> /NBA/H <sub>2</sub> O/NaCl analog liquid system was used.) .....	198
Fig. 4.42: Relative permeabilities determined from horizontal displacements performed in “water-wet” Berea sandstone core. (The C <sub>16</sub> /NBA/H <sub>2</sub> O/NaCl analog liquid system was used.) .....	199
Fig. 4.43: Recovery and differential pressure data for gravity-stabilized displacements in water-wet” glass bead packs. (The C <sub>16</sub> /NBA/H <sub>2</sub> O/NaCl analog liquid system was used.) .....	202
Fig. 4.44: Relative permeabilities determined from gravity-stabilized displacements in “water-wet” glass bead packs. (The C <sub>16</sub> /NBA/H <sub>2</sub> O/NaCl analog liquid system was used.) .....	203
Fig. 4.45: Summary of relative permeabilities in “oil-wet” glass bead packs and Berea sandstone. (The C <sub>16</sub> /NBA/H <sub>2</sub> O/IPA analog liquid system was used. The numbers	

in the legend box represent the IFTs between the NBA-rich “gas” and H <sub>2</sub> O-rich “oil” phases.).....	204
Fig. 4.46: Summary of relative permeabilities in “water-wet” glass bead packs and Berea sandstone. (The C <sub>16</sub> /NBA/H <sub>2</sub> O/NaCl analog liquid system was used. The numbers in the legend box represent the IFTs between the NBA-rich “oil” and C <sub>16</sub> -rich “gas” phases.) .....	205
Fig. 4.47: Recovery of “oil” phase as a function of capillary number.....	206
Fig. 5.1: A schematic of the experimental setup.....	212
Fig. 5.2: Glass bead flow model for the experiments. $\phi = 39.5\%$ , Permeability ratio = 3.7. ....	213
Fig. 5.3: Orientation of glass bead models used in the experiments.....	214
Fig. 5.4: Schematic of fluid compositions used in the experiments. ....	215
Fig. 5.5: First contact miscible displacement of water by dyed water (M= 1). ....	218
Fig. 5.6: Correlation for J-function data using the van Genuchten model.....	219
Fig. 5.7: Capillary pressure data for the high-permeability and low-permeability layers derived from the <i>J</i> -function data presented in Fig. 5.6. ....	222
Fig. 5.8: Measured data of relative permeability for the simulation study. ....	223
Fig. 5.9: Flow regions in low-IFT vertical cross section (VCS) displacements. ....	224
Fig. 5.10: Flow regions in reduced gravity displacements (see Fig. 5.3a,b). ....	225
Fig. 5.11: Flow regions in terms of Bond number. ....	226
Fig. 5.12: Flow regions on the plot of gravity vs. capillary forces. ....	227
Fig. 5.13: Displacement profiles of high-IFT displacements with reduced gravity effects (Exps. #1, 3, and 7). ....	228
Fig. 5.14: Approximate pressure profiles along the porous system.....	230
Fig. 5.15: Comparison of experimental and simulation saturation profiles at PVI = 0.56. ....	231
Fig. 5.16: Production and pressure profiles (High IFT and reduced gravity effects). ....	232
Fig. 5.17: Experimental and simulation displacement profiles for Exp. #9. ....	233
Fig. 5.18: Production and pressure profiles for Exp. #9. ....	234
Fig. 5.19: Experimental and simulation saturation maps of high IFT displacements with gravity effects at PVI=0.49. ....	236
Fig. 5.20: Production and pressure profiles of high-IFT displacements with gravity effects. ....	237
Fig. 5.21: Experimental and simulation displacement profiles of high-IFT displacement with gravity effects. ....	238
Fig. 5.22: Production and pressure profiles of high-IFT displacements with gravity effects in long VCS models. ....	239
Fig. 5.23: Displacement profiles of low-IFT and reduced-gravity displacements (Exps. #2, 4, and 8). ....	241
Fig. 5.24: Eclipse100 runs with different values of density difference for a low-IFT vertical displacement. ....	242
Fig. 5.25: A schematic of pressure profiles in a low-IFT vertical displacement. ....	243
Fig. 5.26: Comparison of effects of capillary and viscous forces (Low-IFT and reduced gravity effects). ....	244
Fig. 5.27: Comparison of experimental and simulation saturation maps. ....	244
Fig. 5.28: Production and pressure profiles low-IFT vertical displacements. ....	246
Fig. 5.29: Simulation and experimental saturation maps for experiment #10. ....	247
Fig. 5.30: Production and pressure profiles for experiment #10.....	247
Fig. 5.31: Saturation profiles for low-IFT VCS displacements. ....	249

Fig. 5.32: Production and pressure profiles for low-IFT VCS displacements.....	251
Fig. 5.33: Saturation profiles for low IFT long VCS displacements. ....	252
Fig. 5.34: Production and pressure profiles for low-IFT long VCS displacements.....	253
Fig. 5.35: Saturation profiles for unfavorable vertical displacements. ....	254
Fig. 5.36: Numerical results of saturation profiles for unfavorable vertical displacements. ....	255
Fig. 5.37: Production and pressure profiles for unfavorable vertical displacements.....	256
Fig. 5.38: Saturation profiles for unfavorable horizontal displacements.....	257
Fig. 5.39: Numerical results of saturation profiles for unfavorable horizontal displacements.....	258
Fig. 5.40: Production and pressure profiles for unfavorable horizontal displacements.....	259
Fig. 5.41: Saturation profiles for unfavorable short VCS displacements. ....	261
Fig. 5.42: Numerical results of saturation profiles for unfavorable short VCS displacements.....	262
Fig. 5.43: Production and pressure profiles for unfavorable short VCS displacements. ....	263
Fig. 5.44: Saturation profiles for unfavorable, long, VCS, high-IFT displacements.....	264
Fig. 5.45: Numerical results of saturation profiles for unfavorable, long, VCS, high-IFT displacements.....	265
Fig. 5.46: Production and pressure profiles for unfavorable, long, VCS, high-IFT displacements.....	266
Fig. 5.47: Saturation profiles for unfavorable, long, VCS, low-IFT displacements.....	267
Fig. 5.48: Numerical results for Saturation profiles for unfavorable, long, VCS, low-IFT displacements.....	268
Fig. 5.49: Production and pressure profiles for unfavorable, long, VCS, low-IFT displacements.....	269
Fig. 5.50: Comparison of low IFT displacements at PVI=0.25 ( $q=2.2 \text{ cm}^3/\text{min}$ ). ....	270
Fig. 5.51: Comparison of high IFT displacements at PVI=0.46 ( $q=2.2 \text{ cm}^3/\text{min}$ ). ....	271
Fig. 5.52: Comparison of high IFT unfavorable displacements ( $q=2.2 \text{ cm}^3/\text{min}$ ). ....	272
Fig. 5.53: Comparison of low-IFT unfavorable displacements ( $q=2.2 \text{ cm}^3/\text{min}$ ). ....	273
Fig. 5.54: Saturation maps (Example 1) from <i>Eclipse</i> and <i>3DSL</i> .....	276
Fig. 5.55: Recovery curves (Example 1) from <i>Eclipse</i> and <i>3DSL</i> .....	277
Fig. 5.56: Saturation map (Example 2) from <i>Eclipse</i> and <i>3DSL</i> .....	278
Fig. 5.57: Recovery Curve (Example 2) from <i>Eclipse</i> and <i>3DSL</i> .....	278
Fig. 5.58: Cross Section of Streamlines.....	280
Fig. 5.59: 2D layered system.....	281
Fig. 5.60: Location of crossflow a) gravity dominated flow b) capillary dominated flow in a two-layer system.....	282
Fig. 5.61 Recovery curve for two fundamentally different displacements.....	283
Fig. 5.62: Saturation maps for case A and case B.....	284
Fig. 5.63: Saturation map showing displacement for increasing capillary number. $M = 1$ ...	285
Fig. 5.64: Saturation difference plot for $M = 1$ .....	286
Fig. 5.65 Recovery curves and recovery difference ( $N_{cv} = 0$ and $N_{gv} = 0$ ).....	286
Fig. 5.66: Saturation difference for $N_{cv} = 0$ at increasing pore volume injected.....	286
Fig. 5.67: Saturation maps for $N_{cv} = 1.5$ , $N_{gv} = 0$ , $M = 1$ .....	287
Fig. 5.68: Saturation difference for $N_{cv} = 1.5$ at increasing pore volume injected. ....	288
Fig. 5.69: Recovery curves/recovery difference for $N_{cv} = 1.5$ .....	288
Fig. 5.70: Saturation maps for $N_{cv} = 3$ , $N_{gv} = 0$ and $M = 1$ .....	289
Fig. 5.71: Saturation difference for $N_{cv} = 3$ at increasing pore volume injected. ....	289
Fig. 5.72: Recovery curves/recovery difference for $N_{cv} = 3$ .....	290

Fig. 5.73: Saturation maps for $N_{cv} = 15$ , $N_{gv} = 0$ , $M = 1$ .	290
Fig. 5.74: Saturation difference for $N_{cv} = 15$ at increasing pore volume injected.	291
Fig. 5.75: Recovery curves/recovery for $N_{cv}=15$ .	291
Fig. 5.76: Effects of mobility ratio on crossflow	292
Fig. 5.77: Differences in predicted saturation.....	293
Fig. 5.78: Recovery curves for different capillary effects. $M = 1$ .....	293
Fig. 5.79: Regions of capillary and mobility ratio for which streamline simulation approach should or should not be used. ....	294
Fig. 5.80: Saturation map for $N_{gv} = 27$ at 0.25 PVI .....	296
Fig. 5.81: Recovery curves for $N_{gv} = 27$ at 0.25 pore volume .....	296
Fig. 5.82: Water saturations predicted by E100 and modified streamline approach .....	299
Fig. 5.83: Pressure distribution in a hypothetical reservoir. ....	300
Fig. 5.84: Effect of pressure gradient on oil recovery in a multicontact miscible displacement. ....	301
Fig. 5.85: Pressure profile at different times in 1D displacements. ....	301
Fig. 5.86: Schematic for pressure distributions for step 3. ....	302
Fig. 5.87: Schematic for pressure distributions for step 4. ....	302
Fig. 5.88: Comparison of analytical solution with FD solutions for various total drops for Displacement-1 at 0.5 PVI.....	304
Fig. 5.89: Comparison of analytical solution with FD solutions for various total pressure drops for Displacement-2 at 0.5 PVI .....	304
Fig. 5.90: Comparison of analytical solution with FD solutions for various total drops for Displacement-1 at 0.55 PVI.....	306
Fig. 5.91: Comparison of analytical solution with FD solutions for various total pressure drops for Displacement-2 at 0.75 PVI .....	306
Fig. 5.92: Analytical solutions at 0.5 PVI for different pressures for the immiscible displacement .....	307
Fig. 5.93: Analytical solutions at 0.5 PVI for different pressures for the near-miscible displacement .....	307
Fig. 5.94: A two-layer system showing pressure variation with front location.....	309
Fig. 5.95: Saturation plots of a two-layer system for permeability contrast of 1.5 at 0.5 PVI. Injection pressure is 190 <i>bar</i> .....	309
Fig. 5.96: Saturation difference plots of a two-layer system for permeability contrast of 1.5 at 0.5 PVI showing crossflow and front advancement. ....	310
Fig. 5.97: Saturation plots of a two-layer system for permeability contrast of 5.0 at 0.5 PVI. Injection pressure is 190 <i>bar</i> .....	310
Fig. 5.98: Saturation plots of a two-layer system for permeability contrast of 5.0. Injection pressure is 190 <i>bar</i> .....	311
Fig. 5.99: Recovery curve of a two-layer system for permeability contrast of 1.5. Injection pressure is 190 <i>bar</i> .....	311
Fig. 5.100: Recovery curve of a two-layer system for permeability contrast of 1.5. Injection pressure is 190 <i>bar</i> .....	312
Fig. 5.101: Porosity and permeability field used in 2D heterogeneous displacements. ....	313
Fig. 5.102: Saturation plots of 10 component system at 0.5 pore volumes injected .....	314
Fig. 5.103: Saturation difference plots of 10-component system at 0.5 pore volumes injected.....	314
Fig. 5.104: Recovery curves for the 10-component system. Injection pressure is 330 <i>bar</i> .....	315

# 1 Introduction

It is now well established that injection of gases such as CO<sub>2</sub>, methane, enriched hydrocarbon gases or nitrogen into an oil reservoir can lead to efficient displacement of the reservoir oil if the displacement pressure is sufficiently high. In such processes, transfer of components from the injection gas mixture to the oil in place in the reservoir and from the oil to the flowing gas phase creates hydrocarbon mixtures that can displace the oil much more efficiently than does water in the portion of the reservoir that is swept by the injected gas. When injection pressures are sufficiently high, these component transfers between phases cause compositions in the transition zone between the injected gas and the displaced oil to pass close to a critical point. When that happens, the local displacement efficiency is high, and the local residual oil saturation is small. The high displacement efficiency that results is a consequence of the transfer of components between phases.

At field scale, local displacement efficiency is only part of the story, however. Injected gas will have lower viscosity than the oil being displaced, and the reservoir rocks that contain the oil will have a wide range of permeabilities. As a result, injected gas will flow preferentially through high permeability zones. It is the combination of local displacement efficiency, determined primarily by compositional phenomena, and sweep efficiency determined primarily by reservoir heterogeneity and gravity segregation, that controls overall process performance. Accurate prediction of process performance at field scale requires, therefore, that the combined effects of component transfers due to phase equilibrium and flow through heterogeneous reservoir rocks be represented adequately. Standard finite difference compositional simulation methods can do just that, of course. Permeability heterogeneity can be represented at the level of detail allowed by the number of grid blocks, and phase equilibrium calculations are performed for each grid block. Very large scale, three-dimensional compositional simulations are rarely attempted, however, for two reasons:

1. Computations with enough grid blocks to give a high-resolution representation of permeability heterogeneity require far too much computation time, and
2. Very large numbers of grid blocks are required to control adverse effects of numerical dispersion.

Computations with coarser grid resolutions are possible, but accuracy may be reduced significantly. If the effects of zones of low and high permeability are not represented accurately displacement efficiency is likely to be seriously in error because sweep efficiency is often determined by the extremes of permeability, not average quantities assigned to large grid blocks. In addition, the effects of numerical dispersion frequently reduce estimates of local displacement efficiency for flows that are above or near the minimum miscibility pressure. Thus, for field-scale computations, conventional finite-difference compositional simulations are usually not feasible. Thus, what is needed for accurate, three-dimensional, field-scale displacements is a very fast simulation method that allows both high resolution representation of heterogeneity and accurate calculation of the effects of phase equilibrium that are not adversely affected by numerical dispersion.

In this report we describe research to develop improved methods for predicting the performance of gas injection processes. The research includes several components:

- Study of analytical solutions for one-dimensional flow of two-phase, multicomponent mixtures,
- Development of fully compositional streamline methods for three-dimensional reservoir simulation
- Experimental investigation of the fundamentals of three-phase flow for gas injection processes, and
- Examination of the limitations of streamline methods.

In the chapters that follow, we describe in some detail the research conducted over the last three years. Chapter 2 of the report describes the effort to develop fully compositional streamline simulation techniques. There are two major parts to this work. The first part describes ways to solve the one-dimensional flow problem that applies along streamlines. We describe methods to obtain the solution analytically (for constant initial and injection compositions) and numerically. In particular, we examine the use of higher order methods to limit the numerical dispersion that arises in the commonly used finite difference approach to solving this problem. In addition, we demonstrate the use of those solution techniques in example simulations for heterogeneous reservoirs, including condensate vaporization. We also describe a method for including the effects of gravity in compositional streamline simulation.

In Chapter 3, we describe experimental work to investigate the fundamentals of three-phase flow in gas injection processes. When these processes are conducted at pressures high enough that the displacement is nearly multicontact miscible, the interfacial tensions between two of the three phases will be low. The experimental work conducted is based on the use of analogue oil-water-alcohol systems, chosen so that interfacial tensions could be controlled carefully to aid interpretation of the experiments. The measured properties of the three-phase systems are reported, and the results of three-phase relative permeability experiments are presented. In addition, results of a series of experiments to investigate the scaling of crossflow, which is not represented in streamline calculations are reported. These experiments help to reveal when it is and when it is not appropriate to use streamline methods for flow prediction.

Chapter 4 reports results of an analysis of the impact of crossflow, the transfer of material across streamlines. These effects are not represented in streamline methods, so it is important to delineate when it is appropriate to use streamline methods and when effects of crossflow are large enough that it is better to use another technique.

The results presented here suggest that in many situations, streamline methods can be used to conduct field-scale reservoir simulations for displacement processes that are

inherently compositional. In addition, it is clear that the streamline simulation approach is orders of magnitude faster than conventional finite-difference simulation approaches, and it is less subject to the numerical errors often referred to as numerical dispersion. The streamline approach, therefore, allows high resolution, field-scale computations for compositional gas injection processes that simply cannot be performed by other available methods. Thus, the results reported here describe significant new tools for simulation of the performance of gas injection processes.

## 2 Efficient Compositional Streamline Methods in 3D Flow

Streamline methods offer an approach that has the potential to satisfy the requirements of high-resolution representation of permeability variation along with representation of the combined effects of phase equilibrium and flow. In this approach, the effects of heterogeneity are captured by calculating the locations of streamlines or streamtubes (Batycky, 1997; Batycky *et al.*, 1996; Thiele *et al.*, 1995a, 1995b, 1996, 1997; Datta-Gupta and King, 1995), and the details of the compositional mechanisms are represented as one-dimensional solutions to the flow equations that are mapped along streamlines (Thiele *et al.* 1995b, 1997). In many flows, the positions of streamlines change slowly, and hence the streamlines need not be updated frequently. Streamline calculations for such flows can be orders of magnitude faster than the corresponding finite difference (FD) compositional simulations because the computationally expensive calculation of the pressure field (from which streamlines are determined) is performed relatively infrequently (in contrast with FD methods which do so each time step).

Most compositional streamline calculations performed to date have used numerical simulation for the solutions along individual streamlines. Use of analytical solutions for the 1D compositional flow problem has been limited by the fact that until recently solutions were available only for systems with a limited number of components (usually three or four) and by limitations on streamline updating. Jessen *et al.* (2001) demonstrated an algorithm with which analytical 1D solutions can be obtained for systems with an arbitrary number of components in the gas or the oil, though the systems considered were limited to those in which components do not change volume as they transfer between phases. The restriction on volume change has recently been relaxed allowing for general application of the analytical 1D solver to streamline simulation as outlined in the following sections.

### 2.1 Analytical 1D solutions in compositional streamline simulation

Performance evaluation of miscible and near-miscible gas injection processes can be assessed through conventional finite difference (FD) compositional simulation. However, low-resolution compositional simulation is adversely affected by numerical dispersion and may fail to represent geological heterogeneities adequately, and high-resolution simulation is too expensive in computation time. The number of components can be reduced but at the price of less accurate representation of phase behavior. Hence, the use of FD simulators in such studies is subject to limitations that can be quite significant in some field settings.

To close this gap, we propose a method combining the use of an analytical one-dimensional (1D) dispersion-free solution for multicomponent gas injection with a representation of flow along streamlines to capture the effects of heterogeneity. The 1D analytical solver allows any number of components to be present in the injected gas as well as in the reservoir fluid and includes the effects of volume change on mixing. The current work is based on a 3D field-scale streamline simulator (3DSL) developed at Stanford University<sup>1</sup>. 3DSL has been modified to use dispersion-free analytical 1D solutions to

propagate compositions along the streamlines. Simulation examples in 2D and 3D heterogeneous porous media are reported to demonstrate the potential speed-up of compositional simulation by the use of analytical solutions in combination with streamlines. We demonstrate that the CPU requirement is reduced by several orders of magnitude compared to conventional FD compositional simulation, even for problems with modest grid resolution.

### 2.1.1 Mathematical model

In this section we derive the equations that are required to trace streamlines in a 3D heterogeneous porous media. The conservation equations for multicomponent multiphase flow can be written in terms of molar compositions and densities as

$$\sum_{j=1}^{n_p} \frac{\partial}{\partial t} (\phi \rho_j x_{ij} S_j) + \nabla \cdot (\underline{u}_j \rho_j x_{ij}) = q_s \rho_j x_{ij} \quad , \quad i = 1, \dots, n_c \quad , \quad (2.1)$$

where  $\phi$  is the porosity,  $\rho_j$  is the molar density of phase  $j$ ,  $x_{ij}$  is the mole fraction of component  $i$  in phase  $j$ ,  $S_j$  is the volume fraction of phase  $j$ ,  $u_j$  is the velocity of phase  $j$  and  $q_s$  represents source/sink terms within the domain. The velocity of phase  $j$  can be expressed by Darcy's law

$$\underline{u}_j = -\underline{\underline{K}} \frac{k_{rj}}{\mu_j} \nabla P_j \quad , \quad \underline{u}_t = \sum_{j=1}^{n_p} \underline{u}_j \quad , \quad (2.2)$$

where  $u_t$  is the total velocity,  $K$  is the permeability tensor,  $k_{rj}$  is the relative permeability of phase  $j$ ,  $\mu_j$  is the viscosity of phase  $j$  and  $P_j$  is the pressure in phase  $j$ . In the examples discussed here we neglect the effects of compressibility and gravity for the purpose of solving for the pressure/velocity field. A summation over all components in Eq. (2.1) combined with the assumption that  $\rho_j$  remains constant leads to the governing volume balance equation for incompressible flow

$$\nabla \cdot \underline{u}_t = q_s \quad (2.3)$$

Neglecting capillary effects ( $P_i = P_j$ ) and introducing the total mobility  $\lambda_t$ , the velocity vector can be rewritten as

$$\underline{u}_t = -\underline{\underline{K}} (\lambda_t \nabla P) \quad (2.4)$$

with  $\lambda_t$  given by

$$\lambda_t = \sum_{j=1}^{n_p} \frac{k_{rj}}{\mu_j} \quad . \quad (2.5)$$

Substitution of Eq.(2.4) into Eq.(2.3) leads to the governing pressure equation for incompressible multicomponent multiphase flow in a porous medium

$$\nabla \cdot \underline{\underline{K}} (\lambda_t \nabla P) = -q_s \quad . \quad (2.6)$$

Eq. (2.6) can be solved by a standard finite difference approach as outlined by Batycky (1997) to obtain the pressure field. Given the pressure field, the face velocities of each gridblock can be evaluated. See Batycky (1997) for further details.

### 2.1.2 Time of flight formulation and coordinate transformation

The time of flight (Pollock, 1988; Datta-Gupta and King, 1995) is the time required for a particle to travel from a reference location (often taken at an injector) to a given location  $s$  along a streamline. The time of flight can be evaluated by the integral

$$\tau(s) = \int_0^s \frac{\phi(\zeta)}{|\underline{u}_t|} d\zeta \quad (2.7)$$

Eq. (2.7) allows the following coordinate transformation (Blunt *et al.* 1996)

$$|\underline{u}_t| \frac{\partial}{\partial s} = \underline{u}_t \cdot \nabla = \phi \frac{\partial}{\partial \tau} \quad (2.8)$$

The key idea behind streamline-based simulation is to decompose the 3D-flow problem into a sequence of 1D displacements along streamlines. To do that we need to transform the component conservation equation from Cartesian coordinates to the time of flight coordinate by the use of Eq. (2.8). Eq. (2.1)

can be rewritten in terms of the overall molar concentration ( $G_i$ ) and the overall molar flux ( $H_i$ ) of component  $i$

$$\phi \frac{\partial G_i}{\partial t} + \nabla \cdot (\underline{u}_t H_i) = 0, \quad i = 1, \dots, n_c \quad (2.9)$$

with

$$H_i = u_d \sum_{j=1}^{n_p} x_{ij} \rho_j f_j \quad G_i = \sum_{j=1}^{n_p} x_{ij} \rho_j S_j \quad (2.10)$$

where  $u_d$  is the dimensionless velocity scaled with respect to the injection velocity and  $f_j$  is the fractional flow of phase  $j$ . The second term on the left-hand side in Eq. (2.9) can be expanded to

$$\nabla \cdot (\underline{u}_t H_i) = \underline{u}_t \cdot \nabla H_i + H_i \nabla \cdot \underline{u}_t \quad (2.11)$$

Assuming that the effect of compressibility on the velocity field is negligible, the second term on the right-hand side of Eq. (2.11) drops out and Eq. (2.9) can be rewritten as

$$\phi \frac{\partial G_i}{\partial t} + \underline{u}_t \cdot \nabla H_i = 0, \quad i = 1, \dots, n_c \quad (2.12)$$

With application of the coordinate transformation outlined in Eq. (2.8), the final form of the conservation equations along a streamline is

$$\frac{\partial G_i}{\partial t} + \frac{\partial H_i}{\partial \tau} = 0, \quad i = 1, \dots, n_c. \quad (2.13)$$

Given constant initial and injection conditions the conservation equations of Eq. (2.13) constitutes a Riemann problem for which the solution is self-similar; the solution can be reported in terms of the dimensionless ratio of independent variables ( $\lambda_{sl} = \tau t$ ). Consequently, any self-similar 1D-displacement problem that can be mapped along streamlines to describe the flow of multiple components in a 3D heterogeneous porous media.

### 2.1.3 Tracing streamlines

Streamlines are curves in the domain of the porous media along which every point is tangent to the velocity field at a specific time (Bear, 1988). Hence, knowing the velocity field allows us to trace the streamlines along which to propagate analytical 1D solutions for any given multicomponent displacement problem. The approach for tracing streamlines in 3DSL use here is based on the work of Pollock (1988), assuming that the total velocity varies linearly within a given gridblock.

In 3DSL, streamlines are traced from injectors to producers taking advantage of the properties of an incompressible velocity field. A number of streamlines, specified by the user, are launched of the grid faces of the gridblocks containing an injector. A given streamline is traced forward from the injector by calculating the locations of entry and exit in the next gridblock, assuming linear variation of the velocity with in each gridblock. The increment in the time of flight is recorded by

$$\tau_{sl} = \tau_{sl} + \Delta \tau_i \quad (2.14)$$

where  $\Delta \tau_i$  is the incremental time of flight through gridblock  $i$ . This procedure is repeated until a producer is reached at which point  $\tau_{sl}$  is the time it would take a particle to travel from injector to producer along the given streamline, provided that the pressure field remains constant. Each gridblock must be assigned a time of flight for the purpose of mapping the 1D solutions on to the pressure grid as discussed in the following section. As several streamlines may pass through the same gridblock an averaging scheme must be introduced (Batycky, 1997):

$$\bar{\tau}_{block_i} = \frac{\sum_{i=1}^{n_{sl}} \Delta \tau_i \bar{\tau}_i}{\sum_{i=1}^{n_{sl}} \Delta \tau_i} \quad (2.15)$$

where

$$\bar{\tau}_i = \frac{\tau_{i,entry} + \tau_{i,exit}}{2} \quad (2.16)$$

### 2.1.4 Mapping 1D analytical solutions to streamlines

The mass conservation equations for multicomponent, dispersion-free two-phase flow in one dimension are written as

$$\frac{\partial G_i}{\partial \tau_a} + \frac{\partial H_i}{\partial \xi} = 0, \quad i = 1, \dots, n_c \quad (2.17)$$

with

$$\tau_a = \frac{u_{inj} t}{\phi L} \quad \xi = \frac{z}{L} \quad (2.18)$$

where  $u_{inj}$  is the injection velocity,  $t$  is the time,  $\phi$  is the porosity,  $L$  is the overall length of the porous medium and  $z$  is the distance from the inlet. Solutions to Eq. (2.17) are self-similar provided constant initial and injection conditions and are constructed by the method of characteristics (MOC). For the 1D problem, the self-similarity variable is given by

$$\lambda_{moc} = \frac{\xi}{\tau_a} = \frac{z\phi}{u_{inj} t} = \frac{\tau_{moc}}{t} \quad (2.19)$$

The analogy between the time of flight  $\tau$  along a streamline and the time required to reach a specific point in the 1D solution  $\tau_{moc}$  is evident. Hence, no additional transformations are necessary for mapping analytical 1D solutions along streamlines. The solution to Eq. (2.17) gives the variation of in overall composition and related properties such as saturation and total mobility as a function of the wave velocity  $\lambda_{moc}$ . Knowing the time of flight in a given gridblock allow us to assign an overall composition to that gridblock. In other words, if the time of flight in a gridblock equals 1 and the real time  $t$  equals 2, the gridblock is assigned the properties of the analytical solution corresponding to a wave velocity of 0.5.

### 2.1.5 Streamline simulation using an analytical 1D solver

As in any simulation, 3DSL starts of by assigning a total mobility to all active gridblocks, based on initial conditions of the porous media in question. The next step is to solve for the pressure field and subsequently evaluating the velocity field. Given the velocity field, a specified number of streamlines can be traced and the time of flight for each gridblock can be determined. In the current approach the analytical solution is then propagated along the streamlines from  $t = 0$  to  $t + \Delta t$  and each gridblock is assigned a new overall composition based on the weighting scheme

$$\bar{G}_j = \frac{\sum_{i=1}^{n_{sl}} \Delta \tau_i q_i G_j(\lambda_i)}{\sum_{i=1}^{n_{sl}} \Delta \tau_i q_i} \quad (2.20)$$

where  $q_i$  is the flux associated with streamline  $i$ .  $G_j(\lambda_i)$  is the overall molar concentration of component  $j$  corresponding to the value of the self-similarity variable  $\lambda_i$  ( $\tau/t$ ) in the specific

gridblock. The flux associated with a given streamline is evaluated by dividing the total flux from the gridblock face, where the streamline is launched, by the total number of streamlines launched from the block face.

As the injected gas invades the porous medium, the mobility distribution changes. The change in mobility distribution results in a varying pressure field and consequently causes the streamlines to change locations. Hence, it is necessary to update the pressure field periodically to account properly for mobility contrasts between the injected fluid and the reservoir fluid. However, in displacement problems where the flow is dominated by heterogeneities (preferential flow paths) the streamlines change only slightly over time reducing the number of pressure solves needed to predict the sweep properly. When a pressure solve is required, the updated overall gridblock compositions are used to evaluate the gridblock mobility, and the trace of streamlines and propagation of fluids along the streamlines are repeated for the next time step. An assumption of the current approach is that the time step from  $t$  to  $t+\Delta t$  can be approximated by a time step from  $t = 0$  to  $t+\Delta t$ . In the following section we demonstrate that this assumption results in good agreement between streamline simulations and conventional FD simulations, at least for the examples considered here.

### 2.1.6 Simulation examples

To demonstrate the combination of analytical 1D solutions with streamlines to evaluate displacement performance of miscible gas injection processes in a heterogeneous porous media we report two examples:

- 2D 100x10 gridblock areal displacement with horizontal wells.
- 3D 50x50x10 gridblock with vertical wells.

In the two examples, phase equilibrium calculations were performed using the Soave-Redlich-Kwong equation of state, whereas the phase viscosities were calculated by the LBC correlation, Lohrenz *et al.* (1964). Relative permeabilities were evaluated by simple quadratic Corey type expressions, with 0.2 residual oil saturation. In both scenarios, the reservoir fluid initially in place was represented by a 15 component mixture. A dry separator gas containing a total of 11 components (81 mole %  $\text{CH}_4$ ) was used to displace the oil. Details of the fluid and relative permeability functions are reported in Jessen *et al.* (2001) At the given reservoir temperature of 368K the minimum miscibility pressure (MMP) is predicted to  $\sim 365 \text{ atm}$ . (Jessen *et al.*, 2001)

#### 2.1.6.1 Two-dimensional example

In the first example we displace the oil by injecting gas at a fixed rate over the entire length of an areal slab. The initial pressure in the reservoir is fixed at  $365 \text{ atm}$  to ensure that the displacement is near the MMP. Oil is produced at the other end of the slab at a fixed bottom hole pressure of  $360 \text{ atm}$ . The displacement process was modeled by three different

approaches: (1) the finite difference based simulator Eclipse 300, (2) streamlines combined with a dispersion-free analytical 1D solution, and (3) by combining streamlines with a dispersed (100 gridblocks) numerical 1D solution. The predicted recoveries and gas to oil ratios are given in Fig. 2.1.

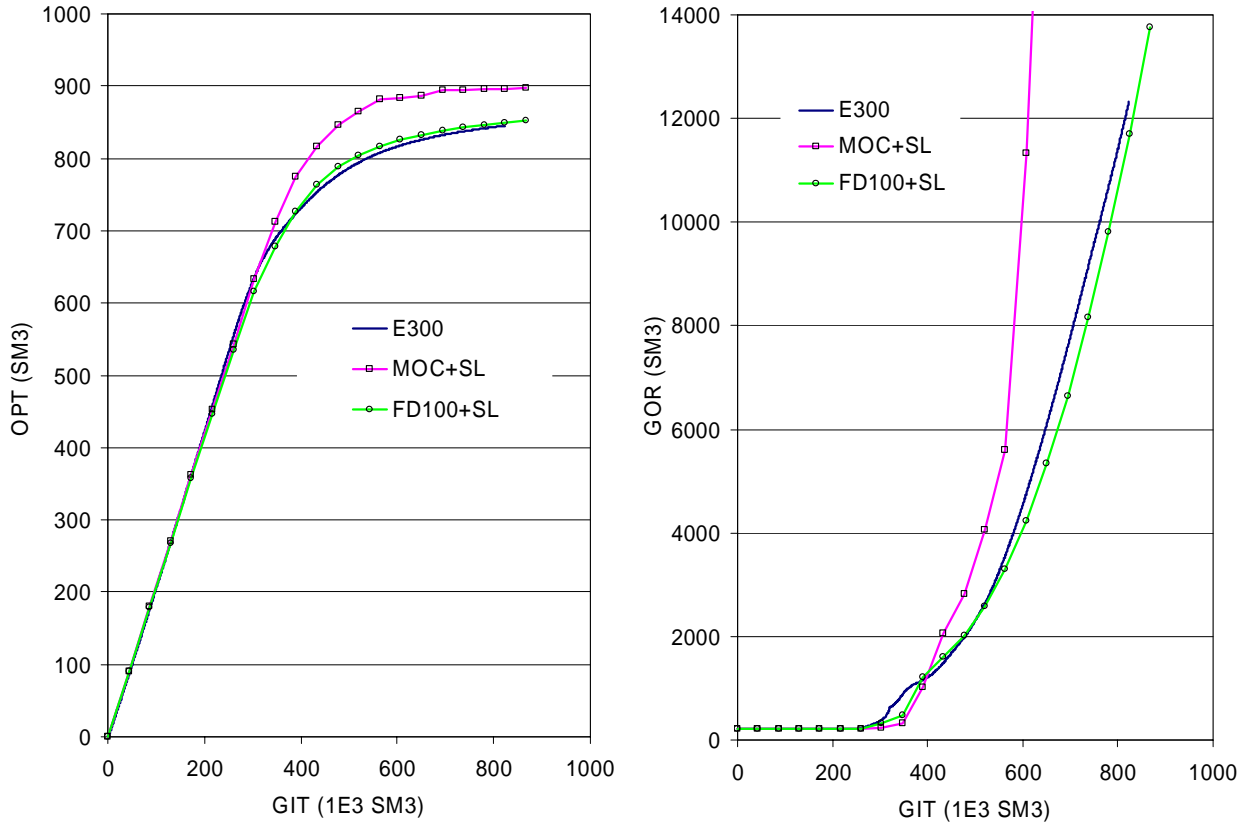


Fig. 2.1: Total oil production (OPT) and gas to oil ratio (GOR) as a function of total gas injected (GIT). (1) E300, (2) analytical 1D solution (MOC) and streamlines (SL), (3) dispersed 1D numerical solution (FD100) + SL.

Fig. 2.1 shows that the recovery predicted by E300 is slightly lower than the equivalent streamline simulation using a dispersion-free 1D solution, whereas the streamline simulation using a numerical 1D solution (dispersed) is in excellent agreement with E300. This is due to the effects of numerical dispersion in E300 (Jessen *et al.*, 2002). The effects of numerical dispersion are more clearly demonstrated in Fig. 2.2.

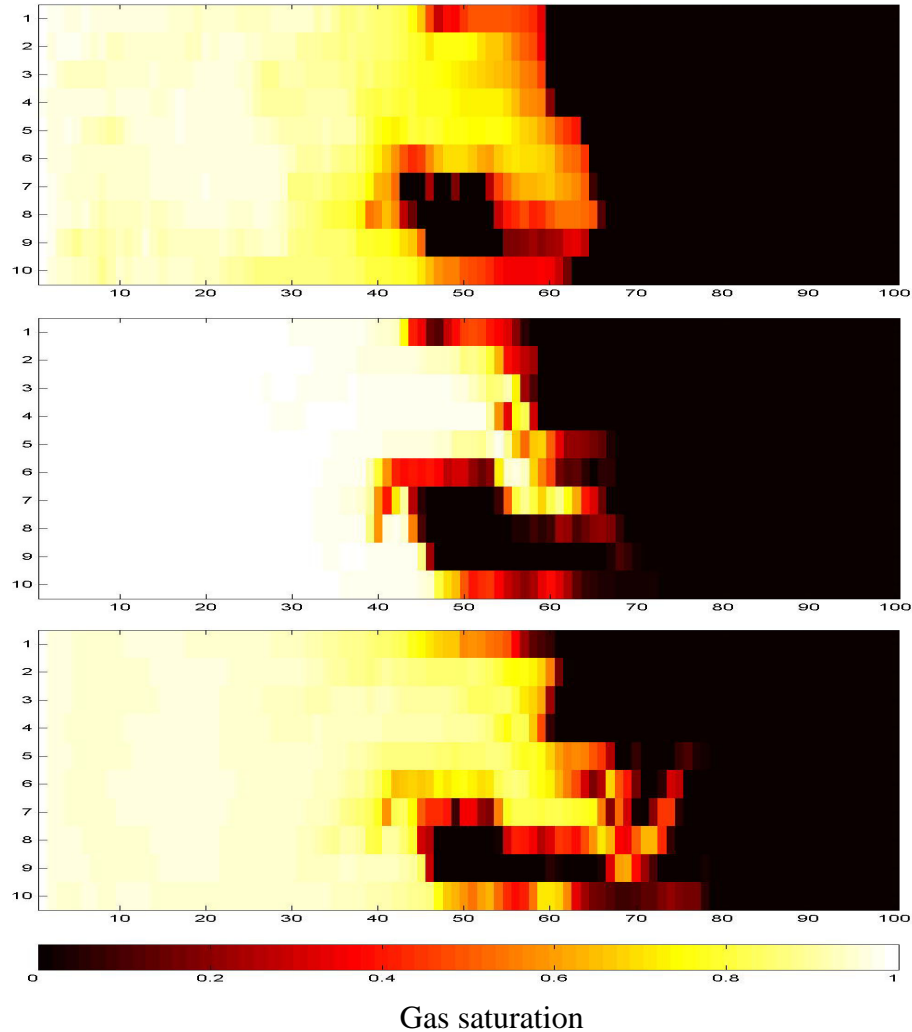


Fig. 2.2: Saturation distribution after 0.4PVI: (1) E300 (top), (2) MOC+SL (middle) and (3) FD100+SL (bottom). CPU requirements: E300 404 sec, 1D+SL: 5 sec.

Fig. 2.2 shows a snapshot of the displacement process in terms of the saturation distribution at  $t = 400$  days. Comparison of the saturation maps from the three simulations indicates that the FD simulation predicts lower local displacement efficiency of the miscible injection process. Numerical dispersion smears out the displacement front resulting in a later breakthrough and a better areal sweep, but with reduced local displacement efficiency in the swept zone. As we add dispersion in the 1D solution to be mapped along streamlines, the saturation distribution approaches more closely that of the E300 simulation. The areal sweep is slightly different, however, due to the fact that viscous cross-flow is not fully captured by the streamline approach (though in this case, at least some of the crossflow predicted by E300 is the result of numerical error). The CPU requirement for the FD and the SL approaches are very different. Using the approach streamline offers a speed-up of about 80, nearly two orders of magnitude, even for this small computational grid of 1000 grid blocks. Speed-ups for larger grids would be greater.

### 2.1.6.2 Three-Dimensional Example

In the second example we displace the reservoir fluid in a 3D formation corresponding to a quarter of a five spot pattern. The injector and producer are completed over the entire column of the formation. The initial reservoir pressure is fixed at 365 atm, and the gas is injected at a fixed rate of 0.001 PV/day. Oil is produced at a fixed bottom hole pressure of 360 atm. The version of the streamline code used for this example does not include gravity. Hence, for the purpose of testing the use of analytical 1D solutions with streamlines and for studying the effects of viscous cross-flow and numerical dispersion, we neglect gravitational forces. Total oil production and GOR predicted by E300 and SL simulation for this displacement process are shown in Fig. 2.3.

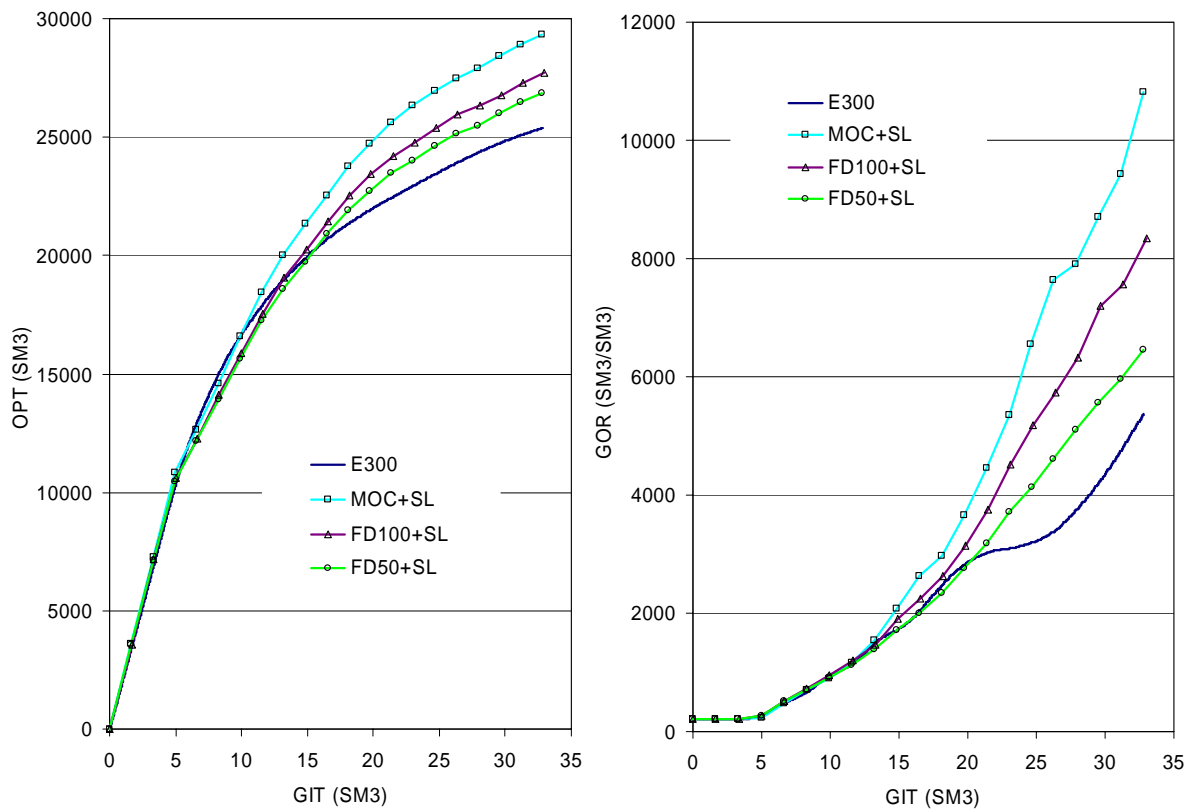


Fig. 2.3: Total oil production (OPT) and gas to oil ratio (GOR) vs. total gas injected (GIT). (1) E300, (2) MOC+SL, (3) FD100+SL and (4) FD50+SL.

The 3D-displacement process summarized in Fig. 2.3 shows behavior similar to the 2D example. The recovery of oil in place predicted by the E300 simulation is somewhat lower than what is predicted by the MOC+SL method, the result of the better local displacement efficiency in the streamline simulation. Again, as we add dispersion to the 1D solutions (FD100 = 100 and FD50 = 50 gridblocks) used in the SL simulations, the predicted oil production and GOR approaches more closely the result of the E300 simulation. Saturation distributions after 200 days of injection are shown in Fig. 2.4 for (a) streamline simulation

using a dispersed 1D solution (FD50) and (b) E300.

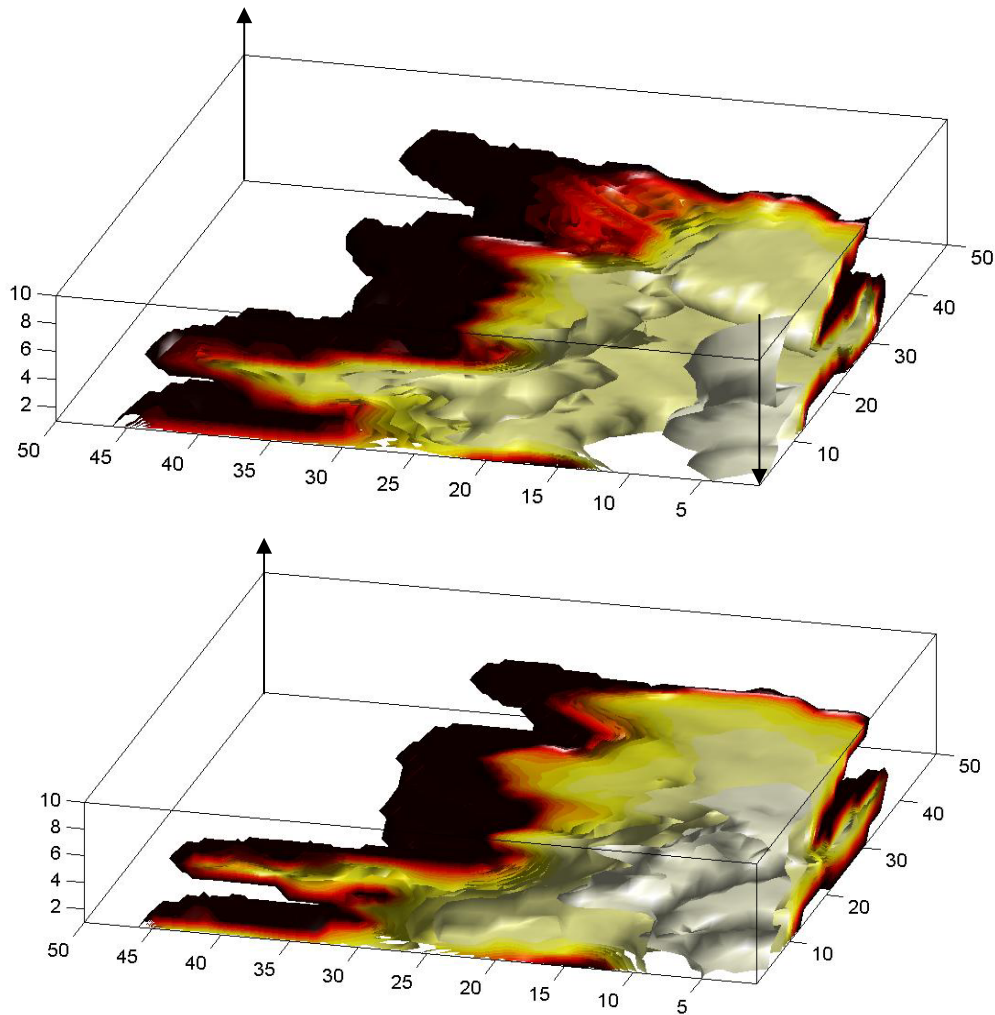


Fig. 2.4: 3D simulation. Saturation distribution after 200 days of injection: (a) E300 and (b) FD50+SL. CPU (2 PVI): E300 = 2083 min, 1D+SL = 2.55min.

Fig. 2.3 and Fig. 2.4 indicate that the numerical dispersion in E300 smears out the displacement front, resulting in a later breakthrough and lower GOR but ultimately in a lower overall recovery. The advantage of using streamlines for compositional simulation is more evident in this example. For this relatively small problem, compared to field scale, the speed-up is close to three orders of magnitude.

### 2.1.7 Discussion and conclusions

In the previous sections, results from combining analytical dispersion-free 1D solutions with streamline simulation have been presented. The major assumption of this work is that the

time step from  $t$  to  $t+\Delta t$  is approximated accurately by a time step from 0 to  $t+\Delta t$ . If the flow in a displacement process is not dominated by gravity, this assumption appears to be an excellent approximation. However, for displacements where gravity plays an important role and components move in directions not aligned with the streamlines, the assumption cannot be expected to provide accurate results. For gravity-dominated flow, the assumption of constant initial and injection conditions used to generate the analytical 1D solutions needs to be relaxed. For gas cycling in condensate fields the effects of gravity are less significant than for oil/gas problems, and the suggested approach is expected to produce accurate results at significantly reduced CPU time requirements.

The examples and analysis presented in this section establish that:

1. Dispersion-free 1D solutions to multicomponent gas injection problems generated by the method of characteristics can successfully be combined with streamline methods to predict the performance of a given multicomponent gas injection process.
2. For studies of displacement processes with low impact of gravitational forces the technology is now available for using compositional streamline simulation. Possible speed-ups of 2-3 orders of magnitude relative to conventional FD simulation are available, for small grids of 100 to 25,000 grid blocks. Larger speed-ups will be observed for larger grids.
3. Compositional streamline simulation using dispersion-free 1D solutions offers a limiting case solution to gas displacement processes. Conventional finite difference simulations offer another (dispersed) limiting case.

## **2.2 Numerical 1D solutions in compositional streamline simulation**

In section 2.1, gas injection was simulated by a streamline method using one-dimensional (1D) method-of characteristics (MOC) solutions along streamlines. Here we investigate a 1D finite difference solver that can also be used to propagate compositions along streamlines. Finite difference schemes improve the range of applicability of streamline simulation but are computationally more expensive and are subject to the errors that arise from numerical dispersion. Our focus here is on finding high order accurate finite difference schemes that are as efficient as possible.

MOC solutions provide fast, accurate representation of the interaction between phase behavior and two-phase flow for multicomponent displacements. The MOC-streamline method was shown to have good potential for predicting the performance of gas injection processes. This method, like other simulation techniques, has limitations. One important assumption required to apply the MOC theory is that compositions along streamlines are initially constant. While this assumption is often reasonable at time  $t = 0$ , it is not valid when streamlines are updated to account for changes in mobility or well status. To satisfy the assumption that initial conditions are constant, compositions must be mapped to the updated

streamlines at time  $t = 0$  rather than at the current time  $t_n$ . Compositions are then moved from time  $t = 0$  to time  $t_n + \Delta t$  along the new streamlines. Finite difference schemes are not limited by constant initial conditions. Compositions can be mapped to the new streamlines at time  $t_n$  and advanced to time  $t_n + \Delta t$ . The restarting of compositions at time  $t = 0$  when streamlines are updated is a potential source of error in the MOC streamline algorithm. The magnitude of the error is related to the difference in position between new and old streamlines. For flow systems that are dominated by heterogeneity, streamlines may move little, and the MOC streamline is reasonable. For systems dominated by other mechanisms such as gravity and changing well conditions, however, the approach is unlikely to be appropriate.

In this section, we investigate high order finite difference schemes for compositional simulation. Results presented for one-dimensional (1D) gas injection problems suggest that a third order, essentially non-oscillatory scheme is more accurate and efficient than first order methods and is more robust than traditional total variation diminishing schemes. We investigate also the use of adaptive mesh refinement (AMR) to further improve the efficiency of high order schemes. Preliminary results indicate that the savings in computation time with AMR can be significant for compositional problems. Our 1D results can be extended to three dimensions through conventional finite difference approaches but we are applying them in our compositional streamline simulator.

### 2.2.1 Motivation and overview

We consider high order upwind schemes for accurately and efficiently modeling two-phase, multicomponent flow. We investigate 1D gas injection problems to focus on the interplay of flow and phase behavior for multicomponent systems. Our goal is to determine methods that capture the effects of phase behavior by accurately propagating solution fronts in 1D. Our 1D results easily can be applied to 3D by conventional approaches or through the use of streamline methods. We plan to use streamline methods because the extension of our 1D schemes is straightforward and because streamline simulation combined with high order methods is a potentially efficient means of accurately modeling 3D gas injection processes. The transfer of components between gas and oil phases determines the displacement efficiency of gas injection processes. To model this transfer, compositional simulators perform flash calculations at each time step to determine the partitioning of components between phases. We seek high order schemes that capture the effects of phase behavior on flow with a minimum number of flash calculations. In particular, we seek schemes that accurately model multicontact miscible and near-miscible displacements. In such cases where phase behavior is strongly coupled to flow, first order methods fail to predict recovery accurately on practical grids. On finer grids, the computational cost due to flash calculations is prohibitively high for use in 3D simulations. We are interested in methods that perform well using coarse grids and fluid descriptions with enough components that phase behavior can be represented with good accuracy. We investigate also the use of adaptive mesh refinement (AMR) to further reduce the number of flash calculations performed and to offset the cost of including more components.

We begin in the next section by considering two-phase, three-component systems with

constant equilibrium K-values. We study these systems because they are the simplest systems that exhibit the essential features of multicomponent behavior (Johns and Orr, 1996). After analyzing the behavior of first and higher order schemes in this setting, we perform tests using a more complicated thermodynamic model and additional components. In all cases, we test our methods on Riemann problems for which analytical or semi-analytical reference solutions are available (Dindoruk, 1992; Wang, 1998). The reference solutions provide an ideal means to validate and analyze numerical schemes for two-phase flow.

High order schemes for the solution of hyperbolic conservation laws have been an active area of research for the past few decades. Many methods of increasingly high order have been proposed, particularly for solving the Euler equations of gas dynamics. Among the most popular are total variation diminishing schemes (TVD), essentially non-oscillatory schemes (ENO) and, more recently, weighted-ENO schemes (WENO). LeVeque (1992) and van Leer (1979) describe TVD schemes. Harten *et al.* (1987) introduced the ENO reconstruction that uses an adaptive stencil to achieve third and higher orders of accuracy. WENO schemes improve upon the order of a base ENO scheme by using all of the information in a given stencil (Jiang and Shu, 1996).

TVD methods have been used in the petroleum literature by several authors (Rubin and Blunt, 1991; Peddibhotla, 1997). Chen *et al.* (1991) used a TVD scheme and a third order ENO scheme to reduce grid orientation effects in two dimensions. The extension of high order methods to compositional problems is nontrivial due to the strong, nonlinear coupling of the advection equations, and also because multicomponent systems are only weakly hyperbolic. Thiele and Edwards (2001) applied TVD schemes to compositional simulation. Their results sparked our interest and began our investigation into the behavior of high order schemes for multicomponent problems. Our approach is similar to theirs, but we have tested a wider range of schemes and make use of reference solutions that have only recently been made available (Jessen, 2000; Ermakov, 2000). We focus initially on simpler systems to gain an understanding of multicomponent problems that motivates treatment of more complicated systems.

We have tested and analyzed several versions of TVD schemes, a third order ENO scheme, and third and fifth order WENO schemes. High order Runge-Kutta (RK) time integration is used in each case to equate temporal and spatial errors. In future work, we will optimize time stepping schemes. Our ENO and WENO schemes perform favorably compared to first order methods on a variety of Riemann problems that are strongly effected by phase behavior. Our third order ENO scheme is more robust than TVD schemes and maintains better accuracy than WENO schemes near points where the solution is weakly hyperbolic. For miscible and near miscible cases our ENO scheme offers significant improvement in solution quality versus first order, single point upstream schemes (SPU). High order schemes allow for much coarser grids than the SPU scheme and hence require fewer flash calculations to produce accurate solutions. The computational time saved on flash calculations outweighs the costs associated with higher order, especially when high order schemes are used in conjunction with AMR.

Three-dimensional (3D) gas injection is a challenging compositional problem because the

flow is dominated by phase behavior, reservoir heterogeneity, gravity and compressibility. Streamline methods can efficiently model flow through heterogeneous reservoirs (Thiele *et al.*, 1997; King, 1998). Bratvedt *et al.* (1996) provided an extension to include gravity in the streamline algorithm by means of operator splitting. Their operator splitting technique is well-established and well-tested (Batycky *et al.*, 1996). Compressibility has only recently been modeled in a streamline context and continues to be an area of active research (Ingebrigtsen *et al.*, 1999; Datta-Gupta *et al.*, 2001). We focus here on the interaction of phase behavior and incompressible flow. We anticipate that high order schemes will improve our ability to predict the local sweep efficiency of gas injection processes in 3D.

## 2.2.2 Governing equations

The hyperbolic conservation equations for multiphase, multicomponent flow in 1D can be written in the vector form,

$$\frac{\partial C}{\partial \tau} + \frac{\partial(v_D F)}{\partial \xi} = 0. \quad (2.21)$$

Here the molar concentrations of each component are given by the entries of the vector  $C$  and the molar flux is given by the vector  $F$ . The jacobian matrix  $\frac{\partial F}{\partial C}$  has real, possibly repeated eigenvalues so Eq. (2.21) is not strictly hyperbolic. The eigenvectors associated with repeated eigenvalues are dependent, hence multicomponent systems can be further classified as weakly hyperbolic. The dimensionless temporal and spatial variables are given by  $\tau = \frac{vt}{\phi L}$  and  $\xi = \frac{z}{L}$  is the total flow velocity,  $t$  is the time,  $\phi$  is the porosity of the porous media,  $L$  is the length of the porous media and  $a$  is the distance from the inlet. Injection takes place at  $\xi = 0$ . The dimensionless time  $\tau$  is measured in pore volumes injected. We assume for now that the total flow velocity and the porosity are constant. For two-phase flow, the overall concentrations are given by,

$$C_i = y_i \rho_g S + x_i \rho_o (1 - S), \quad i = 1, \dots, n_c. \quad (2.22)$$

The mole fractions of component  $i$  in the gas and oil phases are denoted by  $y_i$  and  $x_i$ , respectively, and  $n_c$  is the number of components. We list the components in order of ascending molecular weight. The phase molar densities are given by  $\rho_{g,o}$  and  $0 < S < 1$  is the volumetric saturation of the gas phase. We will also make use of the overall mole fraction,

$$z_i = \frac{C_i}{\sum_{n=1}^{n_c} C_n}, \quad i = 1, \dots, n_c. \quad (2.23)$$

Either  $C$  or  $z$  can be used to specify the composition of a mixture and the phase compositions are determined by  $x$  and  $y$ . The molar flux of the components is given by,

$$F_i = y_i \rho_g f(S) + x_i \rho_o (1 - f(S)), \quad i = 1, \dots, n_c. \quad (2.24)$$

Ignoring gravity, the fractional flow of the gas phase is determined by the relative

permeabilities and viscosities of the phases as,

$$f(S) = \frac{k_{rg}(S)}{k_{rg}(S) + \frac{\mu_g}{\mu_o} k_{ro}(S)} \quad (2.25)$$

We use quadratic relative permeability curves  $k_{rg} = S^2$  and  $k_{ro} = (I - S - S_{or})^2$ . The residual oil saturation  $S_{or}$  is constant in all of our tests. For our initial tests we use a fixed viscosity ratio  $\mu_g/\mu_o$  and for more realistic tests we calculate viscosity using the LBC correlation (Lohrenz *et al.*, 1964).

From Eqs. (2.24) and (2.25) it is clear that the flux of components does not depend directly on the composition of a mixture but rather on the composition of the phases and their properties. This is intuitive since components are only carried along by flowing phases. When only one phase is present, Eq. (2.21) reduces to an uncoupled system of linear advection equations. When two phases form, the composition and properties of the phases must be determined in order to compute the flux. A mixture forms distinct phases in order to achieve local chemical equilibrium. We assume that chemical equilibrium is achieved instantaneously due to the slow rate of flow through porous media. Information about the partitioning of components between phases is frequently expressed in terms of equilibrium ratios also known as K-values,

$$K_i = \frac{y_i}{x_i}, \quad i = 1, \dots, n_c. \quad (2.26)$$

Let  $\beta$  be the molar fraction of an overall composition in the gas phase. A mass balance for each component gives

$$z_i = y_i \beta + x_i (1 - \beta), \quad i = 1, \dots, n_c. \quad (2.27)$$

From Eqs. (2.26) and (2.27) expressions can be written for the mole fractions of the phases,

$$x_i = \frac{z_i}{1 + \beta(K_i - 1)} \quad \text{and} \quad y_i = \frac{K_i z_i}{1 + \beta(K_i - 1)}, \quad i = 1, \dots, n_c. \quad (2.28)$$

Since mole fractions sum to unity,

$$0 = \sum_{i=1}^{n_c} y_i - \sum_{i=1}^{n_c} x_i = \sum_{i=1}^{n_c} \frac{z_i (K_i - 1)}{1 + \beta(K_i - 1)}. \quad (2.29)$$

Given the K-values for a mixture,  $\beta$  can be found from Eq. (2.29) by a scalar Newton-Raphson iteration and the phase mole fractions are given by Eq. (2.28). The phase densities are specified by an equation of state (EOS). Finally, the saturation is given by,

$$S = \frac{\beta}{\beta + \frac{\rho_g}{\rho_o} (1 - \beta)}. \quad (2.30)$$

We will focus on ternary systems initially. To further simplify our initial tests, we will

assume that ideal mixing occurs so that K-values are constant for an entire displacement. At low pressures and temperatures this assumption is reasonable because K-values depend only weakly on composition. In this case the partial molar volume occupied by a component does not depend on composition or phase. Hence,  $S = \beta$  and Eq. (2.21) can be rewritten as a conservation of volume with volume fractions as the primary variables. Since volume fractions sum to unity, only  $n_c - 1$  conservation equations are independent in this case. Fixing the K-values for a displacement completely specifies the thermodynamic behavior of the system. For real multicomponent systems at typical reservoir pressures and temperatures, the K-values depend strongly on composition. The constraints that the K-values satisfy local chemical equilibrium together with Eq. (2.29) and an EOS form a nonlinear system of  $n_c+1$  equations. This system can be solved by estimating the K-values, determining the composition of the phases as described above and iterating on the K-values until convergence is reached. Although convergence can be obtained even for poor initial guesses, the convergence is typically slow. Newton-type iterations can be used to improve the convergence rate. Algorithms that solve this nonlinear system for the partitioning of components into phases are known as flash routines. The flash that we use was developed and described by Michelsen (1998) and incorporates the Peng-Robinson equation of state (Peng and Robinson, 1976).

### 2.2.3 Analytical theory for multicomponent flow

The problem of solving Eq. (2.21) with constant initial and injection conditions is known as a Riemann problem and can be solved by the method of characteristics (MOC). Dindoruk and Wang first obtained MOC solutions to the Riemann problem using constant equilibrium K-values for three- and four-component systems (Dindoruk, 1992; Johns and Orr, 1996). Semi-analytic MOC solutions with arbitrary numbers of components were made available by Jessen (2000). The semi-analytical approach allows phase behavior to be governed by more complex equations of state. Recently, volume change on mixing has been included in the general case (Jessen, 2000; Ermakov, 2000).

Like the Buckley-Leverett solution, solutions to compositional problems consist of segments of shocks and rarefactions. The number of segments increases with the number of components. A solution to a compositional problem can be viewed as a set of profiles and as a single composition path in phase space. Fig. 2.5 gives two MOC solution profiles and the MOC compositional path for a three-component vaporizing drive. The details of this test problem are listed in Table 2-1

The MOC solution for Eq. (2.21) is found by transforming the hyperbolic conservation equations into an eigenvalue problem. The eigenvectors correspond to candidate directions in phase space along which the composition path may vary. The correct composition path is determined by requiring that the path satisfy certain physical rules (Helferich, 1981). The eigenvalues along the path give propagation speeds with which the solution profiles move forward in time. Although phase space does not explicitly show the time dependence of the solution, it lends insight into the behavior of the system that cannot be determined by examining profiles alone. We analyze our high order schemes by comparing both numerical

profiles and composition paths to reference solutions.

Table 2-1: Parameters and component properties used in example 1

	$C_1$	$C_2$	$C_3$
Injection mole fraction	0.90	0.10	0.00
Initial mole fraction	0.00	0.25	0.75
Equilibrium K-values	2.50	1.50	0.05
Residual oil saturation	0.00		
Viscosity ratio, $\mu_g/\mu_o$	1/5		
Pore volumes injected	2/3		
$CFL/V_{max}$	2/5		

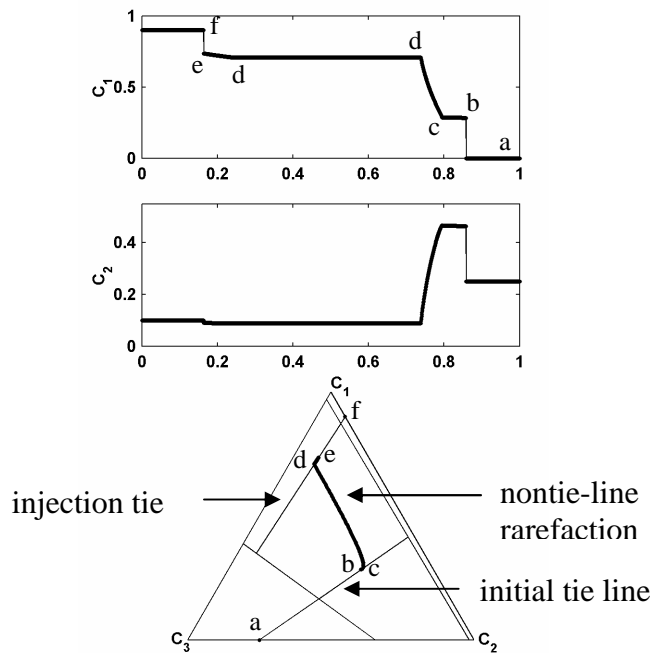


Fig. 2.5: The analytical MOC solution is shown for a three-component vaporizing drive with constant equilibrium K-values,  $K_1=2.50$ ,  $K_2=1.50$ ,  $K_3=0.05$ .

In the example given in Fig. 2.5 the analytical MOC solution is shown for a three-component vaporizing drive with constant equilibrium K-values,  $K_1=2.50$ ,  $K_2=1.50$ ,  $K_3=0.05$ . It illustrates important features of compositional problems. The dew and bubble point curves of the system are drawn as well as two key tie lines that extend through the initial composition (a) and the injection composition (f). Transitions from the single-phase regions to the two-phase region occur as shocks (ab and ef) along extensions of the initial and injection tie lines. We refer to these shocks as the leading and trailing shocks due to their propagation speeds. In the interior of the two-phase region, the solution consists of short rarefactions along the key tie lines (TL), a nontie-line (NT) rarefaction connecting the key tie lines, and a zone of constant state that appears as a single point (d) in phase space.

Depending on the orientation of key tie lines, the NT path may consist of either a shock or a rarefaction. The TL rarefactions need not be present for every solution. The transition point between the initial TL rarefaction and the NT rarefaction is known as the equal eigenvalue point (c). At this point, the propagation speeds of both rarefactions are equal. See Helfferich (1981) and Dumore *et al.* (1984) for a more comprehensive description of three-component theory. Multicomponent systems (Eq. (2.21)) are weakly hyperbolic because the eigenvectors associated with equal eigenvalue points are not independent.

When the number of components in a system increases, the number of key tie lines increases correspondingly. Each additional key tie line introduces an additional NT path, zone of constant state, and possibly a TL rarefaction. The length of the shortest key tie line determines the displacement efficiency of a drive. When all of the TL lengths are long, the propagation speeds vary greatly along the solution path and the displacement is inefficient. If one of the key tie lines is short, the displacement is more efficient. In the limit that one tie line has length zero, miscibility develops and optimal, piston-like displacement is achieved (Orr *et al.*, 1993; Wang and Orr, 1997; Jessen *et al.*, 1998).

#### 2.2.4 First order scheme

MOC solutions provide fast and accurate solutions to one-dimensional gas injection problems when the initial and injection compositions are constant. In many practical settings these compositions are not uniform and finite difference methods provide an alternative solution method. The conservative finite difference form of Eq. (2.21) is given by,

$$C_k^{n+1} = C_k^n - \frac{\Delta\tau}{\Delta\xi} \left[ v_{k+1/2}^{n+1} F_{k+1/2}^n - v_{k-1/2}^{n+1} F_{k-1/2}^n \right] \quad (2.31)$$

$C_k$  is vector containing total moles of each component in the discrete cell  $k$ . The total flux of components between cells  $k$  and  $k+1$  is given by the total dimensionless velocity  $v_{k+1/2}$  times the flux vector  $F_{k+1/2}$ . Since  $C_k^{n+1}$  in Eq. (2.31) depends implicitly on velocity, the velocity must be determined by iteration as described in the appendix. As mentioned previously, in the constant K-value case  $v_{k+1/2}$  is equal to unity for all  $k$  and no iteration is necessary. For the first order method we reconstruct the flux at a cell face by constant interpolation of the upwind, cell-centered flux:

$$v_{k+1/2}^{n+1} F_{k+1/2}^n = v_k^{n+1} F_k^n \quad (2.32)$$

Combining Eqs. (2.31) and (2.32) for the constant K-value case gives the familiar single point upstream (SPU) finite difference form:

$$C_k^{n+1} = C_k^n - \frac{\Delta\tau}{\Delta\xi} \left[ F_k^n - F_{k-1}^n \right] \quad (2.33)$$

We assume that the cell width  $\Delta\xi$  is uniform and choose a stable time step  $\Delta\tau$  according to the relation

$$\Delta\tau = CFL \cdot \frac{\Delta\xi}{(v \cdot \lambda)_{max}} \quad (2.34)$$

$(v \cdot \lambda)_{max}$  is a maximum propagation speed for a displacement and must be chosen to take into account the total flow velocity,  $v$ , as well as the eigenvalues,  $\lambda_i$ , of the Jacobian of (1).  $0 < CFL < 1$  is the Courant-Friedrichs-Lewy number. For single phase flow, each of the eigenvalues is equal to unity. In practice, for two-phase flow we chose the time step size by finding an upper bound for a single eigenvalue  $\lambda_{TL} = \frac{df}{ds}$  corresponding to an eigenvector that is aligned with the tie line for a two-phase composition. The bound can be obtained by calculating the first derivative of the fractional flow over a range of viscosity ratios that could occur in a displacement. For problems involving more than two components it is in general not sufficient to use only the viscosity ratio of the injected gas to the initial oil in place. The tie-line eigenvalue is not the largest eigenvalue for all compositions in the two-phase region, but a bound on the tie-line eigenvalue is sufficient for the other  $n_c-1$  eigenvalues as well.

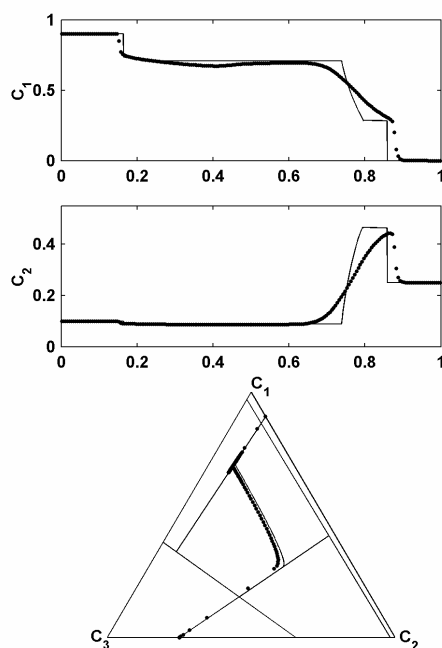


Fig. 2.6: Mole fraction profiles for the first two components and the composition path are shown for the SPU scheme with 200 grid cells.

Fig. 2.6 gives the results of applying Eq. (2.33) to the vaporizing drive illustrated in Fig. 2.5. The first order scheme produces second order truncation errors that mimic excessive amounts of physical diffusion or dispersion. This numerical dispersion pulls the composition path away from the MOC path and towards the line that connects the initial and injection compositions (Jessen *et al.*, 2002). The error in predicting the leading shock speed is due, in part, to the discrepancy between numerical and MOC solutions in phase space. The eigenvalues along the numerical composition path predict that the displacement will be less efficient than the true displacement. The locations of the leading and trailing shocks confirm that this is in fact the case. In a sense, the SPU method captures the correct speed to the wrong shock rather than vice versa.

Along the injection tie line there are errors near the zone of constant state. These errors consist of oil that is left behind due to an underestimation of the displacement efficiency of the leading shock. There is no physical mechanism to remove this oil from the zone of constant state so the errors change very little with time.

To confirm the origin of errors produced by the SPU scheme we reran the above test problem taking as initial data the MOC solution at 0.067 pore volumes injected. The results are shown in Fig. 2.7. The errors observed in the zone of constant state are reduced. This indicates that much of the error seen in the zone of constant state accumulates during early time steps when the solution is not well resolved on the grid. Errors in capturing the leading shock speed are not significantly reduced in this second run. The numerical composition path pulls back from the equal eigenvalue point despite being initialized by the correct path.

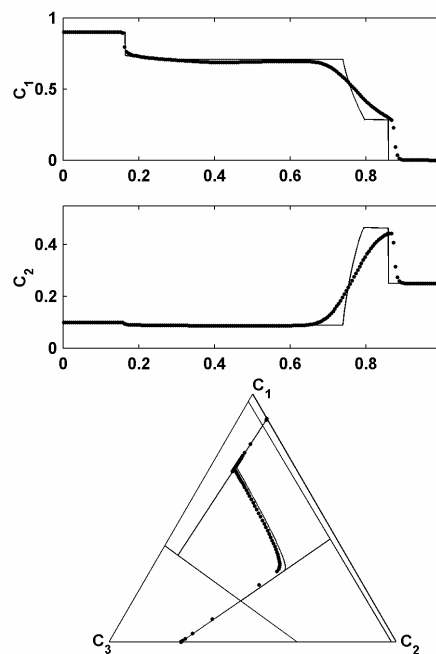


Fig. 2.7: Results for the SPU scheme with 200 grid cells starting with the MOC solution as initial data.

### 2.2.5 High order finite difference schemes

In the examples illustrated in Fig. 2.6 and Fig. 2.7, the SPU scheme failed to predict the correct composition path and hence underestimated the displacement efficiency of the drive. We now seek high order schemes that accurately predict compositional paths in phase space. We also seek schemes that are stable and robust so that they can be applied with confidence to a wide variety of compositional problems independent of the particular representation of phase behavior being used. It is unreasonable to expect a finite difference solution to match a MOC Riemann solution for all time with uniform grids. At early time steps, few grid cells will be used to represent the solution and the displacement efficiency is likely to be underestimated. This observation motivates a need for adaptive mesh refinement (AMR). For

now, we seek methods that minimize the errors made at early time steps. After presenting results for uniform grids, we consider AMR and show preliminary results.

High order methods for conservation laws have been an active area of research for the past few decades. Consider a scalar version of (2.31) applied to the constant K-value case:

$$C_k^{n+1} = C_k^n - \frac{\Delta\tau}{\Delta\xi} \left[ F_{k+1/2}^n - F_{k-1/2}^n \right] . \quad (2.35)$$

High order methods achieve their accuracy by improving upon the approximation (2.32) to the flux at cell faces. The straightforward use of high order interpolation to reconstruct cell-centered variables at the cell faces leads to large oscillations near shocks. Several methods have been proposed to achieve high accuracy without creating oscillations. We now consider methods that fall into 3 categories: total variation diminishing methods (TVD), essentially non-oscillatory methods (ENO), and weighted-ENO methods (WENO). We describe a flux-based version of each reconstruction applied to (2.35).

### 2.2.5.1 Total variation diminishing schemes

To quantify oscillatory behavior, the total variation of a discrete solution is defined as

$$TV(C^n) = \sum_k |C_{k+1}^n - C_k^n| \quad (2.36)$$

TVD schemes mimic continuous conservation laws by requiring that

$$TV(C^{n+1}) \leq TV(C^n) \quad (2.37)$$

The TVD reconstruction makes a correction to linear interpolation that enforces the property of Eq. (2.37). The correction procedure is known as flux or slope limiting and is a two step process. First a measure of the smoothness of the solution is obtained, e.g. the ratio of successive gradients  $\Theta$ . The TVD correction is then applied by a nonlinear limiter based on the smoothness of the solution. Sweby (1984) gives a review of limiters. Here we mention two popular limiters that have been used in the petroleum literature. The simple minmod limiter

$$\Phi(\Theta) = \max(0, \min(1, \Theta)) \quad (2.38)$$

gives solutions that satisfy Eq. (2.37) but are typically too diffused. The Fromm limiter,

$$\Phi(\Theta) = \max\left(0, \min\left(2, 2\Theta, \frac{1+\Theta}{2}\right)\right) \quad (2.39)$$

yields sharper solution profiles. In the following section we give results using the Fromm limiter (TVD-F) and discuss our results obtained using minmod and other limiters. In TVD schemes,  $F_{j+1/2}$  depends on the fixed stencil  $\{F_{j-1}, F_j, F_{j+1}\}$ . The TVD reconstruction reduces to first order at extrema of the solution where  $\Phi = 0$ .

### 2.2.5.2 Essentially non-oscillatory schemes

The motivation behind ENO schemes is to extend the reconstruction step to higher orders of accuracy and to maintain accuracy at smooth extrema. This is accomplished by relaxing the TVD property of Eq. (2.37) to

$$\text{TV}(C^{n+1}) \leq \text{TV}(C^n) + O(\Delta\xi^r) \quad (2.40)$$

where  $r$  is the order of the scheme. Small oscillations on the order of the truncation error are allowed in the reconstruction but do not degrade solution quality. High order accuracy is achieved by polynomial interpolation. Adapting the stencil of the interpolation enforces the property of Eq. (2.40). At each cell face,  $r$  candidate interpolations are performed and the least oscillatory interpolating polynomial is selected. We test a third order ENO scheme (ENO-3) that reconstructs  $F_{k+1/2}$  using quadratic interpolation on the stencils  $\{F_{k-2}, F_{k-1}, F_k\}$ ,  $\{F_{k-1}, F_k, F_{k+1}\}$ , and  $\{F_k, F_{k+1}, F_{k+2}\}$ . In practice, we select the best stencil by examining divided differences. Harten *et al.* (1987) give details of the ENO reconstruction.

### 2.2.5.3 Weighted ENO schemes

WENO schemes improve upon the accuracy of ENO schemes in smooth regions by making full use of the information in a given stencil. Rather than choosing the least oscillatory interpolating polynomial, WENO schemes use a weighted combination of all of the available interpolations. The weights assigned to each stencil are chosen to achieve higher accuracy in smooth regions while still enforcing Eq. (2.40). We test a third order WENO scheme that is based on a compact three point stencil (WENO-3) and a fifth order scheme (WENO-5) that is based on the same five point stencil as ENO-3. Jiang and Shu (1996) give the details of choosing the weights.

### 2.2.6 Extension to multicomponent systems

The traditional approach to solving nonlinear systems of strictly hyperbolic equations has been to decouple the equations by locally changing to characteristic variables (LeVeque, 1992, Harten *et al.* 1987). The decoupled equations can then be solved using the scalar techniques given above. Changing to characteristic variables requires the solution to the same eigenvalue problem discussed previously in the context of MOC solutions. The characteristic approach is impractical for compositional problems because the eigenvalue problem has only been solved analytically for constant K-value phase behavior. Furthermore, the numerical or semi-analytical solution of the eigenvalue problem is computationally expensive and complicated by the weak hyperbolicity near equal-eigenvalue points. For simplicity and efficiency we explore the possibility of using a component-wise reconstruction that does not use a characteristic decomposition. This approach has recently been popularized by the success of high order central schemes for conservation laws (Nessyaho, 1990; Levy *et al.*, 1998). Qiu and Shu (2002) give a comparison of upwind and central WENO schemes with and without a characteristic decomposition.

Within the component-wise framework, we consider two strategies for computing the flux at the cell faces. The flux-based approach is to perform flash calculations and calculate the flux at cell centers. The flux is then reconstructed at the cell faces using one of the schemes described above. Godunov's approach is to reconstruct first the total moles of each component at the cell faces and then perform flash calculations at the cell faces to determine the flux (Godunov, 1959). Thiele and Edwards (2001) recommend a third approach based on reconstructing the saturations, densities, and mole fractions of each phase. We prefer Godunov's approach for the constant K-value case and use the flux-based approach when volume change on mixing is included because our velocity iteration requires flash calculations to be performed at cell centers. The Godunov and flux-based approaches are identical for the first order method.

### 2.2.7 High order time stepping

In the previous subsections we outlined reconstructions that attain high order spatial accuracy. If spatially high order methods are used in conjunction with first order time stepping, temporal errors can dominate the total error. In addition to the lowering the accuracy of the overall scheme, first order temporal errors complicate the analysis of high order spatial reconstructions. Thiele and Edwards (2001) warn against the use of high order spatial reconstructions with first order time stepping for compositional problems for stability reasons. To equate the temporal accuracy with the spatial accuracy, we use explicit, multistage Runge-Kutta (RK) schemes. We use optimal second and third order TVD RK schemes (RK-2 and RK-3) with our second and third order accurate reconstructions, respectively (Shu and Osher, 1988). For our fifth order WENO reconstruction we use a fourth order RK scheme (RK-4) (see Jiang and Shu, 1996). At each stage of an RK scheme, we perform flash calculations and our high order spatial reconstructions. Therefore, the computational cost of each scheme compared to the first order scheme is scaled by a factor equal to the number of stages. Since high order methods allow the use of coarser grids, this added cost is not severe. We use these schemes because they are simple and reliable although other schemes may prove to be more efficient.

As mentioned previously, the total dimensionless velocity  $v_D$  varies in space and time when volume change on mixing is considered. As indicated in Eq. (2.31), the compositions depend on  $v_D$  implicitly. We determine  $v_D$  by an iterative process (Dindoruk, 1992). We review this iteration and outline the modifications needed for higher order RK schemes in the appendix.

### 2.2.8 Results

We have applied the methods described in the previous section to a number of three-component test problems with constant K-values. We give results for the Godunov approach applied to the vaporizing drive illustrated in Fig. 2.6 to Fig. 2.7 and for a condensing drive using the same three-component system.

We present two additional problems to test the ability of our schemes to model flow governed by more realistic phase behavior, including volume change on mixing. In the first test, we displace a mixture of CH<sub>4</sub>, C<sub>4</sub> and C<sub>10</sub> with pure N<sub>2</sub>. The second test is a near-miscible CO<sub>2</sub> flood. We again displace a mixture of CH<sub>4</sub>, C<sub>4</sub> and C<sub>10</sub>. For this second set of test problems we use the flux-based approach.

### 2.2.8.1 Example 1: Vaporizing drive

The results of applying the five schemes to the vaporizing drive (Table 2-1) are given in Fig. 2.8. The high order solutions contain much less numerical dispersion than the SPU solution. The leading shock speed is captured accurately by the TVD-F scheme, but near the equal eigenvalue point the composition path prematurely jumps from the injection tie line onto an incorrect NT path. The size and speed of the trailing shock are both overestimated due to over-squaring. Over-squaring is commonly seen with TVD methods used in conjunction with less diffusive limiters (Rubin and Edwards, 1993). The ENO-3 composition path follows the MOC path closely. The errors in predicting both shock speeds are similar to those seen with the SPU solution but are of smaller magnitude. Errors generated by ENO-3 in the zone of constant state are small but oscillatory compared to SPU. The WENO-3 profiles and composition path are more diffusive than those of ENO-3 are. Hence, errors in predicting the shock speeds and the errors in the zone of constant state are larger for WENO-3 than for ENO-3. WENO-5 is less diffusive and accurately captures both shock speeds. Close inspection of the WENO-5 composition path near the equal eigenvalue point reveals small oscillations. Fig. 2.9 gives a closer look at the numerical composition paths of each high order scheme near the equal eigenvalue point. The ENO-3 composition path stays close to the MOC path but errs on the same side as the SPU path. In the presence of physical diffusion or dispersion, the true solution would also be pulled to this side of the MOC path. Each of the other high order methods contains errors that are not diffusive in nature. For TVD-F, these errors are large enough to impact the solution along the entire NT path and the zone of constant state.

### 2.2.8.2 Example 2: Condensing drive

A condensing drive is obtained for the same constant K-value system by changing the initial and injection compositions (see Table 2-2). The NT path consists of a shock rather than a rarefaction as seen in the previous example. The NT shock reaches the injection tie line at a point close to an equal eigenvalue point, but the MOC composition path does not pass directly through that point. The zone of constant state appears along the initial tie line between the leading shock and the NT shock. Fig. 2.10 gives the results for the condensing drive. The SPU scheme smears the NT shock but maintains a relatively sharp transition at the leading shock. With the exception of the WENO-3 scheme, the high order schemes produce oscillations in the zone of constant state. The magnitude of the oscillations is related to the amount of numerical dispersion in the scheme and to the size of the stencil of the scheme. As in the previous example, TVD-F over-squares the trailing shock and hence overestimates the trailing shock speed. The ENO and WENO schemes accurately predict shock speeds in this example.

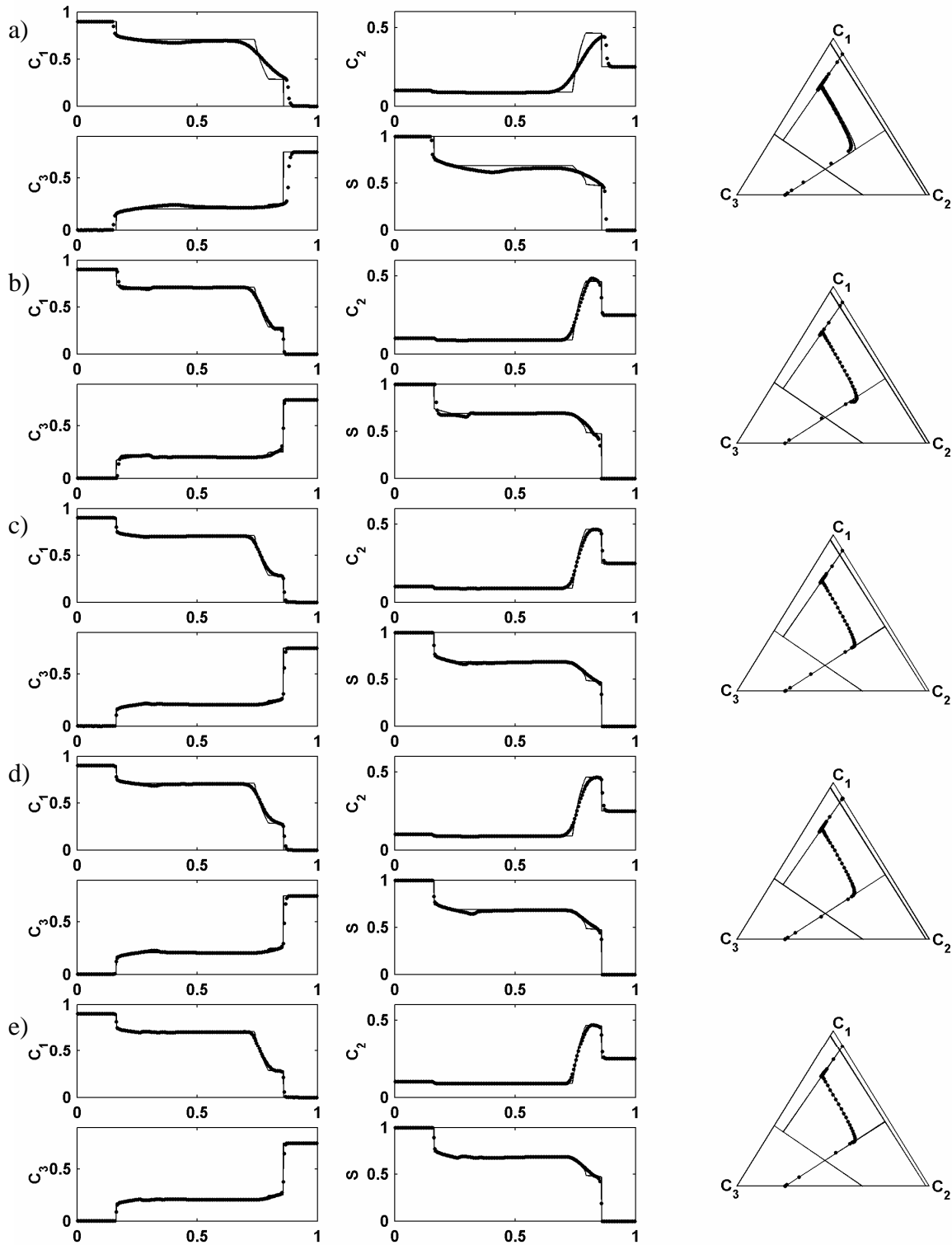


Fig. 2.8: Mole fraction profiles, gas saturation profiles, and composition paths in phase space are given for the following schemes applied to example 1 with 200 grid cells: a) SPU, b) TVD-F, c) ENO-3, d) WENO-3, and e) WENO-5.

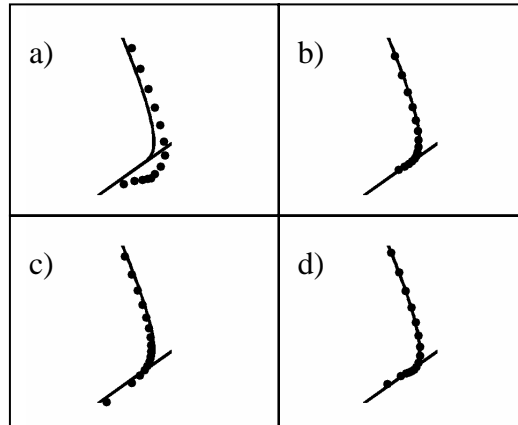


Fig. 2.9: A close view of the numerical composition paths near the equal eigenvalue point is given for the four high order schemes: a) TVD-F, b) ENO-3, c) WENO-3, d) WENO-5.

Table 2-2: Parameters and component properties used in example 2

	$C_1$	$C_2$	$C_3$
Injection mole fraction	0.10	0.90	0.00
Initial mole fraction	0.30	0.00	0.70
Equilibrium K-values	2.50	1.50	0.05
Residual oil saturation	0.00		
Viscosity ratio, $\mu_g/\mu_o$	1/5		
Pore volumes injected	2/3		
CFL/ $V_{\max}$	2/5		

### 2.2.8.3 Summary for constant K-values

In addition to the results presented here, we have tested our high order schemes on condensing and vaporizing drives for constant K-value systems with less volatile intermediate components. Results of those tests are consistent with the findings presented here. The TVD-F scheme over-squares trailing shocks and has a tendency to jump to an incorrect NT path when the composition path passes through an equal eigenvalue point. The ENO-3 and WENO-5 schemes predict shock speeds accurately. The oscillations seen in Fig. 2.10 are the largest that we have observed in constant K-value systems using the Godunov approach. WENO-3 produces smoother solution profiles, but higher levels of numerical dispersion compared to the other high order methods.

Results obtained with the flux-based approach are similar for the third and lower order schemes although shock speeds are captured slightly more accurately with the Godunov approach. Oscillations generated by the flux-based WENO-5 scheme are larger than those

generated by the Godunov approach. The flux-based WENO-5 scheme also displays a greater tendency to jump to an incorrect NT path, although this type of error is much smaller than seen with either the flux-based or Godunov TVD-F schemes.

If the more diffusive minmod limiter replaces the Fromm limiter in the TVD scheme, over-squaring and errors near the equal eigenvalue point are reduced. However, the level of numerical dispersion observed with the minmod limiter is greater than with TVD-F or WENO-3 and shock speeds are not captured accurately. Errors with other limiters are similar to those produced with the Fromm limiter, but the magnitude of the errors is related to the amount of numerical dispersion allowed by the limiter.

### 2.2.8.4 Example 3: Vaporizing N<sub>2</sub> drive

This vaporizing drive (see Table 2-3) contains an NT rarefaction; hence, the solution passes through an equal-eigenvalue point as in example 1. The results of applying the SPU and ENO-3 schemes are given in Fig. 2.11 and Fig. 2.12. As in example 1, the SPU scheme overestimates the leading shock speed and smears the details of the solution within the two-phase region. ENO-3 captures the leading shock speed and resolves the NT rarefaction and the NT shock that occur within the two-phase region with better accuracy than SPU. The ENO-3 composition path passes through the equal eigenvalue point without oscillating or jumping to an incorrect path. For brevity results obtained using the other high order methods are not given. For this problem, the TVD-F scheme again jumped from initial tie line to an incorrect NT path. The results using WENO-3 and WENO-5 also agree with the results of example 1. The solution for both schemes is more accurate than TVD-F near the equal eigenvalue point; however, small errors similar to those shown in Fig. 2.9 are noticeable with both schemes.

Table 2-3: Parameters and component properties used in example 3

	N <sub>2</sub>	CH <sub>4</sub>	C <sub>4</sub>	C <sub>10</sub>
Injection mole frac.	1.0000	0.0000	0.0000	0.0000
Initial mole frac.	0.0000	0.1000	0.2000	0.7000
T <sub>c</sub> (K)	126.25	190.58	425.18	617.65
P <sub>c</sub> (atm)	33.537	45.429	37.463	20.796
Mole. Wt. (g/mole)	28.016	16.043	58.123	142.29
Acentric factor	0.0400	0.0080	0.2010	0.4900
Residual oil sat.	0.2			
Visc. ratio, $\mu_g/\mu_o$	LBC			
Pore volumes inj.	1/3			
CFL/V <sub>max</sub>	1/6			
Pressure	109 atm			
Temp	344 K			

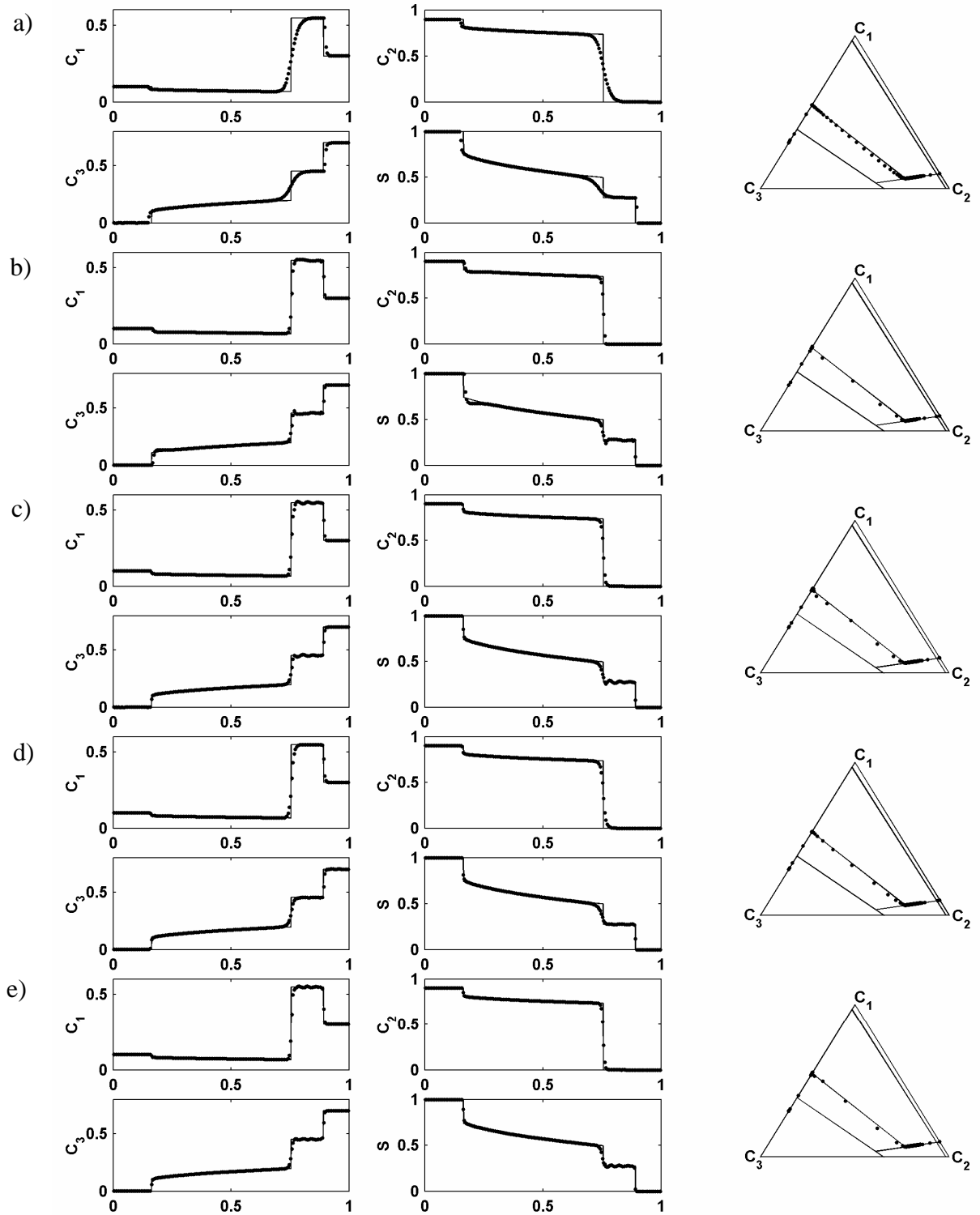


Fig. 2.10: Mole fraction profiles, gas saturation profiles, and composition paths in phase space are given for the following schemes applied to example 2 with 200 grid cells: a) SPU, b) TVD-F, c) ENO-3, d) WENO-3, and e) WENO-5.

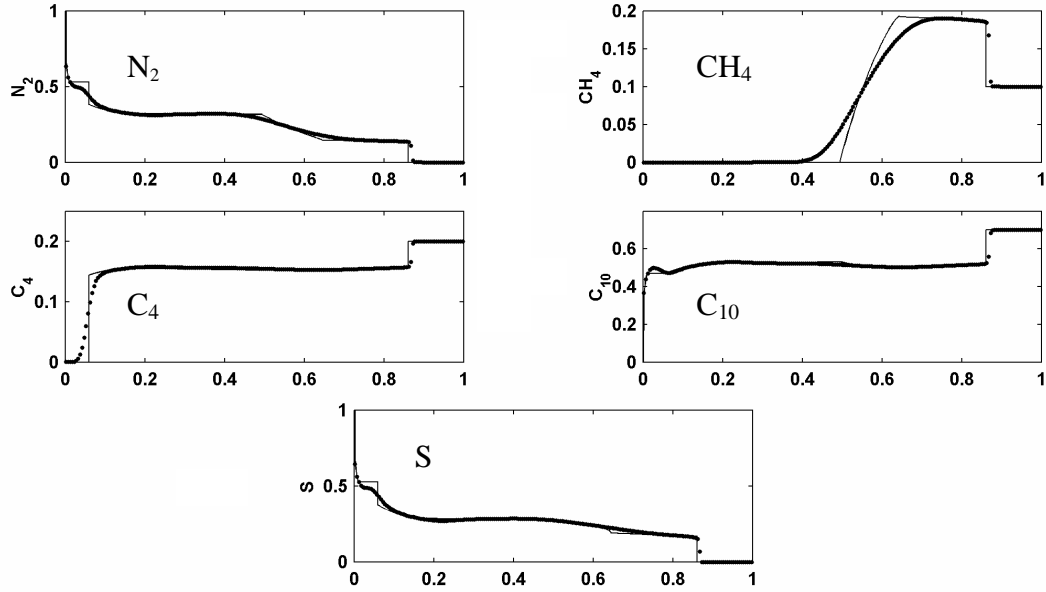


Fig. 2.11: Mole fraction profiles and gas saturation profiles are given for SPU applied to example 3 with 200 grid cells.

### 2.2.8.5 Example 4: Near-miscible CO<sub>2</sub> flood

This problem (see Table 2-4 and Table 2-5) is sensitive to numerical errors since we inject at only two atmospheres below the minimum miscibility pressure. SPU and ENO-3 solutions are given in Fig. 2.13 and Fig. 2.14. We use 400 grid cells in this example because of the increased sensitivity to numerical dispersion. Despite this refinement, numerical dispersion causes the SPU solution to be far from miscible. ENO-3 predicts a much more efficient displacement without generating oscillations. The solutions generated by TVD-F and WENO-5 contain less numerical dispersion than ENO-3 and hence are slightly more accurately than ENO-3 in this example. WENO-3 captures the shock speeds less accurately.

Table 2-4: Parameters and component properties used in example 4

	CO <sub>2</sub>	CH <sub>4</sub>	C <sub>4</sub>	C <sub>10</sub>
Injection mole frac.	1.0000	0.0000	0.0000	0.0000
Initial mole frac.	0.0000	0.3000	0.3000	0.4000
T <sub>c</sub> (K)	304.21	190.58	425.18	617.65
P <sub>c</sub> (atm)	72.857	45.429	37.463	20.796
Mole. Wt. (g/mole)	45.429	16.043	58.123	142.29
Acentric factor	0.2250	0.0080	0.2010	0.4900
Residual oil sat.	0.2			
Visc. ratio, $\mu_g/\mu_o$	LBC			
Pore volumes inj.	2/3			
CFL/V <sub>max</sub>	2/7			
Pressure	110.75 atm			
Temp	344 K			

Table 2-5: Binary interaction coefficients used in examples 3 and 4

	CO <sub>2</sub>	CH <sub>4</sub>	C <sub>4</sub>
CH <sub>4</sub>	0.1000		
C <sub>4</sub>	0.1257	0.0270	
C <sub>10</sub>	0.0942	0.0420	0.0080

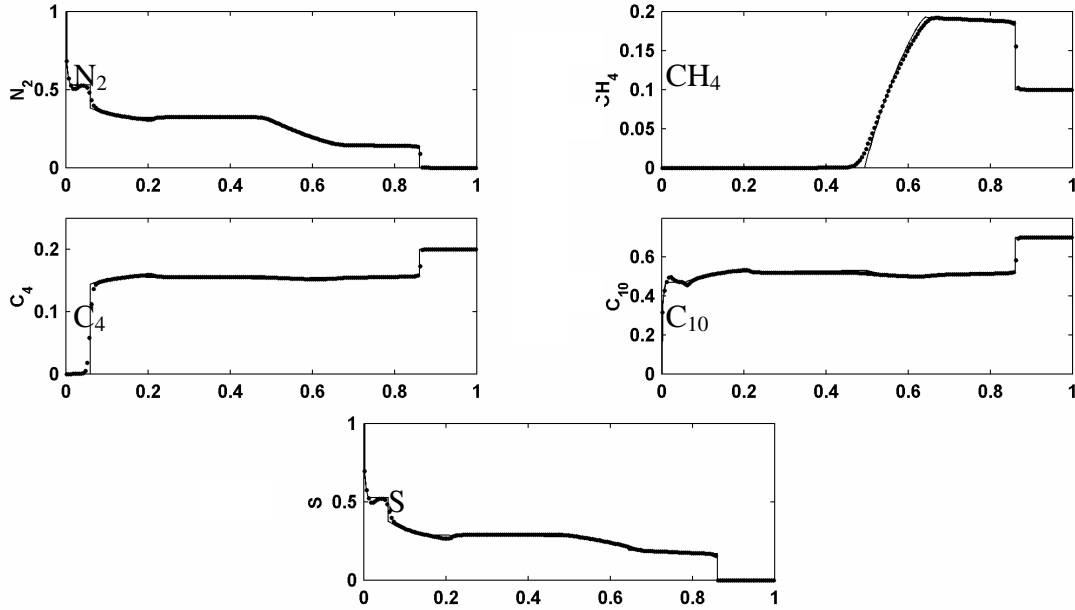


Fig. 2.12: Mole fraction profiles and gas saturation profiles are given for ENO-3 applied to example 3 with 200 grid cells.

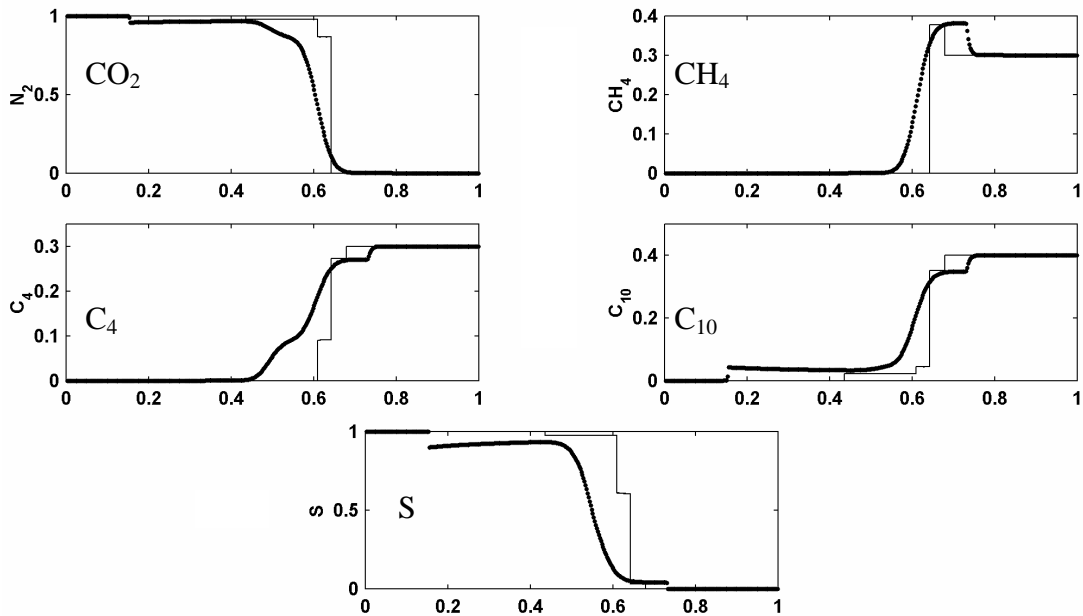


Fig. 2.13: Mole fraction profiles and gas saturation profiles are given for SPU applied to example 4 with 400 grid cells.

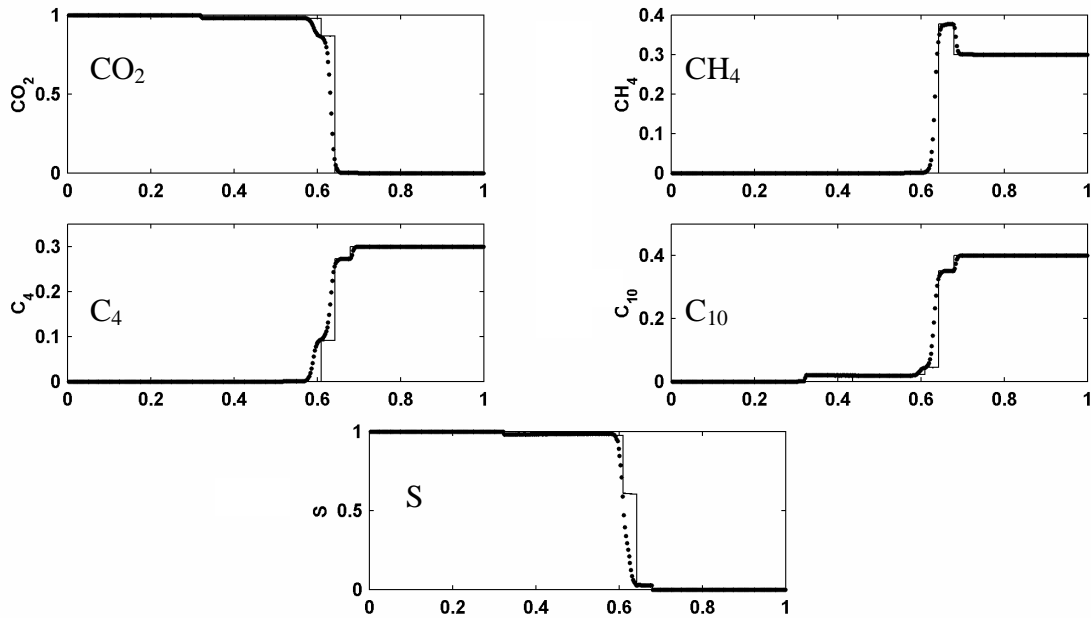


Fig. 2.14: Mole fraction profiles and gas saturation profiles are given for ENO-3 applied to example 4 with 400 grid cells.

### 2.2.9 Efficiency and adaptive mesh refinement

Explicit compositional finite difference schemes spend the majority of computational time performing flash calculations. When volume change on mixing is ignored, ENO-3 performs three times the number of flash calculations as SPU since RK-3 is a three-stage scheme. This added cost is not severe. Refining a grid by a factor necessitates refinement by the same factor in time. Therefore, a grid for SPU can only be slightly finer than a grid for ENO-3 for the same number of flash calculations to be performed by both schemes. For the accuracy of SPU to match ENO-3, refinement by a large factor is required. For a threshold accuracy to be achieved, ENO-3 performs far less flash calculations than SPU.

When volume change is included, the number of flash calculations performed by each scheme increases due to the iteration for the total velocity. The rate of increase is greater for SPU than for the high order schemes. Our experiments indicate that ENO-3 typically performs around twice the number of flashes as SPU on the same grid. Exact count comparisons are difficult to analyze because the composition paths taken by the schemes differ significantly.

We have begun to investigate adaptive mesh refinement (AMR) to further reduce the number of flash calculations required by high order methods. Fig. 2.15 gives AMR results using ENO-3 on example 1.

The AMR algorithm proceeds by solving on the coarsest grid first and then correcting the solution on fine patches where greater resolution is needed (Godunov, 1982). In this test the number of flash calculation performed is half of the number needed to solve the problem on the fine grid alone. We anticipate that the speedup will be greater for near-miscible problems because solution features propagate at nearly the same speed and can be covered with few, relatively small patches. Our preliminary results suggest that AMR will be a useful tool in developing an efficient compositional streamline simulator.

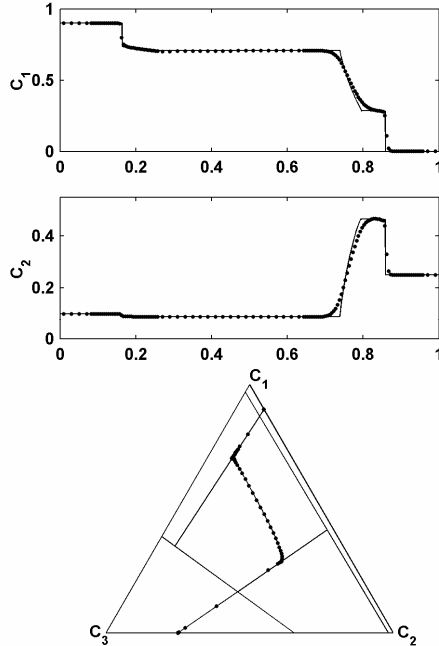


Fig. 2.15: AMR results are shown using ENO-3 with 50 grid cells on the coarse grid and 200 grid cells on the fine grid.

### 2.2.10 Discussion

The ENO-3 scheme investigated in this section provides accurate solutions to 1D gas injection problems compared to the first order scheme and our tests indicate that it is more robust than TVD and WENO schemes. ENO-3 can be used with coarser grids than SPU and still achieves greater accuracy. The scheme is efficient, especially when used in conjunction with AMR. We expect it to be practical for 3D simulation in combination with either streamline methods or conventional 3D finite difference approaches.

In cases where the zone of constant state is located between shocks, ENO-3 may generate small oscillations. The oscillations we have observed are similar to oscillations generated by high order schemes for the Euler equations of gas dynamics. In Sweby (1984), this oscillatory behavior is removed by incorporating a local characteristic decomposition. A similar approach might work here, but we feel that it is unnecessary. Our experiments indicate that the oscillations do not grow in time and have no impact on the prediction of displacement efficiency.

TVD schemes can produce sharp solution profiles but our tests indicate that near equal eigenvalue points they can oscillate and can jump to incorrect NT paths. The WENO schemes that we have investigated show this same tendency but to a lesser degree. We feel more confident in the ENO-3 scheme because it accurately models phase behavior near equal eigenvalue points.

### 2.2.11 Conclusions

The tests and analysis presented here suggest the following conclusions:

1. Compositional finite difference schemes must accurately resolve the effects of phase behavior in order to reliably predict the displacement efficiency of gas injection processes. Of all conservative upwind schemes investigated in this paper, the third order ENO scheme captures the effects of phase behavior most accurately and robustly. Due to the high cost of flash calculations, AMR combined with high order methods is a promising tool for efficient compositional simulation.
2. In this investigation, we have focused on the spatial accuracy of our schemes. We will optimize the time stepping portion of our algorithm in future work. We plan to apply our 1D results to 3D through the use of a streamline method. To take advantage of the adaptive ENO-3 scheme, improved mappings to and from streamlines will be investigated and AMR will be extended to other stages in the streamline algorithm. In addition, we are continuing to investigate the inclusion of gravity and compressibility in compositional streamline simulation.

### 2.2.12 Appendix: Iteration for total velocity

When volume change on mixing is included in a compositional simulation, we determine the total velocity by an iterative process. Dindoruk gives the details of this iteration for the SPU scheme (Dindoruk, 1992). We assume that the change in  $v_D$  due to a gradient in pressure is negligible. Given compositions on a grid, compute the flux at the grid cell faces and make an initial guess to the mixture density at the next time step. For each cell proceeding from injector to producer do the following:

1. Compute  $v_D$  at the exiting face of the cell based on the mixture density.
2. Update the total moles of each component in the cell from Eq. (2.31).
3. Flash the updated cell and calculate a new mixture density.
4. Based on the new mixture density, calculate the mass error for the cell.

If the mass error is below a certain tolerance, proceed to the next cell. If not, repeat starting at 1) with the new mixture density.  $v_D = 1$  at the entrance face to the first cell. We use a tolerance of  $10^{-4}$  moles to ensure that the iteration is not a leading source of error in our schemes although a larger tolerance may certainly be acceptable in some cases. For higher order RK schemes we iterate at each stage to ensure that mass is conserved in our final updated cell. The tolerance at each stage is chosen to reflect the contribution that the stage makes to the flux for the entire step.

## 2.3 Gravity segregation and compositional simulation

### 2.3.1 Introduction

Compositional streamline simulation for assessment of miscible/near-miscible gas injection process performance has significant potential to accommodate requirements for accurate and reliable production forecasts. These requirements include high resolution descriptions of permeability heterogeneity and an appropriate representation of the phase behavior including a sufficient number of components in the equation of state representation of the reservoir fluid. The combination of high spatial resolution and sufficient compositional resolution is needed to resolve the complex coupling between flow and phase behavior.

Conventional finite-difference (FD) or finite-element simulators are presently too slow to permit high resolution compositional simulation at field scale. However, the application of compositional streamline simulation has so far been limited to production scenarios where effects of gravity can be neglected. The lack of suitable methods to include gravity effects has restricted the use of compositional streamline simulation to 2D horizontal displacement problems or 3D displacement problems for fluids with a low-density contrast.

The aim of this work is to extend the area of applicability for compositional streamline simulation by suggesting an efficient method to include gravity segregation on the list of represented physics that control processes performance of gas injection schemes at field scale. Numerous authors have contributed significantly to the development of streamline simulation in general (Bommer and Schechter, 1979; Bratvedt *et al.*, 1992; Datta-Gupta and King, 1995; Thiele *et al.* 1995a, 1995b; Bratvedt *et al.* 1996; Blunt *et al.* 1996; Batycky *et al.*, 1996; Thiele *et al.*, 1996, 1997; Batycky, 1997; King, 1998; Crane, 2000; Ichiro *et al.* 2003; Seto *et al.* 2003). We refer the reader to these contributions for detailed coverage of the fundamentals of streamline simulation.

In the following sections, we start by reviewing the conservation equations for multiphase multicomponent flows in porous media with particular emphasis on handling gravity segregation in compositional streamline simulation. Next, we describe an efficient approach for including the effects of gravity. We then demonstrate, through example calculations, the accuracy of the suggested approach by comparing simulation results with those of a commercial finite difference based simulator.

### 2.3.2 Mathematical formulation

In this section we present the mass conservation equations for multicomponent multiphase flows with emphasis on including gravity segregation in compositional streamline simulation. If effects of dispersion are neglected, mass conservation of  $n_c$  components distributed in  $n_p$  phases, flowing through a heterogeneous porous medium can be written as (Lake, 1989)

$$\phi \frac{\partial}{\partial t} \left\{ \sum_{j=1}^{n_p} \omega_{ij} \rho_{mj} S_j \right\} + \nabla \cdot \left\{ \sum_{j=1}^{n_p} \omega_{ij} \rho_{mj} \underline{u}_j \right\} = 0, \quad i = 1, \dots, n_c, \quad (2.41)$$

where  $\phi$  is the porosity,  $t$  is the time,  $\omega_j$  is the mass fraction of component  $i$  in phase  $j$ ,  $\rho_{mj}$  is

the mass density of phase  $j$ ,  $S_j$  is the gas saturation and  $u_j$  is the velocity of phase  $j$ . According to Darcy's law, the velocity of phase  $j$  can be written in terms of the total permeability ( $k$ ), the relative permeability of phase  $j$  ( $k_{rj}$ ), the viscosity ( $\mu_j$ ) and the mass density ( $\rho_{mj}$ ) of phase  $j$

$$\underline{u}_j = -\frac{kk_{rj}}{\mu_j}(\nabla p + \rho_{mj}g\nabla D) , \quad j = 1, \dots, n_p \quad , \quad (2.42)$$

where  $p$ ,  $D$  and  $g$  are the pressure, depth and gravity (capillary effects are not included). For flow problems that are strongly coupled to the phase behavior of the flowing phases, it is more convenient to work with the conservation equations stated in terms of mole fractions and molar densities;

$$\phi \frac{\partial}{\partial t} \{C_i\} + \nabla \cdot \left\{ \sum_{j=1}^{n_p} x_{ij} \rho_j \underline{u}_j \right\} = 0 , \quad i = 1, \dots, n_c \quad , \quad (2.43)$$

with

$$C_i = \sum_{j=1}^{n_p} x_{ij} \rho_j S_j , \quad i = 1, \dots, n_c \quad , \quad (2.44)$$

where  $x_{ij}$  is the mole fraction of component  $i$  in phase  $j$  and  $\rho_j$  is the molar density of phase  $j$ . For convenience we introduce the overall molar flux  $F_i$ ,

$$F_i = \underline{u}_t \cdot \sum_{j=1}^{n_p} x_{ij} \rho_j f_j , \quad i = 1, \dots, n_c \quad , \quad (2.45)$$

where  $f_j$  is the fractional flow of phase  $j$  and rewrite Eq. (2.43) as

$$\phi \frac{\partial}{\partial t} \{C_i\} + \nabla \cdot \{F_i\} = 0 , \quad i = 1, \dots, n_c \quad . \quad (2.46)$$

In compositional streamline simulation, Eq. (2.46) is decomposed into a sequence of 1D displacement problems along streamlines (Thiele *et al.*, 1997; Crane *et al.*, 2000; Seto *et al.*, 2003). As streamlines are trajectories in space, dictated by the total velocity field, propagation of fluids along the streamlines does not account for gravity effects driven by differences in density between the flowing phases unless explicitly included in terms of in the fractional flow function  $f_j$ . Lake (1989) demonstrates how gravity can be included in the fractional flow function for immiscible flows. However, including gravity in the fractional flow function allows for negative wave velocities and hence complicates the use of otherwise efficient upwind schemes. Another possibility is to locate phase specific streamlines as discussed by Blunt *et al.*, 1996.

Operator splitting is an alternative for including gravity in streamline based simulation and has been applied successfully for immiscible flows by several investigators (Bradtvedt *et al.*, 1996; Batycky *et al.*, 1996; Batycky, 1997). To include gravity by operator splitting, the flux term in Eq. (2.46) must be expanded into a convective term accounting for gradients in pressure and a gravity term accounting for gradients in mass density.

In the following derivation we assume that the gravity vector is aligned with the  $z$  axis in Cartesian coordinates. By summing Eq. (2.42) over all phases, the vertical portion of the total

velocity ( $u_z$ ) can be written as

$$u_z = -k_z \left( \lambda_t \frac{\partial p}{\partial z} + \lambda_g \frac{\partial D}{\partial z} \right) = \sum_{j=1}^{n_p} u_{z,j} \quad , \quad (2.47)$$

with the total mobility ( $\lambda_t$ ) and the total gravity mobility ( $\lambda_g$ ) given by

$$\lambda_t = \sum_{j=1}^{n_p} \lambda_j = \sum_{j=1}^{n_p} \frac{k_{rj}}{\mu_j} \quad \lambda_g = g \sum_{j=1}^{n_p} \lambda_j \rho_{mj} \quad . \quad (2.48)$$

By substituting the Darcy velocity into Eq.(2.43), the conservation equations can be rewritten along a gravity line (vertical line) as

$$\phi \frac{\partial}{\partial t} \{C_i\} - \frac{\partial}{\partial z} \left\{ \sum_{j=1}^{n_p} x_{ij} \rho_j K_z \lambda_j \left( \frac{\partial p}{\partial z} + \rho_{mj} g \frac{\partial D}{\partial z} \right) \right\} = 0 \quad . \quad (2.49)$$

To eliminate the pressure gradient from Eq. (2.49), Eq. (2.47) is rewritten as

$$\frac{\partial p}{\partial z} = -\frac{u_z}{k_z \lambda_t} - \frac{\lambda_g}{\lambda_t} \frac{\partial D}{\partial z} \quad , \quad (2.50)$$

and finally by inserting Eq. (2.50) into Eq. (2.49) we obtain

$$\phi \frac{\partial}{\partial t} \{C_i\} + \frac{\partial}{\partial z} \{F_i^*\} + \frac{\partial}{\partial z} \{G_i\} = 0 \quad , \quad i = 1, \dots, n_c \quad , \quad (2.51)$$

where  $F_i^*$  is the vertical convective flux of component i given by

$$F_i^* = u_z \sum_{j=1}^{n_p} x_{ij} \rho_j f_j \quad , \quad i = 1, \dots, n_c \quad , \quad (2.52)$$

and  $G_i$  is the gravity driven flux of component i given by

$$G_i = k_z \sum_{j=1}^{n_p} x_{ij} \rho_j \lambda_j \left( \frac{\lambda_g}{\lambda_t} - \rho_{mj} g \right) \frac{\partial D}{\partial z} \quad , \quad i = 1, \dots, n_c \quad . \quad (2.53)$$

In streamline simulation of immiscible flows, the equivalent of Eq. (2.49) is commonly solved in a sequential manner by operator splitting (Bratvedt *et al.*, 1996; Batycky *et al.*, 1996; Batycky, 1997). Operator splitting relies on the consistency of treating the convective flux independently from the gravity flux within a given time step of the simulation. In other words, any given time step starts with a convective step solving Eq. (2.46) along a set of streamlines using the standard Buckley-Leverett form of the fractional flow function

$$f_j = \frac{\lambda_j}{\lambda_t} \quad , \quad (2.54)$$

followed by a gravity step solving

$$\phi \frac{\partial}{\partial t} \{C_i\} + \frac{\partial}{\partial z} \{G_i\} = 0, \quad i = 1, \dots, n_c. \quad (2.55)$$

For small time steps the operator-splitting approximation is fairly accurate whereas large time steps may lead to significant operator-splitting errors. In the following section we discuss the consequences of solving the gravity equation, Eq. (2.55), including compositional effects.

### 2.3.3 Solution along gravity lines

A complication that must be addressed in the use of an operator-splitting technique to account for gravity segregation in compositional flows arises from the fact that the performance of compositional displacements can depend strongly on the displacement path. Consider, for example, a gas front in a two-phase gas/oil displacement invading a sequence of gridlocks along the path a shown in Fig. 2.16.

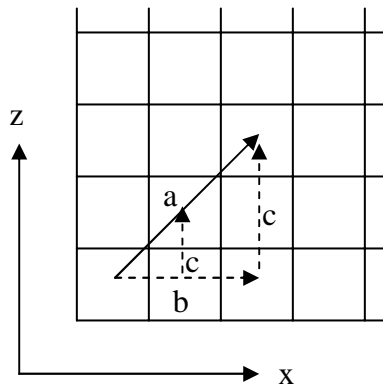


Fig. 2.16: Path dependence of compositional flows.

The corresponding path predicted by an operator-splitting approach could be: a convective step b followed by a gravity step c also shown in Fig. 2.16. If the gas has a low solubility in the oil phase, the two paths would result in a very similar final states corresponding to a small operator-splitting error. If on the other hand the gas is highly soluble in the oil phase (e.g. in undersaturated reservoir fluids), significant amounts of the gas phase would dissolve in the liquid phase as it moves towards the final state. In the worst case, only a small fraction of the original gas phase remains as the gravity step progresses, resulting in a larger operator-splitting error. Furthermore, liquid contacted by the injected phase will have a different density than the original reservoir fluid and hence lighter liquid may seek upwards. Simultaneous liquid-liquid and vapor-liquid segregation corresponds in principle to a three-phase (water-oil-gas) immiscible system.

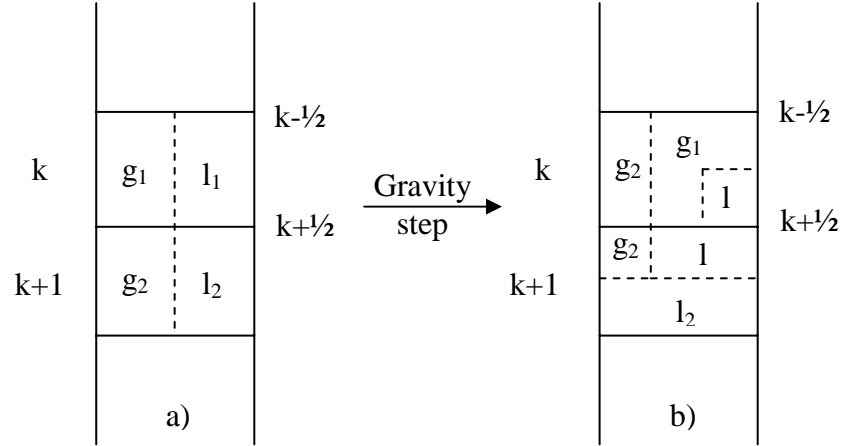


Fig. 2.17: Pseudo-immiscible gravity segregation.

To reduce the path dependence as well as the CPU requirement for gravity steps in compositional streamline simulation, we propose a pseudo-immiscible approach illustrated in Fig. 2.17. At the end of a given convective step, gravity lines are traced. For a Cartesian grid the gravity lines simply correspond to a column of gridblocks. For each gravity line the following steps are performed: equilibrate gridblocks (flash) and record phase saturations, molar densities, viscosities and phase compositions for each gridblock. Each individual phase in a gridblock defines a segment of known composition, molar density, and fluid properties. For two-phase flows, the maximum number of segments along a gravity line is two times the number of gridblocks. This initial state is illustrated in Fig. 2.17a with gas segments  $g_1$ ,  $g_2$  and liquid segments  $l_1$  and  $l_2$ . The pseudo-immiscible gravity step is then performed by moving segments according to the density contrast and relative permeabilities corresponding to the overall phase saturations. For a given gridblock  $k$ , the gas saturation  $S_k$  is evaluated summing the saturations of all gas segments present in the gridblock

$$S_k = \sum_{i=1}^{n_s} S_{i,k}^g, \quad (2.56)$$

where  $S_{i,k}^g$  is the saturation of gas segment  $i$  in gridblock  $k$ . Eq. (2.56) allows the calculation of the relative permeabilities of gas and liquid in any gridblock at any time during a gravity step. Phase viscosities and densities are calculated as saturation averages of the segments present in a gridblock:

$$\mu_k^g = \frac{1}{S_k} \sum_{i=1}^{n_s} \mu_{i,k}^g S_{i,k}^g, \quad (2.57)$$

$$\mu_k^l = \frac{1}{1-S_k} \sum_{i=1}^{n_s} \mu_{i,k}^l S_{i,k}^l, \quad (2.58)$$

$$\rho_{m,k}^g = \frac{1}{S_k} \sum_{i=1}^{n_s} \rho_{m,i,k}^g S_{i,k}^g \quad , \quad (2.59)$$

$$\rho_{m,k}^l = \frac{1}{1-S_k} \sum_{i=1}^{n_s} \rho_{m,i,k}^l S_{i,k}^l \quad . \quad (2.60)$$

Once the phase saturations, relative permeabilities, densities and viscosities are calculated, the saturation of individual segments  $i$  can be updated from time step  $n$  to  $n+1$  by a modified version of the approach for immiscible fluids outlined by Batycky (1997),

$$S_{i,k}^{n+1} = S_{i,k}^n - \frac{\Delta t}{\phi \Delta z_k} \left( \tilde{H}_{i,k+1/2} - \tilde{H}_{i,k-1/2} \right) . \quad (2.61)$$

The flux of segment  $i$  due to gas-liquid segregation is calculated by

$$H_{i,k+1/2} = g \frac{k_{z,k+1} k_{rg,k+1} k_{z,k} k_{ro,k} (\rho_{m,o} - \rho_{m,g})}{\mu_o k_{z,k+1} k_{rg,k+1} + \mu_g k_{z,k} k_{ro,k}} \quad , \quad (2.62)$$

and

$$\tilde{H}_{i,k+1/2} = H_{i,k+1/2} \sum_j^{gas} S_{j,k+1} \quad (2.63)$$

for gas segments, and

$$\tilde{H}_{i,k+1/2} = -H_{i,k+1/2} \sum_j^{liq} S_{j,k} \quad (2.64)$$

for liquid segments. Similar expressions for liquid-liquid segregation can be derived but need not be repeated. The time step  $\Delta t$  in Eq. (2.61) is selected by the CFL condition

$$\Delta t = CFL / \max \left( \frac{H_{i,k+1/2}}{\phi} \right) \quad (2.65)$$

At the end of a gravity step, demonstrated in Fig. 2.17b, the gas and liquid segments in each gridblock are combined to form a new overall molar density and overall mole fraction of component  $i$  in gridblock  $k$  by

$$C_{i,k} = \sum_{j=1}^{N_{seg}} z_{i,j,k} \rho_j S_j \quad , \quad (2.66)$$

$$z_{i,k} = C_{i,k} / \sum_{j=1}^{n_c} C_{j,k} \quad . \quad (2.67)$$

The approach described will always conserve mass as the numerical scheme of Eq. (2.61) conserves the volume of each segment and each segment contains a fixed number of moles determined from the initial state of the gravity line. Furthermore, the CPU requirement of the pseudo-immiscible gravity step is greatly reduced relative to the fully compositional approach, as the gridblocks associated with a gravity line only are flashed at the very beginning of the segregation step.

In the following section we compare the proposed approach with results of simulations performed with the commercial finite difference based simulator, E300. The compositional streamline simulator, CSLS, used in the calculation examples is a modified version of the black-oil simulator, 3DSL, initially developed by Batycky (1997). All calculation examples make use of the Peng-Robinson equation of state to predict phase behavior and the Lohrenz-Bray-Clark correlation to predict phase viscosities.

### 2.3.4 Calculation examples

For all calculation examples, described in the following subsections, the reservoir fluid description given in Table 2-6 was used

Table 2-6: Fluid description used in calculation examples ( $T_{res} = 387.45$  K)

	$P_c$ (atm)	$T_c$ (K)	$\omega$	$M_w$	$Z_c$	$x_{oil}$	$y_{sep}$
$N_2/C_1$	44.61	189.5	0.0085	16.16	0.2898	0.4630	0.8027
$CO_2$	71.95	304.2	0.2280	44.01	0.2706	0.0164	0.0255
C2-C5	39.89	387.6	0.1673	45.57	0.2759	0.2052	0.1582
C6-13	32.58	597.5	0.3861	117.74	0.2567	0.1911	0.0136
C14-24	17.22	698.5	0.8078	248.83	0.2197	0.0811	0
C25-80	11.39	875.0	1.2314	481.52	0.1825	0.0432	0

0						
0.11883	0					
0.00071	0.15	0				
0.000778	0.15	0	0			
0.01	0.15	0	0	0		
0.011	0.15	0	0	0	0	

The fluid description is a 6 component representation of the compositional analysis given in Table 2-7. Throughout the calculation examples, the reservoir temperature was kept constant at 387.45 K. At this temperature the saturation pressure of the reservoir fluid is 220.2 atm. Two injection compositions are used: a separator gas given in Table 2-6, and pure  $CO_2$ . The minimum miscibility pressure (MMP) for injection of the separator gas is 324 atm whereas the MMP for injection of pure  $CO_2$  is 247 atm. Simple quadratic Corey type relative permeability functions were used to determine the phase mobilities.

We present the displacement calculations according to their increasing degree of complexity to gradually build confidence in the predictions of CSLS. The examples include:

- 1D displacement to compare the prediction of local displacement efficiencies predicted by CSLS and E300.

- 2D vertical displacement for a homogeneous porous media with  $k_z = 0.1 k_x$ .
- 2D vertical displacement in a heterogeneous porous media with  $k_z = 0.1 k_x$ .
- 3D quarter five spot displacement in an isotropic heterogeneous porous media.
- 3D five spot pattern in an isotropic heterogeneous porous media.

Table 2-7: Compositional description used for reservoir fluid characterization.

Name	Mole fraction	Name	Mole fraction	M <sub>w</sub> (g/mole)	ρ (g/cm <sup>3</sup> )
N <sub>2</sub>	0.0045	C7	0.0377	92	0.7294
CO <sub>2</sub>	0.0164	C8	0.0428	106	0.7509
H <sub>2</sub> S	0.0000	C9	0.0270	120	0.7739
Methane	0.4585	C10	0.0169	137	0.7835
Ethane	0.0715	C11+	0.1658	288	0.8835
Propane	0.0674				
i-Butane	0.0084				
n-Butane	0.0311				
i-Pentane	0.0103				
n-Pentane	0.0165				
Hexane	0.0252				

### 2.3.4.1 1D Displacement calculation

In the first calculation example the reservoir fluid is displaced by the separator gas at an injection pressure below the MMP. The injection pressure is set at 225 *atm*, and hence the displacement process is sub-miscible. The simulations were performed with 100 grid blocks. Fig. 2.18 reports the production history for the 1D displacement in terms of the recovery of OOIP and the gas-oil ratio (GOR) as a function of pore volumes injected (PVI). Fig. 2.18 shows excellent agreement between the recovery predictions for the two simulators, whereas small differences are found for the calculated gas-oil ratios. The ultimate recovery predicted by both simulators (~80%) is, as expected for a sub-miscible displacement, well below 100%. However, this simple initial test confirms that the local displacement efficiencies predicted by the simulators are in agreement prior to the analysis of more complicated displacement calculations.

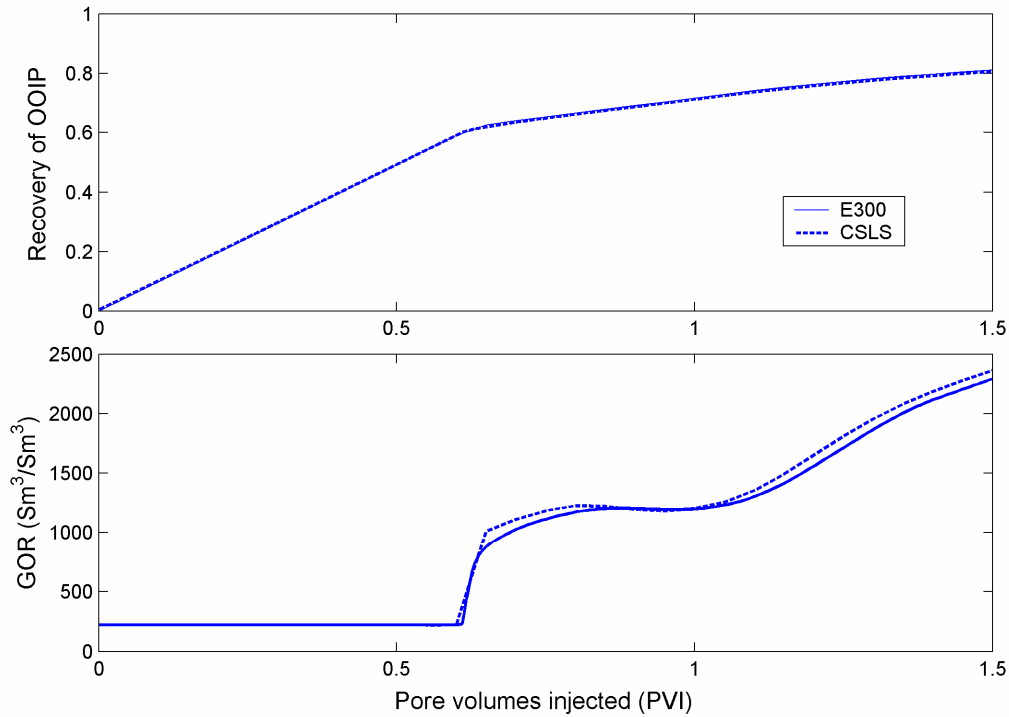


Fig. 2.18: 1D displacement. Recovery and gas-oil ratio predicted by CSLS and E300

### 2.3.4.2 2D Homogeneous displacement

In the second calculation example we displace the reservoir fluid by the separator gas at a pressure above the MMP. The 1000 gridblock vertical slice, representing the porous media, measures 100x10x1 meters with  $k_x = 50 \text{ mD}$  and  $k_z = 5 \text{ mD}$  and a porosity of 0.3.

The separator gas is injected over the entire left hand side of the vertical slice at a constant rate of  $1.5 \text{ Rm}^3/\text{day}$  corresponding to a front velocity of approximately  $1 \text{ m/day}$ . The producer is completed in 1 gridblock only, at the lower right hand side of the domain and is operated at a bottom-hole pressure of  $325 \text{ atm}$ . Hence, the pressure anywhere in the domain will remain above the MMP throughout the displacement.

Fig. 2.19 compares the distribution of the gas phase saturation after 100 and 200 days of injection (0.5 and 1.0 PVI) as predicted by CSLS and E300. Both simulators predict the formation of a gravity tongue as the low density injection gas propagates along the domain. Small differences between the saturation distributions after 100 days are noticed at the front of the displacement. This may be due to the time step selection for pressure-solves/gravity-steps in the streamline method as addressed in the discussion section. Also, small differences are observed in the column of gridblocks containing the production well. The difference can be attributed to the numerical smearing of the displacement front in the FD formulation of the displacement problem used by E300.

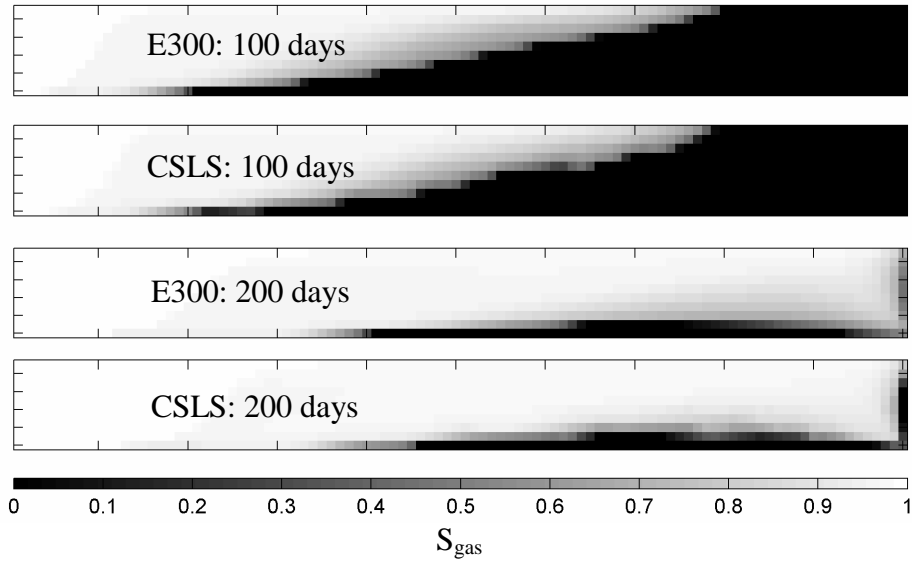


Fig. 2.19: Comparison of gas saturation distribution for 2D homogeneous and anisotropic displacements (100 days = 0.5 PVI and 200 days = 1.0 PVI)

In general, we observe good agreement between the spatial locations of the gas predicted by the two simulation approaches. A comparison of the predicted recovery and producing gas-oil ratios is shown in Fig. 2.20. For this calculation example, the streamline approach predicts slightly higher ultimate recovery than the FD simulation as a result of a slightly lower GOR after the gas breaks through to the producer.

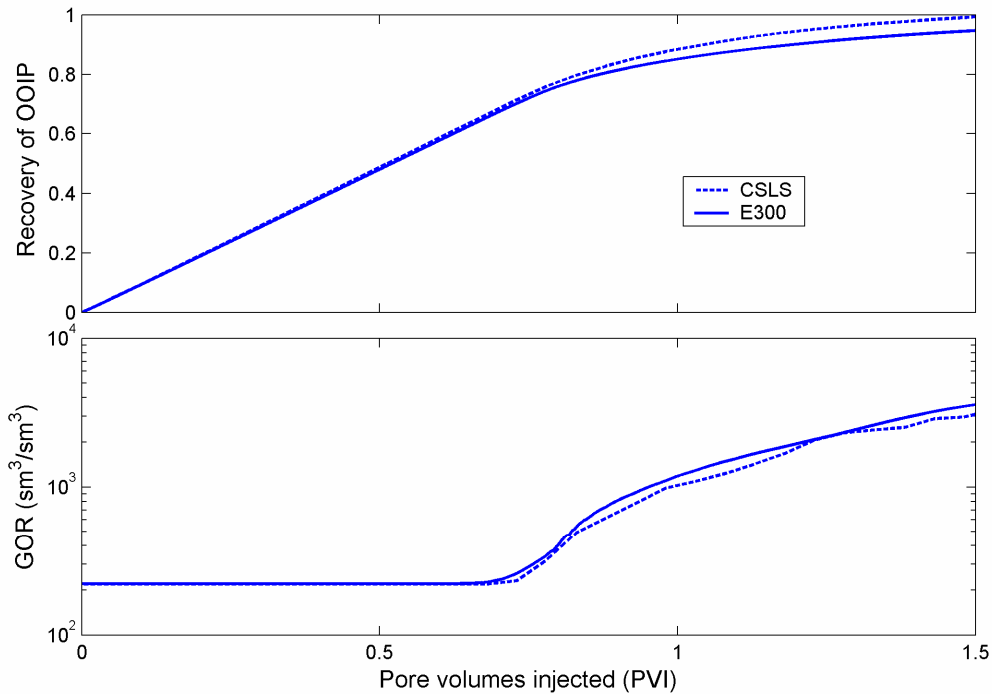


Fig. 2.20: Oil recovery and gas-oil ratio for homogeneous displacement (E300 and CSLS)

### 2.3.4.3 2D Heterogeneous displacement

In the third calculation example, a heterogeneous permeability field, shown in Fig. 2.21, was used with  $k_z = 0.1 \cdot k_x$ .

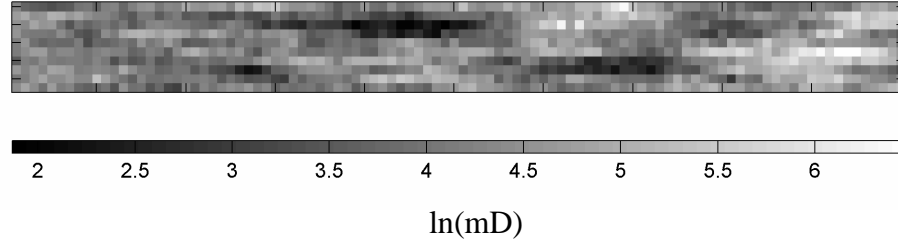


Fig. 2.21: Permeability field,  $\ln(K)$ , for 2D displacement.

The average ( $k_x$ ) permeability is 90 *mD* with a variance of 6000. In this example the reservoir fluid was displaced by pure  $\text{CO}_2$  at near miscible conditions. As in previous example the injector is completed over the entire left-most column and the producer is completed in the lower right hand corner.  $\text{CO}_2$  was injected at a rate of 1.5  $\text{Rm}^3/\text{day}$ , and the producer was operated at a bottom-hole pressure of 225 *atm*.

Fig. 2.22 shows the gas saturation maps after 50 and 100 days (0.25 and 0.5 PVI) as predicted by CSLS and E300. At early times, the injected  $\text{CO}_2$  invades the porous media in a more piston like manner than in the homogeneous case, due to a lower density contrast as well as to the redirection of fluids caused by the heterogeneity. The combined effect results in a better sweep of the lower portion of the reservoir. The redirection of the gas phase is more pronounced after 100 days of injection, where gas from the top of the formation flows downwards through a high permeable zone. Again, we see good agreement between the saturation distributions predicted by CSLS and E300.

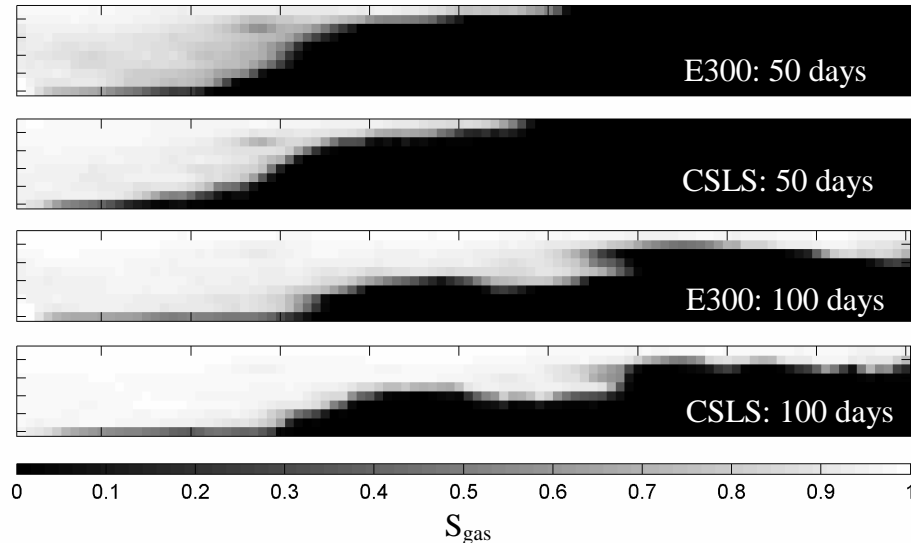


Fig. 2.22: Gas saturation for 2D heterogeneous displacements (0.25 PVI and 0.5 PVI)

The corresponding production history of the two simulations is shown in Fig. 2.23. After gas breakthrough, the recovery predicted by CSLS is slightly higher than that predicted by E300. For this displacement, the difference in the predicted recovery is due to numerical diffusion in the FD simulation. Numerical diffusion acts to smear the displacement front reducing the local displacement efficiency relative to that predicted by the streamline approach, while at the same time marginally delaying the breakthrough of the injected gas.

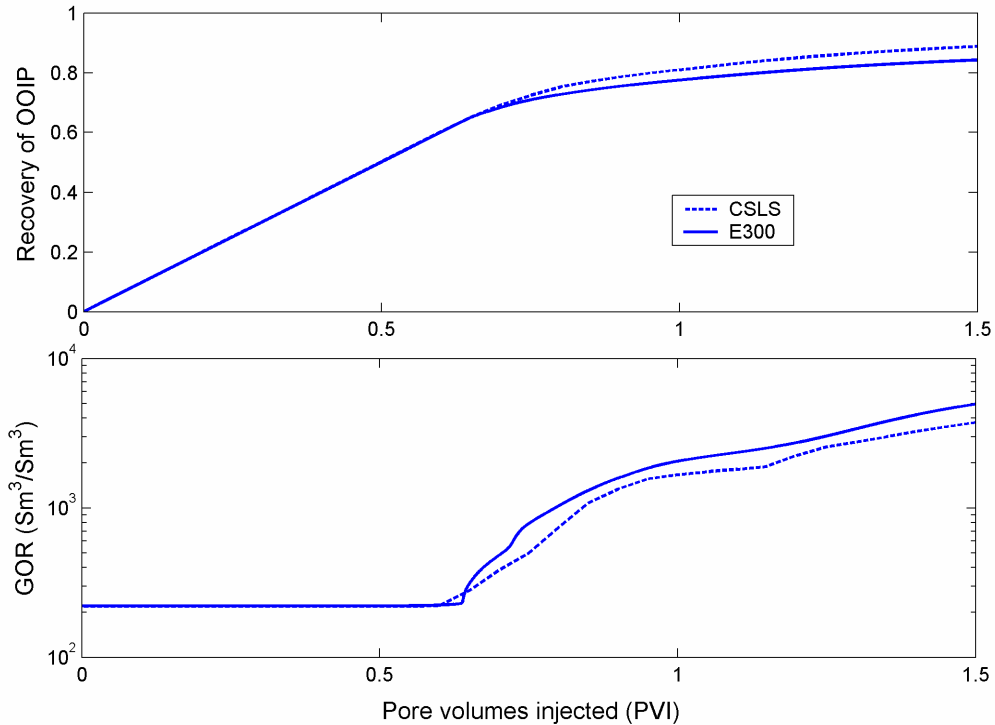


Fig. 2.23: Comparison of recovery and gas-oil ratio for heterogeneous 2D displacement.

#### 2.3.4.4 3D Quarter five spot

Next, CSLS was tested on a 3D quarter five spot pattern with 25000 (50x50x10) gridblocks. The dimensions of each gridblock are  $2 \times 2 \times 2m$  with a porosity of 0.3. The average  $k_x$  permeability is  $90 mD$  with a variance of 11000. The injector and producer were completed over the entire column of the domain. In this example  $CO_2$  was injected at a rate of  $60 Rm^3/day$ , and the producer was operated at a bottom-hole pressure of  $225 atm$ . Fig. 2.24 shows the gas saturation in 3 horizontal slices of the domain (layers 1, 5 and 10) predicted by CSLS and E300 after 300 days (0.3 PVI) of injection.

The predicted saturation distributions are found to be in excellent agreement with only minor variations in local displacement efficiency attributed the different level of numerical diffusion in the two simulation approaches. Fig. 2.25 shows the predicted recovery and producing GOR for the displacement. The agreement of the production history follows that of the saturation distributions and only minor differences are seen for the predicted recovery after 1.5 PVI.

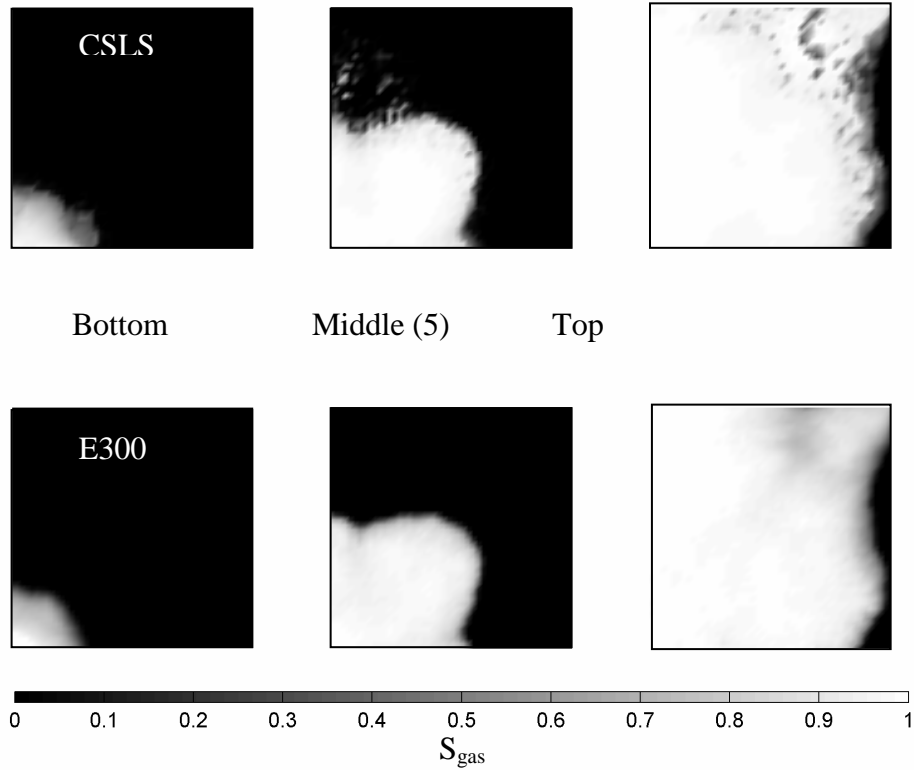


Fig. 2.24: Gas saturation distribution for 3D heterogeneous quarter five-spot (0.3 PV)

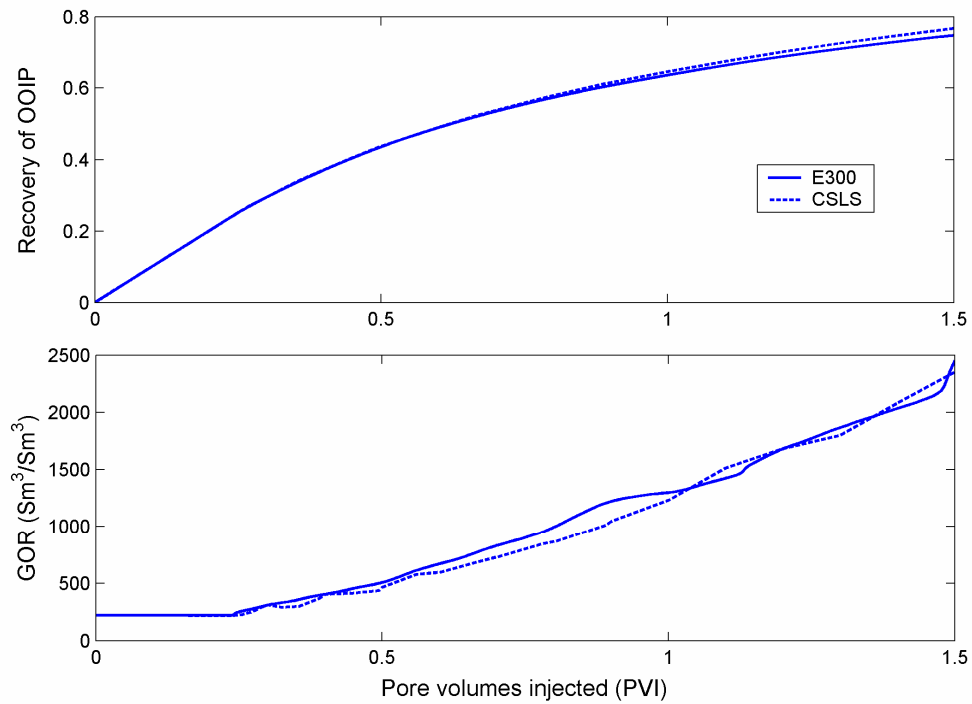


Fig. 2.25: Comparison of recovery and gas-oil ratio for for 3D heterogeneous quarter five-spot.

### 2.3.4.5 3D Five spot

In the final example calculation, the reservoir fluid is displaced by pure CO<sub>2</sub> at near-miscible conditions. The 3D permeability field from previous example is used for a five-spot pattern with an injector located in the middle of the domain and producers located at each corner. All wells are completed over the entire column of the reservoir. CO<sub>2</sub> is injected at 60 Rm<sup>3</sup>/day and the production wells are operated at bottom-hole pressures of 225 atm. The gas saturation distribution after 0.1 PVI (100 days) and 0.2 PVI (200 days) are compared for 3 areal slices in Fig. 2.26 and Fig. 2.27. Fig. 2.26 is a snapshot of the displacement process just before the gas arrives at one of the producers, whereas the gas front has reached two producers in Fig. 2.27. Due to the significant segregation of fluids, the lower portion of the formation is hardly contacted by the injected gas when the top layer breaks through to the producer. Consequently, the ultimate recovery of the initial oil will be relatively low, as Fig. 2.28. Fig. 2.28 reports the recovery of the original oil in place and as well as the producing GOR. At 1.5 PVI as little as ~50% of the oil is produced. As in the previous calculation examples, only marginal differences in the front locations as well as in the predicted production history are observed.

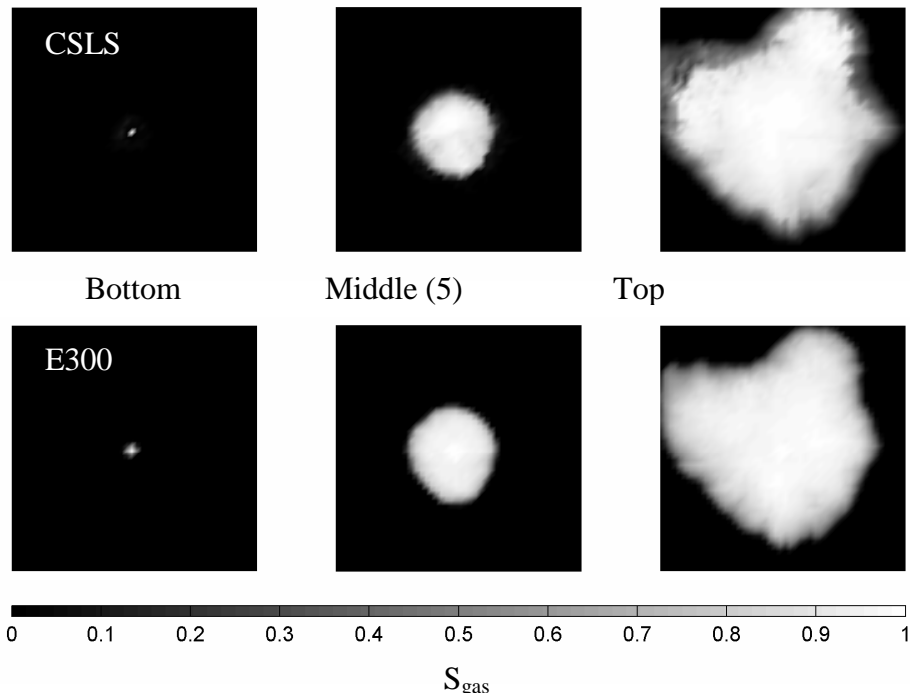


Fig. 2.26: Gas saturation after 100 days of injection (0.1 PVI)

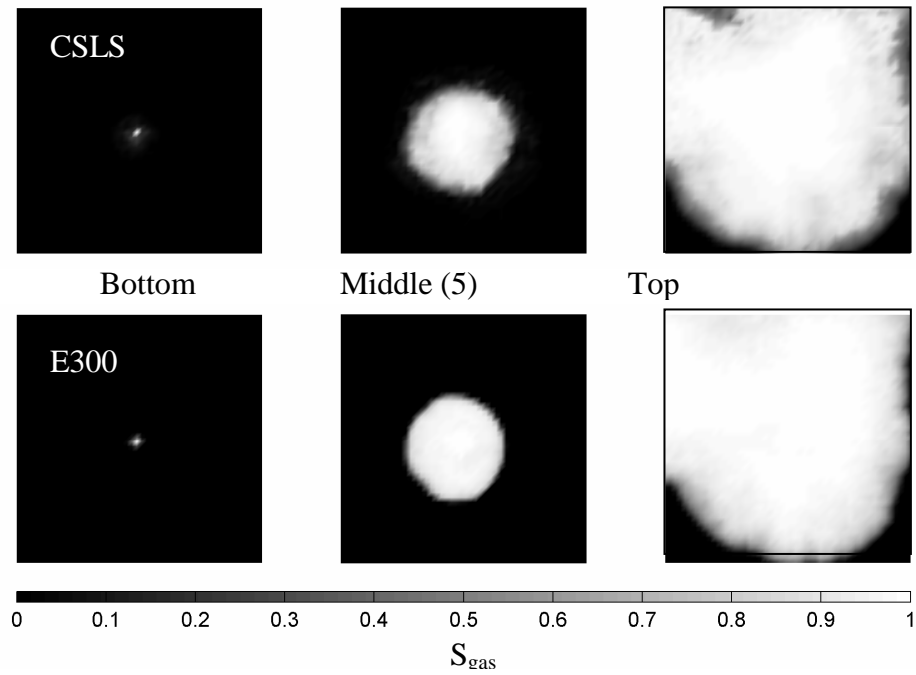


Fig. 2.27: Gas saturation after 200 days of injection (0.2 PVI)

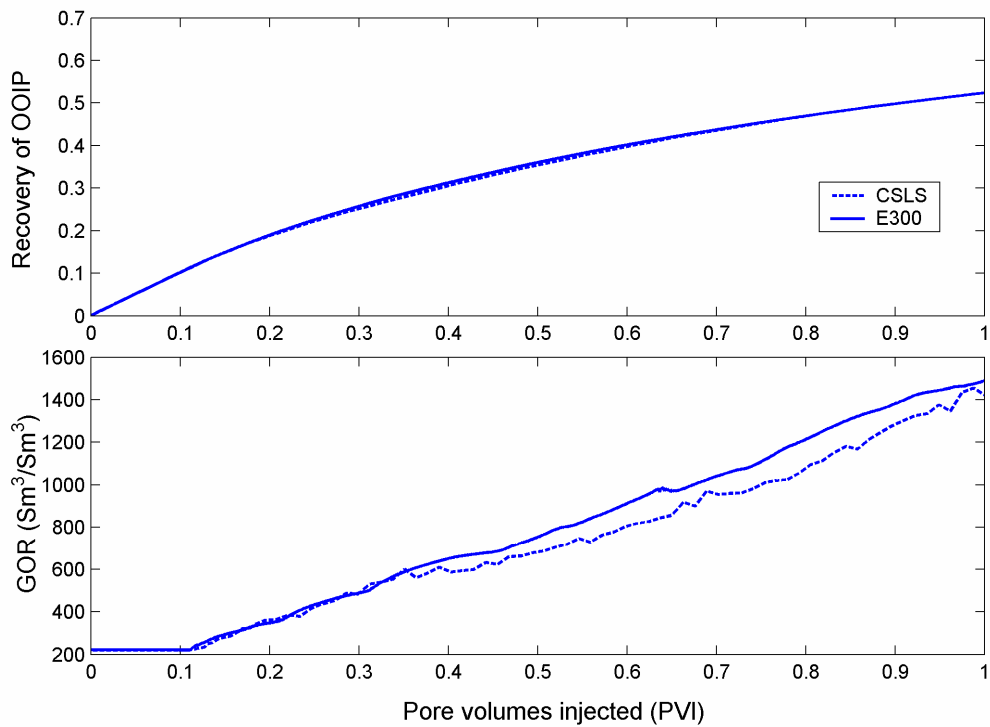


Fig. 2.28: Comparison of oil recovery and gas-oil ratio for five-spot simulation.

### 2.3.5 Results and discussion

A summary of the CPU requirements for the presented calculation examples is given in Table 2-8 for the streamline approach and for the FD approach using implicit pressure explicit saturation (IMPES) and adaptive implicit (AIM) modes.

Table 2-8: Summary of CPU requirements in seconds (2.8 GHz)

Displacement	$N_{\text{gridblock}}$	E300 - AIM	E300 - IMPES	CSLS
2D – homogeneous	1000	N.A.	271 sec	22 sec
2D – heterogeneous	1000	N.A.	398 sec	26 sec
3D – quarter five spot	25000	7457 sec	59353 sec	2701 sec
3D – 5-spot	25000	3356 sec	36568 sec	1680 sec

For the 2D example calculations the implementation of the presented approach in our research code, CSLS, required 12-15 times less CPU time than the equivalent finite difference based IMPES simulation. For the larger calculation examples, CSLS required 22 times less CPU time than the FD IMPES simulation and 2-3 times less CPU time than the equivalent FD AIM simulation. A potential for additional speed-ups are available through adaptive mesh refinement along streamlines (Mallison *et al.* 2003).

In the previous sections we have presented and tested a new method, based on operator-splitting, for including gravity effects in compositional streamline simulation. In the presented calculation examples the time between successive gravity steps was estimated based on the number of gridblocks invaded in the horizontal direction. If more than 5 additional gravity lines were required for a 2D calculation and more than 50 additional gravity lines were needed in a 3D calculation, the subsequent time step was reduced by a factor 2. If this constraint was not violated the time step was doubled. A more sophisticated framework for selecting the length of time steps between successive pressure updates/gravity steps has been suggested by Ichiro *et al.*(2003) but has not yet been implemented and tested in CSLS.

Traditional methods for recording initial conditions along streamline and reassigning compositions on the pressure grid after a convective/gravity step introduce smearing of saturation fronts as well as mass balance errors. If frequent mapping to and from streamlines is required, special care must be taken to reduce these diffusive errors through the use of higher-order accurate mapping as discussed by Mallison *et al.* (2003)

Extension of the presented approach to three-phase flow modeling is straight forward. The presence of a third phase can add a maximum of  $n_g$  segments to the problem, where  $n_g$  is the number of gridblocks along a gravity line. Once the average phase properties are calculated, any 3-phase black-oil formulation can be used to segregate the fluids.

### 2.3.6 Conclusions

The analysis and examples reported lead to the following conclusions.

1. A new approach for including effects of gravity in compositional streamline simulation is proposed and demonstrated.
2. The new approach offers a consistent and efficient method for extending the applicability of compositional streamline simulation to EOR displacements where gravity segregation can play an important role.
3. The implementation of the pseudo-immiscible approach introduces a marginal increase in the overall CPU requirement, as flash calculations are required only to generate the initial state along a gravity line.
4. The pseudo-immiscible approach is demonstrated to produce performance predictions in excellent agreement with a commercial finite difference based simulator.
5. Through a series of calculation examples, the compositional streamline approach has been demonstrated to be up to 22 faster than equivalent IMPES simulations with a finite difference based simulator.

The presented approach is easily extended to three-phase flow problems without significant increase in CPU requirements.

### 2.3.7 Nomenclature

$C_i$  : overall molar density of component  $i$   
 $C_{i,k}$ :  $C_i$  in gridblock  $k$   
 $D$  : depth  
 $f_j$  : fractional flow of phase  $j$   
 $F_i^*$  : velocity scaled total convective flux of component  $i$   
 $g$  : gravity constant  
 $G_i$  : gravity driven flux of component  $i$  (compositional formulation)  
 $H_i$  : gravity driven flux of component  $i$  (black-oil formulation)  
 $k$  : absolute permeability  
 $k_{rj}$  : relative permeability of phase  $j$   
 $k_z$  : absolute permeability in  $z$ -direction  
 $n_c$  : number of components  
 $n_p$  : number of phases  
 $p$  : pressure  
 $S_j$  : saturation of phase  $j$   
 $S_{i,k}^g$ : saturation of gas segment  $i$  in gridblock  $k$   
 $t$  : time  
 $u_j$  : velocity of phase  $j$

$u_z$  : total velocity in  $z$  direction  
 $w_{ij}$  : mass fraction of component  $i$  in phase  $j$   
 $x_{ij}$  : molefraction of component  $i$  in phase  $j$   
 $z$  : distance  
 $z_{i,k}$  : molefraction of component  $i$  in gridblock  $k$

Greek symbols

$\phi$  : porosity  
 $\lambda_t$  : total mobility  
 $\lambda_g$  : total gravity mobility  
 $\mu_j$  : viscosity of phase  $j$   
 $\mu_{i,k}^\alpha$  : viscosity of segment  $i$  of phase  $\alpha$  in gridblock  $k$   
 $\rho_j$  : molar density of phase  $j$   
 $\rho_{i,k}^\alpha$  : molar density of segment  $i$  of phase  $\alpha$  in gridblock  $k$   
 $\rho_{mj}$  : mass density of phase  $j$

## 2.4 Streamline simulation of enhanced condensate recovery

Compositional finite difference simulation is widely used to simulate gas injection processes in condensate reservoirs. However, this method has limitations: it is adversely affected by numerical dispersion, and resolution in the fluid and reservoir heterogeneity fields must be decreased for reasonable computational times. The speed up factors and reduced numerical dispersion associated with streamline simulation make this method an attractive alternative to finite difference methods. Nevertheless, there are also limitations associated with streamline simulation. The primary limitation of streamline simulators is that they do not model crossflow effects. In certain reservoirs, crossflow is an important recovery mechanism, and the inability to model these physical phenomena will result in inaccurate results. In order to effectively exploit the power of streamline based simulators, the user must recognize under which conditions omission of crossflow phenomena is valid.

This section presents a detailed analysis demonstrating the applicability of compositional streamline simulation of gas injection in a condensate reservoir. Analysis of crossflow mechanisms through the use of dimensionless numbers is used to determine the dominant flow forces in these systems. A systematic simulation study comparing the results of the streamline method against one that incorporates crossflow mechanisms demonstrates the validity in exclusion of crossflow when simulating these systems. Computation speeds of the streamline method were orders of magnitude faster than finite difference methods. To conclude this analysis, applications of compositional streamline simulation for reservoir management are presented.

Application to a specific class of reservoirs is presented in this study. Gas condensate reservoirs represent a small, but growing fraction of reserves in the world petroleum supply. This study provides the foundation for demonstrating the relevance of streamline methods in simulating field scale, compositionally driven displacements.

Gas injection for enhanced recovery is one of the most widely used and efficient methods for enhanced hydrocarbon recovery. In zones contacted by the gas, local displacement efficiencies of 80-90% can be achieved (Lake, 1989). Such schemes are inherently compositional. As injection gas propagates through the reservoir, components in the reservoir fluid and the injected fluid mix, altering properties of the fluid. In order to evaluate the performance of gas cycling processes, compositional simulation is necessary. Efficiency of enhanced recovery schemes is dependent on two factors (Pande *et al.*, 1989):

1. local displacement efficiency, which is controlled by phase behavior of mixtures of injection gas and fluid in the reservoir. As a result, the fluid description must adequately capture fluid behavior. Condensate behavior is sensitive to heavy components, (McCain, 1994). To model retrograde behavior in a gas injection scheme, high resolution is required in the heavy end of the fluid description.
2. global sweep efficiency, which is controlled by reservoir heterogeneity. High mobility injection gas will preferentially flow through high permeability paths in the reservoir, efficiently displacing condensate in these regions while bypassing condensate in low permeability zones. Extremes in permeability have a significant impact in determining flow of fluids in the subsurface. To predict flow accurately in a reservoir, these outliers must be retained.

Compositional finite difference simulation is the conventional way to model these systems. In this method, a material balance for each component, over each block, must be calculated. Included in this calculation is at least one flash per grid block per time step. Numerical diffusion and grid orientation effects adversely affect finite difference methods. For large models or complex fluid descriptions, computational times are prohibitively slow. The time step size in fine scale models, calculated using an implicit pressure, explicit saturation (IMPES) method, is limited by the Courant-Fredrichs-Levy stability condition; smaller dimension grid blocks reduces the maximum time step length. Moreover, nonlinearities in the governing equations, introduced by an equation-of-state fluid description, may further reduce time step size (Aziz *et al.*, 2002). In order to obtain results in a reasonable time, simplifications in fluid description and reservoir heterogeneity are necessary, potentially rendering results inaccurate.

An alternative to finite difference simulation is compositional streamline simulation. Streamline methods for simulating reservoir displacements have been applied in the oil industry for several decades. Recent advances in these methods (Batycky *et al.*, 1997; Thiele *et al.*, 1996; Crane *et al.*, 2000; Jessen *et al.*; 2002), coupled with developments in reservoir characterization have resulted in more widespread application in simulating displacement processes, as demonstrated by Grinestaff *et al.* (2000), Samier *et al.* (2001), and Baker *et al.* (2001).

Streamline simulation is an IMPES method, which solves pressure implicitly and then computes streamlines based on this pressure solution. Governing transport equations are recast in terms of a time of flight variable, reducing the physics of the displacement to 1D

solutions along streamlines, decoupling the transport equations from the underlying geological grid. Propagating components along streamlines increases stability, allowing for large time steps. Streamlines are periodically updated to account for changing mobility or field conditions. When this method is coupled with an efficient algorithm for analytical calculation of the displacement, computation times are reduced by orders of magnitude (Ermakov, 2000; Jessen *et al.*, 2001). If Riemann conditions are assumed, self similarity of the solution allows computation of the solution only once, with mappings at the time of interest. The faster computations afforded by the streamline method allow more detailed representation of fluid and reservoir heterogeneity.

The principle limitations of the streamline method is the inability to model flow between streamlines and neglect of complex physical phenomena such as capillarity, changing well conditions, diffusion, viscous and gravity crossflow. In cases where gravity effects are considered by means of operator splitting, computational times in a gravity-dominated displacement are reduced due to streamline retracing. Determining which phenomena dominate flow is key to effective use of this method. Sam-Olibale (2002) demonstrated that streamline methods are most applicable in convection dominated flows, where heterogeneity is the predominant factor governing flow.

In this section, simulation of a gas injection scheme in a condensate reservoir using compositional streamline simulation with analytical solutions is presented as an alternative to compositional finite difference methods. To demonstrate this, the following approach was implemented:

1. Establish the validity in neglecting complex physics involved in gas injection in condensate reservoirs.
2. Demonstrate the viability of the streamline method for simulating gas injection schemes in condensate reservoirs through a detailed simulation study that compares results of compositional streamline simulation against finite difference simulation.
3. Demonstrate applications of compositional streamline simulation for reservoir management.

#### **2.4.1 Dominant flow mechanisms in condensate reservoirs**

Condensate reservoirs are a unique class of reservoirs, to which compositional streamline simulation is well suited. In this section, a discussion on condensate reservoirs and magnitude of forces governing flow in these reservoirs is presented. A schematic of the thermodynamic path a condensate reservoir follows is presented in Fig. 2.29.

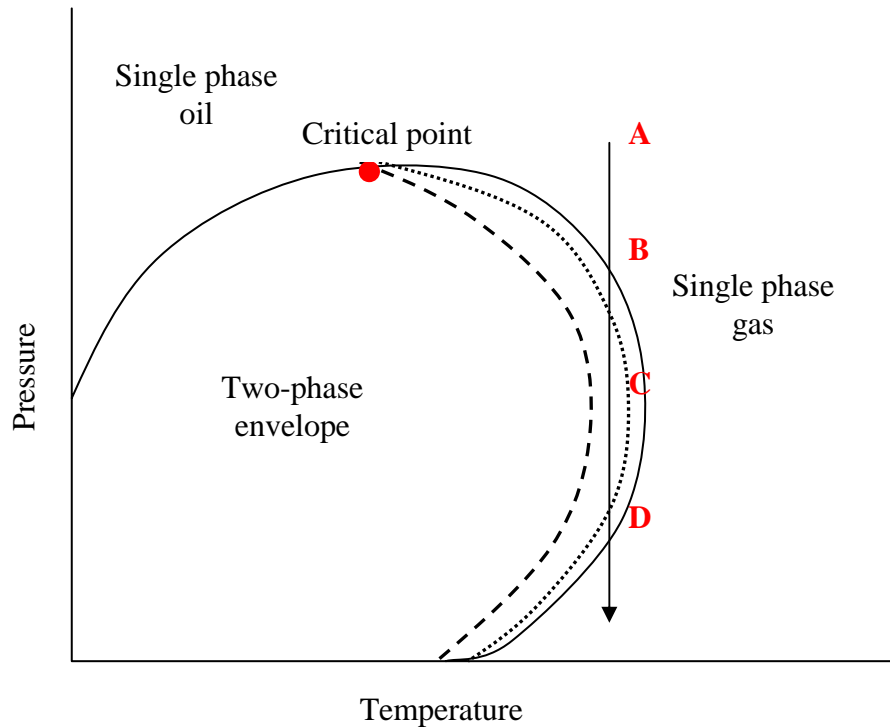


Fig. 2.29: Thermodynamic path followed by depletion of a condensate reservoir.

Initially the reservoir is above dewpoint pressure, and fluid in the reservoir exists as a single-phase (A). As the reservoir is produced, reservoir pressure declines and reaches dew point pressure (B). Once the dew point pressure is reached, liquid begins to condense. The heaviest components drop out first, followed by components of decreasing molecular weight. As the pressure decreases further, more liquid condenses and the condensate saturation increases. Below the critical condensate saturation, condensate is immobile. Once the critical saturation has been reached, condensate is mobile. In most reservoirs, condensate dropout does not exceed critical saturation. This condensate is trapped and will not be recovered through primary means. At a certain pressure, maximum liquid drop out is reached (C). Upon further pressure decrease, condensate re-vaporization occurs (D), with components vaporizing in the reverse order in which they dropped out. In typical field operations, this pressure is below the economic life of the field, and this stage of re-vaporization will not be reached.

One of the most effective methods of recovering dropped out condensate is gas injection. In this process, immobile condensate is vaporized into the mobile injection gas phase. Melean *et al.* (2001) demonstrated that CO<sub>2</sub> is very effective at recovering condensate by reducing interfacial tension and by vaporizing condensate into the mobile phase.

The primary limitation of streamline simulators in modeling fluid flow in a reservoir is their inability to account for transfer of fluid between streamlines; physically, this translates to an inability to incorporate crossflow effects. In the streamline method, flow along each streamline is independent of adjacent streamlines. In some reservoirs, crossflow can significantly impact sweep efficiency. In these systems, if the simulator is unable to capture

these effects, predictions of recovery may be inaccurate.

Crossflow is a result of gradients in the media. There are primarily four types of crossflow that drive fluids in the subsurface (Sam-Olibale, 2002):

1. Viscous, due to viscosity differences between injection and reservoir fluids, creating a pressure gradient in the horizontal direction.
2. Gravity, due to density differences between injection and reservoir fluids, creating crossflow in the vertical direction.
3. Capillary, due to interfacial tension differences between fluids. Heterogeneity distribution in the reservoir will control the degree of capillary crossflow in the transverse and longitudinal directions (Yokoyama *et al.*, 1981).
4. Dispersion, dependent on concentration gradients, local velocity gradients and mechanical mixing within the pores (Mahadevan *et al.*, 2002).

Many researchers have developed scaling relations for comparing magnitudes of crossflow forces in the subsurface. In the following section, scaling relations developed by various researchers were used to assess the relative magnitudes of forces that drive flow in a reservoir.

#### 2.4.1.1 Capillary crossflow

In a miscible displacement, capillary effects are negligible. For critical fluid systems like gas-condensates, interfacial tensions are low. Hamon (1986) classifies capillary dominated displacements as those with  $N_B < 0.05$ , where  $N_B$  is defined as:

$$(2.68) \quad N_B = \frac{\Delta\rho g L^2}{\sigma} .$$

Typical parameters encountered in a field scale displacement in a condensate system are listed in Table 2-9 (Melean *et al.*, 2001).

Table 2-9: Parameters used to calculate expected  $N_B$  in a typical condensate reservoir.

	High	Low
$\Delta\rho$ (kg/m <sup>3</sup> )	50	10
L (m)	2000	1000
$\sigma$ (dynes/cm)	1	0.1
$N_B$	1.92×10 <sup>12</sup>	9.62×10 <sup>11</sup>

Typical  $N_B$  values calculated for a condensate reservoir are  $\gg 0.05$ , suggesting that flow in these systems is far from the capillary dominated regime.

### 2.4.1.2 Gravity-driven crossflow

Gravity-dominated displacements are classified using the following relation developed by Zhou *et al.* (1994):

$$N_{gv} = \frac{\Delta\rho g L k_{avg}}{H v \mu_{res}} , \quad (2.69)$$

where  $N_{gv}$  is the characteristic time ratio for transverse fluid flow due to gravity to fluid flow in the horizontal direction due to viscous forces. Typical ranges for parameters in these systems are listed in Table 2-10.

Table 2-10: Parameters used to calculate expected  $N_{gv}$  in a typical condensate reservoir.

	High	Low
$\Delta\rho$ (kg/m <sup>3</sup> )	50	10
$k_{avg}$ (md)	500	50
H (m)	40	20
v (m/d)	0.5	0.5
$\mu_{res}$ (cP)	0.025	0.01
L (m)	2000	1000
$N_{gv}$	84.7	4.2

$N_{gv}$  is dependent on the velocity of the displacement, vertical communication and reservoir thickness, as well as on the density difference between fluids. Gravity effects will be exacerbated for long, thin reservoirs with good connectivity and slow displacement velocities.

### 2.4.1.3 Viscous cross flow

For viscous dominated cross flow to occur, viscous forces must be much greater than capillary and gravity forces. Zhou *et al.* (1994), classified a viscous dominated regime when:

$$\frac{(N_{gv} + N_{cv})M}{1 + M} \ll 1.0 . \quad (2.70)$$

$N_{cv}$  is the characteristic time ratio for transverse fluid flow due to capillary forces to fluid flow in the horizontal direction due to viscous forces, and M is the mobility ratio between injected fluid and reservoir fluid. As discussed previously, capillary forces in miscible displacements are negligible, and Eq. (2.70) reduces to:

$$\frac{N_{gv}M}{1 + M} \ll 1.0 . \quad (2.71)$$

For the range of  $N_{gv}$  values typically encountered in condensate reservoirs, these systems lie in the transition between viscous and gravity dominated cross flow, Table 2-11.

Table 2-11: Range of values of  $(N_{gv}M)/(1+M)$  in a typical condensate reservoir.

	High	Low
$N_{gv}$	84.7	4.24
$M$	1.0	0.8
$(N_{gv}M)/(1+M)$	42.35	1.88

Similar to  $N_{gv}$ , the position in the transition zone is influenced by scale of the system. Slow rate displacements in long, thin reservoirs lie closer to gravity dominated regime.

#### 2.4.1.4 Dispersion

The Peclet number ( $Pe$ ) is commonly used to assess the magnitude of dispersion in a system. This is a ratio of characteristic times for dispersion to characteristic times for convection.

$$Pe = \frac{vL}{\phi K_l} \quad (2.72)$$

For large  $Pe$ , dispersion effects are small, and displacement is convection dominated. In the field scale displacements,  $Pe$  is very large (Table 2-12). For reservoir displacements, convection dominates.

Table 2-12: Parameters used to calculate expected  $Pe$  in a typical condensate reservoir.

	High	Low
$v$ (m/d)	0.5	0.5
$L$ (m)	2000	1000
$\phi$ (fraction)	0.20	0.05
$K_l$ ( $\text{cm}^2/\text{s}$ )	$1 \times 10^{-3}$	$1 \times 10^{-4}$
$Pe$	$5.79 \times 10^4$	$1.16 \times 10^7$

Through analysis of scaling relations, it is confirmed that gravity, capillary and diffusion forces for instigating crossflow are small in a gas condensate reservoir. Omission of these phenomena in the streamline formulation is therefore reasonable. In the following subsection, the validity of these omissions is demonstrated through a simulation study comparing the streamline method with one that incorporates these physical phenomena.

#### 2.4.2 Comparative simulation study

A simulation study comparing the streamline method with the finite difference method is presented in this section. Predicted recovery, gas oil ratio (GOR) and gas saturation distribution in the reservoir were used to compare methods. Results from both methods were

evaluated for a sequence of increasingly complex reservoir systems, starting at a 1D displacement, and gradually working up to a full field scale 3D displacement. The field scale reservoir description is based on a currently producing reservoir, where gas injection scenarios for enhanced condensate recovery were investigated. Permeability and fluid descriptions for each stage of this study were tied back to the full field system.

In this study, results of CSLS, the compositional streamline simulator developed by Jessen *et al.* (2002), based on the streamline simulator developed by Batycky (1997), were compared against Eclipse 300, Schlumberger’s compositional finite difference simulator. An IMPES scheme was used to solve the finite difference system.

#### 2.4.2.1 Reservoir system

The reservoir that this study is based on is a typical carbonate reservoir found in the Western Canadian Sedimentary Basin. Average reservoir properties are summarized in Table 2-13.

Table 2-13: Average reservoir properties of test reservoir.

Initial reservoir pressure (MPa)	36.5
Dewpoint pressure (MPa)	16.8
Reservoir temperature (°K)	375
Average formation thickness (m)	25
Average porosity (%)	10
Average water saturation (%)	10
Average permeability (md)	125

This is a completely dolomitized barrier reefal complex, located at a depth of 3500 m. The feature strikes northwest, with a southwest dip of 25 m/km (Fig. 2.30). Gas is stratigraphically trapped updip (Fig. 2.31), by overlying shales and underlying mudstones. Gas initially in place is 56 BCM, and 6 MM m<sup>3</sup> condensate is predicted to be left in the reservoir at abandonment.

The field is a large continuous feature, covering over 50 sections of land, and it is penetrated by only 16 wells. Pressure transient analysis was performed on all of the wells; permeability was found to range from 40-275 *mD*. All of the wells were logged and cored. Permeabilities derived from this data range from 1×10<sup>-2</sup> to 1×10<sup>3</sup> *mD*. Permeability fields were generated using sequential Gaussian simulation (Deutch *et al.*, 1998), conditioned to log data. Variogram parameters are summarized in Table 2-14.

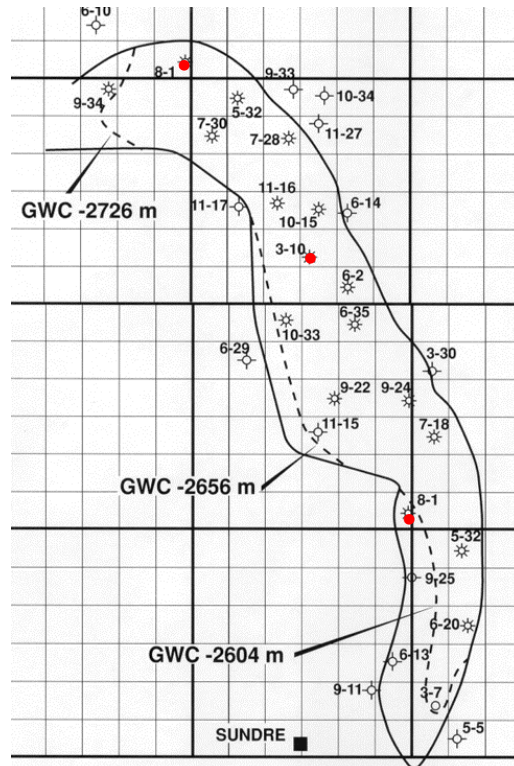


Fig. 2.30: Test reservoir with well locations. Injectors indicated by red dots, producers indicated by open circles.

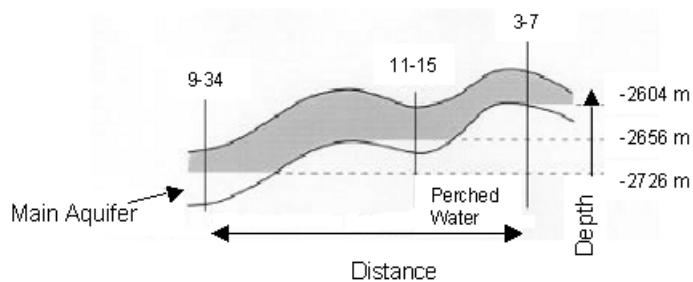


Fig. 2.31: Cross-section of the study reservoir.

Table 2-14: Variogram parameters used to generate permeability realizations.

Nugget	0.2
Angle	0
Radius X	100
Radius Y	100
Radius Z	100

Given that this field is extensively dolomitised, primary depositional facies have undergone extensive diagenesis. In some regions, diagenesis has enhanced reservoir permeability, and in other areas the original matrix structure has been destroyed, reducing permeability. Diagenetic fluids have altered the original correlation structures within a facies; therefore, a sequential Gaussian algorithm is appropriate for generating permeability realizations given this field's geological history.

#### 2.4.2.2 Fluid description

Table 2-15 presents the average composition of the fluid. SPECS, a program for calculating separation and phase equilibrium developed by the Phase Equilibria and Separation Processes Centre in the Department of Chemical Engineering at the Technical University of Denmark, was used to calculate a 13-component Peng-Robinson equation-of-state description of the reservoir fluid. Properties of the characterized fluid are presented in Table 2-16.

Table 2-15: Average fluid composition.

Component	Mol fraction
CO <sub>2</sub>	0.0670
H <sub>2</sub> S	0.3536
N <sub>2</sub>	0.0169
C1	0.3595
C2	0.0790
C3	0.0337
IC4	0.0097
NC4	0.0200
IC5	0.0068
NC5	0.0101
C6	0.0115
C7+	0.0332
MW C7+	113 g/mol
ρC7+	0.9 g/cm <sup>3</sup>

In addition to sensitivity to the heavy components in the fluid, there is a large concentration of H<sub>2</sub>S, requiring a large number of components to adequately capture retrograde behavior. This equation of state model was tuned against a constant volume depletion experiment.

The dewpoint pressure of this fluid is 16800 kPa. In all simulations, the reservoir was initialised at 12000 kPa, below the dewpoint pressure. At initialization, immobile condensate is present everywhere in the reservoir. Maximum liquid dropout is 6.7%, at 14000 kPa. The critical condensate saturation is 20%; dropped out condensate in this system is immobile and the only way to efficiently recover it is through gas injection. For all displacements in this study, the injection fluid was 100% CO<sub>2</sub>.

Table 2-16: Properties of tuned fluid characterization.

Pseudo-component	Mol. Fraction	MW (g/mol)	Tc (°K)	Pc (MPa)	Zcrit	Acentric factor
N <sub>2</sub>	0.0171	28.016	126.2	3.36	0.2895	0.040
CO <sub>2</sub>	0.0576	44.010	304.2	7.29	0.2744	0.228
H <sub>2</sub> S	0.3562	34.076	373.5	8.85	0.2857	0.080
C1	0.3631	16.043	190.6	4.54	0.2737	0.008
C2	0.0798	30.069	304.5	4.82	0.2850	0.980
C3	0.0340	44.096	369.8	4.19	0.2803	0.152
C4	0.0300	58.123	419.6	3.70	0.2737	0.188
C5	0.0171	72.150	465.9	3.33	0.2627	0.241
C6	0.0116	86.177	507.4	2.93	0.2656	0.296
C7	0.0117	94.000	573.9	4.15	0.2631	0.265
C8	0.0126	113.52	648.2	3.25	0.2594	0.344
C10	0.0053	141.52	630.0	3.02	0.2463	0.449
C12	0.0039	190.00	683.2	2.69	0.2373	0.631

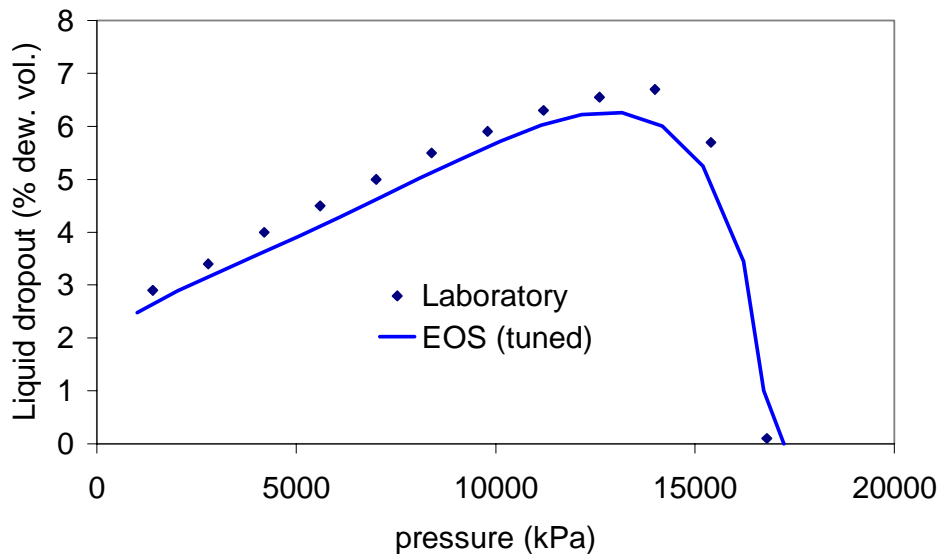


Fig. 2.32: Comparison of tuned 13 component fluid description with laboratory CVD experiment.

### 2.4.2.3 1D Displacement calculation

The analytical solution for this reservoir displacement, calculated using method of characteristics is shown in Fig. 2.33. As the injection fluid propagates through the reservoir, it is clearly shown that condensate is efficiently recovered through a series of vaporizing

shocks. The analytical solution also shows the formation of a condensate bank at the leading edge of the displacement. As components are vaporized by CO<sub>2</sub>, they transfer into the condensate phase as they propagate downstream.

Table 2-17:  $Pe_{Num}$  for finite difference slimtube simulations.

Resolution	$Pe_{Num}$
100	50
500	250
1000	500
5000	2500

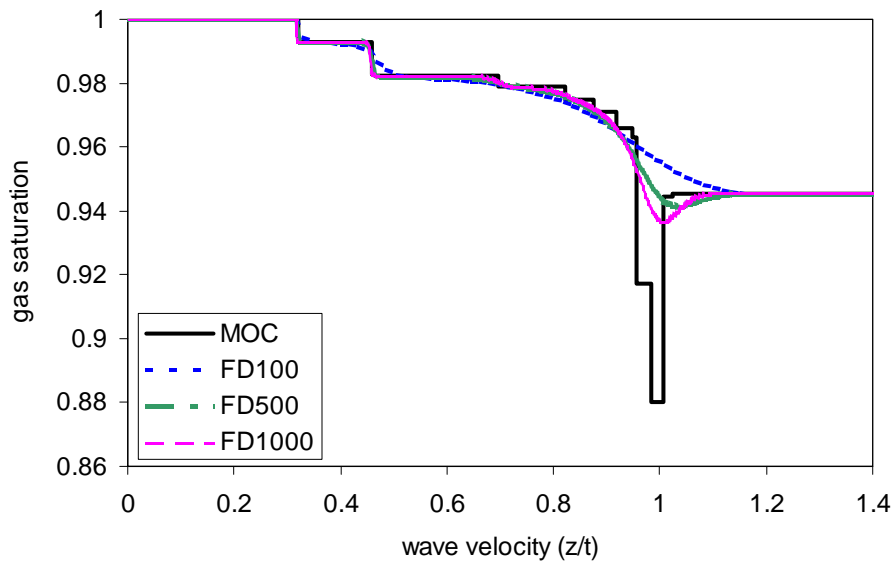


Fig. 2.33 Analytical solution of condensate recovery with 100% CO<sub>2</sub>

A series of finite difference slimtube simulations with resolutions of 100, 500, 1000 and 5000 grid blocks was performed. Fig. 2.33 compares these solutions. Grid block resolutions below 1000 are adversely affected by numerical dispersion. At these resolutions, features of the analytical solution, such as the shocks and the condensate bank are masked by numerical dispersion. As grid block resolution is refined, these features start to become visible. For typical field scale simulations, far fewer grid blocks are modeled between injector and producer.

The numerical 1D solution with dispersion is also presented in Fig. 2.33. When dispersion is incorporated in the 1D solution, good agreement with the low resolution finite difference solution is achieved, demonstrating the sensitivity of this displacement to numerical dispersion. Recall that  $Pe$  represents the ratio of convective forces to dispersive forces, and consequently, large values of  $Pe$  correspond to convection dominated flow. From the finite difference formulation of the dispersion-free conservation equation, Lantz (1971)

demonstrated that the truncation error of a purely convective process is of second order. A finite difference analogue to the  $Pe$  was developed:

$$\frac{1}{Pe_{Num}} = \frac{\Delta\xi}{2} \left[ 1 - \frac{\Delta\tau}{\Delta\xi} \right] . \quad (2.73)$$

Values  $Pe_{Num}$  for the numerical systems investigated are summarized in Table 2-17.

The low values at field scale model resolution indicate the sensitivity of this system to numerical dispersion. To achieve  $Pe_{Num}$  comparable to those calculated in Table 2-12,  $\Delta\tau$  and  $\Delta\xi$  must be very small. Moreover,  $\Delta\tau$  must be less than  $\Delta\xi$  to ensure stability of the solution.

The total mobility of the system as fluids propagate through the reservoir is presented in Fig. 2.34. Mobility variations as the injection gas vaporizes components and moves through the reservoir are small, supporting the assumption that streamlines do not require frequent updates (pressure field varies little in time).

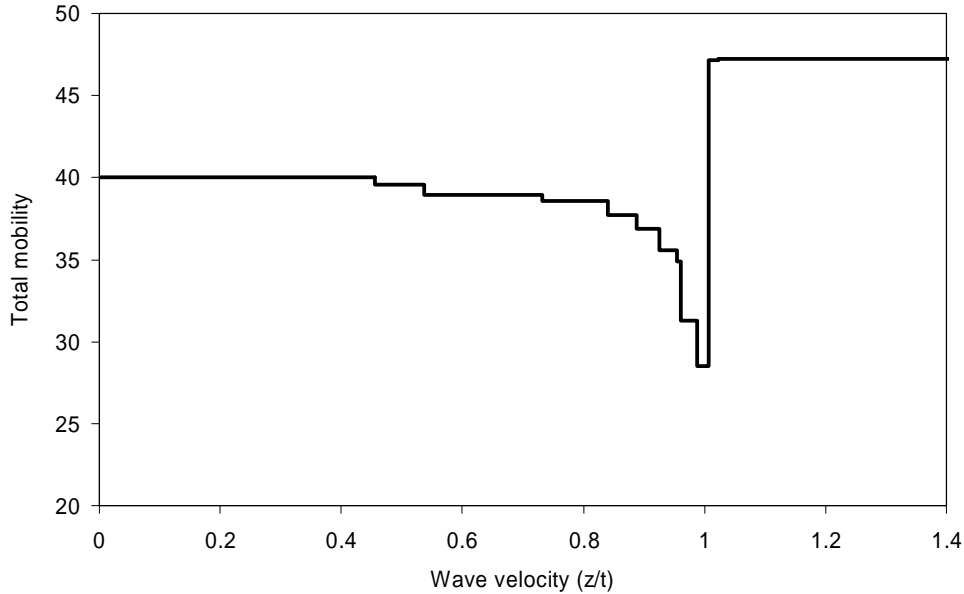


Fig. 2.34: Mobility changes as fluids propagate through reservoir.

#### 2.4.2.4 2D Displacement calculation

In this stage of the study, three finite difference simulations, using identical permeability fields (Fig. 2.35), were performed to assess the magnitude of gravitational effects in this displacement:

- Permeability field oriented vertically, injection at a rate advance of 1.4  $m/d$  (low rate case).
- Permeability field oriented vertically, injection at a rate of advance of 2.8  $m/d$  (high

- rate case).
- Permeability field oriented horizontally, injection at a rate of advance of 1.4 *m/d*.

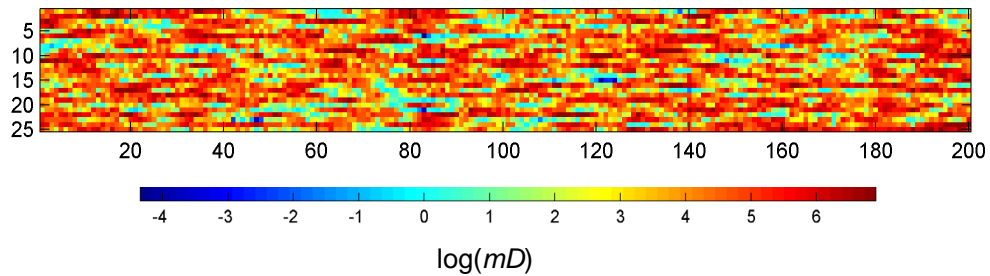


Fig. 2.35. Permeability field of 2D displacement.

An injector-producer pair of the reservoir system was modeled. Model dimensions are summarized in Table 2-18. Streamline and finite difference simulations were run for 2000 days of injection, corresponding to 2 pore volumes injected (PVI).

Table 2-18: Dimensions of 2D displacement model.

Nx	200
Ny	1
Nz	25
Dx (m)	10
Dy (m)	10
Dz (m)	2
Number of wells	2 (1 injector, 1 producer)

A corresponding 2D streamline simulation was performed. Only one orientation of the streamline simulation was performed. Since gravity is neglected in the version of the streamline method used for this example calculation, results from a vertically oriented displacement would be identical to those obtained from a horizontally oriented displacement. The overall character of the saturation plot compares well with results of the finite difference method (Fig. 2.36). Predicted recovery and GOR yield comparable results. Upon closer examination, small differences between the methods emerge. In areas where injection gas contacts the reservoir, very efficient recovery of condensate is achieved. In this system, injected gas flows through high permeability pathways. Due to preferential flow along these high permeability pathways, recovery is not as efficient in low permeability zones.

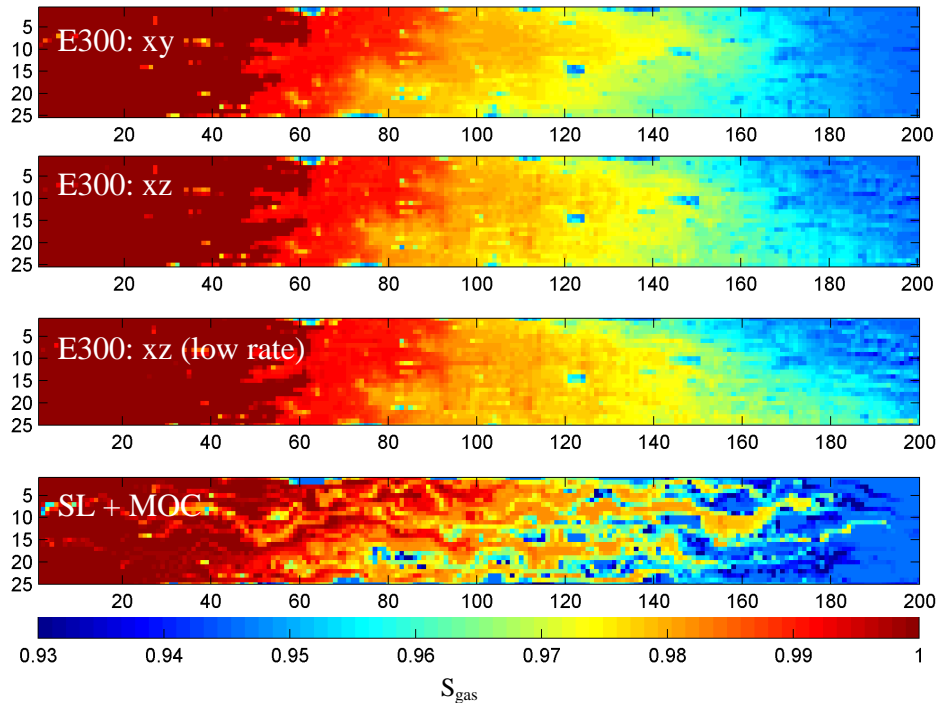


Fig. 2.36: 2D displacement - Gas saturation after 2 PVI.

Fig. 2.37 compares predicted recoveries and GORs for all 2D displacement cases. Between 0.9 PVI and 1.95 PVI, a separation between recovery predicted by streamline methods and finite difference methods is observed. Maximum separation occurs near 1.4 PVI. This difference is due to the production of the condensate bank resolved in the analytical solution. Resolution between injector and producer is 200 grid blocks, far less than the resolution determined in the 1D displacement. As injection continues, the difference in recovery between the two methods converges to a similar value. Once breakthrough occurs in the streamline method, injection gas cycles through the reservoir, making the scheme increasingly inefficient. Numerical dispersion in the finite difference method smears the front of the displacement, artificially increasing the sweep efficiency in low permeability regions. Velocity of the front is also reduced, delaying breakthrough, as indicated by the difference in GOR between the two methods at later times.

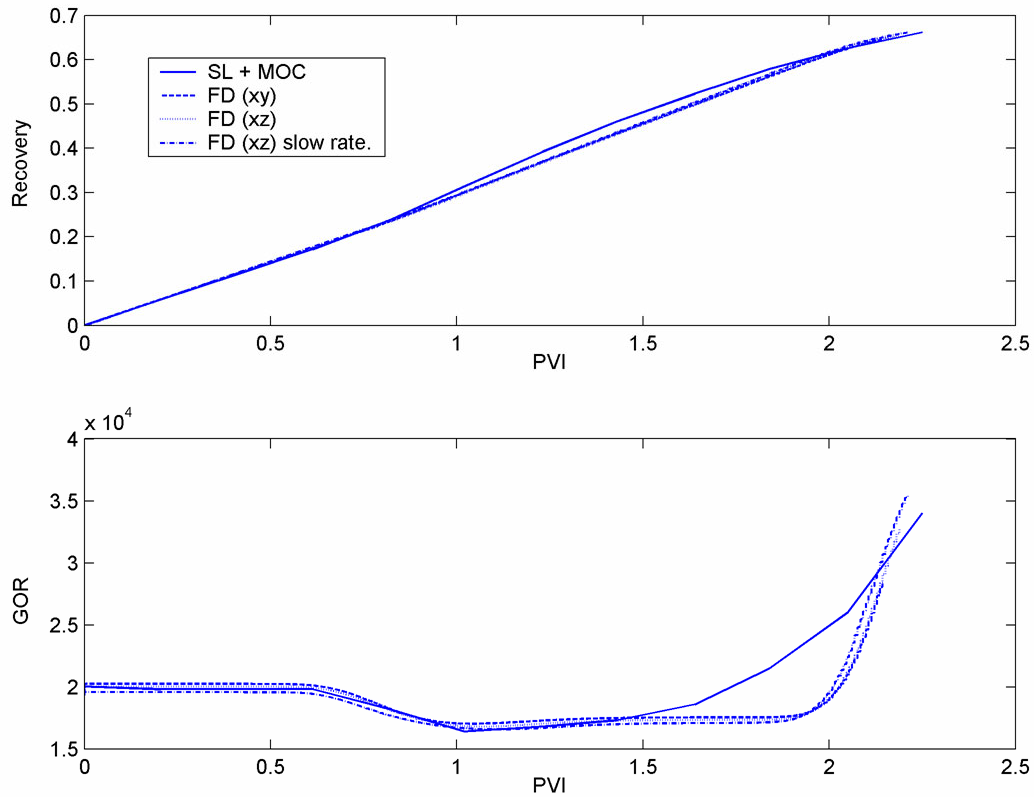


Fig. 2.37: Recovery and GOR predictions for 2D displacement simulations.

### 2.4.2.5 3D Displacement calculation

A section of the reservoir system was extracted to construct a 3D sector model. Permeability distribution and well locations are shown in Fig. 2.38. Model dimensions are summarized in Table 2-19. Streamline and finite difference simulations were run for 2,500 days injection, corresponding to 2 PVI.

Table 2-19: Dimensions of 3D displacement model.

$N_x$	30
$N_y$	90
$N_z$	5
$D_x (m)$	10
$D_y (m)$	10
$D_z (m)$	10
Number of wells	6 (1 injector, 5 producers)

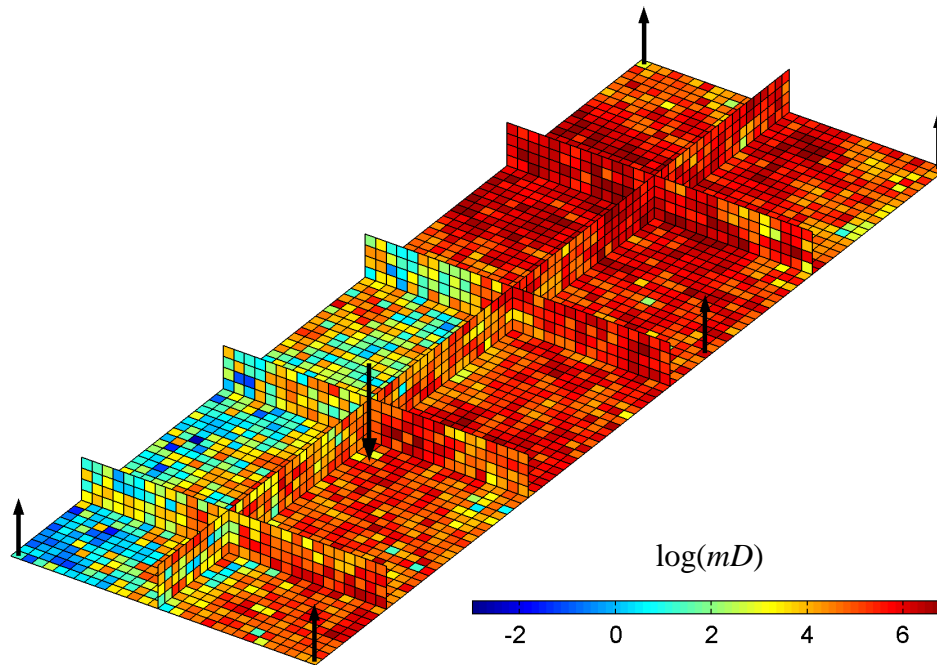


Fig. 2.38. Permeability field and well locations for 3D sector displacement.

Comparison of saturation distributions in the reservoir after 2500 days injection (Fig. 2.39), indicates that numerical dispersion significantly affects sweep efficiency in the reservoir predicted by the finite-difference-based simulator. Injected gas almost entirely covers the lowermost layer in the finite difference simulation, while unswept areas and sharper fronts are observed in the streamline result.

Recovery predicted by finite difference methods is higher than that predicted by the streamline method (Fig. 2.40), even though local displacement efficiency in contacted zones is higher in the streamline calculation than it is in the finite difference version. The lower, and likely more physically realistic, sweep efficiency in the streamline calculation more than offsets the higher local displacement efficiency.

One of the goals of a simulation study is to predict recovery within a reasonable tolerance of uncertainty. Numerical dispersion associated with finite difference methods may adversely impact accuracy, potentially predicting optimistic recoveries. Dispersion free recoveries predicted by the streamline method more accurately predict process recovery. In reality, pore scale dispersion exists; however, physical levels of dispersion are low in field-scale displacements, and convection dominates this displacement. For this system, the Peclet number,  $Pe$ , shown in Table 2-20, is very large. The value for  $L$  in this calculation was the distance between the injector and the closest producer. For larger values of  $L$ , scales linearly.

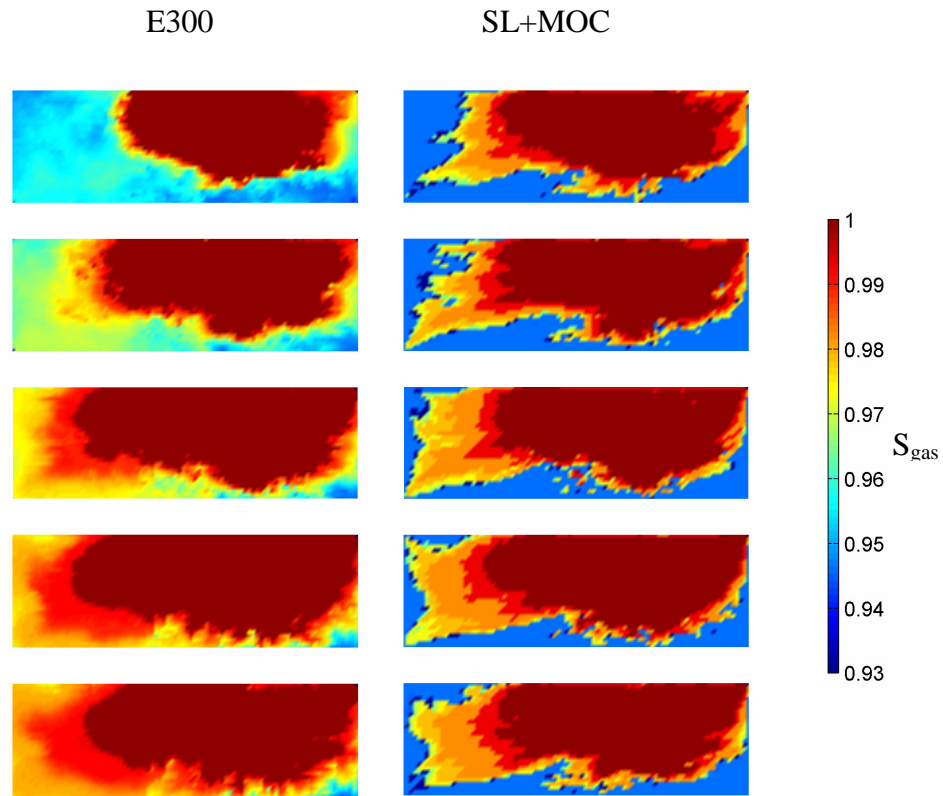


Fig. 2.39. Saturation distribution of areal slices of the 3D sector displacement after 2500 days injection.

Table 2-20:  $Pe$  calculation for sector model displacement.

$v$ (m/d)	0.5
$L$ (m)	440
$\phi$ (fraction)	0.10
$K_l$ (cm <sup>2</sup> /s)	$1 \times 10^{-3}$
$Pe$	$2.55 \times 10^5$

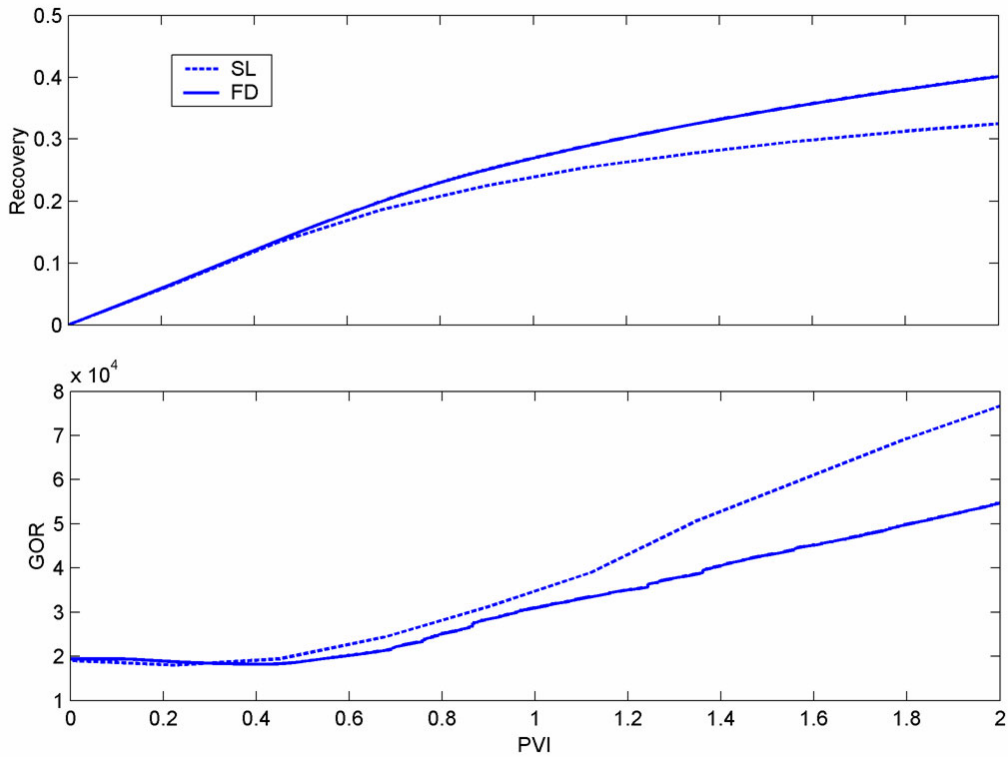


Fig. 2.40. Recovery and GOR predictions for 3D displacement simulations.

### 2.4.2.6 Field scale displacement

A field scale gas injection scheme was modeled for reservoir parameters summarized in Table 2-21.

Table 2-21: Dimensions of field scale displacement model.

Number of active grid blocks	5774
Dx (m)	300
Dy (m)	300
Dz (m)	10
Number of wells	16 (3 injectors, 13 producers)

Grid block dimensions have moved away from a 1:1:1 ratio, reflecting dimensions and aspect ratios commonly used in industry. Due to the sparse well coverage, there is a paucity of hard subsurface data; large uncertainties exist surrounding the permeability distribution between wells. A permeability realization for this field is shown in Fig. 2.41.

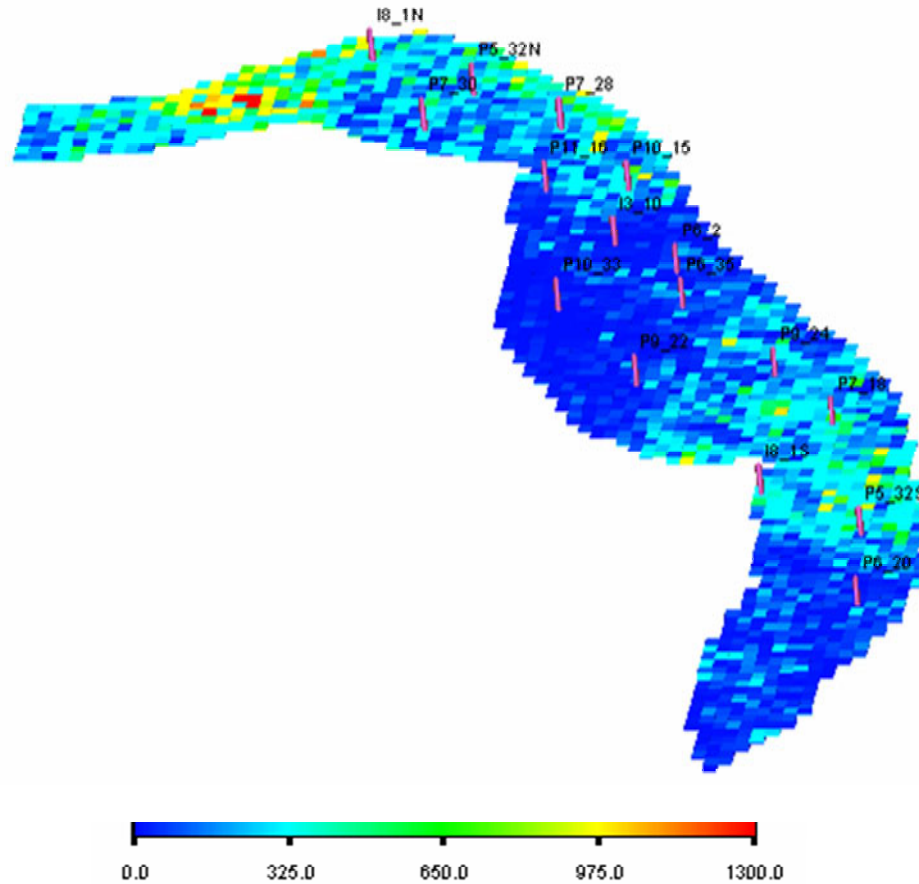


Fig. 2.41. Permeability field ( $mD$ ) and well locations for field scale displacement.

In this development scenario, CO<sub>2</sub> is injected into 3 wells, 8-01N, 3-10 and 8-01 S, indicated by the red dots in Figure 3.1. Injection was modeled from approximately 49 years (1.16 PVI), at fixed reservoir injection rates of 15500, 3000, 14000 m<sup>3</sup>/day, respectively.

Fig. 2.42 shows the saturation distribution in the reservoir at the end of the injection period. Swept zones predicted by both methods are in good agreement. Recovery and GOR predictions are in good agreement prior to breakthrough. Once breakthrough occurs, these predictions deviate, with the finite difference method predicting a higher recovery than the streamline method (Fig. 2.43). As with the sector model, the finite difference method exhibits numerical dispersion, smearing out the fronts and predicting a slightly larger swept zone.

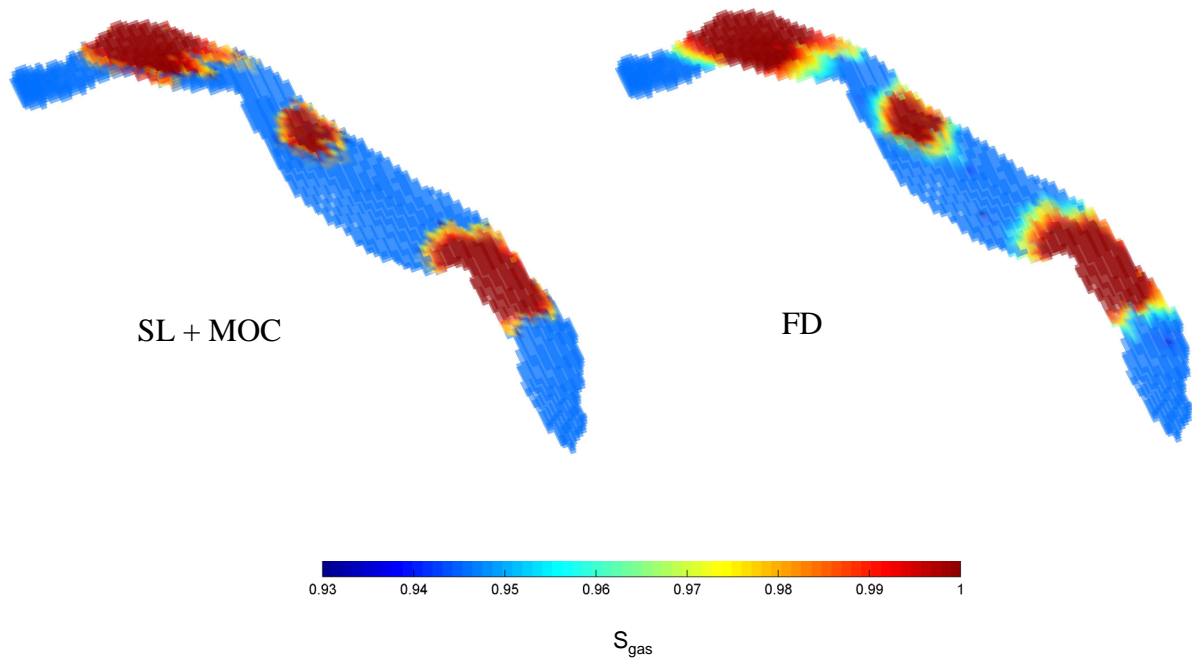


Fig. 2.42. Saturation distribution of field scale displacement after 1.16 PV injection.

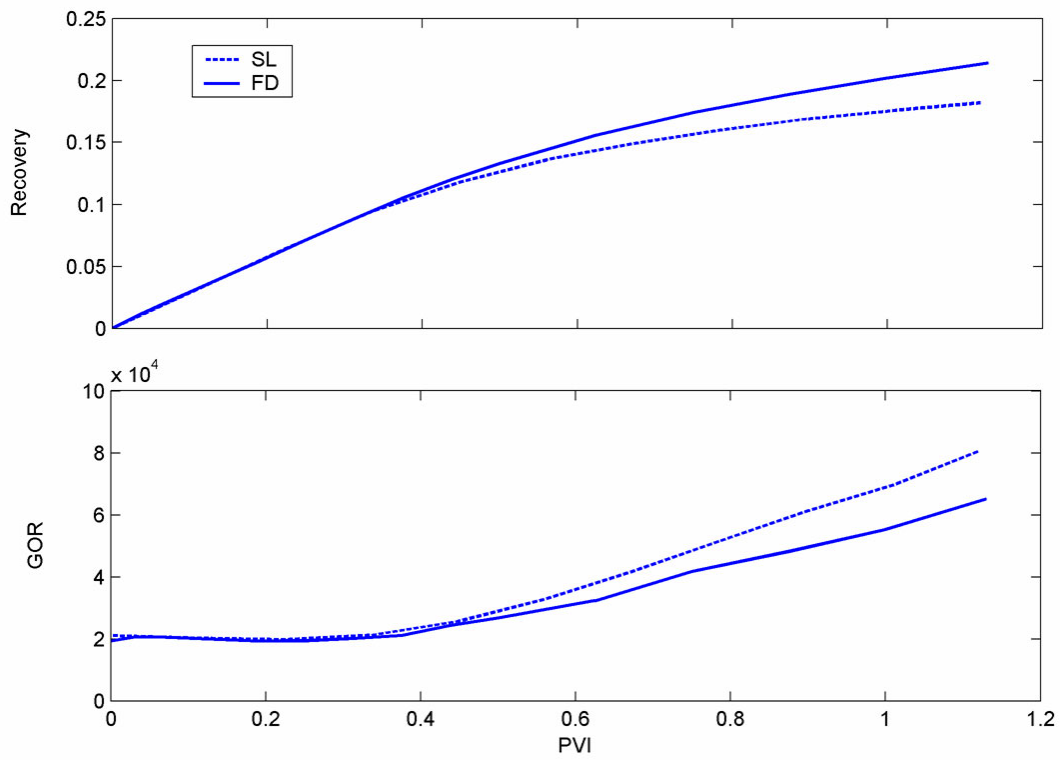


Fig. 2.43. Recovery and GOR predictions for field scale displacement simulations.

### 2.4.2.7 Speed-up factors

Computational times and speed up factors for each phase of this study are summarized in Table 2-22. Speed-up factors observed are in the order of 102-103. These are dependent on system size. Computational time in a streamline simulation scales approximately linearly with model size, while that of a finite difference method scales approximately as the third power of the number of grid blocks. Therefore, the ratio of times is approximately the square of the number of grid blocks. As the number of active grid blocks simulated increases, speed up factors increase approximately quadratically. Finite difference simulations were solved using an IMPES method. If an adaptive implicit scheme is used, speed-up factors are expected to decrease.

Table 2-22: Summary of speed up factors.

Case	Number of active grid blocks	Finite Difference (minutes)	Streamline (minutes)	Speed up factor
2D	5000	123.43	0.23	499
3D	13500	649.85	0.40	1624
Field scale	5774	74.1	0.32	234

The 3D sector displacement case represents a very small volume of the reservoir system (1.4%). If this level of detail were extrapolated to the field scale simulation, a model composed of over 5000000 grid blocks would be required. For this size of model, expected computation times for finite difference methods and streamline methods are on the order of  $1 \times 10^5$  and  $1 \times 10^1$  minutes, respectively. Streamline simulation is the only method currently fast enough to simulate a compositional displacement in a reasonable amount of time.

Decreased simulation times give the simulation engineer the ability to incorporate fine scale permeability distributions and complex fluid descriptions without sacrificing computational requirements. In the following section, we present some of the applications of compositional streamline simulation for reservoir management and uncertainty evaluation.

### 2.4.3 Compositional streamline simulation and reservoir management

The reduced computational run times afforded by streamline simulation allows simulation of gas injection schemes for enhanced condensate recovery in detailed, field scale models in a reasonable amount of time. Due to the paucity of hard data in the subsurface, multiple equiprobable geological models, each honoring the hard data, can be constructed. With developments in reservoir characterization and increases in processor power, generation of high resolution, multi-million cell geological models are now commonplace. This has resulted in a disconnect between the resolution of static reservoir models (on the order of  $10^6$  grid blocks) and dynamic reservoir models (on the order of  $10^4$ - $10^5$  grid blocks). As industry

becomes better able to model geological detail in the static model, there is an increasing awareness of uncertainty surrounding a particular model (Datta-Gupta, 2000). In the following section, some applications of streamline methods for reservoir management are presented.

### 2.4.3.1 Ranking geological models

Streamline techniques can be used to quickly assess geological parameters controlling flow in the subsurface, identifying bounding scenarios of reservoir heterogeneity. This analysis can be used to focus data acquisition efforts by tailoring a data acquisition scheme to specifically seek or disprove geological heterogeneity effects. Once geological scenarios are ranked, detailed simulation that incorporates more complex physics can be carried out for a more rigorous prediction of performance.

Three geological realizations of the 3D sector model were generated to investigate the effects of correlation length and anisotropy. Geostatistical parameters for each realization are summarized in Table 2-23. Well locations were identical to those in the 3D sector displacement simulation.

Table 2-23: Variogram parameters of geological ranking application.

Case	Nugget	Angle	Radius X	Radius Y	Radius Z
Base	0.3	0	50	50	50
Anisotropy	0.3	N17W	50	5	5
Correlation length	0.60	0	50	50	50

Fig. 2.44 shows the permeability distribution in the topmost layer. 4500 days of injection of 100% CO<sub>2</sub> was simulated for each realization. Saturation distributions at the end of the injection period are shown in Fig. 2.45 - Fig. 2.47. Predicted recovery and GOR are shown in Fig. 2.48. For these realizations, high permeability channels with communication between injector and producer have the most impact on recovery. High permeability channels result in premature gas breakthrough. The less tortuous the path from injector to producer, the earlier the breakthrough and lower the ultimate recovery. Permeability fields with short correlation distances, suggestive of a high degree of heterogeneity, result in a more uniform sweep areal sweep efficiency and higher recovery. In distributions with short correlation lengths, high permeability pathways are not developed, hindering premature gas breakthrough.

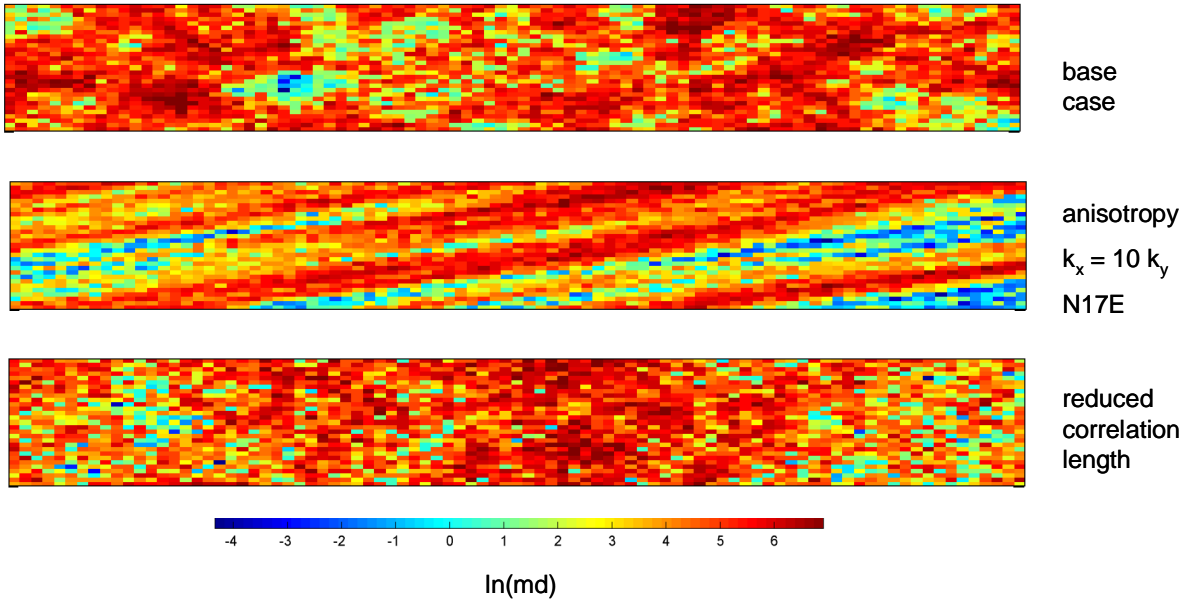


Fig. 2.44. Top layer permeability distributions in geological ranking application.

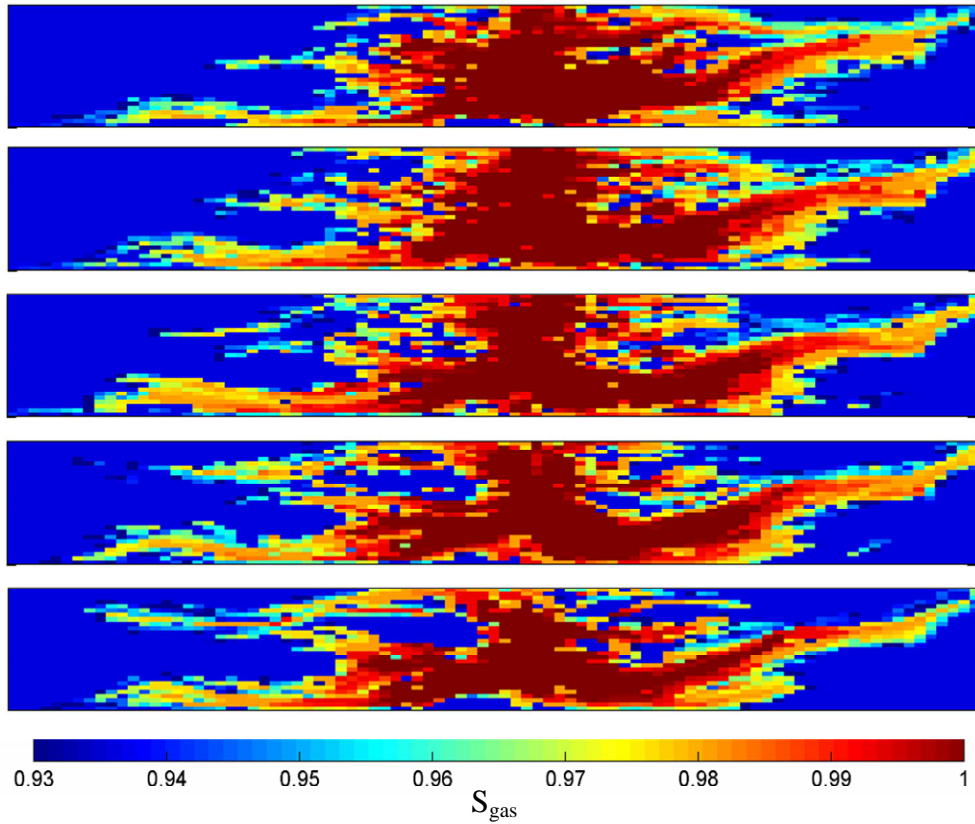


Fig. 2.45. Base case  $S_{gas}$  distribution through reservoir after 2 PVI.

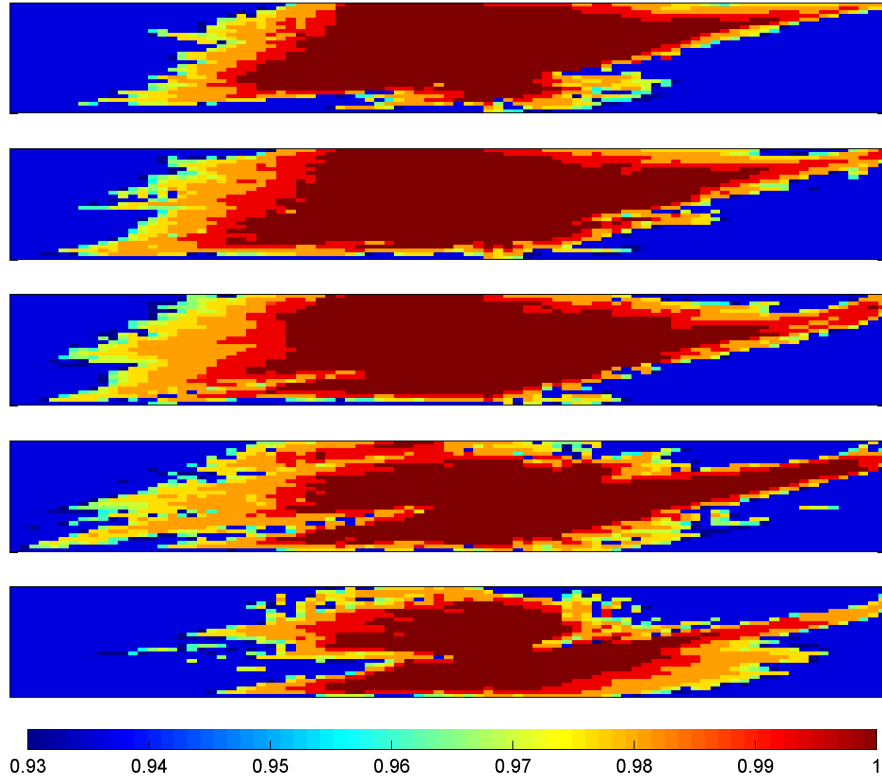


Fig. 2.46. Anisotropy case  $S_{\text{gas}}$  distribution through reservoir after 2 PVI.

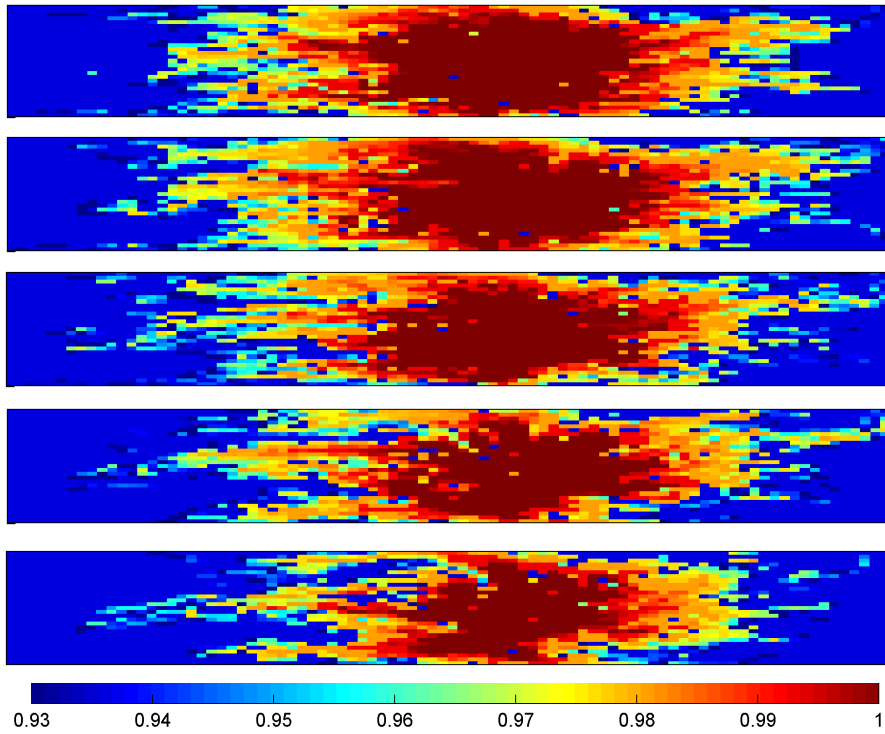


Fig. 2.47. Correlation length case  $S_{\text{gas}}$  distribution though reservoir after 2 PVI.

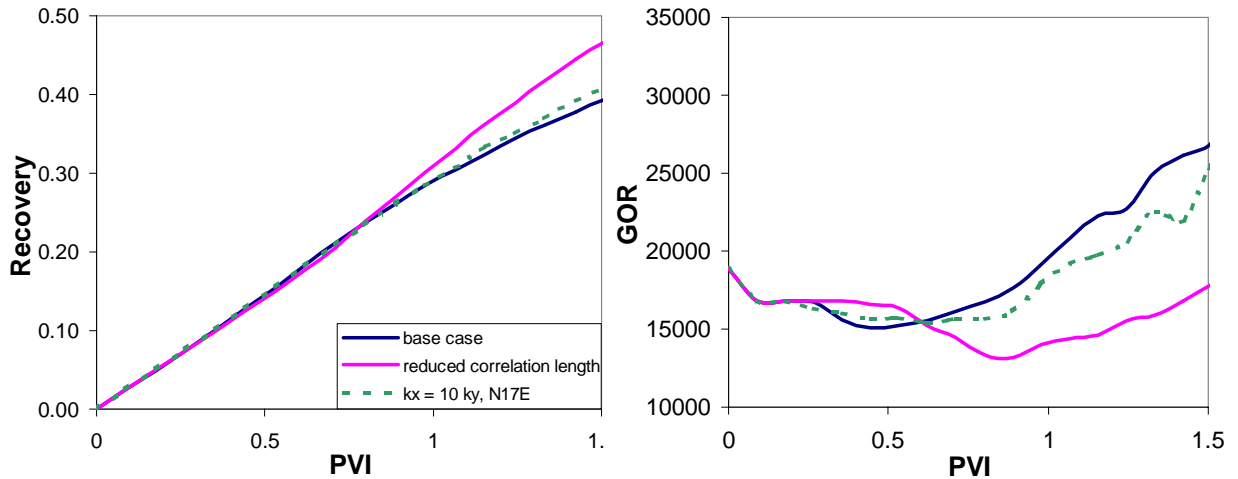


Fig. 2.48. Recovery and GOR predictions from permeability cases used in geological ranking application.

#### 2.4.3.2 Uncertainty analysis on a dynamic reservoir model

To deal with uncertainty, industry has been moving towards a probabilistic estimation of reservoir performance, where P(10), P(50) and P(90) values of predicted performance are reported (Beliveau, 1995). This method of uncertainty analysis requires the reservoir engineer to perform multiple dynamic simulations. The sample size of the simulations must be large enough to be representative of the uncertainty distributions surrounding model parameters.

100 equiprobable realizations of the 3D sector model were generated. Geostatistical parameters were held constant for all realizations, so that the only difference between each permeability realization is the random path by which cells are assigned permeability values, calculated by kriging. The 13-component tuned fluid description was used, and 100% CO<sub>2</sub> was injected. 4500 days of injection were simulated for each realization. Recovery and GOR predictions are presented in Fig. 2.49. For this system, predicted recoveries range from 24 – 42 %; corresponding to a difference of 6775 m<sup>3</sup> recovered (58% of the mean volume recovered). Cumulative distribution of predicted recovery is presented in Fig. 2.50. From this analysis, P(10), P(50) and P(90) recoveries are 28.1, 33.7 and 39.2%, respectively. The total time required to simulate injection over the set of 100 realisations was 34.6 minutes. If this exercise had been performed using finite difference methods, approximately 45 days of computation time would have been required.

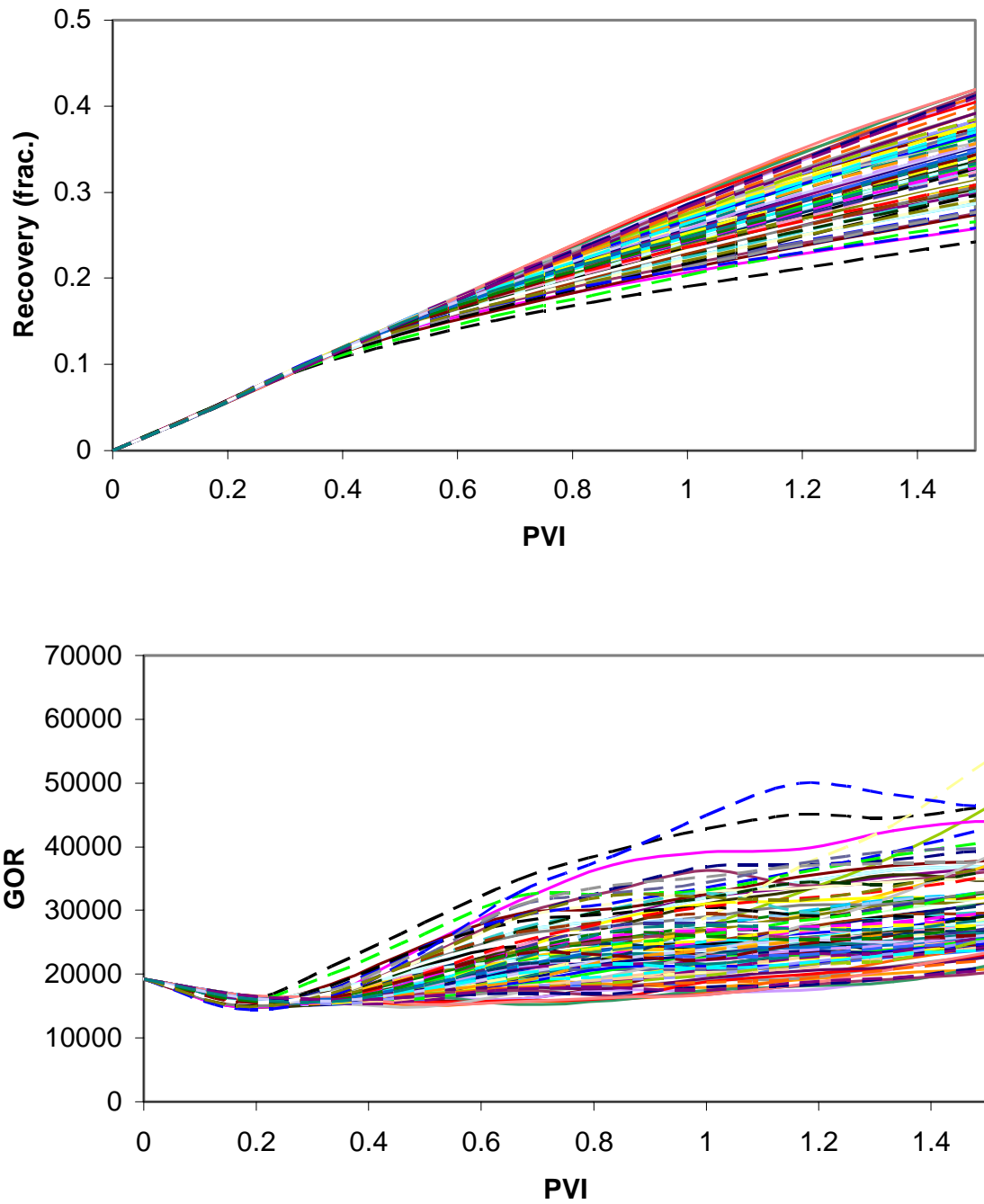


Fig. 2.49. Range of predicted recoveries and GORs for 100 equiprobable sector model displacements.

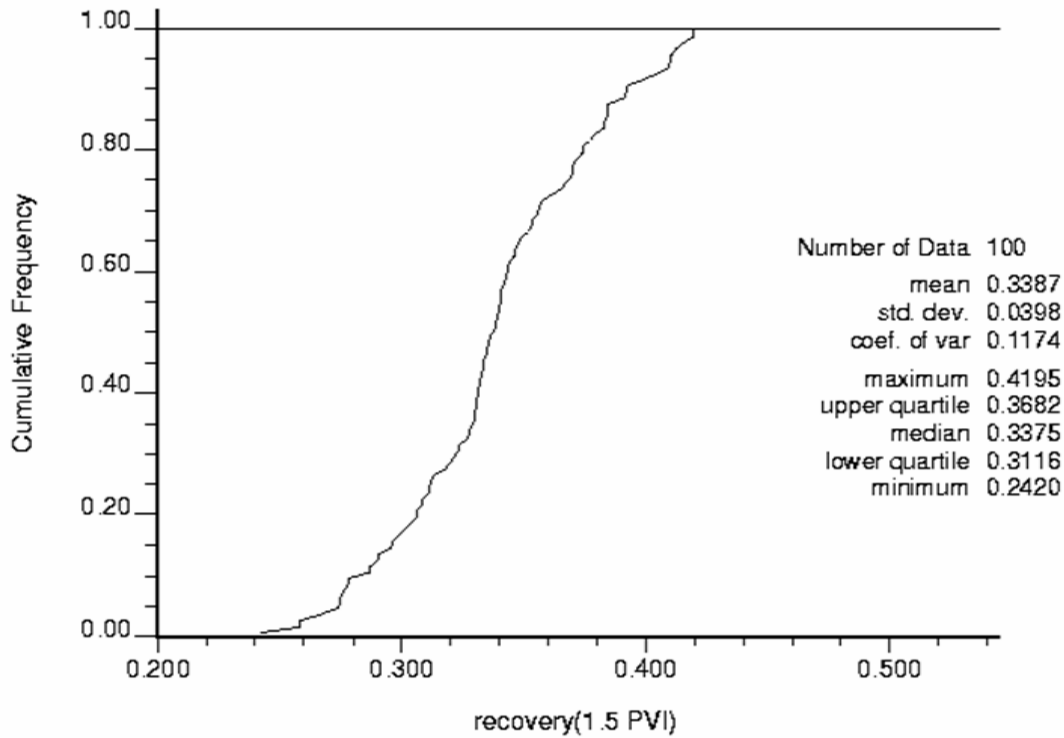


Fig. 2.50. Cumulative distribution function of predicted recovery for 100 equiprobable sector model displacements.

Different permeability realizations influence breakthrough time and well rates. P(10), P(50) and P(90) values for well deliverability are summarized in Table 2-24. Probabilistic analysis of deliverability and breakthrough time allows optimization of facility design and enhances confidence in hydrocarbon recovery, which can then be applied to decisions about reserves estimation, project screening, and nominating forward sales contracts of production.

Table 2-24: Summary of uncertainty analysis on well deliverability.

Well	P(10)	P(50)	P(90)
1	16	41	63
2	74	112	160
3	164	220	281
4	20	43	72
5	48	73	111

#### 2.4.4 Field Scale Fine Reservoir Description

A fine scale permeability realization of the study reservoir was constructed (Fig. 2.51). Model dimensions are summarized in Table 2-25. 100% CO<sub>2</sub> was injected for 45000 days (123 years), corresponding to 1 PVI. Injection well locations and rates were identical to those in the coarse permeability description of the field scale displacement. Simulations took only 31.9 minutes to complete. These computational times could be reduced, if a shorter, more realistic injection period was simulated.

Table 2-25: Dimensions of field scale displacement model.

Number of active grid blocks	606960
Dx (m)	25
Dy (m)	25
Dz (m)	10
Number of wells	16 (3 injector2, 13 producers)

After 1 PVI, ultimate recovery is very low. From the saturation distributions, we can easily visualize the remaining unswept areas of the reservoir (Fig. 2.52). The current injector producer configuration is not optimal.

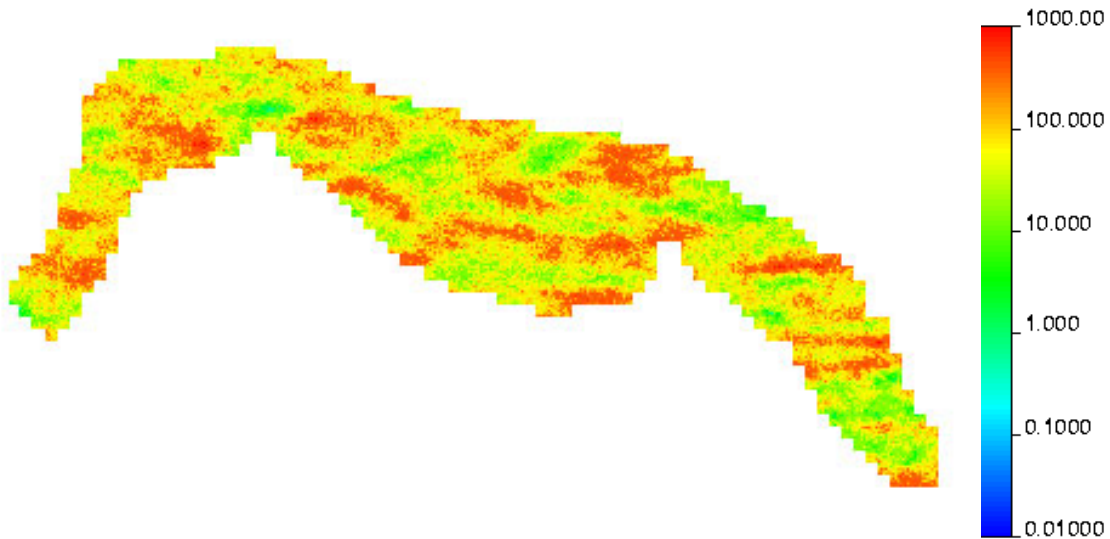


Fig. 2.51. Fine scale permeability distribution (*mD*) of field scale model.

Three simulations assessing alternate development scenarios were performed:

- injectors, alternate injector well placement.
- 4 injectors,
- 5 injectors.

In all cases, positions of existing wells were honored. Additional injectors were added at the expense of removing a producing well. Saturations plots of each development scenario are displayed in Fig. 2.52. Predicted recoveries and GOR as shown in Fig. 2.53. The streamline method allows easy visualization of natural flow paths in the reservoir and injector-producer relationships. Using streamline simulation, we can make quick assessment of alternate development scenarios.

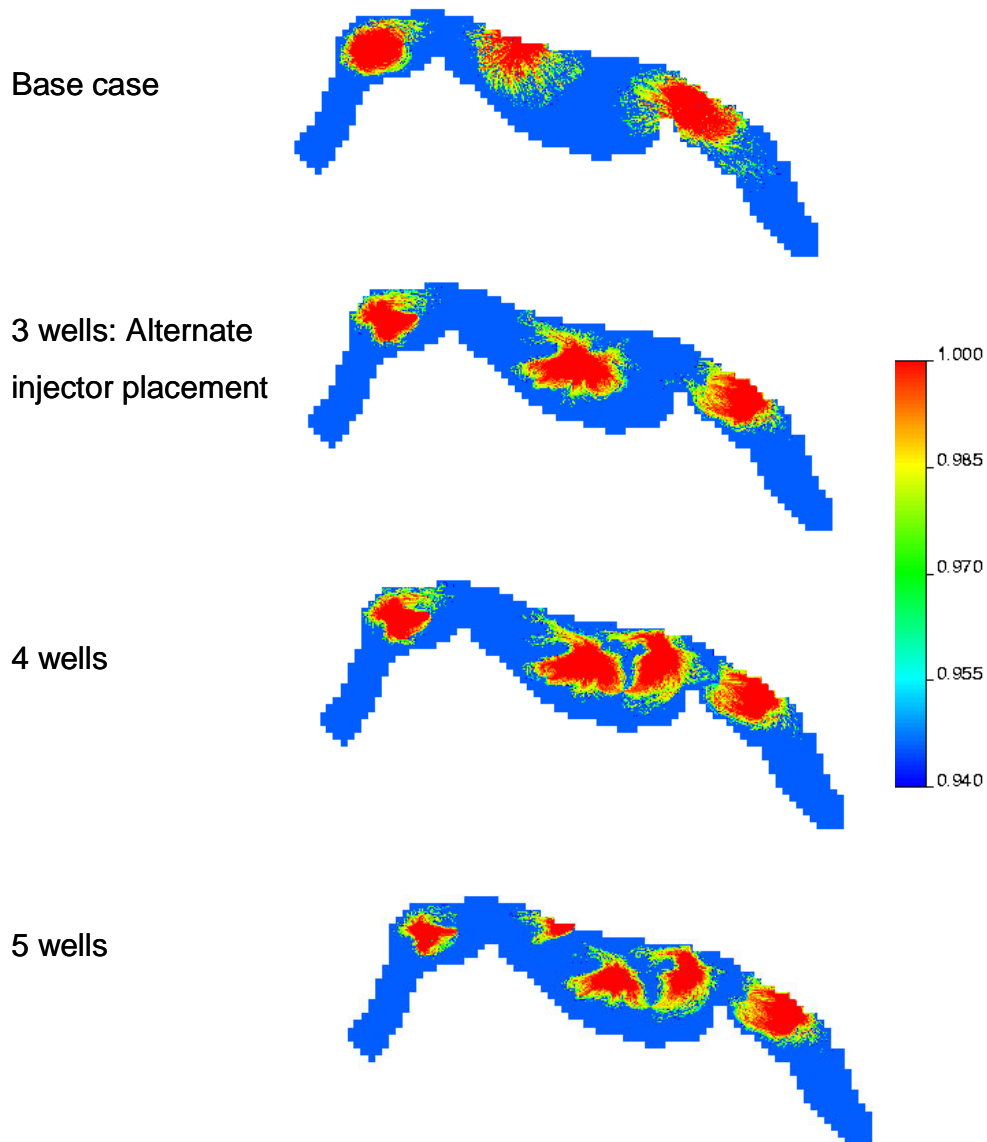


Fig. 2.52. Saturation distributions after 1 PV injected for well placement scenarios of the fine scale geological model.

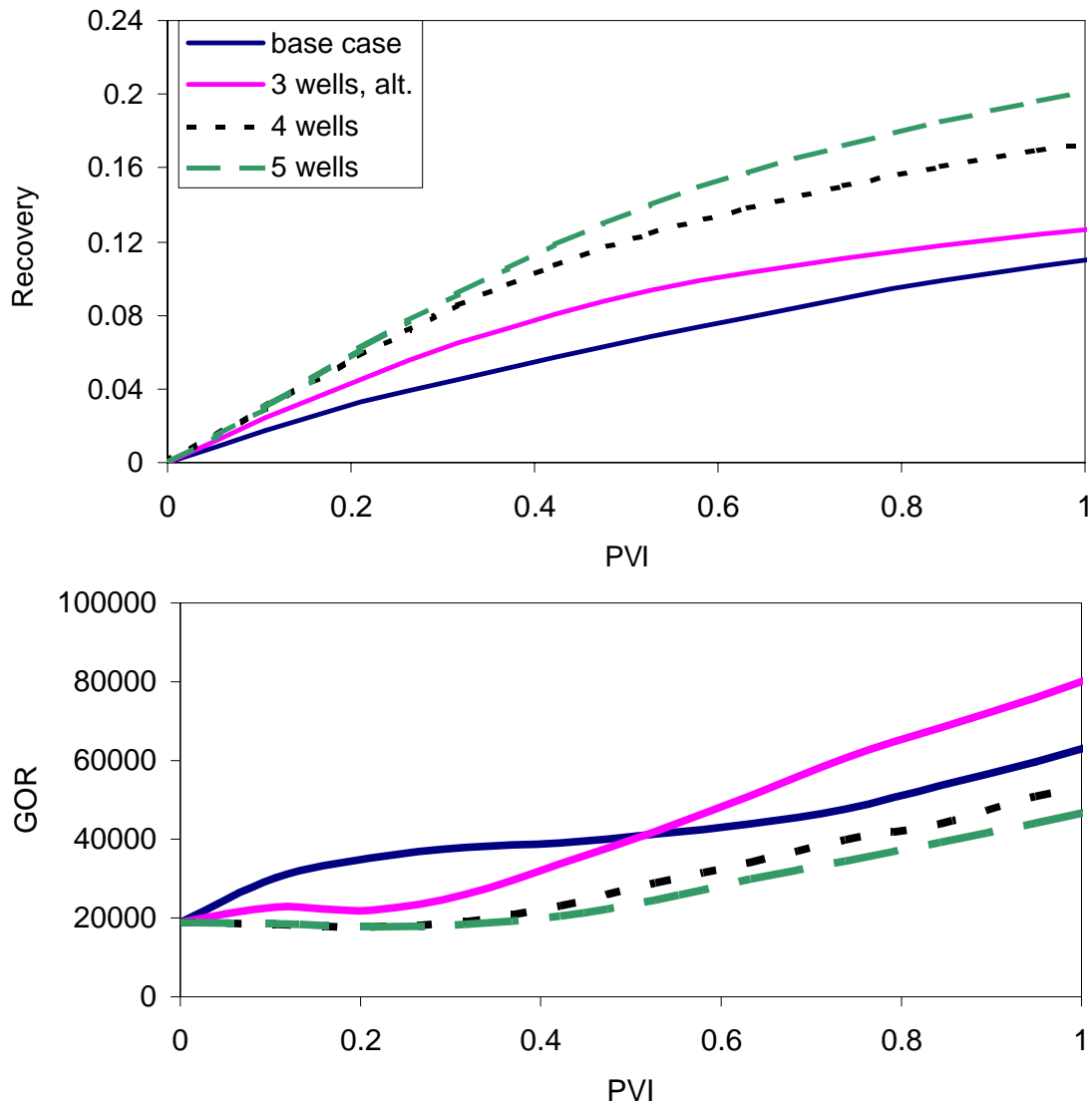


Fig. 2.53. Recovery and GOR predictions for well placement scenarios of the fine scale geological model.

### 2.4.5 Conclusions

In gas cycling schemes for enhanced condensate recovery, the assumptions of no gravity and viscous cross flow, no capillarity and no physical diffusion are valid where the displacement is heterogeneity dominated. Simulations of these systems using streamline methods that neglect these effects yield results comparable to finite difference methods that consider these complex physical phenomena.

Recovery efficiency is a complex balance between local displacement efficiency and global sweep efficiency. For the system investigated, numerical dispersion associated with finite difference simulation increased the contact area of the injection gas and reduced the velocity of the fronts. These effects increased global sweep efficiency and delayed gas breakthrough, respectively, yielding optimistic recovery predictions. The effects of

numerical dispersion are not present in the streamline method with analytical solutions. This results in lower recovery predictions. In systems where physical dispersion is small relative to convection forces, the streamline method more accurately models fluid displacement patterns in the subsurface. Accurate prediction of swept zones is critical in determining placement of infill producers or injectors.

Analytical solutions provide insight concerning physical phenomena occurring in the reservoir. For the reservoir fluid considered, efficient recovery of condensate by injection of pure CO<sub>2</sub> occurs through a series of vaporizing shocks. As the resulting vapor phase propagates through the reservoir, vaporized components dissolved into the condensate phase forming a bank at the leading edge of the displacement. Using finite difference methods, fine resolution (on the order of 1000 grid blocks between injector and producer) is necessary to visualize these features; otherwise they will be masked by numerical dispersion.

The high computation speed afforded by streamline methods make compositional streamline simulation an effective tool for evaluating gas injection in a condensate reservoir. Reduced computational time relative to finite difference methods allow more detailed representation of phase behavior in the equation of state description, and high resolution representation of permeability heterogeneity in the reservoir. Compositional simulation for grids with a million cells in a reasonable period of time is now possible.

This section demonstrates the power that compositional streamline simulation has as a tool for management of condensate reservoirs. Displacement in these systems is dominated by heterogeneity. Complex physics like capillary forces, gravity and natural diffusion can be neglected. In its current formulation, the analytical methods for calculating the 1D solution do not consider these effects. Incorporation of capillary and gravity effects into the analytical solution will make compositional streamline simulation more applicable to a broader range of reservoirs, such as miscible displacements in oil reservoirs.

For the purposes of calculating phase behavior, the analytical solution assumes a fixed pressure (see Chapter 5 for more discussion of this point). As a result of this assumption, near well bore phenomena specific to condensate reservoirs, such as condensate banking, productivity impairment and viscous stripping cannot be incorporated. Such effects can have a dramatic impact on well productivity. Reliable predictions of productivity are essential in establishing the development strategy of an asset. Development of fast numerical methods to account for near well pressure gradients will make productivity prediction more robust. Related to this issue is the assumption of constant injection and production conditions. In many gas cycling schemes, limitations on gas availability result in a partial voidage replacement scheme. As the field are depleted, average reservoir pressure declines. Numerical methods for solving the 1D flow problem as injection and production pressures decline allow consideration of a broader range of development scenarios.

## 2.4.6 Nomenclature

$H$  = reservoir thickness,  $m$   
 $k_{avg}$  = average reservoir permeability,  $m^2$   
 $K_l$  = dispersion coefficient  
 $L$  = reservoir length,  $m$   
 $M$  = mobility ratio  
 $N_B$  = Bond number  
 $N_{cv}$  = transverse capillary number  
 $N_{gv}$  = gravity number  
 $Pe$  = Peclet number  
 $Pe_{Num}$  = numerical Peclet number  
 $v$  = Darcy flow velocity  
 $\phi$  = porosity  
 $\xi$  = dimensionless length  
 $\mu$  = viscosity  
 $\Delta\rho$  = density difference between injected fluid and reservoir fluid  
 $\tau$  = dimensionless time  
 $\sigma$  = interfacial tension

## 2.5 Improved accuracy of compositional streamline simulation

### 2.5.1 Introduction

The overall goal of this research is to improve the accuracy and efficiency of the streamline method in simulating compositional problems such as those that occur in miscible or near-miscible gas injection processes. In Section 2.2 we described a one-dimensional (1D) compositional finite difference solver based on a high order upwind scheme and adaptive mesh refinement that is appropriate for use in a compositional streamline simulator. In this section, we propose new mappings to and from streamlines that improve the accuracy of the streamline method for problems in which the flow pattern does not remain fixed for large time intervals. Such problems require that streamlines be periodically updated in order to account for changing flow directions and the treatment of gravity terms (Thiele *et al.*, 1996; Bratvedt *et al.*, 1996). For each set of streamlines, fluids must be mapped from an underlying background grid to the streamlines, moved forward in time and then mapped from the streamlines to the background grid. The mappings introduce numerical smearing as well as mass balance errors. When streamlines are updated frequently, the mapping error limits the overall accuracy of the streamline method. The improved mapping algorithms described in this section are aimed at minimizing this type of error.

Most methods for compositional simulation are based on Eulerian grids (see Aziz and Settari, 1979). The well-known IMPES methods are limited by severe stability restrictions on the time step size. On the other hand, fully implicit methods (FIM) are limited foremost by the number of unknowns in compositional simulation. Adaptive implicit methods (AIM)

have been formulated to reduce the number of implicit unknowns required by FIM and to alleviate the time step restrictions associated with moving compositions explicitly throughout an entire reservoir (Thomas and Thurnau, 1983). The computation time required for simulation can of course also be reduced through parallelization. Recently an effort has been made to include adaptive mesh refinement (AMR) in compositional simulation (Sammon, 2003). AMR focuses computational effort in regions near fronts to accurately capture the local displacement efficiency.

As an alternative to the above Eulerian methods mentioned above, Euler-Lagrange type methods can be used. The Euler-Lagrange localized adjoint methods (ELLAM) take advantage of the stability of Lagrangian methods over long time steps and do not suffer from the mass conservation errors often observed with similar methods (Celia *et al.*, 1990). Some linearization is required to apply ELLAM to the compositional model (Chen *et al.*, 2000). This linearization may not be suitable for near-miscible displacements. Streamline methods are another class of Euler-Lagrange type methods based on the physical observation that in heterogeneous reservoirs the time scale at which fluids flow along streamlines is often much faster than the time scale at which the streamline locations change significantly. This allows decoupling of the transport problem into a sum of 1D problems along streamlines. Studies have shown that streamline methods can predict the global sweep of water floods in heterogeneous reservoirs effectively (Peddibhotla *et al.*, 1997; Batycky *et al.*, 1997). The extension of streamline methods to compositional simulation is promising and has been discussed in Thiele *et al.* (1997); Crane *et al.* (2000) and Jessen and Orr (2004).

In Section 2.2 we presented a 1D finite difference solver based on a third order upwind essentially non-oscillatory scheme and AMR that is appropriate for predicting local displacement efficiency in a compositional streamline simulator (Malison *et al.*, 2003). Changes in the mobility field can be included by periodically resolving for the velocity field and updating the locations of the streamlines (Thiele *et al.*, 1996). Gravity and other sources of cross flow can be incorporated through operator splitting (Bratvedt *et al.*, 1996). Both techniques can lead to accurate predictions of global sweep; however, as the number of streamline updates and operator-splitting steps increase the errors due to mapping fluids to and from streamlines also increase. When accurate methods are used for transport along streamlines, the mapping errors can be the largest source of error in the streamline algorithm. These mappings smooth saturation fronts and generally introduce mass balance errors. Both of these errors can lead to inaccurate global sweep predictions.

Most previous attempts at reducing mapping errors have focused on mapping from an outdated set of streamlines directly to a newly computed set (Bratvedt *et al.*, 1996; Peddibhotla *et al.*, 1997). This type of projection is problematic in 3D. We map between streamlines and a background grid to allow for the redistribution of fluids on the background grid due to forces that are not aligned with the principal flow direction. The work of several authors relies on fluids residing on a background grid in addition to a set of streamlines (Karlsen, 2000; Berre *et al.*, 2002; Ichiro *et al.*, 2003). Gautier *et al.* (1999) were able to reduce mapping errors by mapping between streamlines and a refined background grid. However, their strategy requires that the streamline method be applied directly to this globally refined grid. For compositional problems where the computation cost of each

streamline solve is significant this approach may not be practical. The mappings proposed here reduce errors and at the same time require fewer streamlines to obtain accurate results.

## 2.5.2 Governing equations

We consider a simple, two-phase model for miscible gas injection based on the assumption of incompressible, Darcy flow. Gravity, capillary forces and dispersive forces are neglected for simplicity although they can be included in streamline methods as mentioned in the previous section (Bratvedt *et al.*, 1996; Berre *et al.*, 2002; Ichiro *et al.*, 2003). These simplifications allow us to isolate the mapping errors.

Darcy's law for the average velocity is given by

$$\bar{u} = k\lambda\nabla p. \quad (2.74)$$

Here  $p$  is the pressure and  $k$  is the (scalar) permeability. The fluid mobility  $\lambda$  will be specified below. Combining Darcy's law with the incompressibility condition  $\nabla \cdot \bar{u} = 0$  yields an elliptic pressure equation:

$$\nabla \cdot (k\lambda\nabla p) = q. \quad (2.75)$$

$q$  represents a source or sink term due to wells or boundary conditions. The specific boundary conditions and permeability fields used in tests of the proposed method are described below.

Mass conservation for the injected fluid gives the following hyperbolic transport equation:

$$(2.76) \quad \phi \frac{\partial S}{\partial t} + \bar{u} \cdot \nabla S = 0,$$

where  $0 \leq S \leq 1$  is the volumetric saturation of the injected fluid. Source and sink terms have been neglected for simplicity.  $\phi$  is the porosity of the porous medium and  $t$  is time. Eq. (2.76) is linear since we have assumed that the transport of the injected fluid is not hindered by the presence of the resident fluid. Generally this is the case when the injected and resident fluids have identical properties. While this is not true in gas injection processes, the development of miscibility serves to reduce the interfacial tension and other differences between the gas and oil phases at the advancing miscible front. So, flow described by Eq. (2.75) and Eq. (2.76) can be used as an approximation to gas injection in the case that miscibility has fully developed.

In gas injection processes, the mobility of the gas is often greater than the mobility of the resident oil. To include this effect in our model we let the mobility depend on the saturation of the injected fluid. First, we introduce the end-point mobility ratio,

$$M = \frac{\lambda_I}{\lambda_o} = \frac{\mu_o}{\mu_I}. \quad (2.77)$$

The viscosities of the injected and resident fluids are  $\mu_I$  and  $\mu_o$ , respectively. For saturations  $0 < S < 1$  we calculate the mobility using a quarter-power mixing rule,

$$\lambda(S) = \left[ (1 - S) + M^{\frac{1}{4}} S \right]^4. \quad (2.78)$$

A potentially strong coupling is introduced between Eq. (2.75) and Eq. (2.76) by allowing the mobility to depend on the saturation of the injected fluid.

In gas injection processes the end-point mobility ratio is typically unfavorable ( $M > 1$ ). In a homogeneous medium the resulting displacement front will be unstable, and so-called viscous fingering can occur. In a heterogeneous medium, however, the variation in permeability serves to channel the injected fluid along high permeability paths (Araktingi and Orr, 1993; Tchelepi and Orr, 1994). We focus on the heterogeneous case to avoid complications and because it is of practical interest.

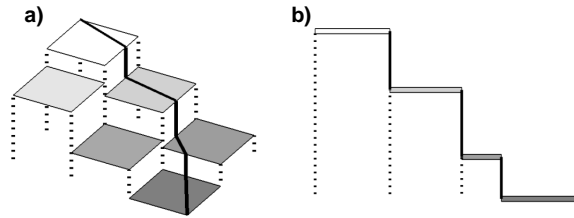


Fig. 2.54: The standard mapping to streamlines assumes a piecewise constant representation of saturations on the background grid (a). The resulting 1D profile along streamlines is also piecewise constant (b).

### 2.5.3 Streamline method

The streamline method solves the coupled system given by Eq. (2.75) and Eq. (2.76) in a sequential fashion. Given suitable initial and boundary conditions, the pressure and velocity fields are found numerically from Eq. (2.75) and Eq. (2.74). This velocity is used to advance the transport equation Eq. (2.76) by some time increment. To avoid the severe time step restrictions imposed by solving Eq. (2.76) explicitly on a fixed background grid, streamline methods interpret the transport equation in a Lagrangian sense using the operator identity,

$$\vec{u} \cdot \nabla = |\vec{u}| \frac{\partial}{\partial \xi}. \quad (2.79)$$

Here  $\xi$  is arc length measured along a streamline. This identity is valid for all time if the velocity field is steady. For the flow considered here, this occurs only for fixed boundary/well conditions and a unit mobility ratio. Streamline methods assume that Eq. (2.79) is valid over some time interval between pressure solves. Eq. (2.76) can be used with Eq. (2.79) to define a transport equation associated with a streamline,

$$\phi \frac{\partial S}{\partial t} + |\bar{u}| \frac{\partial S}{\partial \xi} = 0. \quad (2.80)$$

An additional rescaling of the 1D transport equation along streamlines is often performed using,

$$|\bar{u}| \frac{\partial}{\partial \xi} = \phi \frac{\partial}{\partial \tau}. \quad (2.81)$$

The introduction of the time of flight  $\tau$  leads to the dimensionless form along streamlines,

$$\frac{\partial S}{\partial t} + \frac{\partial S}{\partial \tau} = 0. \quad (2.82)$$

The decomposition (Eq. (2.79) – Eq. (2.82)) replaces the single transport given by Eq. (2.76) with a set of independent 1D equations that must be solved at each time step. See King and Datta-Gupta (1998) for a more detailed discussion of this decomposition. The stages in one time step of the streamline method can be summarized as follows:

**Pressure solve:** Finite difference or finite volume methods are generally used to discretize the pressure equation (Eq. (2.75)) on a fixed background grid. The velocity field is computed using Darcy's law Eq. (2.74). An alternative approach is to solve for the velocity directly with a mixed finite element method (Chen *et al.*, 2000). For simplicity we use a finite difference discretization on a 2D Cartesian grid and a direct sparse solver for the resulting system of equations.

**Streamline Tracing:** Streamlines are traced in the velocity field using a technique developed by Pollock (1988). We trace streamlines forwards (downstream) and backwards (upstream) from points on the interior of our domain until a boundary or a well is encountered. Partial or local streamline tracing is also possible Berre *et al.*, 2002. To ensure adequate streamline coverage we launch streamlines from the centers of background grid cells until at least one streamline crosses every cell. This approach is sufficient for the purpose of studying mapping errors but we are developing a more robust strategy that traces streamlines more selectively. This new strategy for ensuring proper streamline coverage and an improved method for tracing streamlines will be presented in a future paper.

**Mapping to streamlines:** Given a traced streamline, the injected fluid saturation must be initialized along that streamline before that profile can be advanced in time with Eq. (2.82). The first order mapping used in most streamline simulators assumes that saturations are piecewise constant on the cells of the background grid. These constant values are taken from each background grid cell and assigned to the 1D streamline segments that cross those cells (See Fig. 2.54). The assumption that saturation is constant on cells of the background grid introduces a discretization error that smoothes saturation fronts.

The 1D grid defined by tracing a streamline across the background grid is often highly irregular. In fact, there is no bound on the ratio of adjacent grid cell sizes since streamlines can pass arbitrarily close to vertices of the background grid. When finite difference schemes are used for transport along streamlines, the initialized 1D saturation profile is often

remapped to a more regular 1D grid before proceeding. We remap to a uniform 1D grid to simplify the application of adaptive mesh refinement (AMR) in our 1D finite difference solver.

In the following section we propose a more accurate method for mapping from the background grid to streamlines based on a piecewise linear representation of saturations on the background grid.

Transport along streamlines. Several techniques have been proposed to solve the transport equations along streamlines. For the compositional model the solution of the transport equations can be challenging even in 1D but here our task is simplified by the linearity of Eq. (2.82).

If the initial saturation profile is constant then analytical methods can often be applied to solve the resulting Riemann problem (Seto *et al.*, 2003). Also, if a fast Riemann solver is available, front tracking can be performed along streamlines (Berre *et al.*, 2002). We prefer explicit finite difference schemes for solving transport along streamlines due to the relative ease with which they can be applied to complicated transport problems. The often severe time step size restriction associated with explicit finite difference schemes in multi-dimensional simulations is alleviated in this context since time steps can be chosen independently for each streamline.

In Section 2.2 we proposed a third order upwind, essentially non-oscillatory (ENO) finite difference scheme for two-phase, multicomponent flow. Here we use a similar scheme to propagate saturations along streamlines although simpler second order schemes are likely to give comparable results. High order schemes can achieve accurate results more efficiently than first order schemes by using coarser grids along streamlines. To further improve the efficiency of our 1D solver we have incorporated AMR along streamlines as discussed in Berger (1982).

Mapping to the background grid. Saturations must be mapped from the set of streamlines to the background grid in order to complete a time step of the streamline method. The saturation of a background grid cell is typically chosen as a weighted average of the saturations along the  $N$  streamlines crossing the cell, in the form,

$$S_{cell} = \sum_{i=1}^N w_i S_i. \quad (2.83)$$

Here,  $S_i$  is the saturation of a streamline segment. The streamline segments considered here are defined by the tracing and are the same as those shown in Fig. 2.54. The 1D profiles must be remapped to these segments if a different 1D grid was used in stage 4. The weights  $w_i$  are commonly chosen according to their time of flight in the grid cell,

$$w_i = \frac{\Delta\tau_i}{\sum_{k=1}^N \Delta\tau_k}. \quad (2.84)$$

Clearly this mapping requires that at least one streamline cross each background grid cell. In

regions of the domain where saturation is nearly constant we feel that this requirement is overly restrictive. However, where steep fronts in saturation exist several streamlines are required for reasonable predictions. In practice it is not necessary for all of the weights to be known before estimating saturation with Eq. (2.83). As each streamline solve is performed, Eq. (2.83) and Eq. (2.84) can be updated for the underlying grid cells without knowledge of the other streamlines.

In the following section we show that estimating saturations as described above is the primary source of mass balance errors in streamline method. We investigate a new choice for the weights based on Kriging that accounts for the locations of the streamline segments and their proximity to each other.

Each global time step of the streamline method consists of the above five stages. If boundary and well conditions remain fixed, streamline methods can often take large global time steps relative to conventional IMPES methods. When finite difference schemes are used in stage 4, they typically take several local time steps within each global time step. For simplicity we use uniform global time steps here although other strategies have been proposed (Ichiro *et al.*, 2003).

If gravity is included, stages three through five must be repeated at each time step using vertical gravity lines to segregate fluids (Bratvedt *et al.*, 1996). Dispersive forces can be included by introducing a sixth stage in which fluids are redistributed by solving a parabolic equation on the background grid (Karlsen and Risebro, 2000; Berre *et al.*, 2002).

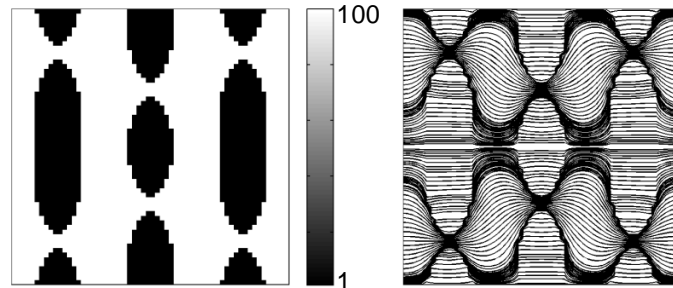


Fig. 2.55: Synthetic permeability field and streamlines used in our first example. The domain is square with unit length and 60 cells in each direction. Pressure at the left boundary is fixed at one and on the right is zero. No flow boundary conditions are imposed on the top and bottom. For simplicity the porosity is constant and equal to unity.

## 2.5.4 Results with standard mappings

In this section we test the streamline method using a unit mobility ratio in order to demonstrate the nature of the mapping errors. With a unit mobility ratio the velocity field and streamline locations do not depend on saturation so only a single global time step is required. By including additional steps we can observe the accumulation of mapping errors. The

synthetic permeability field used in this test is shown in Fig. 2.55 along with the streamlines used for each run. The grid density along streamlines was chosen such that there are twice as many 1D cells as underlying background grid cells. This 1D grid is adaptively coarsened away from saturation front. We used four grid levels with a ratio of two between each level.

Fig. 2.56 shows the saturation fields computed with 1, 5, 10 and 20 global time steps. As the number of time steps increases, the numerical smearing due to the mappings also increases. With a unit mobility ratio the global sweep of the displacement front is not strongly influenced by smearing. Later tests with an adverse mobility ratio demonstrate that this is not always the case. To reduce the numerical smearing we will introduce a more accurate method for mapping saturations to streamlines.

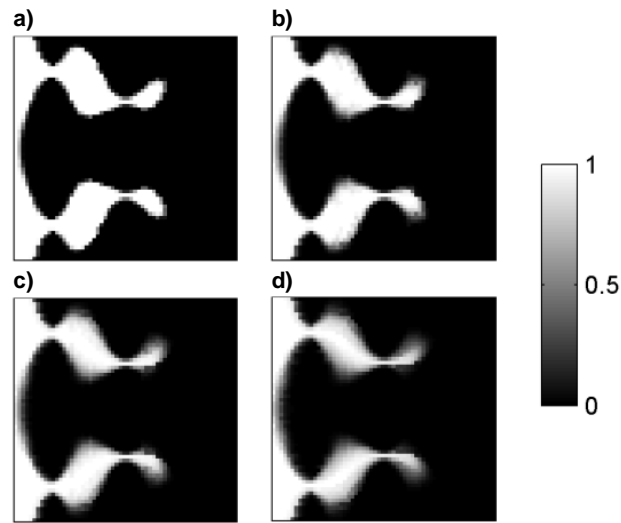


Fig. 2.56: Saturation fields computed using the standard mappings and (a) 1, (b) 5, (c) 10 and (d) 20 time steps. As the number of time steps is increased, the numerical smearing due to the mappings to and from streamlines also increases.

In this test, the mass balance errors for the injected fluid are 1.9%, 5.5%, 9.3% and 15% for runs a) through d), respectively. In each case the mass of injected fluid is underestimated. Similar results are obtained with the weights are determined by arc length rather than time of flight. The mass balance errors are large because the displacement front is sharp, irregularly shaped and not closely aligned with the grid. The permeability field used in this test was chosen specifically to exaggerate these features of the front. If the flow is aligned with the grid or if the saturation field is smooth, then the mass balance errors will generally be smaller. The mass balance problem is due to the mapping from streamlines to the background grid in stage 5 and can be understood by examining the streamline distribution in Fig. 2.55. Many streamlines are clustered near the boundaries of the low-permeability obstructions in the field. The time-of-flight weighting in Eq. (2.84) does not take into account the relative positions of streamlines within cells. Hence, streamlines in close proximity to one another are weighted incorrectly. The situation is not significantly improved by adding more streamlines since the additional streamlines tend to cluster in the same fashion.

One possible strategy to improve these mass balance errors is to assign a flux to each streamline and include this flux when determining the weights. If the flux reflects the clustering of streamlines correctly, then the mass balance errors can be improved. By experimenting with different fluxes we were able to reduce the mass balance error to  $-2.6\%$  in the case with 20 time steps. The flux for each streamline was taken as the flux through the background grid face at the upstream end of the streamline divided by the number of streamlines originating at that face, as suggested in Batycky (1997). In general, the accurate determination of fluxes is difficult without a priori knowledge of all streamline locations. Assigning fluxes to streamlines also places a severe restriction on possible tracing strategies and, in particular, requires that all streamlines begin and end at boundaries or wells. We view this as a severe limitation since we plan use local streamline tracing to gain efficiency in the compositional case. To improve the mass balance of the streamline method we propose a different approach to computing the weights based on Kriging.

### 2.5.5 Improved streamline mappings

As demonstrated in the previous section, the standard mappings introduce numerical smearing and mass balance errors. To reduce this type of error, in this section we introduce more accurate methods for mapping saturations between streamlines and the background grid. We describe our improved mappings in 2D although they have been designed to work well in the 3D case.

### 2.5.6 Improved mapping to streamlines

The numerical smearing observed in Fig. 2.56 is due primarily to errors introduced when mapping saturations from the background grid to streamlines in stage 3. The standard, first order method is based on a piecewise linear approximation of the streamline path and a piecewise constant representation of the saturation field on the background grid. Because the velocity field is typically smooth, we will continue to assume a piecewise linear streamline path. Similar to finite difference schemes, the smearing is due to the assumption of a piecewise constant saturation field. To improve the accuracy of the mapping we will utilize a piecewise linear reconstruction of the saturations on the background grid.

For each cell crossed by a streamline, we find the linear saturation profile within the cell by computing derivatives of saturation with respect to each of the coordinate directions. Unfortunately, the straightforward computation of derivatives can introduce overshoots and nonphysical saturations ( $S < 0$  or  $S > 1$ ) in the mapping. To avoid these complications we use slope limiters when computing derivatives as is common with total variation diminishing (TVD) finite difference schemes (Van Leer, 1979). For simplicity assume a uniform Cartesian background grid. In the  $x$ -coordinate direction we use the approximation,

$$\frac{\partial S_i}{\partial x} \approx \Psi(r_i) \cdot \frac{S_{i+1} - S_i}{\Delta x}, \quad r_i = \frac{S_i - S_{i-1}}{S_{i+1} - S_i}. \quad (2.85)$$

Here  $i$  is the  $x$ -index of the background grid cell and  $\Psi(\cdot)$  is a limiter function. The  $y$ -index has been dropped for clarity. We use the Superbee limiter,

$$\Psi(r) = \max(0, \min(2r, 1), \min(r, 2)). \quad (2.86)$$

Other limiters can also be used. See Sweby (1984) for a comparison of limiters in the context of finite difference schemes. The derivative in the  $y$ -coordinate direction is computed similarly.

Given  $x$ - and  $y$ -derivatives, the saturation at the points where the streamline enters and exits the cell can easily be computed. The resulting 1D profile is piecewise linear with discontinuities where the streamline crosses the background grid. Fig. 2.57a gives an illustration of our improved mapping to streamlines. We remap this profile onto to a uniform 1D grid that is used to initialize the finite difference solver. Fig. 2.57b shows the results of applying our improved mapping to streamlines to the example of the previous section.

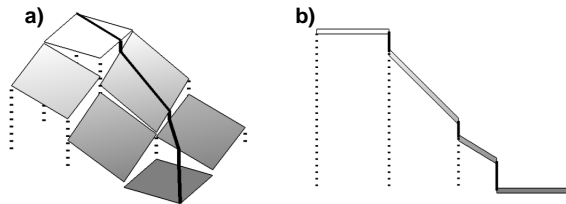


Fig. 2.57: Our improved mapping to streamlines utilizes a piecewise linear representation of saturations on the background grid (a). The resulting 1D profile along streamlines is also piecewise linear (b).

### 2.5.7 Improved mapping to the background grid

By improving the accuracy of the mapping to streamlines, the amount of numerical smearing introduced in the streamline method is reduced. The mass balance errors, however, are not reduced significantly as they are introduced primarily through the mapping from the streamlines to the background grid. We view the mapping to the background grid as an unstructured interpolation problem. The standard mapping given by Eq. (2.83) and Eq. (2.84) is not an accurate interpolator because the weight given to a streamline segment is determined without regard to the positions of other streamlines. Hence, the weights computed with Eq. (2.84) are not able to account for the clustering of streamlines.

To improve the accuracy of the mapping to the background grid we use the same form Eq. (2.83) but account for the correlation between streamline segments when computing the weights. This generalization leads to a Kriging interpolation scheme, or equivalently, radial basis function (RBF) interpolation. The proximity or correlation between a streamline segment  $L$  and a background grid cell  $V$  is given by,

$$\bar{\Phi}(L, V) = \frac{1}{\text{len}(L) \cdot \text{vol}(V)} \iint_{x \in L} \int_{x' \in V} \Phi(|x - x'|) dx' dx.$$

(2.87)

$\Phi(\cdot)$  is the covariance or RBF and  $|\cdot|$  denotes Euclidean distance. The integrals are taken over all points  $x$  along the streamline segment and all points  $x'$  within the grid cell (see Fig. 2.58). The proximity between two streamline segments  $L$  and  $L'$  is given by,

$$\hat{\Phi}(L, L') = \frac{1}{\text{len}(L) \cdot \text{len}(L')} \int_{x \in L} \int_{x' \in L'} \Phi(|x - x'|) dx' dx. \quad (2.88)$$

Fig. 2.58 gives an illustration of correlations Eq. (2.87) and Eq. (2.88).

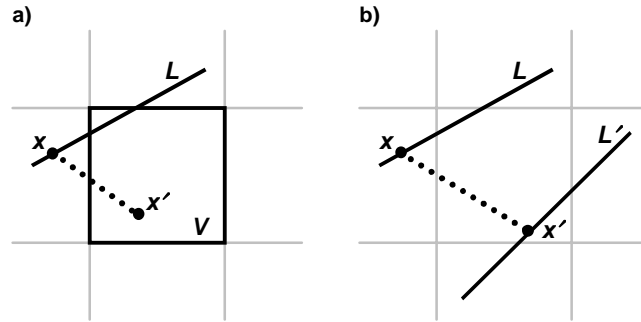


Fig. 2.58: Kriging utilizes both the proximity of streamlines to the background grid cell (a) and the proximity between streamlines (b). Because both of these correlations (shown as dotted lines) are included, the Kriging weights are accurate when streamlines are clustered.

Using Eq. (2.87) and Eq. (2.88) the Kriging system can be constructed in the following matrix form:

$$\begin{bmatrix} K & P \\ P^T & 0 \end{bmatrix} \begin{bmatrix} w \\ c \end{bmatrix} = \begin{bmatrix} k \\ p \end{bmatrix}. \quad (2.89)$$

Here  $K$  is a symmetric  $N$  by  $N$  matrix representing the correlation between streamline segments. Its entries are given by,

$$K_{ij} = \hat{\Phi}(S_i, S_j), \quad i, j = 1 \dots N. \quad (2.90)$$

Similarly, the  $N$ -vector  $k$  has entries  $k_i = \bar{\Phi}(S_i, V)$  and represents the correlation between the streamline segments and the grid cell whose saturation is to be interpolated. In practice we use Simpson's rule to evaluate the volume integral in Eq. (2.87) and the midpoint rule to evaluate the line integrals in Eq. (2.87) and Eq. (2.88). The entries of the  $M$ -vector  $c$  are Lagrange multipliers that constrain the interpolation according to some trend. The trend is typically represented by a polynomial. We use a linear trend that yields three constraints in 2D. These constraints are enforced by choosing the  $M$  by  $N$  matrix  $P$  and the  $M$ -vector  $p$  appropriately. See Deutsch and Journel (1992) for more details on the construction of the

Kriging system.

We use a covariance  $\Phi(h) = h^2 \ln(h)$ . This covariance corresponds to a spline RBF and yields a nonsingular Kriging system if the streamline segments used for interpolation are not collinear. This model has given accurate results in our tests, although other models can be used. For each cell on the background grid we search for the nearest streamline segments and include those segments in the interpolation Eq. (2.83). The number of streamline segments to include is fixed for each example. We directly interpolate from the streamline segments output from our 1D finite difference solver rather than remapping to the traced streamline segments. Because our 1D solver uses AMR, the number of segments to store prior to mapping to the background grid is greatly reduced. Since the nearest streamline segments are always used for interpolation Kriging does not require that every background grid cell be crossed by a streamline. Hence, fewer streamlines are required away from saturation fronts.

Fig. 2.59b shows the results of applying both of our improved mapping strategies to the example of the previous section with 20 steps. 20 streamline segments were included in each Kriging system. The mass balance error remains below 0.5% for this run as well as the runs with 1, 5 and 10 global time steps.

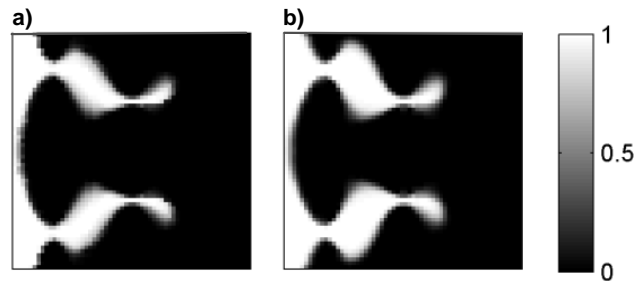


Fig. 2.59: Saturation profiles shown were computed with 20 time steps using (a) improved mapping to streamlines and time-of-flight weighting to map to the background grid, and (b) improved mapping to streamlines and Kriging to map to the background grid.

## 2.5.8 Results

In this section we consider two more realistic examples and compare our improved mappings to the standard mappings. The permeability fields are both taken from the Tenth SPE Comparative Solution Project (Christie and Blunt, 2001). To mimic gas injection processes we use an unfavorable mobility ratio,  $M = 10$ .

Example 2. The permeability field used in this example was taken from slice 9 and is shown in Fig. 2.60 along with a sample of traced streamlines. Despite appearing smooth, the permeability varies by four orders of magnitude in this case. Fig. 2.61 compares the saturation fields computed with the standard streamline mappings to those computed with our improved mappings. Runs with 5, 10 and 20 global time steps are shown. Due to the changes in mobility, the gas front extends further into the domain as the number of steps is increased.

For both methods, the improvement in capturing mobility changes competes with an increase

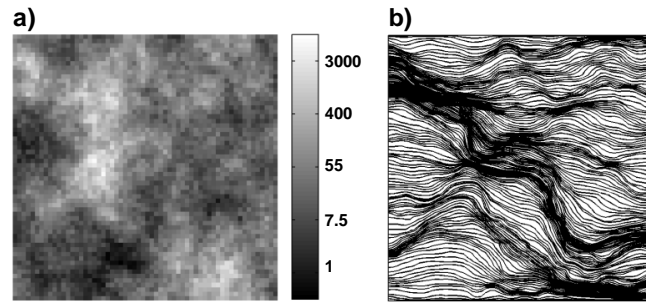


Fig. 2.60: (a) Permeability field used in our second example was taken from layer 9 of the SPE 10 model. (b) Approximately 150 streamlines were required to cover each cell with at least one streamline. Other parameters are used in this example are the same as in the previous example.

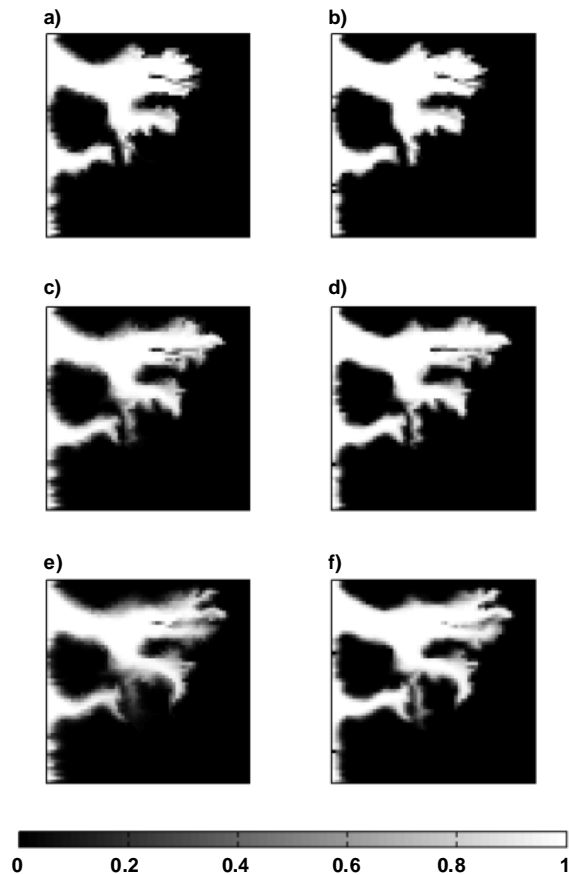


Fig. 2.61: Example 2 was run using 5 (top), 10 (middle) and 20 (bottom) global time steps. Saturation fields (a), (c) and (e) were found using the standard mappings to and from streamlines. The cases shown in (b), (d) and (f) were computed with our improved strategies for mapping saturations to and from streamlines.

in mapping error as more steps are taken. Relative to the standard mappings, our improved mappings introduce less numerical smearing in the solution. Mass balance errors are also reduced with the improved mappings from 1.9% to 0.3% with 5 steps, from 3.8% to 1.1% with 10 steps and from 5.2% to 2.6% with 20 steps. For the standard mappings, the mass balance errors are smaller for this example than with the previous synthetic example. This is due to the fact that the streamlines are more evenly distributed and somewhat aligned with the grid. For the improved mappings the mass balance errors are much higher than in the previous example. This is due to the more irregular shape of the displacement front. We repeated these runs and increased the number of streamlines so that at least two cross every background grid cell. The mass balance error with the improved mappings was reduced to 1.1% with 20 steps. The results with the standard mappings did not improve.

Example 3. The permeability field used in our final example is taken from layer 59 and contains well-defined channels. In this case approximately 350 streamlines were required to cross every background grid cell once. The permeability field and a sample of streamlines are shown in Fig. 2.62. Fig. 2.63 compares the saturation profiles obtained with the standard and improved mappings for the cases of 5, 10 and 20 global time steps. As expected the injected gas flows preferentially down the high permeability channels and achieves a low global sweep efficiency in all cases. With the standard mappings the gas front is smeared by the mappings much more than with the improved mappings. The mass balance errors are also extremely high with the standard mappings: 16% with 5 time steps, 23% with 10 time steps and 30% with 20 time steps. The improved mappings generate 0.2%, 0.5% and 3.3% mass balance error with 5, 10 and 20 global time steps. With enough streamlines to cross every cell twice, the mass balance error with the improved mappings was reduced to 0.6% with 20 steps. As in the previous case, the results with the standard mappings were not improved by adding streamlines.

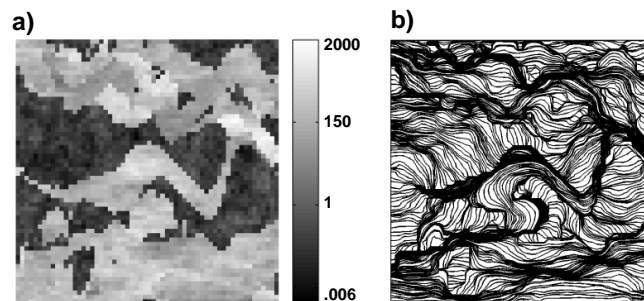


Fig. 2.62: (a) Permeability field used in our final example was taken from layer 59 of the SPE 10 model. (b) Approximately 350 streamlines were required to cross each cell at least once. Other parameters are used in this example are the same as in the previous examples.

### 2.5.9 Discussion

In all of the tests described, the improved mappings reduce numerical smearing of the saturation fronts and reduce mass balance errors relative the standard mappings. The improved method suggested here for mapping saturations to streamlines requires only a small modification to the standard method and does not significantly increase the computation time of streamline-based simulation. In addition, the extension of this improved mapping strategy to the compositional case is straightforward. Here we have used a 1D finite difference solver along streamlines although improved mapping to streamlines will also be beneficial if front tracking is used.

The mapping from streamlines to the background grid is the more challenging of the two mappings. Our tests show that the standard time-of-flight weighting is not sufficiently accurate when streamlines become clustered. Determining weights by considering fluxes along streamlines may improve mass balance errors somewhat; however, our experience suggests that accurate determination of fluxes will prove difficult and will limit the possible tracing strategies that can be used to ensure adequate streamline coverage. In particular, we are interested in using local or partial streamline tracing and fluxes will be difficult to assign in this case.

The Kriging interpolation suggested here for mapping from streamlines to the background grid does not require that fluxes be assigned to streamlines and is not limited to any particular tracing strategy. The Kriging weights naturally account for the clustering of streamlines. We have presented results in 2D, but Kriging in 3D requires few modifications.

The results reported suggest that Kriging can significantly improve the mass balance of streamline-based simulation. The number of streamline segments included in each Kriging system was fixed for each case considered here. A more robust and potentially more accurate strategy would be to vary this number locally according to streamline density. The covariance model used in our tests gave good results, but we will test other models in future work. In particular we suspect that in highly heterogeneous 3D cases some accuracy may be gained by using an anisotropic covariance model. In addition to these improvements we will be investigating new strategies for tracing streamlines that will ensure adequate streamline coverage using a minimal number of streamlines.

Relative to the standard time-of-flight weighting, there is a computational cost associated with Kriging. The additional effort is warranted due to the improvements in accuracy observed. Even with Kriging, the majority of the overall computation time was spent solving the 1D saturation equations along streamlines. When more complicated fluid descriptions such as the compositional model are used, the 1D streamline solves will increase in cost, while the cost associated with Kriging will remain nearly constant. In the case that many components are used in the fluid description, the Kriging system need only be solved once for each cell and the same weights can be used to map each component. Fluid phase behavior must be accounted for when apply this Kriging strategy to the compositional case. This extension will be described in future work.

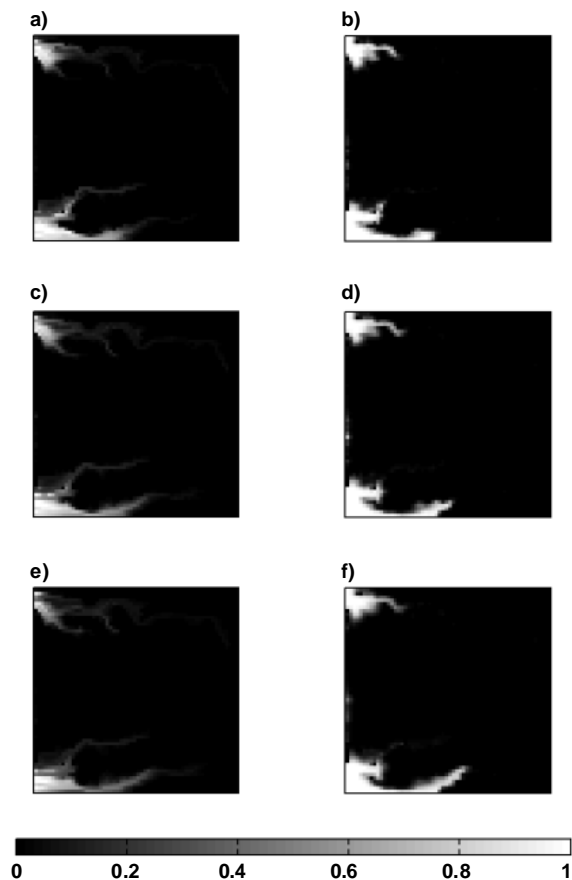


Fig. 2.63: The final example was also run with 5 (top), 10 (middle) and 20 (bottom) global time steps. Saturation fields (a), (c) and (e) were found with the standard mappings. The results shown in (b), (d) and (f) were computed with our improved mappings to and from streamlines.

### 2.5.10 Conclusions

Test results reported here confirm that the streamline method can achieve high-resolution results when applied to a simple model for miscible flooding if few global time steps are taken. These tests also show that as the number of time steps is increased the standard mappings to and from streamlines introduce numerical smearing of saturation fronts and significant mass balance errors. The errors introduced by the mappings can adversely effect the predictions of global sweep as seen in our examples. The mass balance errors reduce the reliability of predictions and in our tests are not improved by including additional streamlines if the standard mappings are used.

The numerical smearing is controlled primarily by the method used to map saturations from the background grid to streamlines. The standard mapping to streamlines uses a piecewise constant representation of saturations on the background grid. By constructing a

piecewise linear representation of saturations we were able to reduce the smearing of saturation fronts in our tests. The improved mapping to streamlines can easily be incorporated in any streamline-based simulator.

Mass balance errors are introduced primarily by the mapping of saturations from streamlines to the background grid. Simple time-of-flight weighting of streamline segments introduces large errors when streamlines become clustered. An alternative is the use of a Kriging interpolation scheme to map saturations from streamlines to the background grid. Kriging naturally accounts for the clustering of streamlines and in our tests reduces mass balance errors relative to time-of-flight weighting. Increasing the number of streamlines further reduces the mass balance errors obtained with Kriging.

## **2.6 Summary**

In this Chapter, we have demonstrated that when reservoir heterogeneity controls flow paths, and when effects of gravity segregation and capillary crossflow are small, compositional streamline simulations are appropriate, and they are orders of magnitude faster than conventional finite-difference compositional simulations. The example given in this chapter of simulation of condensate recovery illustrates that point. In that example, a combination of an analytical solution for the condensate displacement process along a single streamline with a streamline representation of the effects of heterogeneity on the flow was used to perform simulations that were much less subject to the effects of numerical smearing than the corresponding finite difference simulations and much faster to perform. We also demonstrate how to apply higher-order accurate numerical schemes along streamlines for situations where streamlines must be updated periodically to account for changes in mobility in the porous medium. Finally we address the mass-conservation problem associated with the streamline approach and demonstrate how more accurate streamline methods can be devised through application of sophisticated interpolation schemes to and from the background/pressure grid.

### 3 Analytical Solutions for One-Dimensional Flow

The previous chapter demonstrated that analytical solutions for one-dimensional flow can be put to good use in streamline computations. A substantial body of mathematical theory now exists for construction of analytical solutions to the dispersion-free 1D flow problem (Monroe *et al.*, 1990; Johns *et al.*, 1993 and 1996; Johansen *et al.*, 1994; Dindoruk *et al.*, 1992 and 1997). Those investigations considered four-component systems primarily, but special case solutions for systems with more than four components were reported for fully self-sharpening displacements by pure injection gases. The first systematic attempts to describe multicomponent gas/oil systems were restricted to calculation of the minimum miscibility pressure (MMP: Wang and Orr, 1997; Jessen *et al.*, 1998; Wang and Orr, 2000). Those calculations were based on identifications of the key tie lines that control miscibility. Calculation of the full analytical solutions for multicomponent oils and gases was not required to determine the MMP and was not attempted. In the work of Jessen *et al.*, 2001, the results of previous works were integrated in a new approach allowing automatic generation of 1D solutions for the special case of no volume change on mixing. The restriction of no volume change on mixing was later relaxed for fully self-sharpening systems (Ermakov, 2000; Jessen, 2000).

In the following sections, we complete the analytical theory of gas injection processes by combining the work of Ermakov, (2000) and Jessen *et al.* (1999) with an approach for describing systems with nontie-line rarefactions. The resulting tool allows automatic generation of 1D solutions to multicomponent two-phase flow including effects of volume change on mixing. We also apply the theory to obtain the first analytical solutions for condensate displacement.

#### 3.1 Analytical solutions for multicomponent gas/oil displacements

In this section, we consider one-dimensional flow of multicomponent gas/oil mixtures, and we include the effects of volume change as components move from one phase to another. When CO<sub>2</sub> displaces an oil at moderate pressure, for example, CO<sub>2</sub> that dissolves in undisplaced oil occupy significant less volume than CO<sub>2</sub> in the vapor phase. In that situation, volume is lost, and the displacement velocity slows as a result. The mathematical approach described in this section accounts for that volume change in addition to the interactions of phase equilibrium and flow that are so important in gas injection processes.

The mass conservation equations for multicomponent, dispersion-free two-phase flow in one dimension can be written as (Dindoruk, 1992).

$$\frac{\partial G_i}{\partial \tau} + \frac{\partial H_i}{\partial \xi} = 0 \quad , \quad i = 1, \dots, n_c \quad , \quad (3.1)$$

where  $G_i$  is the molar concentration of component  $i$

$$G_i = x_i \rho_{xD} (1 - S) + y_i \rho_{yD} S \quad , \quad (3.2)$$

and  $H_i$  is the molar flux of component  $i$

$$H_i = u_D (x_i \rho_{xD} (1-f) + y_i \rho_{yD} f) \quad (3.3)$$

Eqs. (3.1) - (3.3) are given in dimensionless form. The dimensionless form is obtained by introducing the variables

$$\tau = \frac{u_{inj} t}{\phi L}, \quad \xi = \frac{z}{L}, \quad \rho_{jD} = \frac{\rho_j}{\rho_{ini}}, \quad u_D = \frac{u}{u_{inj}}, \quad (3.4)$$

where  $u_{inj}$  is the injection velocity,  $t$  is the time,  $\phi$  is the porosity and  $L$  is the overall length of the porous medium. The distance from the inlet is given by  $z$  and the molar density of the initial fluid is denoted  $\rho_{ini}$ . The phase equilibrium of the fluids are introduced in the flow equations by the molar density of phase  $j$  and the corresponding equilibrium vapor ( $y_i$ ) and liquid ( $x_i$ ) compositions of component  $i$ . Finally,  $S$  is the volumetric vapor phase saturation and  $f$  is the fractional flow of vapor related to  $S$ . In the examples described here, we use fractional flow functions of the form,

$$f = \frac{S^n}{S^n + \mu_r (1 - S - S_{or})^n} \quad (3.5)$$

In Eq. (3.5),  $\mu_r$  is the ratio of vapor to liquid viscosity and the exponent  $n$  is a constant depending on the system of interest.

Eq. (3.1) is derived based on the assumptions stated by Dindoruk, *et al.* (1992): (1) the flow takes place in a 1D porous medium with uniform properties, (2) the effects of dispersion and capillary pressure can be neglected, (3) that the phases present at any location along a streamline are in local chemical equilibrium (which is specified by the Peng-Robinson equation of state), and (4) for the purposes of the phase equilibrium calculation, the pressure along the streamline is assumed to be constant (See Chapter 5 for a detailed discussion of the accuracy of this assumption). When components can change volume as they transfer between phases, the local flow velocity varies along the displacement length in a way that satisfies at any position,  $\xi$ , a version of the continuity equation obtained by summing Eq. (3.1) over the  $n_c$  components. If, on the other hand, each component has fixed partial molar volume, no matter what phase the component appears in, then the local flow velocity is fixed (see Johns *et al.*, 1993 for the appropriate form of the balance equations).

In the example solutions that follow, the fractional flow function of the vapor phase was taken to be

$$f_v = \frac{S_v^2 / \mu_v}{S_v^2 / \mu_v + (1 - S_{or} - S_v)^2 / \mu_l} \quad (3.6)$$

where  $\mu_v$  and  $\mu_l$  are the viscosities of the vapor and liquid, which were calculated with the viscosity correlation of the Lohrenz *et al.* (1964), and  $S_{or}$  is the residual oil saturation,

assumed to be  $S_{or} = 0.2$  in the example calculations. Phase equilibrium was calculated with the Peng-Robinson equation of state (Peng and Robinson, 1976).

To complete specification of the 1D flow problem, initial and injection compositions and the displacement pressure and temperature (for phase equilibrium calculations) must be given. The initial composition is assumed to be constant throughout the displacement length, and the injection composition is constant for the entire displacement (a Riemann problem).

### 3.1.1 Solution construction

Eq. (3.1) can be solved by the method of characteristics (Dumoreé *et al.*, 1984; Monroe *et al.*, 1990; Dindoruk, 1992, Dindoruk *et al.*, 1992). In that approach, the propagation velocity of a given overall composition is determined by recasting the first-order partial differential equations in terms of an eigenvalue problem. The resulting solutions consist of continuous variations (known as rarefactions) and shocks, jumps in composition and saturation similar to the shocks that arise in a Buckley-Leverett solution for water displacing oil. In Riemann problems, the propagation velocity (which is different from the local flow velocity) of each overall composition or shock is constant throughout the displacement.

#### 3.1.1.1 Shocks

Two types of shocks are observed: (1) shocks that connect a composition in the single-phase region with a composition in the two-phase region and (2) shocks that connect two compositions within the two-phase region. Shocks of the first type must occur along the extension of a tie line (Dumoreé *et al.*, 1984). That is, the single-phase composition lies on the extension of a tie line. If a shock connects two tie lines, the extensions of those tie lines must intersect (Dindoruk, 1992, Dindoruk *et al.*, 1992).

If a shock occurs, it must satisfy an integral material balance of the form,

$$\Lambda^{AB} = \frac{H_i^A - H_i^B}{G_i^A - G_i^B} = \frac{u_D^A \alpha_i^A - u_D^B \alpha_i^B}{G_i^A - G_i^B}, \quad i = 1, n_c, \quad (3.7)$$

where  $\Lambda^{AB}$  is the propagation velocity of the shock that connects composition points A and B,

$$\alpha_i = \sum_{j=1}^{n_p} x_{ij} \rho_{jD} f_j \quad (3.8)$$

The shocks described by Eq. (3.7) have two varieties. When the propagation speed of the shock matches the composition propagation velocity on one side of the shock, then  $\Lambda = u_{D^*}$  ( $df/dS$ ). Such shocks are known as semi-shocks or tangent shocks. For many shocks, however, the shock velocity is not equal to the composition velocities on the upstream and downstream sides of the shock. Shocks of this type are called genuine shocks.

### 3.1.1.2 Continuous variation (tie-line path and nontie-line path)

Two types of continuous variation are found in the analytical solutions. The first type is a continuous variation along a tie line. This type of rarefaction is easily included into the solution as the key tie lines can be located by the intersection approach (Wang and Orr, 1997, 2000; Jessen *et al.*, 1998). In the second type of continuous variation, spreading waves connect neighboring key tie lines. For this type of rarefaction, the eigenvalue problem must be solved for the composition path, where eigenvalues are characteristic wave velocities of a given overall composition subject to composition variation in the eigenvector direction. In the following section we address the eigenvalue problem and demonstrate how to trace nontie-line rarefactions. A method, referred to as the envelope rule (Jessen *et al.* 2001), is now available for the prediction of nontie-line rarefactions in a given 1D-displacement process. This tool allows us design a general algorithm for automatic generation of analytical solutions including volume change on mixing.

In this section we return to the conservation equations to outline the approach for including non-tie line rarefactions in the analytical solutions. The mass conservation equations can be rewritten as an eigenvalue problem by introducing a self-similarity variable  $\eta$ , defined as

$$\eta = \frac{\xi}{\tau} \quad . \quad (3.9)$$

After variable substitution and rearrangement, the resulting eigenvalue problem takes the form (Dindoruk, 1992)

$$(\underline{A} - \lambda \underline{B})\underline{X} = \underline{0} \quad , \quad (3.10)$$

where the coefficients of the matrices A and B are evaluated as

$$A_{ji} = \begin{cases} \frac{\partial H_j}{\partial Z_i} , j = 1, \dots, n_c, i = 1, \dots, n_c - 1, \\ \frac{\partial H_j}{\partial u_D} , j = 1, \dots, n_c, i = n_c, \end{cases} \quad (3.11)$$

and

$$B_{ji} = \begin{cases} \frac{\partial G_j}{\partial Z_i} , j = 1, \dots, n_c, i = 1, \dots, n_c - 1, \\ 0 , j = 1, \dots, n_c, i = n_c. \end{cases} \quad (3.12)$$

The elements of the eigenvector X are given by

$$\underline{X}^T = \left[ \frac{dZ_1}{d\eta}, \dots, \frac{dZ_{n_c-1}}{d\eta}, \frac{du_D}{d\eta} \right] . \quad (3.13)$$

$Z_i$  is the overall composition in mole fractions of component  $i$  along the solution path in compositional space. From a numerical point of view, the eigenvalue problem stated in Eq. (3.10) suffers from the fact that one eigenvalue, associated with the total velocity, will be infinite. This is a result of the fact that changes in velocity and density propagate instantaneously throughout the system. Dindoruk, (1992) developed a method to decouple the total flow velocity,  $u_D$ , and overcome this problem. The decoupling of the total flow velocity facilitates the evaluation of eigenvalues and is the method implemented in the current project.

The decoupling of the total velocity result in the following form of the eigenvalue problem (Dindoruk, 1992),

$$\begin{pmatrix} \underline{C} - \lambda^* \underline{D} & \underline{0} \\ \underline{E} - \lambda^* \underline{F} & \frac{1}{u_d} \end{pmatrix} \underline{X} = \underline{0} \quad , \quad (3.14)$$

where

$$C_{ji} = \frac{\partial H_j^*}{\partial Z_i} - \frac{H_j^*}{H_{n_c}^*} \frac{\partial H_{n_c}^*}{\partial Z_i} , \quad i = 1, \dots, n_c - 1 , \quad j = 1, \dots, n_c - 1 \quad , \quad (3.15)$$

and

$$D_{ji} = \frac{\partial G_j}{\partial Z_i} - \frac{H_j^*}{H_{n_c}^*} \frac{\partial G_{n_c}}{\partial Z_i} , \quad i = 1, \dots, n_c - 1 , \quad j = 1, \dots, n_c - 1 \quad , \quad (3.16)$$

with

$$H_i^* = \frac{H_i}{u_d} \quad , \quad \lambda^* = \frac{\lambda}{u_d} \quad . \quad (3.17)$$

The entries of the vectors  $E$  and  $F$  are given by

$$E_j = \frac{1}{H_{n_c}^*} \frac{\partial H_{n_c}^*}{\partial Z_j} , \quad j = 1, \dots, n_c - 1 \quad , \quad (3.18)$$

and

$$F_j = \frac{1}{H_{n_c}^*} \frac{\partial G_{n_c}}{\partial Z_j} , \quad j = 1, \dots, n_c - 1 \quad . \quad (3.19)$$

The decoupled eigenvalue problem stated in Eq. (3.14) can now be solved in two steps. The first step is to evaluate the eigenvalues/eigenvectors from

$$(\underline{C} - \lambda^* \underline{D})\underline{e} = \underline{0} \quad . \quad (3.20)$$

Eq. (3.20) is solved independently from the total velocity,  $u_D$ , with  $e$  given by

$$\underline{e}^T = \left[ \frac{dZ_1}{d\eta}, \dots, \frac{dZ_{n_c-1}}{d\eta} \right] \quad (3.21)$$

The new overall composition along the nontie-line path is obtained by taking a small step  $\delta$  in the eigenvector direction

$$Z_i^{new} = Z_i^{old} + \delta e_i, \quad i = 1, \dots, n_c - 1, \quad (3.22)$$

and

$$Z_{n_c}^{new} = 1 - \sum_{i=1}^{n_c-1} Z_i^{new}. \quad (3.23)$$

Subsequently the change in the total velocity can be evaluated from

$$u_D^{new} = u_D^{old} e^{-\gamma\delta}, \quad (3.24)$$

where the exponent  $\gamma$  is evaluated as

$$\gamma = (\underline{E} - \lambda^* \underline{F}) \underline{e}. \quad (3.25)$$

After updating the overall composition and the total flow velocity, the stepwise procedure is repeated for the new overall composition, and the nontie-line path is constructed. For details on the decoupling procedure, the reader is referred to Dindoruk, 1992 (section 3.4.1, pp. 35).

In the following, we assume that all key tie lines have been determined by the intersection approach. If a pair of neighboring key tie line is connected by a nontie-line rarefaction, according to the envelope rule, the integration of the nontie-line path begins on the shortest of the two tie lines. The equal-eigenvalue points of interest ( $n_c-2$ ) are located by the approach outlined by Dindoruk, (1992). The equal-eigenvalue points are points where a tie-line path can change to a nontie-line path without violation of the velocity rule. Only one of the equal-eigenvalue points is associated with the appropriate nontie-line path that connects the two key tie lines in question. For regularly S-shaped fractional flow curves, the values of the nontie-line eigenvalues stay ordered on either side of the inflection point (maximum value of  $df/dS$ ). As the solution for oil-gas systems is restricted to the region of  $f > S$ , this fact enables us to select the correct equal-eigenvalue point by evaluating the eigenvectors for composition points between two equal-eigenvalue points. Between two equal-eigenvalue points on a key tie line, only one eigenvector will point in the direction of the neighboring key tie line. Hence, the ordering of eigenvalues (eigenvectors) allows selection of the proper equal-eigenvalue point from which the nontie-line path integration is started. Once the appropriate equal-eigenvalue point has been determined, stepwise numerical integration of the eigenvectors is used to trace the nontie-line path. In the vicinity of the equal-eigenvalue point, small steps must be used to ensure appropriate accuracy, whereas larger steps can be used away from this point. The typical behavior of a nontie-line path integration is shown in Fig. 3.1.

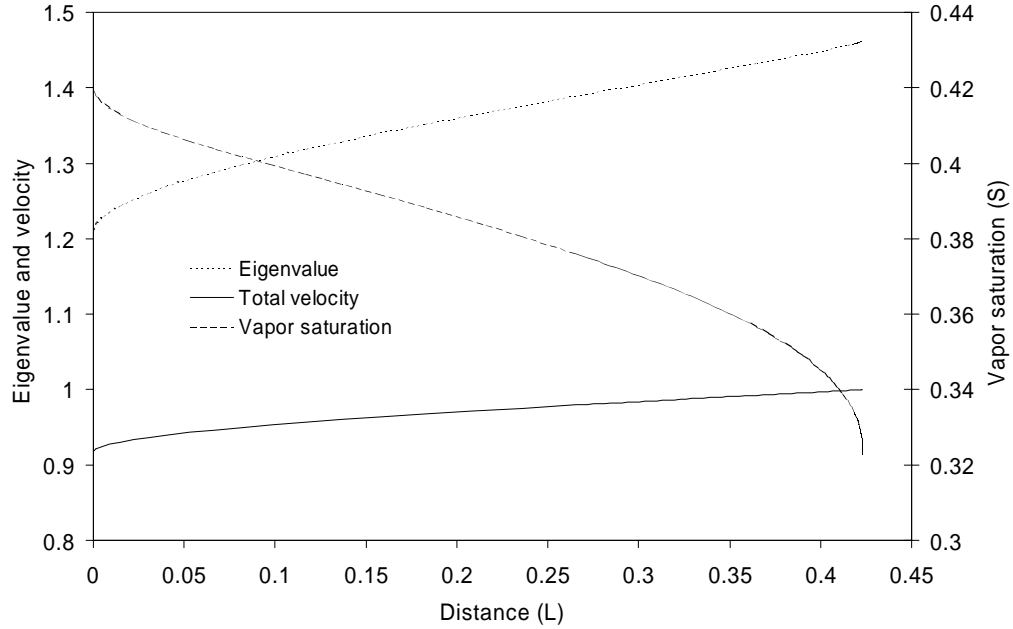


Fig. 3.1: Variation of wave speed, saturation and total velocity along a non-tie line path.

Fig. 3.1 shows the variation in wave velocity (eigenvalue), vapor saturation and total velocity along a nontie-line path. The location on the nontie-line path is given as the distance  $L$  at a given location on the path to the target tie line (neighboring tie line). The distance is defined as

$$L = \sum_{i=1}^{n_c} \left( x_{i,target} - x_{i,current} \right)^2 + \left( y_{i,target} - y_{i,current} \right)^2 . \quad (3.26)$$

In Fig. 3.1, the stepwise integration of the non-tie line path starts from the right hand side of the figure and terminates on the neighboring key tie line at the left hand side. The slope of the eigenvalue vs. distance curve is steeper in the vicinity of the equal eigenvalue point. Hence, using small initial steps minimizes the error introduced by the stepwise integration.

As the total flow velocity varies along nontie-line paths, special care must be taken in including this effect in the analytical solution. For each nontie-line rarefaction, the total flow velocity at the equal-eigenvalue point is assumed to be unity. The total velocity along the nontie-line path can then be rescaled later following the approach outlined in Ermakov (2000) and Jessen (2000).

### 3.1.2 Analytical solutions for self-sharpening systems

Displacement problems where all key tie line are connected by shocks (fully self-sharpening) allow for a simpler solution strategy than implied by the precious section. The self-sharpening behavior of a displacement eliminates the need for performing the integration of the nontie-line path and requires only an efficient approach for locating all key tie lines. Wang and Orr (2000) and Jessen *et al.*, (1998) demonstrated how key tie lines can be located for multicomponent gas/oil displacement problems. Their approach was used in the first

automatic approach for generating solutions to multicomponent gas/oil displacements without volume change on mixing (Jessen *et al.*, 1999). The algorithm for constructing solutions for fully self-sharpening displacements is:

1. Determine the key tie lines by the tie line intersection approach (Wang and Orr, 2000; Jessen, 1998).
2. Locate the primary (shortest) tie line.
3. Construct the upstream and downstream portions of the solution by solving sequentially the shocks balances for each adjacent pair of key tie lines. The upstream and downstream segments each begin with a shock that is tangent at the primary tie line.

In this section, we consider only fully self-sharpening displacements, in which all tie lines are connected by shocks. To solve the problem for systems in which volume change plays a role, the form of the equations derived by Dindoruk (1992) is used. He showed that the tie lines intersect in a molar concentration space at the intersection point X,  $(\rho_{zi})^X$ , defined by the equations of the intersecting tie lines. Once the intersection point is known, the shock balances can be written conveniently as (details of the derivations are given by Dindoruk, 1992; Ermakov, 2000 and Jessen, 2000)

$$\Lambda^* = \frac{\Lambda^{AB}}{u_D^A} = \frac{f^A - S^{XA}}{S^A - S^{XA}} = \frac{u_D^A}{u_D^B} \frac{f^B - S^{XB}}{S^B - S^{XB}} = \left( \frac{df}{dS} \right)^A \quad (3.27)$$

Eq. (3.27) is written for a tangent shock from point A to point B, in which the shock velocity matches the composition wave velocity at point A. The saturation and fractional flow,  $S^{XA}$  and  $f^A$  or  $S^{XB}$  and  $f^B$ , refer to the values at the shock landing points A and B on the tie lines that contain those points. The saturations  $S^{XA}$  and  $S^{XB}$  refer to the tie-line intersection point.  $S^{XA}$  is the saturation at that point measured on the tie line that contains point A, and similarly,  $S^{XB}$  is the saturation measured on the tie line that contains point B. The saturation at any point on a tie line can be calculated easily from a tie-material balance

$$z_i = Vy_i + (1-V)x_i \quad , \quad i = 1, n_c \quad , \quad (3.28)$$

where  $V$  is the vapor mole fraction, and  $x_i$  and  $y_i$  are the mole fractions of component  $i$  in the equilibrium liquid and vapor. The saturation at overall composition  $z_i$  is

$$S_v = \frac{V/\rho_v}{V/\rho_v + (1-V)/\rho_l} \quad (3.29)$$

Similar equations apply if the shock is a genuine shock. In that case,  $\Lambda^*$  does not equal  $df/dS$ , but the composition on one side of the shock is known.

The ratio of flow velocities on either side of the shock can be determined from Eq. (3.27). To determine the actual flow velocities, the velocity ratios for all the shocks between tie lines

are calculated, and then the velocity ratios for the leading and trailing phase change shocks are calculated. Because the flow velocity at the inlet is  $u_D = 1$ , all the remaining flow velocities can be found from the ratios. For any shock in which the composition on one side of the shock is a single-phase mixture (see Dindoruk, 1992 or Jessen, 2000 for details)

$$\Lambda^* = \frac{\Lambda}{u_D^II} = \frac{f^{II} - S^I}{S^{II} - S^I} = \left( \frac{df}{dS} \right)^{II} \quad (3.30)$$

where the superscript II refers to the two-phase side of the shock, and  $S^I$  is the saturation at the single-phase composition (greater than one or less than zero). The velocity ratio for the shock is given by

$$\frac{u_D^I}{u_D^{II}} = \frac{1 - \Lambda^*}{\rho_D^I} \{ \rho_{ID} + S^I (\rho_{vD} - \rho_{ID}) \} \quad , \quad (3.31)$$

where  $u_D^I$  and  $u_D^{II}$  refer to the dimensionless flow velocities on the single- and two-phase sides of the shock, and  $\rho_D^I$  is the dimensionless molar density of the single-phase mixture.

The theory outlined above was used to find solutions for several gas displacement problems that illustrate the effects of volume change on mixing. Fig. 3.2 shows the results for a displacement of a five-component oil containing equal mole fractions of methane ( $\text{CH}_4$ ), n-butane ( $\text{C}_4$ ), decane ( $\text{C}_{10}$ ), tetradecane ( $\text{C}_{14}$ ), and eicosane ( $\text{C}_{20}$ ) by pure  $\text{CO}_2$  at 109 atm (1600 psia) and 71 C (160 F).

Fig. 3.2 compares the saturation profiles for solutions with and without volume change. Additional details of the solution, such as the compositions at the shock landing points and the flow velocities on each key tie line are given by Ermakov (2000). In this example, volume change reduces the flow velocity.  $\text{CH}_4$  from the oil present in the transition zone appears in a leading  $\text{CH}_4$  bank, and when the injected  $\text{CO}_2$  encounters the undisplaced oil, it dissolves, losing volume in the process. In displacements in which the pressure is high enough that the solubility of  $\text{CO}_2$  in the oil is appreciable, but not high enough that the displacement is very efficient, the loss of volume can actually cause  $\text{CO}_2$  breakthrough to occur after one pore volume of injection (see Orr *et al.* (1983), for experimental results that show this effect and Dindoruk (1992), for theoretical examples).

Fig. 3.3 compares the analytical solution including the effects of volume change with results of a FD compositional simulation performed with single-point upstream weighting, 1000 grid blocks and  $\Delta x/\Delta t$  set to 5. Also shown in Fig. 3.3 is a numerical solution obtained by a TVD scheme (unpublished simulator written by Marco Thiele and Michael Edwards). While the numerical solutions show some smearing of the shocks, it is clear that the numerical and analytical solutions agree very well.

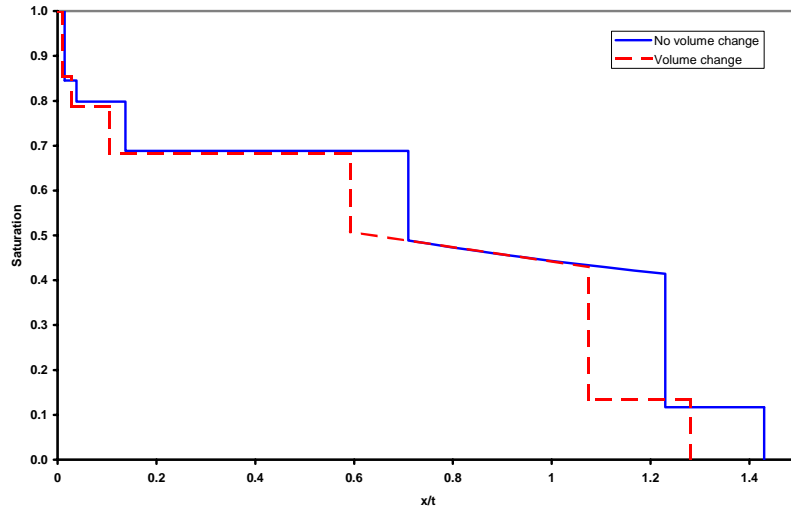


Fig. 3.2: Saturation profiles for displacement of a five-component oil by  $\text{CO}_2$  at 109 atm (1600 psia) and 344 K (160 F).

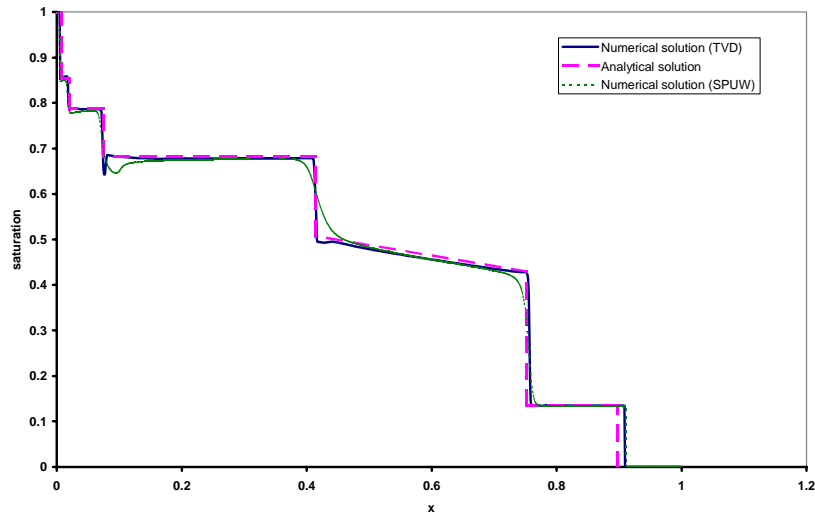


Fig. 3.3: Analytical and numerical solutions for a five-component oil at 0.7 pore volumes injected.

Fig. 3.4 shows that the effects of volume change become much smaller as miscibility is approached, however. At a displacement pressure 1 atm below the minimum miscibility pressure (MMP), nearly all the oil is displaced, and the change in flow velocity that results from the dissolution of  $\text{CO}_2$  in the small amount of oil remaining in the transition zone is small. Hence, the solutions with and without volume change differ only slightly. The flow behavior in the vicinity of the MMP is dominated by phase behavior as represented by the

key tie line that is approaching the critical locus, and that behavior is determined by the geometry of the tie lines, which is not affected by volume change.

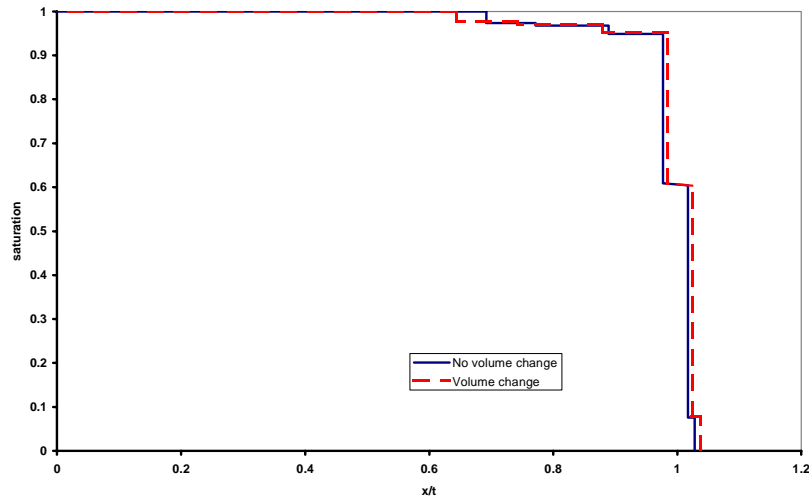


Fig. 3.4: Saturation profile for a displacement of a near-miscible five-component oil by  $\text{CO}_2$  at 161 atm and 344 K.

Fig. 3.5 shows the results of a more realistic displacement problem. In this example, Oil 1, a 15-component oil, is displaced by Gas 1, which is mostly methane (Høier, 1997) at 275 atm and 387 K. The compositions of Oil 1 and Gas 1 are given in Table 3-1.

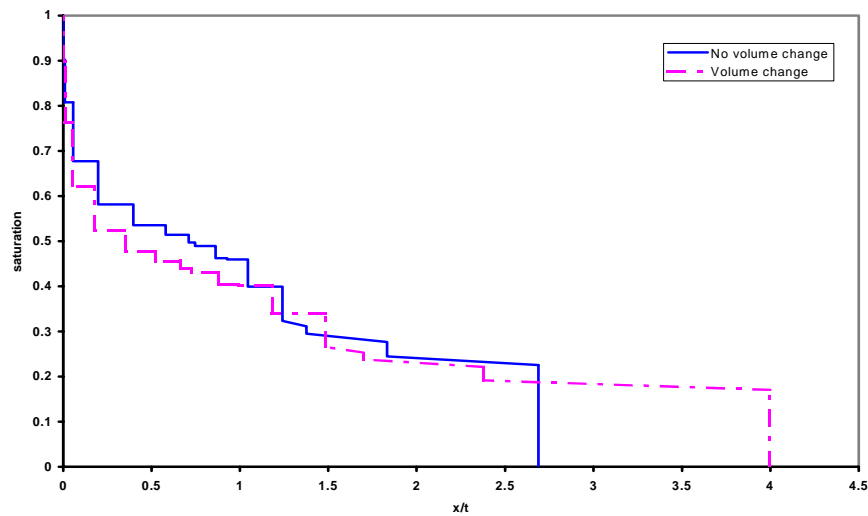


Fig. 3.5: Effects of volume change in displacement of Oil 1 by Gas 1 at 275 atm and 387 K.

In this case, the effect of volume change is to increase the flow velocity. Substantial quantities of  $\text{CH}_4$  are present in the oil, and when the vapor phase created by the injected gas appears,  $\text{CH}_4$  dissolved in the oil transfers to the vapor phase, where it occupies more volume. Fig. 3.5 demonstrates that it is possible to solve problems analytically with enough

components present that the phase behavior of the system can be represented accurately.

Table 3-1: Oil and injection gas compositions for the 15-component displacements.

Comp.	Oil 1 (Mol %)	Oil 2 (Mol %)	Gas 1 (Mol %)	Comp.	Oil 1 (Mol %)	Oil 2 (Mol %)	Gas 1 (Mol %)
N <sub>2</sub>	0.785	0.450	1.5858	n-C5	1.406	1.650	0.0226
CH <sub>4</sub>	45.622	45.850	92.8772	C6	2.097	2.520	0.1133
CO <sub>2</sub>	0.265	1.640	0.5973	C7+(1)	4.902	12.440	0.1205
C <sub>2</sub>	6.090	7.150	3.6638	C7+(2)	9.274	6.320	0.0914
C <sub>3</sub>	4.429	6.740	0.3888	C7+(3)	9.880	5.024	0.0001
i-C <sub>4</sub>	0.865	0.840	0.3389	C7+(4)	7.362	3.240	0.0000
n-C <sub>4</sub>	2.260	3.110	0.0851	C7+(5)	3.804	1.996	0.0000
i-C <sub>5</sub>	0.957	1.030	0.1154				

Fig. 3.6 shows results of a displacement of Oil 1 (Table 3-1) by a mixture of 75% CO<sub>2</sub> and 25% CH<sub>4</sub> at 275 atm and 368 K. The MMP for this system is 291 atm, so this displacement is nearly miscible. Also shown are numerical solutions obtained with single-point upstream weighting and  $\Delta x/\Delta t = 10$ . The adverse effects of numerical dispersion are significant in this example, with poor agreement between the numerical and analytical solutions unless a very fine grid is used, though it is clear that the numerical solutions do converge to the analytical solution as the grid is refined.

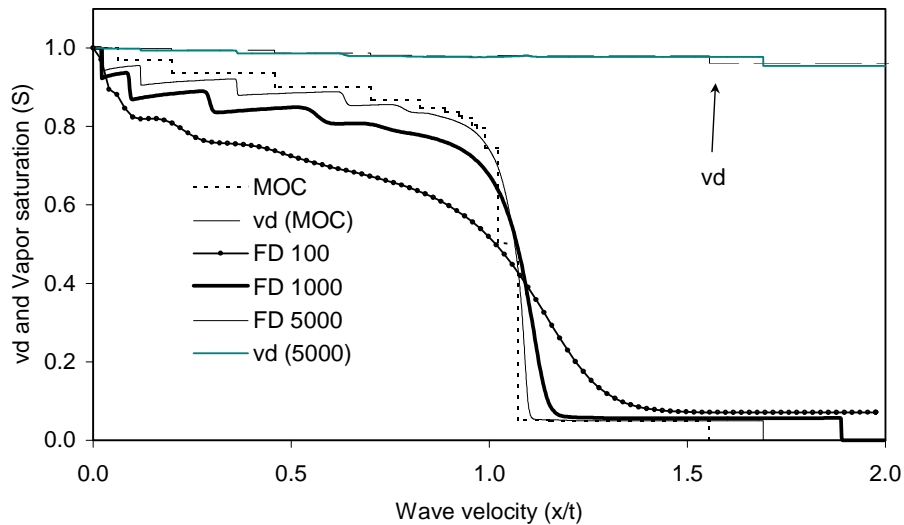


Fig. 3.6: Comparison of numerical and analytical solutions with volume change for displacement of Oil 3 by a gas containing 75% CO<sub>2</sub> and 25% CH<sub>4</sub> at 275 atm and 368 K.

Calculated recoveries at 1.2 pore volumes injected are shown for a displacement of Oil 2 by pure N<sub>2</sub> at 387 K in Fig. 3.7. For the fully self-sharpening examples considered here calculation of recovery is straightforward. As Fig. 3.2 to Fig. 3.6 show, the solution profiles consist mainly of zones of constant state separated by shocks. A material balance can be performed easily for those zones by multiplying the molar concentration of each component, which is known from the key tie line information, by the length of the zone, which is known

from the propagation speeds of the shocks. For the small number of segments that represent continuous variations along tie lines, the equivalent of the theory used to calculate recovery in a Buckley-Leverett displacement applies. An overall material balance on the components remaining in the unit displacement length at the time in question (in this case 1.2 PV) gives the desired recovery.

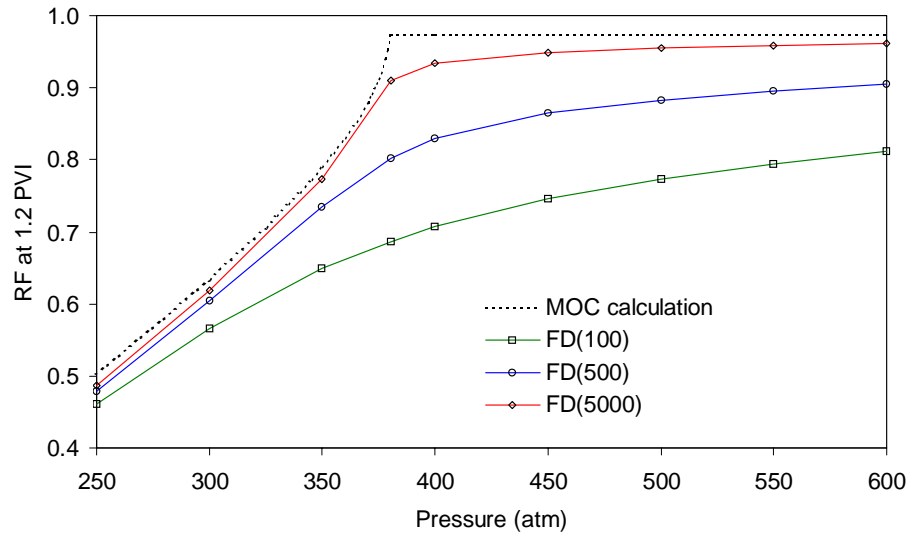


Fig. 3.7: Comparison of recovery curves for the displacement of Oil 2 by pure N<sub>2</sub> at 387K generated by analytical calculations and numerical simulations.

In this example, again, the effects of numerical dispersion are evident in the calculated recovery as a function of pressure. While the numerical computations are clearly converging to the analytical solution, the rate of convergence is slow. The slow convergence illustrated in Fig. 3.7 demonstrates that careful grid refinement is required if conventional FD compositional simulations are to be used to estimate minimum miscibility pressure. The speed advantage of the analytical approach is illustrated in Table 3-2.

Table 3-2: CPU requirements for analytical and numerical solutions for gas displacements

Components	Analytical Solution (sec)	Simulation Length (PV)	Numerical Solution 1000 Blocks (sec)	Numerical Solution 5000 Grid Blocks
6	1.1	0.70	300	8160
15	10	0.25	720	14820

The analytical solutions are self-similar, so the computation time required for any length of displacement is the same. That is not true, however, for FD compositional simulation. The computation times shown are only approximate because the simulations were run on a multiuser server, but even so, they indicate clearly that the analytical approach is orders of magnitude faster than FD simulation for grids that are fine enough to resolve the composition path well. FD simulations for coarser grids would be faster, of course, but significant adverse

effects of numerical dispersion would be present in the solutions.

### 3.1.3 Analytical solutions for general displacements

In this section we demonstrate some results obtained by the general algorithm for generating analytical solutions including volumetric effects. The algorithm required for generating general solutions to the 1D dispersion-free displacement problem includes an extra step as compared to the algorithm for self-sharpening systems. The general algorithm is:

1. Locate all key tie lines by the tie-line intersection approach (Jessen *et al.* 1998).
2. Apply the envelope rule for each neighboring pair of key tie lines. If no rarefactions are predicted, switch to the simplified algorithm for fully self-sharpening systems outlined in section 3.1.2.
3. For each predicted rarefaction, locate the equal-eigenvalue point and integrate the eigenvector to obtain the corresponding nontie-line path.
4. Locate the primary key tie line (the shortest tie line) and start the shock construction downstream. Switch points between the nontie-line paths and the tie-line paths are introduced in the solution requirements in parallel with the velocity rule. The downstream solution is traced until the initial oil composition is reached.
5. Continue constructing the upstream solution by the approach of step 4 until the injection gas composition is reached.

Two examples of displacement calculations using the algorithm described above are reported:

1. Pure N<sub>2</sub> displacing a mixture of CH<sub>4</sub>, C<sub>4</sub> and C<sub>10</sub> at 344 K and 108.4 atm. In this process the parameter  $n$  entering the fractional flow function, Eq.(3.5), is set to 3 and the residual oil saturation  $S_{or}$  is set to 0.05.
2. Pure N<sub>2</sub> displacing a multicomponent reservoir fluid (represented by 15 pseudo components) at 387 K and 275 atm. In this process  $n=2$  and  $S_{or}=0.2$ .

Input to the thermodynamic model can be found in Dindoruk (1992) and Jessen (2000). Fig. 3.8 shows the result of applying the new algorithm to the quaternary system. Four different solutions are reported:

1. the MOC solution, which is obtained by assuming that all key tie lines are connected by shocks (fully self-sharpening system);
2. the MOC solution combined with integration of the nontie-line rarefaction connecting the initial tie line to the first cross over tie line;

3. a coarse grid finite difference (FD) solution obtained by using 100 grid blocks and a  $\Delta\xi/\Delta\tau=10$  in a one point upstream formulation of the conservation equations; and
4. a fine grid FD solution obtained by using 5000 grid blocks and  $\Delta\xi/\Delta\tau=10$ .

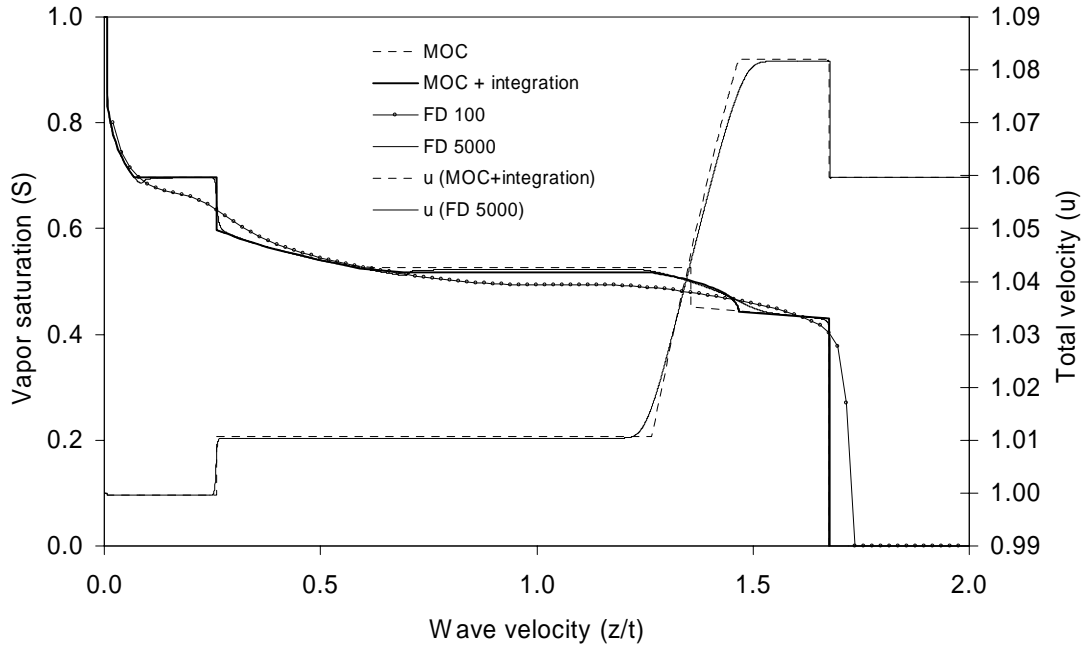


Fig. 3.8: Analytical solution and FD simulations for a quaternary displacement.

The analytical solution combined with integration of nontie-line paths is in excellent agreement with the fine grid FD simulation. Another important observation is that the fully self-sharpening solution is a better approximation to the exact solution than the coarse grid FD simulation. The coarse grid numerical solution describes the general variation of the dispersion-free solution but fails to capture the details of the shock fronts and the non-tie line rarefaction. This is due to the strong effects of numerical dispersion in coarse grid numerical simulations.

Next we apply the general analytical approach for the displacement of a real reservoir fluid by pure  $N_2$ . The result of this test example is reported in Fig. 3.9. Analytical solutions with and without integration of nontie-line rarefactions are compared with numerical simulations using 100, 1000 and 5000 grid blocks in Fig. 3.9. Fig. 3.9 demonstrates again that the fully self-sharpening analytical solution is a far better approximation to the true dispersion-free solution (MOC + integration) than the coarse (100 grid block) grid FD solution. An increasing amount of the detail in the dispersion-free solution is captured as the number of grid blocks is increased. However, the CPU requirement increases rapidly as Table 3-3 shows.

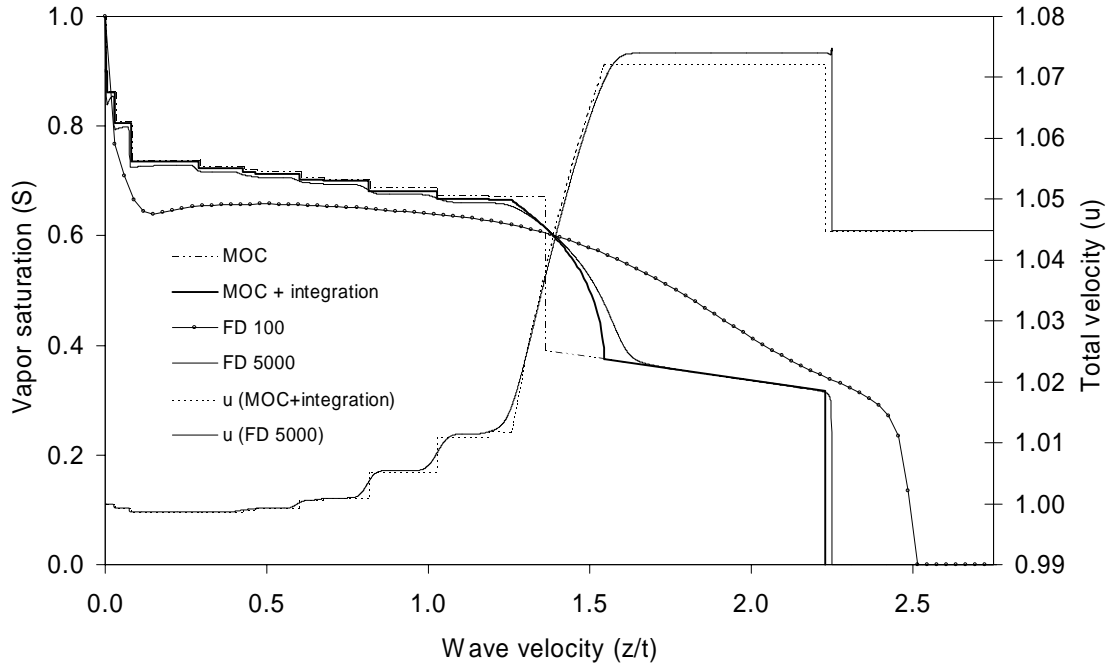


Fig. 3.9: Comparison of analytical solutions and FD simulations for a 15 component system.

Table 3-3: Comparison of CPU (sec.) requirement for the MOC and FD approaches

Example	MOC (shock)	MOC (general)	FD 100	FD 5000
1	<1	<1	4	1506
2	1	7	3	5965
All calculations were performed on a 800 MHz PC.				

### 3.1.4 Discussion

A general approach for automatic generation of dispersion-free solutions for 1D-gas injection processes has been developed and demonstrated. The previous restriction of no volume change as components transfer between phases has been relaxed without adding substantial complexity to the algorithm. The CPU time required for generating the analytical solutions is still small compared to the time required for FD simulations of comparable accuracy.

A comparison of the FD simulator performance for the two test examples demonstrates the fact that a system becomes increasingly sensitive to numerical dispersion as the displacement pressure approaches the minimum miscibility pressure. This behavior strongly suggests that dispersion-free 1D solutions should be used in connection with streamline and streamtube simulators when the transfer of components between phases interacts strongly with two-phase flow to determine displacement efficiency. It is just those situations where the effects of numerical dispersion cause FD simulation results to be misleading.

### 3.1.5 Conclusions

The examples and analysis presented in this section establish that:

1. The analytical theory of multicomponent gas injection processes has been extended to represent volume change on mixing and to include systems with nontie-line rarefactions connecting key tie lines.
2. Results of fine grid numerical simulations based on one point upstream weighting are in excellent agreement with the presented algorithm.
3. Coarse grid numerical simulations are strongly affected by numerical dispersion and may lead to a misleading interpretation of the displacement process.
4. The analytical approach is orders of magnitude faster than fine-grid numerical simulations. Coarse grid numerical simulations can be faster than the general analytical approach but at a significant loss of accuracy.
5. The new general approach for generating 1D dispersion-free solutions is suitable for combination with streamline simulators, which would allow very fast assessment of displacement performance.

### 3.2 Analytical solutions for enhanced condensate recovery

A significant portion of current hydrocarbon reserves exists in gas condensate carrying formations. In analog to oil reservoirs, production of condensate fields by primary production only will result in significant loss of the heavy ends due to liquid drop-out below the dew point pressure. Gas cycling/injection schemes are often applied to enhanced condensate recovery by vaporization. Successful design and implementation of enhanced condensate recovery schemes require accurate prediction of the compositional effects that control the local displacement efficiency.

Many contributions to the development of the analytical theory of gas injection processes can be found in the literature: Monroe *et al.* (1990), Johns *et al.* (1993, 1996), Dindorouk *et al.* (1992, 1993, 1997), Johansen *et al.* (1994), Helfferich (1981), Zanotti *et al.* (1983), Cere' *et al.*, (1985), Jessen *et al.* (2001). The previously published research in this field has been aimed at construction of analytical solutions to problems of gas displacing oil. In this work we extend the analytical theory to include the important process of enhanced condensate recovery by gas injection.

Numerical studies of miscibility variation in compositionally grading reservoirs by Hoier and Whitson (2001) demonstrated a significant potential for efficient gas cycling in condensate reservoirs below the dew-point pressure due to the development of miscibility by the combined condensing and vaporizing mechanism. In their study, rich separator gas was injected to obtain a miscible displacement at pressures far below the dew-point pressure.

With the emerging focus and efforts in the area of greenhouse gas capture and sequestration, CO<sub>2</sub> may in the near future become widely available for enhanced oil recovery as well as enhanced condensate recovery projects. Seto *et al.* (2003) demonstrated, based on simulation studies, that CO<sub>2</sub> can be used as an effective solvent in enhanced condensate recovery processes at pressures well below the dew point pressure or the initial condensate.

In this section we focus on analyzing the development of miscibility during gas cycling in condensate reservoirs that after primary production leave significant amounts of retrograde condensate trapped in the formation.

We start out by presenting the conservation equations that describe multicomponent two-phase flow in a porous media including volume change on mixing and list the key assumptions made to apply the analytical solution strategy. We then describe, through analytical example calculations, the different mechanisms that control the development of miscibility in retrograde condensate reservoirs. The mathematical background is outlined in section 3.1.

### 3.2.1 Solution construction for condensate displacements

In the following sections we demonstrate the solution construction for enhanced condensate problems for three different fluid systems. All phase equilibrium calculations were performed using the Peng-Robinson equation of state while phase viscosities were calculated by the Lohrenze-Bray-Clark correlation.

#### 3.2.1.1 Vaporizing drives

Consider the simple representation of a condensate given by a ternary mixture of methane (C<sub>1</sub>), Ethane (C<sub>2</sub>) and n-pentane (C<sub>5</sub>) reported in Table 3-4.

Table 3-4: EOS parameter for the ternary displacement. All  $K_{ij} = 0$

Component	T <sub>c</sub> (K)	P <sub>c</sub> (atm)	Ω	M <sub>w</sub> (g/mole)	Z <sub>c</sub>	Z <sub>condensate</sub>
Methane	190.6	45.389	0.0080	16.043	0.2896	0.5
Ethane	305.4	48.083	0.0980	30.070	0.2818	0.4
n-Pentane	465.9	33.340	0.2413	72.150	0.2685	0.1

The phase envelope (PT-diagram) of the fluid is shown in Fig. 3.10. At a temperature of 325K this ternary system behaves like a retrograde condensate system below the dew-point pressure of 100 atm. To demonstrate how development of miscibility by a vaporizing mechanism develops, pure C<sub>1</sub> is injected into the condensate at 75 atm ( $S_{or} = 0$ ). The binodal curve corresponding to a pressure of 75 atm along with the location of the initial and injected composition is shown on a ternary diagram in Fig. 3.11. From the analytical theory of gas injection processes, we know that the composition path connecting the initial and injection compositions must pass through a sequence of  $n_c - 1$  key tie lines.

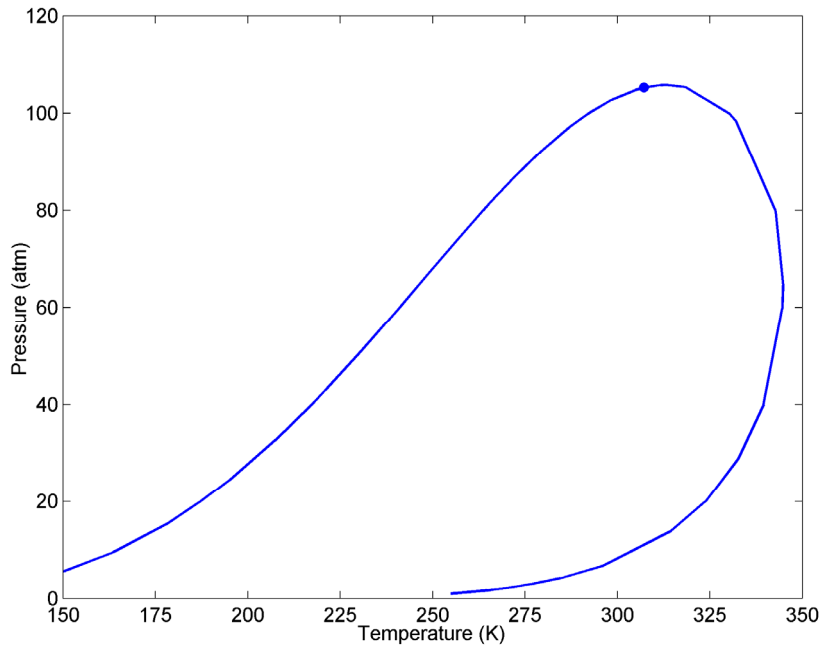


Fig. 3.10: Phase envelope of a ternary C<sub>1</sub>/C<sub>2</sub>/C<sub>5</sub> mixture. Near-critical retrograde behavior is observed at 325 K.

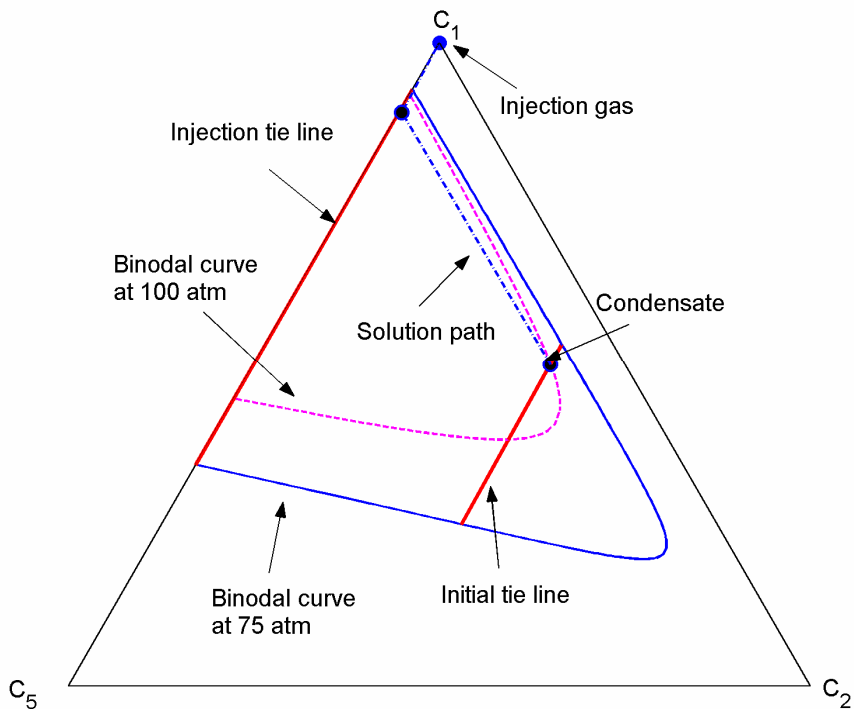


Fig. 3.11: Displacement of 3 component condensate by pure C<sub>1</sub> at 325 K and 75 atm (MMP = P<sub>dew</sub> = 100 atm)

For ternary displacements the key tie lines are the initial tie line and the injection tie line. The initial tie line extends through initial fluid composition, or in the case of a two-phase initial condition: the initial tie line is given directly by a PT-flash calculation. And, the injection tie line is the tie line that extends through the injection composition. Both key tie lines are shown in Fig. 3.11. A sketch of the fractional flow curves corresponding to the initial and injection tie lines is shown in Fig. 3.12.

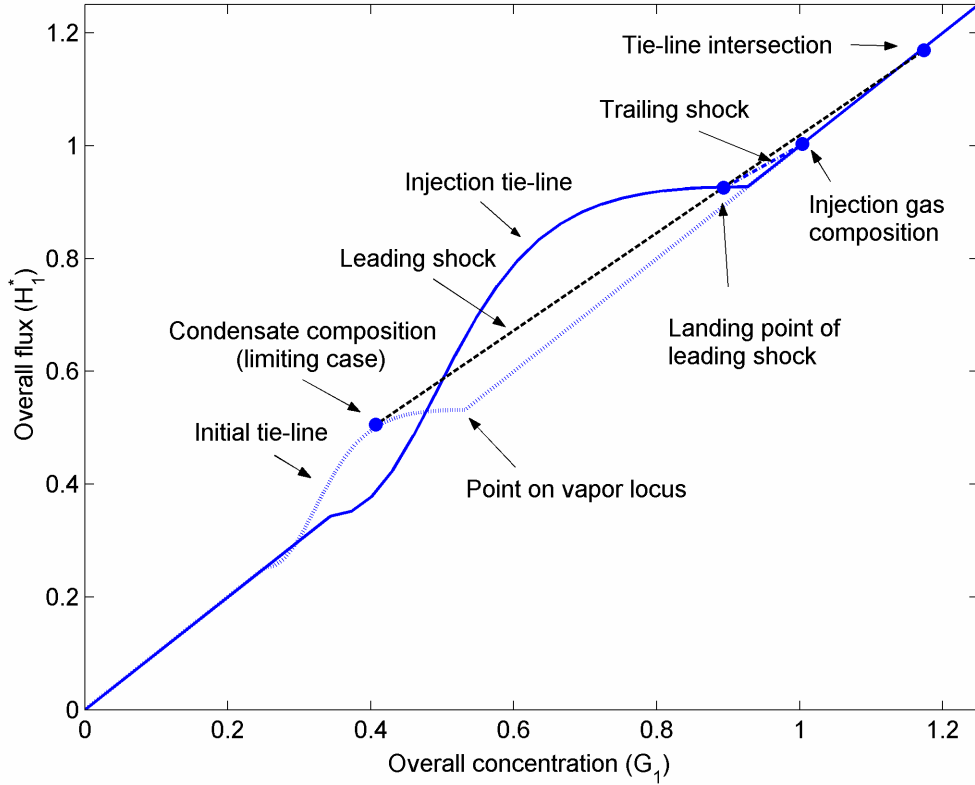


Fig. 3.12: Displacement of 3 component condensate by pure  $C_1$  at 325 K and 75 atm (MMP =  $P_{\text{dew}} = 100 \text{ atm}$ )

The solution path connecting the initial tie line to the injection tie line must in this case be a shock. This particular solution structure is a direct result of the orientation of the key tie lines and the envelope rule (Jessen *et al.*, 2001). The envelope rule states that for vaporizing displacement with a vapor-side envelope curve (the curve which is tangent to the extensions of all tie lines in the surface spanned by the key tie lines) the key tie lines must be connected by a shock for the solution to stay single-valued. Johns *et al.* (1993) and Dindoruk, *et al.* (1992) proved that two tie lines that are connected by a shock must intersect. This observation allow us to write the shock balance as

$$\Lambda = \frac{H_i^a - H_i^b}{G_i^a - G_i^b} = \frac{H_i^a - H_i^x}{G_i^a - G_i^x} = \frac{H_i^b - H_i^x}{G_i^b - G_i^x}, \quad i = 1, \dots, n_c, \quad (3.32)$$

where superscripts  $a$ ,  $b$  denote the different sides of the shock and  $x$  denotes the intersection

point. The graphical interpretation of Eq. (3.32) is shown in Fig. 3.12. The limiting case demonstrated in Fig. 3.12 corresponds to the highest saturation of the initial fluid for which it is possible to determine the shock velocity by a Welge tangent construction. For all condensate displacements examined in this section, the initial composition is located between the limiting composition and the equilibrium vapor composition, and hence the shock velocity is determined by a direct jump from the initial composition to the neighboring tie line. The only question remaining before solving this ternary displacement problem is how to deal with the change in the total flow velocity across the shock. In the formulation of the conservation equations we scaled the total flow velocity with respect to the injection velocity. Hence, the injection composition corresponds to a dimensionless velocity of one. As we start the solution construction at the downstream end of the displacement, we do not know the total velocity that enters the shock balance equations (Eq. (3.32)). To overcome this problem, we rescale the conservation equations with respect to the velocity of the compositions on the initial tie line (the total velocity is constant for composition changes along a given tie line within the two-phase region). To calculate the shock velocity we locate the intersection point and evaluate the overall molar concentration by

$$\Lambda_{a,b} = \frac{H_1^a - H_1^x}{G_1^a - G_1^x} = \frac{H_1^a - G_1^x}{G_1^a - G_1^x}, \quad (3.33)$$

with

$$G_1^x = x_1^a \rho_x^a (1 - \theta) + y_1^a \rho_y^a \theta, \quad (3.34)$$

where  $\theta$  is the fictive saturation corresponding to the intersection point measured from the initial tie line. The landing point and the total velocity on the injection tie line are then evaluated by the shock balances for  $C_1$  and  $C_5$ . The injection composition is connected to the landing point on the injection tie line by a direct jump as a tangent construction would violate the velocity rule, as Fig. 3.12 shows. Hence, the total velocity corresponding to the injection composition (rescaled value) can be found from the shock balance equation. A final transformation to rescale all shock velocities with respect to the injection velocity is required to obtain the full solution. The analytical solution is shown on the ternary diagram (Fig. 3.11) and is reported in terms of saturation and composition profiles along with a finite difference (FD) simulation using 100 grid blocks in Fig. 3.13. Tabulated values are given in Table 3-5.

Table 3-5: MOC solution for ternary displacement

Segment	$\lambda (= z/t)$	$S_{gas}$	$v_d$	$z_{C1}$	$z_{C2}$	$z_{C5}$
1	0.9551 - $\infty$	0.9515	1.0488	0.5	0.4	0.100
2	0.9551 - 0.6222	0.9762	1.0246	0.888	0.0	0.112
3	0.6222 - 0	1.0000	1.0000	1.000	0.0	0.000

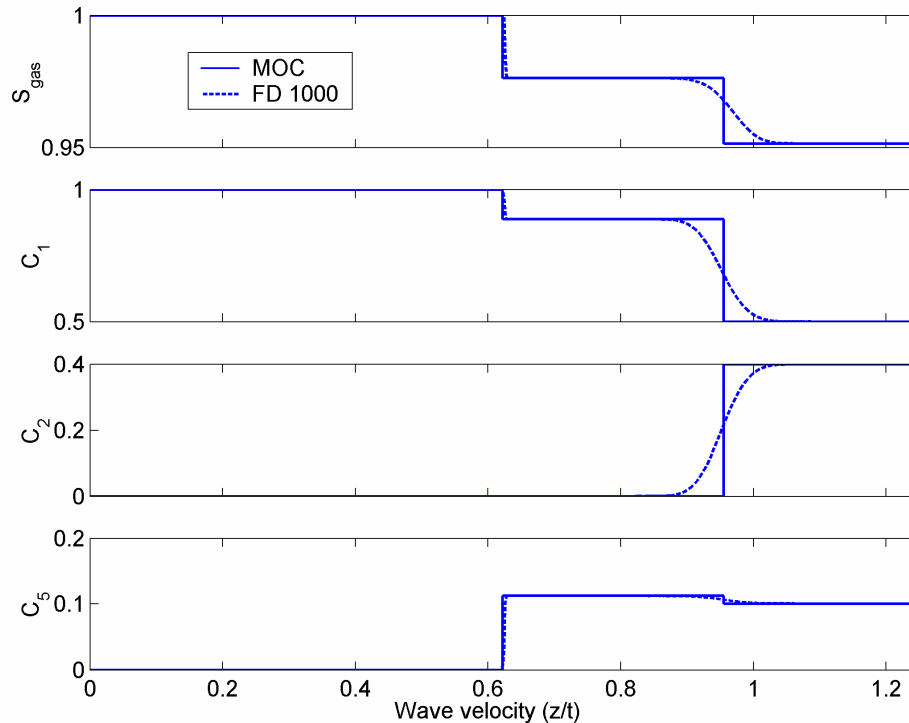


Fig. 3.13: Semi-analytical and numerical (1000 grid blocks) solution profiles for the displacement of a 3 component condensate by pure  $C_1$  at 75 atm and 325 K.

### 3.2.1.2 Development of miscibility in vaporizing drives

The solution to the displacement of the ternary condensate by pure methane at 75 atm and 325K is clearly not a miscible displacement (piston like). If the initial composition is moved toward the vapor locus along the initial tie line, the slope of the line in Fig. 1.12 that connects the intersection point to the initial compositions increases. The slope of this line is equivalent to the shock speed of the leading edge of the displacement. Hence, to achieve a piston like displacement we must move the initial composition all the way to the vapor locus of the binodal curve at which point, the shock speed will be equal to one. Alternatively, the pressure could be increased to obtain the same effect. Fig. 3.11 shows a second binodal curve corresponding to a pressure of 100 atm. As the pressure is changed from 75 atm to 100 atm the binodal curve moves closer to the initial composition. As the binodal curve reaches the initial composition a piston-like displacement is achieved, and the displacement is multicontact miscible. If the pressure is increased above the dew point pressure the displacement switches from multicontact miscible to first contact miscible. This is not necessarily the case for all vaporizing drives. If the dilution line, connecting the initial composition to the injection composition, intersects the two-phase region at pressures above the dew point pressure, the displacement will still be multicontact miscible, but at a pressure above the minimum miscibility pressure (MMP), because the initial composition lies outside the region of tie-line extensions.

The development of miscibility described for the ternary displacement is valid also for multicomponent vaporizing drives. This due to the fact that the initial tie line controls the development of miscibility in any given vaporizing displacement.

### 3.2.1.3 Combined condensing and vaporizing drives

To illustrate the development of multicontact miscibility in combined condensing/vaporizing (C/V) displacements of condensate we turn to the 4-component system described in Table 3-6.

Table 3-6: EOS parameter for the quaternary displacement.

Component	$T_c$ (K)	$P_c$ (atm)	$\Omega$	$M_w$ (g/mole)	$Z_c$	$Z_{\text{condensate}}$
$C_1$	190.6	45.389	0.0115	16.043	0.2896	0.80
$CO_2$	304.2	72.865	0.2236	44.010	0.2709	0.00
n- $C_4$	425.1	37.464	0.2002	58.123	0.2730	0.15
n- $C_{10}$	617.7	20.824	0.4923	142.29	0.2474	0.05
Non-zero $K_{ij}$ : $K_{CO_2,C_4} = 0.12$ , $K_{CO_2,C_{10}} = 0.115$						

The condensate is made up by 80% (mole)  $CH_4$ , 15% n-butane ( $C_4$ ) and 5% decane ( $C_{10}$ ) and we inject pure  $CO_2$  ( $S_{or} = 0.2$ ). The phase envelope of the condensate is given in Fig. 3.14.

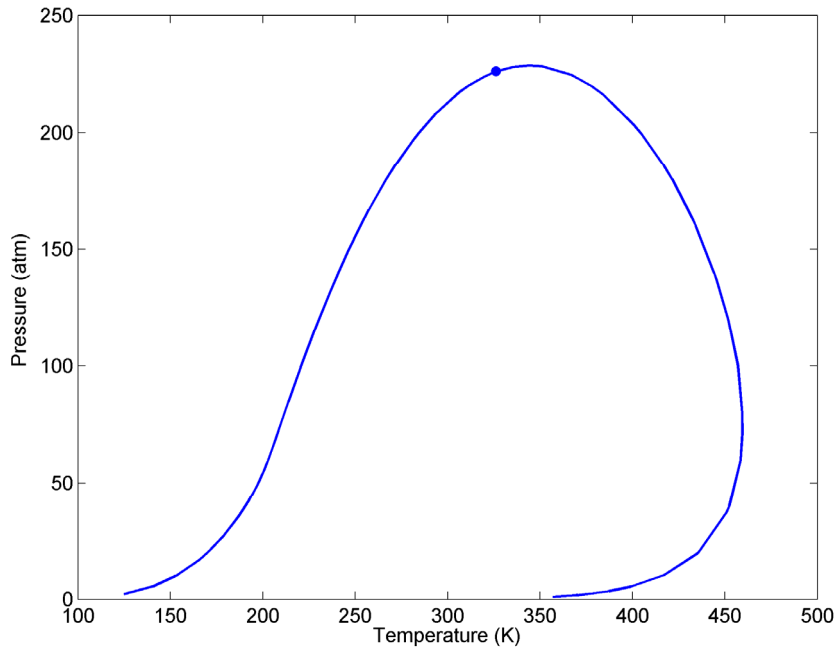


Fig. 3.14: Phase envelope of 4 component mixture. Near-critical behavior at 344 K

At a temperature of  $344\text{K}$  the fluid system represents a near-critical condensate. A significant difference between ternary and quaternary displacement is the introduction of a third key-tie line known as a crossover tie line, Monroe *et al.* (1990). Johns *et al.* (1993) demonstrated that the crossover tie line is responsible for the development of combined C/V miscibility as reported by Zick (1986) and Stalkup (1987).

It is well known that miscibility for gas/oil displacements can develop by the C/V mechanism at pressures far below the vaporizing drive. Hoier and Whitson, (2001) demonstrated similar behavior for the displacement of retrograde condensate by injection of a rich gas. In the following example calculation we demonstrate that  $\text{CO}_2$  injection is also similar. To generate a semi-analytical solution to the displacement of the condensate by pure  $\text{CO}_2$  we set the pressure to  $100\text{ atm}$  ( $P_{\text{dew}} = 228\text{ atm}$ ). The key tie lines that make up the solution in composition space can be located (Jessen *et al.* (1998), Wang and Orr (2000), Yuan and Johns (2002)) by applying the tie-line intersection equations. Once the key tie lines are located (See Fig. 3.15) the solution strategy from the ternary displacement example is repeated.

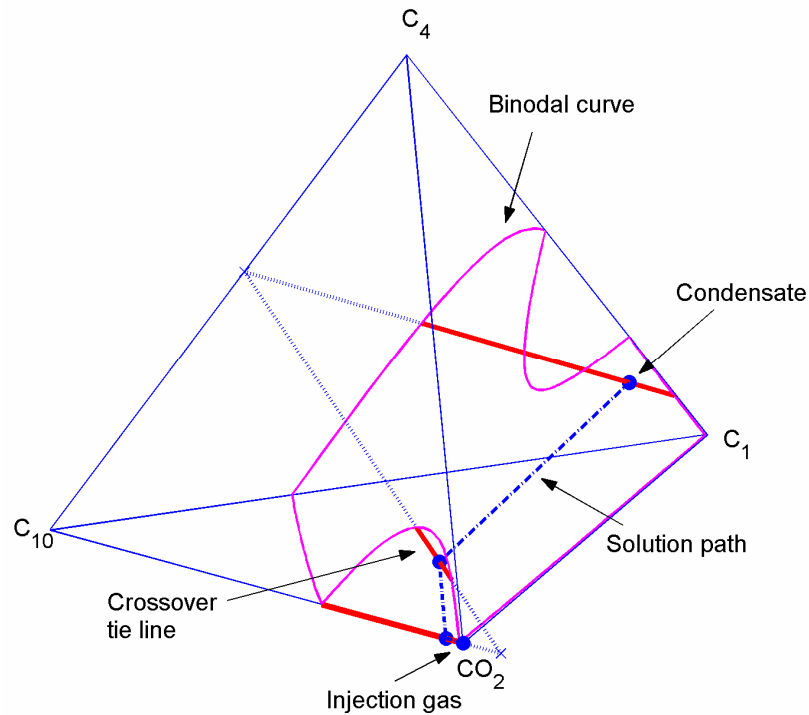


Fig. 3.15: Near-miscible displacement of 3 component condensate by pure  $\text{CO}_2$  (4 components) at  $344\text{ K}$  and  $100\text{ atm}$  ( $\text{MMP} = 106\text{ atm}$ )

We start by connecting the initial composition to the crossover tie line by evaluating the shock velocity from the information about the tie-line intersection point. As in the previous example calculation we, rescale the shock velocities with respect to the total velocity of the compositions on the initial tie line. Knowing the landing point on the crossover tie line we construct the shock from the crossover to the injection tie line also like in the ternary displacement. In essence, solving a quaternary displacement problem corresponds to solving two coupled ternary displacement problems. The solution path for the quaternary

displacement is shown in Fig. 3.15 whereas the saturation and composition profiles are shown in Fig. 3.16 together with coarse and fine grid FD simulations. Tabulated results are given in Table 3-7.

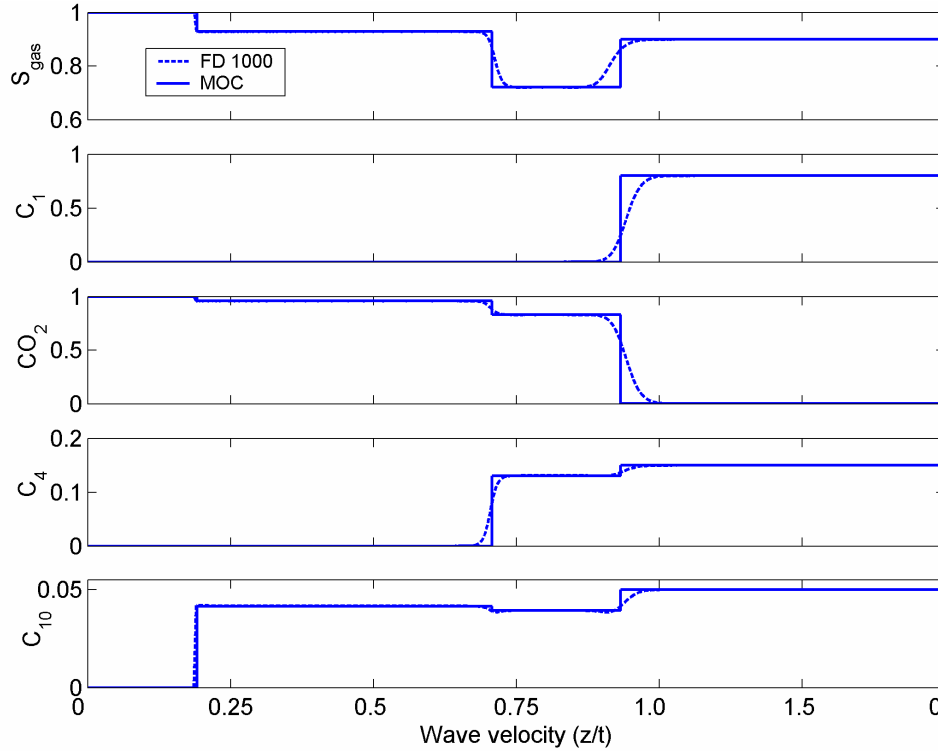


Fig. 3.16: Semi-analytical and numerical (1000 grid blocks) solution profiles for the displacement of a 4 component condensate by pure CO<sub>2</sub> at 100 atm and 344 K

Table 3-7: MOC solution for quaternary displacement

Seg.	$\lambda (= z/t)$	$S_{\text{gas}}$	$v_d$	$z_{C1}$	$z_{CO2}$	$z_{C4}$	$z_{C10}$
1	0.9325 - $\infty$	0.8994	0.9133	0.8000	0.0000	0.1500	0.05
2	0.9325 - 0.7076	0.7215	0.9691	0.0000	0.8301	0.1307	0.0393
3	0.7076 - 0.1918	0.929	0.9693	0	0.9586	0	0.0414
4	0.1918 - 0	1	1	0	1	0	0

A major difference in the solution profiles is seen for the quaternary C/V displacement relative to the pure vaporizing ternary displacement. At the leading edge of the displacement, a condensate bank is formed with high concentration of C<sub>4</sub> and CO<sub>2</sub>. In this case the retrograde liquid saturation of the bank exceeds the residual liquid saturation and hence becomes mobilized. The condensate bank is a result of the location of the landing point on

the crossover tie line that is closer to the critical locus than is the initial or the injection tie line. If the pressure is increased, the condensate bank shrinks in width and grows in height until the point where the crossover tie line becomes critical (zero length tie line), and a piston-like displacement develops. The pressure at which the crossover tie line becomes critical is the C/V MMP. From Fig. 3.15 it is clear that C/V miscibility will be much lower than the dew point pressure (228 atm) of the condensate. Another interesting feature of the C/V drive can be deduced from Fig. 3.15. Hoier and Whitson (2001) found, from numerical simulations, that the MMP of a C/V drive could be determined from the composition of the retrograde liquid and the injection gas composition. Their finding is consistent with the analytical theory as the retrograde liquid will specify the initial tie line.

### 3.2.2 Multicomponent displacements

To test the new approach for generating semi-analytical solutions to condensate displacement problems on a multicomponent reservoir fluid, we select the fluid reported by Seto *et al.* (2003). Based on the equation of state input is given in Table 3-8, the phase envelope shown in Fig. 3.17 was generated.

Table 3-8: EOS parameter for the 13 component displacement.

Comp.	zcond	Tc (K)	Pc (atm)	$\Omega$	Mw (g/mole)	Zc
N2	0.0171	126.2	33.60	0.0400	28.016	0.287050
CO2	0.0576	304.2	72.90	0.2280	44.010	0.270553
H2S	0.3562	373.5	88.50	0.0800	34.076	0.283540
Methane	0.3631	190.6	45.40	0.0080	16.043	0.289858
Ethane	0.0798	305.4	48.20	0.0980	30.069	0.281961
Propane	0.0340	369.8	41.90	0.1520	44.096	0.277222
Butane	0.0300	419.6	37.01	0.1875	58.123	0.274107
Pentane	0.0171	465.9	33.34	0.2413	72.150	0.269386
C6	0.0116	507.4	29.30	0.2960	86.177	0.264586
C7	0.0117	573.9	40.47	0.2651	94.000	0.267297
C8	0.0126	648.3	32.53	0.3437	113.52	0.260400
C10	0.0053	630.1	30.17	0.4489	141.52	0.251169
C12+	0.0039	683.2	26.92	0.6305	190.00	0.235234
Non-zero Kij: N2-C1 = 0.02, N2-C2 = 0.06, N2-C3+ = 0.08, CO2-H2S = 0.12, CO2-C1 = 0.12, CO2-C2+ = 0.15, H2S-C1 = 0.08, H2S-C2 = 0.07, H2S-C3 = 0.07, H2S-C4 = 0.06, H2S-C5 = 0.06, H2S-C6 = 0.05 ,						

The reservoir fluid is represented by 13 components, and again we use pure CO<sub>2</sub> as injection gas. First we consider the displacement of condensate at 335 K to achieve a near-critical reservoir fluid. The dew point pressure of the initial fluid is 158 atm and the MMP predicted by the key tie line approach is 93 atm.

To generate the solution we locate the key tie lines (Jessen *et al.* (1998), Wang and Orr

(2000), Yuan and Johns (2002)) at 90 atm. In a 13 component system, there exist  $n_c - 1$  key tie lines, out of which  $n_c - 3$  are crossover tie lines. Hence, the construction of the analytical solution corresponds to solving 10 coupled pseudo-ternary displacements, starting from the initial tie line through to the injection tie line. For the fluid system in consideration the second crossover tie line controls the development of miscibility and hence, the displacement is a C/V drive.

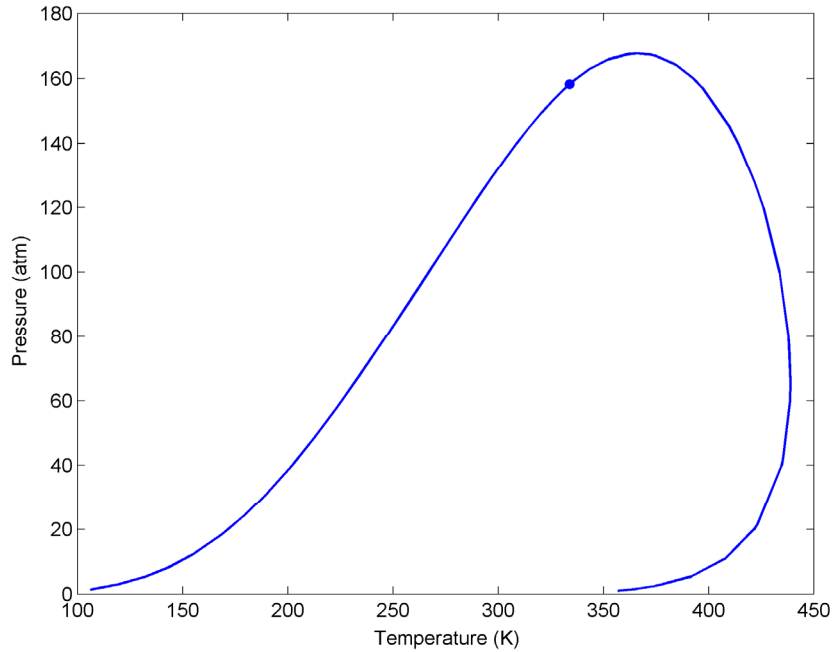


Fig. 3.17: Phase envelope of 13 component mixture. Near-critical retrograde behavior at 335 K

Table 3-9: MOC solution for near-miscible 13 component displacement

Seg.	$\lambda (= z/t)$	$S_{\text{gas}}$	$v_d$	$z_{\text{CO}_2}$
1	0-0.0855	1	1	1
2	0.0855-0.1616	0.9927	0.9965	0.9929
3	0.1616-0.1665	0.9777	0.9872	0.9761
4	0.1665-0.3799	0.9763	0.9863	0.9740
5	0.3799-0.5602	0.9687	0.9795	0.9604
6	0.5602-0.6644	0.957	0.9712	0.9431
7	0.6644-0.7570	0.9452	0.9663	0.9207
8	0.7570-0.8270	0.9232	0.9644	0.876
9	0.8270-0.8350	0.8737	0.9719	0.7884
10	0.8350-0.9256	0.7378	1.065	0.594
11	0.9256-0.9809	0.5817	1.0771	0.4886
12	0.9809-1.024	0.8949	0.9748	0.0582
13	1.024- $\infty$	0.8966	0.9723	0.0576

The full solution to the displacement of the retrograde condensate at 90 atm ( $S_{or} = 0.2$ ) is tabulated in Table 3-9 and shown in terms of saturation and composition profiles in Fig. 3.18. Additional FD simulations are reported in Fig. 3.18 also. At the leading edge of the displacement we see a significant condensate bank that by far exceeds the residual saturation of 0.2. However, inspection of the phase envelope suggests that small variations in the initial composition will bring relatively large variations in saturation.

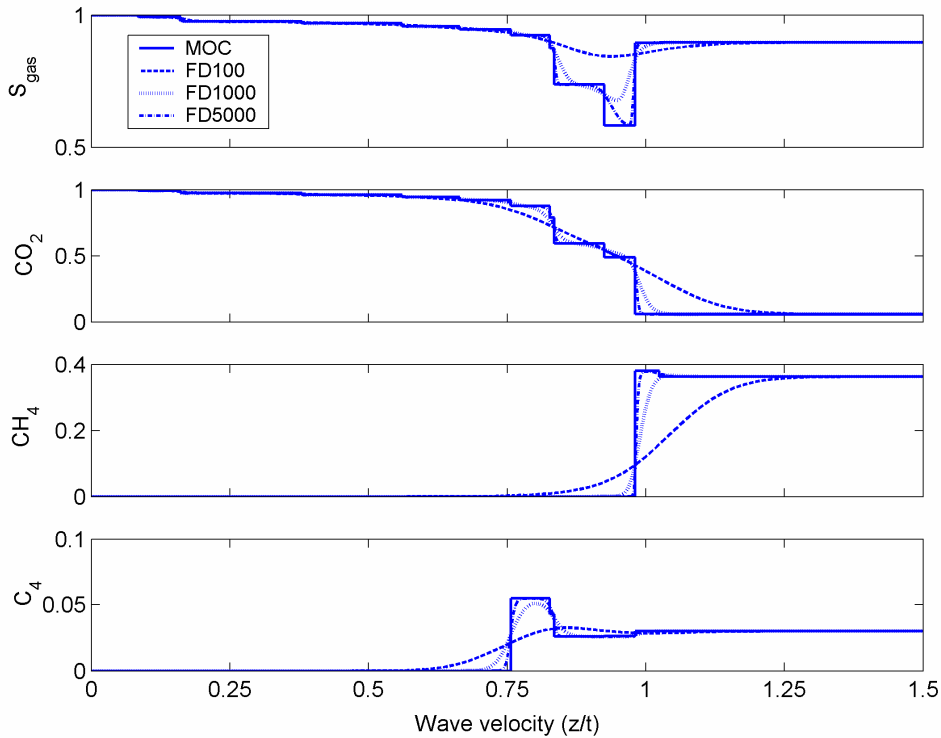


Fig. 3.18: Semi-analytical and numerical solution profiles for the displacement of a 13 component condensate by pure CO<sub>2</sub> at 90 atm and 335 K (MMP = 93 atm)

To investigate the significance of the initial composition relative to the critical point (temperature) we repeat the displacement problem at 375 K (moving right in the phase envelope). At this temperature the dew-point pressure is 167 atm, and the MMP is predicted to be 128 atm. The dispersion-free solution for this displacement problem is reported in Fig. 3.19. The solution shows a significantly smaller condensate bank that hardly exceeds the residual saturation. Hence, the location of the initial condensate relative to the critical point on the phase envelope and hence the 0.5 quality line appears to have a significant impact on the formation of a condensate bank at the leading edge of the displacement.

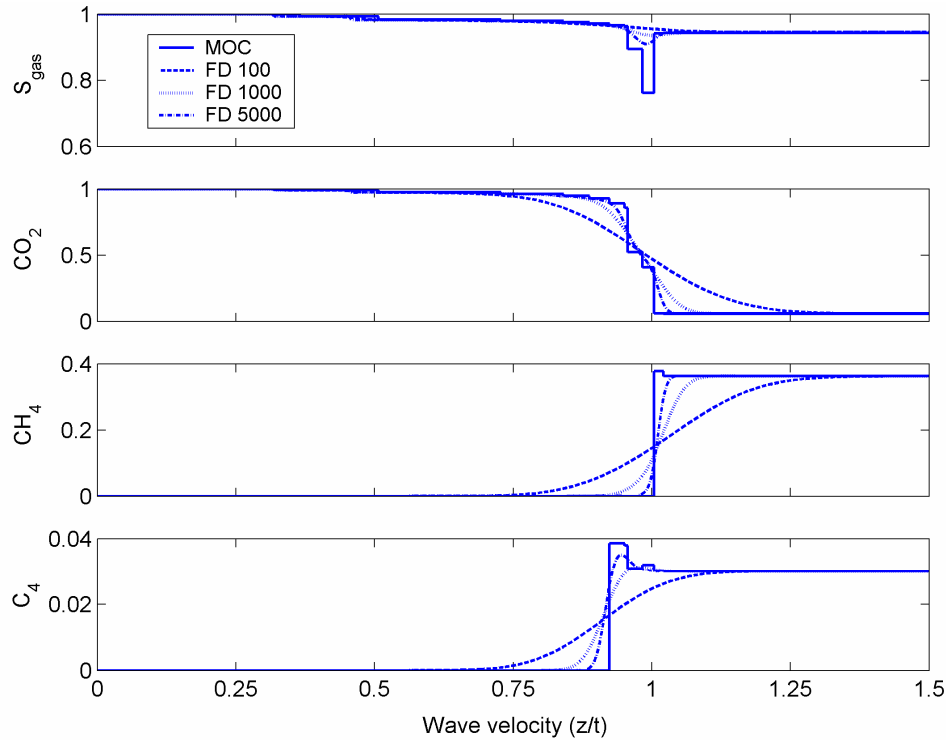


Fig. 3.19: Semi-analytical and numerical solution profiles for the displacement of a 13 component condensate by pure CO<sub>2</sub> at 126 atm and 375 K (MMP = 128 atm)

### 3.2.3 Discussion

In the previous sections we have applied the analytical theory of gas injection processes to predict the displacement behavior of gas injection into retrograde condensates. One of the major assumptions of this approach is to neglect the gradient in pressure for the purpose of evaluating phase behavior. Hence, semi-analytical predictions should not be expected to be highly accurate in near-well settings where steep gradients in pressure certainly exist. However, far from production wells, important information about the expected behavior of an enhanced condensate recovery scheme may still be at hand. The formation of condensate banks that exceed the residual liquid saturation suggests that gravity segregation could reduce displacement performance by draining valuable retrograde liquid away from high permeability zones at the cost of a reduction in recovery. To predict accurately the extent of a condensate bank with finite-difference simulations we have demonstrated that significant grid refinement is required. Hence, coarse grid simulation of field development scenarios may fail to predict the true effects of gravity in these flow settings.

### 3.2.4 Conclusions

The examples and analysis presented in this section establish that:

1. The analytical theory of gas displacement can be used to describe enhanced condensate recovery by gas injection. Semi-analytical dispersion-free 1D solutions to 3-, 4- and 13-component fluid descriptions have been presented. The presented analytical solutions are in excellent agreement with fine grid numerical simulations. However, coarse grid numerical simulations fail to capture the formation of condensate banks.
2. Development of miscibility in gas cycling schemes may be achieved at pressures far below the dew-point pressure of the condensate by injection of CO<sub>2</sub>.
3. Formation of a condensate bank at the leading edge of the displacement for C/V drives is reported. The magnitude of the saturation change in the condensate bank is related the location of the initial condensate with respect to the critical point of the original condensate.
4. The fairly low miscibility pressures obtained for injection of CO<sub>2</sub> in a retrograde condensate suggests that mature condensate carrying formations may be suitable targets for CO<sub>2</sub> sequestration offset by a possible increase in condensate recovery.

### 3.2.5 Nomenclature

$f$	Fractional flow of vapor	$z$	Distance from inlet
$G_i$	Molar concentration of component $i$	$Z_i$	Overall mole fraction of $i$
$H_i$	Molar flux of component $I$	$\phi$	Porosity
$L$	Total length of system	$\Lambda$	Shock speed
$n_c$	Number of components	$\mu_r$	Gas to oil viscosity ratio
$S$	Gas saturation	$\theta$	Fictive saturation
$S_{or}$	Residual liquid saturation	$\rho_x$	Molar density of liquid
$t$	Time	$\rho_y$	Molar density of vapor
$u$	Total velocity	$\rho_j$	Molar density of phase $j$
$u_D$	Dimensionless total velocity	$\rho_{jD}$	Dim. less density of phase $j$
$u_{inj}$	Injection velocity	$\rho_{ini}$	Molar density of initial fluid
$x_i$	Liquid mole fraction of component $I$	$\tau$	Dim. less time (PVI)
$y_i$	Vapor mole fraction of component $i$	$\xi$	Dimensionless length

### 3.3 Additional analytical solutions

The analytical solutions discussed in this chapter are useful additions to the toolkit for prediction of process performance in gas injection processes, but they do not cover all the situations of interest. The area of three-phase flow is one such area. Recent work by Juanes (2004) has demonstrated a systematic procedure for constructing solutions to Riemann problems in which the compositions of the three phases remain fixed. Those solutions can be used with the streamline approach, but they do not describe what happens when the phase behavior of gas/oil mixtures change the compositions of the phases. A first step towards the solution of the more general has been taken by Force and Johns (2004). They reported solutions for a ternary system in which the compositions of the three equilibrium phases were

fixed, but with variable phase compositions in the two-phase regions bounding the three-phase region. The general multicomponent three-phase flow problem remains to be solved, though it now appears that it might be possible to do so. In the meantime, the numerical 1D solutions described in Chapter 2 can be used to describe these flow situations.

Analytical solutions for the non-Riemann problems would also be useful. When streamline locations are updated, compositions along the new streamlines will vary spatially, as compositions are mapped from the grid on which the pressure equations is solved to the new streamlines. In principle, this problem can be solved by the method of characteristics. In these problems, eigenvalues are not constant, at least for an initial period in which the compositions evolve to a set of compositions for which they are constant. The same situation arises when injection gas compositions are not constant. Integration along evolving composition paths will be required for a period, after which solutions related to those described here will apply. These integrations would have to be done numerically for realistic phase behavior. No general approach to solving this problem for more than two components has been reported. These problems are sufficiently difficult that it is appropriate to use numerical simulations along the lines described in Chapter 2 to solve them.

### **3.4 Summary**

Analytical solutions are presented in this chapter for a general 1D multicomponent gas injection process in which the phase behavior of the gas/oil mixtures is evaluated as a fixed pressure, the initial composition in the 1D porous medium is constant, the injection gas composition is constant, and the components have a partial molar volume that is not constant. For some reservoir settings these assumptions are reasonable. The example solutions presented for condensate reservoirs in Chapter 2, for example, demonstrate that the analytical solution can be use effectively to model a condensate recovery process that would be very difficult to simulate accurately with conventional compositional simulation approaches. They also show that when it is reasonable to use the analytical solutions, the resulting predictions of process performance can be obtained with orders of magnitude less computation time than is required for conventional compositional simulation. This speed advantage arise both from the inherent speed of the streamline approach, which requires fewer pressure solves than conventional simulation, and from the fact that the analytical solution can be constructed once for the entire simulation, and the computation time to construct that solution is negligible. The combination of analytical solutions with streamline simulation will be useful for screening of heterogeneous reservoirs for application of gas injection processes and for evaluation of the uncertainties associated with variable reservoir properties.

## 4 Physics and Chemistry of Multiphase Flow

In this chapter, we report results of experiments to examine the effects of variations in the interfacial tension (IFT) of phases that might arise during three-phase displacements in gas injection processes. Variations in gas and oil relative permeabilities as a function of IFT are of particular importance in the area of compositional processes like high-pressure gas injection, where oil and gas compositions can vary significantly both spatially and temporally. Because gas injection processes routinely include three-phase flow (either because the reservoir has been previously waterflooded or because water is injected alternately with gas in order to improve overall reservoir sweep efficiency), the effect of variations in IFT on three-phase relative permeabilities must be delineated if the performance of gas injection process is to be predicted accurately. The development of multicontact miscibility in a gas injection process will create zones of low IFT between gas and oil phases in the presence of water. In the sections that follow, changes in phase relative permeabilities with IFT are described for a variety of porous media and wetting situations.

### 4.1 Analogue three-phase systems

Because they allow control of IFT in experiments performed at atmospheric pressure, hydrocarbon/alcohol/water systems are useful for investigations of the effects of IFT variations. The use of analog liquid phases offers many advantages in the laboratory determination of relative permeabilities: relatively low IFT reduces capillary end effects during displacements, IFT can be varied by changing the composition, and it is possible to create two phases that have low IFT in the presence of a third phase, just as gas/oil tensions can be low while oil/water and gas/water IFTs are not. Several researchers have reported phase behavior and applications for two-phase systems, isooctane (IC<sub>8</sub>) / isopropyl alcohol (IPA) / brine (Taber and Meyer, 1964, Pongpitak, 1980, Morrow *et al.*, 1988, Schechter *et al.*, 1994) and for three-phase systems, hexadecane (C<sub>16</sub>)/n-butanol (NBA)/water (Pongpitak, 1980) and decane/benzyl alcohol/water (Grader and O'Meara, 1988). For example, dilution of IC<sub>8</sub> and brine phases with IPA can reduce IFT to very low values as the critical composition is approached. This is, of course, a good analogy to miscible gas injection, in which the interfacial forces between the oil and gas phases become weaker as displacement composition paths approach the critical locus.

The selection of reasonable liquid pairs with different IFT behavior for three-phase relative permeability measurements requires the knowledge of the phase behavior of appropriate components. Knickerbocker *et al.* (1982) presented the phase behavior of a variety of hydrocarbon/alcohol/water combinations, which yield different three-liquid-phase patterns when salt is added. They studied phase patterns for combinations of 10 alcohols, 6 even-numbered n-alkanes having from 6 to 16, and water with salinity from zero to 32  $cg/cm^3$ . The results presented by Knickerbocker *et al.* suggest that oil/alcohol/water systems can be formulated that mimic the behavior of gas/oil systems in the presence of water.

In this report we consider mixtures of C<sub>16</sub>, NBA, and water, which form three liquid phases in equilibrium at ambient conditions. The C<sub>16</sub>/NBA/H<sub>2</sub>O system gives appropriate

phase behavior when IPA or NaCl is added to the mixtures. Adding IPA or NaCl changes the compositions of the three equilibrium phases that form in a way that alters IFT appreciably.

In the sections that follow we report experimental results of phase composition, phase density and viscosity, and IFT measurements of three-phase  $C_{16}$ /NBA/ $H_2O$ /IPA and  $C_{16}$ /NBA/ $H_2O$ /NaCl analog liquid systems under ambient conditions. We describe the correspondence between these systems and reservoir fluids that will be employed in the three-phase relative permeability experiments described in the preceding sections.

#### 4.1.1 Experimental procedures

The chemicals used in the experiments were  $C_{16}$  (Fisher Chemicals, 99.4%), NBA (EM Science, 99.94%), IPA (Fisher Chemicals, 99.9%),  $IC_8$  (Fisher Chemicals, 99.4%) and NaCl (Baker, 99.6%). The aqueous phase was distilled, de-ionized  $H_2O$ .

All experiments were performed at room temperature,  $22 \pm 0.4$  °C. All components were mixed in the  $60\text{-cm}^3$  glass vials based on their weights taken with the balance with 0.001 g reproducibility. After the mixtures were shaken by hand the equilibrated phases separated in times that ranged from minutes to one day (depending on the IFT between pairs of phases – low IFT mixtures took longer to separate).

The equilibrated phases were sampled by syringe and transported to  $1.5\text{-cm}^3$  vials for composition measurements by gas chromatography. To prevent contamination by the phases above when sampling  $H_2O$ -rich and NBA-rich phases, a small amount of air withdrawn by syringe before sampling was pushed out in the correspondent phase to clean any contamination at the edge of the needle. Liquid phase compositions were analyzed with a Hewlett-Packard 5880A temperature programmable gas chromatograph. Satisfactory separations were obtained by using the  $6' \times 1/8" \times 0.085"$  stainless steel column packed with 10% Carbowax 20M on 80/100 Chromosorb W-HP (Alltech Associates). The peaks for the components,  $C_{16}$ , NBA, IPA, and  $H_2O$ , were calibrated with mixtures containing known amounts of the components. The amount of NaCl in the phases was determined from the amount of  $H_2O$ , with the assumption that NaCl dissolves only in the  $H_2O$  component.

The IFTs between the phases were measured with a spinning drop tensiometer manufactured by the University of Texas (Model 300), which is reliable for low IFTs (Manning and Scriven, 1977). The tensiometer was calibrated using known IFT values of tie lines on the phase diagram of the  $IC_8/2\%CaCl_2$   $H_2O$ /IPA system presented by Taber and Meyer, 1964.

Densities were measured gravimetrically using a  $10\text{-cm}^3$  Gay-Lussac bottle. Viscosities were measured using a Cannon-Fenske viscometer.

## 4.1.2 Experimental results and interpretation

### 4.1.2.1 Compositional data

The effects of increasing IPA fraction or of increasing NaCl concentration were examined for  $C_{16}$ /NBA/ $H_2O$  mixtures that formed three phases. Fig. 4.1 reports the base ternary phase diagram for the  $C_{16}$ /NBA/ $H_2O$  system. It shows a large three-phase region surrounded by three unconnected two-phase regions. The  $C_{16}$ -rich phase (88%  $C_{16}$ )\* contained a small amount of  $H_2O$  (approx. 0.5%). The NBA-rich phase (74% NBA) also contained 17%  $C_{16}$  and 9%  $H_2O$ . Almost no  $C_{16}$  was detected in the  $H_2O$ -rich aqueous phase which contained 8% NBA. Each of the edges of the three-phase region is also a tie line for the associated two-phase region. The two-phase regions on the  $H_2O$ /NBA and  $H_2O$ / $C_{16}$  sides of the three-phase triangle extend all the way to the binary  $H_2O$ /NBA and  $H_2O$ / $C_{16}$  axes. In binary mixtures of  $C_{16}$  and  $H_2O$ , the  $C_{16}$ -rich phase contained only  $C_{16}$ , whereas a very small amount of  $C_{16}$  (0.1%) was detected in the  $H_2O$ -rich phase. The binary mixture of NBA and  $H_2O$  yields an NBA-rich phase consisting of 83% NBA and 17%  $H_2O$  and an  $H_2O$ -rich phase of 8% NBA and 92%  $H_2O$ . The fact that all binary mixtures of  $C_{16}$  and NBA are completely miscible at 22 °C indicates that the two-phase region connected to the tie line of three-phase region between the  $C_{16}$ -rich and NBA-rich phases must lie inside the ternary triangle. As a result, there must be a critical point on the two-phase envelope associated with the  $C_{16}$ /NBA side of the three-phase region.

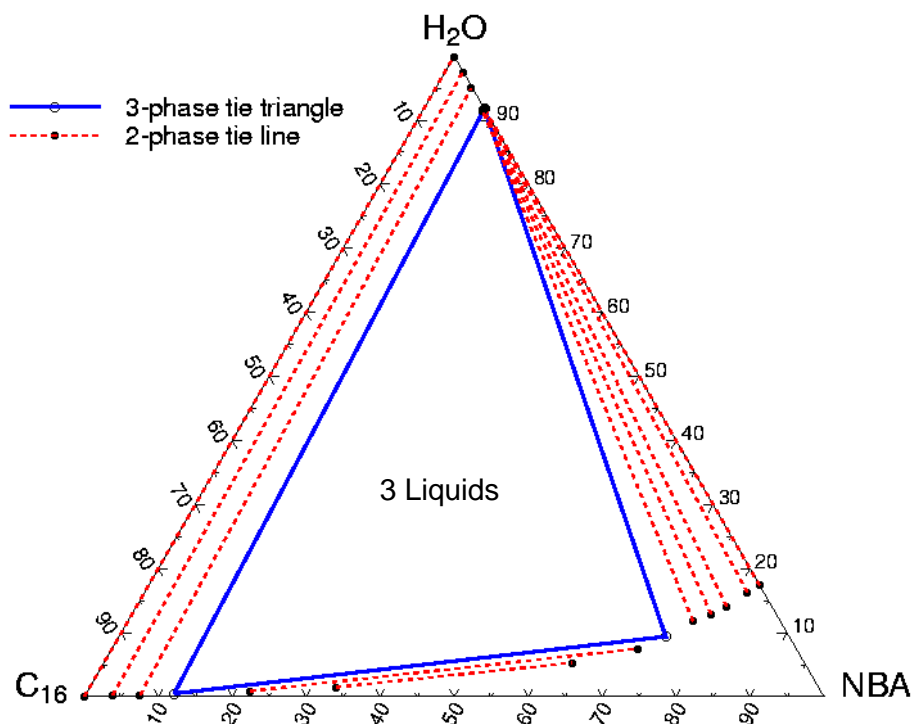


Fig. 4.1: Ternary phase diagram for the  $C_{16}$ /NBA/ $H_2O$  system at ambient conditions.

\* All compositions are in mass fractions unless otherwise specified.

Starting from an overall composition on the base tie triangle, we added IPA in steps to obtain a quaternary phase diagram that shows a sequence of tie triangles, shown in Fig. 4.2. The arrows in Fig. 4.2 show the directions of change of the respective phase compositions caused by adding IPA. C is the critical end point, and AC represents the approximate location of the critical tie line. As the concentration of IPA increases, the NBA-rich and H<sub>2</sub>O-rich phase compositions approach each other, and three-phase behavior reduces to two-phase behavior at the critical tie line.

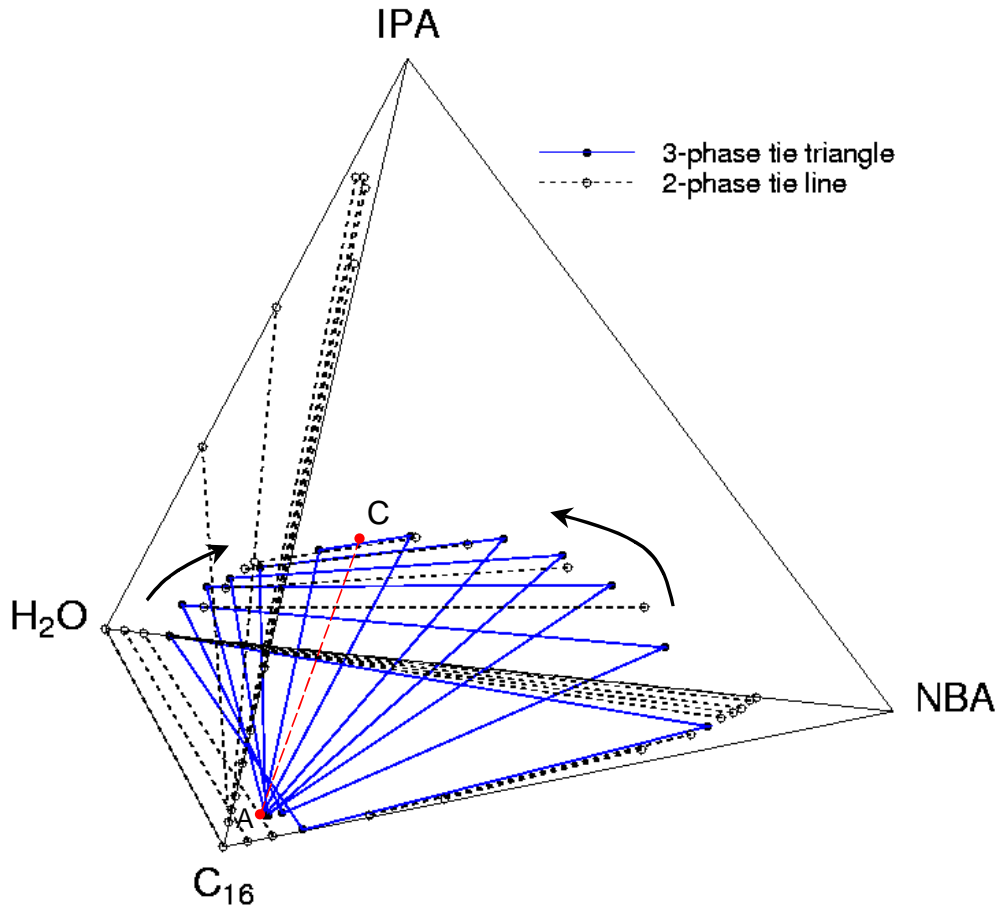


Fig. 4.2: Quaternary phase diagram for the C<sub>16</sub>/NBA/H<sub>2</sub>O /IPA system.

Phase compositions for the range of IPA mass fractions for which three phases coexist are shown in Fig. 4.3. The x-axis shows the overall mass fraction of IPA at the center of each tie-triangle. As IPA was added to the mixtures, most of it partitioned between the NBA-rich and H<sub>2</sub>O-rich phases, while the IPA fraction in the C<sub>16</sub>-rich phase was small (about 3%) and approximately constant. As the IPA fraction increased, the C<sub>16</sub> moved out of the NBA-rich phase to the C<sub>16</sub>-rich phase. The NBA moved from the NBA-rich phase to the H<sub>2</sub>O-rich phase, and some H<sub>2</sub>O transferred to the NBA-rich phase from the H<sub>2</sub>O-rich phase. In other words, the H<sub>2</sub>O-rich and NBA-rich phase compositions approached each other as the IPA concentration increased.

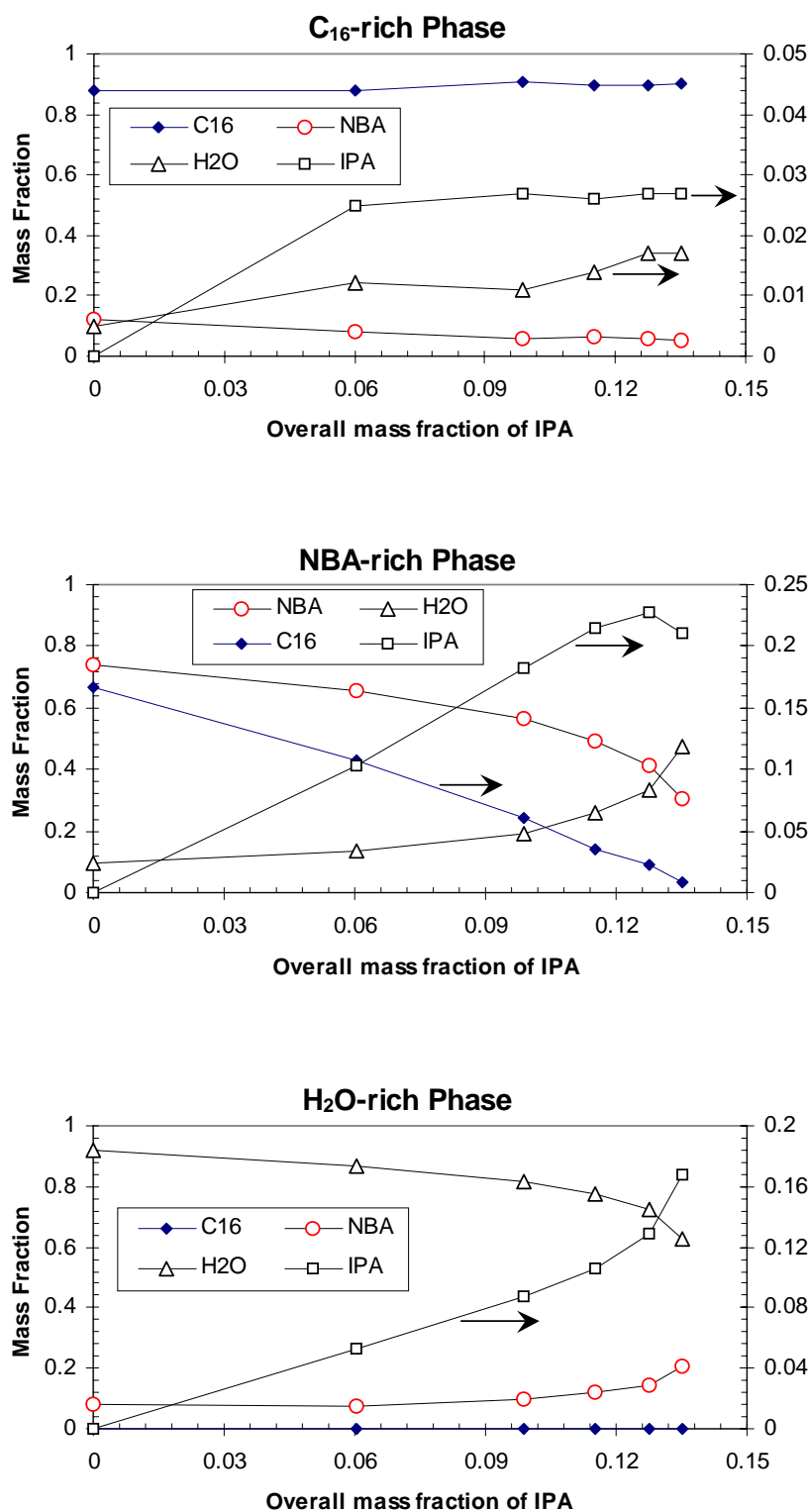


Fig. 4.3: Phase compositions for mixtures of C<sub>16</sub>/NBA/H<sub>2</sub>O /IPA system.

By adding IPA to the binary mixtures of the components we also obtained ternary diagrams that represent two sides of the quaternary diagram. All two- and three-phase compositional data are summarized in Table 4-1, Table 4-2, Table 4-3, and Table 4-4.

Table 4-1: Three-phase compositional data for C<sub>16</sub>/NBA/H<sub>2</sub>O/IPA system.

Sample		Composition in mass fraction			
		NBA	C <sub>16</sub>	IPA	H <sub>2</sub> O
Mix 1	C <sub>16</sub> -rich	0.119	0.876	0.000	0.005
	NBA-rich	0.739	0.167	0.000	0.094
	H <sub>2</sub> O-rich	0.082	0.000	0.000	0.918
	Overall	0.284	0.312	0.000	0.404
Mix 2	C <sub>16</sub> -rich	0.083	0.880	0.025	0.012
	NBA-rich	0.654	0.107	0.103	0.136
	H <sub>2</sub> O-rich	0.077	0.000	0.053	0.870
	Overall	0.271	0.298	0.045	0.385
Mix 3	C <sub>16</sub> -rich	0.057	0.905	0.027	0.011
	NBA-rich	0.563	0.061	0.182	0.194
	H <sub>2</sub> O-rich	0.095	0.000	0.087	0.818
	Overall	0.258	0.284	0.091	0.366
Mix 4	C <sub>16</sub> -rich	0.062	0.898	0.026	0.014
	NBA-rich	0.493	0.035	0.214	0.258
	H <sub>2</sub> O-rich	0.118	0.000	0.106	0.776
	Overall	0.193	0.271	0.110	0.426
Mix 5	C <sub>16</sub> -rich	0.058	0.898	0.027	0.017
	NBA-rich	0.415	0.022	0.227	0.336
	H <sub>2</sub> O-rich	0.146	0.000	0.129	0.725
	Overall	0.169	0.239	0.138	0.454
Mix 6	C <sub>16</sub> -rich	0.053	0.903	0.027	0.017
	NBA-rich	0.305	0.009	0.211	0.475
	H <sub>2</sub> O-rich	0.207	0.000	0.168	0.625
	Overall	0.179	0.263	0.151	0.407

Table 4-2: Two-phase compositional data for the base ternary system shown in Fig. 4.1.

Sample		Composition in mass fraction		
		C <sub>16</sub>	NBA	H <sub>2</sub> O
Mix 1a	C <sub>16</sub> -rich	1.000	0.000	0.000
	H <sub>2</sub> O-rich	0.001	0.000	0.999
	Overall	0.500	0.000	0.500
Mix 2a	C <sub>16</sub> -rich	0.961	0.037	0.002
	H <sub>2</sub> O-rich	0.001	0.024	0.975
	Overall	0.485	0.485	0.03
Mix 3a	C <sub>16</sub> -rich	0.923	0.074	0.030
	H <sub>2</sub> O-rich	0.002	0.048	0.950
	Overall	0.470	0.470	0.060
Mix 1b	NBA-rich	0.000	0.826	0.174
	H <sub>2</sub> O-rich	0.000	0.082	0.918
	Overall	0.000	0.500	0.500
Mix 2b	NBA-rich	0.022	0.815	0.163
	H <sub>2</sub> O-rich	0.001	0.081	0.918
	Overall	0.012	0.494	0.494
Mix 3b	NBA-rich	0.061	0.798	0.141
	H <sub>2</sub> O-rich	0.002	0.081	0.916
	Overall	0.032	0.484	0.484
Mix 4b	NBA-rich	0.088	0.783	0.129
	H <sub>2</sub> O-rich	0.003	0.081	0.916
	Overall	0.048	0.476	0.476
Mix 5b	NBA-rich	0.118	0.764	0.118
	H <sub>2</sub> O-rich	0.004	0.081	0.915
	Overall	0.066	0.467	0.467
Mix 1c	C <sub>16</sub> -rich	0.652	0.333	0.015
	NBA-rich	0.314	0.633	0.053
	Overall	0.482	0.483	0.035
Mix 2c	C <sub>16</sub> -rich	0.771	0.220	0.009
	NBA-rich	0.215	0.710	0.075
	Overall	0.479	0.476	0.045

Table 4-3: Two-phase compositional data for NBA/H<sub>2</sub>O/IPA ternary system.

Sample		Composition in mass fraction		
		NBA	IPA	H <sub>2</sub> O
Mix 1d	NBA-rich	0.635	0.130	0.235
	H <sub>2</sub> O-rich	0.105	0.053	0.842
	Overall	0.490	0.109	0.401
Mix 2d	NBA-rich	0.517	0.182	0.301
	H <sub>2</sub> O-rich	0.118	0.089	0.793
	Overall	0.348	0.143	0.509
Mix 3d	NBA-rich	0.383	0.203	0.414
	H <sub>2</sub> O-rich	0.130	0.124	0.746
	Overall	0.326	0.185	0.489
Mix 4d	NBA-rich	0.315	0.205	0.480
	H <sub>2</sub> O-rich	0.137	0.136	0.727
	Overall	0.235	0.174	0.591

Table 4-4: Two-phase compositional data for C<sub>16</sub>/H<sub>2</sub>O/IPA system.

Sample		Composition in mass fraction		
		C <sub>16</sub>	IPA	H <sub>2</sub> O
Mix 1e	C <sub>16</sub> -rich	0.967	0.030	0.003
	H <sub>2</sub> O-rich	0.002	0.320	0.679
	Overall	0.400	0.200	0.400
Mix 2e	C <sub>16</sub> -rich	0.950	0.046	0.004
	H <sub>2</sub> O-rich	0.003	0.565	0.432
	Overall	0.300	0.402	0.298
Mix 3e	C <sub>16</sub> -rich	0.933	0.063	0.004
	H <sub>2</sub> O-rich	0.050	0.810	0.140
	Overall	0.300	0.599	0.101
Mix 4e	C <sub>16</sub> -rich	0.894	0.105	0.001
	H <sub>2</sub> O-rich	0.083	0.824	0.093
	Overall	0.380	0.561	0.059
Mix 5e	C <sub>16</sub> -rich	0.850	0.147	0.003
	H <sub>2</sub> O-rich	0.115	0.815	0.070
	Overall	0.484	0.480	0.036
Mix 6e	C <sub>16</sub> -rich	0.770	0.226	0.004
	H <sub>2</sub> O-rich	0.237	0.730	0.033
	Overall	0.481	0.499	0.020

Fig. 4.4 shows the quaternary phase diagram for three-phase  $C_{16}$ /NBA/ $H_2O$  system with NaCl. As NaCl was added to the mixture, most of the salt went to the  $H_2O$ -rich phase, and increasing salt concentration drove alcohol out of the  $H_2O$ -rich phase (see Fig. 4.5 for phase compositions). No measurable amount of  $C_{16}$  was detected in the  $H_2O$ -rich phase. With increasing salinity, the  $C_{16}$  concentration increased in the NBA-rich phase, which lost some of its NBA. In a similar manner, additional NBA partitioned into the  $C_{16}$ -rich phase, while some  $C_{16}$  moved out of that phase. The  $C_{16}$ -rich and NBA-rich phase compositions approach each other as the tie triangles shrink with increasing NaCl concentration. The related three-phase compositional data are given in Table 4-5.

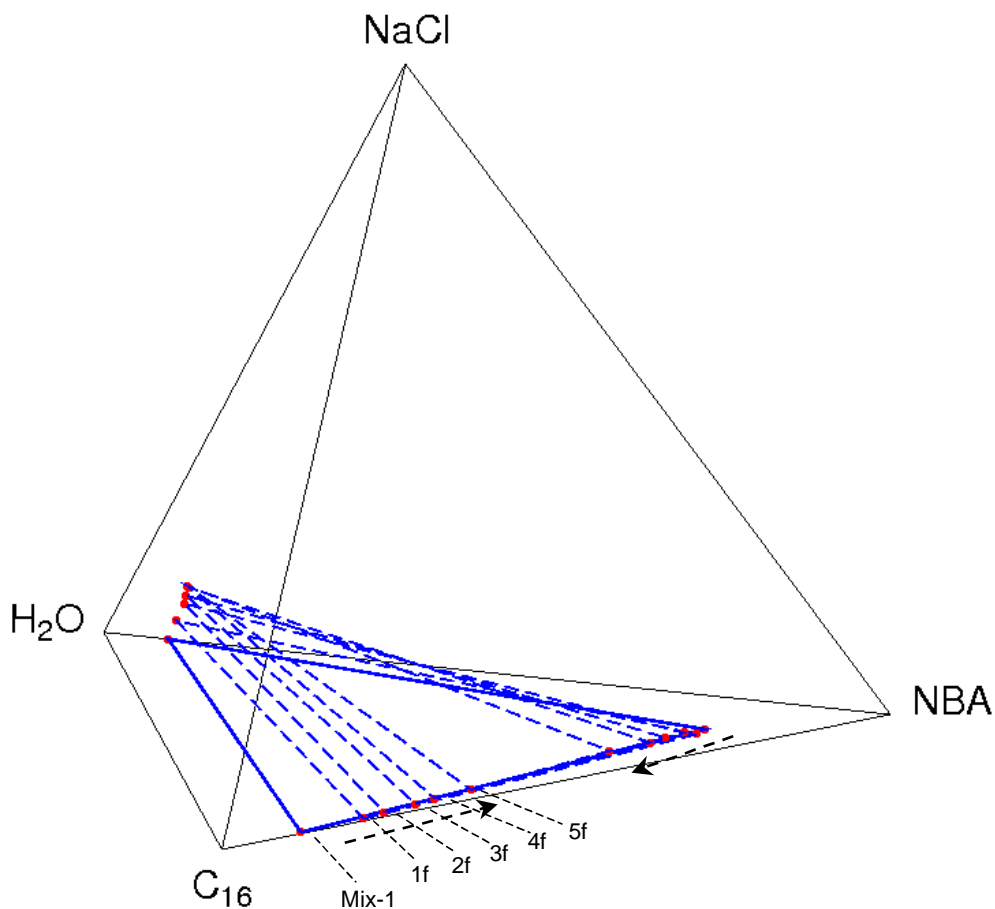


Fig. 4.4: Quaternary phase diagram for the  $C_{16}$ /NBA/ $H_2O$ /NaCl system.

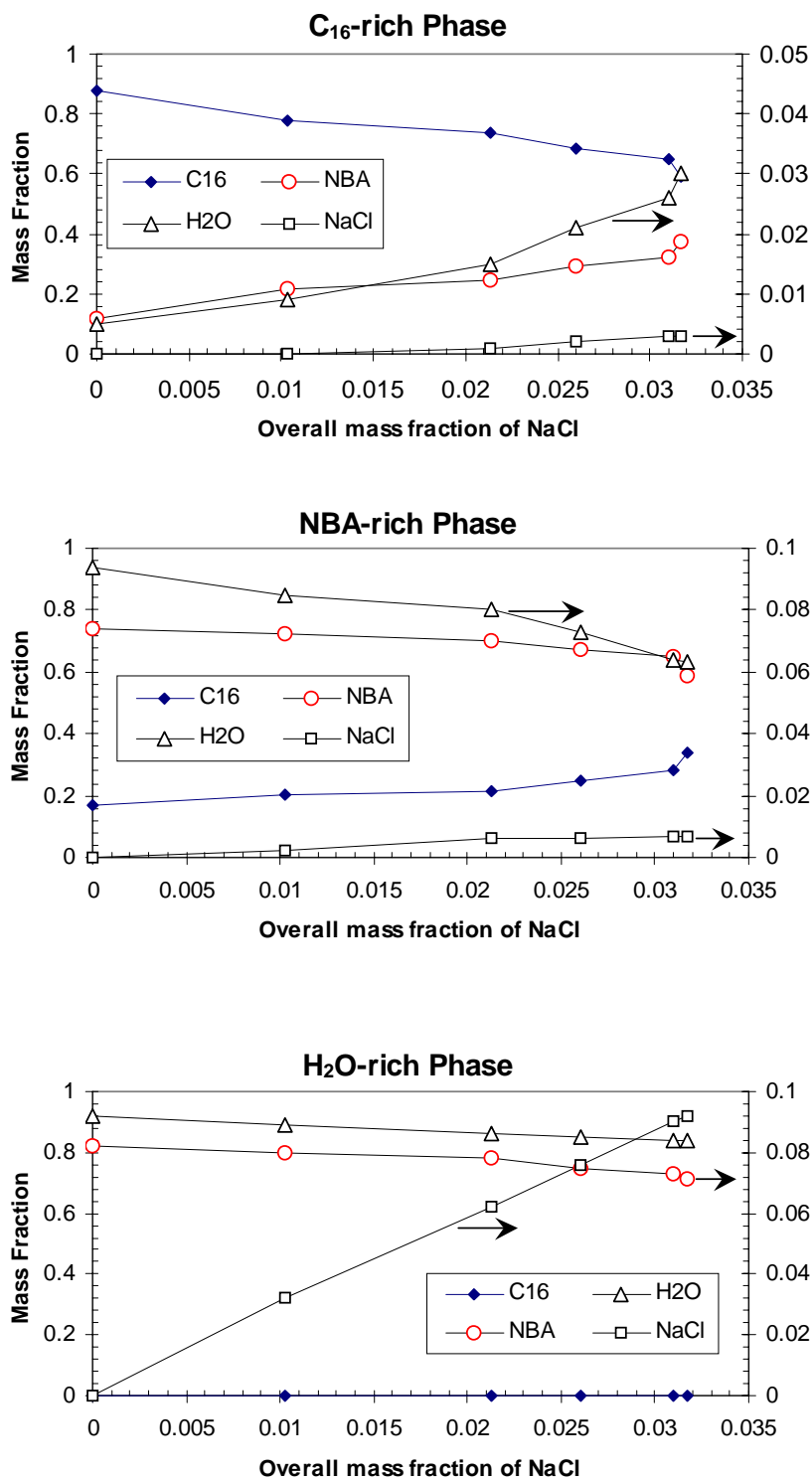


Fig. 4.5: Phase compositions for mixtures of C<sub>16</sub>/NBA/H<sub>2</sub>O/NaCl system.

Table 4-5: Three-phase compositional data for C<sub>16</sub>/NBA/H<sub>2</sub>O/NaCl system.

Sample		Composition in mass fraction			
		NBA	C <sub>16</sub>	H <sub>2</sub> O	NaCl
Mix 1	C <sub>16</sub> -rich	0.119	0.876	0.005	0.000
	NBA-rich	0.739	0.167	0.094	0.000
	H <sub>2</sub> O-rich	0.082	0.000	0.918	0.000
	Overall	0.284	0.312	0.404	0.000
Mix 1f	C <sub>16</sub> -rich	0.214	0.777	0.009	0.000
	NBA-rich	0.722	0.201	0.085	0.002
	H <sub>2</sub> O-rich	0.080	0.000	0.888	0.032
	Overall	0.329	0.330	0.329	0.012
Mix 2f	C <sub>16</sub> -rich	0.245	0.739	0.015	0.001
	NBA-rich	0.703	0.212	0.080	0.006
	H <sub>2</sub> O-rich	0.078	0.000	0.860	0.062
	Overall	0.326	0.326	0.325	0.023
Mix 3f	C <sub>16</sub> -rich	0.293	0.684	0.021	0.002
	NBA-rich	0.675	0.246	0.073	0.006
	H <sub>2</sub> O-rich	0.075	0.000	0.849	0.076
	Overall	0.324	0.324	0.324	0.029
Mix 4f	C <sub>16</sub> -rich	0.322	0.651	0.026	0.003
	NBA-rich	0.649	0.280	0.064	0.007
	H <sub>2</sub> O-rich	0.073	0.000	0.837	0.090
	Overall	0.321	0.323	0.321	0.035
Mix 5f	C <sub>16</sub> -rich	0.377	0.590	0.030	0.003
	NBA-rich	0.589	0.341	0.063	0.007
	H <sub>2</sub> O-rich	0.071	0.000	0.837	0.092
	Overall	0.322	0.321	0.321	0.036

The two systems presented offer some flexibility in the design of displacement experiments to investigate effects of IFT variations in three-phase flow. For example, injection of pre-equilibrated three-phase systems should allow control of IFT between pairs of phases with low IFT between one pair.

#### 4.1.2.2 Computational model for compositional data

In the development of compositional reservoir simulations, a reliable computational model of phase and chemical equilibria is needed. Many computational algorithms for computing phase equilibrium exist in the phase equilibria literature [Raal and Muehlbauer (1997)]. In this section, we describe our attempt to define a model of the three-phase equilibrium data.

We used SPECS Ver. 4.64, a phase behavior modeling program developed by the Institute of Chemical Engineering at the Technical University of Denmark, to model the phase behavior of the four component (C<sub>16</sub>, NBA, H<sub>2</sub>O, IPA), three-phase system shown in Fig. 4.2. Table 4-6 gives fluid characterization data for the components. Although it is difficult to model three-phase liquid/liquid/liquid systems, we found that, among others, the CPA (Cubic Plus Association, Kontogeorgis *et al.*, 1996 using the Soave-Redlich-Kwong equation of state gives reasonable results. Fig. 4.6 shows the model match to the experimental data using a quadratic mixing rule with a binary interaction ( $k_{ij}$ ) obtained by matching the equilibrium data. As Fig. 4.6 shows, the model deviates from the experimental data around the critical point and at the critical tie line. Otherwise the model representation of the three-phase behavior is reasonable. This model of the phase equilibria for this system can be used to interpolate the data reported or to examine interactions of phase behavior and flow.

Table 4-6: Fluid characterization constants.

	C <sub>16</sub>	NBA	H <sub>2</sub> O	IPA
T <sub>c</sub> , °K	722	563.05	647.13	508.3
P <sub>c</sub> , atm	14.1	43.652	217.666	46.997
ω	0.742	0.5935	0.3449	0.6677
M	225.448	74.123	18.015	60.096

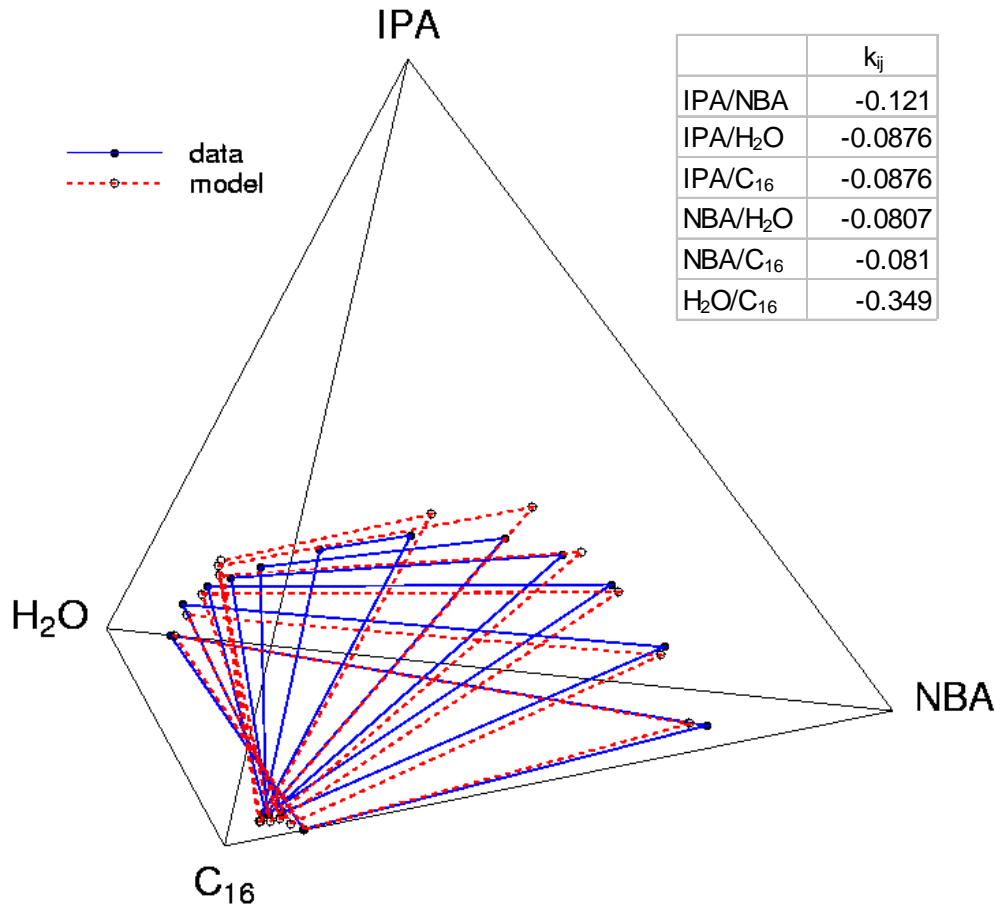


Fig. 4.6: Soave-Redlich-Kwong+Association (CPA) model for 3-phase compositional data of C<sub>16</sub>/NBA/H<sub>2</sub>O/IPA system.

#### 4.1.2.3 Analogy to reservoir fluids based on IFT data

The physical properties of the phases of the C<sub>16</sub>/NBA/H<sub>2</sub>O/IPA system are given in Table 4-7. As the IPA concentration in the mixture was increased, the IFT between H<sub>2</sub>O-rich and NBA-rich phases decreased (Fig. 4.7). The IPA % in the figure refers to the value at the center of each tie triangle representing three-phase compositions (see Table 4-7). With the same increase in the IPA concentration, the IFT between C<sub>16</sub>-rich and NBA-rich phases increases, whereas the IFT between C<sub>16</sub>-rich and H<sub>2</sub>O-rich phases stays almost constant. When the IFT between H<sub>2</sub>O-rich and NBA-rich phases reaches zero, the other two IFTs become identical, which means that only two phases exist in the system. By comparison of the results with those obtained by Amin and Smith, 1998 for three-phase flow experiments shown in Fig. 4.8, which represent multicontact miscible gas injection processes with water present, we choose the H<sub>2</sub>O-rich phase to represent the gas phase, the NBA-rich phase to represent the oil phase, and the C<sub>16</sub>-rich phase to represent the aqueous phase. Note that density and viscosity of analog liquids don't match with those of reservoir fluids.

Table 4-7: Physical properties of the phases obtained from C<sub>16</sub>/NBA/H<sub>2</sub>O/IPA system.

Samples		Mix 1	Mix 2	Mix 3	Mix 4	Mix 5	Mix 6
Density (g/cm <sup>3</sup> )	C <sub>16</sub> -rich	0.776	0.774	0.774	0.772	0.772	0.773
	NBA-rich	0.824	0.837	0.846	0.858	0.870	0.903
	H <sub>2</sub> O-rich	0.987	0.983	0.976	0.969	0.960	0.946
Viscosity (mPa.s)	C <sub>16</sub> -rich	2.942	3.071	3.065	3.046	3.084	3.111
	NBA-rich	2.973	3.145	3.279	3.237	3.510	3.749
	H <sub>2</sub> O-rich	1.216	1.563	1.824	1.833	2.416	3.043
IFT (mN/m)	C <sub>16</sub> -rich / H <sub>2</sub> O-rich	2.465	2.068	1.893	1.776	1.749	1.622
	C <sub>16</sub> -rich / NBA-rich	0.239	0.551	0.794	1.106	1.491	1.583
	NBA-rich / H <sub>2</sub> O-rich	2.297	1.157	0.654	0.308	0.086	0.028
IPA % at the center of tie triangle		0.00	6.03	9.87	11.53	12.77	13.53

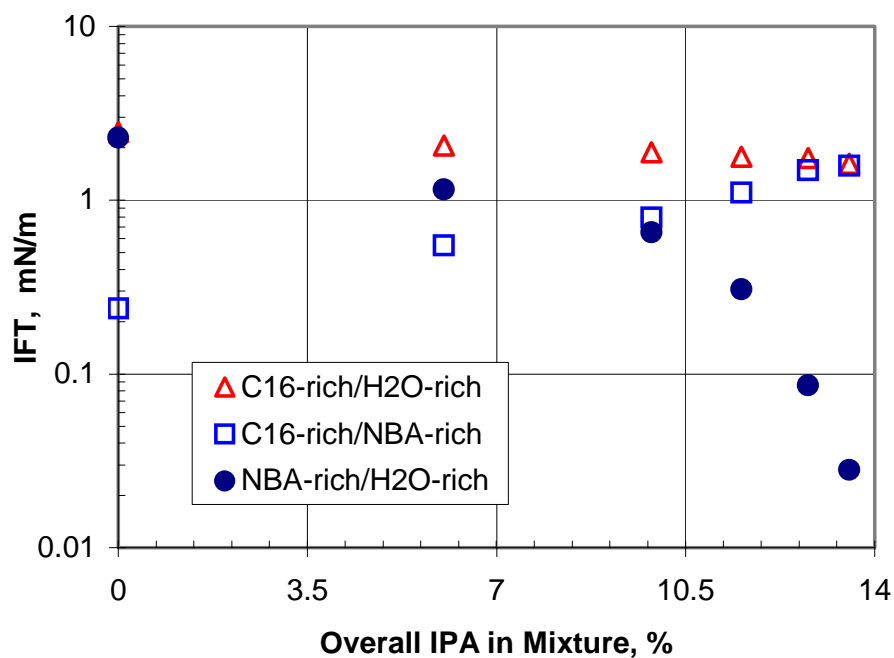


Fig. 4.7: IFT variation of C<sub>16</sub>/NBA/H<sub>2</sub>O/IPA quaternary system as a function of IPA concentration at the center of each tie triangle.

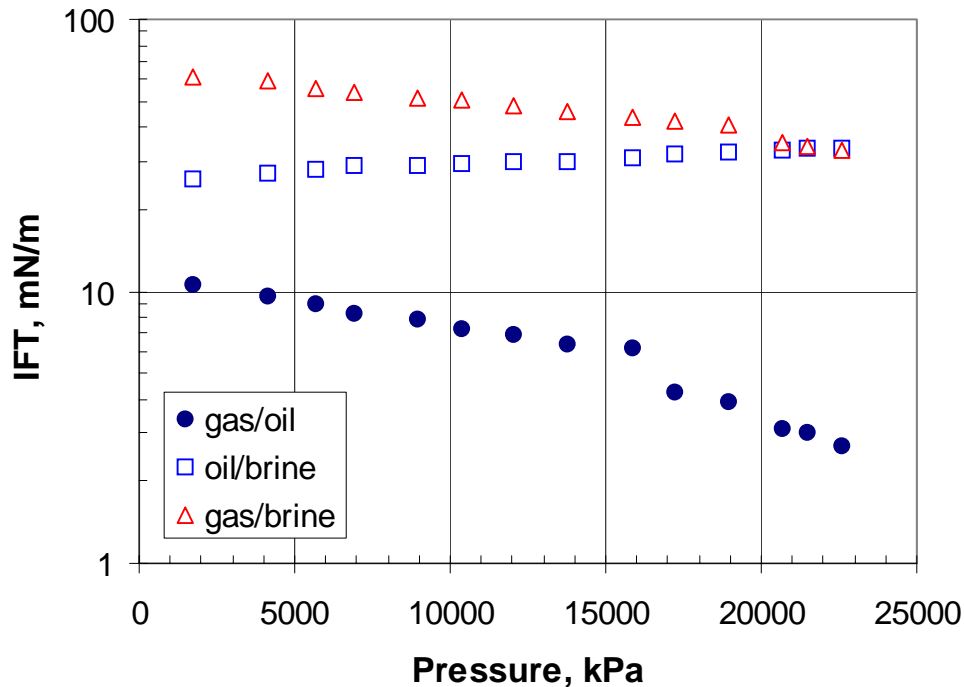


Fig. 4.8: IFT between oil, gas and brine phases as a function of pressure at reservoir conditions ( $T=82.2\text{ }^{\circ}\text{C}$ ) [Amin and Smith (1998)].

As the NaCl concentration in the mixture was increased, the IFT between  $C_{16}$ -rich and NBA-rich phases decreased (see Table 4-8 and Fig. 4.9). The NaCl % in the figure refers to the value at the center of each tie triangle representing three-phase compositions. With the same increase in the NaCl concentration, the IFTs of  $C_{16}$ -rich/ $H_2O$ -rich and NBA-rich/ $H_2O$ -rich increase. When the IFT between  $C_{16}$ -rich and NBA-rich phases reaches zero, the other two IFTs become identical, which means that only two phases exist in the system.

Comparison of the results in Fig. 4.9 with those in Fig. 4.8 indicates that there is an analogy of  $C_{16}$ /NBA/ $H_2O$ /NaCl system to three-phase fluid systems in field scale gas injection processes. For three-phase displacement experiments, the  $C_{16}$ -rich phase represents the gaseous phase, the NBA-rich phase is the analog of the oleic phase, and the  $H_2O$ -rich phase represents the aqueous phase.

A relation between IFT and phase density differences is shown in Fig. 4.10. Our data with IPA show trends similar to the data given by Morrow *et al.* (1988) and Bardon and Longeron (1978). The data with NaCl are different in that small concentration differences result in dramatic changes in IFT but without accompanying changes in density. As previously stated, most of NaCl goes to the aqueous phase. This is why adding NaCl does not affect the density of the  $C_{16}$ -rich and NBA-rich phases, but forces the component movement between those phases, which in turn changes the related IFT.

Table 4-8: Physical properties of the phases obtained from C<sub>16</sub>/NBA/H<sub>2</sub>O/NaCl system.

Samples		Mix 1	Mix 1f	Mix 2f	Mix 3f	Mix 4f	Mix 5f
Density (g/cm <sup>3</sup> )	C <sub>16</sub> -rich	0.776	0.776	0.780	0.784	0.783	0.786
	NBA-rich	0.824	0.816	0.810	0.809	0.803	0.798
	H <sub>2</sub> O-rich	0.987	1.022	1.043	1.055	1.066	1.067
Viscosity (mPa.s)	C <sub>16</sub> -rich	2.942	2.999	3.020	3.048	3.062	3.090
	NBA-rich	2.973	3.082	3.095	3.110	3.131	3.140
	H <sub>2</sub> O-rich	1.216	1.300	1.310	1.318	1.323	1.330
IFT (mN/m)	C <sub>16</sub> -rich / H <sub>2</sub> O-rich	2.465	3.244	4.265	4.267	4.714	4.645
	C <sub>16</sub> -rich / NBA-rich	0.239	0.083	0.038	0.012	0.005	0.001
	NBA-rich / H <sub>2</sub> O-rich	2.297	3.187	3.824	4.182	4.172	4.179
NaCl % at the center of tie triangle		0.00	1.03	2.13	2.60	3.10	3.17

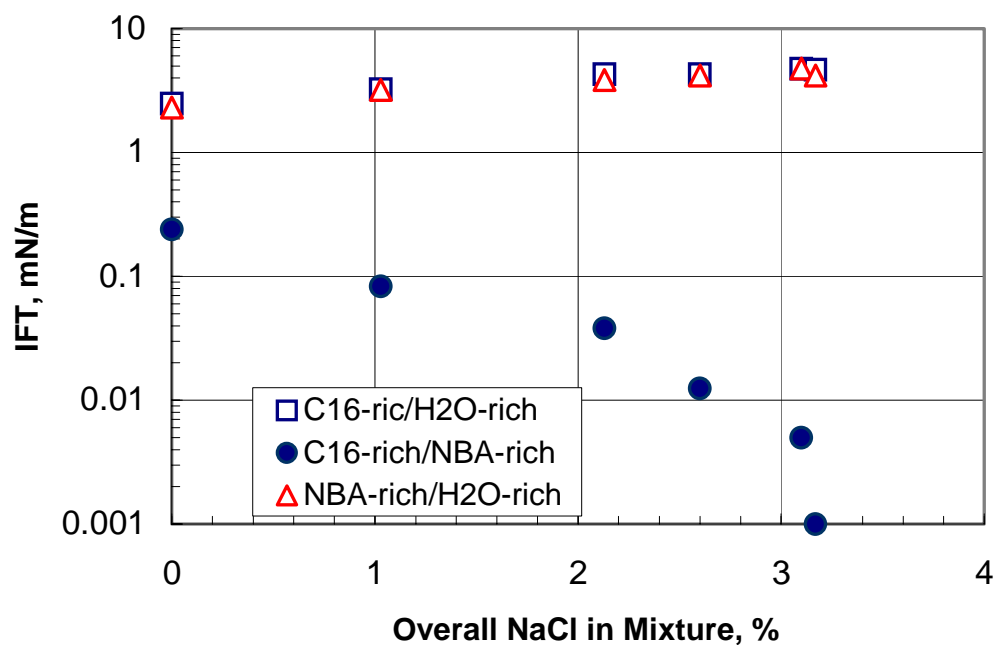


Fig. 4.9: IFT variation of C<sub>16</sub>/NBA/H<sub>2</sub>O/NaCl quaternary system as a function of NaCl concentration at the center of each tie triangle.

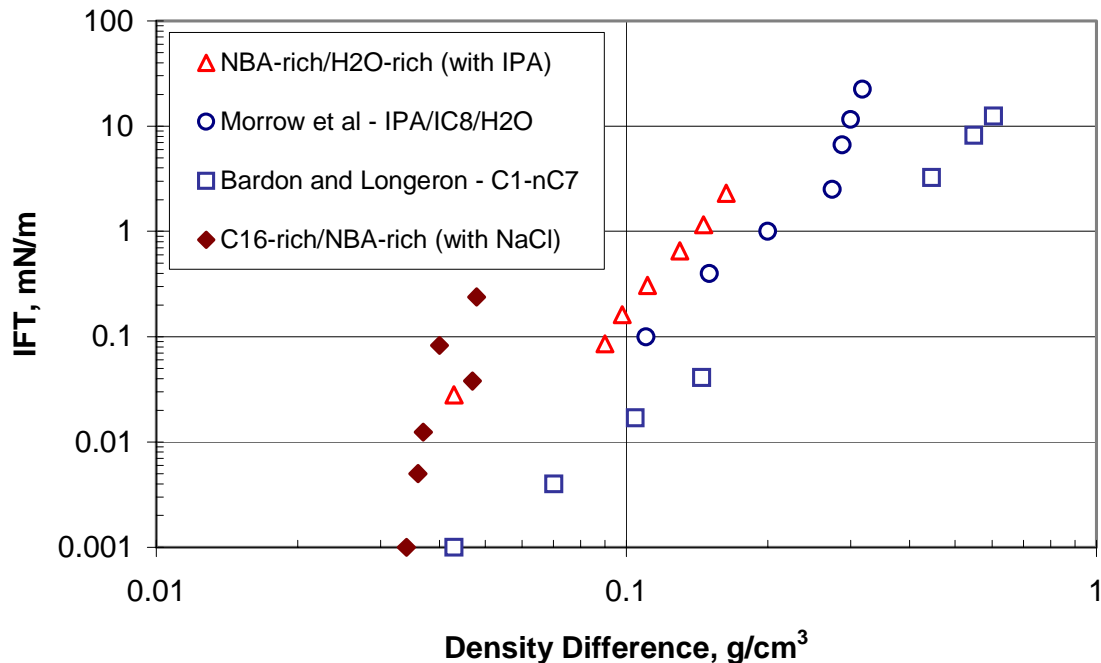


Fig. 4.10: Correlation between IFT and density difference.

#### 4.1.3 Effect of IFT variation and wettability on three-phase relative permeability in unconsolidated media

For compositional processes such as high-pressure gas injection, in which oil and gas compositions can vary significantly, variations in gas and oil relative permeabilities as a function of IFT are of interest. In displacements of oil by gas, considerable exchanges between these phases can exist, which can substantially modify the physical and chemical properties of the fluids, especially at their interfaces. The creation of lower IFT between the oil in place and the injected gas results in a reduction of the capillary forces, which may make possible reductions in the residual oil saturation and may modify phase relative permeabilities. With the presence of water (in a pre-waterflooded reservoir or in WAG processes), tertiary recovery processes such as gas injection routinely involve three-phase flow. Thus, the effect of IFT variations on three-phase relative permeabilities must be delineated for accurate predictions of the performance of gas injection processes.

Although there have been studies of the effect of low IFT on two-phase relative permeability (Talash, 1976, Bardon and Longeron, 1978, Batycky and McCaffery, 1978, Amaefule and Handy, 1982, Asar and Handy, 1983, Harbert, 1983, Torabzadeh and Handy, 1984, Fulcher *et al.*, 1985, Delclaud *et al.*, 1987, Tehrani *et al.*, 1997, McDougall *et al.*, 1997), there are limited experimental data published so far that examine the effect of low IFT on three-phase relative permeabilities (Delshad *et al.*, 1987). Because the IFT between oil and displacing fluid is an important parameter for most of enhanced oil recovery techniques, almost all authors have focussed on the effect of IFT on oil and displacing fluid relative

permeabilities (Lake, 1989). Experimental results show that residual oil saturation and relative permeability are strongly affected by IFT, especially when the IFT is lower than about 0.1  $mN/m$  (corresponding to a range of capillary number of  $10^{-2}$ - $10^{-3}$ ). Bardon and Longeron observed that oil relative permeability increased linearly as IFT was reduced from about 12.5  $mN/m$  to 0.04  $mN/m$  and that for IFT below 0.04 the oil relative permeability curves shifted more rapidly with further reductions in IFT. Later Asar and Handy showed that oil relative permeability curves began to shift as IFT was reduced below 0.18  $mN/m$  for a gas-condensate system near the critical point.

Delshad *et al.* presented experimental data for low IFT three-phase relative permeabilities in Berea sandstone cores. The measurements were done at steady-state conditions with a constant capillary number of  $10^{-2}$ . They employed a brine/oil/surfactant /alcohol mixture that included a microemulsion and excess oil and brine. The IFTs of microemulsion/oil and microemulsion/brine were low, while the IFT between oil and brine remained high. They concluded that low IFT three-phase relative permeabilities are functions of their own saturations only. Amin and Smith (1998) have recently published experimental data showing that the IFTs for each binary mixture of brine, oil and gas phases vary as pressure increases (see Fig. 4.8 in the previous section). Fig. 4.8 shows that the IFT of gas/oil pair decreases as the pressure increases whereas the IFTs of the gas/brine and oil/brine pairs approach to each other. Similar variations can be induced by phase composition changes that occur during gas displacement processes.

In the sections that follow we report experimental results dealing with the effect of IFT variation on the three-phase flow. We employed the analog  $C_{16}/NBA/H_2O/IPA$  liquid system defined in the previous section to represent reservoir fluids. We used both teflon bead packs and glass bead packs to analyze effects of wettability on low-IFT relative permeabilities. Finally we report results of experiments to investigate effects of IFT gradient on three-phase relative permeability functions.

#### **4.1.4 Experimental approach**

##### **4.1.4.1 Analysis procedure**

In the project proposal, we proposed to use computerized tomography (CT) to determine the saturation profiles along the porous medium and to derive the relative permeabilities therefrom. Employing analog liquid phases instead of appropriate reservoir fluids, on one hand, offers flexibility in the experimental analysis of effects of IFT variation on relative permeabilities, but, on the other hand, resulted in some difficulties with visible attenuation contrast between the phases in the scanned images. One way to enhance the attenuation contrast between the liquid phases is to add some tracers to the liquids, such as iodated oils to oleic phase, or high atomic number salts like sodium iodide to the aqueous phase (Siddiqui *et al.*, 1996). However, as we have shown in the previous section, compositions data and physical properties of two of three phases are very close to each other, especially around the critical point (see Table 4-7 and Table 4-8). Tracers that are miscible with individual

components cannot enhance the attenuation contrast to our desired degree and may influence phase behavior. To overcome these difficulties, we decided to employ another experimental technique to evaluate three-phase relative permeabilities.

The method proposed by Welge (1952) and Johnson *et al.* (1959), known as the combined Welge/JBN-Method, is based on the following assumptions in the determination of saturation and relative permeabilities from two-phase dynamic displacement experiments:

1. Fluids are incompressible,
2. Flow is one-dimensional and isothermal,
3. Three immiscible phases flow, with no mass transfer between phases, and
4. Capillary effects are ignored.

As it can be seen from the measured phase properties in the previous section (see Table 4-7 and Table 4-8), the pre-equilibrated, incompressible three-liquid-phase system (without IPA or NaCl) has an order of magnitude lower IFT than those of reservoir fluids containing a gaseous phase. Typical values of IFT for hydrocarbon/water/gas systems at ambient conditions have a range of 20-70 *mN/m*. Thus, using the analog liquid system we proposed in the three-phase displacement experiments is reasonably consistent with the assumptions required for the application of the Welge/JBN method.

The Welge/JBN method was later extended by Virnovski (1985) and Grader and O'Meara (1988) independently to three-phase dynamic displacements. The method is applied as follows. Plots of the recovered pore volumes (PV) of each phase as a function of the injected PV are generated (Fig. 4.11). The saturation of phase *i* at the outlet of the core,  $S_i$  is given by,

$$S_i = S_i^o - L_i + Q \frac{dL_i}{dQ}, \quad (4.1)$$

where  $S_i^o$  is the initial saturation of phase *i* before injecting the third phase,  $L_i$  is the pore volume (PV) recovery of phase *i*, and  $Q$  is the PV of the third phase injected.

The relative permeability to phase *i*,  $k_{ri}$ , is calculated using the following equation, including gravity,

$$k_{ri} = \frac{q_i \mu_i l}{kA} \frac{f_i}{((\Delta p)_{x=1} - \rho_i g l)}, \quad (4.2)$$

where  $(\Delta p)_{x=1}$  is the differential pressure at the downstream end of the core, which is defined by Johnson *et al.* (1959) as (Fig. 4.12),

$$(\Delta p)_{x=1} = \Delta p - Q \frac{d(\Delta p)}{dQ}, \quad (4.3)$$

where  $q_t$  is the total flow rate,  $\mu_i$  the viscosity of phase *i*,  $l$  the length of the core,  $f_i$  the fractional flow of phase *i*,  $k$  the absolute permeability,  $A$  the cross-sectional area of porous medium, and  $\Delta p$ , the differential pressure across the core. The fractional flows ( $f_i$ 's) at the

outlet of the core were determined from the slopes of tangents drawn to the recovery curves. Eq. (4.3) was evaluated from the differential pressure values at the intercepts of the tangents to the graph of differential pressure vs PV injected after breakthrough.

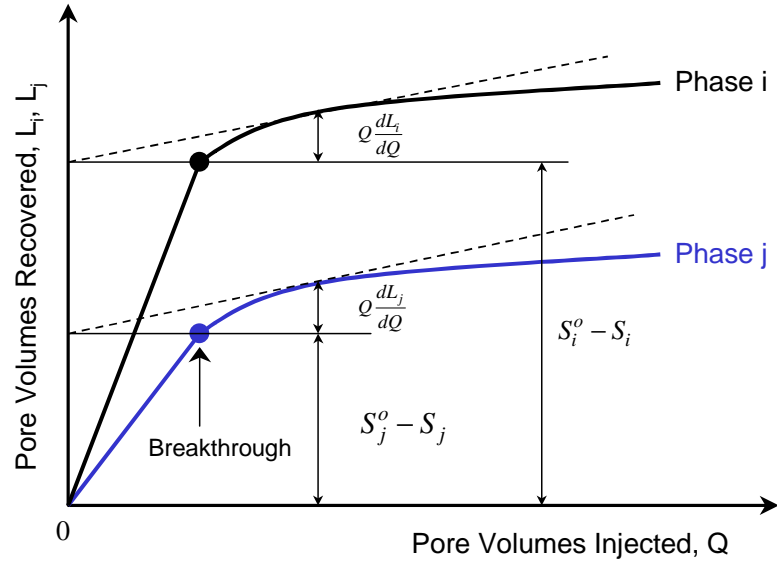


Fig. 4.11: The Welge method for the determination of saturations at the end of core.

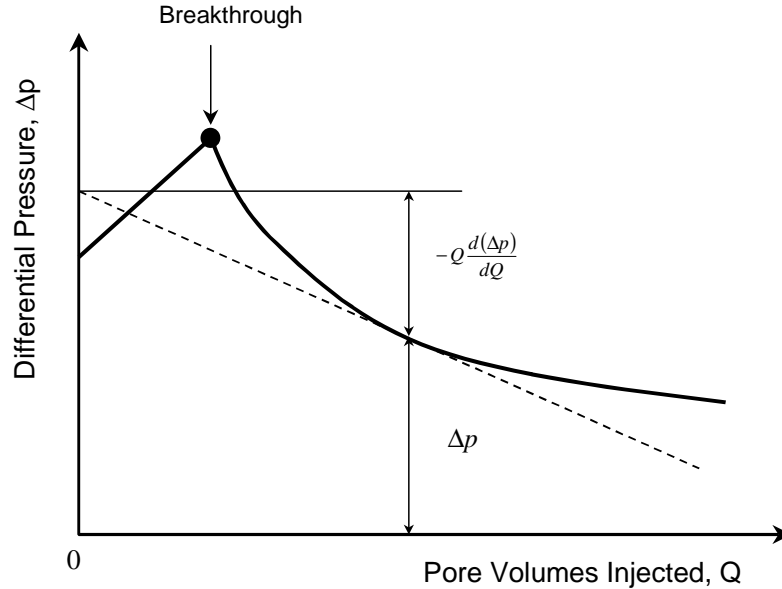


Fig. 4.12: The JBN method for the determination of the pressure gradient at the end of core.

#### 4.1.4.2 Porous medium

Because the  $C_{16}$ -rich phase always represents the water in the reservoir system (according to the selection criteria for the  $C_{16}$ /NBA/ $H_2O$ /IPA system presented in the previous section), we

employed an oil-wet porous medium in the laboratory to simulate the fluid flow in a water-wet oil reservoir. Alternately, employing a water-wet porous medium in the flow experiments simulates displacements in an oil-wet reservoir as long as the wetting H<sub>2</sub>O-rich phase represents the reservoir oil. Table 4-9 summarizes those phase correspondences for the analog displacements.

Morrow and McCaffery (1978) performed experiments with compressed porous polytetrafluoroethylene (PTFE, teflon) media to analyze effects of wetting conditions of reservoirs on displacement performance. They measured a contact angle exhibited by a given fluid pair at a smooth PTFE surface to 108° for the water/air pair and 44° for the n-tetradecane/air pair, an indication that hydrocarbons are wetting and water is non-wetting to PTFE materials.

Table 4-9: Correspondence of analog and reservoir phases.

Analog Liquids from C <sub>16</sub> /NBA/H <sub>2</sub> O/IPA Quaternary System	Water-wet reservoir system (Oil-wet lab system) (i.e., Teflon bead pack)	Oil-wet reservoir system (Water-wet lab system) (i.e., Glass bead pack)
C <sub>16</sub> -rich phase	WATER	WATER
NBA-rich phase	OIL	GAS
H <sub>2</sub> O-rich phase	GAS	OIL

We employed PTFE powder (purchased from Aldrich Chemical Co.) and glass bead packs (purchased from Cataphote Co.) to mimic a water-wet porous medium and an oil-wet porous medium, respectively, with our analog fluids. The wetting situation for those porous media was investigated in the following simple experiments. We measured contact angles directly by taking images of solid-liquid-liquid interface in a PTFE capillary tubing as well as in a glass capillary and determining the contact angle. Those measurements were also verified by series of capillary rise measurements. The results tabulated in Table 4-10 show that the C<sub>16</sub>-rich phase wets the PTFE tubing more than the other phases whereas the H<sub>2</sub>O-rich phase is the most non-wetting phase (see Fig. 4.13). On the contrary, the H<sub>2</sub>O-rich phase is the most wetting phase in the glass capillary (see Fig. 4.14). The NBA-rich phase always represents intermediate phase when all phases coexist in the tubing.

Table 4-10: Contact angles of analog liquids in teflon and glass tubing.

Phases from Mix 1	Phase in which contact measured	Contact angle, degrees	
		Glass capillary (ID=0.02cm)	Teflon tubing (ID=0.02cm)
C <sub>16</sub> -rich/ NBA-rich	C <sub>16</sub> -rich	143 (NBA-rich wets)	38 (C <sub>16</sub> -rich wets)
C <sub>16</sub> -rich/ H <sub>2</sub> O-rich	C <sub>16</sub> -rich	108 (H <sub>2</sub> O-rich wets)	45 (C <sub>16</sub> -rich wets)
NBA-rich/ H <sub>2</sub> O-rich	H <sub>2</sub> O-rich	76 (H <sub>2</sub> O-rich wets)	138 (NBA-rich wets)

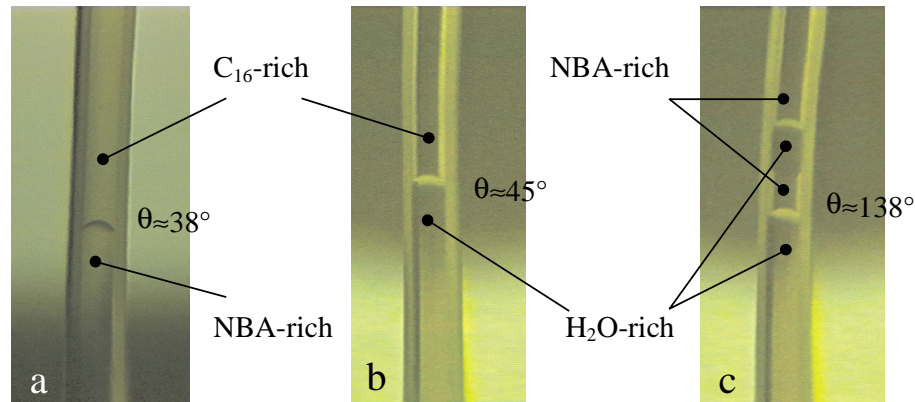


Fig. 4.13: Coexistence of analog liquid phases of Mix. 1 (Table 4-1) in the teflon tubing.

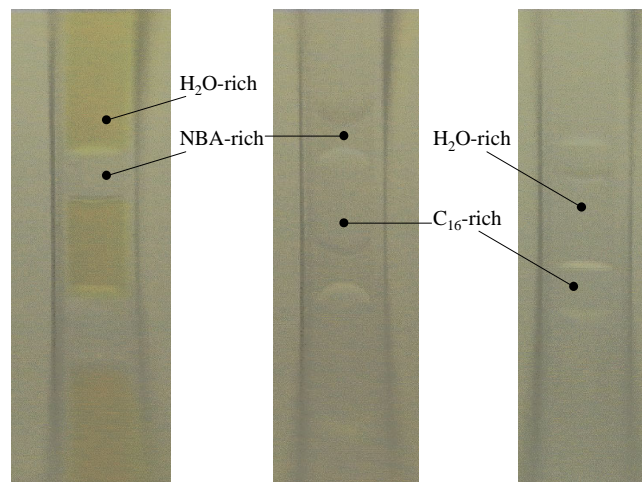


Fig. 4.14: Coexistence of analog liquid phases of Mix. 1 (Table 4-1) in the glass capillary.

#### 4.1.4.3 Fluids

The fluids used in this series of displacement experiments were  $C_{16}$ -rich, NBA-rich, and  $H_2O$ -rich phases with three different compositions taken from Table 4-1 in the previous section, namely Mix 1, Mix 4, and Mix 6. Fig. 4.15 shows the related phase tie-triangles. We prepared all mixtures in a  $4000\text{-cm}^3$  Erlenmeyer, waited for phase equilibrium, and checked their properties again. As illustrated in Fig. 4.15, the IFT between NBA-rich and  $H_2O$ -rich phases is very sensitive to changes in IPA concentration in the mixture, especially around the critical point. Because IPA is relatively volatile, special care was required in displacement experiments to avoid composition changes due to evaporation. Therefore we tried to prevent

the mixture from contacting air as much as possible. IFT checks before and after the experiments indicated that changes in IFT due to evaporation were small.

For the data given in Table 4-7, the largest viscosity ratio is about 2.5 (between the NBA-rich and H<sub>2</sub>O-rich phases of Mix 1) and the largest density ratio is about 1.3 (between the H<sub>2</sub>O-rich and C<sub>16</sub>-rich phases of Mix 1). The phase correspondence between the analog phases and reservoir fluids were previously presented in Table 4-9 for both teflon powder and glass bead packs.

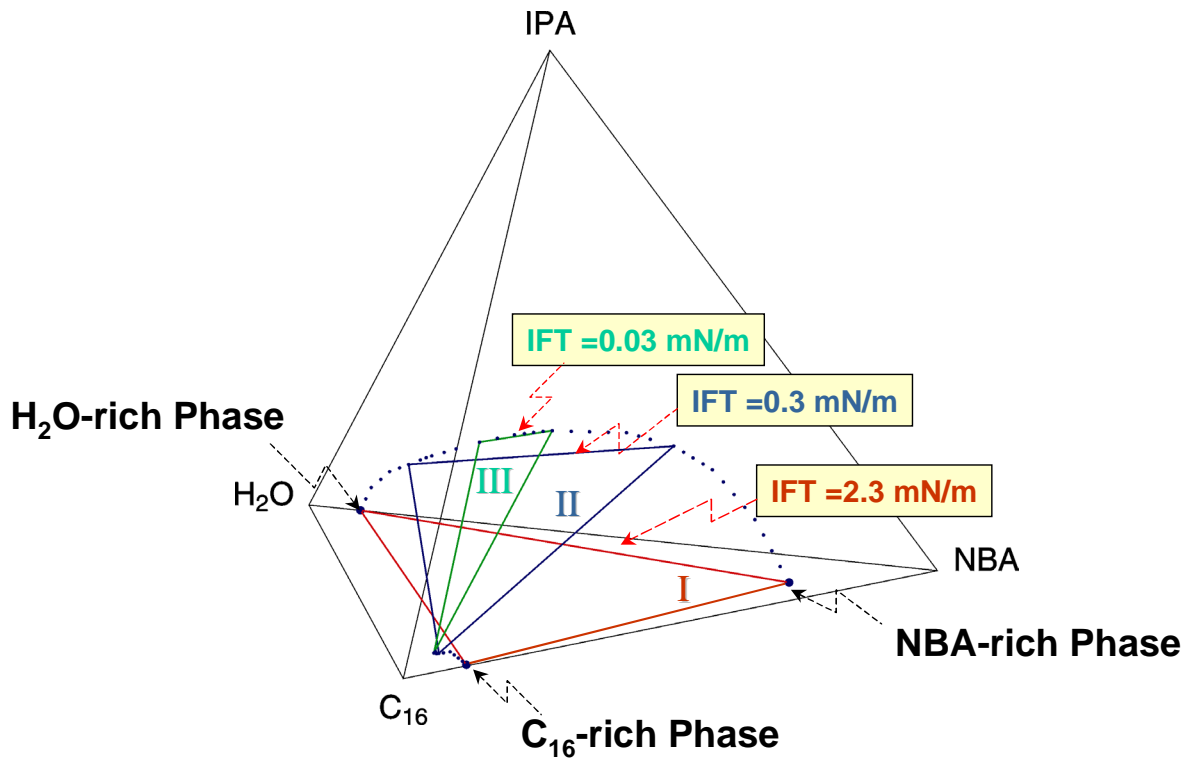


Fig. 4.15: Three-phase compositions used in the experiments.

#### 4.1.4.4 Apparatus

A simplified schematic of the three-phase dynamic displacement apparatus is shown in Fig. 4.16. The apparatus is capable of injecting one or two phases into the porous medium. The phases were always kept in one container to avoid any non-equilibrium conditions. The pump used was a Masterflex Easy-Load Pump with the capacity of 0.06-30  $cm^3/min$ . The console drive of the pump allowed the use of two pump heads for the injection of two different liquids simultaneously.

The core holder is made of a 3.18- $cm$  outside diameter by 0.34- $cm$  thick Plexiglas tube

with two end plugs of the same material. Holes were drilled through both end plugs to allow fluids to enter and exit the core. The injection pressure across the core was measured by an analog gauge with  $0.05\text{-kPa}$  precision. During dynamic displacement experiments, we used glass vials with  $0.1\text{-cm}^3$  precision to collect the effluent.

We prepared two cores for the experiments. The core holder was packed dry in a vertical position with either PTFE powder or glass beads. The physical properties of the cores are presented in Table 4-11. The porosity and homogeneity of the PTFE porous medium were verified by CT scanning.

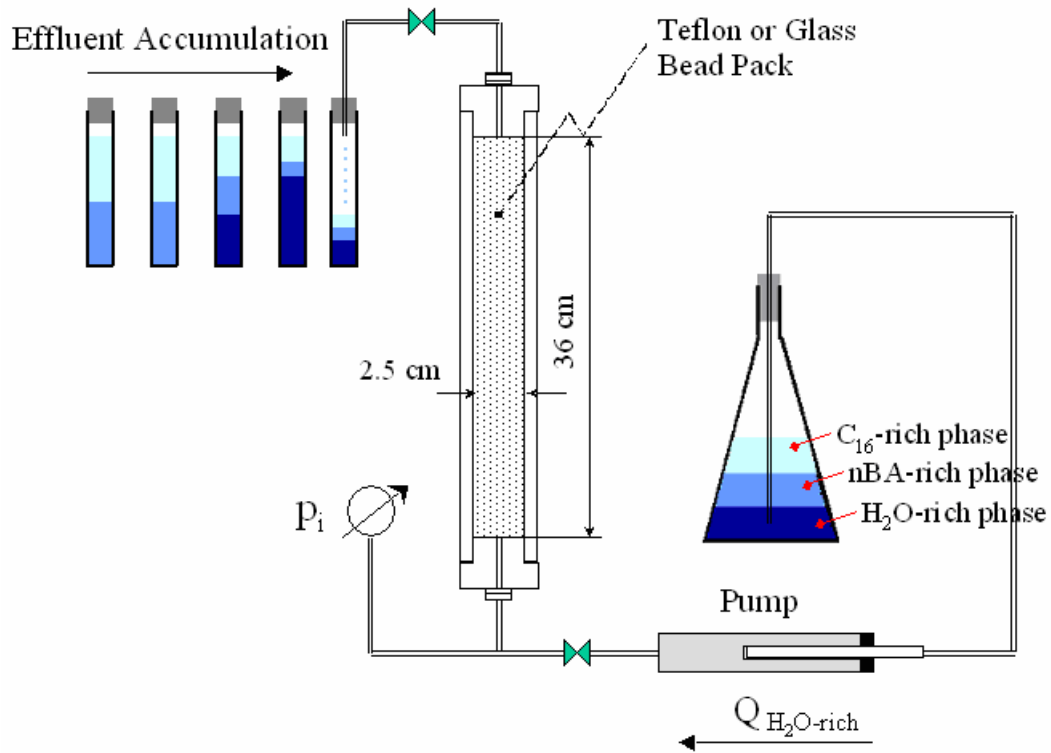


Fig. 4.16: Experimental equipment for displacement experiments.

Table 4-11: Core properties.

	Teflon Pack	Glass Pack
Length, cm	36	33
Diameter, cm	2.5	2.5
Pore volume, $\text{cm}^3$	104.3	64.8
Porosity, %	59	40
Absolute Permeability, D	19	35

The core holder was positioned vertically to allow creation of a stable displacement front. Because for the experiments in the teflon pack the gas phase was represented by the denser H<sub>2</sub>O-rich phase, this phase was injected from the bottom of the core holder to displace the less dense C<sub>16</sub>-rich and NBA-rich phases. For the experiments in the glass bead pack, however, we injected the NBA-rich “gas” phase from the top of the core to have a gravity stable displacement of the H<sub>2</sub>O-rich “oil” phase. There was gravity instability between the injected NBA-rich “gas” phase and the displaced C<sub>16</sub>-rich “water” phase. This will be discussed later in detail.

#### 4.1.4.5 Experimental procedure

##### Analogue Water-Wet Medium (Teflon powder)

An expected saturation path for displacement experiments can be represented for a given mixture from the base tie triangle as shown in Fig. 4.17. To obtain this saturation path we used the following experimental procedure:

1. We first let the C<sub>16</sub>-rich phase (wetting (W), “water”) flow into the porous medium from the bottom of the core. We did not evacuate the porous medium to avoid causing any change in the composition of liquid phase containing IPA, but we flushed the porous medium by CO<sub>2</sub> to displace air from the pores. Then we injected about five more PVs of the C<sub>16</sub>-rich phase (W, “water”) into the porous medium to make sure that the PTFE bead packs were saturated completely. We determined the porosity from the total amount of the C<sub>16</sub>-rich phase (W, “water”) stored in the pores and measured the absolute permeability of the porous medium.
2. Then we injected the NBA-rich phase (intermediate wetting (IW), “oil”) into the porous medium until no additional C<sub>16</sub>-rich phase (W, “water”) was produced. At this point we determined the effective phase permeability.
3. We simultaneously injected C<sub>16</sub>-rich (W, “water”) and NBA-rich (IW, “oil”) phases with the same flow rate to set the initial condition of the porous medium before injection of the H<sub>2</sub>O-rich phase (nonwetting (NW), “gas”).
4. We started the dynamic displacement experiment for measuring relative permeabilities by injecting the H<sub>2</sub>O-rich phase (NW, “gas”) into the uniformly saturated porous medium.
5. We collected the effluents and measured the differential pressure across the core as a function of pore volumes injected (PVI).
6. After the experiment, we cleaned the PTFE porous medium by flooding three PVs of IPA and flushing with dry air for 24 hours before the next experiment.

We repeated the steps 1-6 with another mixture having lower IFT.

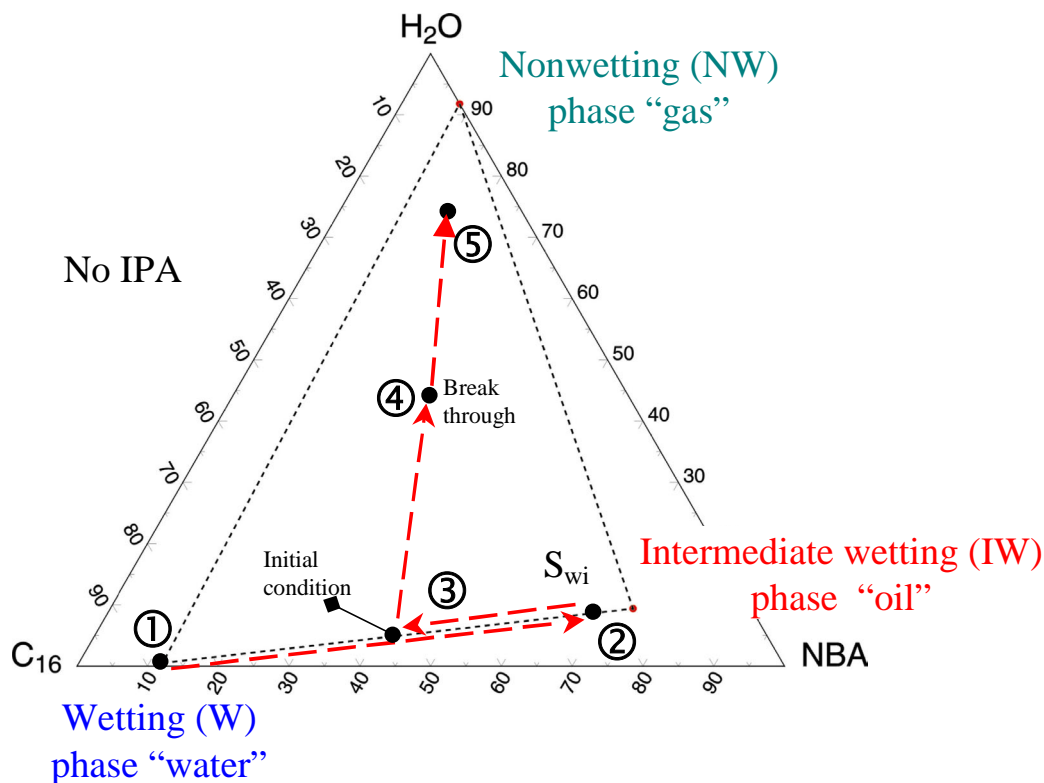


Fig. 4.17: Sample saturation path for three-phase displacement experiment in an artificial water-wet porous medium.

#### Analogue Oil-Wet Medium (Glass beads)

To investigate the behavior of an oil-wet porous medium, we employed a similar displacement procedure, except that we used a glass bead pack and followed a different sequence of fluids injected to the core representing different fluid analogs for the alternate wetting system. Glass beads are widely documented as a naturally water wet material. We then adopted the H<sub>2</sub>O-rich phase of the analog C<sub>16</sub>/NBA/H<sub>2</sub>O/IPA ternary system to represent “oil” and initially saturated the core with this phase to simulate an oil-wet system (see Table 4-9 for the analogy between analog liquids and reservoir fluids). Since the NBA-rich phase has a density between those of the other two phases, this selection for phase correspondences inevitably introduces the possibility of gravity instabilities into the vertical dynamic displacement experiments. How these density differences affect the relative permeabilities as the IFT is increased between two of the three phases will be discussed later.

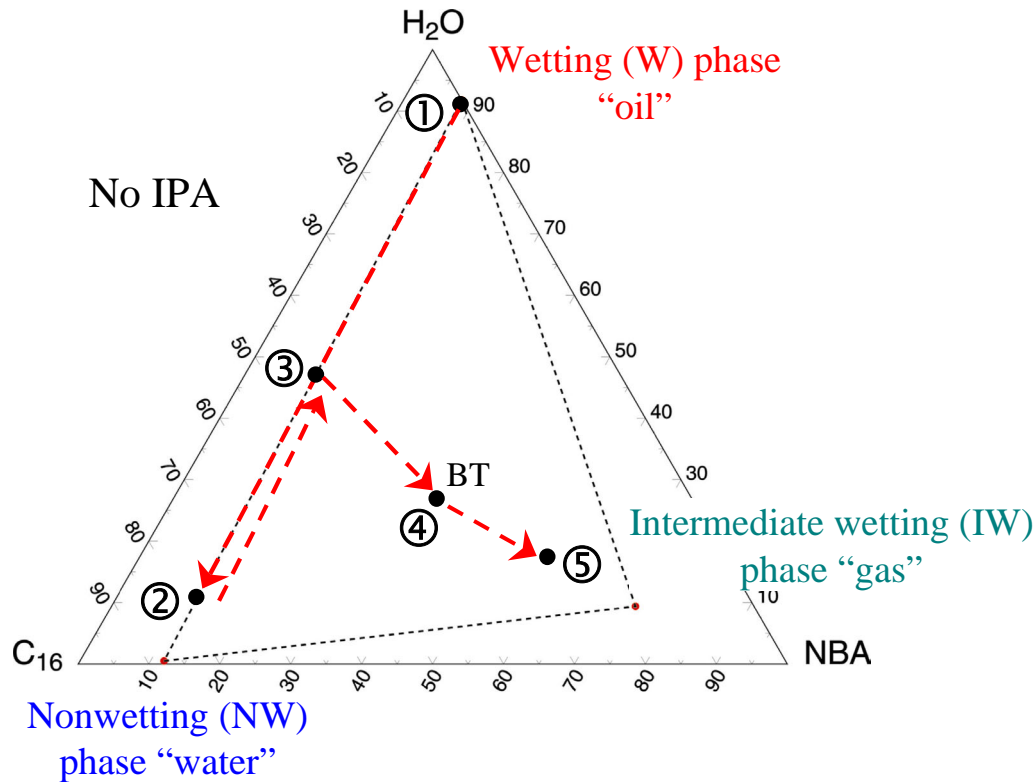


Fig. 4.18: Sample saturation path for dynamic displacement experiments in an artificial oil-wet porous medium.

A sample saturation path for this system is shown in Fig. 4.18. The following procedure was used to conduct the displacement processes:

1. We first saturated the core with the H<sub>2</sub>O-rich phase (W, “oil”) by injecting this phase from the bottom of the core. We then determined the porosity and absolute permeability of the porous medium in a similar manner as the water-wet system.
2. Then we injected the C<sub>16</sub>-rich phase (NW, “water”) into the porous medium from the top of the core until we reached a residual oil saturation, at which time no additional H<sub>2</sub>O-rich phase (NW, “water”) was collected from the core outlet. In the same manner as the water-wet system, we determined the effective phase permeability at this stage.
3. Simultaneous injection of both the C<sub>16</sub>-rich (W, “oil”) and H<sub>2</sub>O-rich (NW, “water”) phases using the same flow rate was then conducted until equal amounts of both fluids were collected at the core outlet. This procedure allows set up of the initial condition (50/50 wetting and intermediate wetting phase) of the porous medium before the injection of the NBA-rich phase (IW, “gas”).
4. We then introduced the NBA-rich phase (IW, “gas”) into the uniformly saturated oil wet medium from the top of the core and conducted a dynamic displacement experiment for measuring relative permeabilities.

5. Effluents were collected from the core outlet while differential pressure across the core as a function of pore volumes injected (PVI) was measured, to aid in the computation of the three phase relative permeabilities using the Welge/JBN method.
6. The glass bead core was then flooded with about 3 PVI's of IPA and air-dried for 24 hours in preparation for another experimental run.

Steps 1-6 were repeated with two other mixtures with lower IFTs.

#### 4.1.5 Experimental results

##### 4.1.5.1 Analogue water-wet porous medium (PTFE powder pack)

Displacement experiments were performed with different IFT pairs. All data are summarized in Table 4-12. After primary drainage of the C<sub>16</sub>-rich phase (W, “water”) by the NBA-rich phase (IW, “oil”) up to a residual phase saturation, we found that the residual C<sub>16</sub>-rich phase (W, “water”) saturation was very high (61.5%), although we applied a relatively high injection flow rate of 10 cm<sup>3</sup>/min. The porosity and absolute permeability of porous PTFE packs were also very high. We speculate that this high irreducible value of C<sub>16</sub>-rich phase (W, “water”) might have resulted from the plastic behavior of PTFE powder and the packing procedure of the core at ambient conditions. Morrow and McCaffery (1978) presented two-phase displacements in uniformly wetted teflon porous media. They prepared the teflon cores by compressing the powder in a metal pipe and then sintering at about 370°C. Having varied the sintering procedure, they obtained solidified cores having a porosity range of 0.24-0.47 and a permeability range of 0.02-2.9 D. The procedure used here to pack and compress the PTFE particles gave reproducible porosities, permeabilities, and residual C<sub>16</sub>-rich phase.

The initial condition in the table represents the NBA-rich (IW, “oil”) and the C<sub>16</sub>-rich (W, “water”) phase saturations after they were simultaneously injected with about the same rate. The procedure was documented before. They also represent the initial saturation distribution in the core before the gas injection.

Table 4-12: Data for the displacement experiments in water-wet system ( $q_t = 1.5 \text{ cm}^3/\text{min}$ )

Fluids	IFT NBA-rich/ H <sub>2</sub> O-rich mN/m	Initial Condition		Capillary Number x10 <sup>-5</sup>		NBA-rich “Oil” Recovery %
		S <sub>NBA-rich</sub>	S <sub>C16-rich</sub>	C <sub>16</sub> -rich/ H <sub>2</sub> O- rich	NBA- rich/ H <sub>2</sub> O- rich	
Mix 1	2.297	0.208	0.792	4	4	52.2
Mix 4	0.308	0.190	0.810	7	41	67.9
Mix 6	0.028	0.191	0.809	14	745	71.1

Fig. 4.19 and Fig. 4.20 show the recoveries of the C<sub>16</sub>-rich (W, “water”) and NBA-rich (IW, “oil”) phases and the overall pressure drop across the core, respectively, recorded during each dynamic displacement of a mixture of C<sub>16</sub>-rich (W, “water”) and NBA-rich (IW, “oil”) phases by H<sub>2</sub>O-rich (NW, “gas”) phase. The IFT values on the figure represent those of the NBA-rich (IW, “oil”)/H<sub>2</sub>O-rich (NW, “gas”) pair. Before the analysis, all data after breakthrough were smoothed by fitting the data to an easily differentiable function. By applying the Welge tangent construction method to the smoothed data, we obtained a saturation path for the downstream end of the core. The saturation paths for each experiment are shown in Fig. 4.21. The symbols marked on the C<sub>16</sub>-rich/NBA-rich side of the ternary diagram represent the initial saturations in the reservoir before the H<sub>2</sub>O-rich (NW, “gas”) phase injection. Saturation and permeability data were not obtained for phase saturation values lower than the saturation at the front. This saturation shock (so-called Buckley-Leverett shock) causes the outflow saturation to jump over lower part of the saturation trajectory. After breakthrough, drainage of the C<sub>16</sub>-rich (W, “water”) and NBA-rich (IW, “oil”) phases occurs and the saturation of the H<sub>2</sub>O-rich (NW, “gas”) phase increases.

The capillary number is often used to generalize the effect of capillary forces on trapping of oil within the pores of the reservoir rock during immiscible displacements. One version of the capillary number is defined as the ratio of viscous to capillary forces:

$$N_{vc} = \frac{v\mu_D}{\sigma \cos \theta}, \quad (4.4)$$

where  $v$  and  $\mu_D$  are the velocity and viscosity, respectively, of the displacing fluid, and  $\sigma$  and  $\theta$  are the IFT and contact angle, between the displacing and displaced fluids. The capillary number is inversely proportional to the IFT, by definition. The values of  $N_{vc}$  for the experiments are given in Table 4-12. As expected, the  $N_{vc}$  for the displacement of the NBA-rich (IW, “oil”) by the H<sub>2</sub>O-rich (NW, “gas”) increases as the IFT between them decreases, and hence the NBA-rich (IW, “oil”) recovery improves (see Fig. 4.22). The change in the  $N_{vc}$  for the H<sub>2</sub>O-rich (NW, “gas”)/C<sub>16</sub>-rich (W, “water”) pair is relatively small. The range of  $N_{vc}$  (from  $10^{-5}$  to  $10^{-2}$ ) for the displacements presented here represents a transition in the capillary desaturation of non-wetting phase from the capillary-viscous equilibrium to the only viscous-dominated flow (Lake, 1989). At values of  $N_{vc} < 10^{-5}$ , it is assumed that capillary forces strongly dominate in the flow of non-wetting phases.

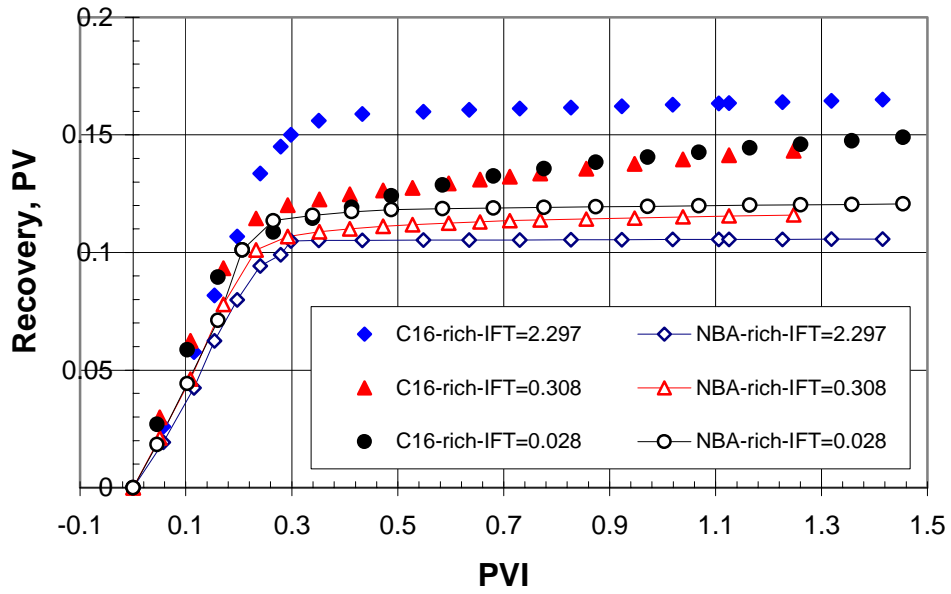


Fig. 4.19: Pore volume effluents as a function of pore volumes injected. (The IFT values in the legend box represent those between the NBA-rich “oil” and H<sub>2</sub>O-rich “gas” phases).

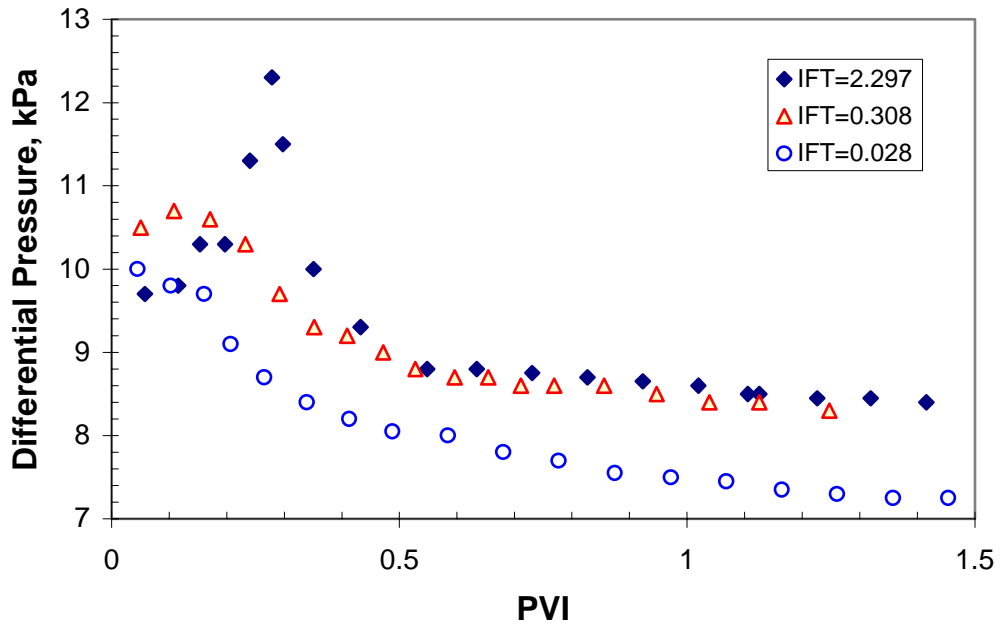


Fig. 4.20: Pressure drops as a function of pore volumes injected. (The IFT values in the legend box represent those between the NBA-rich “oil” and H<sub>2</sub>O-rich “gas” phases).

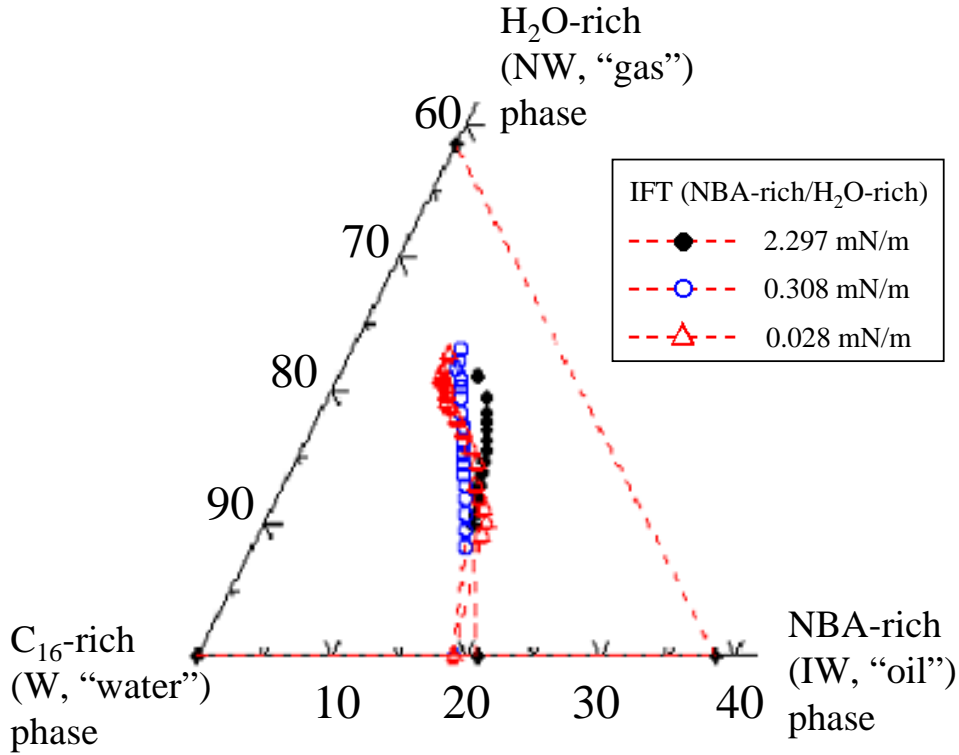


Fig. 4.21: Saturation paths for the displacement experiments.

Rapoport and Leas (1953) derived scaling coefficients to indicate when capillary pressure effects will be important:

$$N_{RL} = \left( \frac{\phi}{k} \right)^{0.5} \frac{lv\mu_D}{\sigma \cos \theta}, \quad (4.5)$$

where  $l$  and  $\phi$  are the length and porosity of the core, respectively. They primarily focussed on the product  $lv\mu_D$ , because of the experimental difficulties in the measurement of interfacial tensions and contact angles. They verified the theory with experimental results and concluded that, above a limiting value of  $lv\mu_D$ , the flooding behavior becomes independent of core length, flow rate, viscosity of injected fluid and capillary end effects. Later Lake (1989) combined Eqs. (4.4) and (4.5) to obtain:

$$N_{RL} = \left( \frac{\phi}{k} \right)^{0.5} N_{vc} l, \quad (4.6)$$

They suggested that there is a critical value of about 3, above which the capillary pressure will not affect 1D displacements. The  $N_{RL}$  values for our experiments (2.3 for the experiments with the highest IFT and higher for the other experiments) indicate that capillary end effects were not significant in the displacement experiments performed.

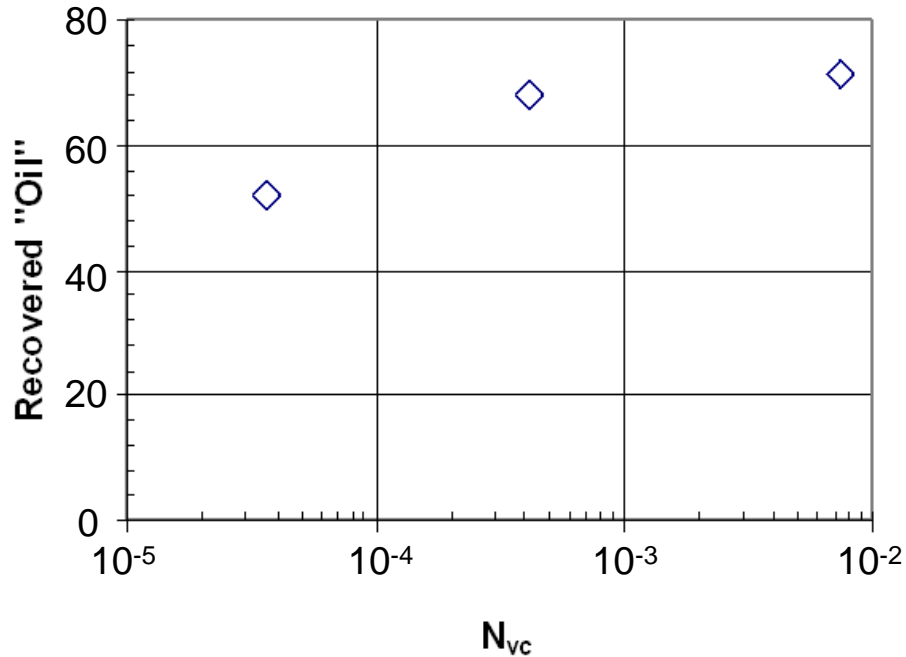


Fig. 4.22: The NBA-rich “oil” recovery versus capillary number.

#### Relative Permeabilities

Using the combined Welge/JBN technique, we derived the relative permeabilities using the smoothed pressure data and Eq. (4.2) for each phase employed in the experiments. The fractional flows for each phase were determined from the slopes of the recovery curves. The relative permeabilities to the  $C_{16}$ -rich (W, “water”), NBA-rich (IW, “oil”), and  $H_2O$ -rich (NW, “gas”) phases are shown in Fig. 4.23, Fig. 4.24, and Fig. 4.26, respectively.

Fig. 4.23 shows a modest change in the relative permeability to the  $C_{16}$ -rich phase (W, “water”) as IFT is varied. Many other investigators have shown that the wetting-phase relative permeability ( $k_{rw}$ ) is a function of its own saturation and is independent of the initial saturation distribution (Delshad *et al.*, 1987, Dria *et al.*, 1993). Sahni *et al.* (1998) found from their large experimental data set that  $k_{rw}$  is a function of  $S_w^a$ , with  $a \sim 5$ . Our data, however, correlate best to a third order polynomial, but with trends similar to those reported by Sahni *et al.* In related work, Sahni *et al.* (1996) obtained good agreement between a fifth order polynomial and three-phase relative permeability data published by Grader and O’Meara (1988).

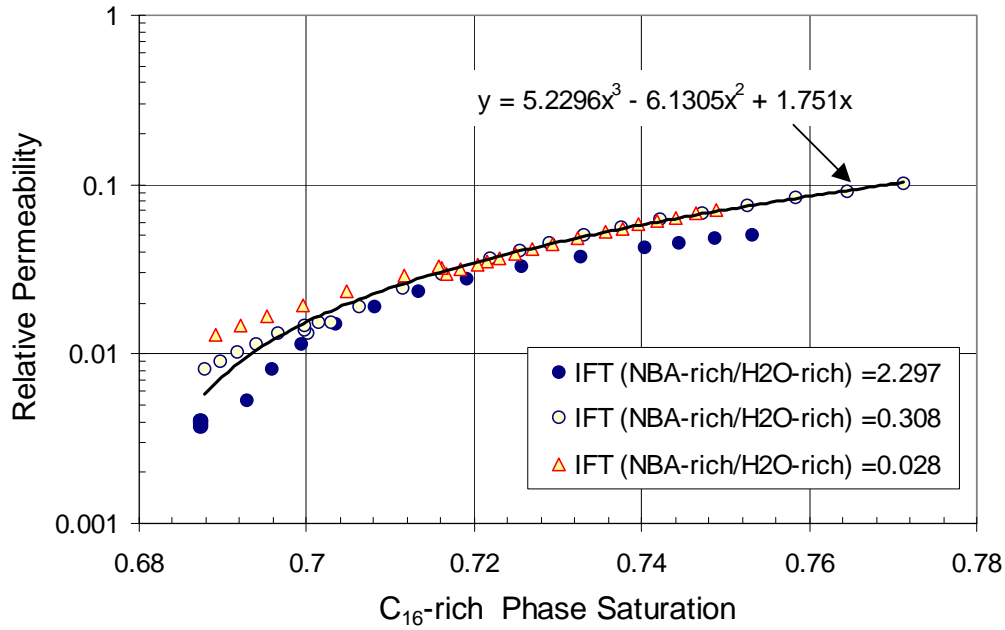


Fig. 4.23: Relative permeability of the  $C_{16}$ -rich (W, “water”) phase as a function of its own saturation.

The relative permeability to the NBA-rich (IW, “oil”) phase shown in Fig. 4.24 is clearly dependent on the IFT variations. The data at high phase saturations are fit well by a function of the form,  $k_{ro} \sim S_o^2$ , which is represented by the dashed line on the figure. Many researchers have obtained similar expressions for oil relative permeability and many of them also concluded that the oil relative permeability was a function of its own saturation only and independent of initial condition (Blunt, 2000). Our data actually deviate from the quadratic correlation at the low end of the saturation range. We fitted the data best with a third order polynomial. At lower saturations the data converge to a constant oil saturation, presumably trapped oil in some pores. The existence of this so-called residual oil might be due to non-spreading conditions or to the nature of porous medium. It has been established that three-phase flow in a porous medium is affected by spreading coefficient, which is defined by

$$C_s = \sigma_{gw} - (\sigma_{ow} + \sigma_{go}) \quad (4.7)$$

Fig. 4.25 shows a pore scale configuration of analog liquid system on a flat teflon surface. As it can be seen from the figure, a positive spreading coefficient indicates that spreading of NBA-rich (IW, “oil”) phase will occur between  $C_{16}$ -rich (W, “water”) and  $H_2O$ -rich (NW, “gas”) phases. The spreading coefficients for our experiments are determined to be -0.071, 0.362, 0.011 mN/m for the IFT values of 2.297, 0.308, and 0.028 mN/m, respectively. According to these values, in the experiment with the highest IFT of “oil”/“gas” pair, the “oil” is expected to be trapped between the “gas” and “water” phases whereas, in other

experiments, it is supposed to flow between other two phases as layer drainage. However, the values here are not conclusive because they are around zero within some experimental error. Moreover, Adamson (1990) stated that, when the fluids are in equilibrium, a positive spreading coefficient can not occur. But, in relatively rapid displacement experiments like ours, it is very difficult to see the effects of layer drainage of “oil” due to the positive spreading coefficients. Gravity drainage experiments of longer duration will be required to establish whether layer drainage does occur in these systems.

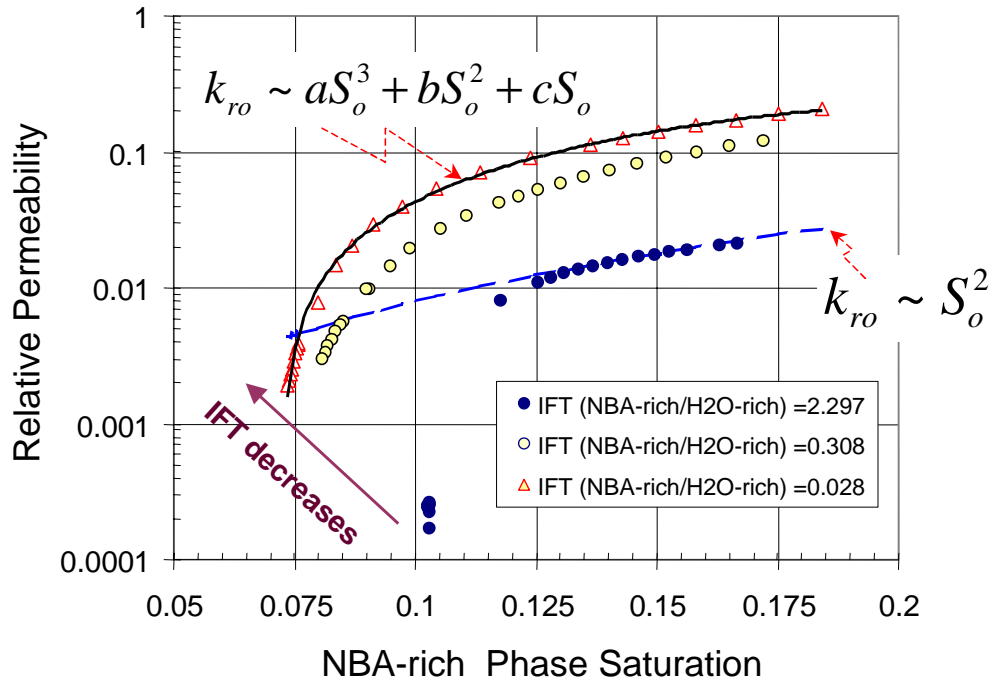


Fig. 4.24: Relative permeability of NBA-rich (IW, “oil”) phase as a function of its own saturation.

The gas relative permeabilities shown in Fig. 4.26 are also sensitive to IFT variations, as expected due to the fact that the composition and physical properties of the H<sub>2</sub>O-rich phase (NW, “gas”) change with IFT variation. The experimental data for H<sub>2</sub>O-rich phase (NW, “gas”) relative permeabilities show similar trends to those observed for NBA-rich phase (IW, “oil”) relative permeabilities. The data obtained were fit with reasonable accuracy by a third order polynomial.

Fig. 4.27 and Fig. 4.28 show the changes in the NBA-rich (IW, “oil”) and H<sub>2</sub>O-rich (NW, “gas”) relative permeabilities as a function of IFT at determined saturation values. Quantitatively, we observed about a 10-fold increase in the relative permeabilities against a 100-fold decrease in the IFT.

The experiments performed so far demonstrate that there is a significant effect of IFT on the flow of the nonwetting phases in the presence of a third wetting phase. Additional

experiments with lower IFTs around the critical tie line and with different initial conditions will be required to investigate effects of near-critical flow in the presence of a third phase.

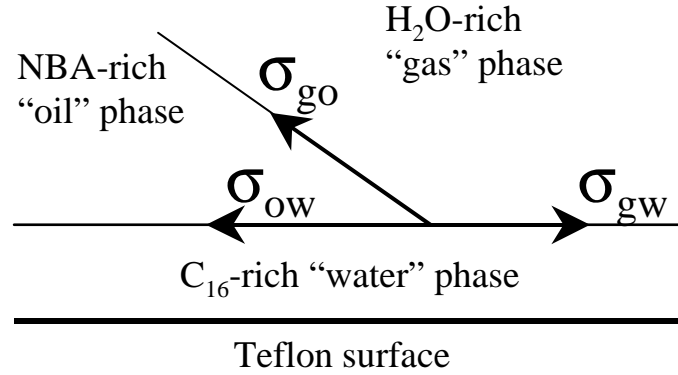


Fig. 4.25: Configuration of analog liquids on teflon surface.

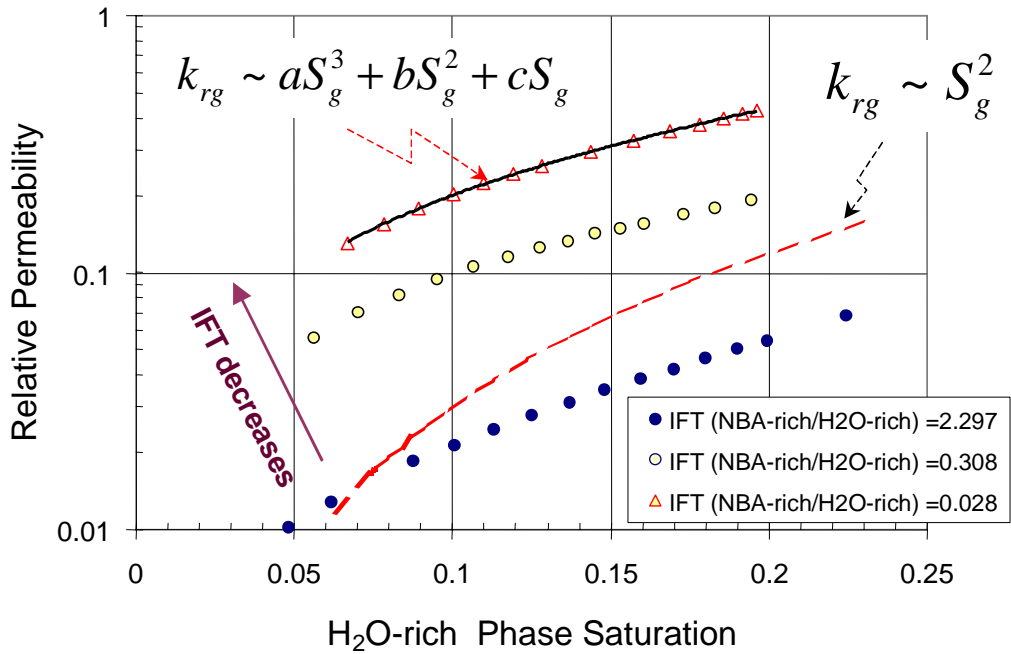


Fig. 4.26: Relative permeability of H<sub>2</sub>O-rich (NW, “gas”) phase as a function of its own saturation.

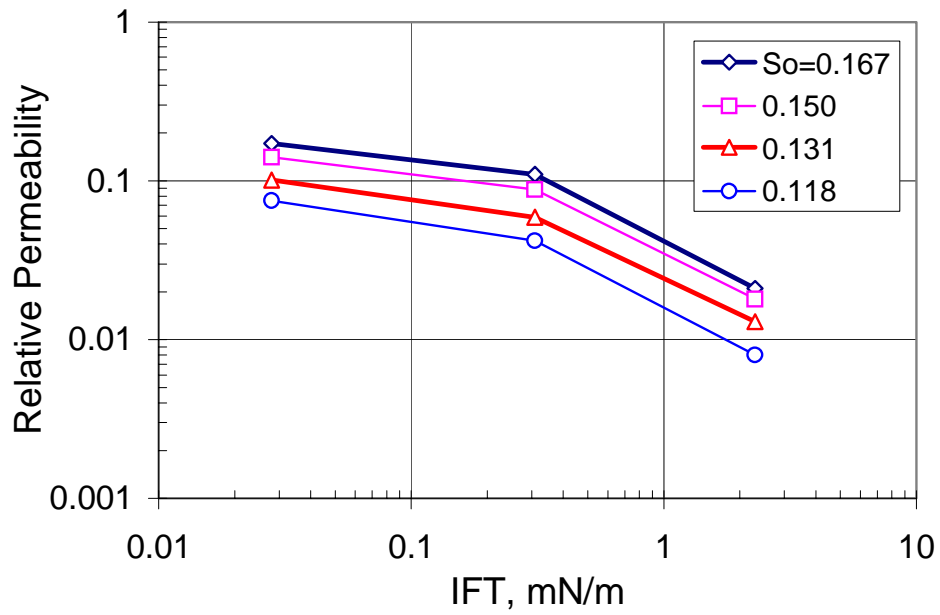


Fig. 4.27: Relative permeability of NBA-rich (IW, “oil”) phase as a function of IFT.

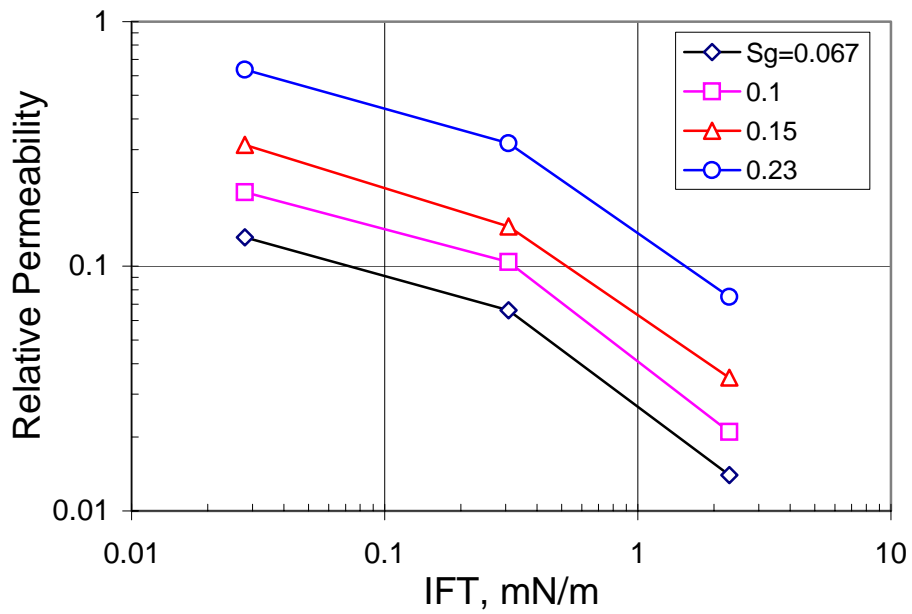


Fig. 4.28: Relative permeability of H<sub>2</sub>O-rich (NW, “gas”) phase as a function of IFT.

#### 4.1.5.2 Artificial oil-wet porous medium (glass bead packs)

Using the same set of fluid mixtures as the water-wet system (refer to Table 4-12) and applying the procedures described previously, three sets of experiments with different fluid systems having different set of IFT data were also conducted for an artificial oil-wet porous medium that was glass bead pack. The physical properties of the core are given in Table 4-11. A summary of the experiments is presented in Table 4-13. The Rapoport-Leas numbers ( $>15$ ) for the experiments indicate that capillary effects on the displacements were negligible. The dimensionless capillary numbers for the displacement of the H<sub>2</sub>O-rich (W, “oil”) phase by the NBA-rich (IW, “gas”) phase increase dramatically as the IFT between them decreases. The capillary numbers for the displacement of the C<sub>16</sub>-rich (NW, “water”) by the NBA-rich (IW, “gas”), however, decrease slightly because of the small increase in the IFT between them (see Table 4-7).

Table 4-13: Data for the displacement experiments in oil-wet system ( $q_t = 5.2 \text{ cm}^3/\text{min}$ ).

IFT H <sub>2</sub> O-rich/ NBA- rich mN/m	Initial Condition		Capillary Number $\times 10^{-5}$		Density Difference g/cm <sup>3</sup>		H <sub>2</sub> O-rich “Oil” Recover y %
	S <sub>H<sub>2</sub>O- rich</sub>	S <sub>C<sub>16</sub>- rich</sub>	C <sub>16</sub> -rich/ NBA- rich	NBA- rich/ H <sub>2</sub> O-rich	C <sub>16</sub> -rich/ NBA- rich	NBA- rich/ H <sub>2</sub> O-rich	
2.297	0.552	0.448	275	95	0.048	0.163	51
0.308	0.552	0.448	65	767	0.086	0.111	63
0.028	0.552	0.448	52	9772	0.130	0.043	72

Note that the analogy for the fluids used experiments, constructed upon the phase behavior and IFT variation of the analog and reservoir fluid systems, does not represent other properties like density and viscosity of the phases. For example, the lightest C<sub>16</sub>-rich phase represents the “water” phase, which is mostly the heaviest one in an oil reservoir. The heaviest H<sub>2</sub>O-rich phase in the analog system represents “oil” that is intermediate phase in the reservoir whereas the lightest reservoir “gas” is represented by the intermediate the NBA-rich analog phase (see Fig. 4.29). And, the analogy does not include the wettability of the system either. Because the intermediate wetting analog phase (NBA-rich) in the glass bead pack represents the “gas” phase which is supposed to be the most non-wetting in the reservoir. However, DiCarlo *et al.* (2000) pointed that the wettability of the gas phase could be in the same degree of water wettability in oil-wet reservoir porous media.

We injected the NBA-rich (IW, “gas”) phase from the top of the core to have a gravity stable displacement of the H<sub>2</sub>O-rich (W, “oil”) phase. However, in this case, there was gravity instability between the injected NBA-rich (IW, “gas”) phase and the displaced C<sub>16</sub>-rich (NW, “water”) phase. Density differences between the displacing NBA-rich phase and displaced phases presented in Table 4-13 indicate that, as the IFT is lowered, the gravity instability can be important because of the increases in density difference between the NBA-rich and C<sub>16</sub>-rich phases.

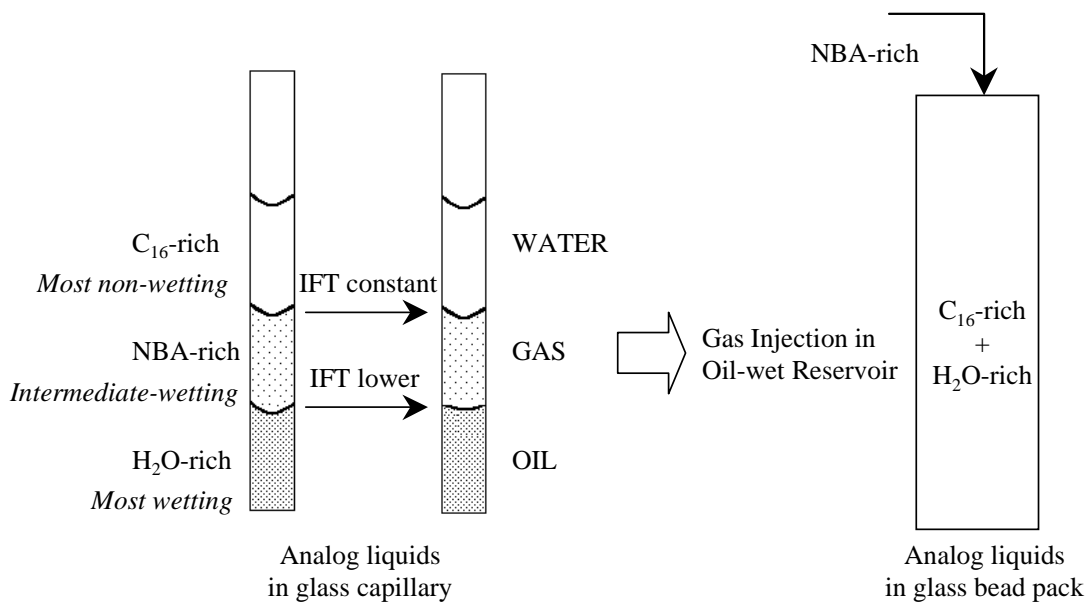


Fig. 4.29: Schematic illustration of using analog liquid system in the experiments.

Fig. 4.30 shows the recoveries of the C<sub>16</sub>-rich (NW, “water”) and the H<sub>2</sub>O-rich (W, “oil”) phases as they were displaced by the NBA-rich (IW, “gas”) phase. Fig. 4.31 shows the recorded pressure drop along the core through each dynamic displacement experiment.

As the recovery plots show, breakthrough occurs at about 0.5 PVI of the injected “gas” phase for each displacement. All experiments were conducted at the same flow rate, so the effect of IFT variation is apparent in the behavior of the recovery slopes after breakthrough and in the differential pressures measured through each experiment. Lower IFT between the H<sub>2</sub>O-rich (W, “oil”) and NBA-rich (IW, “gas”) phases evidently caused less interference of each phase with the flow of other, allowing the injected NBA-rich (IW, “gas”) phase to pass more freely and causing smaller pressure drops across the core, as shown in Fig. 4.31. The effect of IFT variation on the breakthrough time is negligible.

As the IFT between the H<sub>2</sub>O-rich (W, “oil”) and NBA-rich (IW, “gas”) phases is lowered, the production of the C<sub>16</sub>-rich (NW, “water”) phase is decreased, as Fig. 4.30 shows. The behavior observed in the C<sub>16</sub>-rich (NW, “water”) phase may be explained by various reasons. First, as the IFT of NBA-rich (IW, “gas”)/H<sub>2</sub>O-rich (W, “oil”) pair is lowered, the H<sub>2</sub>O-rich (W, “oil”) phase is displaced more easily with the NBA-rich (IW, “gas”), causing the C<sub>16</sub>-rich (NW, “water”) to be bypassed by both the H<sub>2</sub>O-rich (W, “oil”) and NBA-rich (IW, “gas”) phases. The IFT between the C<sub>16</sub>-rich (NW, “water”) and the NBA-rich (IW, “gas”) increases as the IFT between H<sub>2</sub>O-rich (W, “oil”) and NBA-rich (IW, “gas”) phases decreases (see the capillary numbers in Table 4-13), increasing the capillary forces that further resist the ability of C<sub>16</sub>-rich (NW, “water”) to be displaced. The bypassed C<sub>16</sub>-rich (NW, “water”) in the large pores is then surrounded by other phases and stays

immobile unless very high pressure gradients are applied. Note that the measured pressure drop across the core shown in Fig. 4.31 decreases as IFT is lowered.

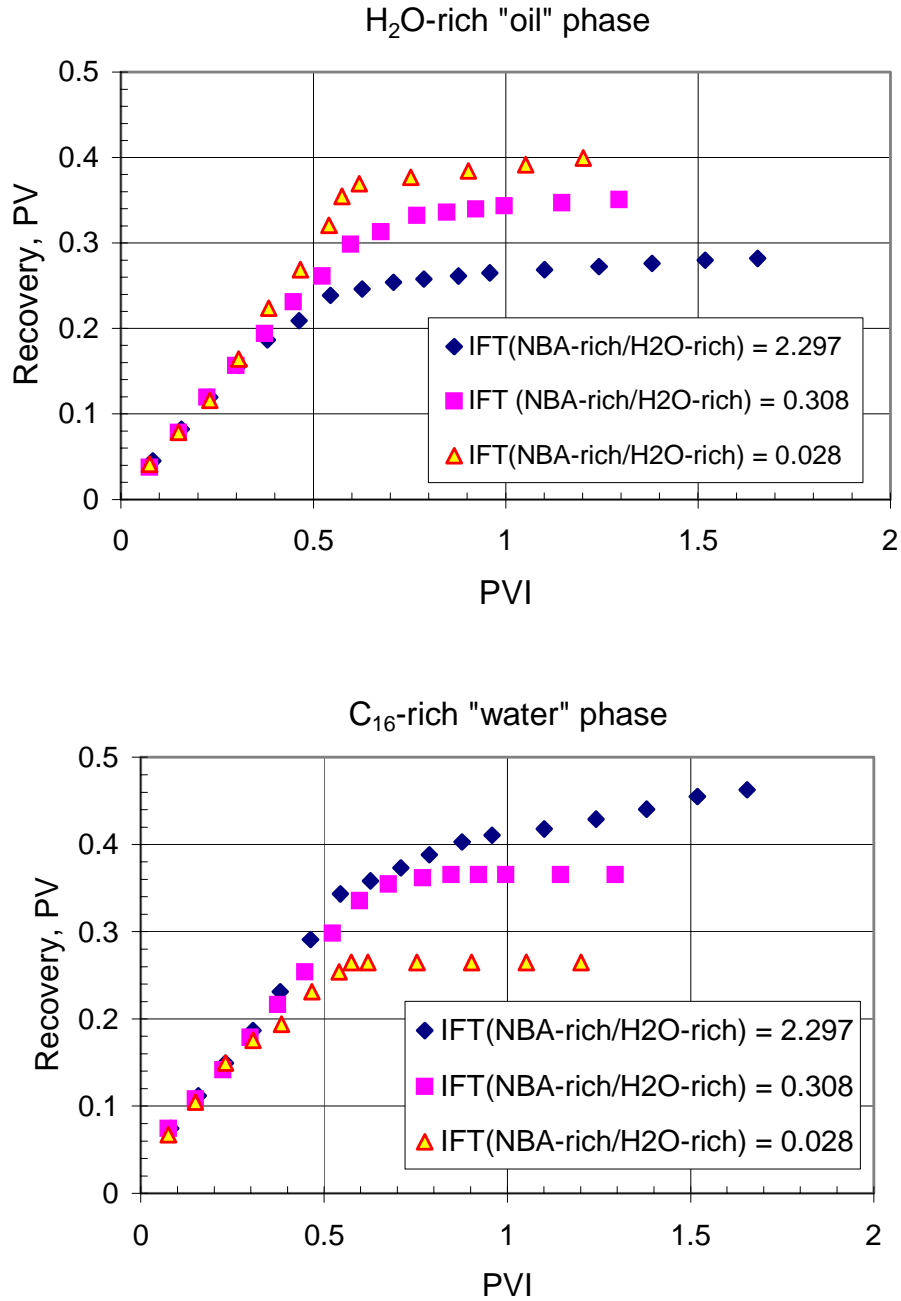


Fig. 4.30: Recovery plots for displaced phases.

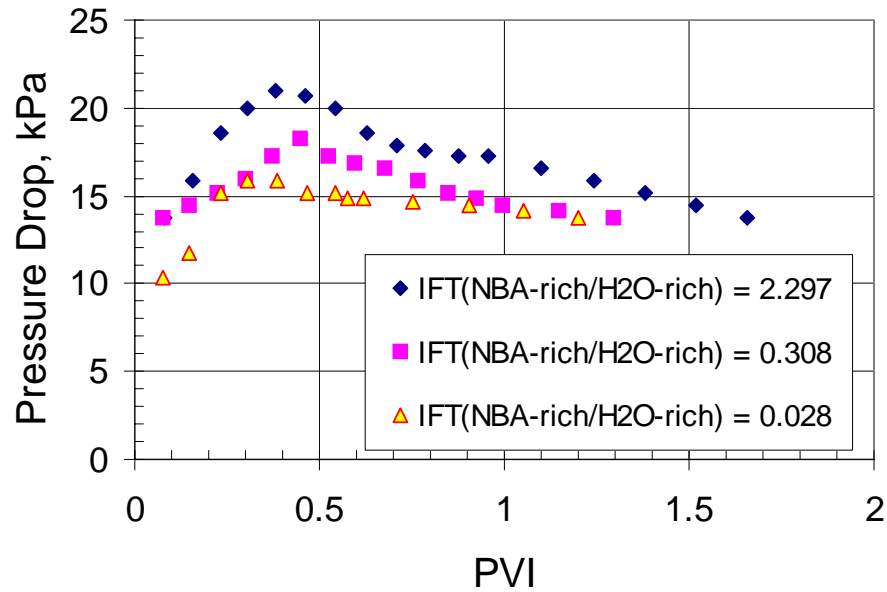


Fig. 4.31: Differential pressure across the core.

In general, as the degree of rock preferential wettability for any phase decreases, the relative permeability to that phase increases whereas relative permeabilities to other phases decrease (Honarpour *et al.*, 1986). The  $C_{16}$ -rich phase is the most non-wetting phase in the glass bead system and occupies center of the large pores, sometimes as discontinuous droplets. By lowering the IFT between the NBA-rich (IW, “gas”) and the  $H_2O$ -rich (W, “oil”), we also change the rock preferential wettability for both phases. This leads to a consequence that the NBA-rich phase displaces more  $H_2O$ -rich phase bounded along the walls of the pore, but traps more  $C_{16}$ -rich “water” in the center of the large pores.

Another possible explanation for the trapping behavior of the most nonwetting phase is the gravity instability between the  $C_{16}$ -rich (NW, “water”) and NBA-rich (IW, “gas”) phases, caused by the inconsistent densities of these phases with respect to the physical values that would be expected in a “gas”/“oil” system (see density differences in Table 4-13). Recall that for this artificially oil-wet system, “water” is now represented by the lightest  $C_{16}$ -rich phase. As can be seen from the data in Table 4-7, with increasing IPA content of the mixtures, the density difference between the  $C_{16}$ -rich and NBA-rich phases increases. Upon the injection of the NBA-rich “gas” phase from the top of the core, this phase remained in gravity equilibrium with the  $H_2O$ -rich “oil” phase, but not with the lightest  $C_{16}$ -rich “water” phase. It is possible that gravity instability caused the injected phase to finger through the  $C_{16}$ -rich “water” phase, reducing the amount recovered.

## Relative Permeabilities

All data after breakthrough were smoothed to obtain a differentiable function for use in the application of Welge tangent construction method to calculate the saturation path at the downstream end of the core. The method described by Grader and O’Meara (1988), which extends the JBN method to calculating relative permeabilities for three-phase flow, was used to compute the relative permeabilities for the oil-wet system from the smoothed pressure and recovery data. Fig. 4.32, Fig. 4.33, and Fig. 4.34 show the resulting relative permeabilities for the C<sub>16</sub>-rich (NW, “water”), NBA-rich (IW, “gas”), and H<sub>2</sub>O-rich (W, “oil”) phases, respectively.

The reduction in recovery of the C<sub>16</sub>-rich (NW, “water”) phase is manifested in Fig. 4.32 where the relative permeability values for this phase drop sharply as the IFT of the “gas”/“oil” pair is decreased. Note that the IFT between displaced C<sub>16</sub>-rich (NW, “water”) and injected NBA-rich “gas” stays almost constant. “Water” in this case is bypassed by the “oil”, which is moving with the injected “gas” phase at a lower resistance. At higher saturations, there is almost no discernible effect of IFT variations on the relative permeability of water. The apparent reduction in relative permeability becomes significant only at lower saturations.

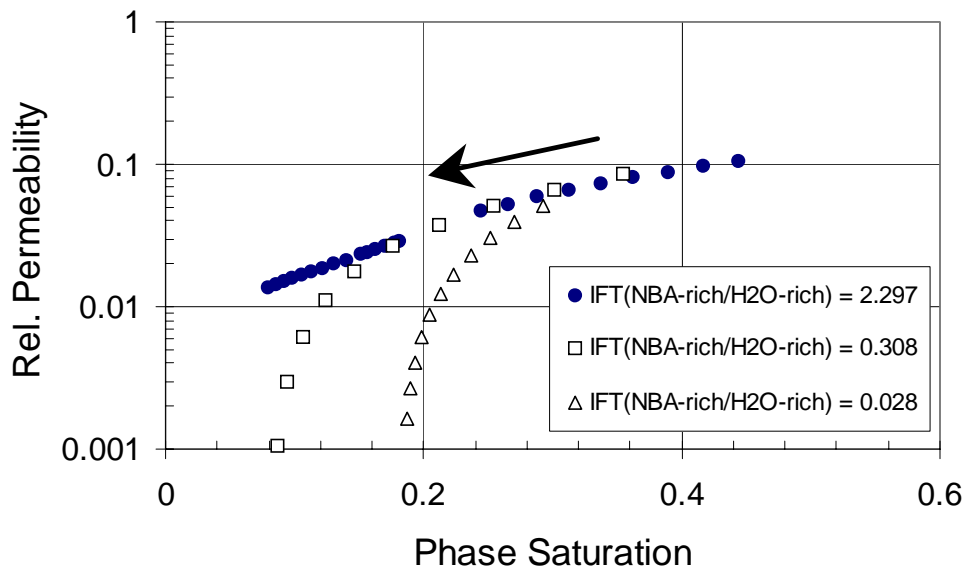


Fig. 4.32: The C<sub>16</sub>-rich “water” relative permeability as a function of its own saturation.

The H<sub>2</sub>O-rich “oil” recovery plots in Fig. 4.30 do not manifest any change in its recovery slopes despite lowering the IFT between the H<sub>2</sub>O-rich (W, “oil”) and NBA-rich (IW, “gas”) phases. However, they reflect a higher cumulative H<sub>2</sub>O-rich “oil” recovery despite the same flow rate albeit at a lower IFT. This behavior results in higher relative permeability curves of the H<sub>2</sub>O-rich “oil” phase, as can be seen in Fig. 4.33. The NBA-rich “gas” phase on the other

hand reveals a small effect of IFT variation on relative permeability. This can be explained by increasing the degree of rock preferential wettability for that phase, which makes its relative mobility lower, and trapping the most non-wetting  $C_{16}$ -rich phase, which occupies much volume that restricts the flow of the NBA-rich “gas” phase.

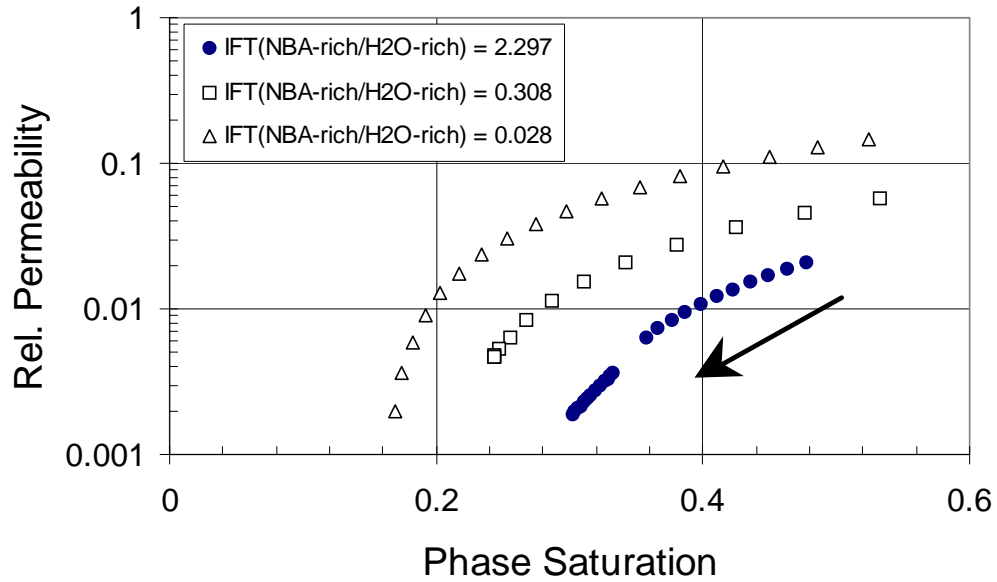


Fig. 4.33: The H<sub>2</sub>O-rich “oil” relative permeability as a function of its own saturation.

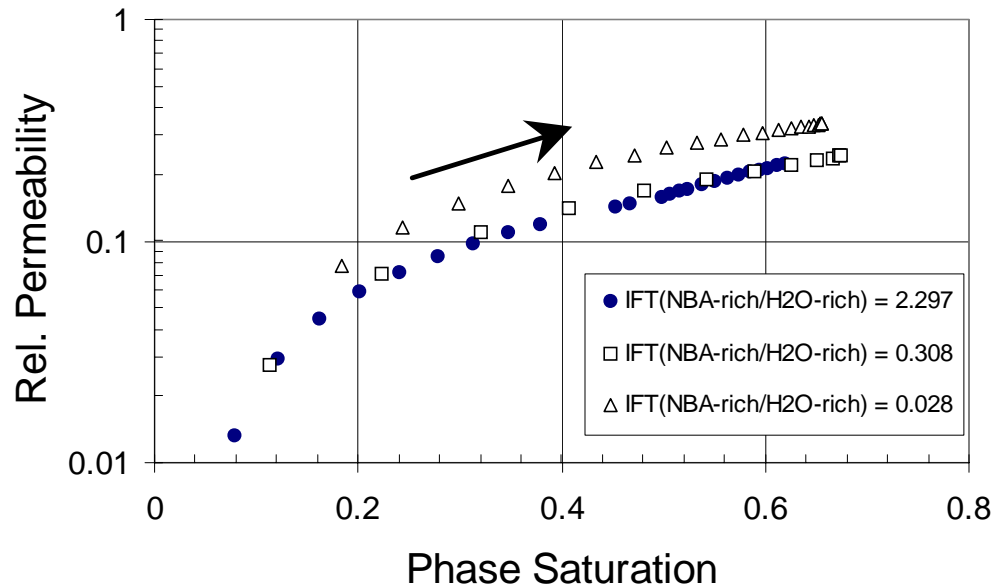


Fig. 4.34: The NBA-rich “gas” relative permeability as a function of its own saturation.

#### 4.1.6 Discussion

Fig. 4.35 and Fig. 4.36 show summaries of all relative permeability data obtained from displacements in oil-wet and water-wet porous systems. In Fig. 4.35, we observe that except for the observed reduction in “water” relative permeability and a slight increase in the “gas” phases, IFT variation has minimal effect on both the C<sub>16</sub>-rich (NW, “water”) and the NBA-rich (IW, “gas”) phases. The effect of IFT variation is very distinct in the H<sub>2</sub>O-rich (W, “oil”) phase for an artificially oil-wet porous medium. A two-order of magnitude reduction in IFT of the “oil”/“gas” pair results in about a one-order of magnitude increase in the “oil” relative permeability, which is similar to that observed for “oil” relative permeability in a water-wet system as shown in Fig. 4.36. Although the trends of “oil” relative permeability in both wettabilities are found to be similar, the relative permeability in the water-wet system is slightly higher than that of an oil-wet system. The residual oil saturation in both wettability systems is decreased with lowering the IFT between “oil and “gas” phases.

In the analogue oil-wet system (glass bead), where the C<sub>16</sub>-rich phase was the most non-wetting fluid, very little effect of IFT variations on the C<sub>16</sub>-rich “water” relative permeability was observed at higher saturations. However, at lower phase saturations, the C<sub>16</sub>-rich “water” phase showed sharp declines that may have been due gravity instability between the injected NBA-rich “gas” phase and displaced C<sub>16</sub>-rich “water”.

In the analogue water-wet system (teflon beads), the effect of lower IFT resulted in identical changes in relative permeability for both non-wetting NBA-rich “oil” and H<sub>2</sub>O-rich “gas” phases. For the oil-wet system, however, we observed that the effect of variations in IFT is smaller for the NBA-rich (IW, “gas”) phase, especially at higher saturations. It is also interesting to note that reduction of C<sub>16</sub>-rich (NW, “water”) phase due to the IFT variation and/or gravity instability resulted in keeping the injected NBA-rich “gas” phase relative permeability roughly constant.

For the NBA-rich phase, which was the intermediate wetting phase in both analogue water-wet and oil-wet systems, the relative permeability curves exhibited a more abrupt drop at lower saturations even though they represented different fluids for the two different wetting systems.

For the H<sub>2</sub>O-rich phase, a distinct effect on the relative permeability is observed in both the oil-wet and water-wet systems. In the water-wet system where this phase represented “gas”, the relative permeability curves manifested a more steady decrease at lower saturation whereas the oil-wet system, where this fluid now represents “oil”, showed a more abrupt drop in the relative permeability at lower saturations. But, it should be noted that, its saturation increased in the water-wet displacements, whereas it decreased in the oil-wet displacements. In both cases, we demonstrated higher relative permeabilities at lower IFT between “oil” and “gas” phases for the water-rich phase.

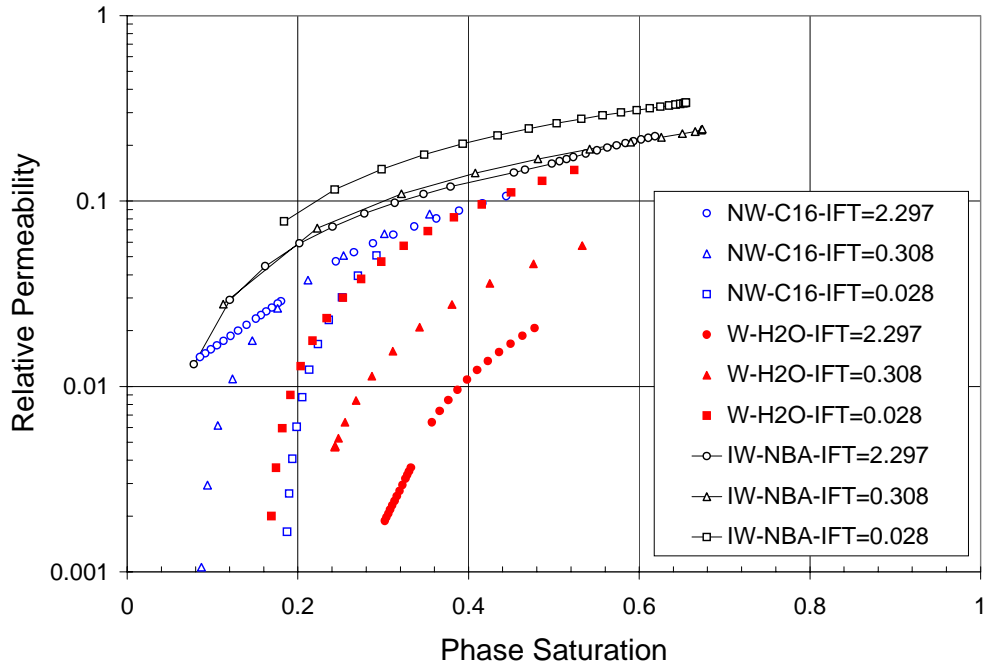


Fig. 4.35: Summary of relative permeabilities for artificial “oil”-wet system. ( $S_{or} = 0.1$ ). NW: Non-wetting, IW: Intermediate wetting, W: Wetting. The IFTs in the legend box represent those between the NBA-rich and H<sub>2</sub>O-rich phases.

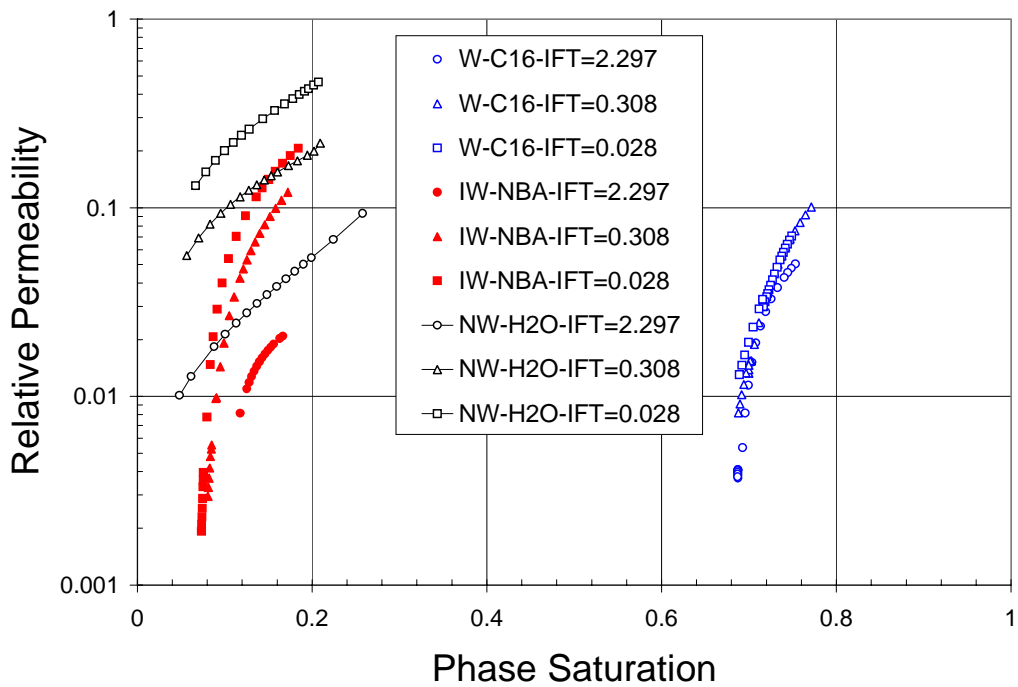


Fig. 4.36: Summary of relative permeability for artificial “water”-wet system ( $S_{wr} = 0.615$ ).

Reviewing the relative permeability data for both the water-wet and oil-wet systems, we find that there are some similarities in the behavior of relative permeability curves in both wetting systems, if we track the changes in the order of increasing fluid density. Regardless of the wetting fluid or the wetting system, a more distinct effect on the relative permeability is observed in the densest fluid, i.e., H<sub>2</sub>O-rich phase, which suggests that vertical displacements were influenced by the density differences between the fluids in our analog system. Comparison of the results of vertical displacements with those of horizontal displacements for the same fluid system might be able to delineate the extent of the influence of these density differences.

#### 4.1.7 Summary

Use of the analog liquids instead of real reservoir fluids requires the use of appropriate porous medium because of system wettability. Teflon bead packs were employed in the displacement experiments to simulate a water-wet porous medium with the analog liquids whereas glass bead packs were employed to mimic an oil-wet reservoir. Three dynamic displacement experiments with IFTs of 0.028, 0.308, and 2.297 *mN/m* of NBA-rich phase - H<sub>2</sub>O-rich phase pairs were performed. The relevant three-phase relative permeabilities were obtained from the recovery and pressure drop data by applying the Welge/JBN method.

In the water-wet porous system (teflon beads), the wetting phase (C<sub>16</sub>-rich) relative permeability was not much affected by the IFT variation whereas the relative permeabilities to both non-wetting NBA-rich “oil” and H<sub>2</sub>O-rich “gas” phases were clearly affected. As IFT decreases the NBA-rich “oil” and H<sub>2</sub>O-rich “gas” phases become more mobile at the same phase saturations, with an increase in relative permeability of about an order of magnitude resulting from a two-order of magnitude reduction in IFT between the two non-wetting phases.

In the analog oil-wet system, where the C<sub>16</sub>-rich phase was the most non-wetting fluid, the H<sub>2</sub>O-rich “oil” phase relative permeability increased with one order of magnitude against about two-order of magnitude reduction in IFT of NBA-rich “gas”/ H<sub>2</sub>O-rich “oil” pair. The trends of “oil” relative permeability in both wettabilities were similar, however. The “oil” phase was more mobile in the water-wet system than in the oil-wet system. At higher phase saturations there was little change in the “water” relative permeability whereas, at its lower saturations, the “water” became trapped, possibly due to the variations in the IFT and a possibility of a gravity instability between the injected “gas” and displaced “water”. The “gas” relative permeability was roughly constant, compared to that for a gravity-stabilized gas injection in a water-wet porous system.

#### 4.1.8 Effect of IFT variation and wettability on three-phase relative permeability in Berea sandstone

Because of considerable experimental difficulties in the measurement of three-phase relative permeabilities, most of researchers have first employed experiments in unconsolidated porous materials, such as sand packs or bead packs. For example, almost all gravity drainage experiments, which have recently contributed much to understand physical mechanisms underlying three-phase displacements, have been done in unconsolidated sandpacks (Skauge *et al.*, 1994, Vizika and Lombard, 1996, Sahni *et al.*, 1998, DiCarlo *et al.*, 2000). However, it is also useful to consider consolidated porous media, in which capillary forces are greater than in unconsolidated sand packs. Higher capillary forces in relatively low-permeability consolidated rocks may change behavior of relative permeabilities to the corresponding phases. In this section, we report results of measurements of three-phase relative permeabilities in Berea sandstone.

A summary of the experimental work on three-phase relative permeability in consolidated porous materials is given in Table 4-14. This summary was obtained from three sources that reviewed available data (Honarpour *et al.*, 1986 for three-phase relative permeability data obtained in consolidated porous media until eighties and Blunt, 2000 and Pejic and Maini, 2003 for the experiments done later). As can be seen from the table, Berea sandstone has often been preferred because of its relative uniformity and general acceptability as an industry standard. Although consolidated cores with different wettabilities were considered, gravity drainage experiments that can investigate the effects of spreading behavior of three phases on the displacement behavior in consolidated media are still lacking. Such experiments have recently been attempted by some authors for unconsolidated porous media (DiCarlo *et al.*, 2000). They measured the three-phase relative permeabilities for water-wet and oil-wet unconsolidated sandpacks. They concluded that the gas relative permeability was lowered significantly when water was present in an oil-wet system. This was apparently due to the water competing for the large pore spaces, hindering the gas flow. The smaller gas relative permeability can lead to less preferential flow and less gravity override, enhancing the sweep of the gas injection. Important features such as the lowered gas relative permeability and the low residual saturations are unique to three-phase systems and are not included in current three-phase relative permeability models that just extrapolate two-phase relative permeabilities.

Almost all researchers used fluids that had high interfacial tensions (IFTs). Only Delshad *et al.* (1987) and Dria *et al.* (1993) attempted to measure low-IFT three-phase relative permeabilities. Delshad *et al.* presented experimental data for low-IFT three-phase relative permeabilities in Berea sandstone cores. The measurements were done at steady-state conditions with a constant capillary number of  $10^{-2}$ . They employed a brine/oil/surfactant/alcohol mixture that included a microemulsion and excess oil and brine. The IFTs of microemulsion/oil and microemulsion/brine were low, whereas the IFT between oil and brine was high. They concluded that low-IFT three-phase relative permeabilities are functions of their own saturations only. Dria *et al.* injected CO<sub>2</sub> gas, oil, and brine into a

carbonate core at high temperature (71 °C) and high pressure (9.65 MPa) so that phase behavior and flow would be similar to reservoir conditions. Results showed that significant differences existed between the three-phase gas/oil/brine relative permeabilities measured when the gas was high pressure CO<sub>2</sub> and those measured when the gas was low pressure N<sub>2</sub>. They reported that the IFT between the oil and CO<sub>2</sub> phases was about an order of magnitude lower than that for the low pressure N<sub>2</sub>/oil mixture.

Table 4-14: Summary of three-phase flow experiments in consolidated porous media.

Authors	Porous Material	Experimental Method
Caudle <i>et al.</i> (1951)	Consolidated sandstone	The Penn State method
Corey <i>et al.</i> (1956)	Berea Sandstone	Hassler's capillary pressure method
Sarem (1966)	Berea sandstone	Unstead-state method
Donaldson and Dean (1966)	Berea sandstone Arbuckle limestone	Unsteady-state method
Saraf and Fatt (1967)	Boise sandstone	Single core dynamic method
Schneider and Owens (1970)	Torpedo sandstone	Dynamic method
Van Spronsen (1982)	Tensleep sandstone Berea sandstone	Stead-state centrifuge method
Delshad <i>et al.</i> (1987)	Berea sandstone	Steady-state method
Oak (1990)	Berea sandstone, water-wet	Stead-state method
Oak (1991)	Berea sandstone, intermediate wet	Stead-state method
Dria <i>et al.</i> (1993)	Baker dolomite	Steady-state
Skauge and Larsen (1994)	Sandstones, water-wet, intermediate, and oil-wet	Unstead-state method
Eleri <i>et al.</i> (1995)	Berea and Clashach sandstones	Both stead-state and unsteady- state methods
Baker (1993)	Sandstones, water-wet, intermediate-wet, and oil- wet	Steady-state method
Akin and Demiral (1997)	Berea sandstone	Dynamic method
Sahni <i>et al.</i> (1998)	Berea sandstone	Gravity drainage

## 4.1.9 Experimental design

### 4.1.9.1 Porous medium

We employed a Berea sandstone core in the experiments. The core properties are presented in Table 4-15. We fired the core at about 800 °C to avoid interactions between the clay content of the core and water. For this core we determined a residual water saturation of about 22%.

Table 4-15: Core properties.

Length, <i>cm</i>	27.5
Diameter, <i>cm</i>	2.5
Pore volume, <i>cm</i> <sup>3</sup>	28
Porosity, %	20.7
Absolute Permeability, <i>D</i>	0.294

### 4.1.9.2 Fluids

We employed two analogue three-phase systems, in which the IFT between two of the phases could be varied systematically while holding the IFTs between the other pairs of phases roughly constant. The first system included fluid mixtures of C<sub>16</sub>, NBA, H<sub>2</sub>O, and IPA, in which only the IFT between the H<sub>2</sub>O-rich and NBA-rich phases varies. Using this system in a naturally water-wet Berea sandstone core with an analogy that the wetting H<sub>2</sub>O-rich analog phase represents the reservoir “oil”, the intermediate wetting NBA-rich phase mimics the injected “gas”, and the nonwetting C<sub>16</sub>-rich analog phase represents the “water” phase in reservoir, we measured three-phase relative permeabilities for an oil-wet porous medium. We obtained the second analog system by replacing the IPA in the mixtures by sodium chloride (NaCl), which gives a different phase behavior and shows IFT variations between the pair of C<sub>16</sub>-rich/NBA-rich phases. Employing this analog system with an analogy that the wetting H<sub>2</sub>O-rich, the intermediate wetting NBA-rich, and the nonwetting C<sub>16</sub>-rich phases represent the “water”, the “oil”, and the “gas” in a reservoir, respectively, and the same sandstone core in the displacement experiments, we derived water-wet three-phase relative permeabilities. The phase behavior and physical properties of these systems were presented in Section 4.1.2.

We used three different compositions from the C<sub>16</sub>/NBA/H<sub>2</sub>O/IPA system (Mixtures 1, 4, and 6 in Fig. 4.2 and Table 4-1). These compositions give the phases that have an IFT variation of one pair of three phases from 2.297 to 0.028 *mN/m*. Such a fluid system in a naturally water-wet Berea sandstone core should represent an “oil”-wet porous medium based on the IFT variation of the compositional system (see Table 4-9). For water-wet reservoir systems, we considered four different mixtures from the C<sub>16</sub>/NBA/H<sub>2</sub>O/NaCl

system (Mixtures 1, 1f, 3f, and 4f in Fig. 4.4 and Table 4-5). The IFT between the  $C_{16}$ -rich and NBA-rich phases varies from  $0.239 \text{ mN/m}$  to  $0.005 \text{ mN/m}$ .

#### 4.1.9.3 Experimental set-up

A schematic of the experimental design is shown in Fig. 4.37. The pre-equilibrated analog liquid phases were injected by means of positive displacement pumps at constant flow rates. Careful attention was paid to prevent any contact of fluids with air, which could cause changes in phase compositions. The core holder was a modified Hassler design machined from PVC material. All displacements were performed horizontally. The injection pressure was read at the inlet of the core holder by an analog pressure gauge with a  $0.5\text{-psi}$  (about  $3.5 \text{ kPa}$ ) resolution. The outlet of the core was held at atmospheric pressure so that the injection pressure was taken as the pressure drop across the core. A confining pressure was applied by means of gas supply on a plastic sleeve, which was mounted on the core to prevent any leak between the sleeve and the core. Effluents were accumulated at the outlet by means of glass vials with a resolution of  $0.1 \text{ cm}^3$ . During the experiment 16 glass vials were used to obtain 16 data points for recovery and pressure drop plots.

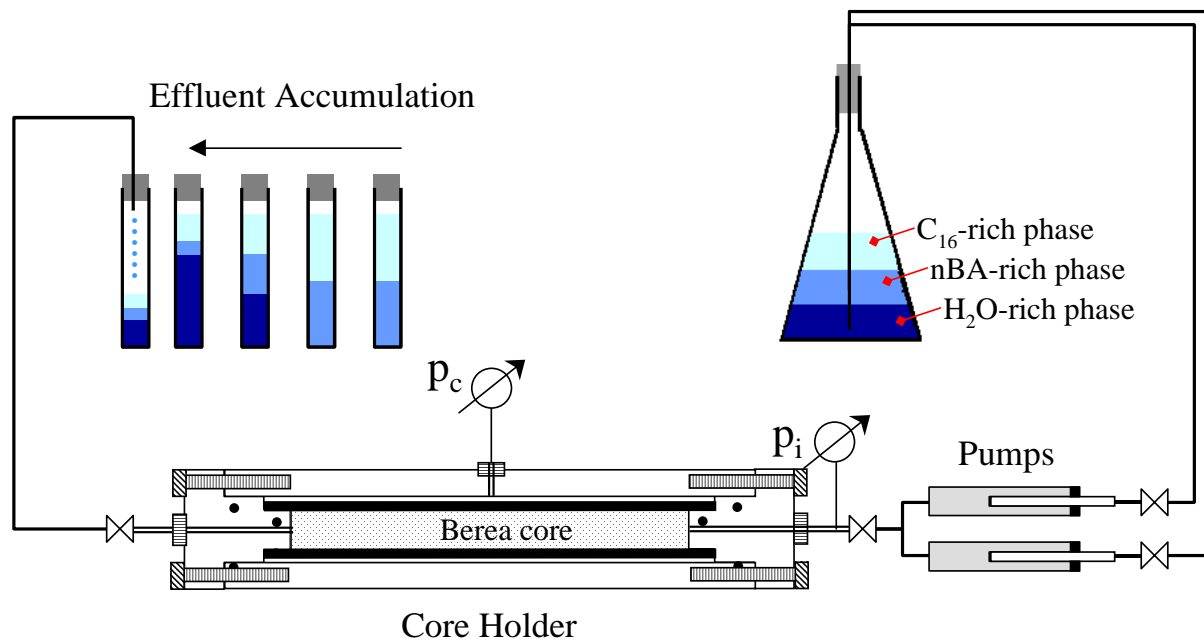


Fig. 4.37: Experimental set-up for displacements in consolidated porous medium.

For the displacement experiments with the  $C_{16}$ /NBA/ $H_2O$ /IPA analogue system, we employed similar experimental and data evaluation procedures described in the previous sections for “oil-wet” experiments with glass bead packs.

For the water-wet displacements in Berea sandstone with  $C_{16}$ /NBA/ $H_2O$ /NaCl analogue system, we started by saturating the core by the  $H_2O$ -rich (W, “water”) phase, which was then displaced by the NBA-rich (IW, “oil”) phase until no  $H_2O$ -rich phase was produced. At this point we determined a residual “water” saturation of about 22%. A simple saturation path for this kind of displacement is depicted in Fig. 4.38.

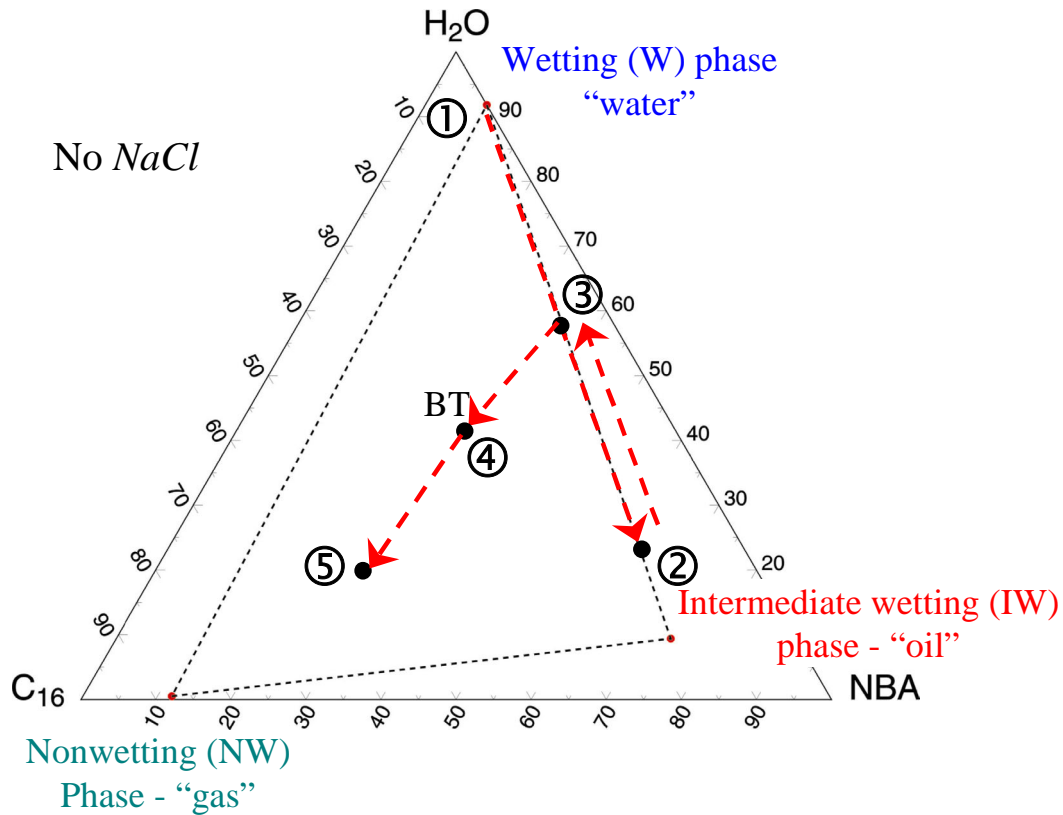


Fig. 4.38: Saturation path for three-phase displacement experiment in a water-wet Berea sandstone core.

Simultaneous steady-state injection of the  $H_2O$ -rich (W, “water”) and NBA-rich (IW, “oil”) phases was conducted to establish an initial saturation distribution through the porous medium just before the gas injection process. A  $C_{16}$ -rich (NW, “gas”) phase injection was then performed. Recovery and differential pressure data were recorded for each experiment to derive relative permeabilities therefrom using an extension of Welge and JBN methods. After each experiment, the core was cleaned by injecting about five PV of IPA+ $H_2O$  mixture and air-dried for the next experiment.

#### 4.1.10 Displacements with $C_{16}$ /NBA/ $H_2O$ /IPA liquid system

Using this analog liquid system in the displacements through a naturally water-wet Berea

sandstone core, we represent a three-phase flow in an “oil”-wet porous medium. So, our phase correspondence was that the nonwetting C<sub>16</sub>-rich phase represented “water”, the wetting H<sub>2</sub>O-rich phase represented “oil” and the intermediate wetting NBA-rich phase represented “gas” in the experiments. These experiments were similar to those done before with glass bead packs, except that the flow here was horizontal, in an attempt to limit effects of gravity instability between C<sub>16</sub>-rich “water” and NBA-rich “gas” phases on displacement.

A summary of experiments is given in Table 4-16. The recovery data for the C<sub>16</sub>-rich (NW, “water”) phase and H<sub>2</sub>O-rich (W, “oil”) phase and total pressure drop across the core are presented in Fig. 4.39. The three-phase relative permeability to all phases derived from the data given in Fig. 4.39 using the combined Welge/JBN method is shown in Fig. 4.40. Smaller production of any displaced phase after breakthrough results in relative permeability data for narrower saturation interval.

Table 4-16: Data for the displacement experiments in Berea core ( $q_t = 1.1 \text{ cm}^3/\text{min}$ ).

Fluids	IFT H <sub>2</sub> O-rich /NBA-rich <i>mN/m</i>	Initial Condition		Capillary Number $\times 10^{-5}$		H <sub>2</sub> O-rich “Oil” Recovery %
		S <sub>H<sub>2</sub>O-rich</sub>	S <sub>C<sub>16</sub>-rich</sub>	NBA-rich/ C <sub>16</sub> -rich	NBA-rich/ H <sub>2</sub> O-rich	
Mix 1	2.297	0.612	0.388	58	20	42.8
Mix 4	0.308	0.631	0.369	13	159	53.7
Mix 6	0.028	0.623	0.377	11	2049	62.6

In the displacements we observed very early breakthroughs at about 0.2 PVI. This could have resulted from the fact that a gravity tongue of the injected phase could form in the horizontal displacement. The injected NBA-rich “gas” phase had an intermediate density in the system. This could result in a gravity tongue with respect to the lightest C<sub>16</sub>-rich phase and a gravity override with respect to the heaviest H<sub>2</sub>O-rich phase. As can be seen in Fig. 4.39, both recovery plots show clear changes in response to decreasing IFT. The ultimate H<sub>2</sub>O-rich “oil” recovery increased in response to lowering the IFT. As observed in the vertical displacement experiments with the same set of compositional system in unconsolidated glass bead packs, less C<sub>16</sub>-rich “water” was produced as the IFT of H<sub>2</sub>O-rich “oil”/NBA-rich “gas” pair was lowered. Hence more C<sub>16</sub>-rich “water” was bypassed by “oil” and “gas”. The differential pressure was measured to be higher than those for experiments in unconsolidated media, as expected for a lower-permeability consolidated porous medium.

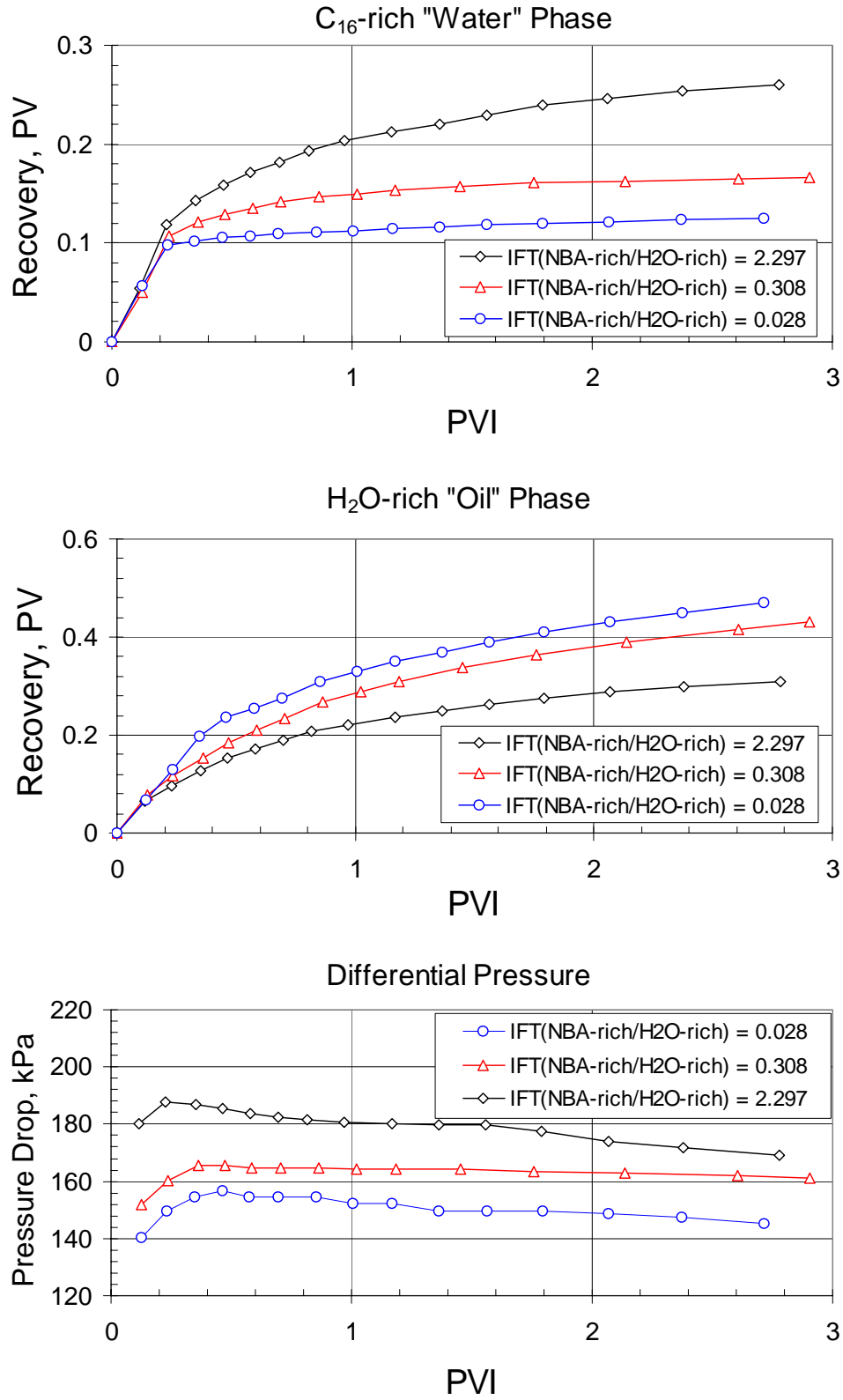


Fig. 4.39: Recovery and differential pressure data for horizontal displacements in “oil-wet” Berea sandstone core. (The C<sub>16</sub>/NBA/H<sub>2</sub>O/IPA analog liquid system was used.)

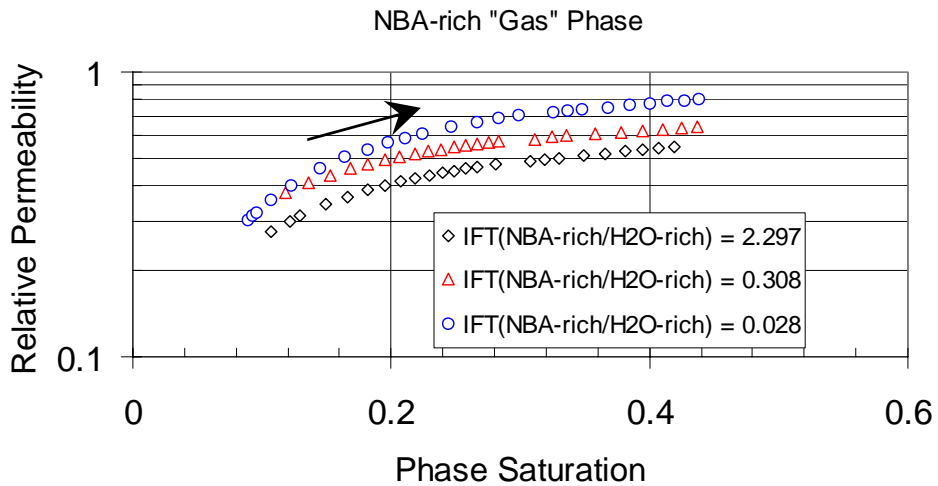
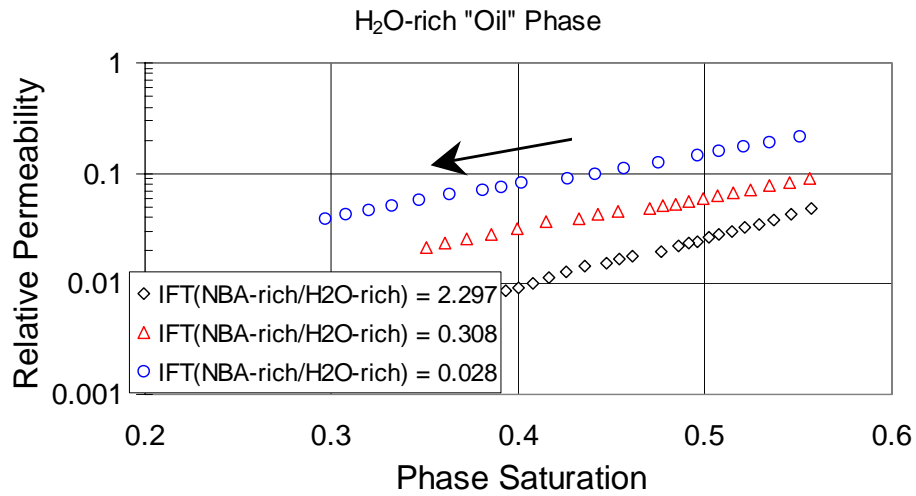
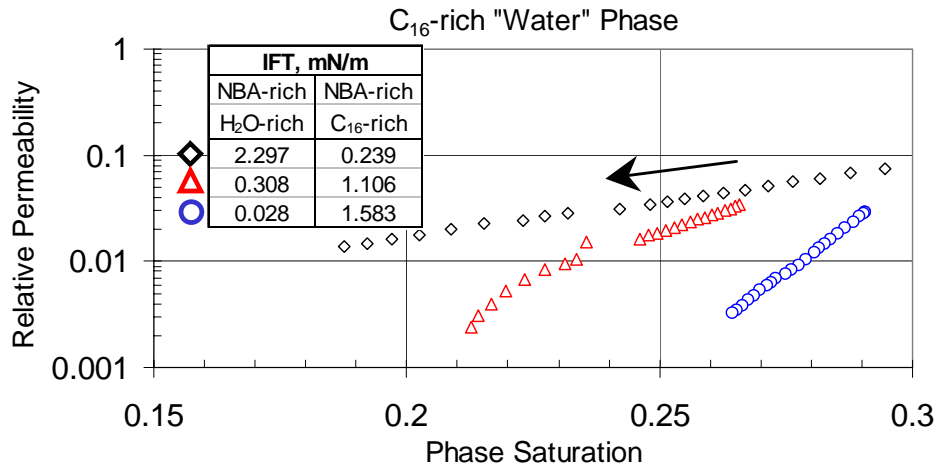


Fig. 4.40: Relative permeabilities determined from horizontal displacements performed in "oil-wet" Berea sandstone core. (The C<sub>16</sub>/NBA/H<sub>2</sub>O/IPA analog liquid system was used.)

The apparent “trapping” of C<sub>16</sub>-rich (NW, “water”) phase can be better seen in “water” relative permeability shown in Fig. 4.40. Recall that the IFT between the C<sub>16</sub>-rich “water” and NBA-rich “gas” phases increases as shown in Fig. 4.7, which, in turn, increases the capillary resistance between the injected NBA-rich “gas” and displaced C<sub>16</sub>-rich “water”. However, reducing capillary effects between the NBA-rich (IW, “gas”) and H<sub>2</sub>O-rich (W, “oil”) phases by lowering the IFT between them makes the “gas” displace the “oil” more easily. This also reduces the displacement pressure drop as can be seen Fig. 4.39. Consequently, the nonwetting “water” is bypassed by the other two phases and retained in the porous system.

We observed distinct increases in H<sub>2</sub>O-rich “oil” and NBA-rich “gas” relative permeabilities in response to reduction in their IFT. However, the change in the NBA-rich “gas” relative permeability was relatively small compared to that in the H<sub>2</sub>O-rich “oil” relative permeability and also to that in “water-wet” teflon packs. This is a consequence of the “water” trapping, just like in WAG processes.

#### 4.1.11 Displacements with C<sub>16</sub>/NBA/H<sub>2</sub>O/NaCl liquid system

This analog liquid system in naturally water-wet Berea sandstone represents three-phase flow in actual water-wet porous medium, which means that the H<sub>2</sub>O-rich phase represents “water”, the intermediate NBA-rich phase represents “oil” and the lightest C<sub>16</sub>-rich phase represents “gas”. A summary of experiments is given in Table 4-17. The recovery data for the H<sub>2</sub>O-rich “water” phase and NBA-rich “oil” phase and total pressure drop across the core are presented in

Fig. 4.41. The three-phase relative permeability to all phases derived from the data given in Fig. 4.41 using the Welge/JBN method is shown in Fig. 4.42. An additional experiment with the phases of Mix 1 was run vertically to show differences between horizontal and vertical displacements. In general the horizontal and vertical displacements in Berea sandstone yielded similar recovery and pressure data.

Table 4-17: Data for the displacement experiments with Berea core ( $q_t = 1.1 \text{ cm}^3/\text{min}$ ).

Fluids	IFT C <sub>16</sub> -rich /NBA-rich <i>mN/m</i>	Initial Condition		Capillary Number $\times 10^{-5}$		NBA-rich “Oil” Recovery %
		S <sub>H<sub>2</sub>O-rich</sub>	S <sub>NBA-rich</sub>	C <sub>16</sub> -rich/ H <sub>2</sub> O-rich	C <sub>16</sub> -rich/ NBA-rich	
Mix 1	0.239	0.615	0.385	15	58	42.9
Mix 1f	0.083	0.619	0.381	11	171	50.8
Mix 3f	0.012	0.637	0.363	9	1177	34.6
Mix 4f	0.005	0.638	0.362	8	2863	30.8

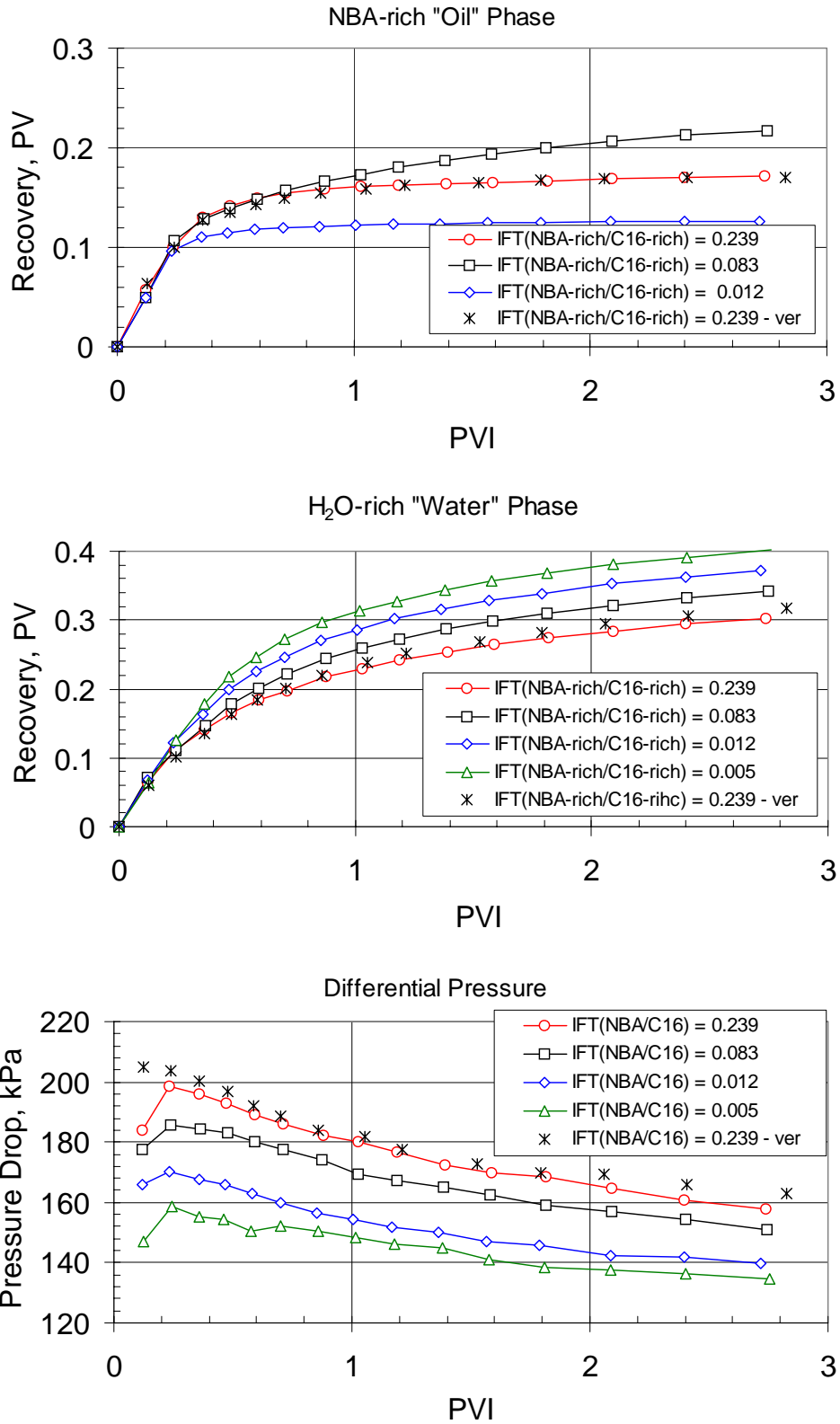


Fig. 4.41: Recovery and differential pressure data for horizontal displacements performed in "water-wet" Berea sandstone core. (The C<sub>16</sub>/NBA/H<sub>2</sub>O/NaCl analog liquid system was used.)

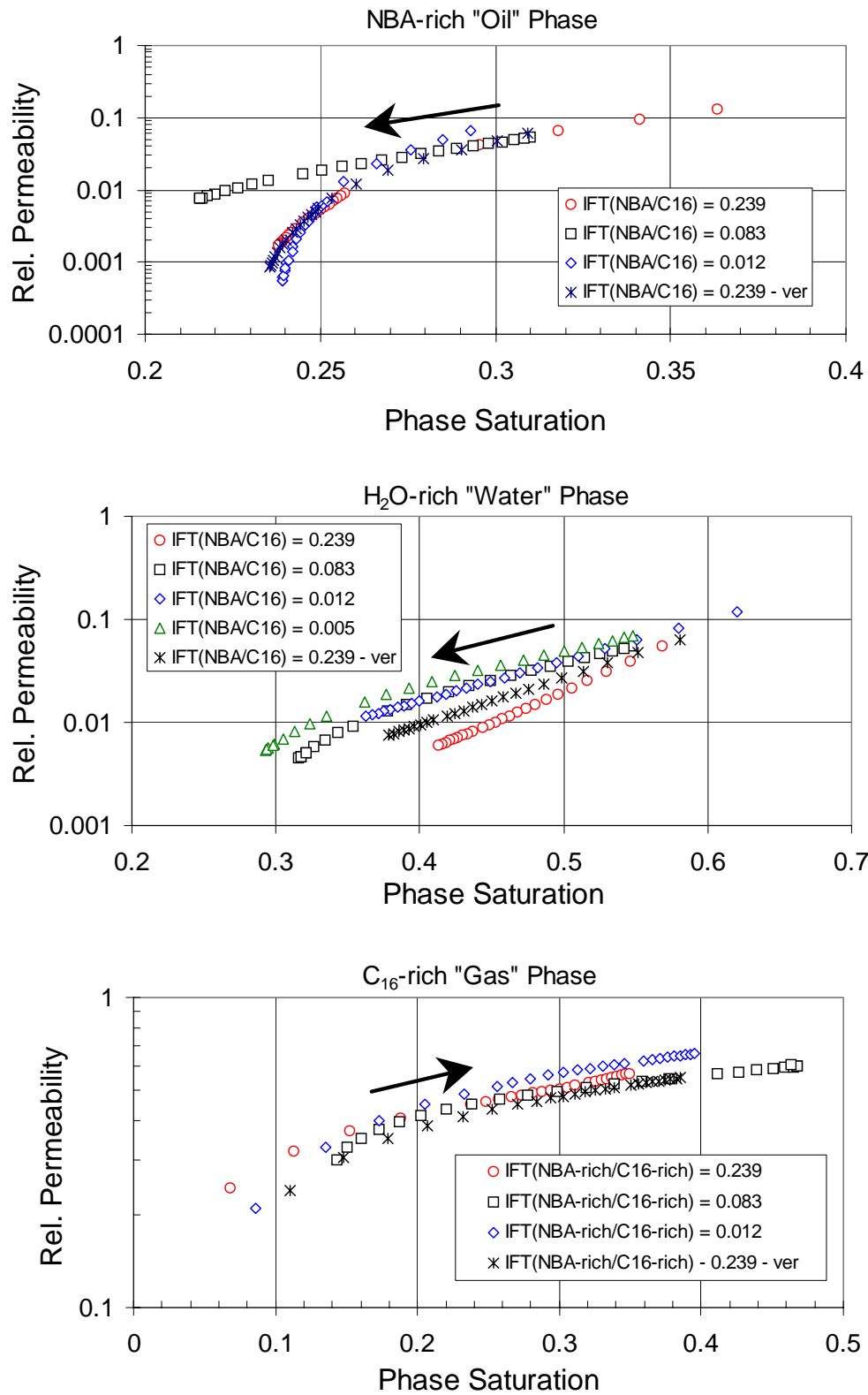


Fig. 4.42: Relative permeabilities determined from horizontal displacements performed in "water-wet" Berea sandstone core. (The C<sub>16</sub>/NBA/H<sub>2</sub>O/NaCl analog liquid system was used.)

The recovery data presented in Fig. 4.41 show very interesting behavior. The NBA-rich “oil” recovery with the second mixture (Mix 1f) increased as the IFT was lowered. However, when we lowered the IFT further more to 0.012  $mN/m$ , the NBA-rich “oil” recovery surprisingly decreased. This was unexpected behavior based on our previous experiences with the experiments in teflon bead packs designed to mimic a “water-wet” reservoir. If we further lowered the IFT into 0.005  $mN/m$ , we observed only two-phase at the outlet. We obtained steady increases in the H<sub>2</sub>O-rich “water” phase, so this phase should not be much affected by IFT variations. The other phase must be a composed of the NBA-rich “oil” and C<sub>16</sub>-rich “gas” phases.

This behavior could be the result of the fluid-rock interactions. It is conceivable that the interaction between the sandstone and NaCl could cause some changes in the phase behavior of the fluid system. More work will be needed to determine the reason for the observed behavior.

This effect can also be seen in the determined relative permeabilities shown in Fig. 4.42. The H<sub>2</sub>O-rich “water” relative permeability data should be more or less correct, because of minimum interaction between other phases and itself. For the displacement with 0.005  $mN/m$ , no data for NBA-rich “oil and C<sub>16</sub>-rich “gas” phase relative permeability are reported. The data obtained from the first and maybe the second mixtures allow only limited comparisons. To investigate further the behavior of water-wet systems, we performed a series of similar displacement experiments in unconsolidated glass bead packs that eliminate potential fluid-rock interactions.

We used the same glass bead pack used in the experiments described in Section 3.2.3. We employed gravity-stabilized vertical displacement experiments by injecting the lightest phase (C<sub>16</sub>-rich) from the top. A summary of experiments is given in Table 4-18. Recovery, differential pressure, and evaluated three-phase relative permeability are presented in Fig. 4.43 and Fig. 4.44. The gravity-stabilized experiments resulted in later breakthrough values and higher ultimate recoveries of the NBA-rich “oil” phase. In these displacements, we did not observe any disturbing effect on the low-IFT phases.

The NBA-rich “oil” recovery increased steadily as the IFT of NBA-rich “oil”/C<sub>16</sub>-rich “gas” pair was lowered. Especially with the lowest IFT the recovery reached at a very high value, which says that we were very close to miscible region. Although moderate changes in water production were observed, the production in the lowest-IFT displacement decreased.

The effect of the IFT variation on the NBA-rich (IW, “oil”) phase relative permeability was significant. Although the C<sub>16</sub>-rich (NW, “gas”) phase relative permeability also increased as the IFT was lowered, the change was relatively small. We observed considerable changes in the H<sub>2</sub>O-rich (W, “gas”) phase relative permeability obtained from the displacements in teflon bead packs.

For the corresponding saturation interval we obtained moderate changes in the H<sub>2</sub>O-rich (W, “water”) phase relative permeability. This is comparable with the result we obtained using teflon bead packs.

Table 4-18: Data for the displacement experiments in glass bead packs ( $q_t = 2.3 \text{ cm}^3/\text{min}$ ).

Fluids	IFT C <sub>16</sub> -rich /NBA-rich <i>mN/m</i>	Initial Condition		Capillary Number $\times 10^{-5}$		NBA-rich “Oil” Recovery %
		S <sub>H<sub>2</sub>O-rich</sub>	S <sub>NBA-rich</sub>	C <sub>16</sub> -rich/ H <sub>2</sub> O-rich	C <sub>16</sub> -rich/ NBA-rich	
Mix 1	0.239	0.562	0.438	31	125	77.4
Mix 1f	0.083	0.591	0.409	24	361	82.3
Mix 3f	0.012	0.592	0.408	18	2462	93.9
Mix 4f	0.005	0.534	0.466	17	6014	98.5

#### 4.1.12 Results and discussion

Fig. 4.45 and Fig. 4.46 show a summary of all three-phase relative permeabilities determined in both consolidated and unconsolidated porous media with different wettabilities. In the previous section, three-phase relative permeability data were summarized in Fig. 4.35 and Fig. 4.36. The following is a comparison of all three-phase experimental data obtained.

Similar trends in C<sub>16</sub>-rich (NW, “water”) phase relative permeability, observed in unconsolidated “oil-wet” system (glass beads), were also observed in consolidated “oil-wet” system (Berea sandstone). However, we found that more C<sub>16</sub>-rich “water” was retained in Berea sandstone for the same relative permeability. This fact that can be explained by the differences in capillary pressure functions of consolidated and unconsolidated porous systems also provides evidence that the trapping of C<sub>16</sub>-rich “water” phase in an “oil-wet” medium had to be caused by the variations in the IFT of the fluid system. At high saturations, the effects of IFT variation on C<sub>16</sub>-rich “water” relative permeability were small. Having used different analog liquids to represent the “water” in “water-wet” unconsolidated porous media (C<sub>16</sub>-rich phase of C<sub>16</sub>/NBA/H<sub>2</sub>O/IPA analogue system in teflon beads and H<sub>2</sub>O-rich phase of C<sub>16</sub>/NBA/H<sub>2</sub>O/NaCl system in glass beads), we observed moderate changes in “water” relative permeability. The “water” relative permeability in “water-wet” Berea sandstone had the same trend with that in glass bead packs, but shifted to higher saturations because of a high residual saturation in the Berea sandstone.

The H<sub>2</sub>O-rich (W, “oil”) phase relative permeabilities in “oil-wet” systems (simulated by employing C<sub>16</sub>/NBA/H<sub>2</sub>O/IPA analog system in glass bead packs and Berea sandstone) showed almost the same trends and changes in response to the IFT variations at intermediate phase saturations. At lower saturations more residual “oil” is left in the Berea sandstone due to a high residual saturation. “Oil” relative permeability in “water-wet” porous media showed big differences at low saturations. For the lowest IFT, the residual “oil” in unconsolidated glass bead packs was almost zero. The “oil” relative permeability in both unconsolidated glass bead and teflon bead packs is comparable in magnitude. The residual “oil” saturation in “water-wet” Berea sandstone was found to be higher.

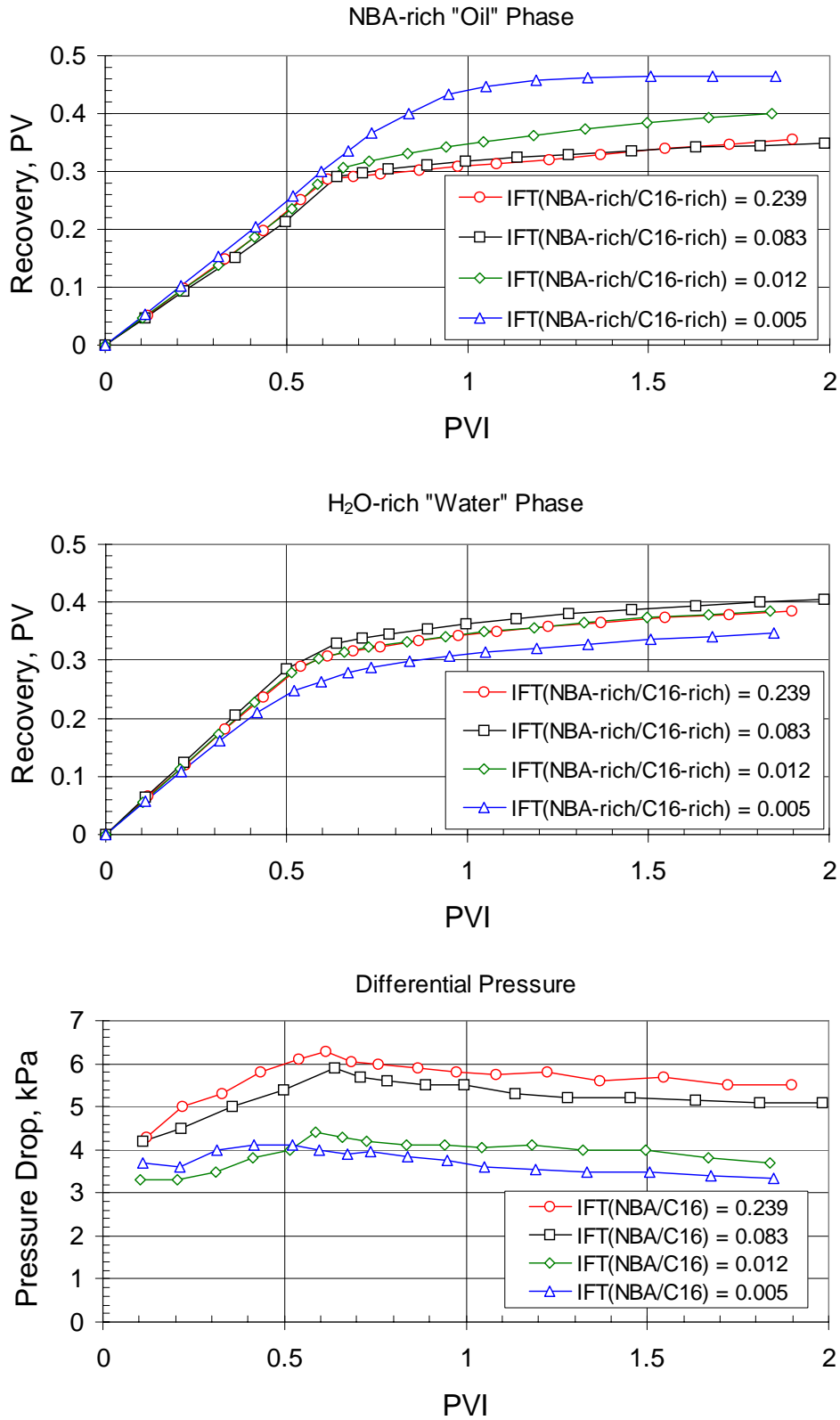


Fig. 4.43: Recovery and differential pressure data for gravity-stabilized displacements in water-wet glass bead packs. (The C<sub>16</sub>/NBA/H<sub>2</sub>O/NaCl analog liquid system was used.)

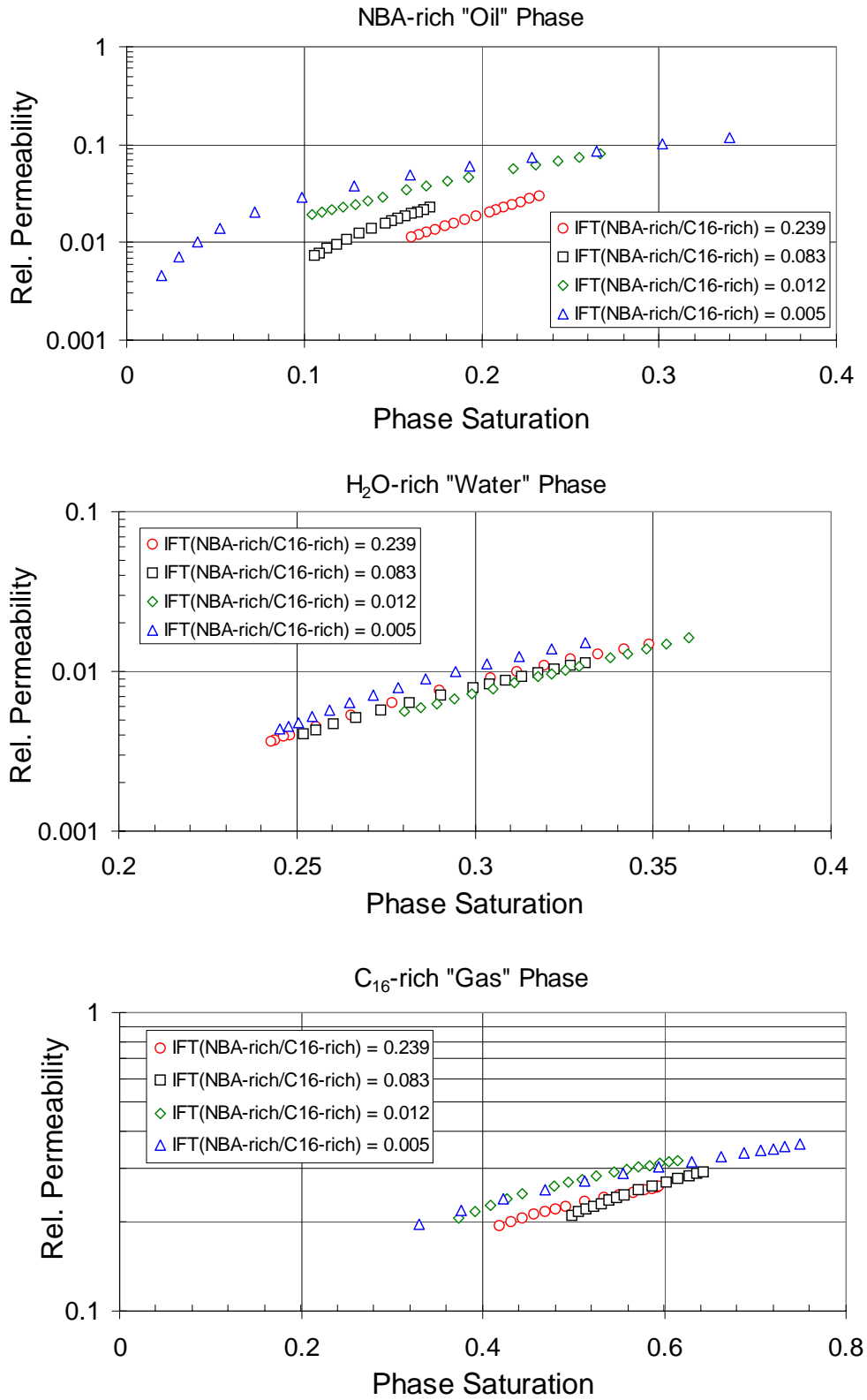


Fig. 4.44: Relative permeabilities determined from gravity-stabilized displacements in “water-wet” glass bead packs. (The C<sub>16</sub>/NBA/H<sub>2</sub>O/NaCl analog liquid system was used.)

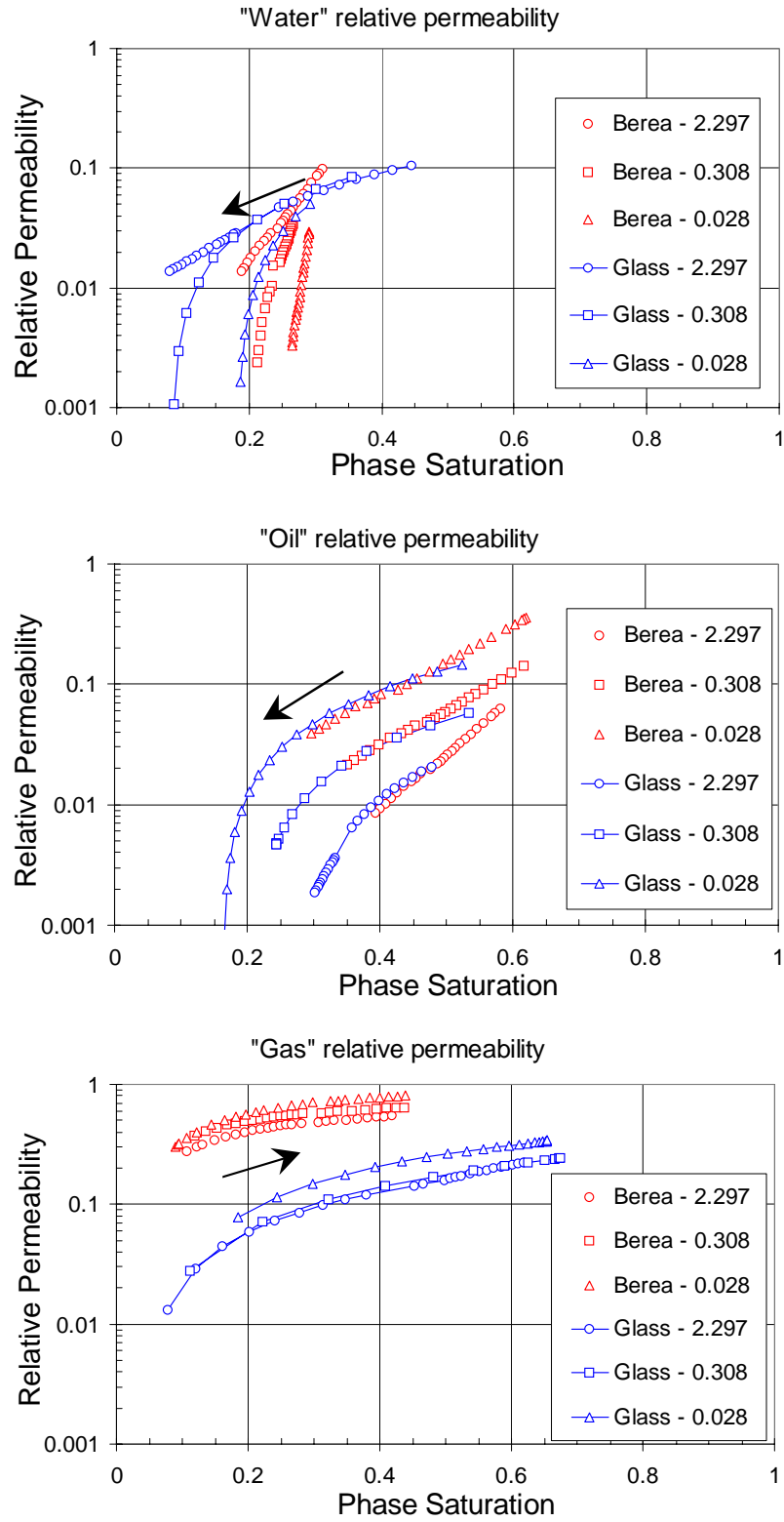


Fig. 4.45: Summary of relative permeabilities in “oil-wet” glass bead packs and Berea sandstone. (The  $C_{16}/NBA/H_2O/IPA$  analog liquid system was used. The numbers in the legend box represent the IFTs between the NBA-rich “gas” and  $H_2O$ -rich “oil” phases.)

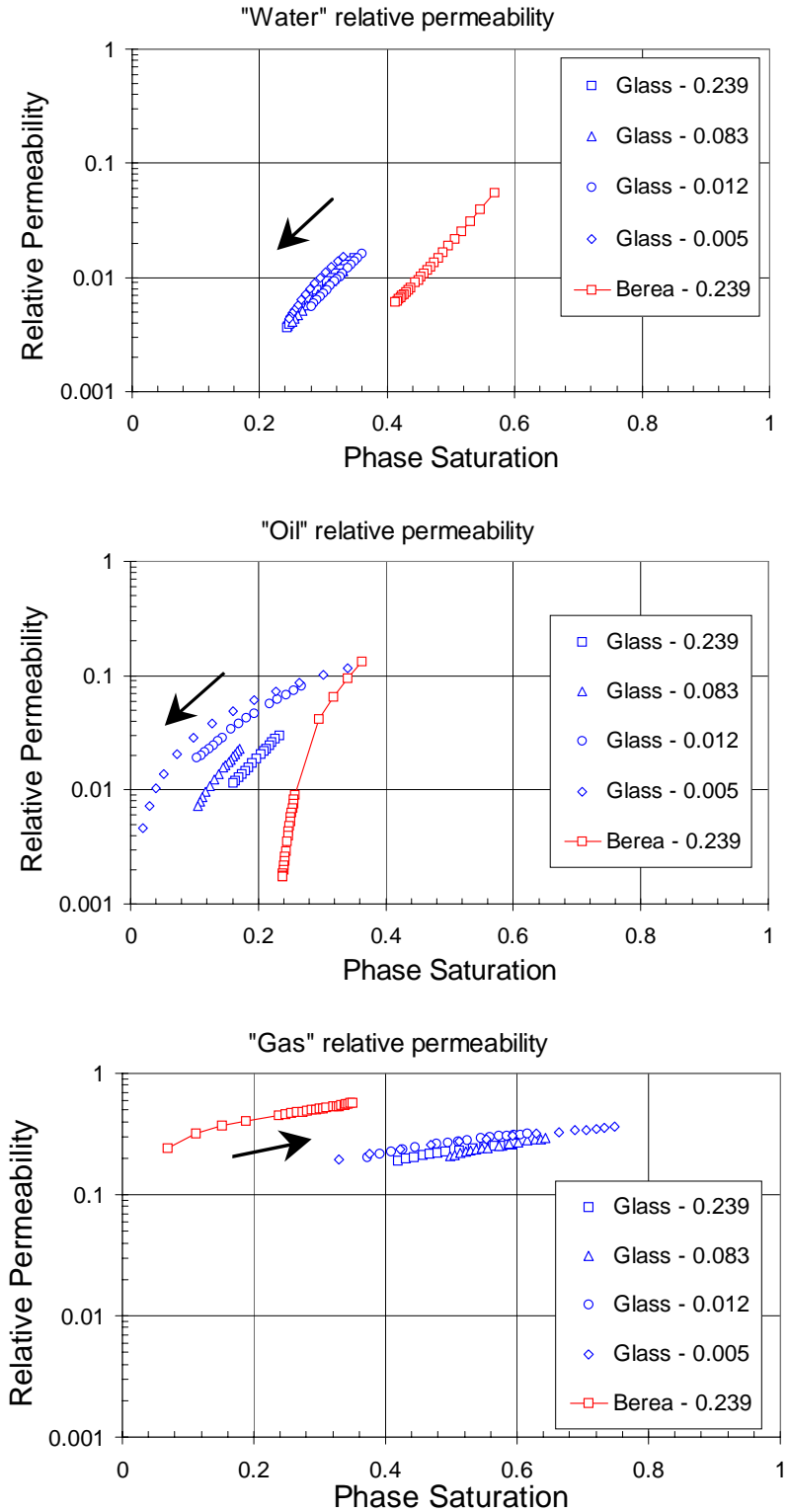


Fig. 4.46: Summary of relative permeabilities in “water-wet” glass bead packs and Berea sandstone. (The  $C_{16}/NBA/H_2O/NaCl$  analog liquid system was used. The numbers in the legend box represent the IFTs between the NBA-rich “oil” and  $C_{16}$ -rich “gas” phases.)

“Oil” and “water” relative permeabilities are comparable to those obtained by Oak (1990) for water-wet Berea sandstone. The “oil” relative permeability in “oil-wet” system behaves similarly to the “water” relative permeability in “water-wet” system, and vice versa. A similar observation was obtained by DiCarlo *et al.* (2000).

“Gas” phase relative permeabilities show similar trends in both “oil”-wet and “water”-wet systems, but have different values for different wetting conditions. “Gas” relative permeability in the Berea sandstone core was found to be higher. Experiments in the Berea sandstone core with both wettability systems show that “gas” relative permeability was very similar in both systems. The change in “gas” relative permeability due to lowering the IFT was very small for “oil-wet” systems. We obtained higher changes in “gas” relative permeability in the “water-wet” teflon bead system than in all other porous and liquid systems.

Lowering IFT apparently reduced the amount of residual “oil” in all kind of porous media. Fig. 4.47 shows a relationship between the recovery of “oil” phase versus the dimensionless capillary number. The “oil” recovery is directly proportional with the capillary number. There is a distinct difference between recoveries of consolidated Berea sandstone and unconsolidated bead packs, independent of the wetting condition. We recovered more “oil” from unconsolidated porous systems. Recoveries of “water-wet” unconsolidated bead packs with different liquid systems have similar trends. Limited data with Berea sandstone do not show any difference in recoveries of different wettability systems. We obtained more “oil” recovery from unconsolidated “water-wet” system than that from unconsolidated “oil-wet” system.

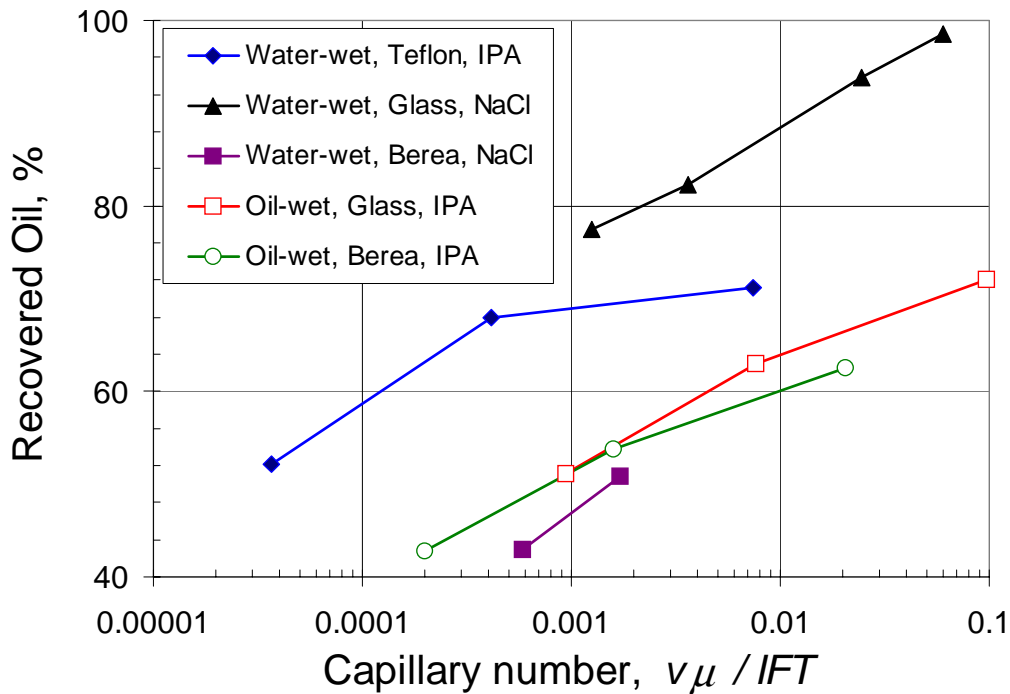


Fig. 4.47: Recovery of “oil” phase as a function of capillary number.

### 4.1.13 Conclusions

We employed three-phase displacement experiments in Berea sandstone, a naturally water-wet consolidated porous rock, to investigate effects of variations in the IFTs of three-phase systems on three-phase relative permeability. We used two three-phase analog liquid systems that have different phase behavior to change the wettability condition of the porous system. The  $C_{16}/NBA/H_2O/IPA$  system, which has a varying IFT between wetting  $H_2O$ -rich and NBA-rich phases with increasing IPA content in the mixture, represented an “oil-wet” system in Berea sandstone. The  $C_{16}/NBA/H_2O/NaCl$  system, which has a varying IFT between non-wetting  $C_{16}$ -rich and NBA-rich phases with increasing NaCl content in the mixture, represented a “water-wet” system in the same Berea sandstone core. In this system, we observed some disturbances in the phase behavior of the analog liquid system that made the analysis of the investigation difficult.

The following are the main results:

1. In the “oil-wet” consolidated and unconsolidated systems, we observed that at low saturations the “water” phase was retained in the porous medium as the IFT of the “gas”/“oil” pair was lowered. In consolidated Berea sandstone the trapped volume was larger. At high saturations, the effects of IFT variation on “water” relative permeability was observed to be small. Moderate changes were observed in “water” relative permeability in “water”-wet porous systems.
2. “Oil” relative permeabilities in all experiments showed similar trends, but more residual “oil” left in the Berea sandstone. The “oil” relative permeability in “oil”-wet system behaved similarly to the “water” relative permeability in “water”-wet system, and vice versa. Lowering IFT apparently reduced the amount of residual “oil” in all kinds of porous media employed in this study.
3. “Gas” phase relative permeabilities showed similar shapes in both “oil”-wet and “water”-wet systems, but had different values for different wetting conditions. Gas relative permeability in the Berea sandstone core was found to be higher, compared to that in unconsolidated porous media. Experiments in both wettability Berea sandstone cores show that “gas” relative permeability behaves the same.
4. We observed a distinct difference between recoveries of consolidated Berea sandstone and unconsolidated bead packs, independent of the wetting condition. We recovered more “oil” from unconsolidated porous systems.

## 4.2 Summary

Accurate reservoir simulation of multicontact gas injection processes requires information about the physics and chemistry of three-phase flow in porous media because such processes routinely include flow of three mobile phases (either because the reservoir has been previously waterflooded or because water is injected alternately with gas in order to improve overall reservoir sweep efficiency). An important and significant difference of three-phase

flow during multicontact processes from other three-phase flows is that such processes have variations in IFT between one pair of the three phases. Hence effects of the IFT gradients along the displacement path on three-phase relative permeabilities must be understood sufficiently for the accurate prediction of the performance of gas injection processes.

The experimental study described in this chapter was designed and executed to delineate the effects of variations in IFT between one pair of the three phases on relative permeabilities of all three phases. The main results of this investigation are:

1. Two four-component three-liquid-phase quaternary phase diagrams have been determined that allow investigation of the effects of IFT variation on three-phase flow. The phase diagrams demonstrate that three-phase systems can be created that exhibit low IFT between one pair of phases, a situation that is analogous to that created in multicontact miscible gas injection processes with water present.
2. In analog water-wet porous systems, we observed that when the displaced phase (“oil”) had low IFT with the displacing phase (“gas”), the relative permeability of that phase increased about an order of magnitude in response to a two-order of magnitude reduction in its IFT with the displacing “gas” phase. We also obtained similar increases in the displacing “gas” phase, which is consistent with the idea that the displacing “gas” flowed more easily along the paths the displaced “oil” occupied. Moderate changes in relative permeability were observed for the other displaced phase (the most wetting “water”), which had roughly constant IFT with the displacing “gas” phase.
3. In analog oil-wet porous systems, we observed similar trends in the relative permeability to the wetting displaced phase (“oil”), but it was less mobile compared to that in water-wet systems. The relative permeability to the displacing “gas” phase, which was intermediate wetting in the porous system, was roughly constant as its IFT with the displaced “oil” was lowered. The other displaced phase (“water”), which occupied the centers of pores, was trapped in porous media in response to lowering IFT between other two phases.
4. Lowering IFT between one pair of three-phases (namely, IFT between displacing “gas” and displaced “oil”) reduced the amount of residual “oil” in all the porous media investigated. We observed a distinct difference between recoveries from consolidated Berea core and unconsolidated bead packs, independent of wetting condition. We recovered more “oil” from the unconsolidated systems.
5. The calculated capillary numbers ( $10^{-5}$ - $10^{-1}$  for “gas”/“oil” pair and  $10^{-5}$ - $10^{-4}$  for “gas”/“water” pair) show that multicontact gas injection processes create regions with IFT gradients where the displacement of “oil” by “gas” can be governed by a combination of viscous and capillary forces while the displacement of the “water” can still be driven by capillary forces.

## 5 Limitations of Streamline Simulation

While streamline methods offer many advantages for field-scale simulation, they are not without limitations. Because these methods treat flow along each streamline as independent of adjacent streamlines, effects of the transfer of components transverse to streamlines are not represented in the simulations. If users of streamline methods are to interpret simulation results reliably, they will need to assess whether any of the mechanisms not modeled in the simulations are important enough to limit appreciably the accuracy of the simulations. In this chapter, we examine the effects of crossflow from several points of view.

We begin with an experimental investigation of the interplay of gravity, capillary, and viscous forces in two-layer glass bead packs. These experiments examined whether the transitions from capillary- to gravity-dominated flow proposed previously are reasonable. In addition, we report results of a simulation study to delineate situations in which it is reasonable to use the basic streamline approach and when the inclusion of gravity effects or capillary crossflow is required. Finally, we examine the accuracy of the assumption used in the construction of analytical solutions that the pressure at which the phase equilibrium is calculated is fixed.

### 5.1 Crossflow effects in two-phase displacements

Transfer of fluid in the direction transverse to streamlines can result from diffusion and dispersion, crossflow due to viscous and capillary forces, and gravity segregation. The scaling of diffusion and dispersion has been investigated in a variety of previous studies. If the injected gas is miscible or partially miscible with the oil, diffusion and dispersion mechanisms may play a significant role in the displacement (Jiang and Butler, 1994, Fayers and Lee, 1994, Tchelep, 1994, Mohanty and Johnson, 1993). In particular, Burger and Mohanty (1997) showed that diffusion through the oil phase can limit mass transfer from oil residing in low permeability regions. Similar arguments can be applied to other mechanisms of crossflow: viscous crossflow, capillary crossflow, and gravity segregation (Burger and Mohanty, 1997, Zhou *et al.*, 1994, Fayers and Lee, 1994). Experimental investigations at the short core scale have shown that crossflow effects can be significant in some settings, especially in heterogeneous media where high and low permeability zones exist (Ahmed, 1984, Schechter *et al.*, 1994, Fayers and Lee, 1994, Firoozabadi and Markeset, 1994, Firoozabadi and Tan, 1994, Burger and Mohanty, 1997, Wylie and Mohanty, 1997, Ma *et al.*, 1997, Peters *et al.*, 1998). In this section, we describe a systematic analysis of the scaling of crossflow mechanisms applied to the situations in which streamline models are used.

Starting from material balance equations Zhou *et al.* (1994) presented dimensionless scaling groups that determine the regime of flow during two-phase displacement. The relevant scaling groups are the transverse gravity and capillary numbers, which are given by:

$$N_{gv} = \frac{\Delta\rho g L k_{av}}{H v \mu_o}, \quad (5.1)$$

$$N_{cv} = \frac{L P_c^* k_{av}}{H^2 v \mu_o}. \quad (5.2)$$

$N_{gv}$  and  $N_{cv}$  are the characteristic time ratios for fluid to flow in the transverse direction due to gravity or capillary forces to that in horizontal direction due to viscous forces\*.  $P_c^*$  is a characteristic transverse capillary pressure of the medium, which is defined by,

$$P_c^* = \int_{S_{wc}}^{1-S_{or}} \frac{P_c(S_w)}{(1-S_{or}-S_{wc})} dS \quad (5.3)$$

Using the simulation and experimental results presented in the literature, Zhou *et al.* reported criteria that determine when capillary forces become dominant in the displacement as well as when gravity forces or viscous forces do. They defined the transients between them as equilibrium conditions such as gravity-capillary, viscous-capillary, and viscous-gravity equilibrium. Table 5-1 summarizes related scaling factors and dominated regions.

Table 5-1: Conditions for flow regions (Zhou *et al.*, 1994).

Flow Region	Condition
Capillary-dominated	$N_{cv} \gg N_{gv}$ and $\frac{MN_{cv}}{1+M} \gg 1.0$
Gravity-dominated	$N_{gv} \gg N_{cv}$ and $\frac{MN_{gv}}{1+M} \gg 1.0$
Capillary-gravity equilibrium	$N_{cv} \approx N_{gv}$ and $\frac{MN_{gv}}{1+M} \gg 1.0$
Viscous-dominated	$\frac{M(N_{cv} + N_{gv})}{1+M} \ll 1.0$

$M$  in the table is the mobility ratio:

$$M = \frac{\lambda_w}{\lambda_o} \approx \frac{\mu_o}{\mu_w} \quad (5.4)$$

While several components of the crossflow process have been investigated, a full set of experiments designed to examine individually and simultaneously the effects of capillary, diffusion, dispersion, gravity, and viscous forces in two- and three-phase immiscible (or partially miscible) gas injection has not been carried out. In this section we examine miscible and immiscible displacements in 2-D models of glass bead packs or sandpacks. Such models allow visualization of displacement fronts as well as the area affected by crossflow.

Ahmed (1984) investigated the effects of capillary imbibition, gravity segregation and viscous pressure gradient on oil recovery. He employed a 2-D model that consisted of three communicating layers of equal thickness of water-wet sand with a permeability ratio of 2:4:1 from top to bottom. He reported that oil recovery increased with decreases in flow rate and in

---

\* All other symbols are defined in the nomenclature, Section 5.1.5.

oil viscosity. He also employed low-IFT displacements but did not report any considerable change in oil recovery.

Brock and Orr (1991) investigated the combined effect of viscous fingering and permeability heterogeneity. They employed four different glass bead models with different permeability heterogeneities, which were made by packing unconsolidated glass beads in a quasi-2-D linear geometry. They used first-contact miscible fluids in the experiments to eliminate capillary effects. They controlled the effect of viscous forces with different flow rates. They employed particle tracking simulations of unstable flows to simulate experiments. In homogeneous media, viscous fingers grow by spreading and splitting at their tips. In heterogeneous media fingering patterns develop along the same streamlines followed during flow at unit mobility in the same porous medium. In general, simulations reproduced the fingering patterns of the experiments well. However, the experimental fingers were more diffuse at their tips than were fingers in the simulations, probably due to some edge flow of fluids in the experimental models.

Dawe *et al.* (1992) performed an experimental investigation of capillary pressure effects on immiscible displacement in lensed and layered glass bead porous media. They reported that capillary forces became of greater importance at permeability boundaries. They also concluded that the balance between capillary and viscous forces is rate dependent; the effects of capillary forces become larger as the flow rate decreases.

Peters *et al.* (1998) worked out the effect of gravity on miscible displacements. They performed a series of experiments in two layered glass bead systems where gravity forces favored flow in the low-permeability layer. They observed that increasing the gravity number forced fluid from the high-permeability layer into the low-permeability layer, increasing crossflow and improving recovery. They also stated that, for the favorable mobility (mobility ratio,  $M < 1$ ), viscous and gravity crossflow forces opposed each other whereas they acted in the same direction for the unfavorable mobility ( $M > 1$ ).

In this section we present experimental results that demonstrate effects of capillary, viscous, and gravity crossflow on two-phase displacement in layered porous systems. The ultimate goal of doing experiments is to quantify limitations of streamline simulations. The experiments designed span a wide range of capillary and gravity numbers, by adjusting the flow rate and the IFT and by performing experiments with horizontal and vertical (upward or downward) flow, and also flow in vertical cross section (VCS).

## **5.1.1 Experimental approach**

### **5.1.1.1 Apparatus**

Glass beads were used to build a two-dimensional, two-layered flow model. Such models allow the displacement to be directly visible, and they enable control permeability heterogeneities. A schematic of the apparatus used in this study is shown in Fig. 5.1.

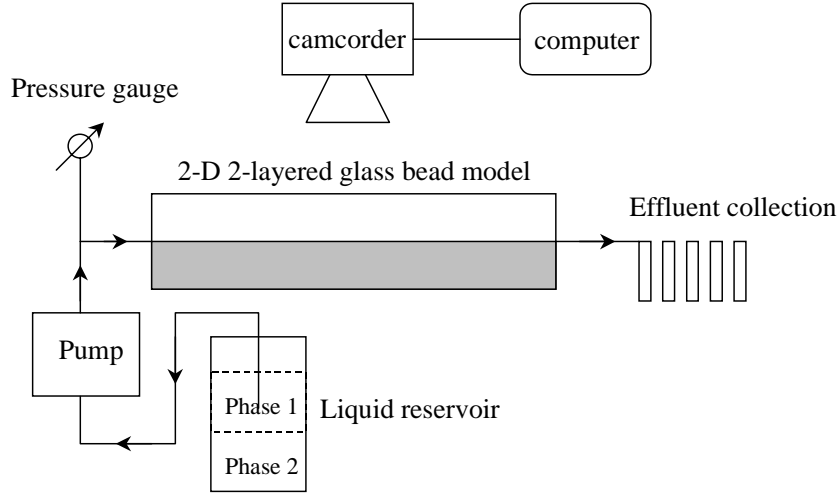


Fig. 5.1: A schematic of the experimental setup.

The glass bead model was the key part of the apparatus. The model was built in the following way (see Fig. 5.2). First, glass blocks and fluid distribution parts were glued together with epoxy to form a box with one side open. This box was then attached to two pneumatic vibrators. As a first, small-sized glass beads (Mesh size: 60, bead size  $\approx 0.021$  cm), and then large glass beads (Mesh size: 35, bead size  $\approx 0.043$  cm) were dropped into the model under vibration. After that some water was let into the model to make sure have a better compaction of glass beads and then the packing was pressed firmly by means of a plastic plate. The final piece of the box was then glued in place by applying an additional forced on that piece. The water was drained and the model was flushed by dry air for 24 hours.

The porosity of each layer was measured separately, and found to be approximately 39.5%. The permeability of each layer was also measured separately using homogeneous packs in a cylindrical tube:  $190 D$  for high-permeability layer and  $52 D$  for low-permeability layer. Using the individual permeabilities, the average permeabilities of the model in the horizontal and vertical directions can be calculated by the following formulas:

$$k_{ah} = \frac{\sum_i k_i H_i}{\sum_i H_i}, \quad (5.5)$$

$$k_{av} = \frac{\sum H}{\sum_i H_i / k_i}, \quad (5.6)$$

where the  $H$  represents the height of the layer. The calculated average permeabilities are  $82 D$  and  $121 D$  for vertical and horizontal directions, respectively. The horizontal permeability

of the model was verified experimentally. We prepared short and long models to investigate effects of gravity.

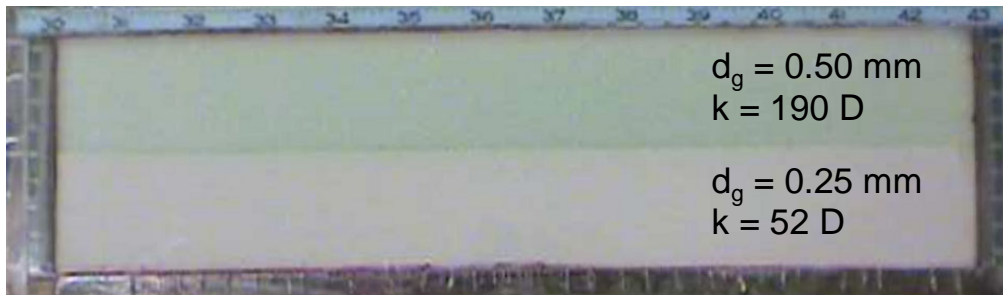
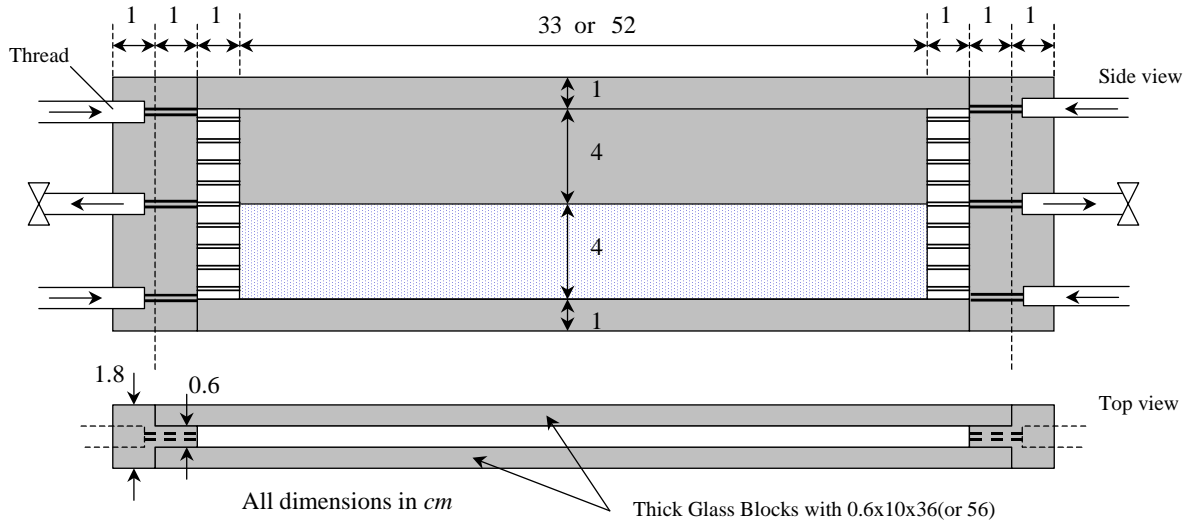


Fig. 5.2: Glass bead flow model for the experiments.  $\phi = 39.5\%$ , Permeability ratio = 3.7.

In the experiments, we systematically changed the orientation of the glass bead models to investigate different type of crossflow mechanisms. Fig. 5.3 shows a sketch of orientations of glass bead models used. We reduced the effects of gravity by employing vertical displacements in two-layered system and injected heavier fluid at the bottom of the model to displace lighter fluid, or vice versa (see Fig. 5.3a). The interfacial tension (IFT) between the fluids and the flow rate determine which of the crossflow mechanism dominates the displacement. Gravity effects on crossflow in the vertical displacements should be different from those in gravity-stabilized horizontal displacements depicted in Fig. 5.3b. For example, in a vertical near miscible flooding the front in the high-permeability layer is expected to be faster than that of the low-permeability layer, and consequently, there will be a difference in the hydrostatic heads of the layers. Depending on the flow rate and the density difference of the fluids, this effect can be important to crossflow. To investigate the combined effects of

viscous, gravity, and capillary forces on the displacement behavior, we employed horizontal displacements in glass bead models oriented as shown in (c) and (d). We built one short and one long model to analyze the effect of the L/H ratio on the displacement behavior. We also inverted these models for the other set of similar displacements to have the high-permeability layer at the top of the porous system.

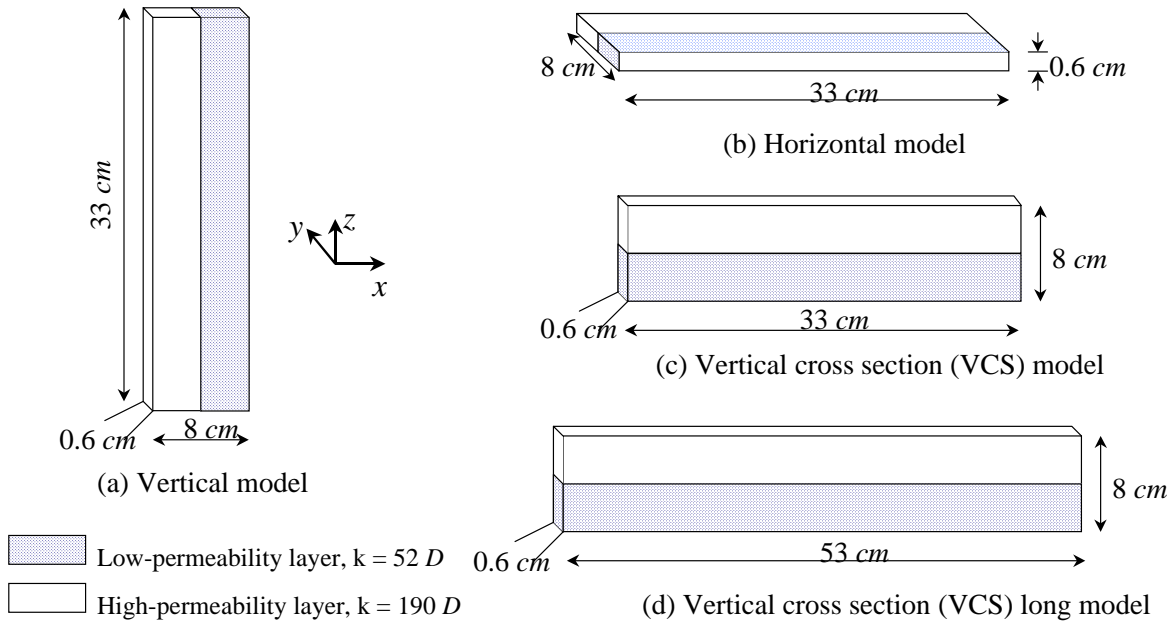


Fig. 5.3: Orientation of glass bead models used in the experiments.

Pressure drops across the model and production of the phases at the end of the model were measured during the experiment. The pressure was measured by means of an analog gauge with an accuracy of  $0.2\text{ kPa}$ . The effluent fluids were collected in plastic graduated cylinders. After suitable delay for phase separation, the production data were then determined by reading the liquid levels in the cylinders with an accuracy of  $0.1\text{ cm}^3$ . All displacements were recorded using a video camera to obtain areas invaded across the model.

### 5.1.1.2 Fluid system

We employed two different sets of overall phase compositions from the ternary isooctane ( $\text{IC}_8$ )-isopropanol (IPA)-water system, in which IFT can be controlled systematically (Fig. 5.4). The first set of phases was composed of binary mixture of  $\text{IC}_8$  and water that represented high-IFT immiscible displacements in the experiments. The other one was composed of all ternary components (42%  $\text{IC}_8$ , 11.5%  $\text{H}_2\text{O}$ , 46.5% IPA by weight), which represented low-IFT near miscible displacements. The fluid properties of the phases are given in Table 5-2. The  $\text{IC}_8$ -rich and the  $\text{H}_2\text{O}$ -rich phases were dyed by the Oil Red O

(Sigma) and the Brilliant Green (Harleco), respectively, to track the fluid movements in the experiments.

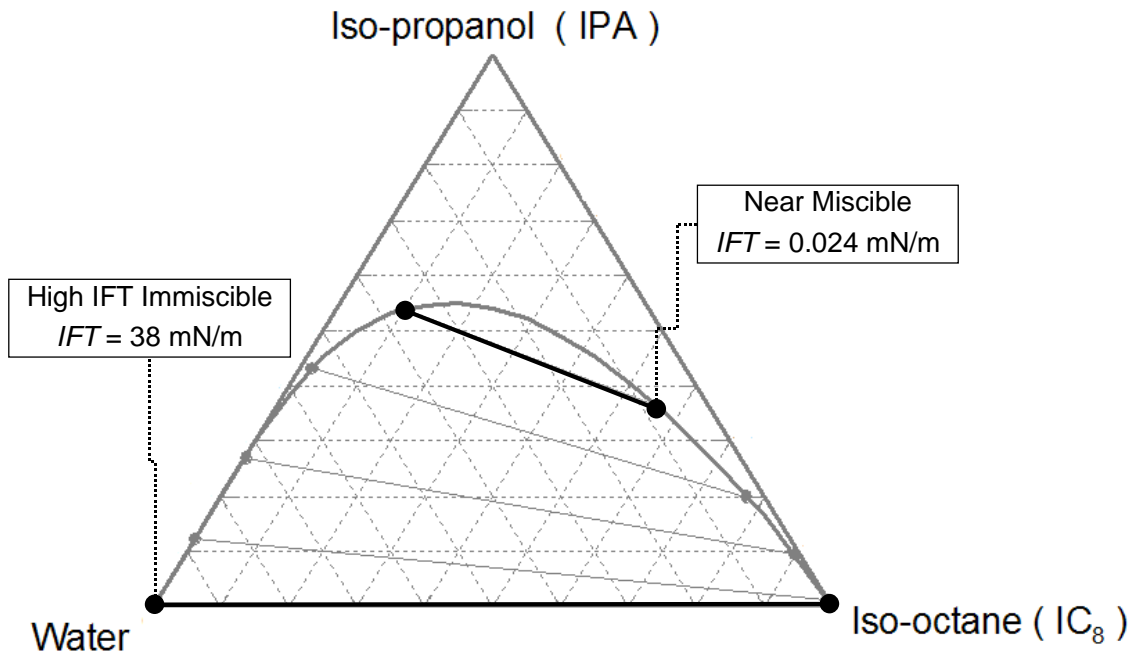


Fig. 5.4: Schematic of fluid compositions used in the experiments.

Table 5-2: Physical properties of the phases.

	Immiscible (Fig. 5.4)		Near Miscible (Fig. 5.4)	
	IC <sub>8</sub> -rich	H <sub>2</sub> O-rich	IC <sub>8</sub> -rich	H <sub>2</sub> O-rich
$\rho, g/cm^3$	0.692	0.998	0.723	0.795
$\mu, mPa.s$	0.48	1.00	0.836	2.027
IFT, mN/m	38.1		0.024	
$\Delta\rho, g/cm^3$	0.306		0.072	
M (H <sub>2</sub> O-rich disp. IC <sub>8</sub> -rich)	0.48		0.41	
M (IC <sub>8</sub> -rich disp. H <sub>2</sub> O-rich)	2.48		2.44	

### 5.1.1.3 Experimental procedures

Table 5-3 gives a preliminary strategy for all experiments. We used the following steps to investigate the combined effects of crossflow forces:

1. We employed two different glass bead models (one short, one long) to investigate L/H ratios on crossflow formed by gravity forces.
2. We employed gravity-reduced and gravity-stabilized experiments to investigate the combined effects of only viscous and capillary forces.
3. We injected fluids with three different flow rates to control viscous forces.
4. We used one low and one high IFT to study the effect of capillary crossflow with/out gravity forces.
5. We repeated some of the experiments with an unfavorable mobility ratio.
6. For the experiments with gravity, the model was located such that the low-permeability layer was at the bottom. Later we inverted the glass bead model such that the high-permeability layer was at the bottom and repeated some of the experiments.

Table 5-3: Summary of the displacement experiments.

Glass Bead Model	Gravity Effects	$q$ <i>cm<sup>3</sup>/min</i>	Favorable displacement $M < 1$		Unfavorable displacement $M > 1$	
			38 mN/m $M = 0.48$	0.02 mN/m $M = 0.41$	38 mN/m $M = 2.08$	0.02 mN/m $M = 2.44$
Short vertical Fig. 5.3a)	reduced	0.6	Exp. #1	<b>Exp. #2</b>		
		2.2	# 3	# 4	# 5	#6
		8.5	# 7	# 8		
Short horizontal Fig. 5.3b)	negligible	2.2	# 9	# 10	# 11	# 12
Short horizontal Fig. 5.3c)	large	0.6	# 13	# 14		
		2.2	# 15	# 16	# 17	# 18
		8.5	# 19	# 20		
Long horizontal Fig. 5.3d)	large	2.2	# 21	# 22	# 23	# 24
Long horizontal Fig. 5.3d) High-perm layer at the bottom	large	2.2	# 25	# 26	# 27	# 28

We employed the following experimental procedure:

1. Displace air in the pores with CO<sub>2</sub>.
2. Displace the CO<sub>2</sub> with two PVs of either the dyed IC<sub>8</sub>-rich phase or the dyed H<sub>2</sub>O-rich phase depending on displacement type: the “imbibition”, “favorable” displacement or the “drainage”, “unfavorable” displacement. Make sure that the porous system is saturated completely.
3. Then start injecting the dyed H<sub>2</sub>O-rich phase or the dyed IC<sub>8</sub>-rich phase to view the saturation profile using Camcorder. Record the pressure drop across the model and the production of phases.
4. Compare the experimental results with simulation results.

At the beginning of experiments of favorable imbibition displacements, we tried to create a residual saturation of the H<sub>2</sub>O-rich phase in the porous system to represent displacements in real reservoirs. However, after preliminary test runs, we determined that we could not obtain a reasonably uniform residual saturation of the H<sub>2</sub>O-rich phase for the porous system. This was because the injected IC<sub>8</sub>-rich phase did not sweep the water-rich phase in the low-permeability layer after breakthrough in the high-permeability layer. We separately measured a residual water saturation of about 9% for glass bead packs. In the end, we skipped the steps for the residual saturation and performed experiments of the H<sub>2</sub>O-rich phase displacing the IC<sub>8</sub>-rich phase fully saturated in pores. Hence the results obtained from these experiments might not be fully representative for water-wet systems, which initially contain connate water.

#### **5.1.1.4 Homogeneity of the flow model**

The homogeneity of the flow model was checked by the following experiment. The model was first saturated completely by water. Then first-contact miscible dyed water was injected to the porous medium. Because the fluids were miscible, and there were no capillary effects, no density difference, and viscosity difference, the effects of capillary, viscous, and gravity crossflow on the displacement were eliminated. The displacement fronts in each layer should then be determined by the individual layer permeabilities. The experimental results are shown in Fig. 5.5. The model was held vertically and all fluids were injected from bottom. The first image shows the situation at the start of the experiment, whereas the second shows the saturation profile at the time the pore volume injected (PVI) was 0.35. The displacement front in the high-permeability layer (at  $x \sim 29$  cm of the total length of 54 cm) is faster than that in the low-permeability layer ( $x \sim 9$  cm). The ratio of the front locations (about 3.2) is comparable to the permeability ratio (3.7). The third image shows the saturation distribution in the layers at the breakthrough. The images prove an acceptable homogeneity of the individual layers.

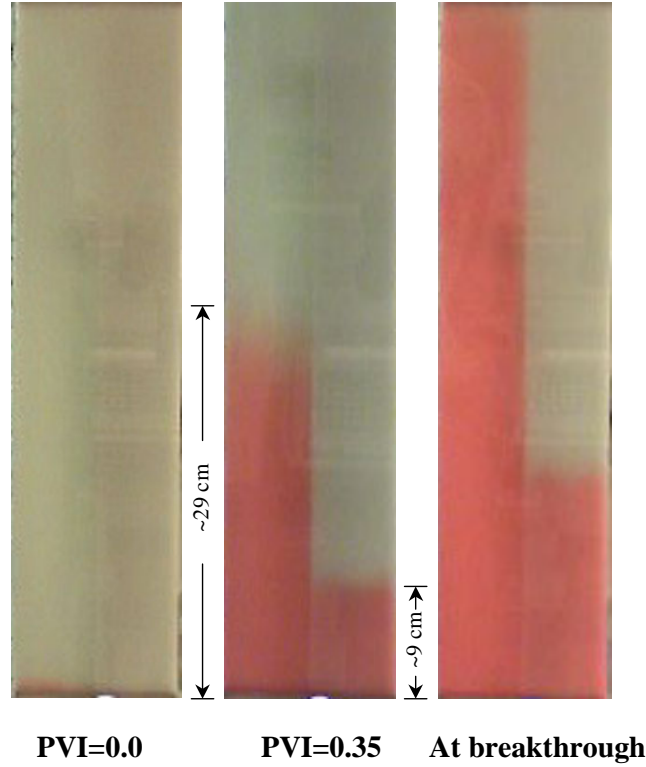


Fig. 5.5: First contact miscible displacement of water by dyed water (M= 1).

### 5.1.2 Experimental results

The related crossflow scaling groups for all experiments were calculated using Eqs. (5.1) and (5.2). A summary of data and calculations is given in Table 5-4. The so-called characteristic capillary pressure,  $P_c^*$ , was evaluated from the capillary pressure experimental data using the van Genuchten (1980) capillary pressure model given by:

$$p_c = p_d \left( S_{wd}^{-1/m} - 1 \right)^{1/n}. \quad (5.7)$$

With this model, Eq. (5.3) can be rewritten as it follows:

$$P_c^* = \int_o^1 p_d \left( S_{wd}^{-1/m} - 1 \right)^{1/n} dS_{wd}, \quad (5.8)$$

where,

$$S_{wd} = \frac{S_w - S_{wr}}{1 - S_{wr} - S_{or}}. \quad (5.9)$$

Here  $p_d$  is the displacement pressure,  $m$  and  $n$  are fitting parameters,  $S_w$  is the water saturation, and  $S_{wr}$  and  $S_{or}$  are residual saturations. Using experimental capillary pressure data  $p_d$ ,  $m$  and  $n$  can be determined. We used the capillary pressure data presented by Dawe *et al.* (1992) for various unconsolidated glass bead packs for oil/water fluid system. Before

matching with the models we converted all capillary pressure data into the Leverett  $J$ -functions to obtain a more general definition using the following equation (Lewerett, 1941):

$$J(S_w) = \frac{p_c}{\sigma \cos \theta} \sqrt{\frac{k}{\phi}}. \quad (5.10)$$

Because Dawe *et al.* did not report any IFT value for their fluid system, we took 38.1  $mN/m$  for the IFT between oil and water in the data conversion. Fig. 5.6 shows the results of correlation of the van Genuchten model with experimental data. Table 5-5 reports the matching parameters. The figure shows a good model match with the experimental data. The calculated characteristic capillary pressures are listed in the table. Other data have already been given before. We assumed that glass bead packs were strongly water-wet.

Fig. 5.7 shows the capillary pressure functions of high-permeability and low-permeability layers for both imbibition and drainage cases. The data were derived using the  $J$ -functions shown in Fig. 5.6 and other physical data of the layers in Eq. (5.10). For the imbibition case, we shifted the original  $J$ -function to zero water saturation, which was the initial condition in our experiments. These data show that capillary pressure was a considerable driving force in the displacements with a high-IFT fluid system.

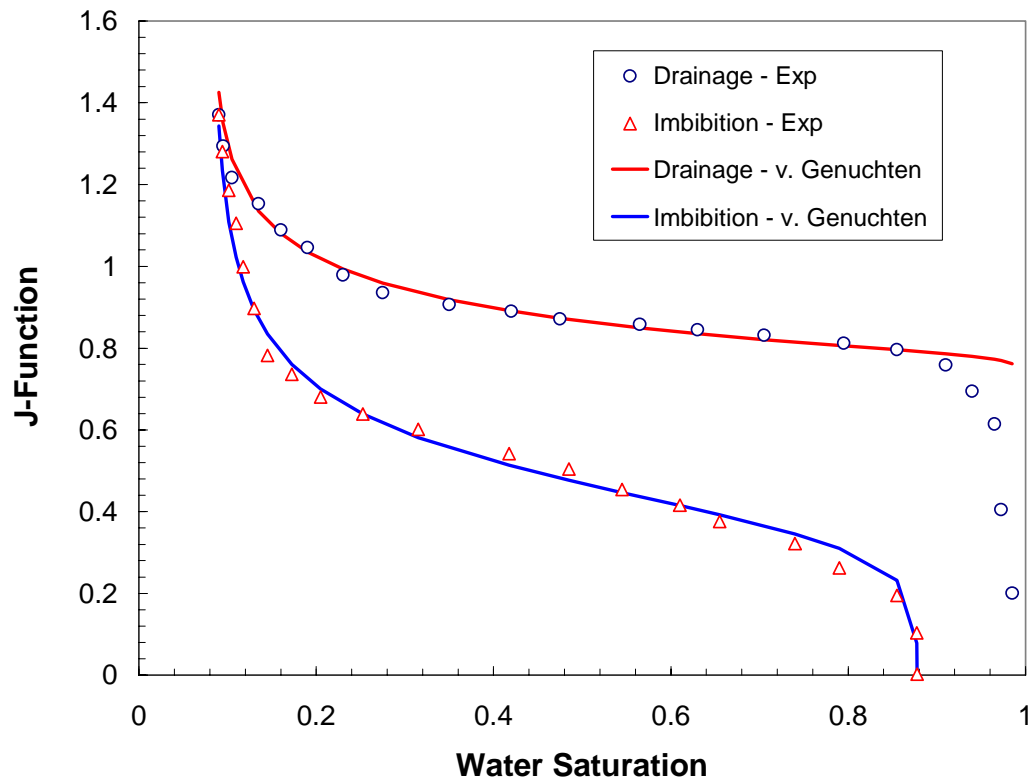


Fig. 5.6: Correlation for  $J$ -function data using the van Genuchten model.

Table 5-4: Summary of displacement experiments.

Exp. #	$q$ $cm^3/min$	$L$ $cm$	$W$ $Cm$	$H$ $cm$	$p_c^*$ $Pa$	$N_{gv}$	$N_{cv}$	$\frac{N_{gv}M}{1+M}$	$\frac{N_{cv}M}{1+M}$	$N_B$	$R_l^2$	Remarks on Flow	Recovery @ PVI=1	
													Exp.	ECL100
1	0.57	33	0.65	8	1095	N/a	525.72	N/a	170.51	N/a	11.48	Capillary-dominated	0.899	0.849
2	0.62	33	0.65	8	0.7	N/a	0.18	N/a	0.05	N/a	11.48	Viscous-dominated	0.925	0.890
3	2.31	33	0.65	8	1095	N/a	129.72	N/a	42.07	N/a	11.48	Capillary-dominated	0.902	0.851
4	2.08	33	0.65	8	0.7	N/a	0.05	N/a	0.02	N/a	11.48	Viscous-dominated	0.884	0.912
5	2.16	31	0.57	8	1926	N/a	95.59	N/a	68.12	N/a	10.13	Capillary-dominated	0.595	0.529
6	2.16	31	0.57	8	1.2	N/a	0.03	N/a	0.02	N/a	10.13	Viscous-dominated	0.631	0.707
7	8.45	33	0.65	8	1095	N/a	35.46	N/a	11.50	N/a	11.48	Capillary-dominated	0.908	0.862
8	8.53	33	0.65	8	0.7	N/a	0.01	N/a	0.00	N/a	11.48	Viscous-dominated	0.900	0.842
9	2.2	36	0.57	8	1095	$\approx 0.00$	130.30	$\approx 0.00$	42.26	$\approx 0.00$	13.67	Capillary-dominated	0.812	0.774
10	2.27	33	0.65	8	0.7	$\approx 0.00$	0.05	$\approx 0.00$	0.01	$\approx 0.00$	11.48	Viscous-dominated	0.881	0.841
11	1.82	34	0.57	8	1926	$\approx 0.00$	124.42	$\approx 0.00$	88.67	$\approx 0.00$	12.19	Capillary-dominated	0.629	0.468
12	2.2	33	0.65	8	1.2	$\approx 0.00$	0.04	$\approx 0.00$	0.03	$\approx 0.00$	11.48	Viscous-dominated	0.611	0.607
13	0.6	36	0.57	8	1095	104.68	477.78	33.95	154.96	$\approx 0.22$	13.67	Gravity-Capillary Transition	0.717	0.774
14	0.57	33	0.65	8	0.7	15.56	0.19	4.52	0.06	80.64	11.48	Viscous-Gravity Transition	0.922	0.930
15	2.13	36	0.57	8	1095	29.49	134.59	9.56	43.65	0.22	13.67	Gravity-Capillary Transition	0.817	0.797
16	2.21	33	0.65	8	0.7	4.01	0.05	1.17	0.01	80.64	11.48	Viscous-Gravity Transition	0.906	0.913

**Table 5-4** (continued)

Exp. #	$Q$ $cm^3/min$	L $cm$	W $cm$	H $cm$	$P_c^*$ $Pa$	$N_{gv}$	$N_{cv}$	$\frac{N_{gv}M}{1+M}$	$\frac{N_{cv}M}{1+M}$	$N_B$	$R_l^2$	Remarks on Flow	Recovery @ PVI=1	
													Exp.	ECL100
17	2.16	31	0.57	8	1926	12.02	95.59	8.56	68.12	0.13	10.13	Gravity-Capillary Transition	0.442	0.433
18	2.02	31	0.57	8	1.2	1.49	0.03	1.06	0.02	47.04	10.13	Viscous-Gravity Transition	0.537	0.557
19	8.53	36	0.57	8	1095	7.36	33.61	2.39	10.90	0.22	13.67	Gravity-Capillary Transition	0.848	0.851
20	8.94	33	0.65	8	0.7	0.99	0.01	0.29	0.00	80.64	11.48	Viscous-Gravity Transition	0.919	0.856
21	2.26	53	0.57	7.6	1095	40.91	196.57	13.27	63.75	0.21	32.82	Gravity-Capillary Transition	0.910	0.786
22	2.16	52	0.65	7.9	0.7	6.48	0.08	1.89	0.02	79.63	29.35	Viscous-Gravity Transition	0.929	0.925
23	2.23	53	0.57	7.8	1926	19.90	162.35	14.18	115.70	0.12	31.16	Gravity-Capillary Transition	0.390	0.444
24	2.18	53	0.57	7.8	1.2	2.36	0.05	1.68	0.04	45.86	31.16	Viscous-Gravity Transition	0.564	0.570
25	2.26	53	0.57	7.8	1095	40.91	191.53	13.27	62.12	0.21	31.16	Gravity-Capillary Transition	0.840	0.754
26	2.29	53	0.57	7.8	0.7	5.45	0.07	1.59	0.02	78.62	31.16	Viscous-Gravity Transition	0.937	0.831
27	2.2	53	0.57	7.8	1926	20.17	164.56	14.38	117.28	0.12	31.16	Gravity-Capillary Transition	0.520	0.573
28	2.25	53	0.57	7.8	1.2	2.29	0.05	1.62	0.04	45.86	31.16	Viscous-Gravity Transition	0.606	0.844

Table 5-5: Model parameters for experimental J-function data.

	$\frac{p_d}{\sigma \cos \theta} \sqrt{\frac{k}{\phi}}$	$m$	$N$	$S_{wr}$	$S_{or}$	$P_c^*, Pa$ High IFT	$P_c^*, Pa$ low IFT
Drainage	0.78	0.1	75	0.08	0.0	1926	1.2
Imbibition	0.45	0.8	5	0.08	0.122	1095	0.7

We used Eclipse100, a commercial black oil simulator, to simulate experiments. The J-function and relative permeability data used in the simulations are presented in Fig. 5.8 for both drainage and imbibition cases. The symbols in Fig. 5.8 represent experimental data, obtained from dynamic experiments with Isooctane (IC<sub>8</sub>)-water fluid system in glass bead packs ( $\phi = 40\%$  and  $k = 52 D$ ). The data were then smoothed before entering to the simulators. For low-IFT displacements we simply used roughly X-shaped diagonal relative permeabilities that represent near-miscible floods.

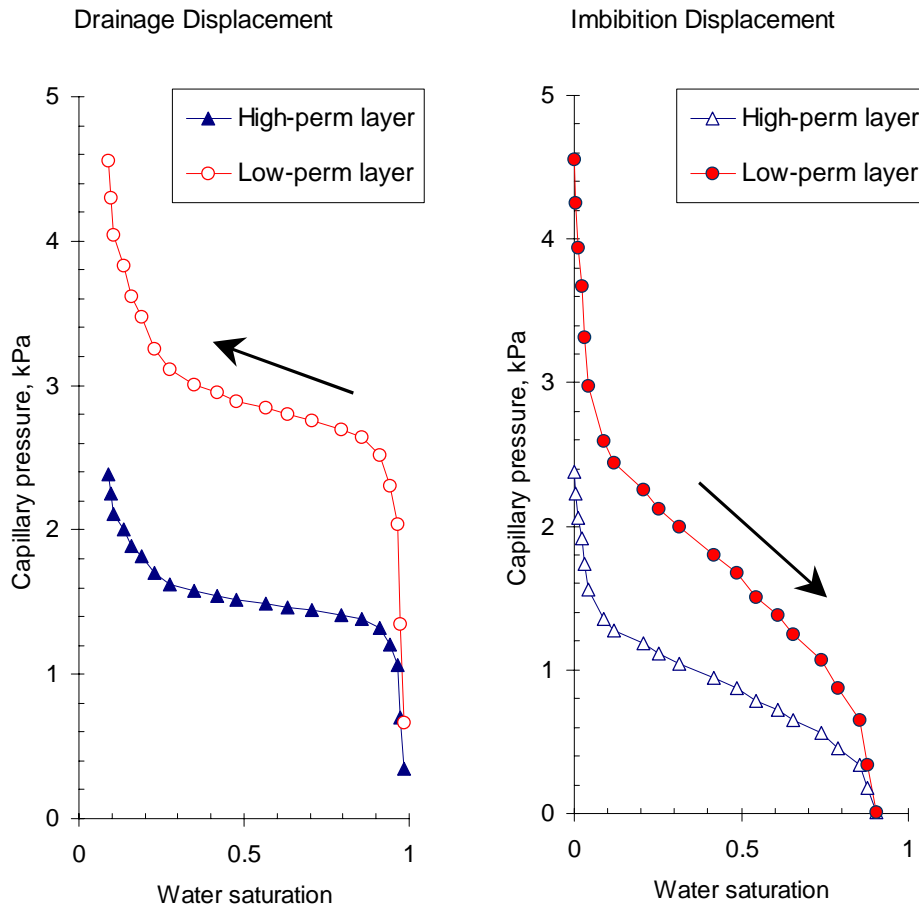


Fig. 5.7: Capillary pressure data for the high-permeability and low-permeability layers derived from the  $J$ -function data presented in Fig. 5.6.

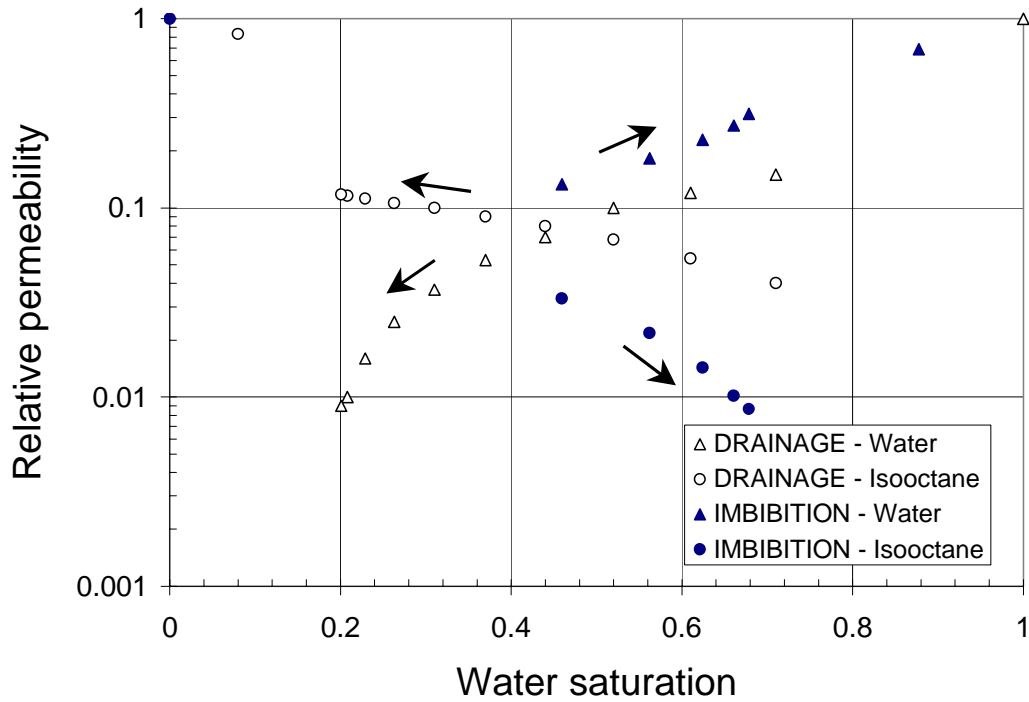


Fig. 5.8: Measured data of relative permeability for the simulation study.

### 5.1.2.1 Scaling groups for flow regions in displacements

A derivation of scaling groups for different crossflow mechanisms has been presented by several authors (Zhou *et al.*, 1994, Tchelepi and Orr, 1994) for near-miscible as well as immiscible displacements. The scaling data we calculated for our experiments are given in Table 5-4.

Fig. 5.9 shows data of scaling groups for gravity and viscous crossflow mechanisms in near-miscible displacements (Experiments with the low-IFT, 0.024 *mN/m* fluid pair). The dotted lines show the boundaries between flow regions, suggested by Zhou *et al.* They determined these approximate boundaries using experimental and simulation results given in the literature through 1994. The boundary for viscous effects was proposed by Ekraan (1992) from the simulation results.  $R_l^2$  is called the effective shape factor and given by,

$$R_l^2 = \left( \frac{L}{H} \right)^2 \frac{k_{av}}{k_{ah}} \quad (5.11)$$

$R_l^2$  also represents the time ratio for a fluid to flow a distance  $L$  in the horizontal direction to the distance  $H$  in the vertical direction with the same potential difference across the distance.

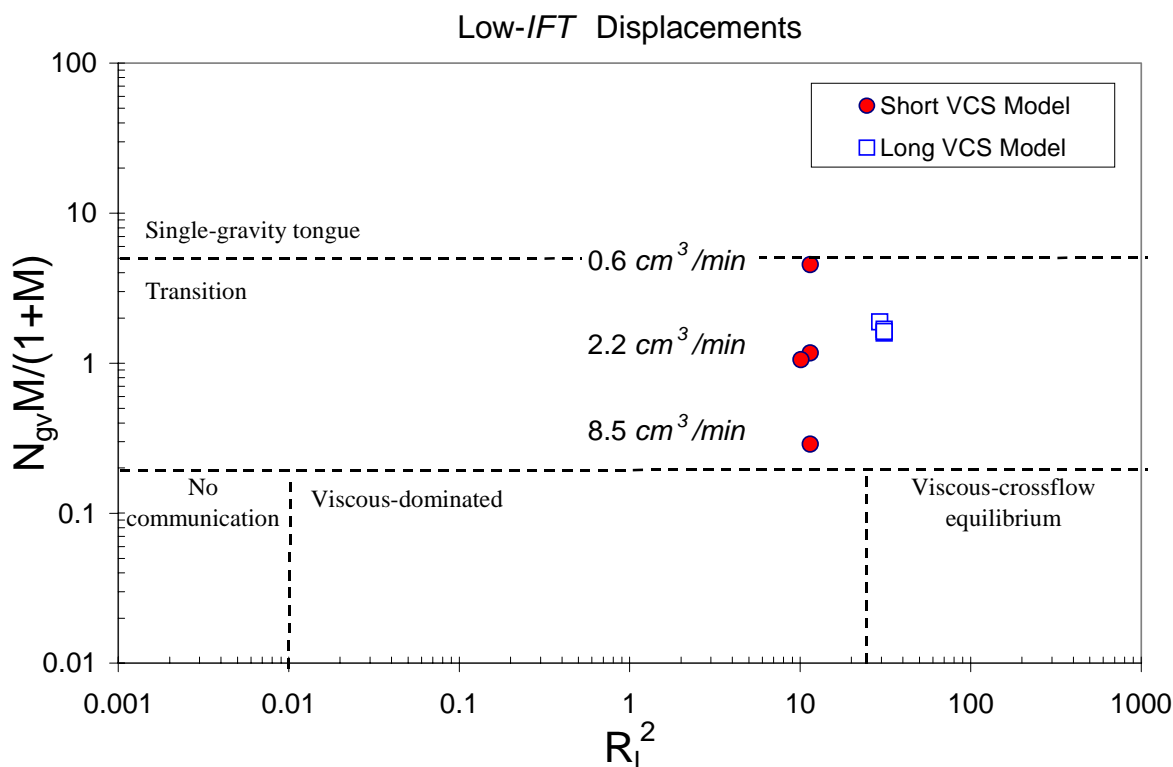


Fig. 5.9: Flow regions in low-IFT vertical cross section (VCS) displacements.

According to this plot, all displacements with VCS glass-bead models lie in the transition region, depending on the flow rate of the displacement. So, the effect of gravity increases in the slower displacements. We used two glass-bead models: one was a short model that gave a smaller  $R_1^2$  value of about 11.5 and the other was a long model that gave a higher  $R_1^2$  value of about 31. Displacements with the longer model had slightly higher gravity numbers at the same flow rate of  $2.2 \text{ cm}^3/\text{min}$ , which shows that the longer models are affected by gravity forces more than the shorter ones. Inverting the model, which means that the orientation of high- and low-permeability layers was changed, also did not affect the condition of crossflow effects.

We did not calculate any gravity numbers for gravity-stabilized displacements, assuming that they had almost negligible gravity effect. However, this assumption is not strictly satisfied for the vertical displacements, where the density difference of the fluids in the fast and slow layers includes gravity effects on the displacement front. In the near-miscible displacements like those described here, the fluids with lower IFT also have a low density difference, which in turn makes the effects of gravity on crossflow small. Thus, we expect in our experiments that the low-IFT displacements had flows dominated by viscous forces. However, this situation might be different for miscible displacements in similar layered systems, because the density difference of fluids might be higher. This will be discussed later in detail.

Fig. 5.10 is a plot of modified capillary number versus  $R_l^2$ . It indicates that our high-IFT gravity-reduced immiscible displacements are definitely in the capillary-dominated region. The highest value of capillary number represents the experiment with the vertical displacement and the slowest flow rate. All experiments were performed in short glass bead models. Moderate variations in the horizontal-axis result from the dimensions of various glass-bead models. The low-IFT displacements done in the similar short models are found to be in the viscous-dominated regions. The higher flow rates cause the larger viscous effects. Any IFT value between 0.024 and 38.1  $mN/m$  would bring the displacement into the capillary-viscous transition zone.

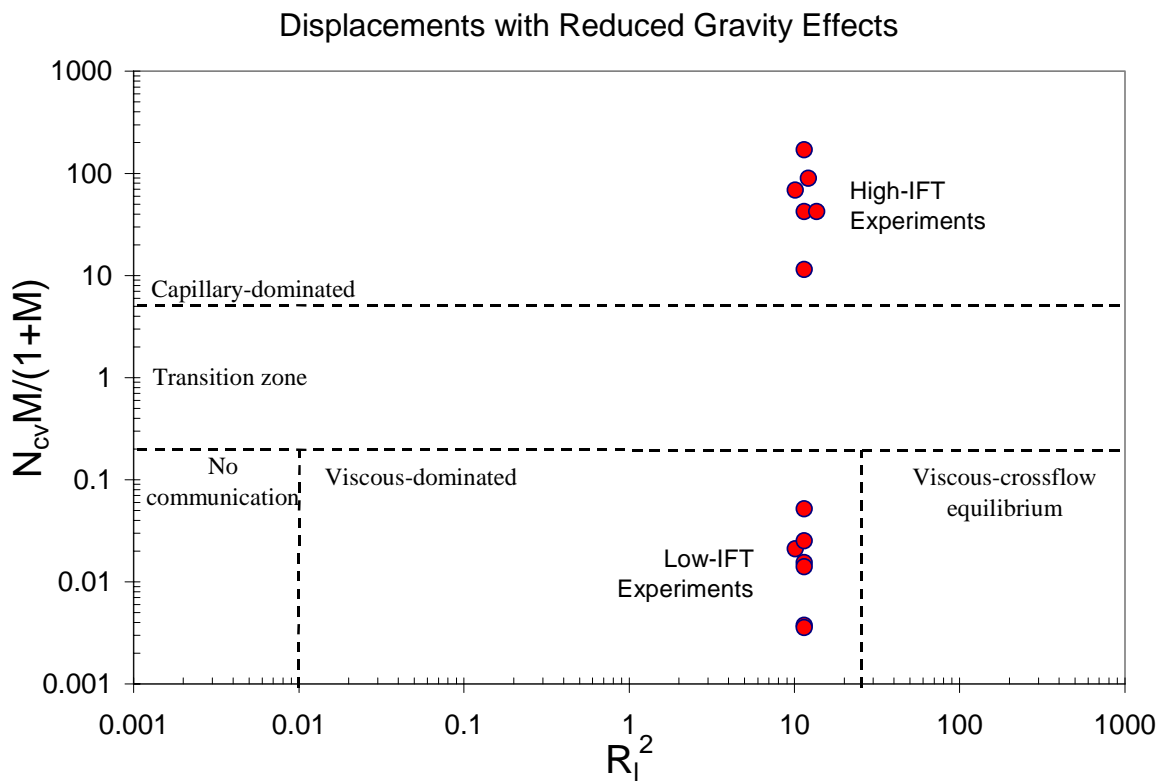


Fig. 5.10: Flow regions in reduced gravity displacements (see Fig. 5.3a,b).

Fig. 5.11 shows the Bond number, a ratio of gravity forces to the capillary forces, for the VCS displacements with gravity effects. In the figure we only present the displacements at a constant flow rate of about 2.2  $cm^3/min$ . The displacements with the longer model are indicated by a higher  $R_l^2$ -value. The figure shows that the flow in the high-IFT VCS displacements was mainly governed by the capillary forces. All data in the gravity-dominated region represent the low-IFT displacements in VCS setups depicted in Fig. 5.3c-d.

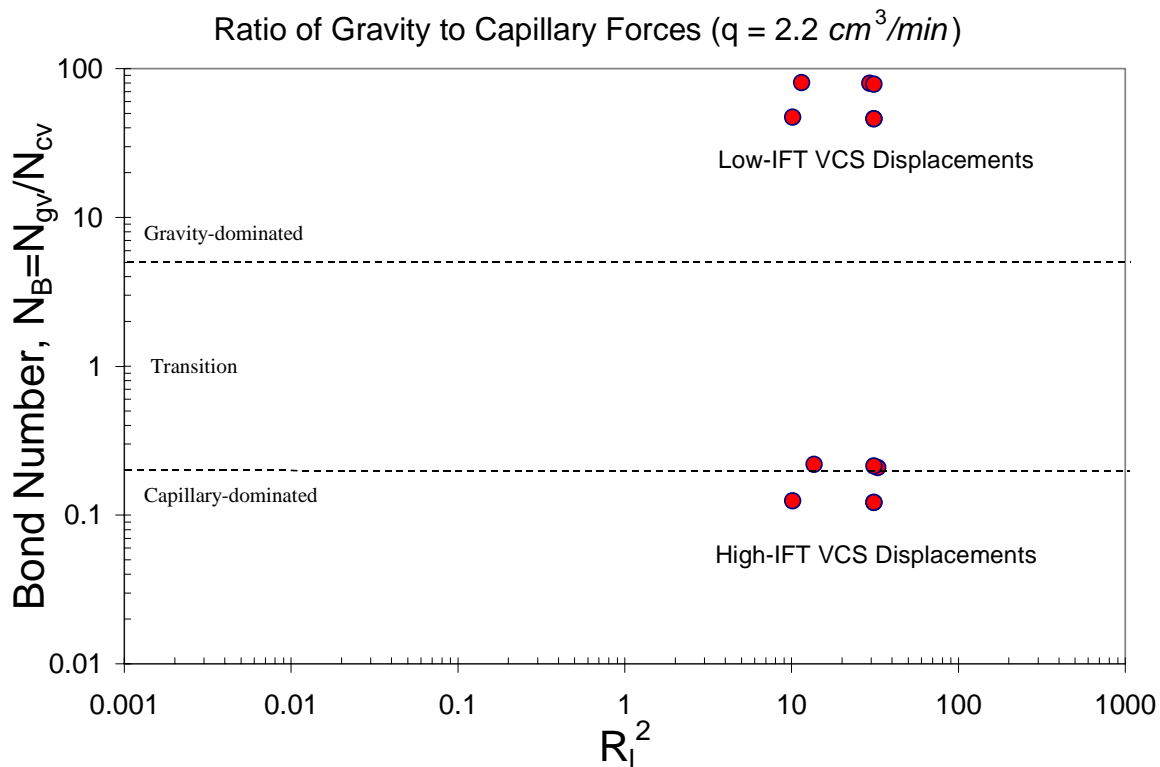


Fig. 5.11: Flow regions in terms of Bond number.

Fig. 5.11 does not delineate the effects of viscous forces, especially in the transition zone. In this region, the capillary or gravity numbers can be smaller, but greater than one another relatively, while viscous forces dominate the displacement. A plot of modified gravity and capillary numbers shown in Fig. 5.12 can represent this difference more clearly. Based on the boundary values given before, all three crossflow mechanisms can be clustered as shown in the figure. This plot does not include the displacements run with gravity-reduced or gravity-stabilized set-ups. It is important to note that we do not have any displacement in the capillary-dominated region. In this version displacements found in the capillary-dominated region previously (Fig. 5.10 and Fig. 5.11) shifted to the region of gravity-capillary equilibrium. Increasing flow rate shifts the displacements to the viscous-influenced regions without changing the ratio of the gravity/capillary forces, i.e., the Bond number. As shown in the figure, the high  $R_l^2$  values ( $=31$ ) increase the gravity and capillary effects in the displacements.

The displacement results presented below examine whether the general delineations of flow regions shown in Fig. 5.9 - Fig. 5.12 are reasonable for a simple flow setting. They are compared with simulation results to verify that simulations can be used to explore regions of the parameter space not tested experimentally.

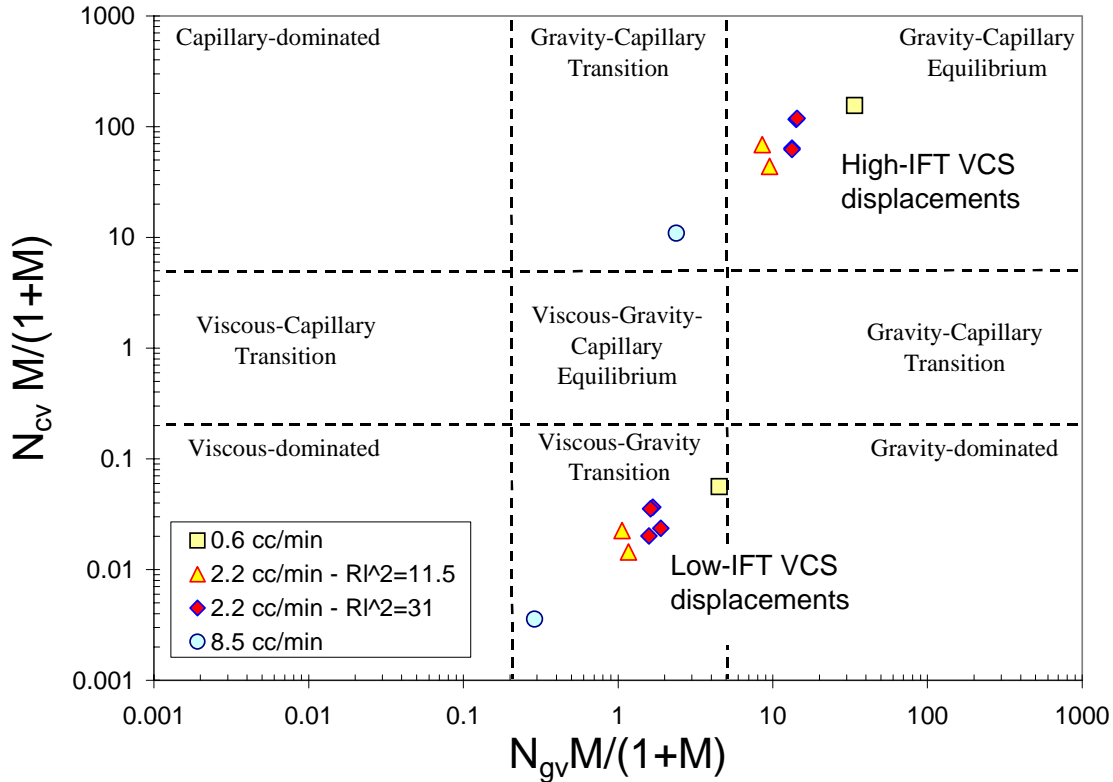


Fig. 5.12: Flow regions on the plot of gravity vs. capillary forces.

### 5.1.2.2 Favorable displacements

#### *High-IFT Vertical Displacements (Experiments #1, 3, and 7)*

A significant cause of mixing in immiscible displacements is capillary imbibition. In the displacements with high-IFT fluid systems we can see the capillary imbibition clearly. In this section, we discuss the results of favorable, immiscible, imbibition displacements that were run with an experimental setup depicted in Fig. 5.3a. We employed vertical displacements with the flow rates of 0.6, 2.2, and 8.5  $cm^3/min$ .

All three displacements had capillary numbers that are greater than unity, and the experimental results show that the flow mechanism controlling the sweep efficiency was clearly capillary-dominated. However, the displacement profiles shown in Fig. 5.13 show that the effects of capillary forces on the flow decrease dramatically as the flow rate is increased. The images show the  $H_2O$ -rich phase (red) displacing the  $IC_8$ -rich phase (light green) with no irreducible water in the porous system. In the first set of images at PVI= 0.19, there is a clear capillary interaction to be seen at the interface between the layers. At the slow flow rate, the displacement front in the low-permeability layer is faster than that in the high-permeability layer because of longitudinal capillary imbibition. The front looks like a tongue along the interface. The pressure profiles along the porous system are depicted approximately in

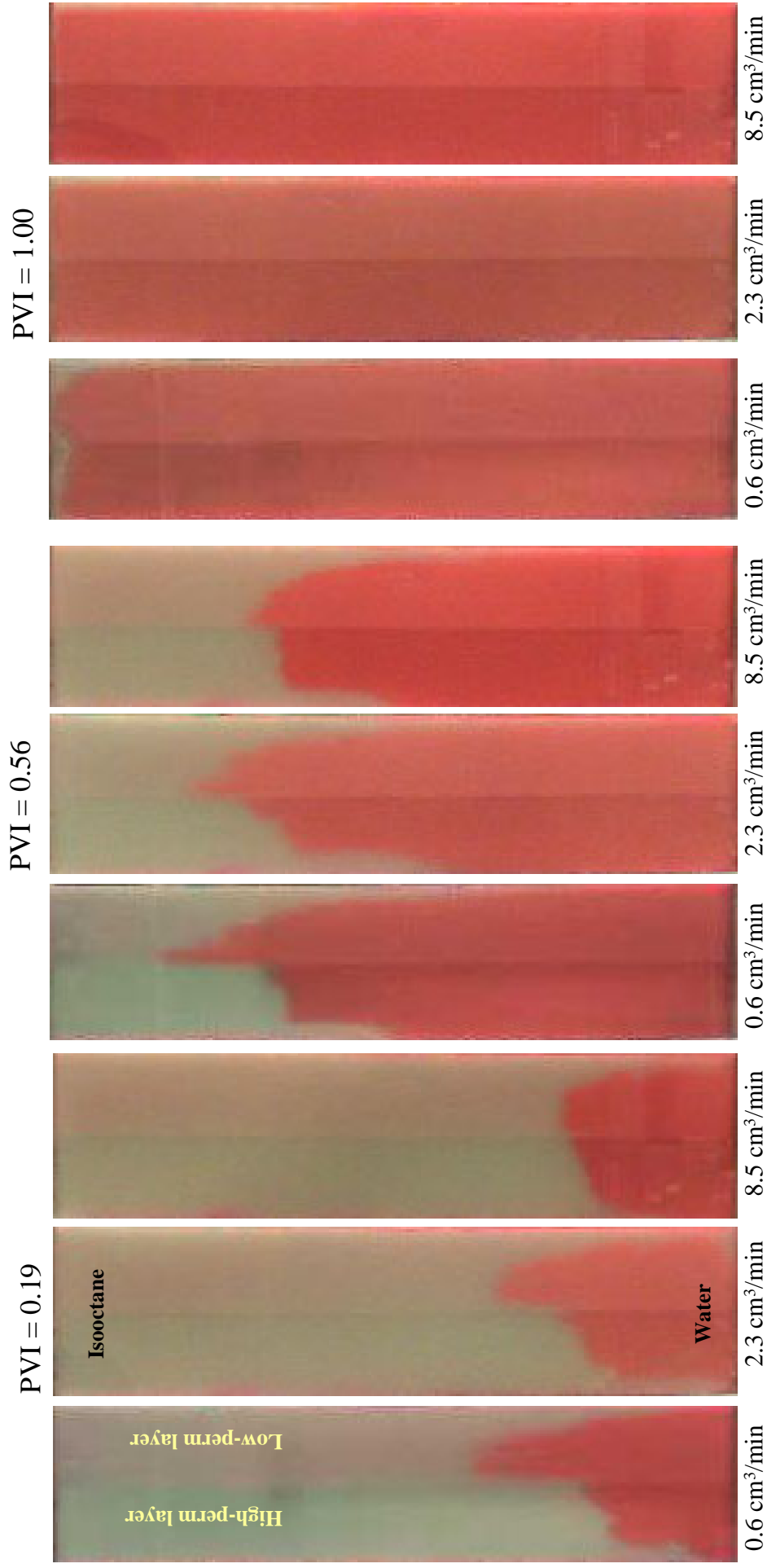


Fig. 5.13: Displacement profiles of high-IFT displacements with reduced gravity effects (Exps. #1, 3, and 7).

Fig. 5.14. At the trailing edge of the displacement, the pressure in the high-permeability layer is higher than that in the low-permeability layer because of capillary effects. Consequently, the injected phase cannot crossflow into the high-permeability layer. The sweep efficiency, therefore, is lower than at the faster velocities, where longitudinal capillary imbibition is too slow to create a leading tongue in the low-permeability layer. If the displacement had been miscible or submiscible, we would have observed faster flow in the high-permeability layer and viscous crossflow at the interface. As the flow rate is increased by a factor of four, the front in the low-permeability layer slows down, and the front in the high-permeability layer moves faster, which indicates that the effects of viscous forces increase in magnitude compared to the effects of the capillary forces. The leading edge of the displacement front is still tongue-like but smaller. As the flow rate is increased one more time by a factor of four, the displacement fronts in both layers stabilize as can be seen from Fig. 5.13. The capillary number still suggests that capillary forces can dominate the flow, but a capillary-viscous equilibrium can also be interpreted from that image. Compared to previous two images, better sweep efficiency can be seen in this case. At later stages of the displacement, for example at  $PVI = 0.56$ , similar displacement profiles were obtained for the relevant flow rates.

Fig. 5.15 and Fig. 5.16 show a comparison of experimental and simulation saturation distributions and recovery data. Note that the color scales in the simulation and the displacement were not the same, so the colors should be taken only as an indication of areas of each porous medium invaded. The images taken during the experiment show very sharp saturation distributions. We observed significant boundary effects on both sides of the experimental displacements. The simulation is affected by numerical diffusion, especially where capillary forces strongly dominate the displacement. In general, the simulations reproduce the observations, though they appear to show faster invasion of the low-permeability layer and slower invasion of the high-permeability layer.

Fig. 5.16 compares the production and pressure profiles for the experiments and corresponding simulation. Compared to capillary pressure data given in Fig. 5.7, we see that the measured pressure drop along the core was close to the capillary pressure. In general, the simulation results agreed very well with the production profiles, though the pressure data did not agree well. The simulated pressure is the difference between the block pressures at the first and last blocks in the vertical direction. The experimental pressure was it measured at the entrance outside the porous model. The pressure drop that occurred in the tubings before and after the glass bead model due to the viscous flow (0.01-0.3  $kPa$  depending on the flow rate and viscosity of the injected fluid) was excluded from the overall measured pressure drop. This could result in some differences in the simulated and measured pressures. Especially at the situations where capillary forces were strongly dominant, the simulation predictions for the pressure drop are far from the error limits of experimental data. As the effect of capillary forces decreased (Exp #7 in Fig. 5.15), the simulator gave better predictions for the pressure drop.

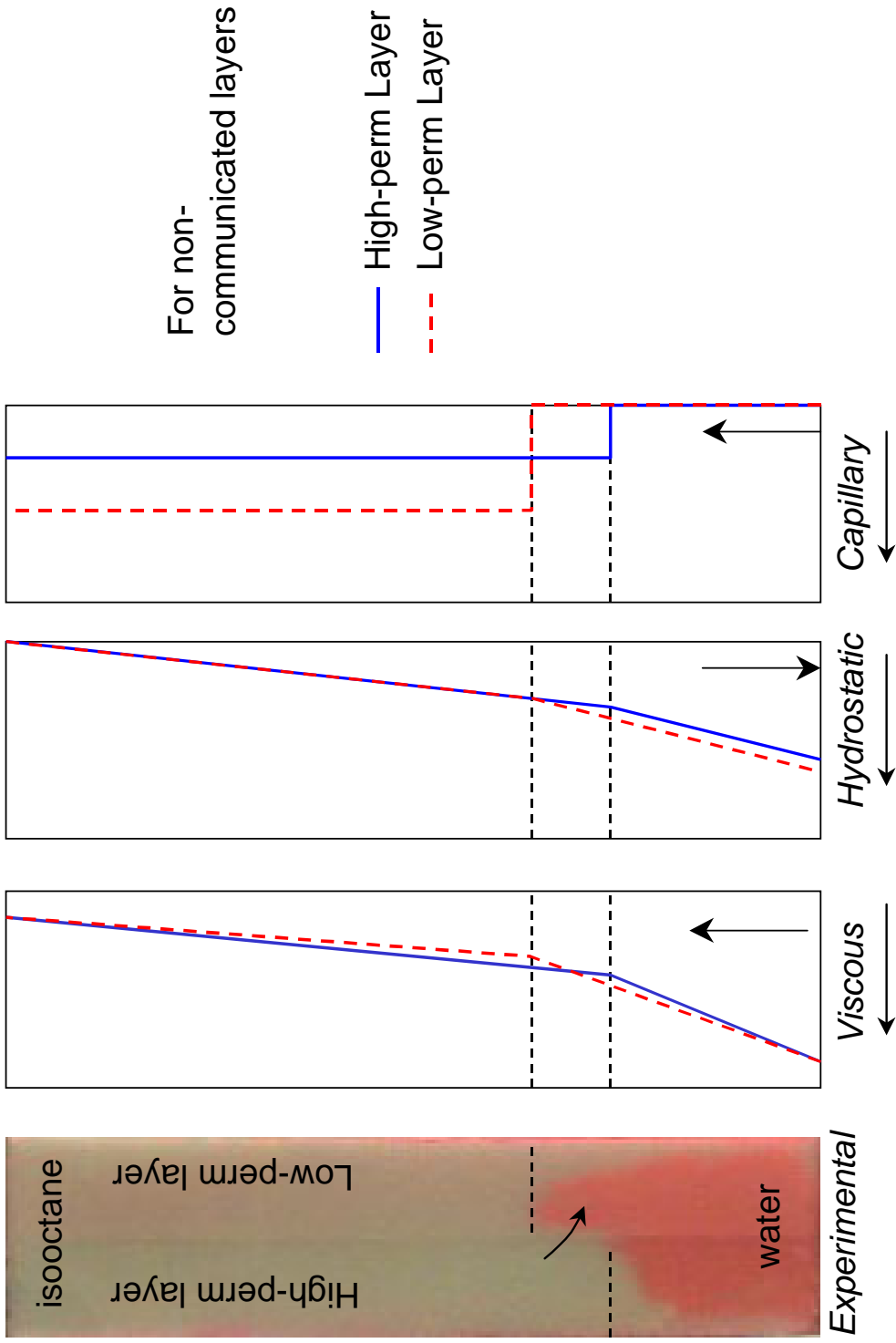


Fig. 5.14: Approximate pressure profiles along the porous system.

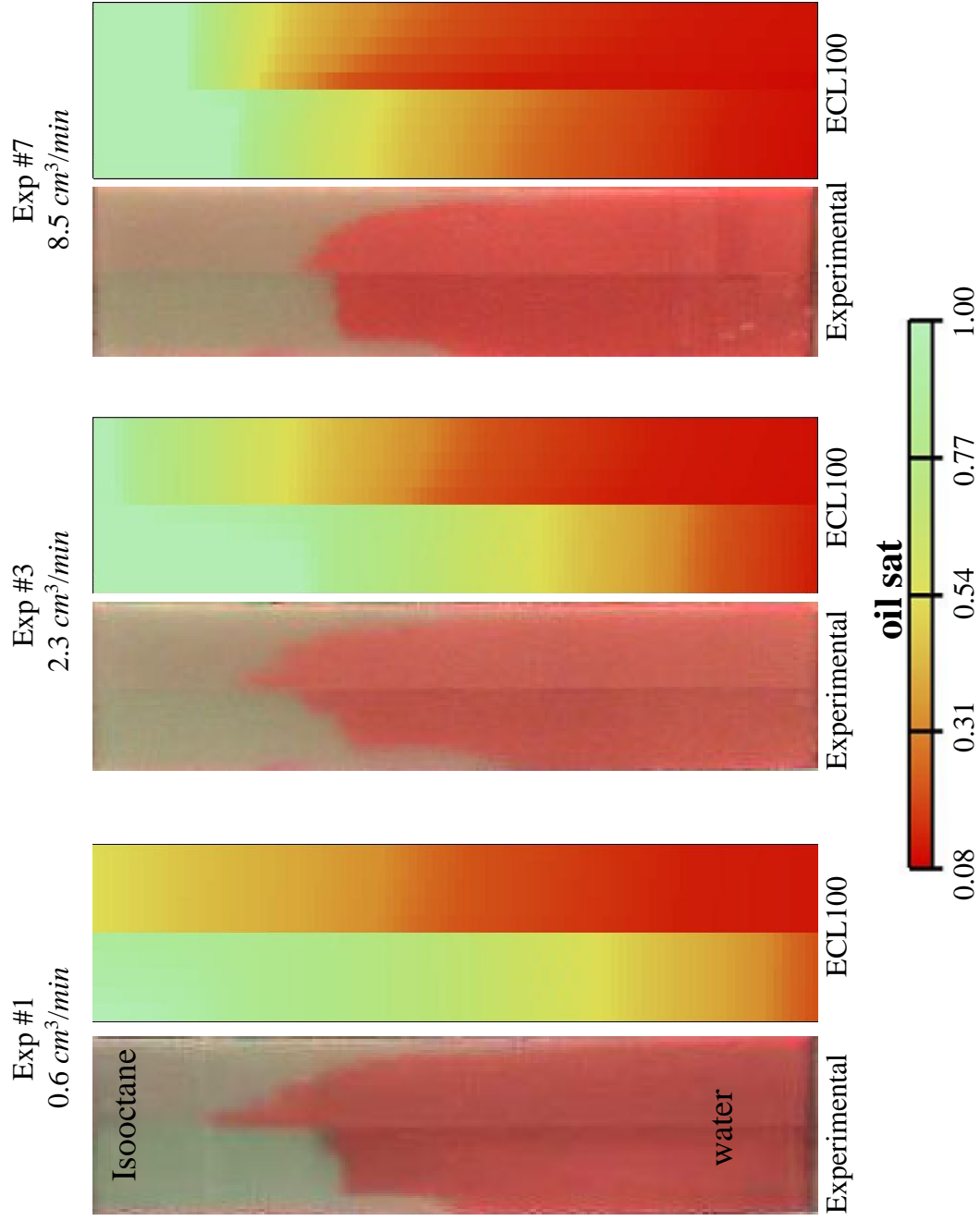


Fig. 5.15: Comparison of experimental and simulation saturation profiles at PVI = 0.56.

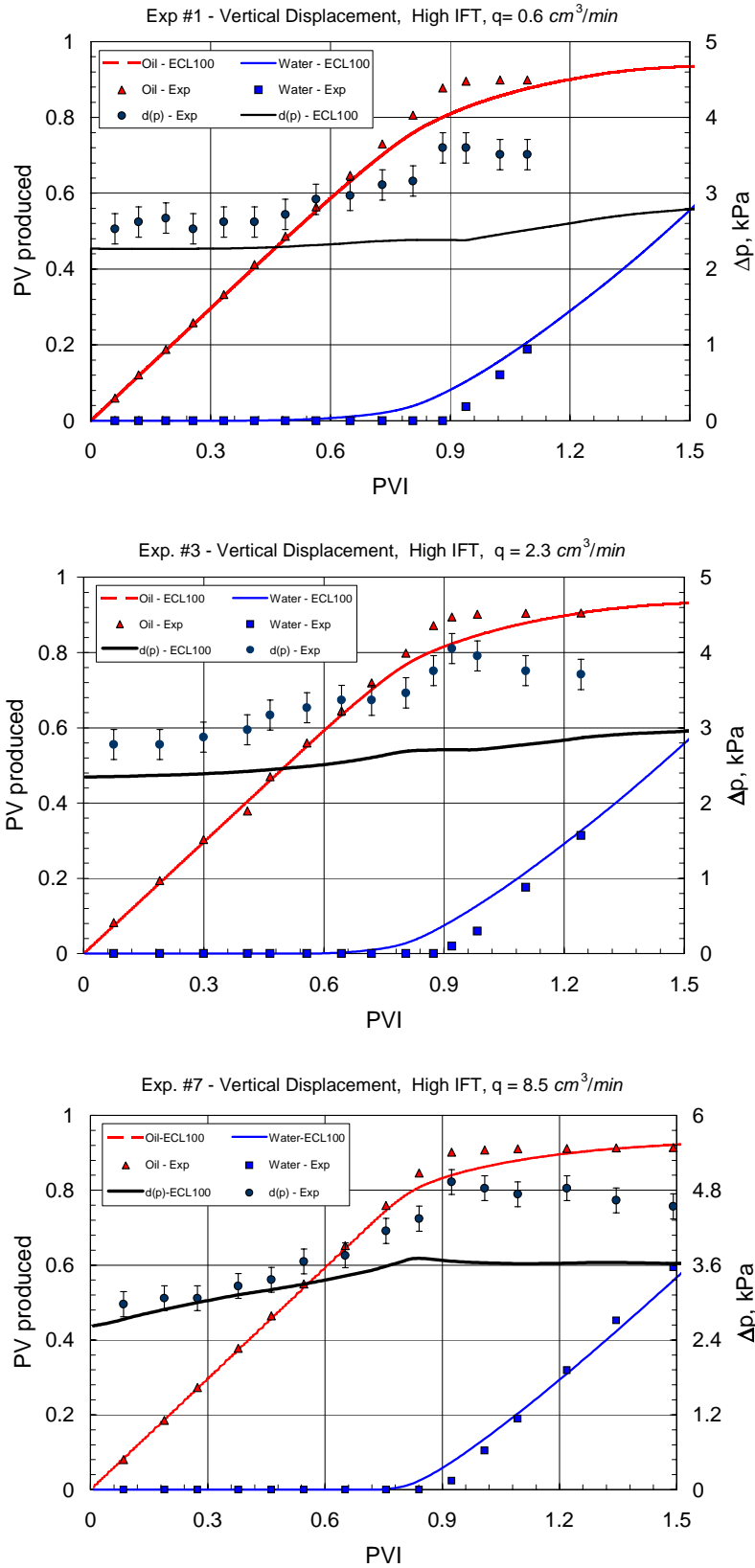


Fig. 5.16: Production and pressure profiles (High IFT and reduced gravity effects).

*High-IFT Horizontal Displacement (Experiment #9)*

In the vertical experiments, we eliminated most of the effects of gravity, but the difference between locations of the fronts in the fast and slow layers still caused to some effects of hydrostatic head on the crossflow. For comparison purposes, we employed imbibition flooding in a setup shown in Fig. 5.3b to eliminate the effects of gravity completely. Only one experiment with the flow rate of  $2.2 \text{ cm}^3/\text{min}$  was performed.

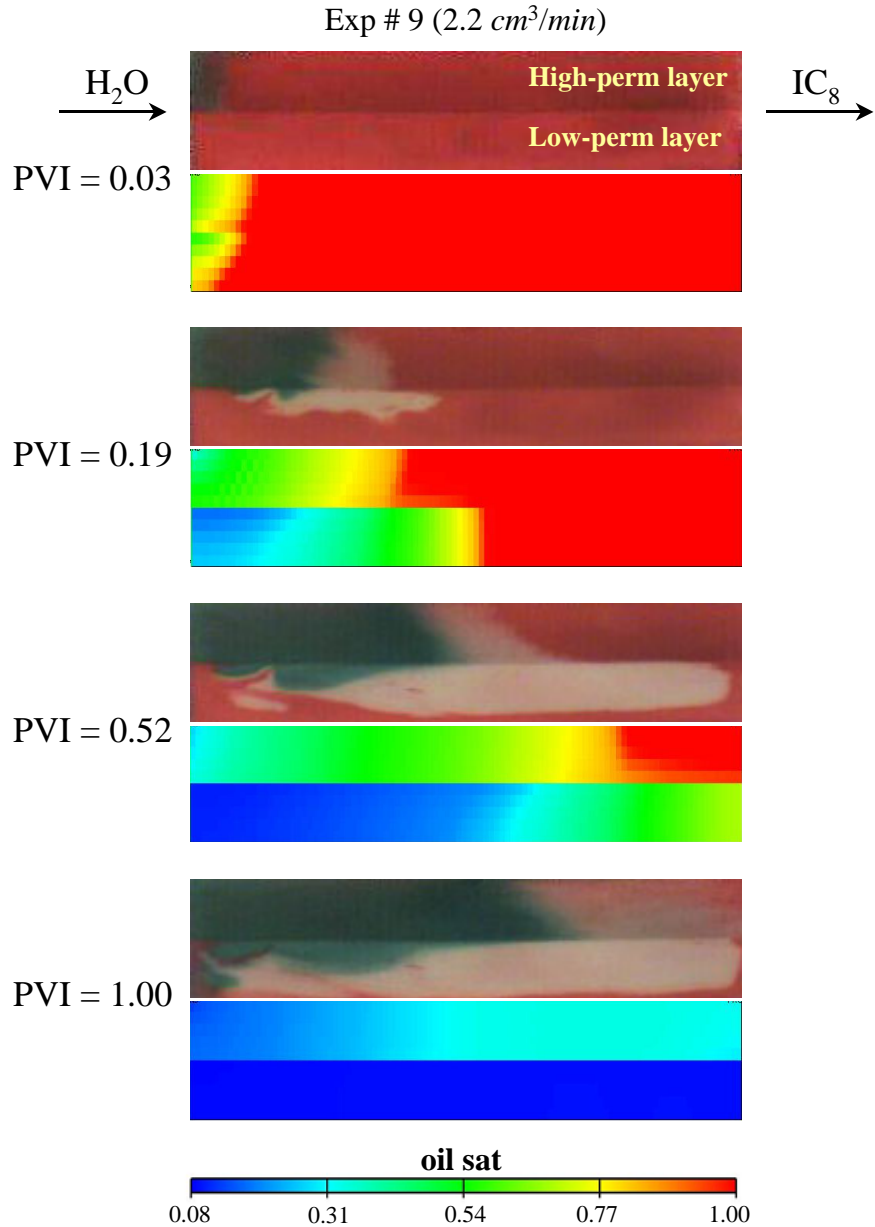


Fig. 5.17: Experimental and simulation displacement profiles for Exp. #9.

Fig. 5.17 shows the experimental and simulation saturation distributions through the porous system at certain PVI. At early times of the displacement, the water first entered the high-permeability layer and then transferred to the low-permeability layer. This can be explained by the fact that, at the interface of injection port, the pressure in the high-permeability layer was lower than that in the low-permeability layer. The flow was subsequently dominated by capillary imbibition, and consequently, the water reached the outlet first in the low-permeability layer. Evidently, there was also some adsorption of the dye from the H<sub>2</sub>O-rich phase as well.

The simulation also shows that the water first entered the high-permeability layer, then entered the low-permeability layer as a result of capillary imbibition. In the vertical displacements, we also observed similar development of the displacement front, but the sweep area in the high-permeability layer was much smaller than that observed here. This is reasonable because of the different direction of gravity forces in both experiments. This difference also makes the vertical setup more efficient in terms of ultimate recovery. Recovery and pressure data for this experiment obtained by the simulation are shown in Fig. 5.18. The recovery of oil is less than that obtained with vertical displacements. Moreover, the simulation predicts the breakthrough time of Exp. #9 correctly. The recovery data match excellent although there is some mismatch with pressure data. The pressure profile along the core should be similar to that shown in Fig. 5.14 except for the hydrostatic pressure.

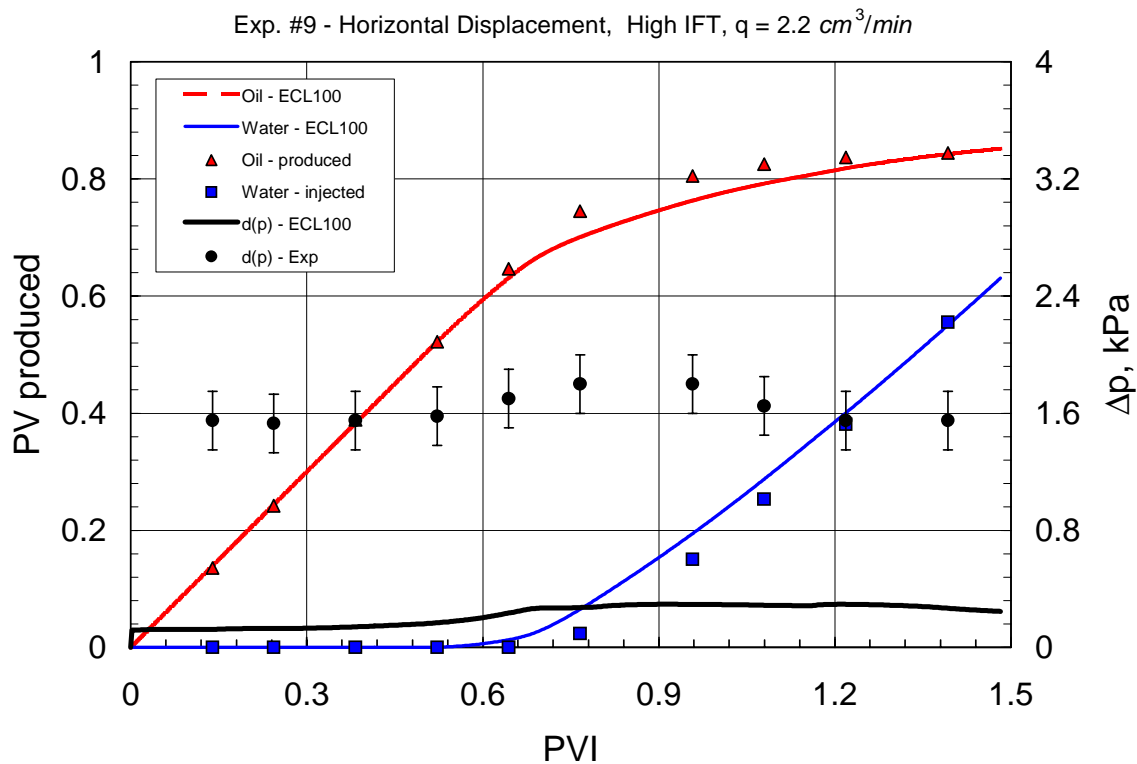


Fig. 5.18: Production and pressure profiles for Exp. #9.

### *High-IFT VCS Displacements (Experiments #13, 15, 19, 21, and 25)*

In this section, we discuss the results of the experiments that investigate the combined effects of gravity, viscous, and capillary forces on the displacement performance. The effects of gravity were included in these experiments by the way that the glass bead model was oriented as vertical cross section shown in Fig. 5.3c-d.

Fig. 5.19 shows the experimental and simulation saturation maps for different flow rates. Here again, the water first entered the high-permeability layer. But, the sweep area in the high-permeability layer was smaller for the low-rate displacement due to gravity effects, which aided vertical flow of the water. Later the capillarity forced the water to enter the low-permeability layer. As can be seen from the experiments, capillary forces strongly affected the displacement at the slower flow rate, i.e.  $0.6 \text{ cm}^3/\text{min}$ , which resulted in an early breakthrough in the low-permeability layer. At breakthrough, very little  $\text{IC}_8$  was produced from the high-permeability layer, resulting in a very poor sweep efficiency. As the flow rate was increased by a factor of four, capillary forces still dominated flow, but in this case we had later breakthrough in the low-permeability layer and better sweep area in the high-permeability layer. When the flow rate was increased further by a factor of about four, we observed slow capillary imbibition in the low-permeability layer and a faster front in the high-permeability layer.

Fig. 5.20 shows a comparison of experimental recovery and pressure data with those obtained by simulation. Although a good match between recoveries was achieved, the simulation and experimental pressure data did not agree well.

To see the effect of  $L/H$  ratio of the glass bead models on the displacements, we also performed additional high-IFT VCS displacements in two long models. One of the models had an orientation with the high-permeability layer at the bottom. The experimental and simulation images and recovery data are shown in Fig. 5.21 and Fig. 5.22, respectively.

In terms of capillary effects, displacement profiles similar to those obtained in the short models were also observed in the long models. However, we observed a weak gravity-tongue in the long model, especially at the later stage of the displacement. In the displacement with the inverted model, the water initially flowed in the high-permeability layer, longer than that in the original model, which enhanced the sweep efficiency in the high-permeability layer. But, at the later stage of the flooding, the capillary imbibition dominated, forcing the water to flow in the low-permeability layer.

We observed higher ultimate recovery with the long model than with the short model, which is consistent with the idea that gravity effects contributed to the sweep efficiency. But, the simulation results are almost the same. The recovery with the inverted model was lower than that observed for the model with the high permeability layer at the top. This can be explained by the observation that gravity and capillary forces opposed each other in the displacements with the high-permeability layer at the bottom.

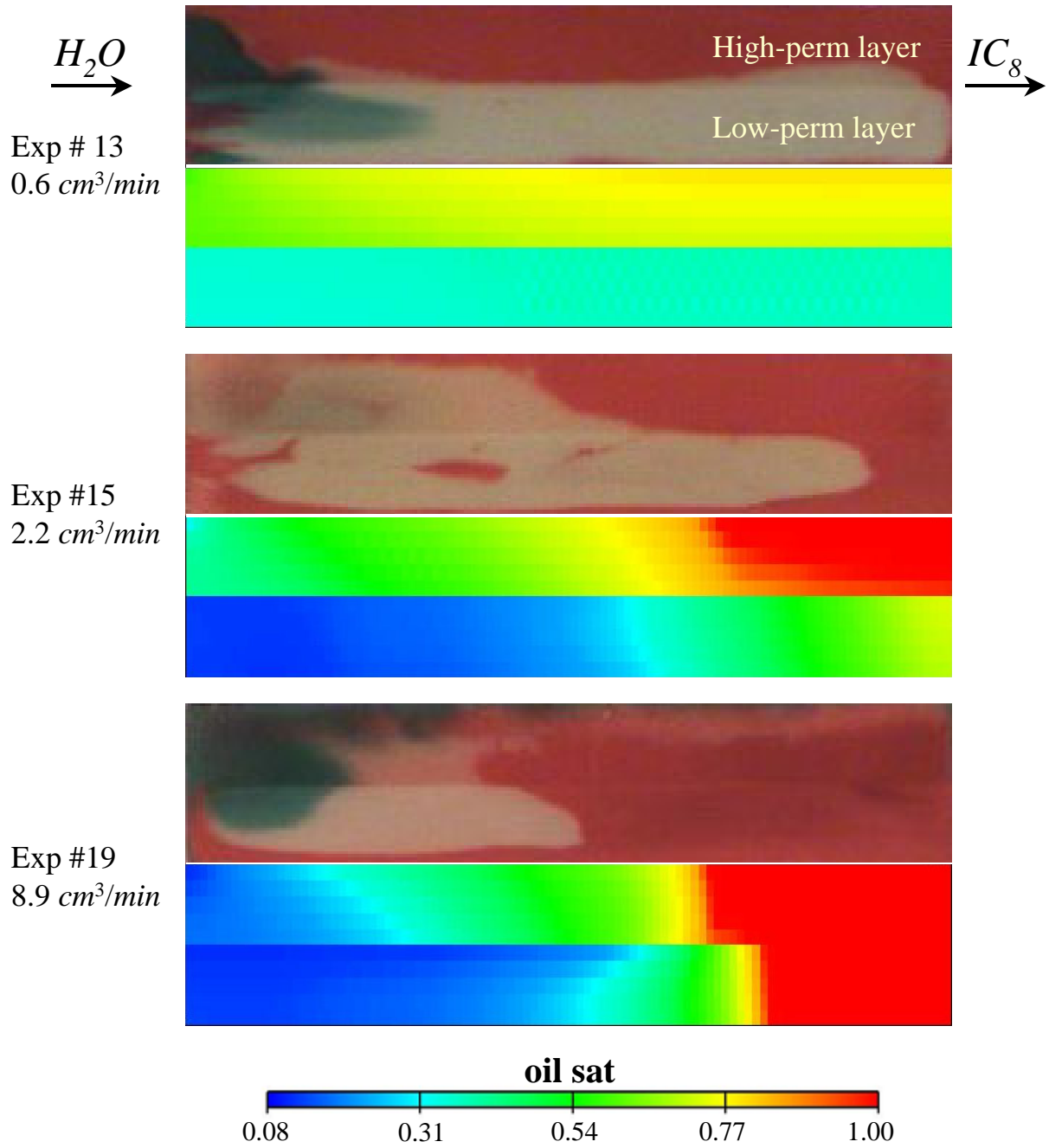


Fig. 5.19: Experimental and simulation saturation maps of high IFT displacements with gravity effects at PVI=0.49.

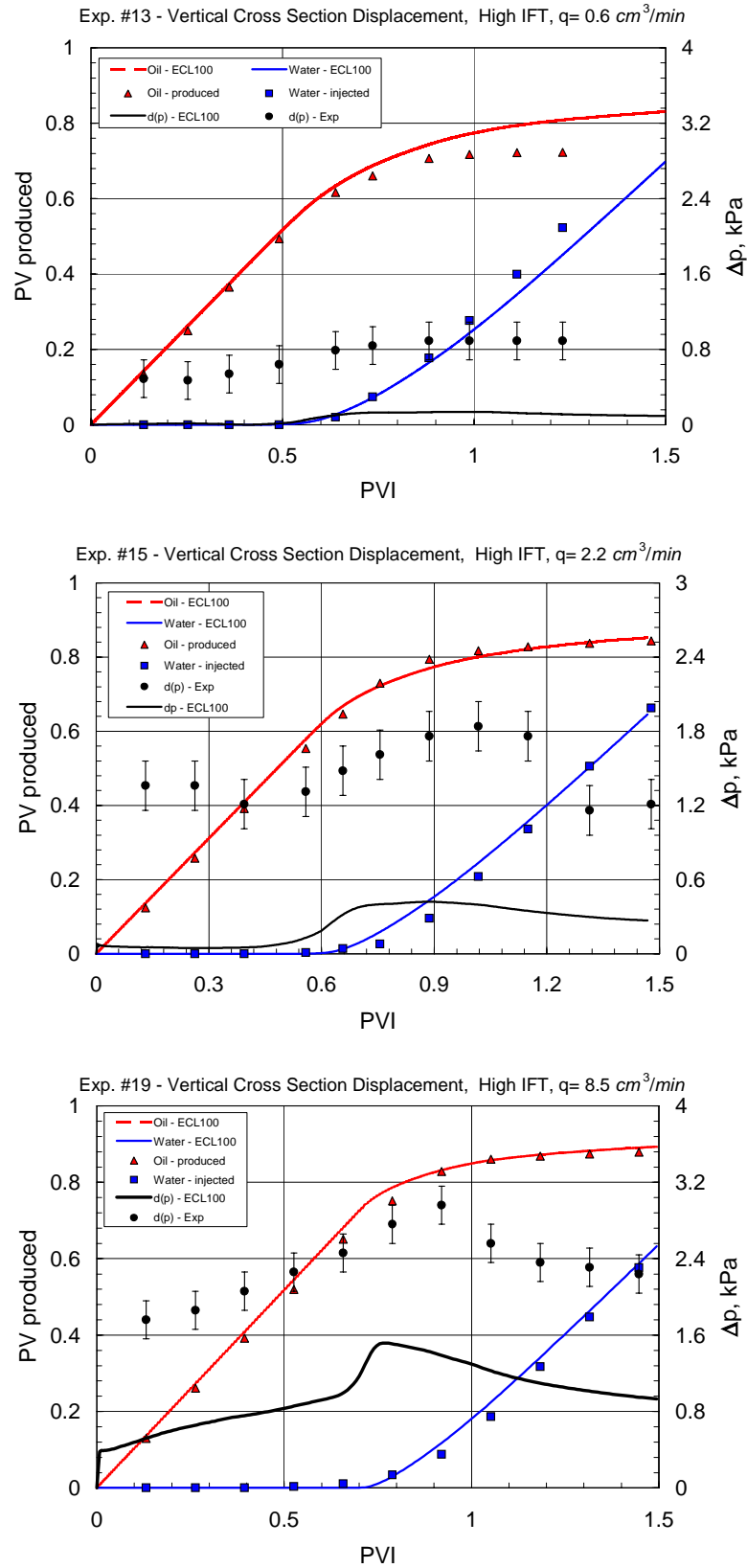
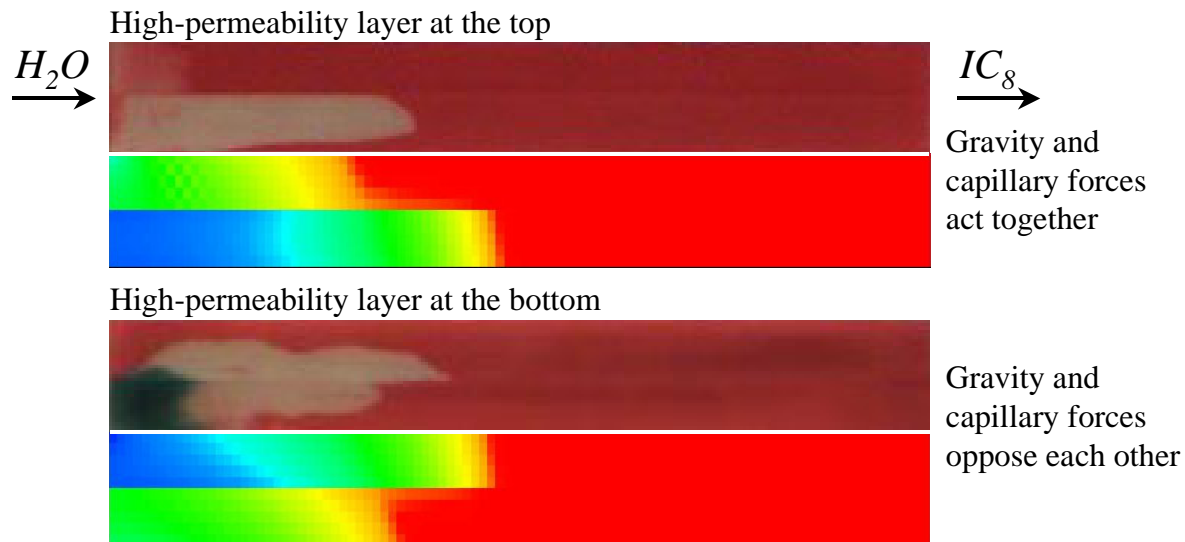


Fig. 5.20: Production and pressure profiles of high-IFT displacements with gravity effects.

Exp. #21 & 25 ( $2.2 \text{ cm}^3/\text{min}$ )

PVI = 0.20



PVI = 0.50

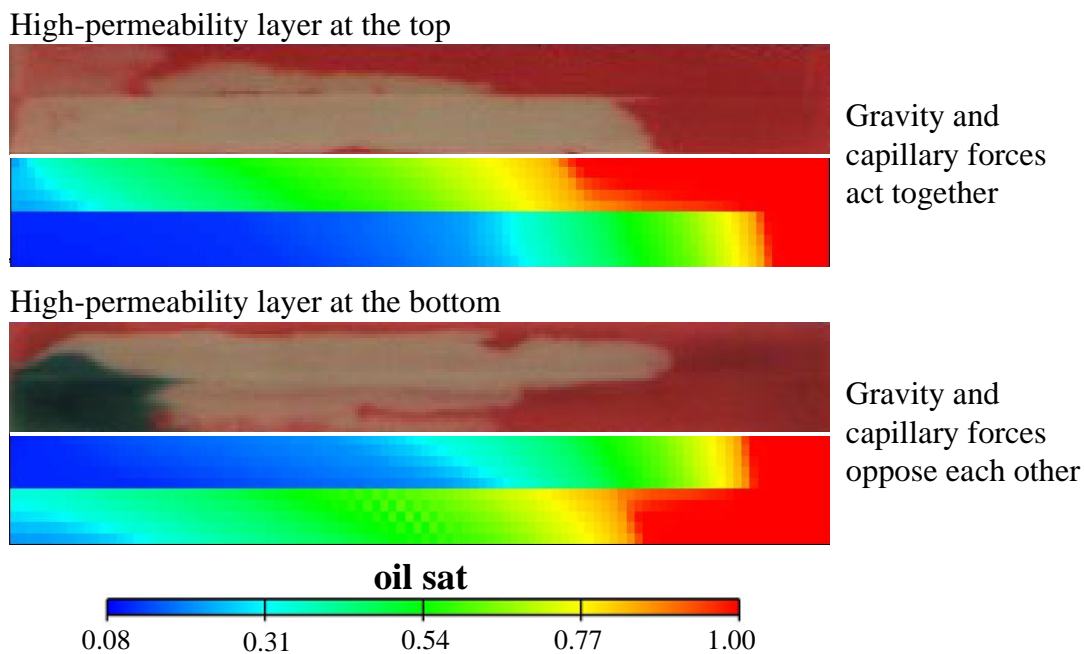


Fig. 5.21: Experimental and simulation displacement profiles of high-IFT displacement with gravity effects.

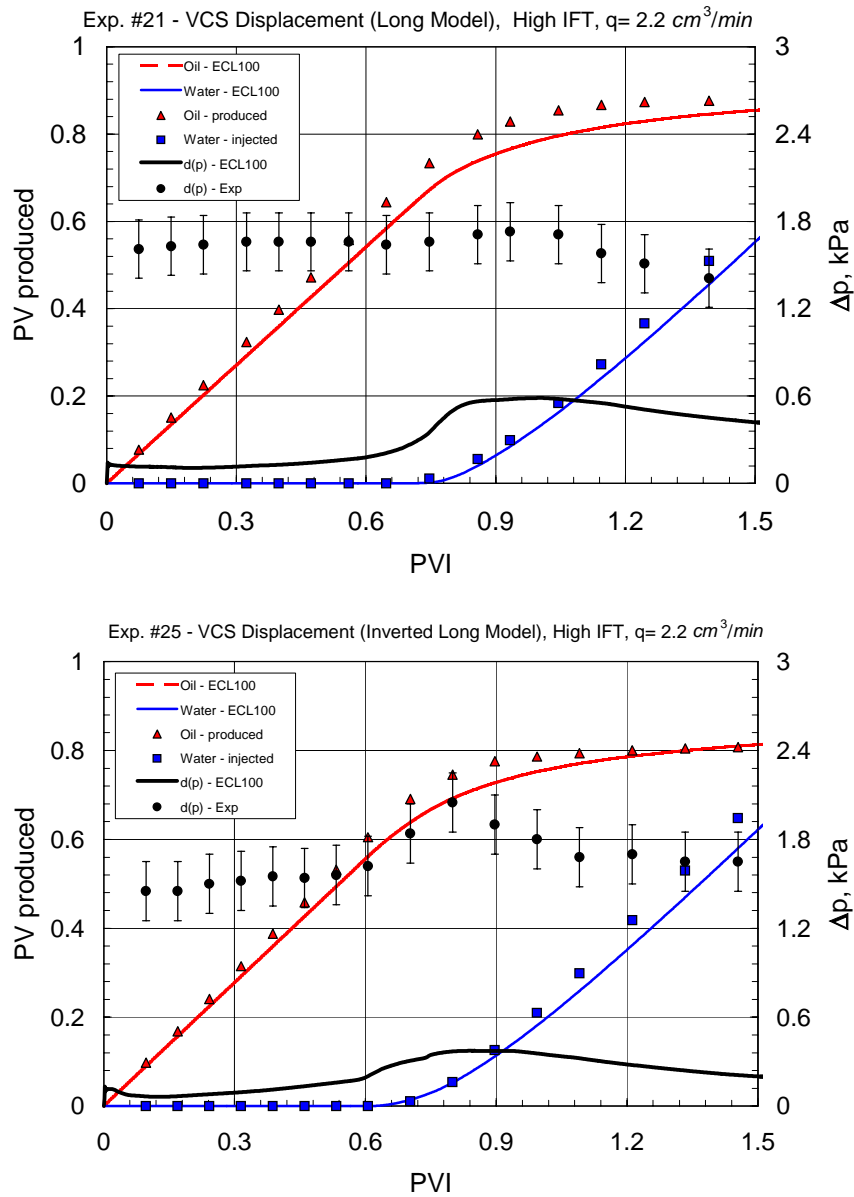


Fig. 5.22: Production and pressure profiles of high-IFT displacements with gravity effects in long VCS models.

For experiments, we previously determined that the displacements were in the capillary-gravity equilibrium region (see Fig. 5.12). But, we did not observe a large effect of gravity on the experimental images of short models shown in Fig. 5.19 even though the simulation results showed some gravity effects. Compared to the experimental saturation distribution in Exp. #9 for  $\text{PVI}=0.52$  (see Fig. 5.17), the saturation distribution in Exp. #15 (Fig. 5.19) is very similar, showing that the effects of gravity on the displacement are small. However, the experiments performed with original and inverted long VCS models demonstrate that there

was definitely an effect of gravity in the displacements shown in Fig. 5.21. In the displacements with the original model, gravity and capillary forces acted together, which improved sweep area in the low permeability layer, while viscous forces opposed both of them to force the water to flow in the high-permeability layer. This made the low-permeability layer be swept efficiently, however, resulted in a very poor sweep in the high-permeability layer. But, in the displacements with the inverted model, gravity and viscous forces acted together to force the water to flow in the high-permeability layer while capillarity acted oppositely that forced the water to enter the low-permeability layer. This enhanced the swept area in the high-permeability layer, however in parallel, reduced the area in the low-permeability layer, as can be seen in Fig. 5.21.

#### *Low-IFT Vertical Displacements (Experiments #2, 4, and 8)*

In this section we discuss the experimental and simulation results that demonstrate the effects of crossflow mechanisms in near-miscible displacements. A relatively low characteristic capillary pressure because of the low-IFT (see Table 5-5) results in low capillary numbers. It is, therefore, expected that viscous forces should be dominant in this kind of displacements, which had reduced gravity effects (see Fig. 5.3a).

The images taken at different PVI values during the experiment are shown in Fig. 5.23. In this experiment, the injected H<sub>2</sub>O-rich fluid was dyed green, and the IC<sub>8</sub>-rich fluid was red. The first impression from the images is that the displacement fronts are totally different from those obtained with high-IFT fluid system. This can be explained by the fact that the three-order of magnitude reduction in IFT (from 38.1 to 0.024 *mN/m*) reduces the capillary pressure by the same magnitude.

Although we also reduced the effects of gravity by performing gravity-stabilized vertical displacements, the difference between the fronts of the fast and slow layers leads to some effect of gravity on displacement performance in such systems. To show the magnitude of this effect, we ran the simulator with different values for density differences (see Fig. 5.24). The figure shows that an increase in density difference of the phases causes the front in the fast layer to slow down, whereas it advances the slow layer. This effect results in an improved sweep of the porous medium. However, in the related experiment where the density difference was about 0.07 *g/cm<sup>3</sup>*, gravity affects on the displacement performance were small. Moreover, in two-phase submiscible displacements like ours here, the density difference between the phases scales with the IFT, which means that lower IFT values correspond to the lower density differences.

Since gravity and capillary effects were minimized by lowering IFT and employing gravity-stabilized vertical displacements, the front position in each layer is determined by viscous forces as well as the level of communication between the layers. If there is no communication between the layers, the front position in each layer may be determined from Darcy's law (Lake, 1989). However, communication between layers leads to crossflow due to the different pressure gradients in the layers driven by viscous and gravity forces. Zapata and Lake (1981) presented a theoretical analysis of viscous crossflow in layered reservoirs with

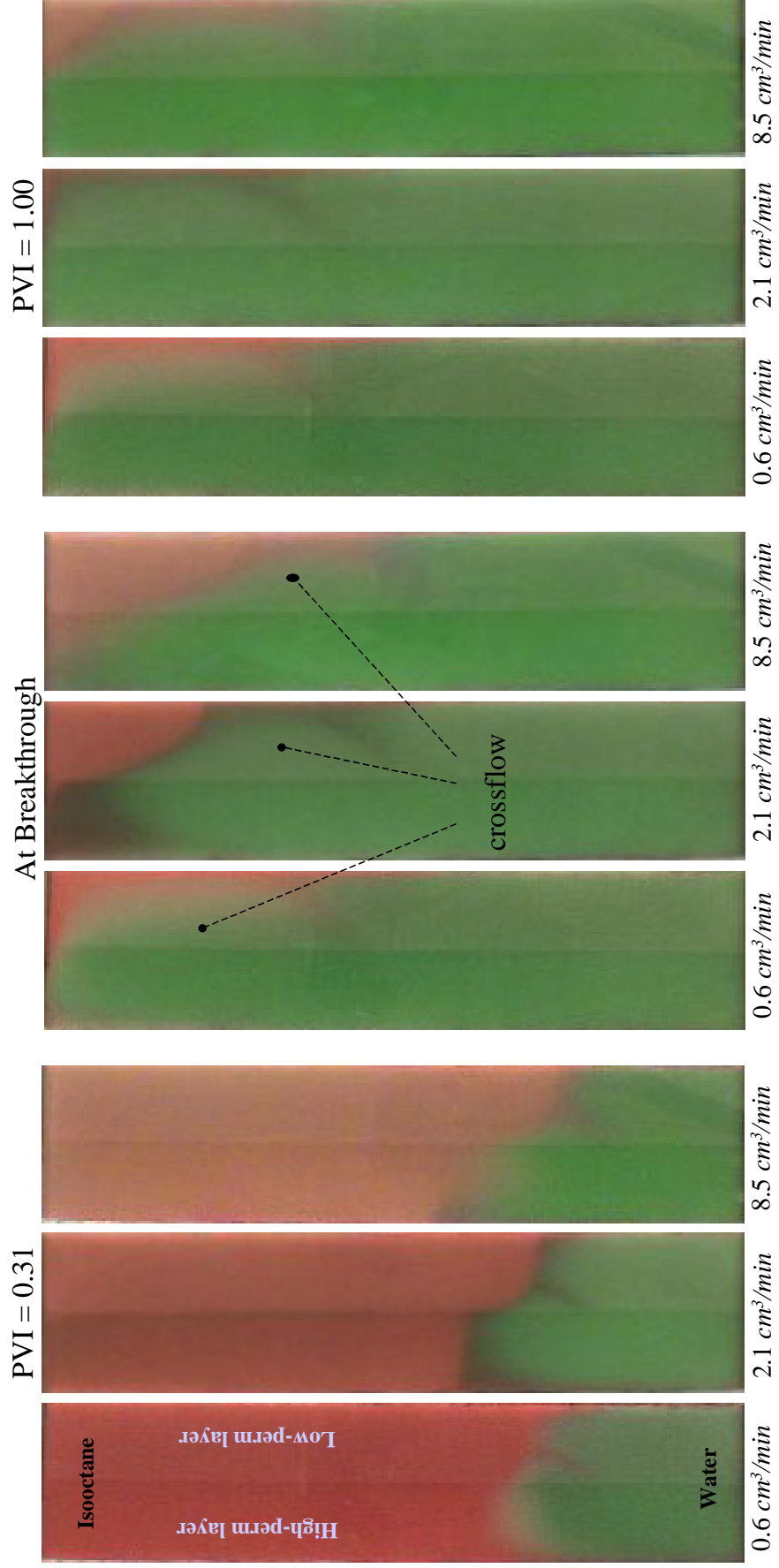


Fig. 5.23: Displacement profiles of low-IFT and reduced-gravity displacements (Exps. #2, 4, and 8).

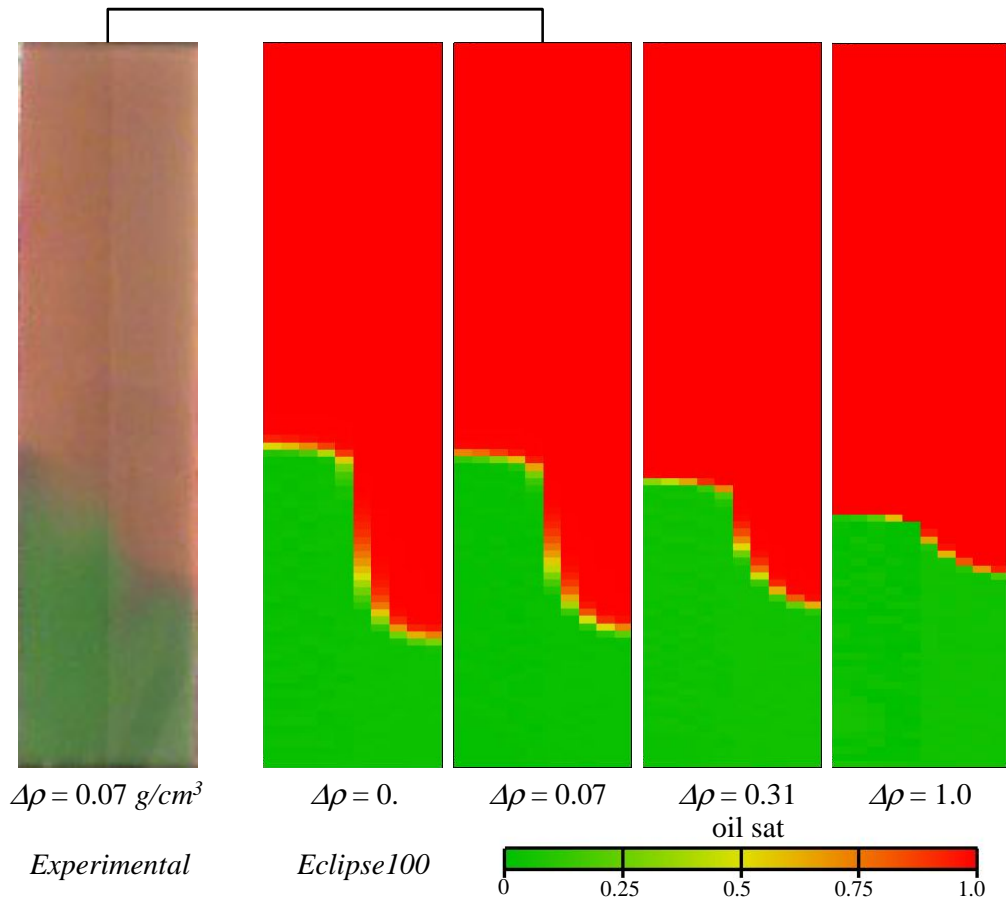


Fig. 5.24: Eclipse100 runs with different values of density difference for a low-IFT vertical displacement.

absence of capillary and gravity effects. They explained viscous crossflow in both favorable and unfavorable displacements starting from pressure profiles for two non-communicating layers. They concluded that for favorable displacements the direction of crossflow is from the low to high permeability layer at the leading water front and in the reverse direction at the trailing water front. Thus crossflow causes the leading and trailing fronts to recede and advance, respectively, over their no-crossflow positions. This, in turn, improves the vertical sweep efficiency over that of the situation without crossflow.

Fig. 5.25 shows an explanation schematic for one of the reported favorable displacements in terms of the pressure profiles. Neglecting the effects of capillary pressure (a reasonable assumption for the low IFT of  $0.024 \text{ mN/m}$ ) and assuming no communication between the layers, we can consider viscous and gravity forces to determine the pressure profile along the porous medium. The gravity forces slightly increase the rate of crossflow depending on the density difference as shown in Fig. 5.24. Applying the pressure profiles in a communicating layer system, we have two different crossflows in the system. The first one takes place at the leading front, and its direction is from the slow layer into the fast layer. The second one is the

crossflow from fast layer into the slow layer at the trailing front. The displacement profile obtained experimentally is clearly consistent with the directions of crossflow obtained from this simple analysis.

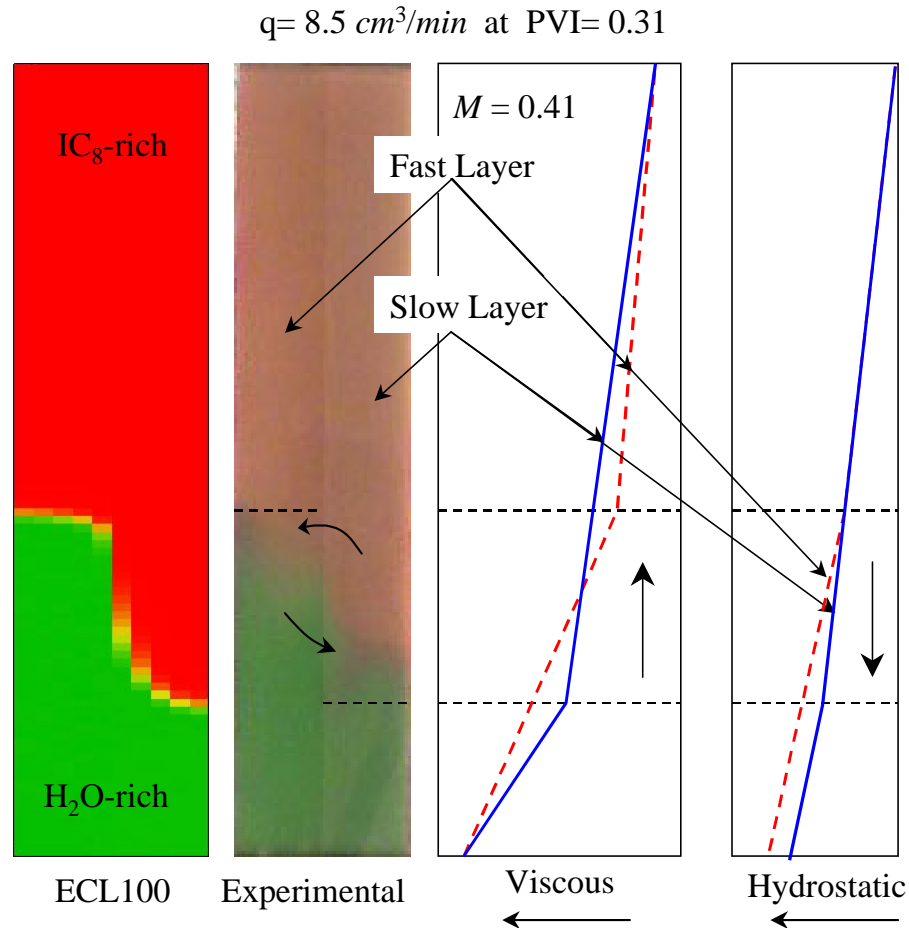


Fig. 5.25: A schematic of pressure profiles in a low-IFT vertical displacement.

It is also interesting to note that when we put the images at  $\text{PVI} = 0.31$  with those from Fig. 5.13 ( $\text{PVI} = 0.19$ ) together (Fig. 5.26), we clearly see the effects of the transitions from capillary to viscous dominated flow on the displacement profile. Capillary and viscous forces opposed each other in the displacements in a way that capillary imbibition pulled the injected water to the low-permeability whereas viscous forces drove the water into the high-permeability layer. Providing that gravity forces are small ( $N_{gv}M/(M+1) \ll 1$ ), we can argue that an equilibrium between capillary and viscous forces ( $0.2 < N_{cv}M/(M+1) < 5$ ) should result in more stabilized fronts in both layers, which in turn enhances sweep efficiency for the displacement.

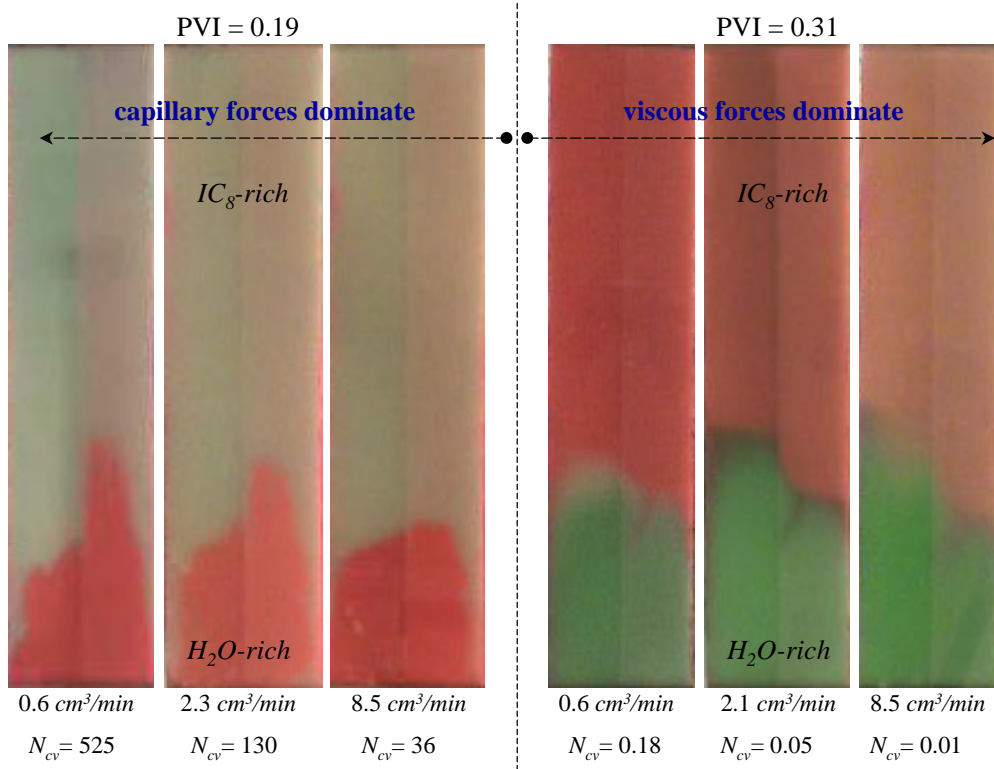


Fig. 5.26: Comparison of effects of capillary and viscous forces (Low-IFT and reduced gravity effects).

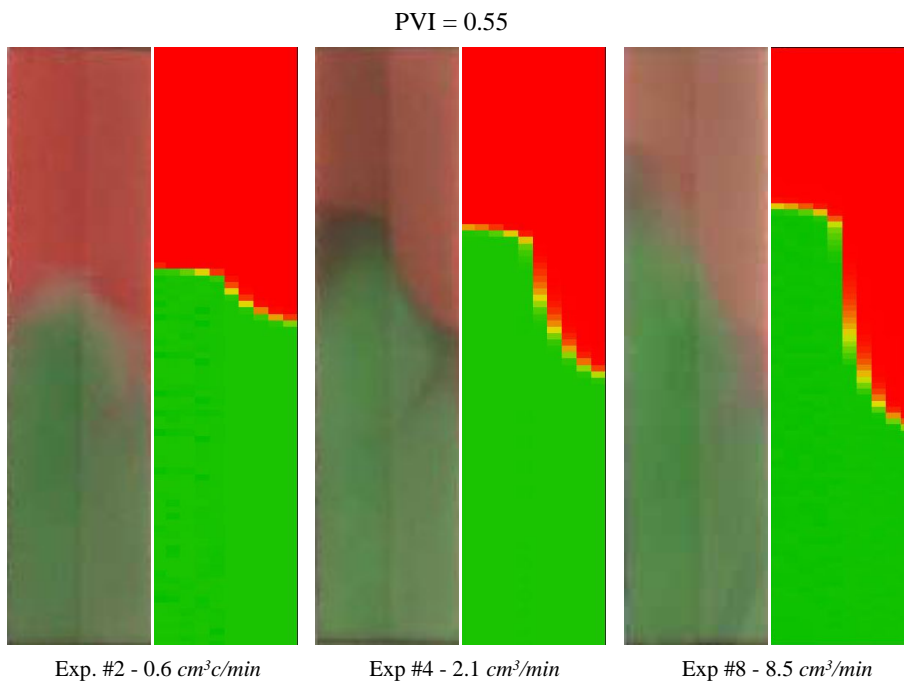


Fig. 5.27: Comparison of experimental and simulation saturation maps.

Experimental and simulation results for the saturation profiles, production and pressure drop are given in Fig. 5.27 and Fig. 5.28. Simulation predictions for the saturation distributions are very good. Because the displacements were run under the stability of viscous and gravity forces, there were no big differences obtained in the recoveries. The simulation results represent the experimental production and pressure data very well. This is mainly because IFT was low, which reduced the effects of capillary pressure.

#### *Low-IFT Horizontal Displacement (Experiment #10)*

In this experiment, we employed a low-IFT displacement in a setup shown in Fig. 5.3b to eliminate the effects of gravity. Fig. 5.29 shows experimental and simulation saturation distributions through the porous system at certain PVIs. Contrary to the situation observed in high-IFT displacements (see Fig. 5.17), the high-permeability layer is the fast layer. The flow is dominated by viscous forces, and consequently, significant viscous crossflow from the high-permeability layer into the low-permeability layer takes place due to the differences in the pressure gradients in the layers. In general, the simulation predicts saturation distributions that are similar to the experimental results. But, the shape of the crossflow area in the low-permeability layer is quite different from that predicted by the simulation.

Experimental and simulation recovery and pressure data for this experiment are shown in Fig. 5.30. The recovery and pressure data match the simulation data satisfactorily. The pressure data agree better with the simulation results than in high-IFT displacements. The saturation and recovery data are in good agreement with those of the low-IFT vertical displacements, except for the breakthrough time. The reason for that might be due to the different directions of gravity forces in both experiments.

#### *Low-IFT VCS Displacements (Experiments #14, 16, 20, 22, and 26)*

In this section, we report the results of the experiments that demonstrate the combined effects of gravity and viscous forces on the displacement performance. The low-IFT liquid system was employed, so capillary effects were small (see the low modified capillary numbers in Table 5-4). The effects of gravity were included in these experiments by the way that the glass bead model was oriented horizontally. The high-permeability layer was at the top of the model for experiments #14, 16, 20, and 22 and at the bottom of the model for experiment #26. The scaling parameters for these experiments are given in Table 5-4. Here we used favorable displacements to avoid viscous instabilities in the experiments.

Based on the criteria for the flow regions (see Table 5-1), the low-rate displacement should show the largest gravity effects. But, this effect should become weaker as the rate is increased. The experiment with the highest flow rate should be controlled by viscous forces if the estimates based on the gravity to viscous ratio are correct.

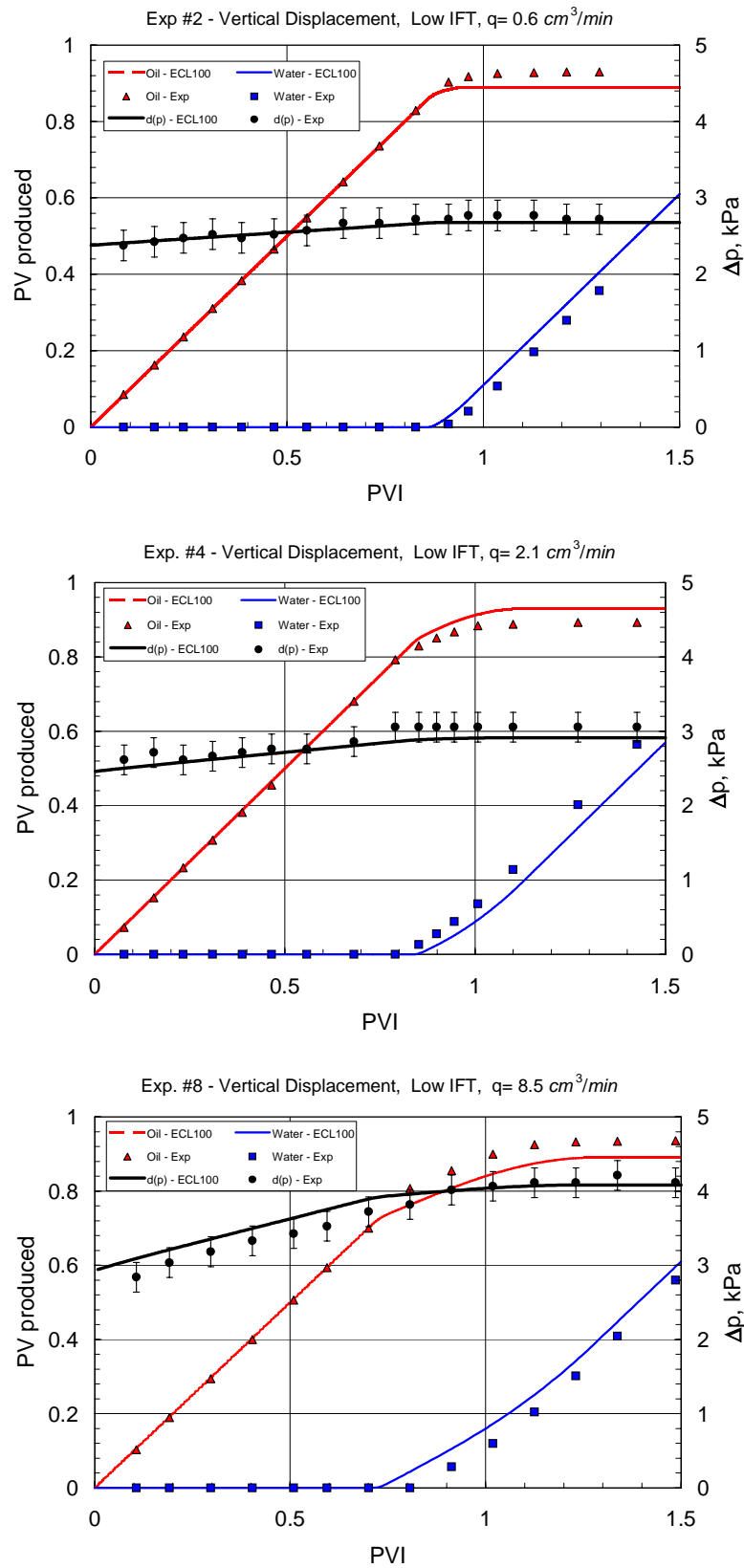


Fig. 5.28: Production and pressure profiles low-IFT vertical displacements.

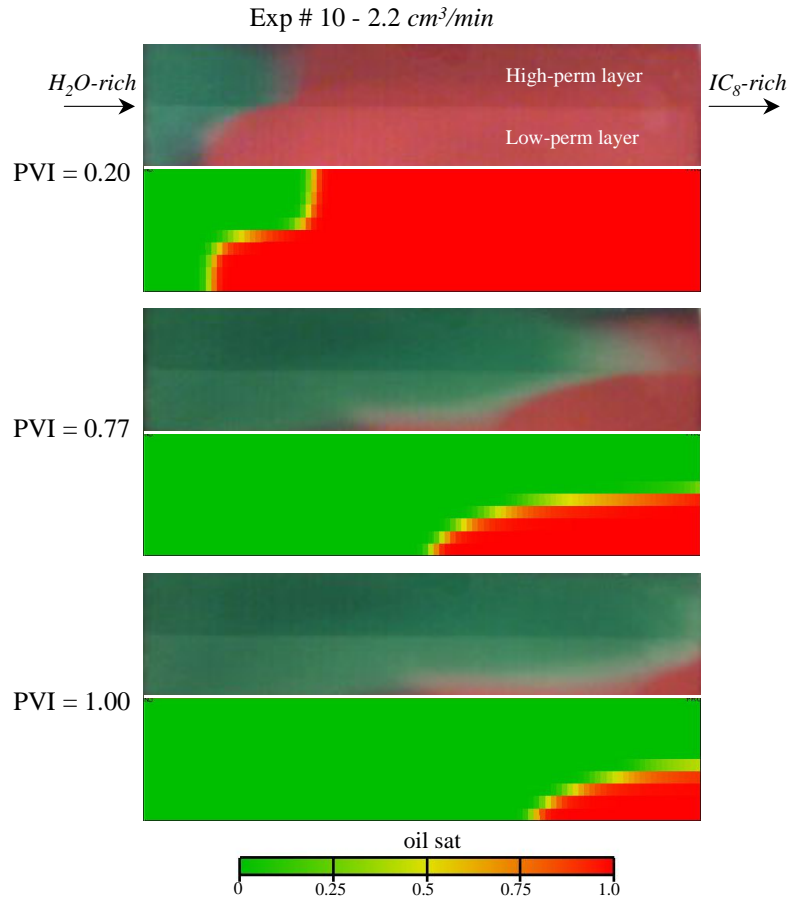


Fig. 5.29: Simulation and experimental saturation maps for experiment #10.

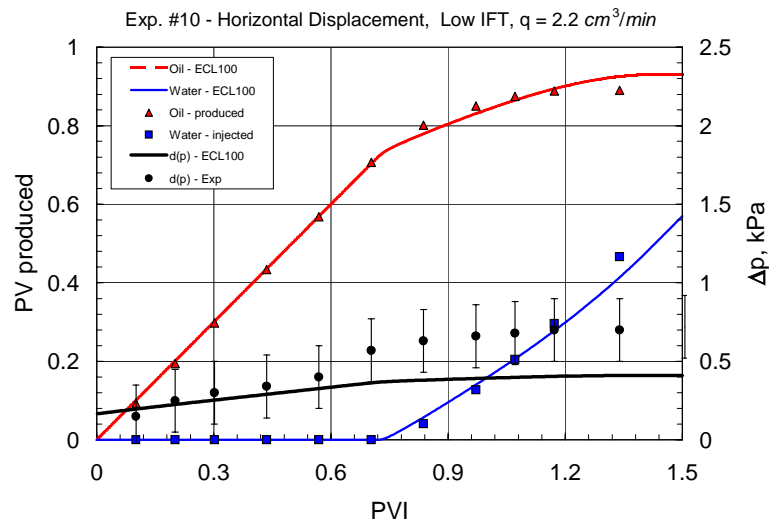


Fig. 5.30: Production and pressure profiles for experiment #10.

Fig. 5.31 shows the images at two different PVI that illustrate the crossflow regions in the low-permeability layer. Two gravity tongues in both layers can be distinguished clearly on the images of the low-rate experiment. At lower flow rate, the gravity tongue in the high-permeability layer and crossflow in the low-permeability layer propagate together to the outlet. However, the crossflow that occurs from the upper layer into the lower layer makes the upper tongue smaller than it would otherwise be. With increasing the flow rate the gravity tongues in both layers disappear. The fronts in both layers look more stabilized with a small crossflow region. As it can be seen from the images, the highest sweep efficiency is found for the low-rate displacement, which is affected by gravity. Thus, for this combination of displacement and flow model, crossflow increases the ultimate sweep efficiency.

Fig. 5.32 shows production and pressure profiles for the experiments. Simulation results agree with the experimental recovery data satisfactorily. However, the predictions for the pressure drop deviate from the experimental data.

Comparing to those obtained with the vertical experiments (see Fig. 5.23), here we observed saturation profiles with weak gravity tongues. We recovered slightly more oil here than in the gravity-reduced vertical experiments, which means that gravity effects positively contributed to the recovery. In this kind of displacements, the viscous and gravity forces act together in the same direction, which increases the crossflow area. The shape of the crossflow area is found to be similar for both vertical and horizontal displacements. Because of the gravity tongue, the breakthrough here was earlier than that observed in the vertical displacements.

Fig. 5.33 and Fig. 5.34 show experimental and simulation results for longer models. One experiment was performed with the inverted model. In general, we did not observe any difference between the saturation profiles and recovery of short and long models. The saturation profiles of the inverted long model are almost symmetrical to the original model as can be seen from Fig. 5.33. In these displacements, the viscous and gravity forces acted in opposite directions. Because the fast layer is now at the bottom, gravity effects force the injected fluid flow into the high-permeability layer. However, we obtained a large crossflow area in the low-permeability layer at the later stage of the flooding. This crossflow occurred due to viscous forces that overcame the gravity forces. Recall that the density difference here was relatively small because of the low IFT. Because the driving forces acted oppositely, the recovery of oil also was little reduced in this experiment, compared to that of original model. This can be seen in the recovery plots shown in Fig. 5.34. The experimental and simulation results show very good agreement. The experimental crossflow area was not predicted by the simulation well.

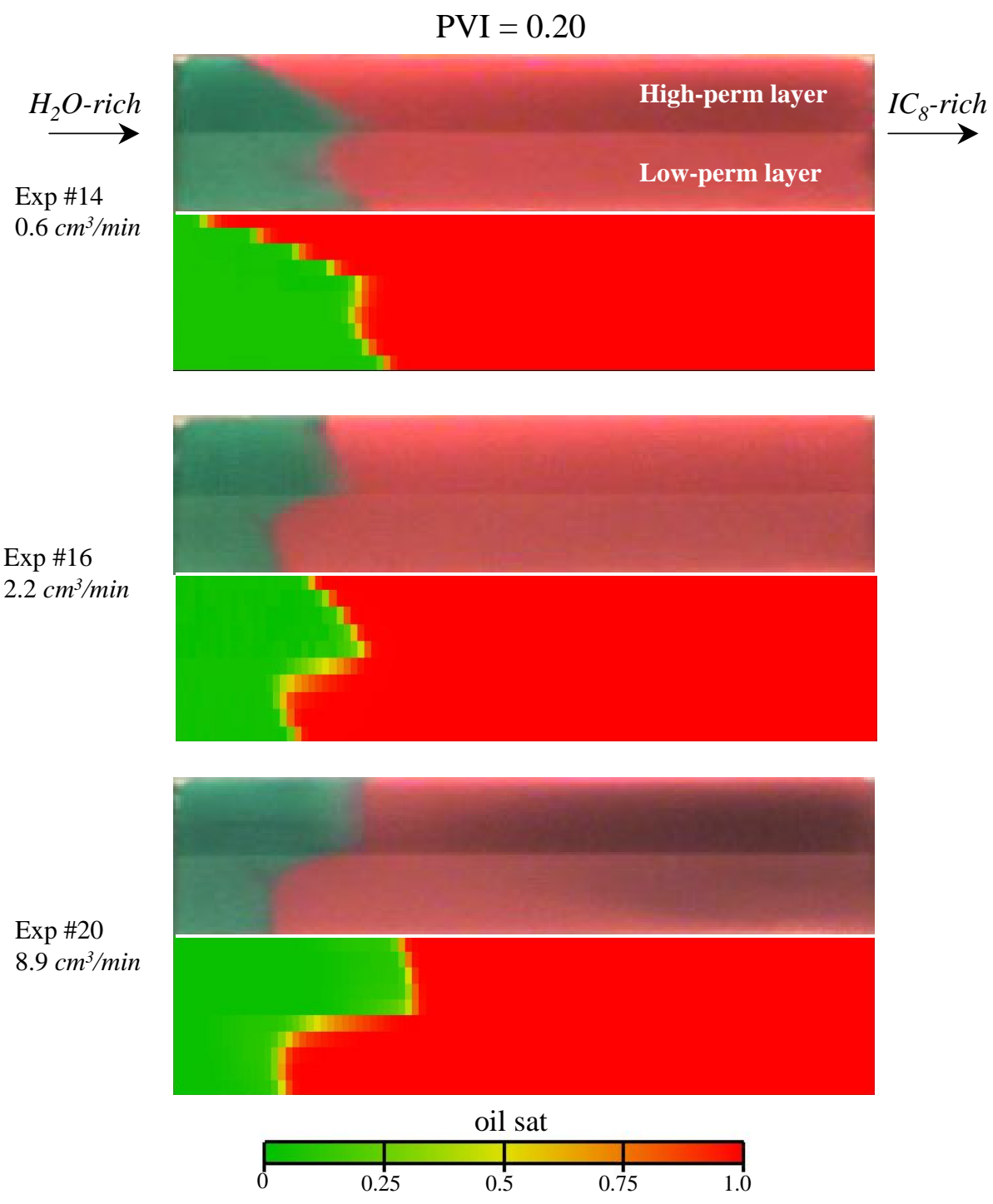


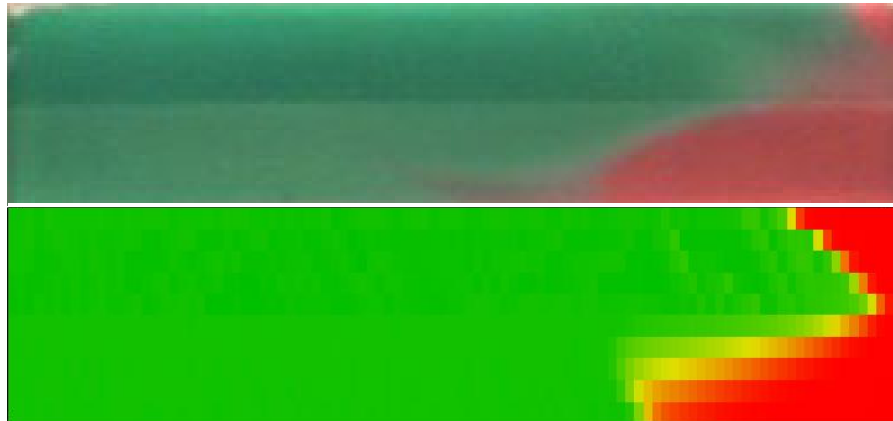
Fig. 5.31: Saturation profiles for low-IFT VCS displacements.

PVI = 0.81

Exp #14  
 $0.6 \text{ cm}^3/\text{min}$



Exp #16  
 $2.2 \text{ cm}^3/\text{min}$



Exp #20  
 $8.9 \text{ cm}^3/\text{min}$

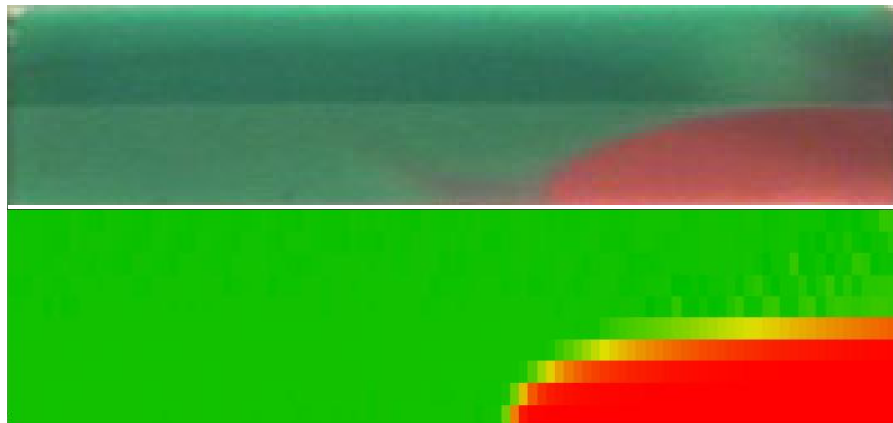


Fig. 5.31: (continued).

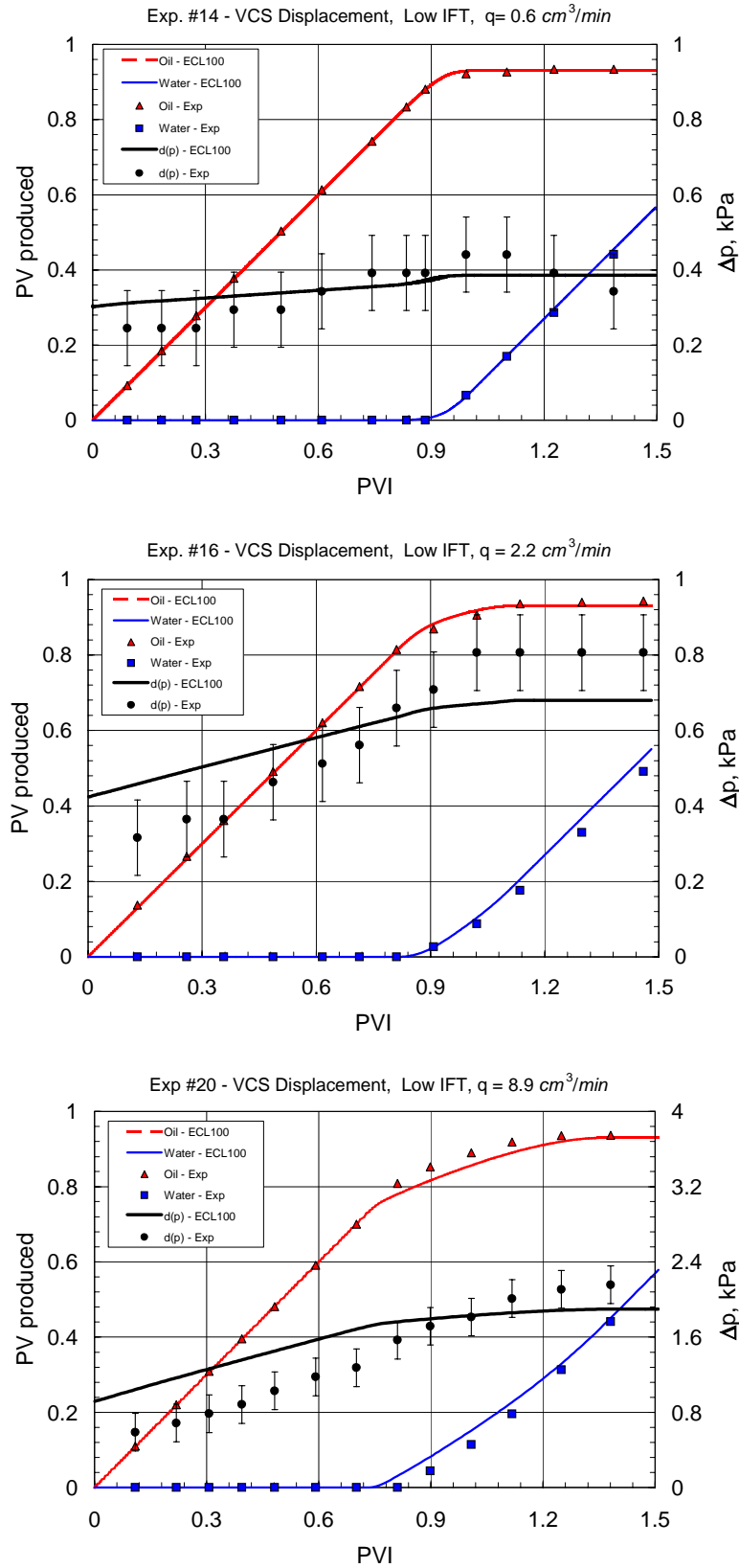


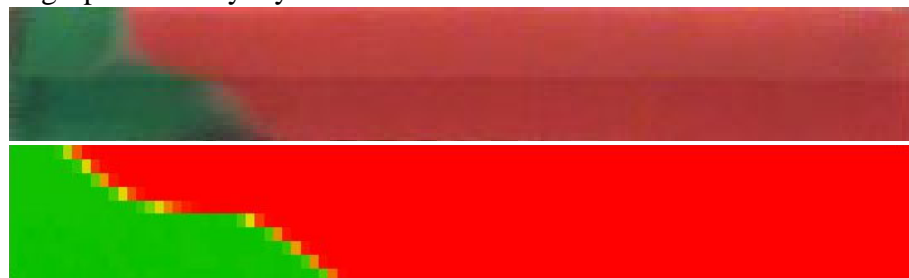
Fig. 5.32: Production and pressure profiles for low-IFT VCS displacements.

Exp # 22 & 26 -  $2.2 \text{ cm}^3/\text{min}$

PVI = 0.20



High-permeability layer at the bottom



PVI = 0.78

High-permeability layer at the top



High-permeability layer at the bottom

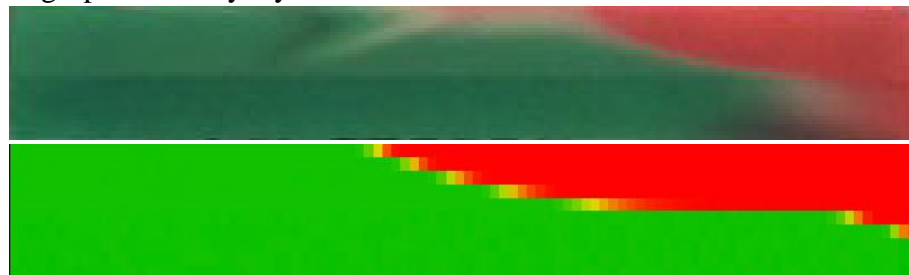


Fig. 5.33: Saturation profiles for low IFT long VCS displacements.

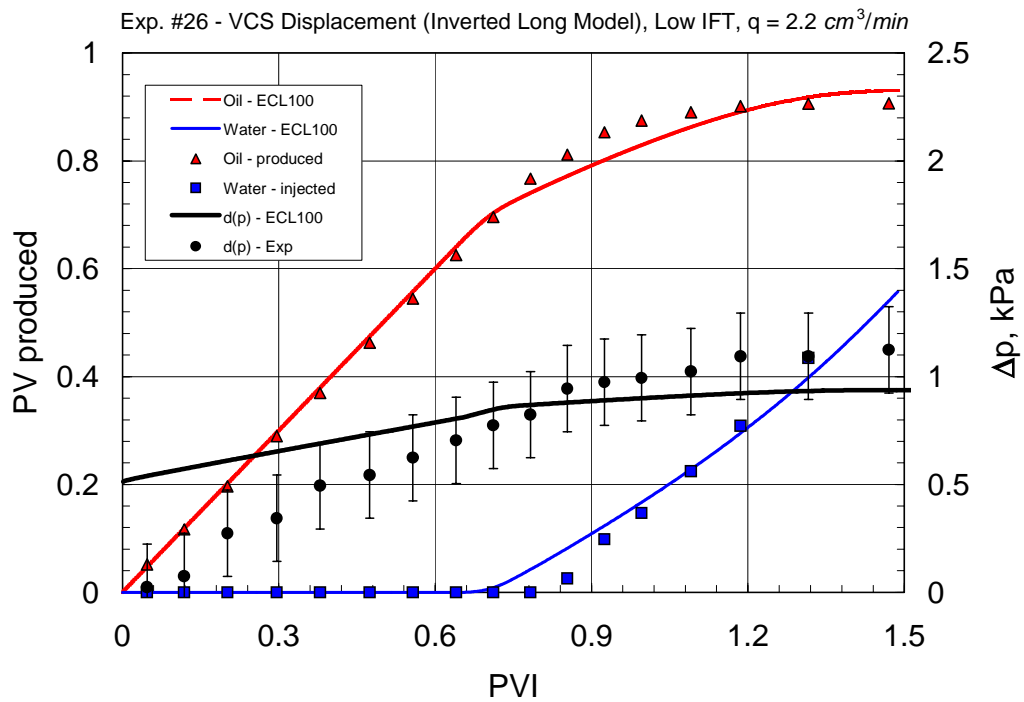
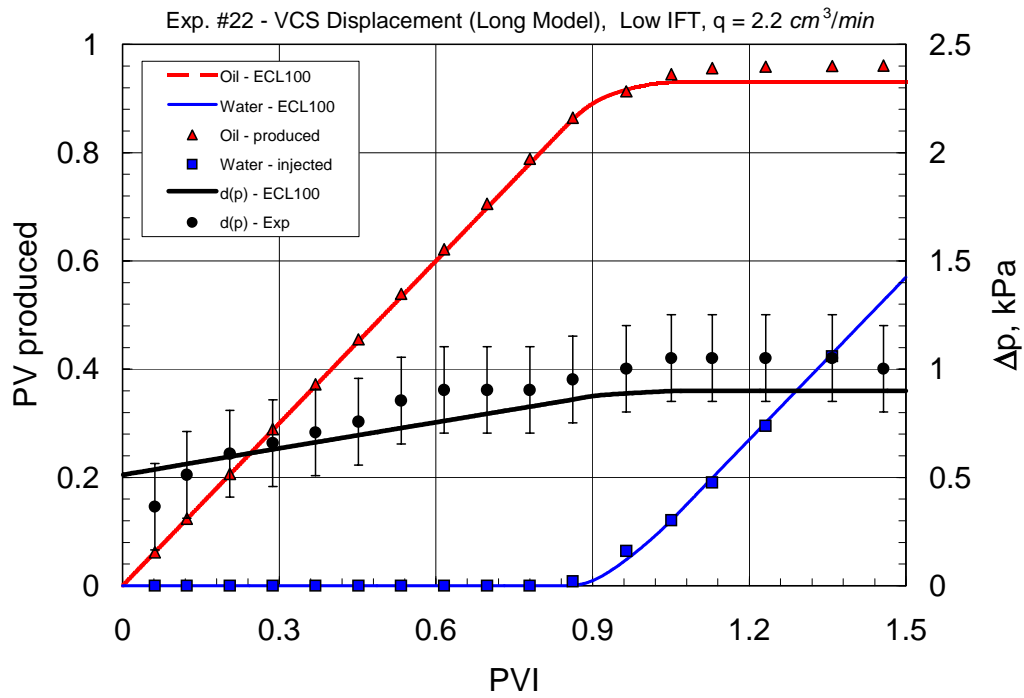


Fig. 5.34: Production and pressure profiles for low-IFT long VCS displacements.

### 5.1.2.3 Unfavorable displacements

#### *Vertical Displacements (Experiments #5 and 6)*

In this series of experiments, we injected the  $IC_8$ -rich phase into the completely  $H_2O$ -rich phase-saturated glass bead model. These displacements were unfavorable. We injected the  $IC_8$ -rich phase from the top of the model to have gravity-stabilized flood. We employed both high- and low-IFT drainage displacements to compare with those favorable imbibition displacements.

Fig. 5.35 shows the images taken at various times during the experiment. As can be seen from the figure, the flow took place mostly in the high-permeability layer and reached at the production end of the flow model very early (about  $PVI=0.4$ ). Breakthrough for the imbibition displacement (Exp. #3) was about  $PVI=0.75$ . Consequently here, a large portion of the low-permeability layer was left unswept. The numerical prediction of saturation profiles is shown in Fig. 5.36.

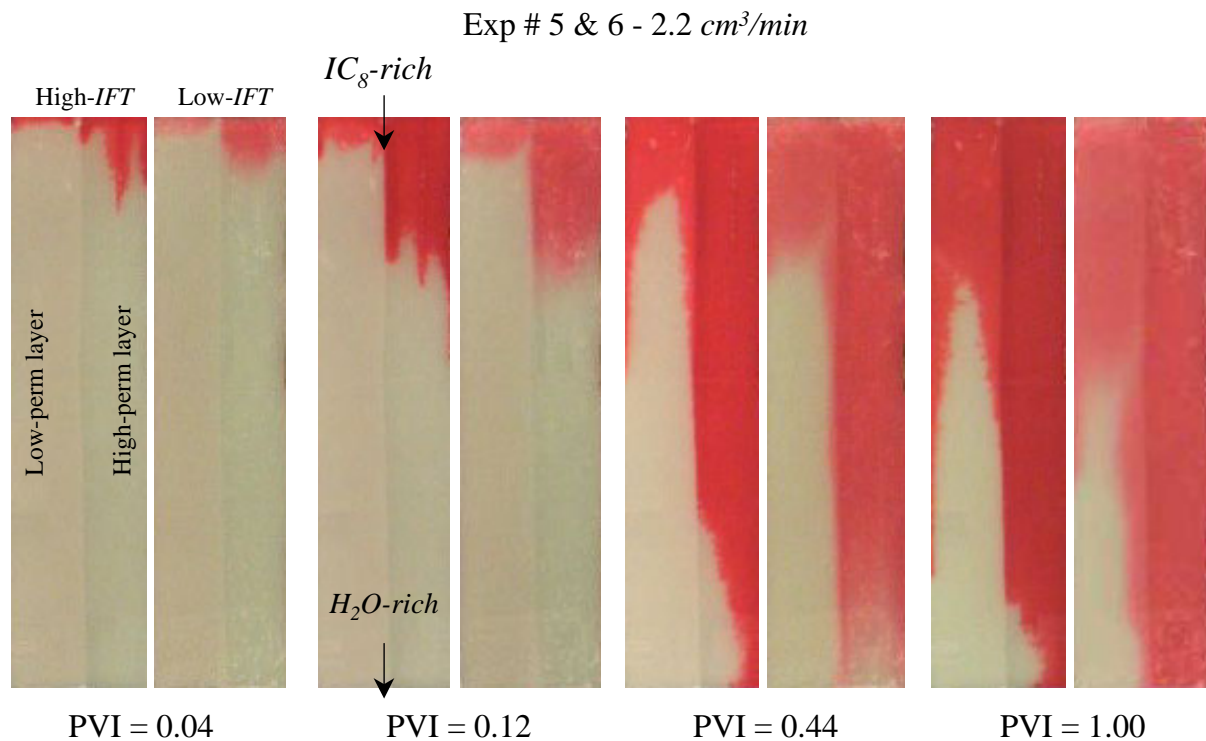


Fig. 5.35: Saturation profiles for unfavorable vertical displacements.

At the early stage of the high-IFT flooding, small viscous fingers occurred, but later these fingers merged to form big fingers in the layers. We observed one main finger in the high-permeability layer, and two main fingers in the low-permeability layer. Interestingly, each

layer had a main finger at its side. The reasons for that could be either due to the packing of glass beads or that might be caused by the thin oil-wet plastic rod (0.6 cm thick) used to close both ends of the glass bead model. Glass beads packed in the smooth-surfaced model may lead to a high-porosity region just near the surface, which in turn this region acts like a high-permeability streak in the porous system. However, we observed an opposite situation in the high-IFT imbibition displacements (Exp. #1), which might be explained by the wettability of the plastic rod. The other finger in the low-permeability layer occurred at the interface with the other layer, which shows an existence of crossflow.

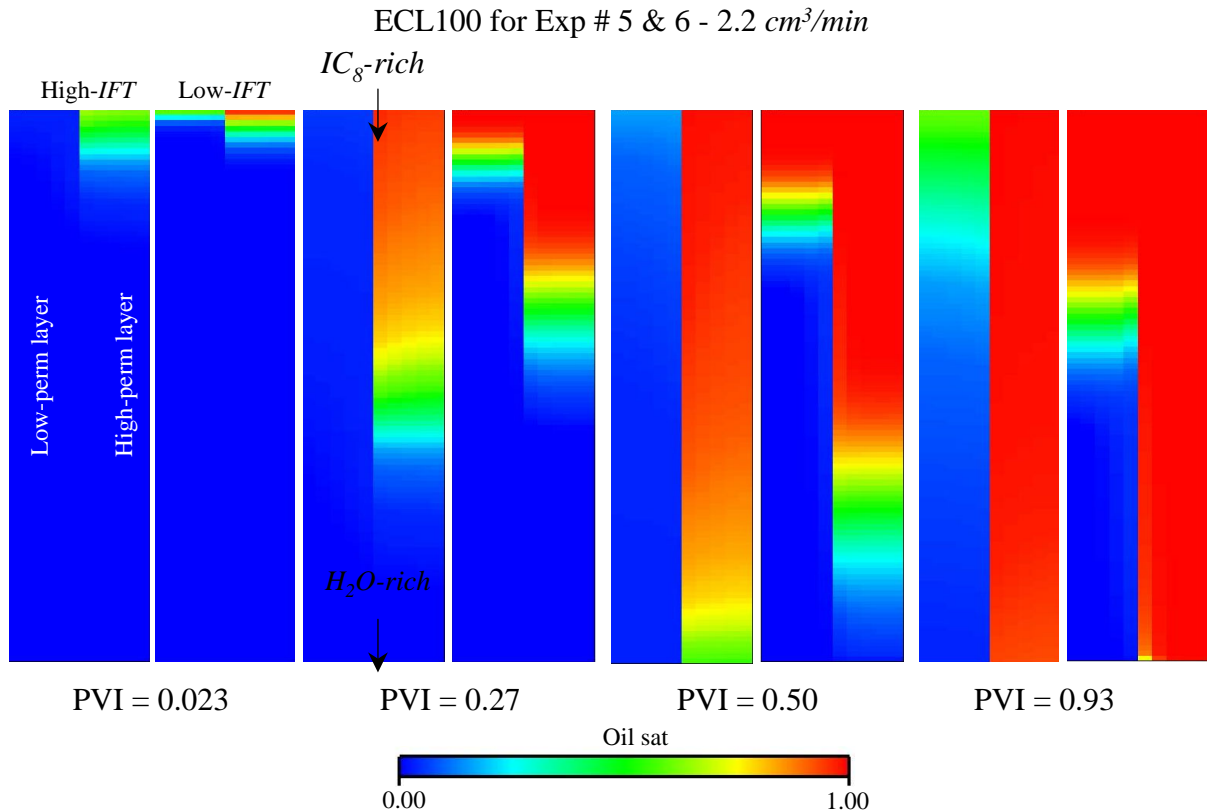


Fig. 5.36: Numerical results of saturation profiles for unfavorable vertical displacements.

Fig. 5.37 shows the production and pressure data. Due to the early breakthrough as well as the very poor sweep efficiency, the recovery of displaced phase was very small. The lower IFT enhanced the recovery with about 10%. The pressure data shown in the figure were those measured at the top of the flow model. Due to the positive contribution of the gravity, this pressure must be summed with the hydrostatic head to find the total pressure drop.

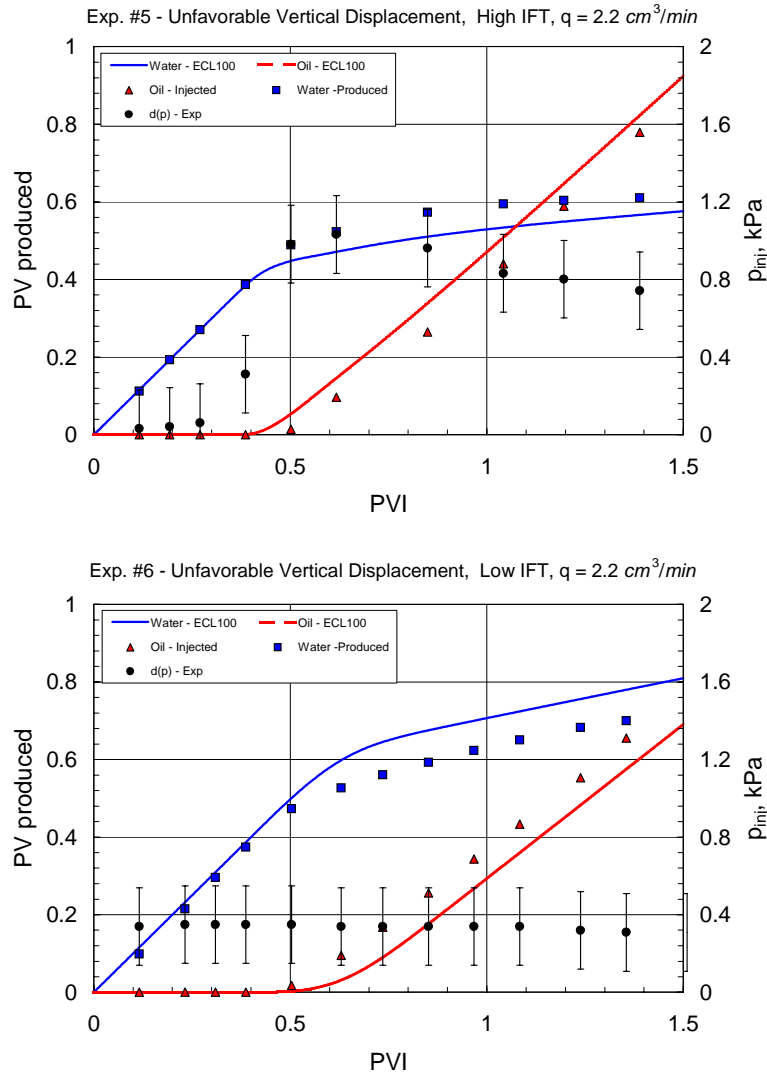


Fig. 5.37: Production and pressure profiles for unfavorable vertical displacements.

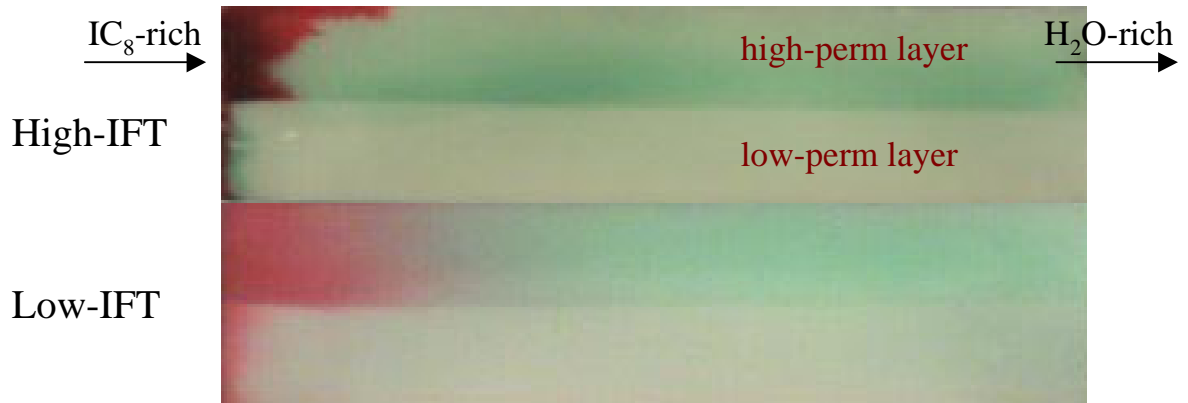
Lowering IFT between the fluids weakened the viscous fingering and enhanced the crossflow, as can be clearly seen at the later stage of the flooding. With reduced capillary effects, this crossflow should be caused by viscous forces, because the density difference between fluids forces a crossflow in the opposite direction.

#### *Horizontal Displacements (Experiments #11 and 12)*

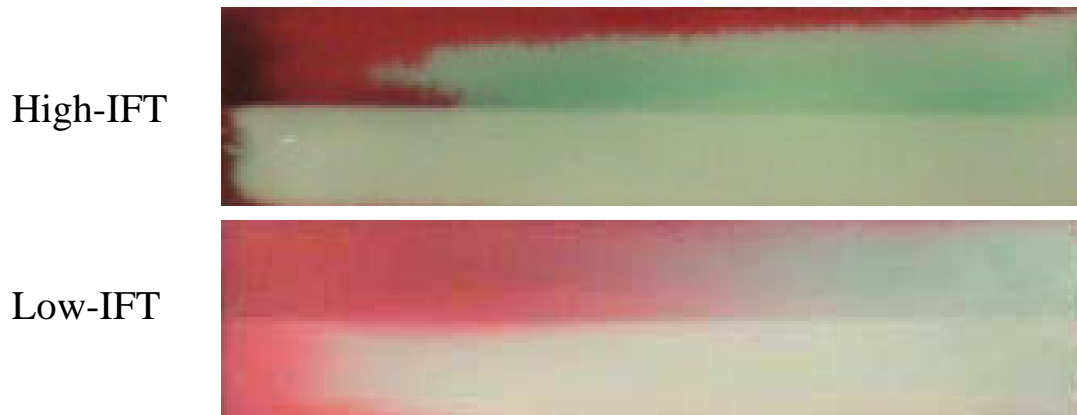
We repeated experiments # 9 and #10 (see Fig. 5.17 and Fig. 5.29), but with unfavorable conditions. Fig. 5.38, Fig. 5.39, and Fig. 5.40 show the experimental results. For the high-IFT displacement, we observed development of fingering similar to that shown in Fig. 5.35, but the sweep efficiency in the low-permeability layer was worse than that in the vertical dis-

Exp # 11 & 12 -  $2.2 \text{ cm}^3/\text{min}$

PVI = 0.06



PVI = 0.22



PVI = 1.00

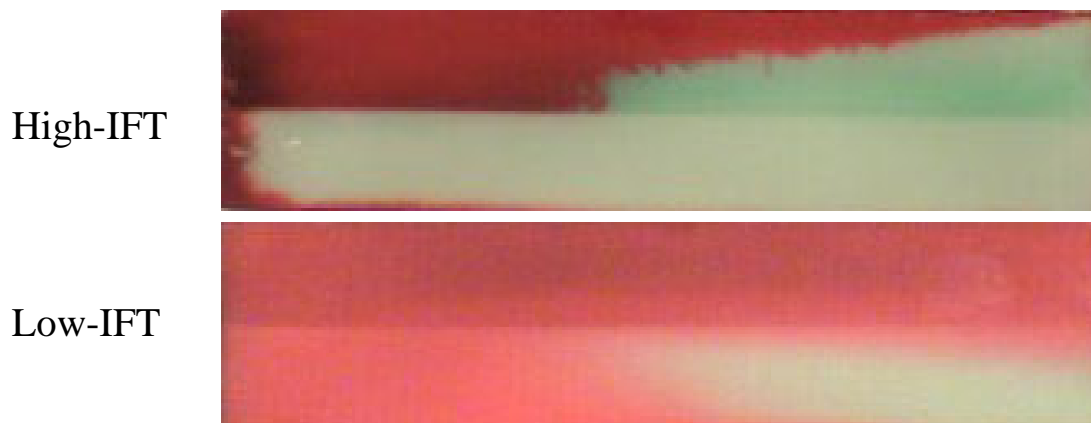


Fig. 5.38: Saturation profiles for unfavorable horizontal displacements.

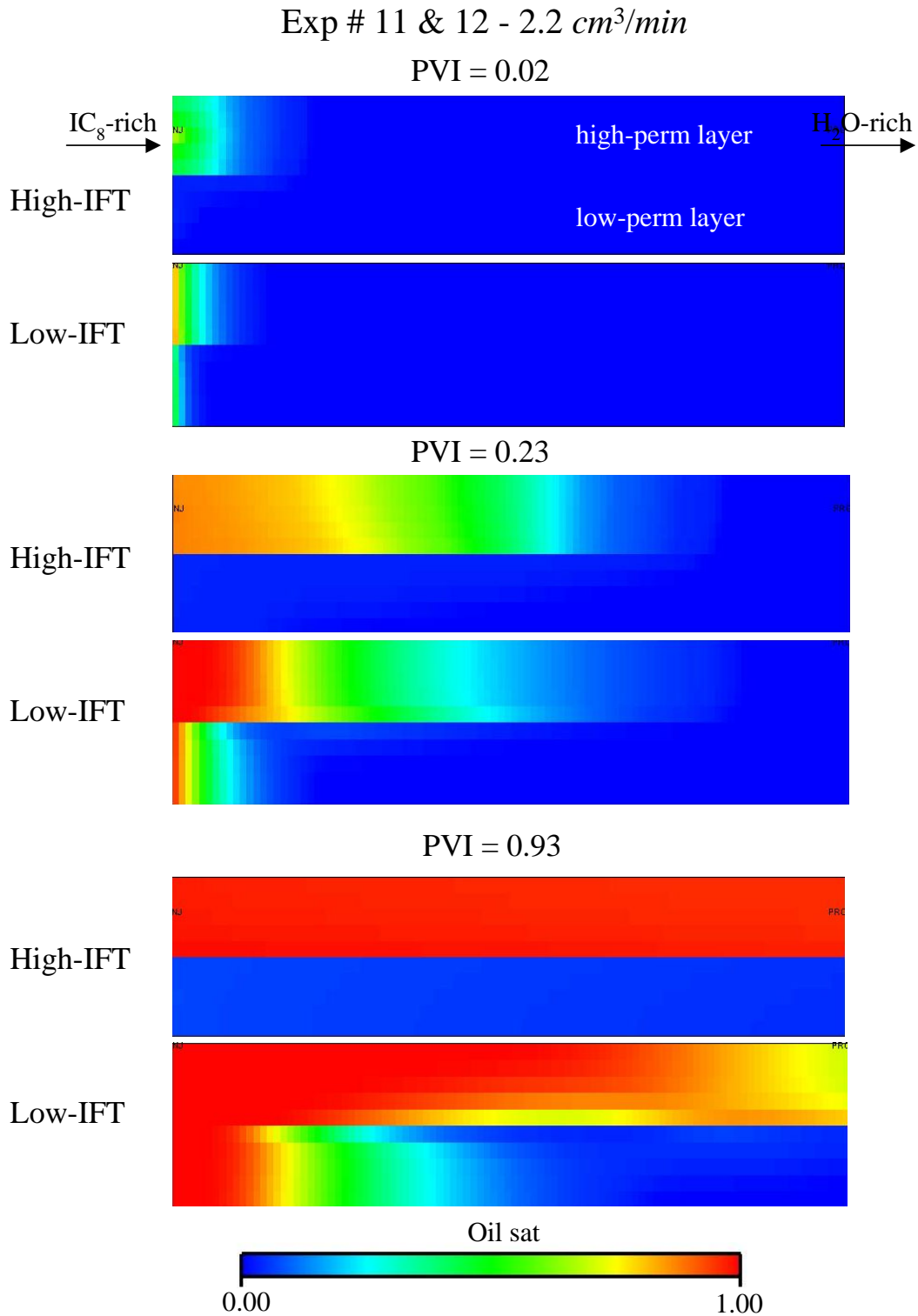


Fig. 5.39: Numerical results of saturation profiles for unfavorable horizontal displacements

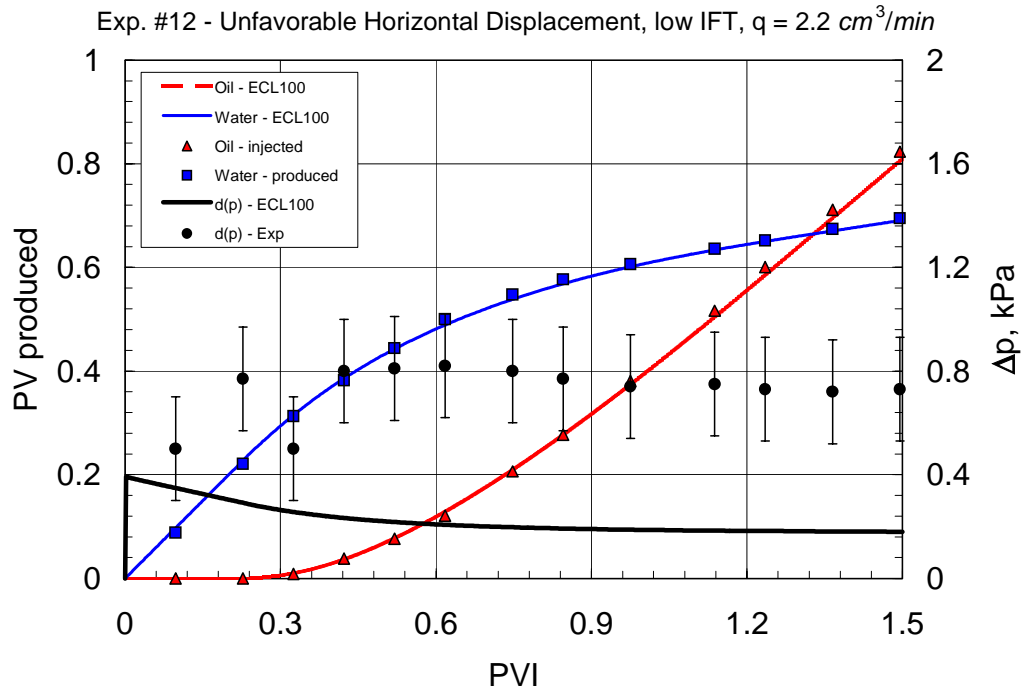
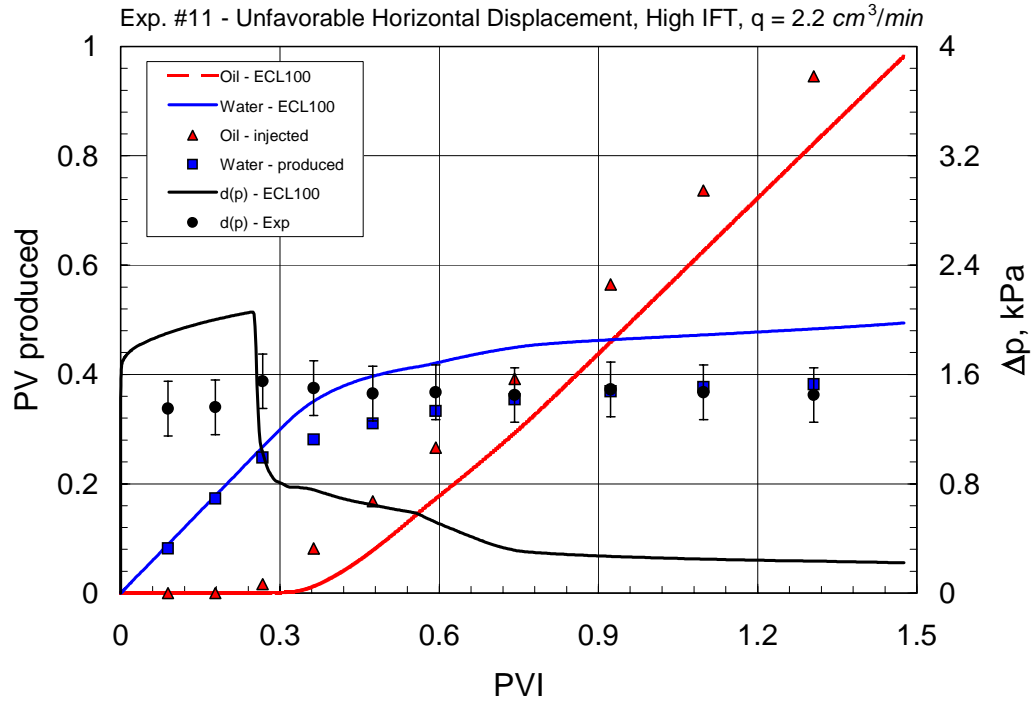


Fig. 5.40: Production and pressure profiles for unfavorable horizontal displacements.

placement. We can also see this difference on recovery curves shown in Fig. 5.37 and Fig. 5.40. The horizontal and vertical low-IFT displacements gave almost the same saturation profiles and recovery data.

The main difference between favorable and unfavorable displacements is that the favorable flow dominated by capillary imbibition takes place in the low-permeability layer whereas the unfavorable flow develops in the high-permeability layer, and there is no imbibition of the nonwetting phase. Thus, the displacement performance was influenced strongly by the direction of saturation (imbibition or drainage) rather than the mobility ratio. The mobility ratio affected the sweep efficiency of single layer, while the direction of saturation change determined whether or not the neighbor layer was swept.

#### *VCS Displacements (Experiments #17, 18, 23, 24, 27 and 28)*

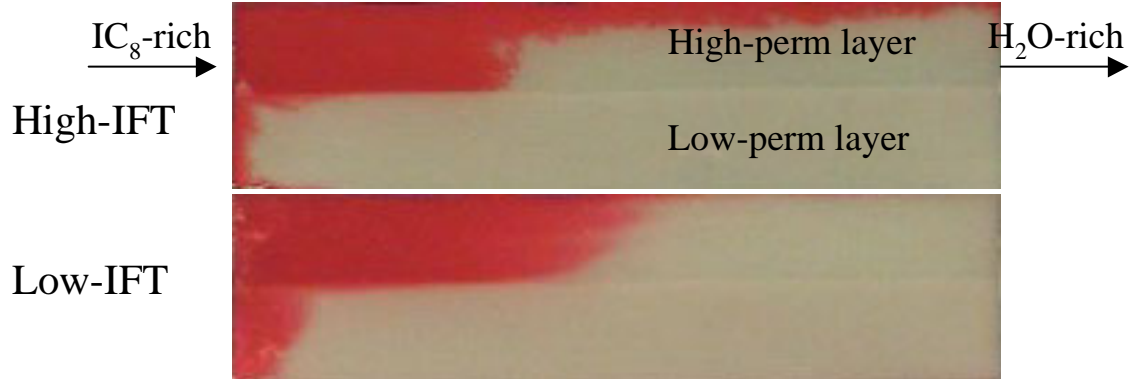
In this series of experiments, we employed unfavorable displacements where the IC<sub>8</sub>-rich phase was injected to displace the H<sub>2</sub>O-rich phase from the model that included the effects of gravity. Fig. 5.41, Fig. 5.42, and Fig. 5.43 show the related experimental and simulation data.

Both high-IFT and low-IFT displacements show similar characteristics obtained before for all unfavorable displacements. In the high-IFT displacement, we had better sweep in the high-permeability layer, but almost no sweep in the low-permeability layer. The sweep area in the low-permeability layer was almost identical with gravity-stabilized experiment, while the sweep area in the high-permeability layer was almost identical with horizontal displacement case. These results show that gravity effects in the high-permeability layer were stronger than that in the low-permeability layer. A small crossflow area in the low-permeability layer might be caused by the effects of gravity. Recovery of the high-IFT displacement was about 50%, which was less than the amount obtained from vertical displacement (~60%) and higher than that obtained from horizontal setup (~40%). The low-IFT displacement, however, indicates less recovery (~60%) than those obtained from vertical and horizontal experiments (~70%), which can be explained by the fact that gravity forces act oppositely in the VCS experiments.

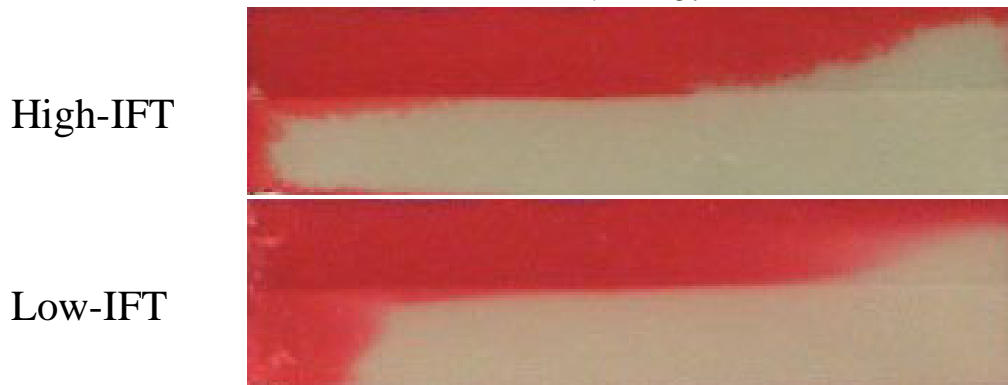
We also performed further similar experiments in the long model to investigate the effect of L/H ratio on the displacement performance. Fig. 5.44, Fig. 5.45, and Fig. 5.46 show the experimental and simulation data for high-IFT displacements in the long model and the inverted long model, respectively. Although displacement characteristics are similar to those of the short models, we obtained less recovery of the displaced phase (~40%) in the long model than the short model (~50%). However, we obtained higher recovery (~60%) from the displacements in the inverted long model. This can be explained by the fact that the lighter IC<sub>8</sub>-rich phase swept more of the low-permeability layer because of gravity override.

Exp # 17 & 18 -  $2.2 \text{ cm}^3/\text{min}$

PVI = 0.21



PVI = 0.44



PVI = 1.00

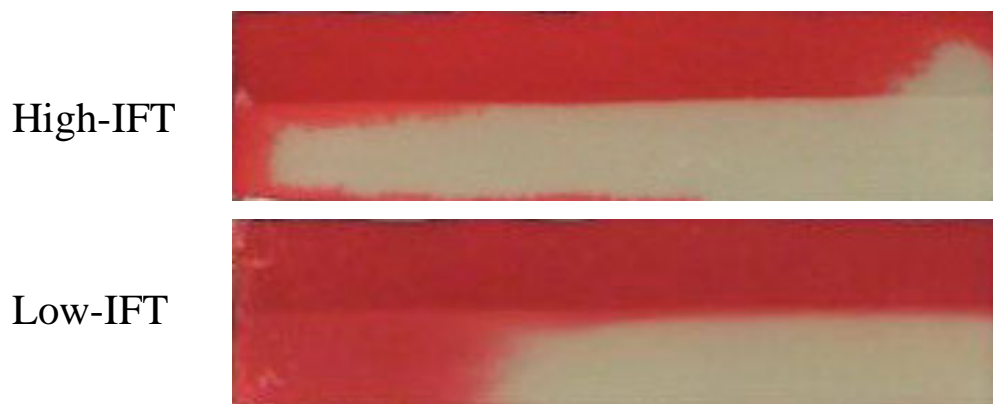


Fig. 5.41: Saturation profiles for unfavorable short VCS displacements.

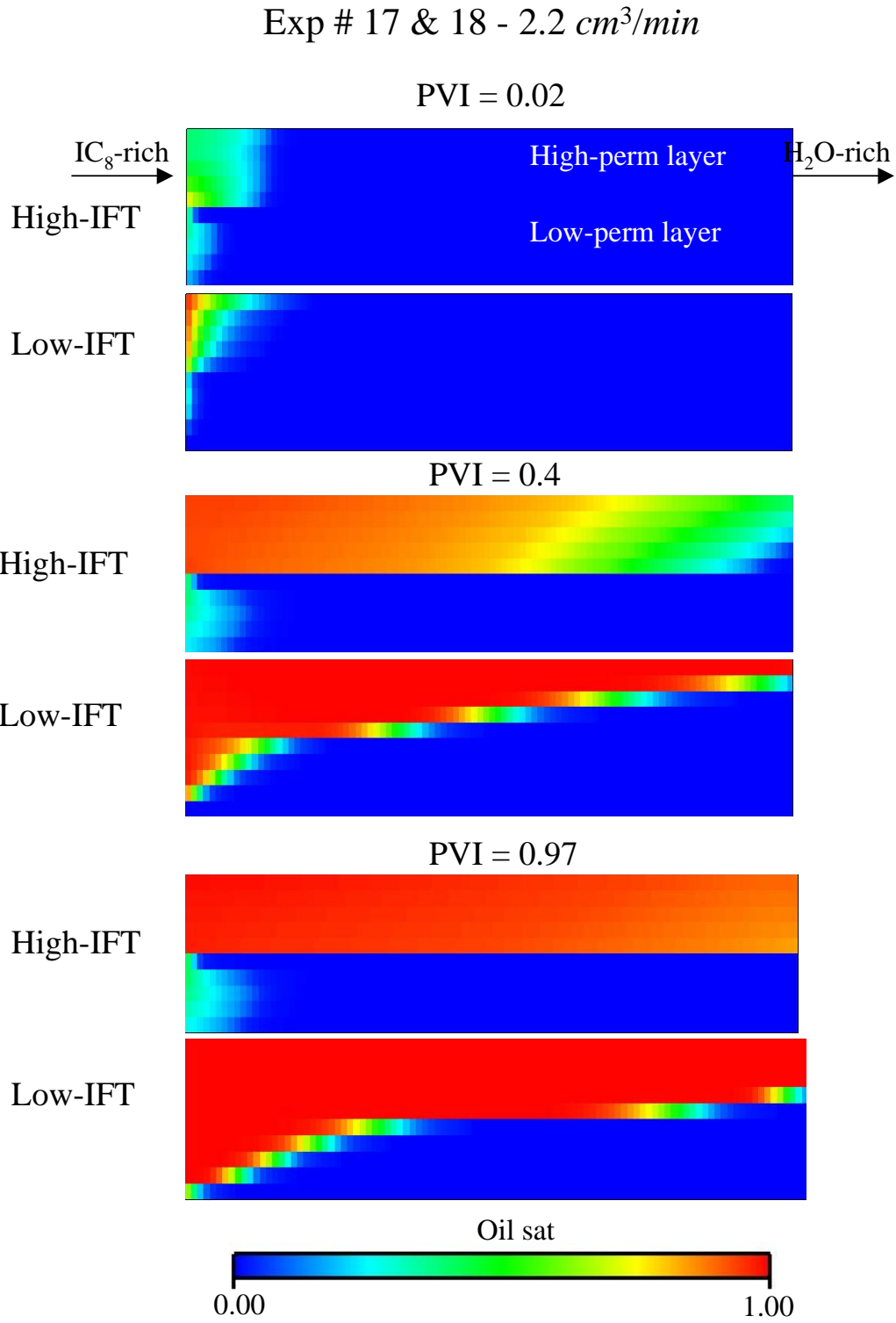


Fig. 5.42: Numerical results of saturation profiles for unfavorable short VCS displacements.

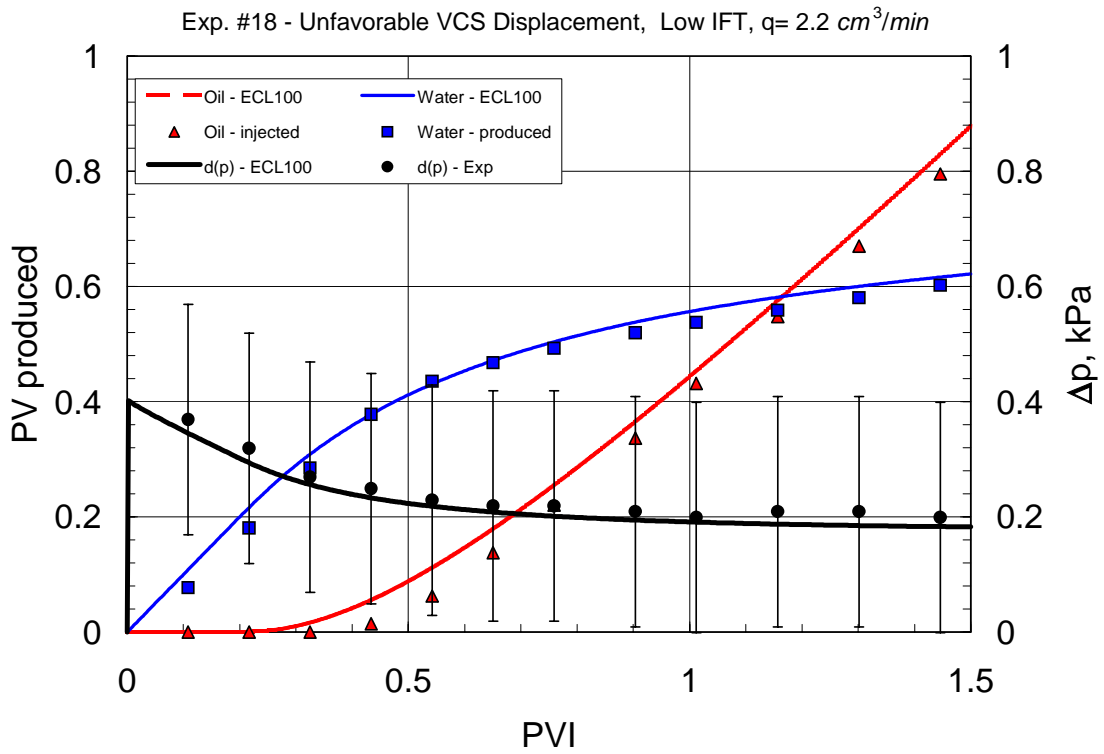
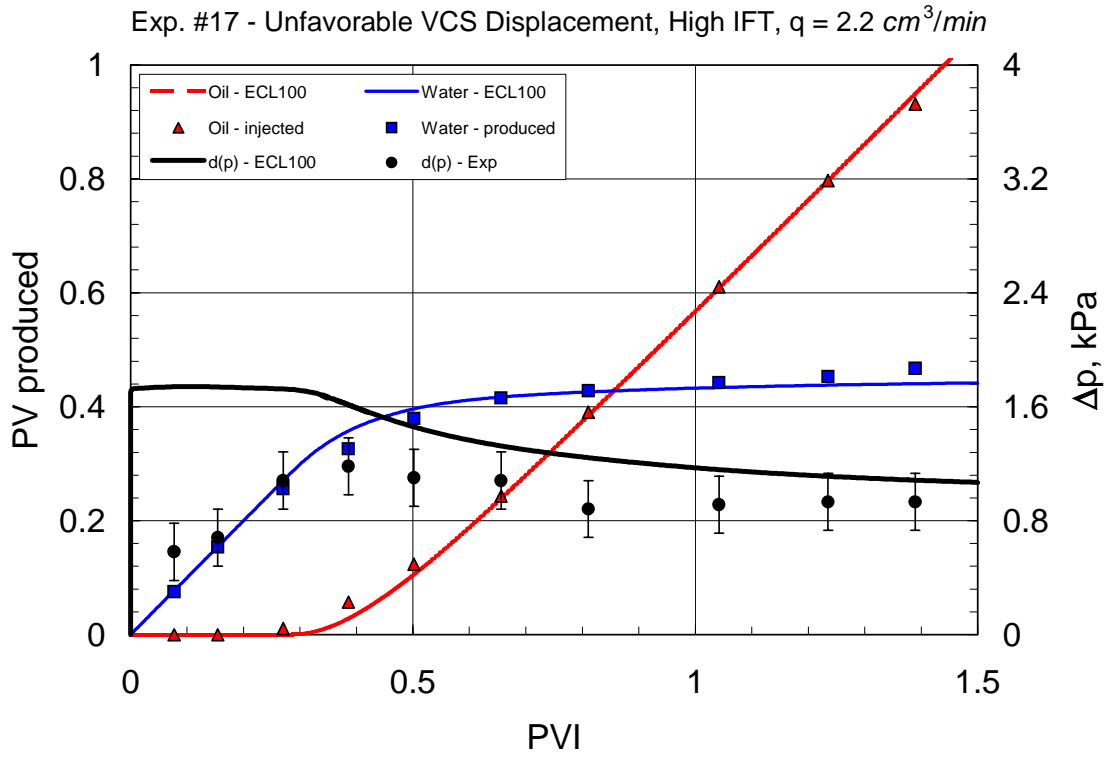
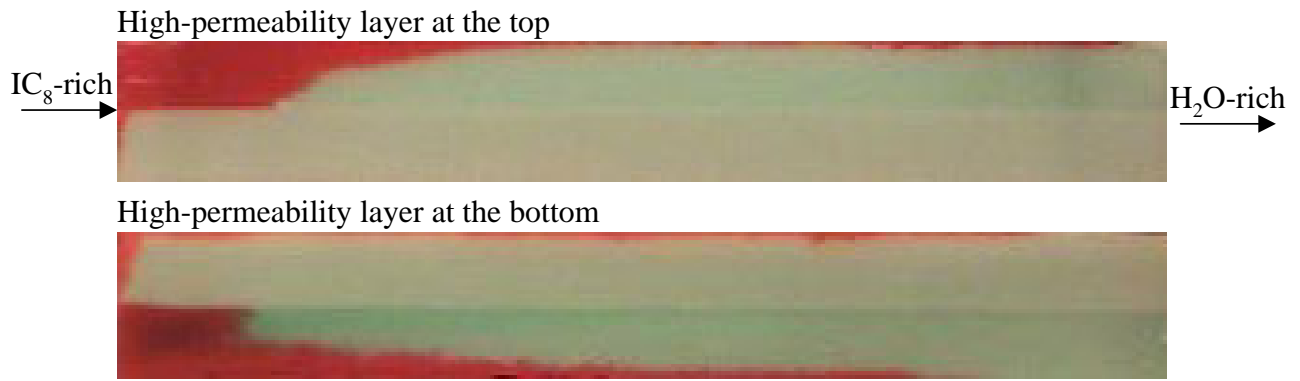


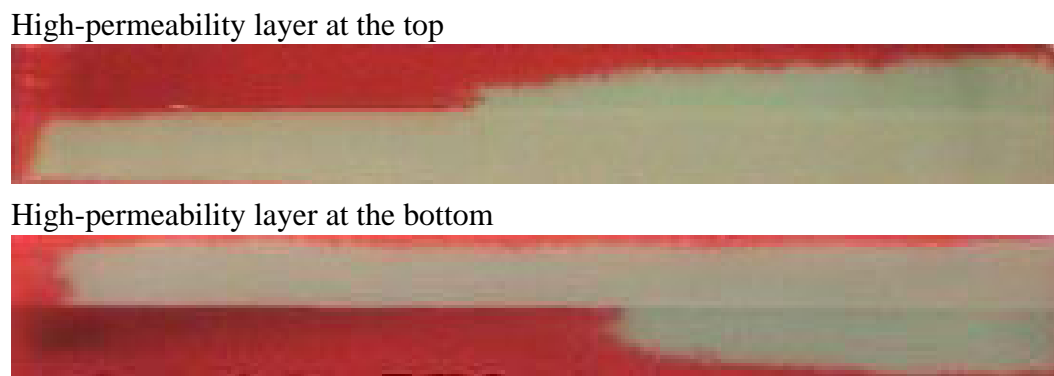
Fig. 5.43: Production and pressure profiles for unfavorable short VCS displacements.

Exp # 23 & 27 - 2.2 cm<sup>3</sup>/min

PVI = 0.14



PVI = 0.45



PVI = 1.00

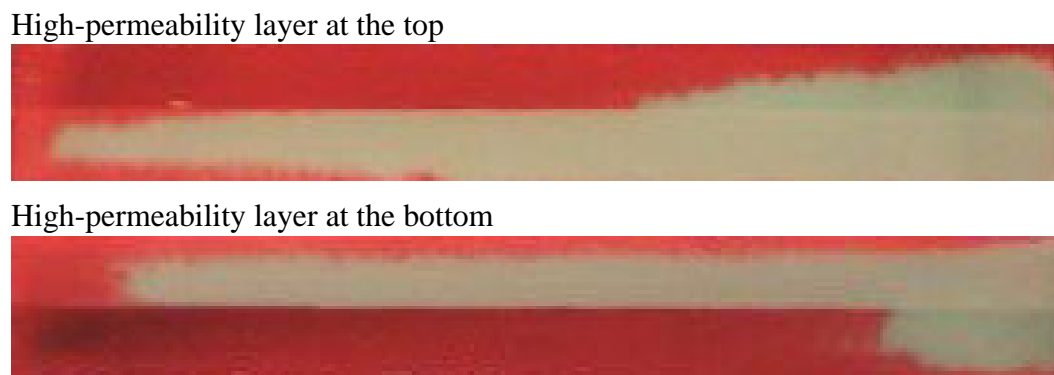
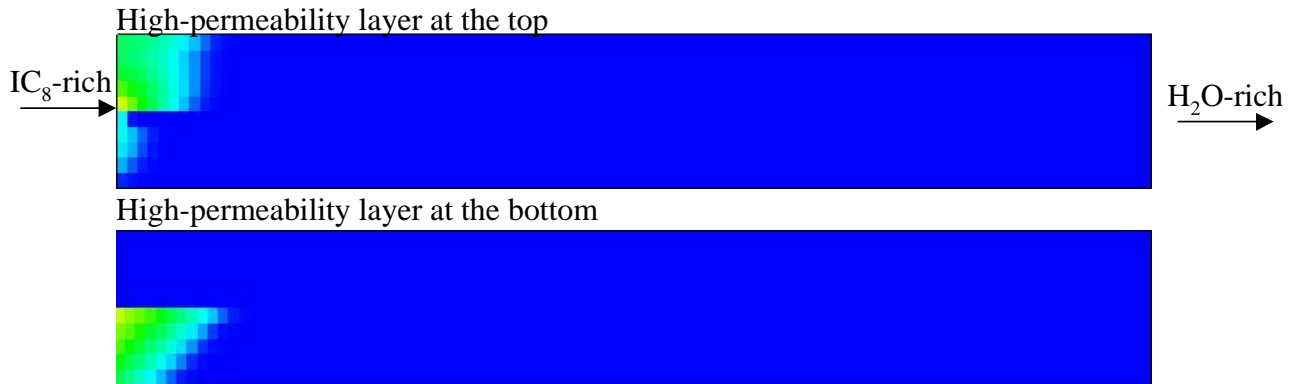


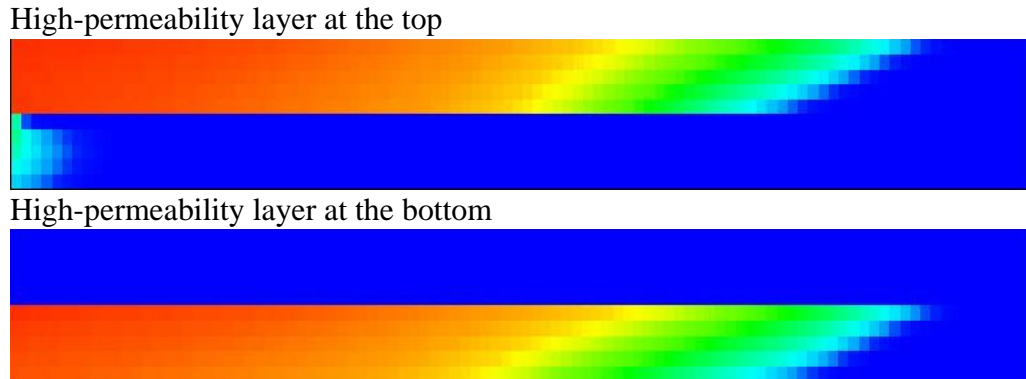
Fig. 5.44: Saturation profiles for unfavorable, long, VCS, high-IFT displacements.

Exp # 23 & 27 - 2.2 cm<sup>3</sup>/min

PVI = 0.014



PVI = 0.31



PVI = 0.95

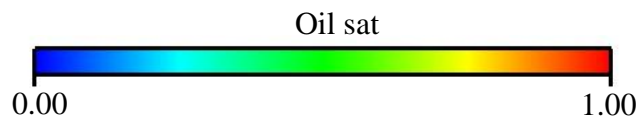
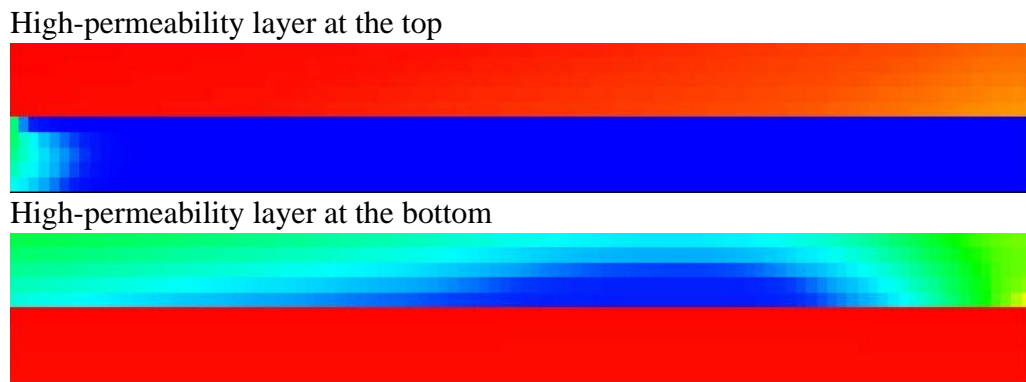


Fig. 5.45: Numerical results of saturation profiles for unfavorable, long, VCS, high-IFT displacements.

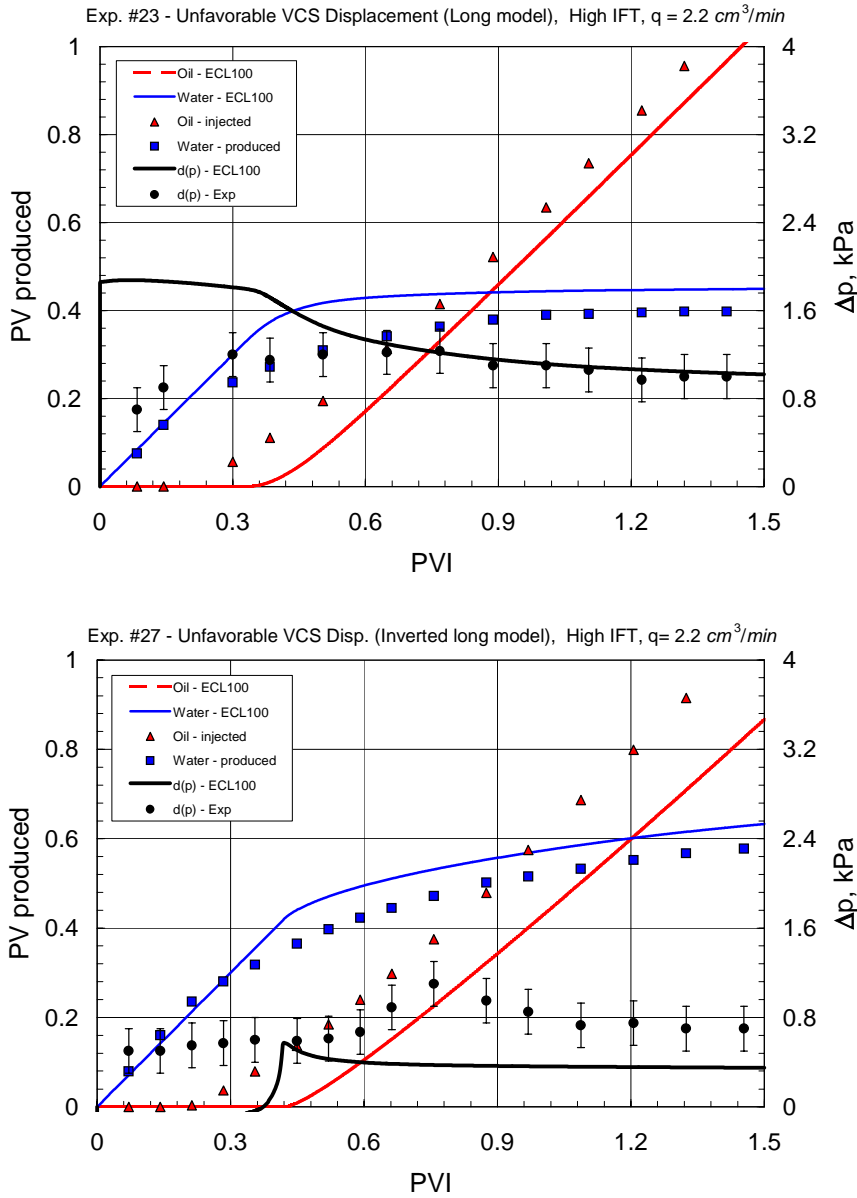
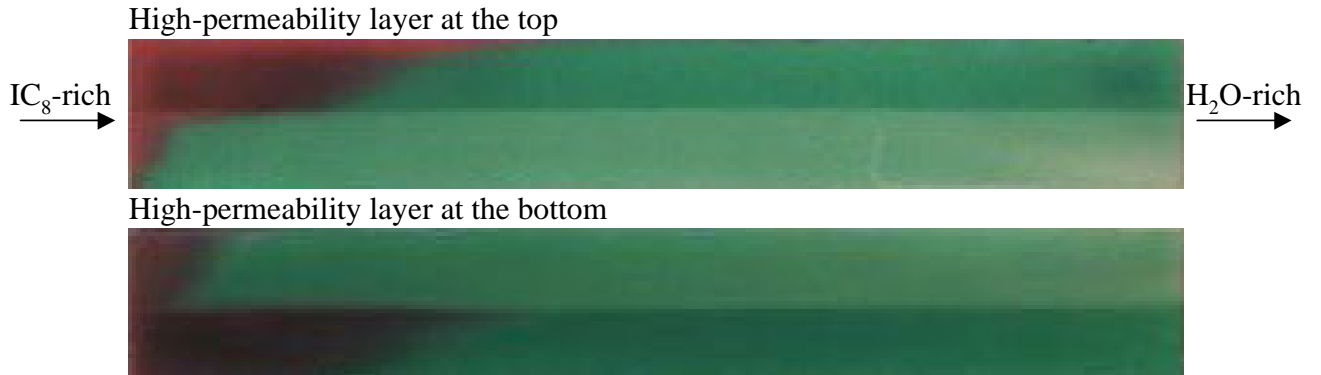


Fig. 5.46: Production and pressure profiles for unfavorable, long, VCS, high-IFT displacements.

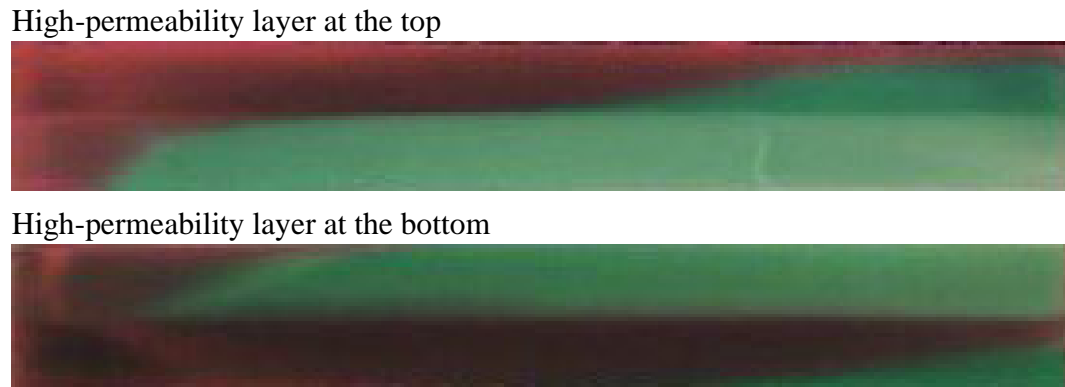
Fig. 5.47, Fig. 5.48, and Fig. 5.49 show the experimental and simulation results for the low-IFT displacements. The displacement in the long model has almost the same saturation profiles and recovery data as in the short model (about 60% recovery of the displaced phase from both models). The displacement with the inverted long model showed an enhancement in the sweep efficiency of the low-permeability layer, which in turn increased the recovery to a value of about 70%. The predictions of the low-IFT displacements by simulation are acceptable in general, but the simulation overestimated the recovery data for the inverted model.

Exp # 24 & 28 - 2.2  $cm^3/min$

PVI = 0.14



PVI = 0.45



PVI = 1.00

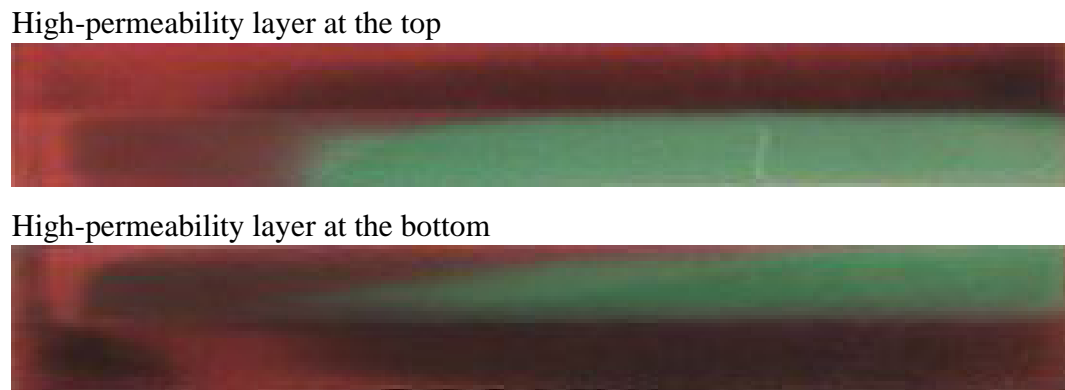
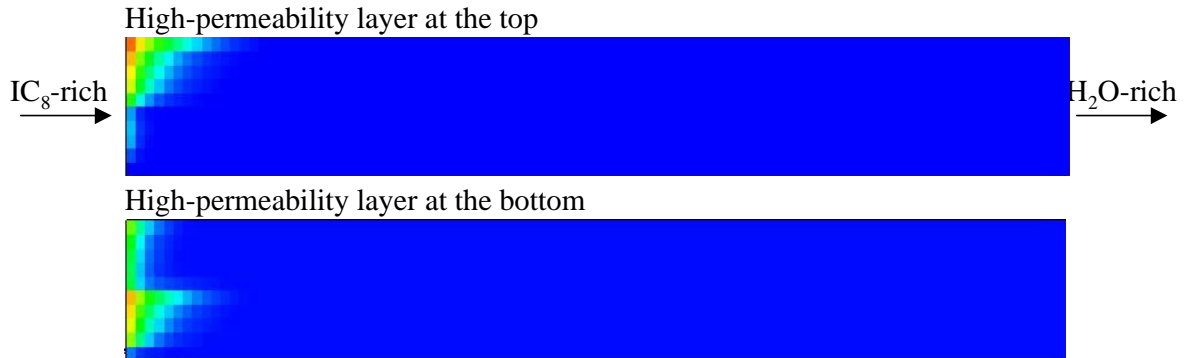


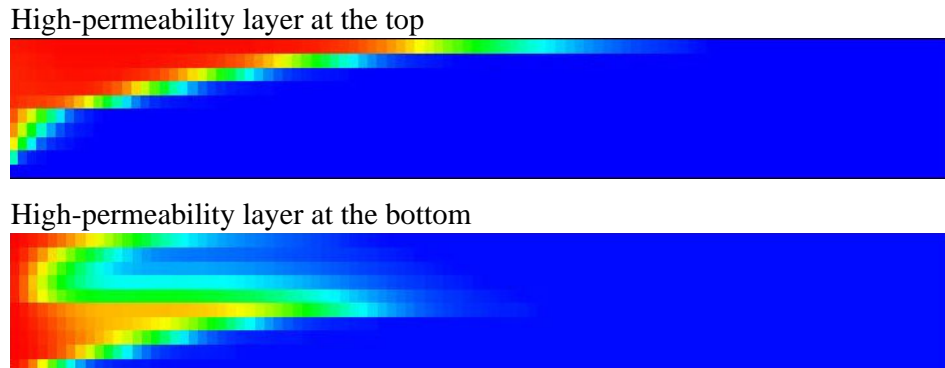
Fig. 5.47: Saturation profiles for unfavorable, long, VCS, low-IFT displacements.

Exp # 24 & 28 - 2.2 cm<sup>3</sup>/min

PVI = 0.15



PVI = 0.17



PVI = 0.43

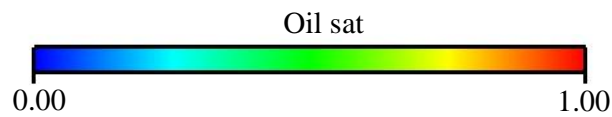
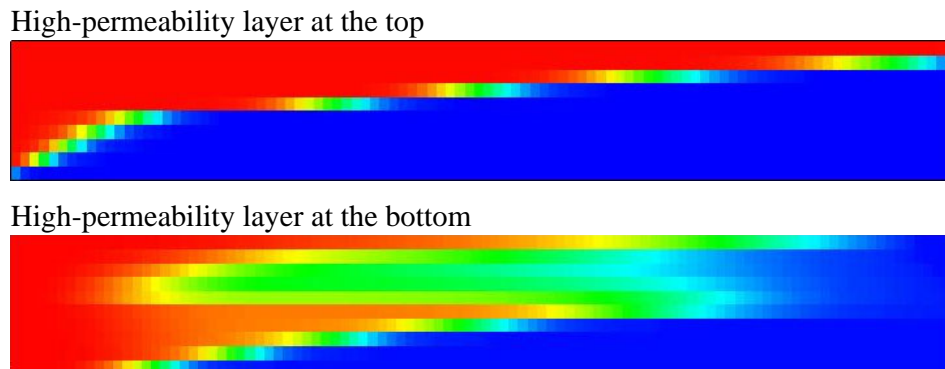


Fig. 5.48: Numerical results for Saturation profiles for unfavorable, long, VCS, low-IFT displacements.

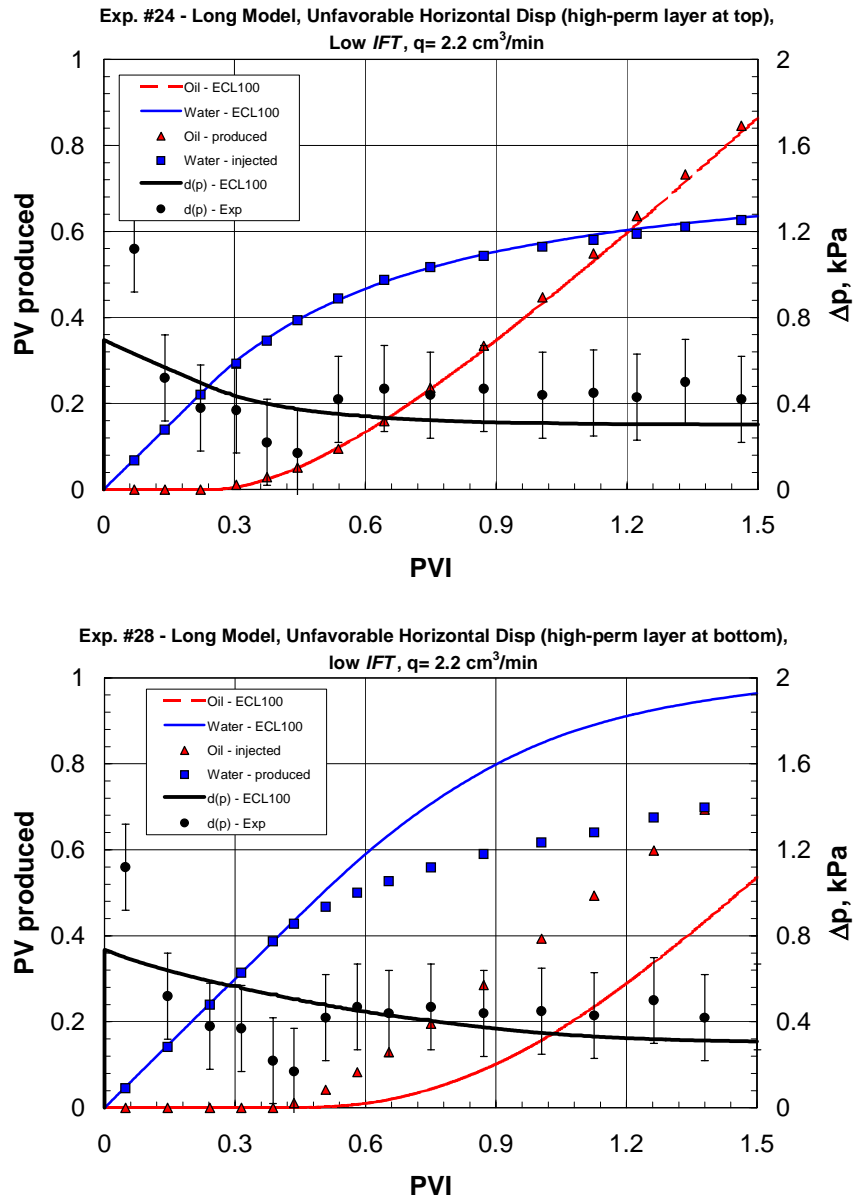


Fig. 5.49: Production and pressure profiles for unfavorable, long, VCS, low-IFT displacements.

### 5.1.3 Discussion: Analysis of scaling groups

The conditions for the transitions from capillary to gravity, from viscous to capillary, and from viscous to gravity flow regions can be generalized as:  $0.2 < S_g < 5.0$  (Zhou *et al.*, 1994), where  $S_g$  is the scaling group and can be either  $MN_{cv}/(1+M)$ , or  $MN_{gv}/(1+M)$ , or  $N_B$ .

In the low-IFT experiments ( $N_{cv} \approx 0$ ), we examined the combined effects of gravity and viscous forces. Fig. 5.50 shows images taken at a certain time ( $PVI=0.25$ ) for three different experiments with different orientations. Related scaling groups are given in Table 5-4. The first experiment was performed with horizontal setup and there was only viscous forces driving the flow ( $N_{gv} \approx 0$ ). The crossflow occurred from the high-permeability layer into the low-permeability layer was caused by the difference between layer pressures due to the viscosity contrast. The second experiment was a vertical cross-section (VCS) displacement, which included both gravity and viscous forces. The scaling group for this experiment is calculated to be,  $N_{gv}M/(1+M) = 1.2$ , which suggests that the displacement was governed by a combination of viscous and gravity forces. The value of  $N_B$  (about 81) also suggests that gravity forces were more important than capillary forces. Viscous forces drive the fluid to flow in the high-permeability layer (Exp. #10), causing a viscous crossflow into the low-permeability layer as can be seen in Fig. 5.50. In the situation where Exp.#16 was performed, however, gravity forces also forced the water to crossflow, and consequently, the water swept more area in the low-permeability layer. Weak gravity tongues in both layers can also be seen in the figure. In the third experiment with the vertical setup, we obtained more stabilized fronts in both layers, which were also dominated by viscous and gravity forces.

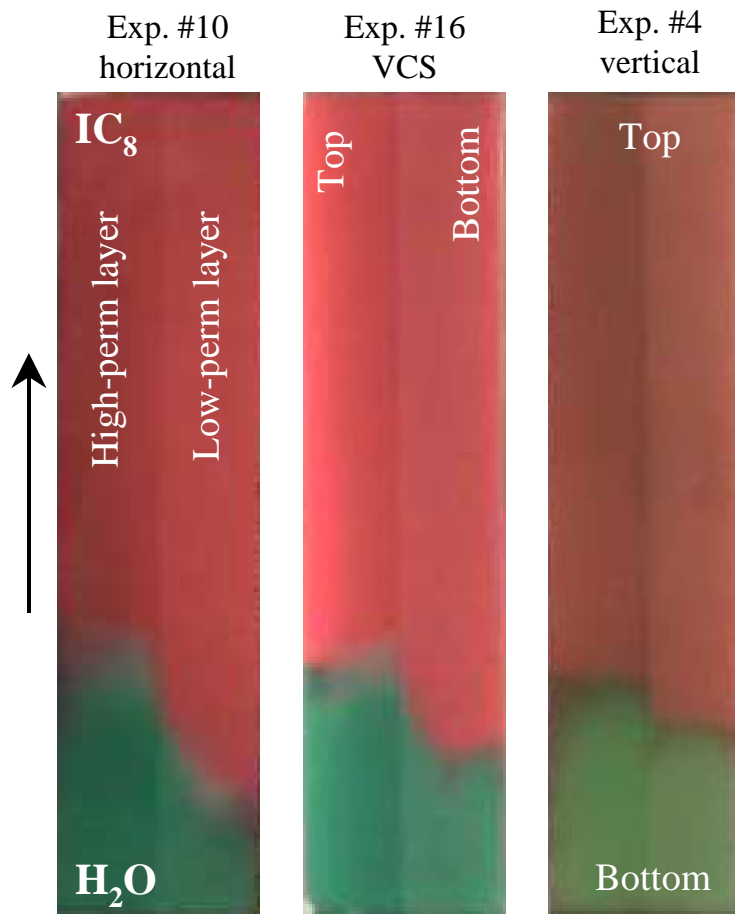


Fig. 5.50: Comparison of low IFT displacements at  $PVI=0.25$  ( $q=2.2 \text{ cm}^3/\text{min}$ ).

Fig. 5.51 shows saturation profiles of the high-IFT experiments performed with different orientations of flow model. The displacement in the horizontal setup included only viscous and capillary forces ( $N_{gv}$ ,  $N_B \approx 0$ ,  $N_{cv}M/(1+M) = 42.3$ ). The scaling group suggests that the displacement was dominated by capillary forces. The capillary imbibition shown in the low-permeability layer in displacement #9 is consistent with that scaling argument. The displacement in the VCS experiment, however, included all three driving forces ( $N_{gv}M/(1+M) = 9.6$ ,  $N_B = 0.22$ ,  $N_{cv}M/(1+M) = 43.7$ ). The scaling groups suggest that gravity and capillary forces more strongly influenced the flow than did viscous forces. But, the  $N_B$  with its lower boundary for the transition region suggests that, in the displacement, capillary forces were more important than gravity forces. The significantly faster flow in the low-permeability layer is consistent, again, with strong capillary imbibition in the experimental image of Exp. #15. It is also interesting to note that when we turned the direction of flow upwards, gravity effects on the displacement increased dramatically. The scaling groups defined by Zhou *et al.* do not provide guidance for the effects of gravity on this kind of displacement, because the analysis that produced the scaling groups was based on the assumption that gravity acts transverse to the average flow direction. Nevertheless, it is clear that gravity acted to reduce the impact of longitudinal capillary imbibition in displacement #3.

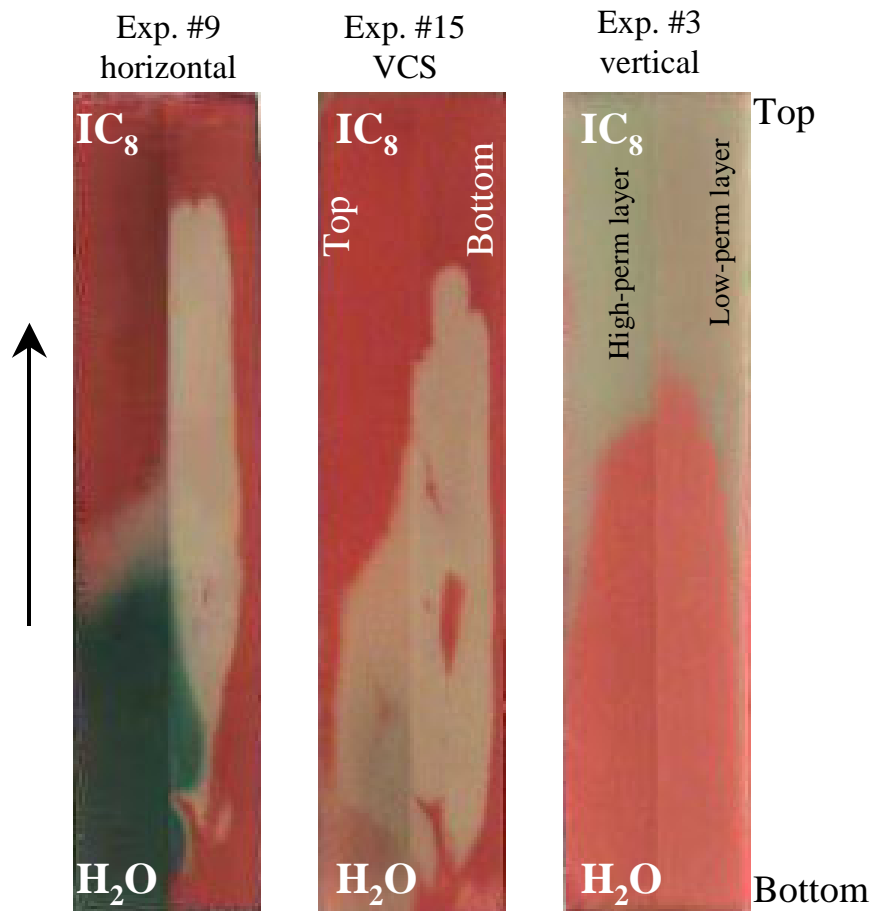


Fig. 5.51: Comparison of high IFT displacements at PVI=0.46 ( $q=2.2 \text{ cm}^3/\text{min}$ ).

The scaling groups for the high-IFT unfavorable drainage displacements also show similar characteristics to those obtained for favorable displacements. Because the capillary pressure for flow in drainage mode (see Fig. 5.7) was high, the corresponding values for the scaling groups of capillary/viscous forces were also larger. For example, the experiment #11 was a horizontal displacement with scaling groups of  $N_{gv}$ ,  $N_B \approx 0$ , and  $N_{cv}M/(1+M) = 88.7$  that was influenced only by the permeability differences and capillary forces. Note that the capillary number for the same liquid system in the same porous model was about half of that value for the imbibition experiment. The values of  $N_{cv}M/(1+M)$  and  $N_{gv}M/(1+M)$  were 68.1 and 8.6, respectively for a similar experiment (#17) in the VCS setup. These values suggest that the displacement in experiment #17 was sharply influenced by both capillary and gravity forces, with smaller effects of viscous forces. But the  $N_B$  for this experiment was 0.13, which is consistent with the idea that the flow was strongly affected by capillary forces. Fig. 5.52 shows the images taken during the related experiments. Capillary forces apparently drove the nonwetting fluid to flow in the larger pores of the high-permeability layer. Comparison of the images of experiments #11 and #17 shows that the gravity effects in the VCS experiment were relatively weak. The vertical displacement (experiment #5) was still influenced by capillary forces, but gravity helped produce more stable fronts and a larger swept area in the low-permeability layer.

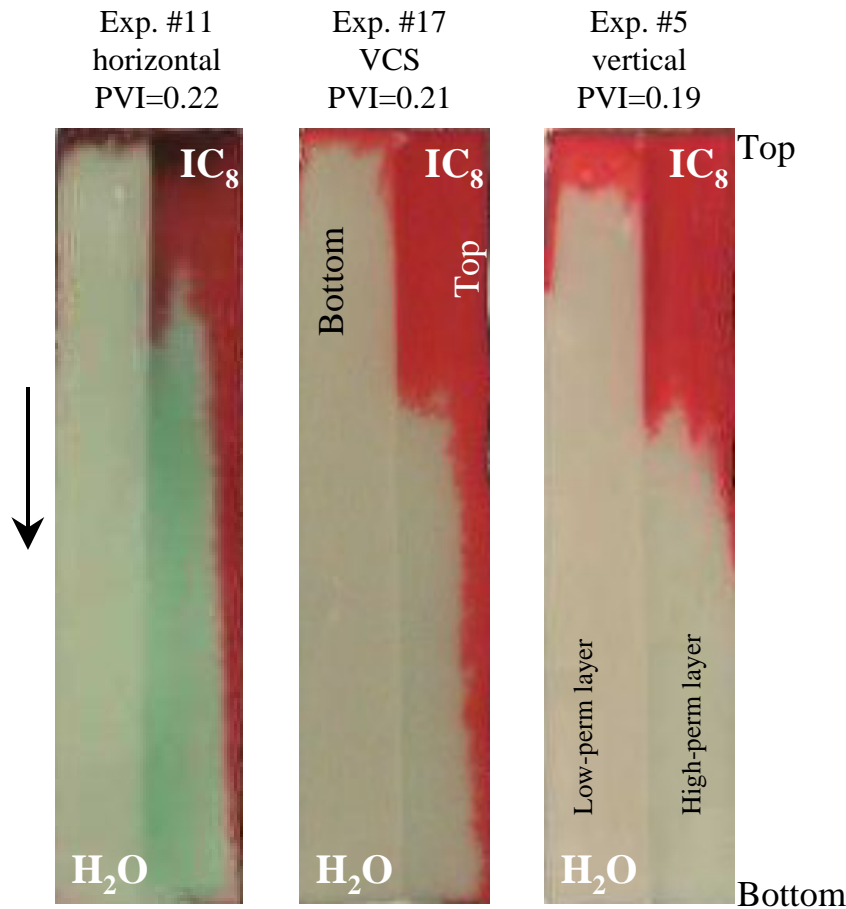


Fig. 5.52: Comparison of high IFT unfavorable displacements ( $q=2.2 \text{ cm}^3/\text{min}$ ).

In the low-IFT unfavorable horizontal displacement (experiment #12), the flow was governed primarily by viscous forces ( $N_{gv}$ ,  $N_B \approx 0$ ,  $N_{cv}M/(1+M) = 0.03$ ). The image shown in Fig. 5.53 shows evidence of unstable viscous flow. Scaling parameters for a similar displacement in the VCS model (experiment #18) are 0.02, 1.06, and 47 for  $N_{cv}M/(1+M)$ ,  $N_{gv}M/(1+M)$ , and  $N_B$ , respectively. These numbers suggest that the VCS displacement was governed by viscous and gravity forces. The image with gravity override in Fig. 5.53 also supports this argument. The displacement in the vertical setup was similar to that in the horizontal setup.

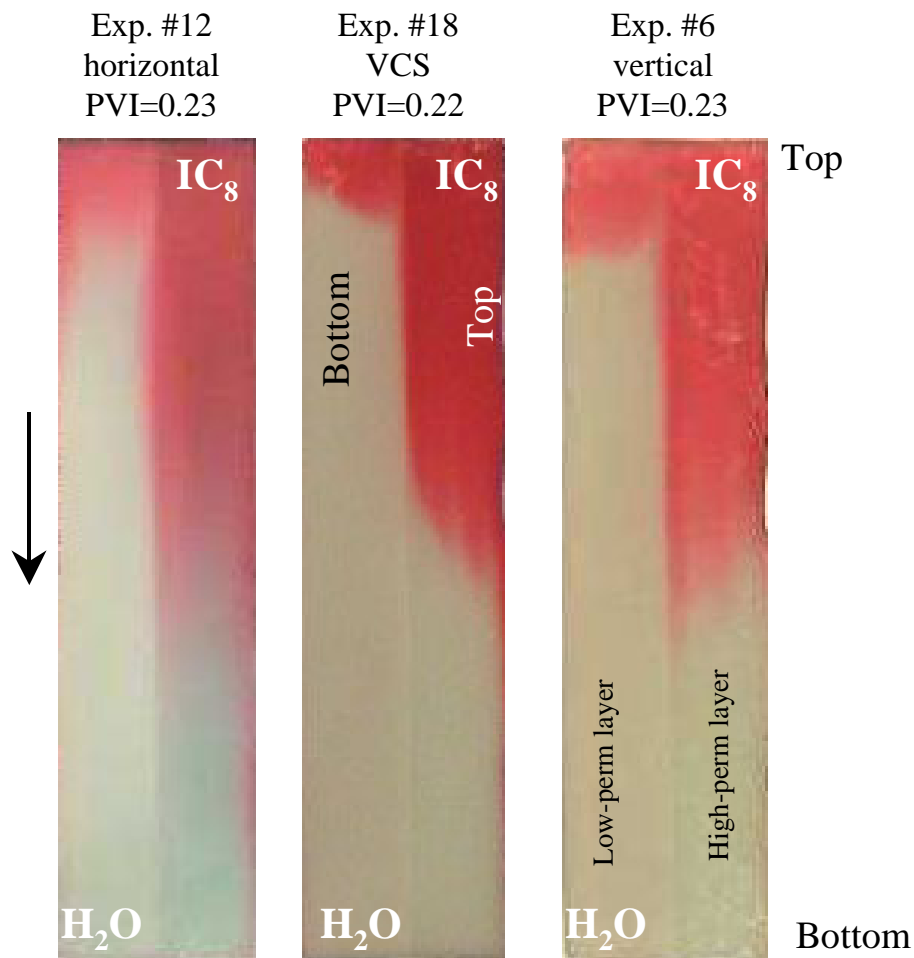


Fig. 5.53: Comparison of low-IFT unfavorable displacements ( $q=2.2 \text{ cm}^3/\text{min}$ ).

The combination of experimental results for low- and high-IFT displacements for imbibition and drainage experiments, and for various orientations with respect to gravity confirm that the ranges of the scaling groups suggested by Zhou *et al.* are reasonable, at least for the regions where capillary or gravity forces were most important. Confirmation of the details of the transition regions would require more experimental work, but it is clear that the

broad outlines of the scaling analysis are consistent with the experimental observations.

#### 5.1.4 Conclusions

A series of experiments was designed and run to investigate combined effects of capillary, viscous, and gravity forces on displacement efficiency in layered systems. Two-phase displacements with favorable and unfavorable mobility ratio were performed. A wide span of capillary and gravity numbers was investigated.

The high-IFT experimental results with small gravity effects show that IFT and flow rate determine how capillary and viscous forces affect a displacement. At high values of the capillary number, capillary forces caused the imbibition displacement front to move more rapidly in the low-permeability layer. In contrast at low values of the capillary number, the front moved more rapidly in the high-permeability layer due to viscous forces. The vertical displacements gave better sweep areas than the horizontal displacements, for both high- and low-IFT fluids. The 2-D images show that displacements in which capillary and viscous forces are roughly balanced give displacement fronts that move at comparable velocities in both low- and high-permeability layers, a situation that results in the optimum sweep efficiency.

The high-IFT displacements in the vertical cross-section model show that all three crossflow mechanisms affected the flow. Though capillary forces affected the flow in these experiments more than others, increasing flow rates and changing the location of permeability heterogeneity resulted in dramatic changes in behavior of displacement. In the experiments with the high-permeability layer at the top, it was observed that capillary and gravity forces acted together, whereas viscous forces opposed them. In the experiments with the inverted flow model, however, gravity and viscous forces acted together while opposing capillary forces.

The results of the low-IFT experiments show that slow displacements produce larger area affected by crossflow. The presence of gravity in the displacements contributed positively to the total sweep efficiency in these experiments except for the displacement with the high-permeability layer at the bottom where gravity crossflow opposed the viscous crossflow.

In all unfavorable drainage displacements, a large portion of the low-permeability layer was left unswept. The unswept area in the high-IFT displacements was even worse.

Numerical simulation of the displacements matched the experimental production history and sweep efficiencies very well. Observed and calculated pressure drops in the situations did not agree well where capillary forces dominated the displacement. Numerical verification of experimental results suggests that further simulation can be used for displacements with a combination of flow rate and IFT that are chosen from an interval we studied.

The experimental results including effects of viscous and capillary forces and gravity segregation confirm that the ranges of scaling groups, suggested by Zhou et al. (1994), are

reasonable. Though confirmation of the details of the transitions would require more experimental work, it is clear that the broad outlines of the scaling analysis are consistent with the experimental observations.

### 5.1.5 Nomenclature

$g$	gravitational force	$H$	height of the layers
$k_{ah}$	horizontal permeability of the model	$k_{av}$	vertical permeability of the model
$k_i$	permeability of layer I	$L$	length of the model
$M$	viscosity ratio	$N_{cv}$	modified capillary number
$N_{gv}$	modified gravity number	$P_c^*$	characteristic capillary pressure
$p_c$	capillary pressure	$p_d$	displacement pressure
$S_{or}$	residual oil saturation	$S_{wc}$	residual water saturation
$q$	flow rate	$v$	Darcy velocity
$W$	width of the model	$\mu_o$	oil viscosity
$\phi$	porosity	$\Delta\rho$	density difference
IFT	interfacial tension	IPA	isopropanol
PVI	pore volume injected	VCS	vertical cross section

## 5.2 When is the streamline approach accurate?

While streamline methods offer many advantages for field scale simulation they also have certain limitations. In general the streamline method is not well suited for displacements with complex physics (high compressibility, capillary effects, complicated phase behavior or more generally, any effect that will move the fluids across streamlines). This is because the streamline method treats flow along each streamline as independent of adjacent streamlines, and thus the effects of fluids crossflow are not represented in the simulations (though an operator splitting technique described by Bratvedt *et al.* (1996), does a good job in approximating crossflow due to gravity effects).

If users of streamline methods are to interpret simulation results, they will need to assess whether any of the mechanisms not modeled in the simulation are important enough to limit the accuracy of the simulation. Thus it is very important to quantify what the limitations of the method are, so that the users can determine when calculated results can be trusted and when other computational approaches should be considered. There is no one numerical method that can solve the governing equation for all cases efficiently. Depending on which mechanism dominates, different techniques should be used.

Generally, the finite difference methods tend to be better in compressible gas drives (gas cap, solution gas). It has been noted (Baker, 2001) that the streamline simulation method gives inaccurate results for water floods that do not have good voidage balance. A rule of thumb given by Baker (2001) for streamline simulation is that streamline simulation should be avoided when the voidage replacement ratio is less than 0.9. This rule requires that the

majority of the reservoir energy comes from a water flood or water drive and not from expansion or solution gas drives. Also in gravity-dominated situations, significant speed up, which is one of the most important advantages of streamline simulation, is rarely achieved.

The focus of the section is on the limitations to the use of streamlines brought about by crossflow effects. Crossflow due to dispersion is neglected. We will present results from *Eclipse* (a finite difference simulator), and *3DSL* (streamline based simulator). Both are commercially available.

Two calculation examples are initially presented to illustrate the advantages as well as the limitations of the streamline approach:

1. a viscous dominated displacement
2. a gravity dominated displacement

The first calculation example is an immiscible water-oil displacement. The properties of the reservoir and the fluid properties were chosen such that the crossflow effects of capillary and gravity forces were removed. To remove the effect of gravity, the densities of the fluids were made equal at the reservoir condition, while using surface tension of zero ensures no capillary crossflow. Viscous crossflow was greatly minimized by setting the end point mobility ratio to one and a total mobility ratio that remains constant throughout the displacement process. The saturation profile from both simulators at 0.125, 0.25 and 0.5 pore volumes of injected fluid is shown in the Fig. 5.54.

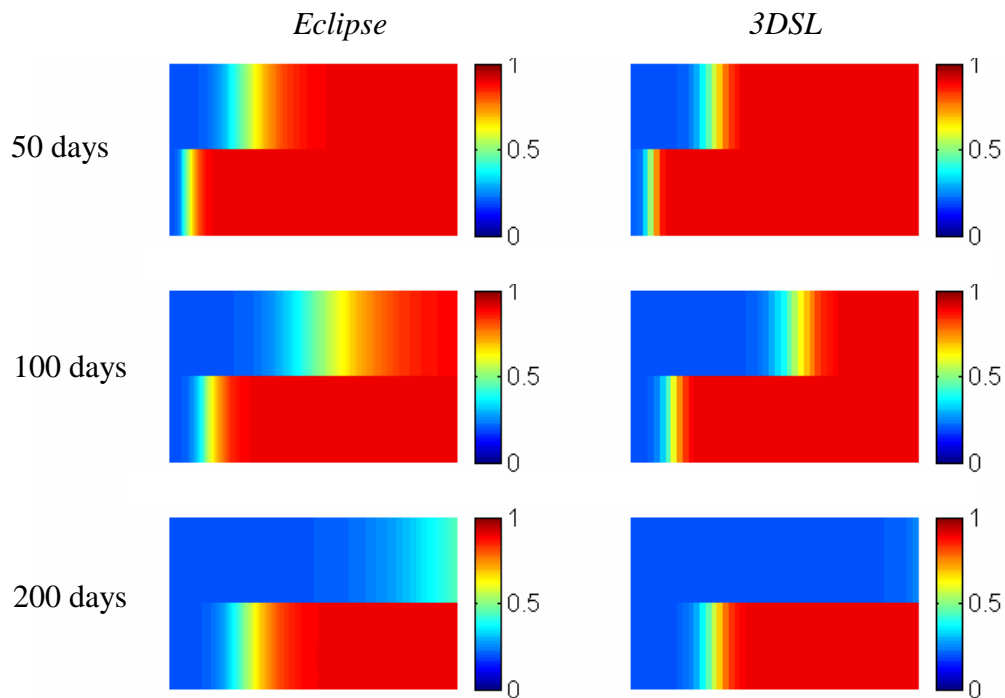


Fig. 5.54: Saturation maps (Example 1) from *Eclipse* and *3DSL*

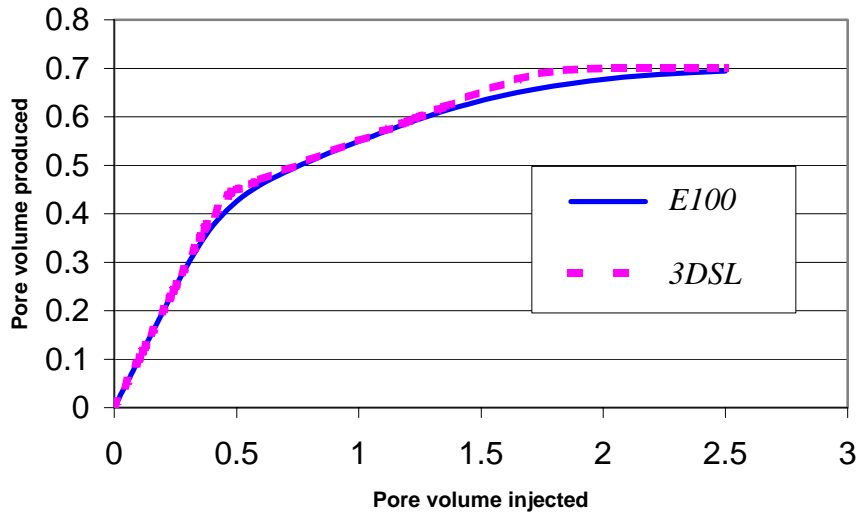


Fig. 5.55: Recovery curves (Example 1) from *Eclipse* and *3DSL*

As can be seen from Fig. 5.54 and Fig. 5.55, the predictions from *3DSL* and *Eclipse* are in excellent agreement. The streamline method actually does a somewhat better job of capturing the breakthrough of the two distinct layers, while the fronts in the *Eclipse* simulation are smeared by numerical dispersion. The time for this simple streamline simulation was seven times faster than for *Eclipse* (See Table 5-6) for this relatively small 200 x 50 grid (note that the difference in computation time increases with grid refinement).

Table 5-6 Simulation times (Example 1: 200x1x50)

Simulator	Elapsed CPU time
<i>Eclipse</i>	350 secs
<i>3DSL</i>	50 secs

In the second set of example calculations, crossflow mechanisms were introduced in the displacement process such that the convective force is no longer the dominant mechanism. This was achieved by introducing density difference between the fluids and also introducing capillary pressure between the phases. The results of the simulation runs at 0.125, 0.25 and 0.5 pore volumes of injected fluid are shown in Fig. 5.56. The recovery curves and the CPU requirements for this example calculation are shown in Fig. 5.57 and Table 5-7.

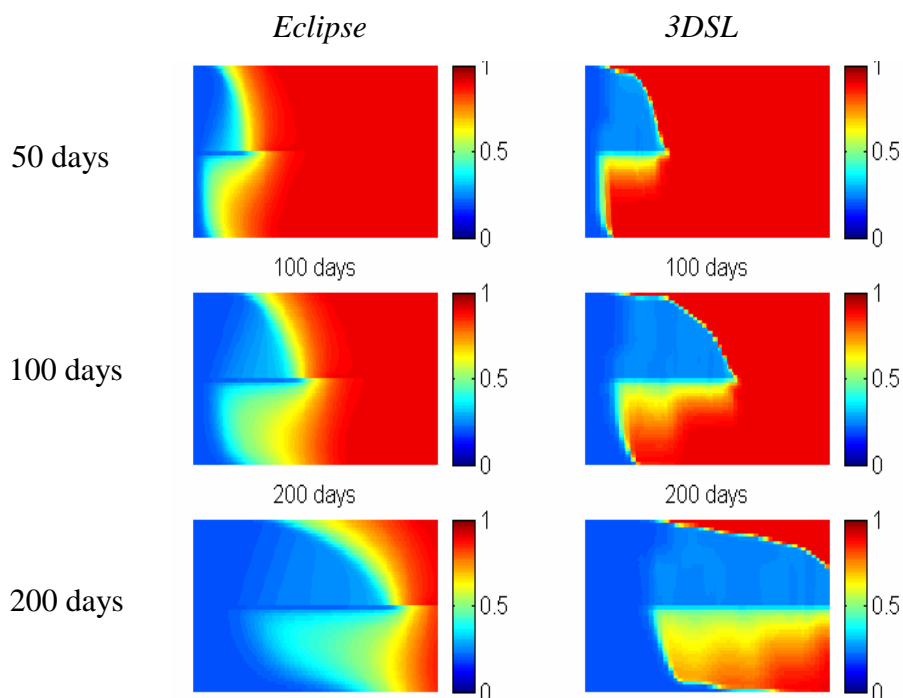


Fig. 5.56: Saturation map (Example 2) from *Eclipse* and *3DSL*

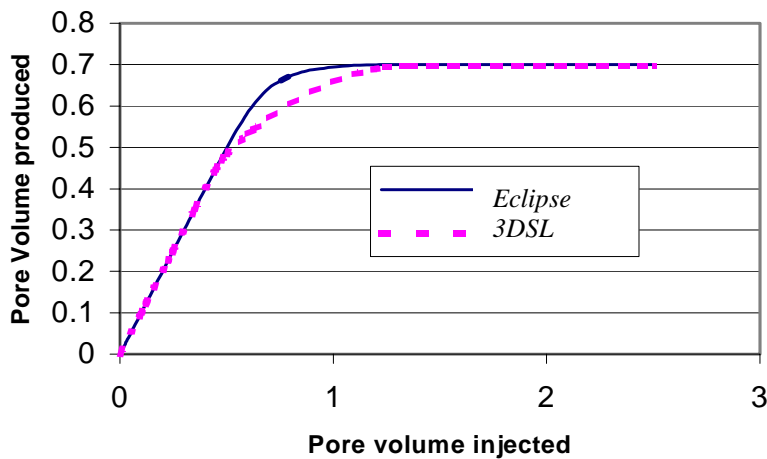


Fig. 5.57: Recovery Curve (Example 2) from *Eclipse* and *3DSL*

Table 5-7 Simulation time (Example 2: 200x1x50)

Simulator	Elapsed CPU time
<i>Eclipse</i>	480 secs
<i>3DSL</i>	300 secs

The results shown in Fig. 5.56 and Fig. 5.57 indicate that the simulation approaches give quite different results, both in the spatial distribution of the fluids and also in the integrated production curves. Delayed water breakthrough in the Eclipse results occurs because of the

imbibition of water by the low permeability region. Also the front moves faster in the low permeability layer for the Eclipse simulations, which is not observed in the 3DSL simulations. The recovery curves also show almost a 20% difference in the recovered oil at the breakthrough of the injected fluid with Eclipse predicting a higher recovery.

For the user, the problem is to determine to what extent these crossflow effects can be neglected with reasonable assurance that the results of streamline based simulation are fairly accurate (at least compared to the other uncertainties in the simulation data). The simulation engineer is interested in knowing (before running simulations) when he can safely use the streamline-based simulators. He ought to be able to look at his reservoir and its fluid properties and be able to take a decision on which method of simulation to use without jeopardizing the accuracy of the results. This is not a trivial issue, and in this section we will try to understand the transition from a very good match between the different methods of simulation to a complete mismatch, so that guidance can be given as to when use of streamlines is appropriate.

### **5.2.1 Crossflow mechanisms**

A lot of work has been done to understand the effect of crossflow on displacements. In simple terms, the word crossflow is used to describe any mechanism that moves fluids in direction transverse to the streamlines (away from the direction of bulk flow). Fig. 5.58 shows a cross section of streamlines. In the streamline simulation approach fluids in a particular streamline is confined to that streamline and movement of fluids between streamlines (crossflow) is not modeled. Fluid crossflow can significantly affect sweep efficiency in heterogeneous reservoirs. The importance of fluid crossflow relative to purely longitudinal convective transport in a two-dimensional domain depends on several factors: rock properties (porosity, permeability, ratio of vertical and horizontal permeability), fluid properties (phase densities, phase viscosities and interfacial tension), wettability, relative permeability and capillary pressure.

There are basically four types of crossflow: viscous crossflow, gravity crossflow, capillary crossflow and crossflow due to dispersion. These crossflow mechanisms affect flow in different ways depending on the type of displacement, and as experimental investigations have shown, tend to be more significant in heterogeneous (poorly sorted) media where high and low permeability zones exist. For displacements where viscosity differences exist between the fluids, and a transverse pressure differential exists, then viscous crossflow will be present. Gravity will induce flow in the vertical direction when the densities of the fluids are different, and this will produce different effects depending on whether the high permeable layer is above or below the low permeable layer. Capillary crossflow is caused by differences in saturation and possibly interfacial tension between the fluids in a displacement system. Crossflow due to dispersion occurs when differences in concentration and local flow velocity exist in a domain. Table 5-8 summarizes the crossflow types and the driving force.

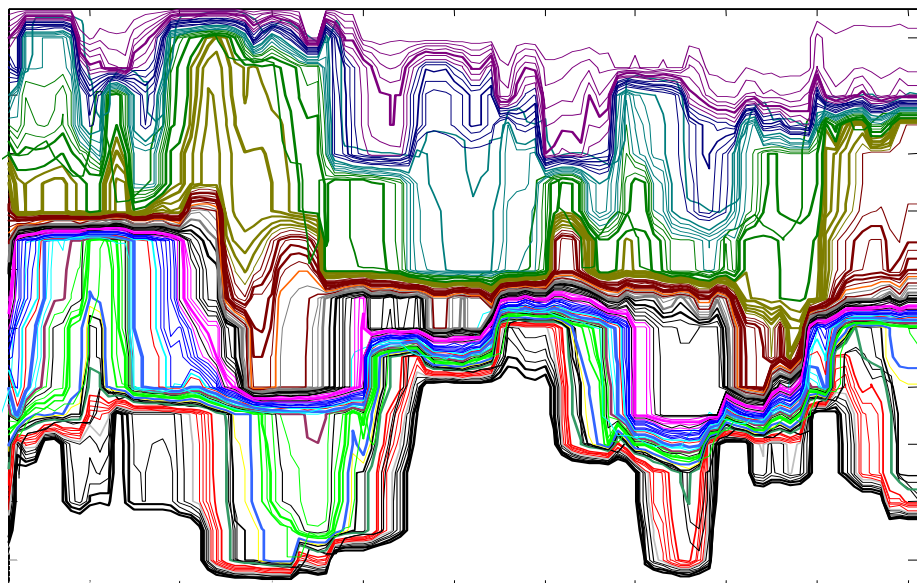


Fig. 5.58: Cross Section of Streamlines

Table 5-8: Types of Crossflow

Crossflow Type	Driving force
Viscous	$\Delta P$ (pressure)
Capillary	$\Delta\sigma, \Delta S$
Gravity	$\Delta\rho$ (density)
Dispersion	$\Delta C, \Delta v$

Dimensionless scaling groups from the mathematical statement of a particular process are very important for a number of reasons. The scaled groups are used to generalize results derived from a set of systems to offer guidelines to understanding other systems. Another good reason is to be able to obtain limiting behavior of systems, as the scaling groups become large or small. Scaling is also used to gauge the effects of various system parameters. We use these scaling groups to map out the parameter space of interest so that a reasonable number of physical and/or numerical experiments can be performed (See Section 5.1).

In this work, as in the work of Zhou, Fayers and Orr (1992), we are interested in transverse flow (or flow away from the streamline). Hence, we consider the gravity to viscous ratio, the capillary to viscous ratio and the mobility ratio defined in Section 5.1.

The gravity to viscous ratio quantifies the average balance between the viscous forces in the x-direction and the gravity forces in the z-direction. In addition to the obvious fact that this ratio requires that the densities of the injected and displaced components be different, the

ratio indicates that the effectiveness of gravity forces is increased in slow average velocity displacements, large vertical permeability communication and longer thinner reservoirs.

The capillary to viscous ratio quantifies the balance between the viscous forces in the x-direction and the capillary forces in the z-direction and it requires that the pressure of the phases be different. Like the gravity-viscous ratio, capillary forces dominate more in long, thin high vertical permeability reservoirs with low displacement velocities.

Finally, the mobility ratio describes the relative ease of flow of one phase to the other.

The definitions of these scaling groups are for a two-dimensional homogenous permeability field though could be easily extended to three-dimensional domain (Tchelepi, 1989). The interest is in relative comparison of the groups for different displacement processes so an average value of  $N_{gv}$  or  $N_{cv}$  will be quoted for each displacement. The ratio  $M/(1+M)$  is treated as a constant in the system though in reality, the mobility ratio  $M$  is a function of saturation.

### 5.2.2 Simulation model

Displacements in a 2D layered system (Fig. 5.59) are used to analysis the accuracy of streamline simulations over a wide range of flow settings. The model parameters are summarized in Table 5-9.

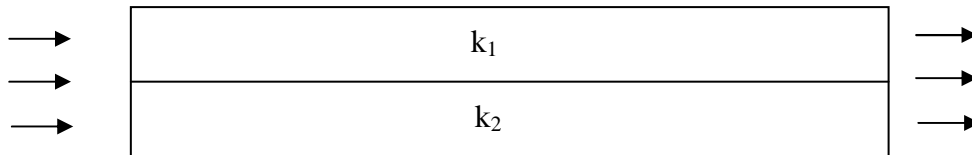


Fig. 5.59: 2D layered system

Table 5-9: Model parameters for calculation examples

Layer	1	2
Permeability ( $mD$ )	100	400
Hight ( $m$ )	2.5	2.5
Length: 100 $m$ , Width: 10 $m$ , Porosity: 0.2, Initial water ( $S_{wi}$ ): 0.1 Residual $S_{or}$ Interfacial tension from 0-500 $dynes/cm$ . Oil/water viscosity varied to achieve the desired mobility ratio. Oil/water density varied to achieve the desired scaling number.		

To evaluate the magnitudes of crossflow terms for different displacement processes and at a particular time step, we calculate the contribution of different crossflow term in each grid cell and then average over the entire number contributing grid cells. This average which gives an indication of the contribution of the particular flow mechanism is then plotted as the dimensionless scale group increases. The interest here is not on the absolute number but on the relative magnitude of the forces compared to each other. In other words, the trend as the scaled groups are increased will give a first guess to the regions of dominance and when the forces realign themselves. Application of this approach is illustrated in Fig. 5.60 demonstrating the locations of areas of maximum crossflow for a) gravity dominated flow and b) capillary dominated flow.

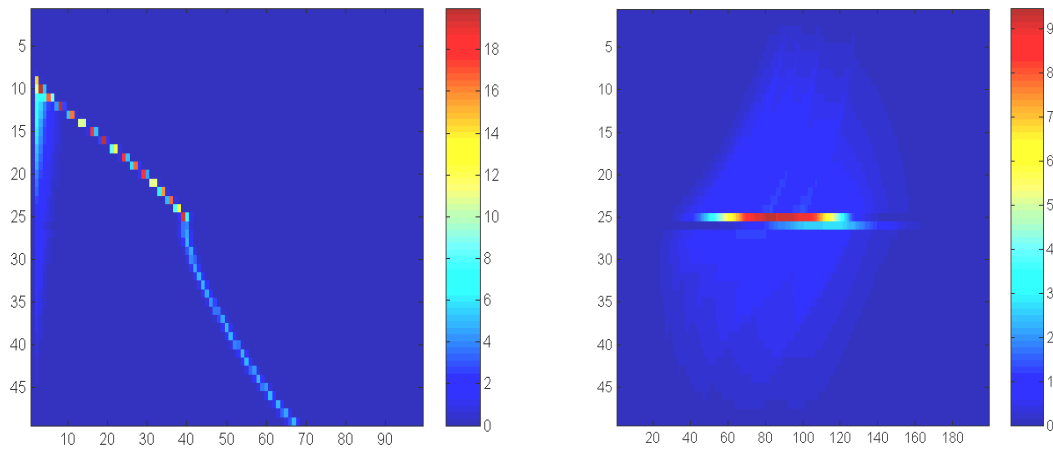


Fig. 5.60: Location of crossflow a) gravity dominated flow b) capillary dominated flow in a two-layer system.

For more detailed comparison of the simulators, recovery curves, saturation maps as well as saturation difference plots were used.

The comparison of the simulators was done in two stages:

1. First a comparison based only on the effects of capillary forces (gravity was removed by setting the density of the fluids equal).
2. The second comparison was based only on the gravity effects and the capillary effect between the fluids was neglected.

This is clearly a simplification as the interplay of gravity and capillary effects exists, as the experimental results of Section 5.1 demonstrate. The idea in this study is to be able to suggest (in terms of the dimensionless numbers) where the crossflow mechanisms are dominant in a displacement such that neglecting them, as is the case in streamline simulators, would be significantly inaccurate.

The study was also done separately for water-flood displacement and gas injection but in gas injection, the fluids were still assumed to be immiscible. In high-pressure gas injection processes, phase behavior effects can reduce the surface tension significantly, and therefore capillary crossflow may be small, though no quantitative analysis of the impact of low surface tension in such displacement has been performed. Volume change on mixing was neglected.

Recovery curves are normally used to compare simulation results. The difficulty associated with using only recovery curves is that it is an integrated response of so many mechanisms going on in a displacement process. Two displacement dominated by two different displacement mechanisms can be shown to have almost same recovery curve. It becomes very difficult to tell from the recovery curve what mechanism is actually responsible for the distribution of the fluids in the reservoir. A typical example to illustrate the point is shown in Fig. 5.61.

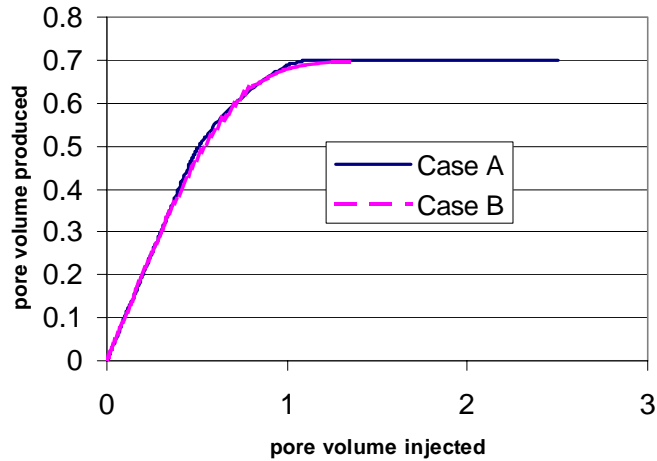


Fig. 5.61 Recovery curve for two fundamentally different displacements

In the example in Fig. 5.61 both cases have the same rock properties and volume, but the fluid properties are different. Looking at the recovery curves alone one could think that both curves represent the same type of displacement. In case A, the fluids have been moved by gravity effects, but the second case is purely a capillary-dominated flow with no gravity effects at all. The fluid properties are given in Table 5-10.

Table 5-10: Fluid properties

Property	Case A	Case B
Water Density ( $kg/m^3$ )	1089	1089
Oil Density ( $kg/m^3$ )	589	1089
Surface tension ( $dynes/cm$ )	0	90
Rate ( $m^3/day$ )	2.5	0.5

The saturation maps for the two cases show the obvious differences between the displacements, which proves that using recovery curves alone in judging simulation results could be misleading. The saturation maps should in all cases complement recovery curves.

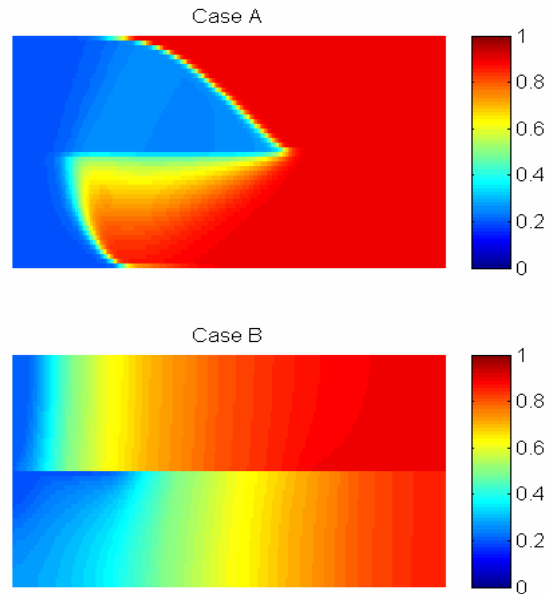


Fig. 5.62: Saturation maps for case A and case B

Saturation profiles are another qualitative tool used for comparison. For this study, the saturation map was interpreted based on the location of the fronts in both layers. Flow is considered capillary-dominated when the location of the front in the low permeability layer almost catches up (or is faster) with the location of the front in the high permeability layer.

Also as part of the saturation comparison tool we considered the saturation difference plot. In this plot, we take the absolute difference in the saturation values at the grid blocks. The plot emphasizes where the differences exist between the simulators thus showing us where crossflow of fluids happen most.

Fig. 5.63 illustrates the use of saturation maps. From the plots one could (though subjective) consider capillary effects to begin to be important above a capillary-to-viscous ratio of around 3.

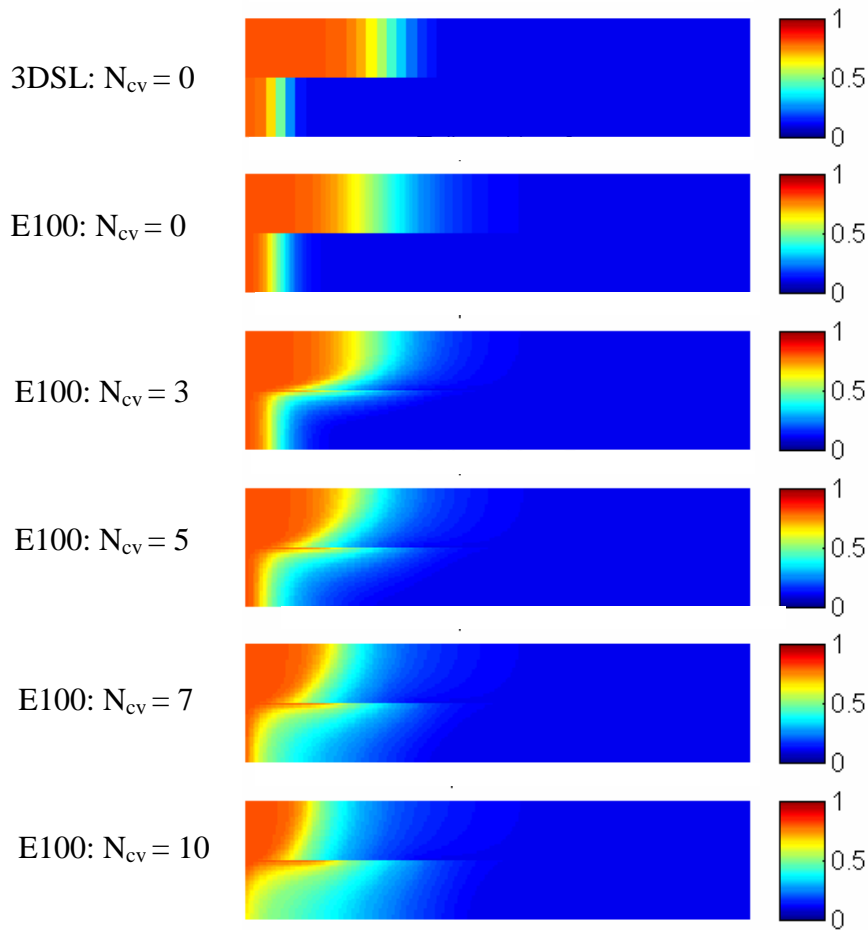


Fig. 5.63: Saturation map showing displacement for increasing capillary number.  $M = 1$

The corresponding saturation difference plots for this displacement at 0.5 PV injected are shown in Fig. 5.64.

### 5.2.3 Quantifying effects of numerical dispersion

The first step in the comparison using these tools would be to compare the results of the simulators for a displacement without any crossflow mechanism (Both capillary-to-viscous ratio and gravity-to-viscous ratio of zero). Ordinarily the results from the different simulators should be the same. Any difference between them for this case will give us an idea of the magnitude of numerical dispersion and smearing in the finite difference method. It also allows us avoid trying to match effects of numerical dispersion. From the recovery curves predicted by the two simulators given in Fig. 5.65, we see that the difference in recovery for the simulators actually depends on the time of analysis, but on average, there is a seven percent difference in recovery that can be attributed to the effects of numerical smearing. This factor should be intuitively removed in subsequent comparisons.

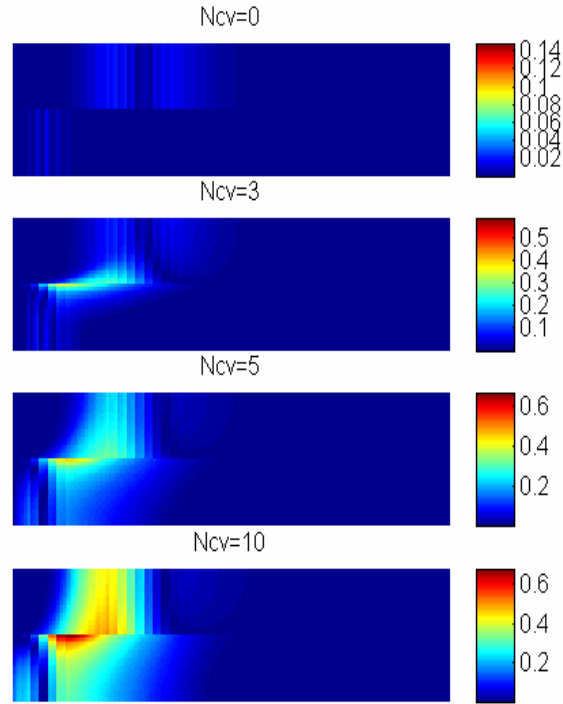


Fig. 5.64: Saturation difference plot for  $M = 1$

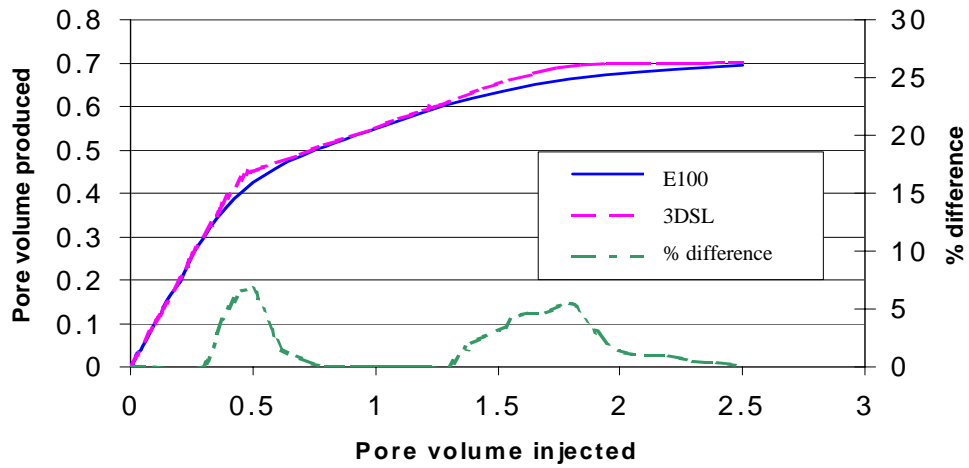


Fig. 5.65 Recovery curves and recovery difference ( $N_{cv} = 0$  and  $N_{gv} = 0$ ).

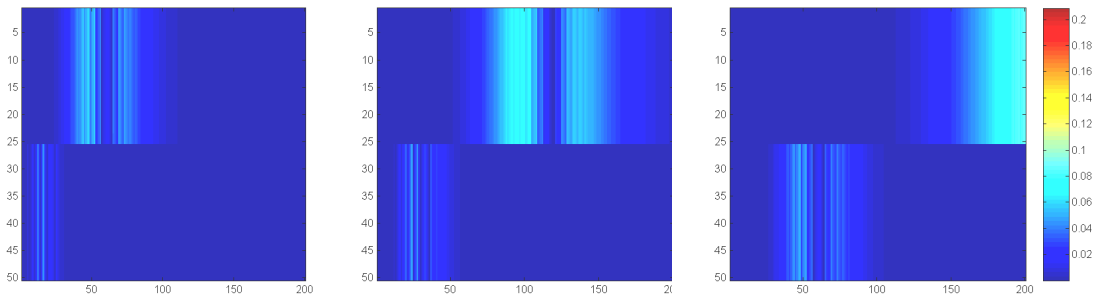


Fig. 5.66: Saturation difference for  $N_{cv} = 0$  at increasing pore volume injected.

The saturation difference plots for the displacement illustrated are given in Fig. 5.66. Again the difference between the two simulators is emphasized especially around the fronts. The difference in the saturation profiles is purely the effect of numerical dispersion.

## 5.2.4 Results

The comparison of the simulators was done separately to investigate the effects of the two mechanisms of crossflow (gravity and capillary). The interplay of gravity and capillary effects was not investigated in this study, though it certainly can exist and could modify displacement performance significantly.

### 5.2.4.1 Capillary effects

This study covers the range of capillary-to viscous number ( $N_{cv}$ ) from zero to twenty (0-20) and a mobility ratio up to fifty ( $M < 50$ ). The analysis of three displacement processes at different capillary to viscous ratio ( $N_{cv} = 1.5$ ,  $N_{cv} = 3$  and  $N_{cv} = 15$ ) using the comparative tools is shown below. The saturation maps (Fig. 5.67, Fig. 5.70 and Fig. 5.73) and the saturation difference plots reported in Fig. 5.68, Fig. 5.71 and Fig. 5.74 are shown for 0.125, 0.25 and 0.5 pore volumes of injected fluid. The recovery curves and the difference in recovery (Fig. 5.69, Fig. 5.72 and Fig. 5.75) are also shown. As pointed out earlier, these comparisons are sensitive to the time of analysis.

The saturation plots clearly show an increase in flow into the low permeability region as we move up higher in  $N_{cv}$  scale. Also notice the increase in the highest value of percentage recovery difference. While  $N_{cv} = 1.5$  has about 5%,  $N_{cv} = 3$  has about 15% and  $N_{cv} = 15$  has about 25% difference.

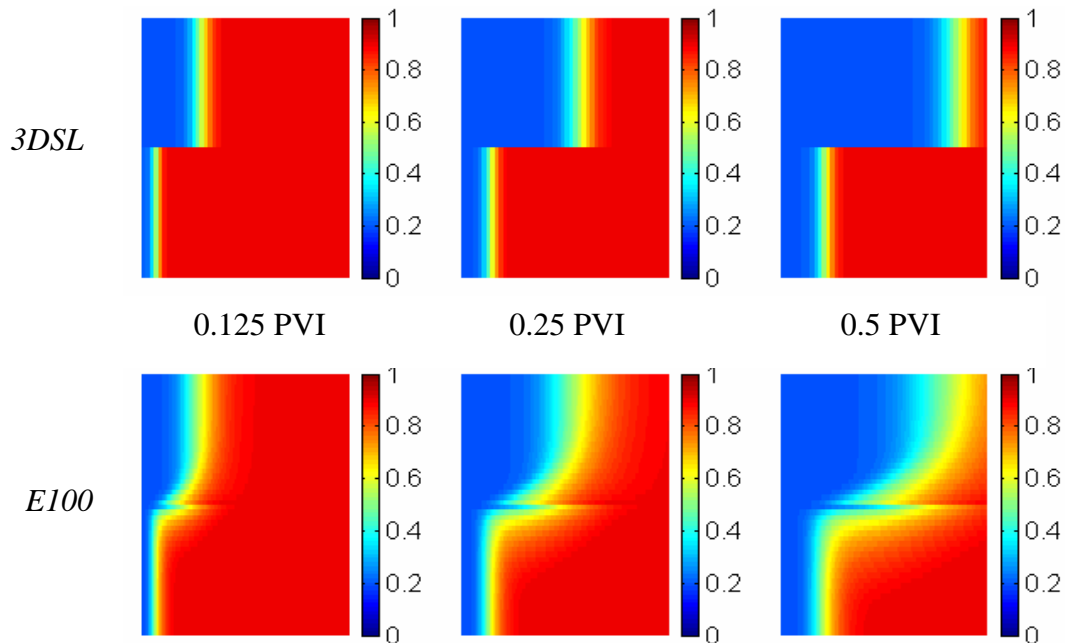


Fig. 5.67: Saturation maps for  $N_{cv} = 1.5$ ,  $N_{gv} = 0$ ,  $M = 1$

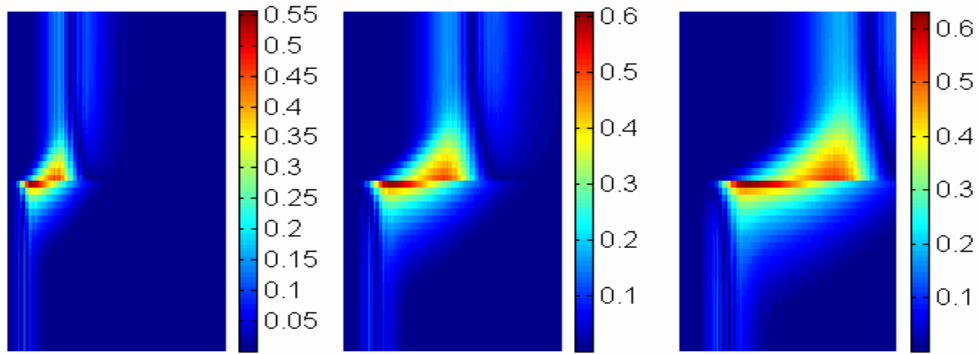


Fig. 5.68: Saturation difference for  $N_{cv} = 1.5$  at increasing pore volume injected.

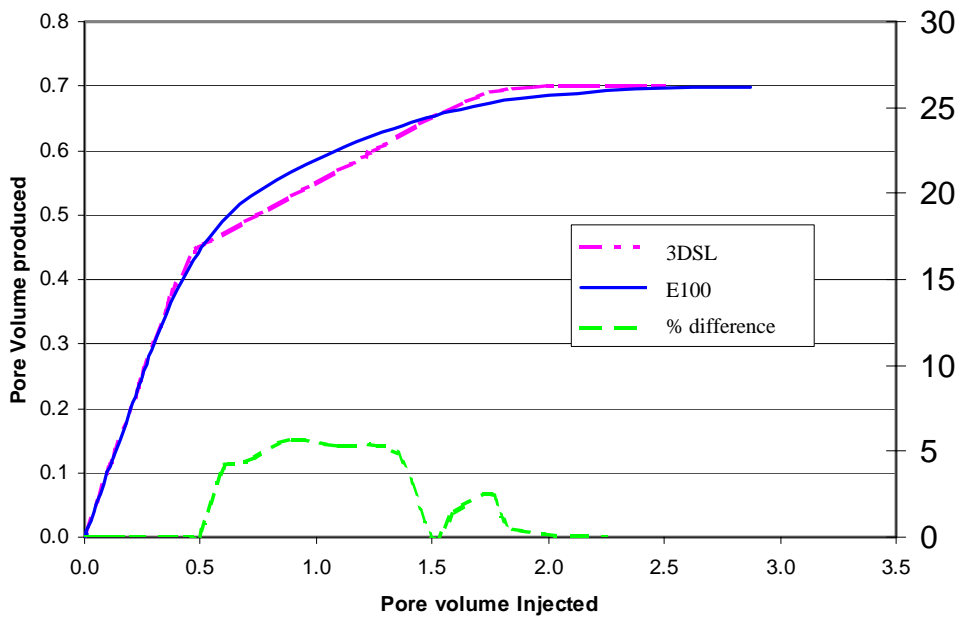


Fig. 5.69: Recovery curves/recovery difference for  $N_{cv} = 1.5$

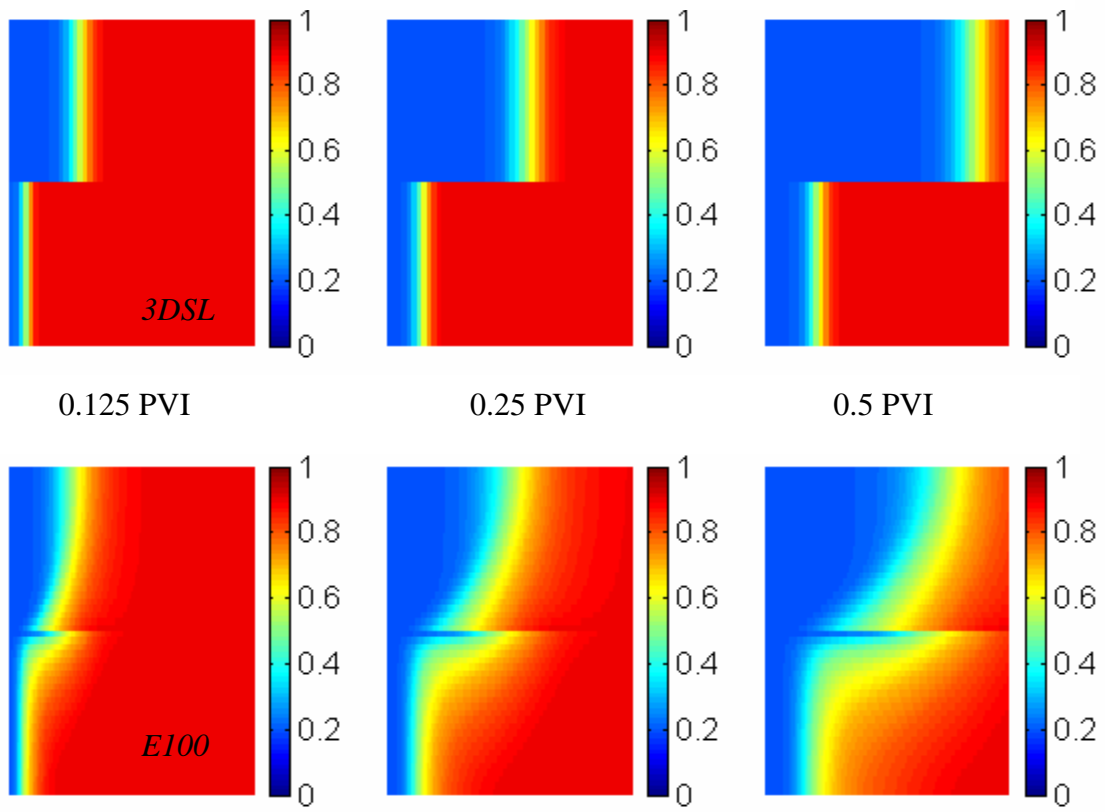


Fig. 5.70: Saturation maps for  $N_{cv} = 3$ ,  $N_{gv} = 0$  and  $M = 1$

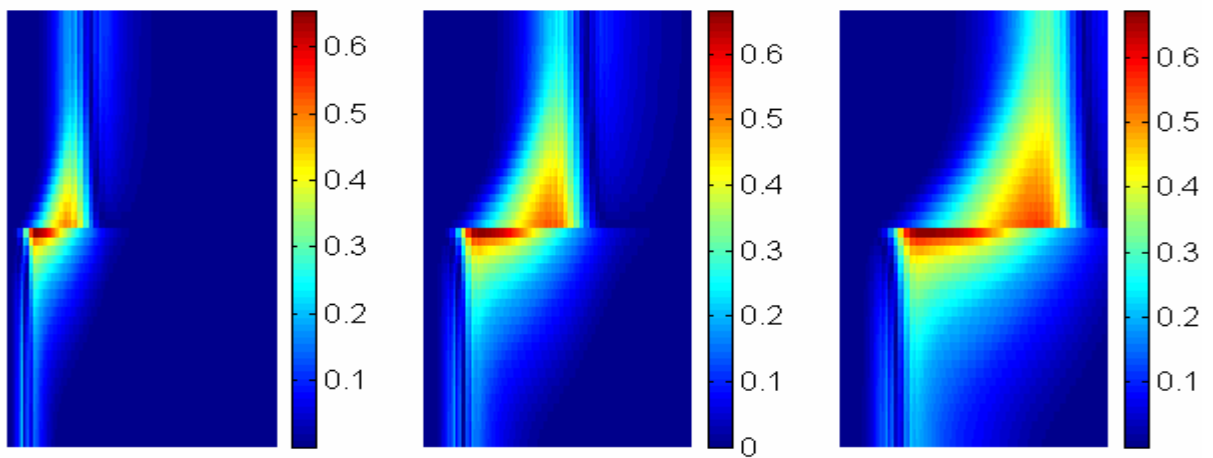


Fig. 5.71: Saturation difference for  $N_{cv} = 3$  at increasing pore volume injected.

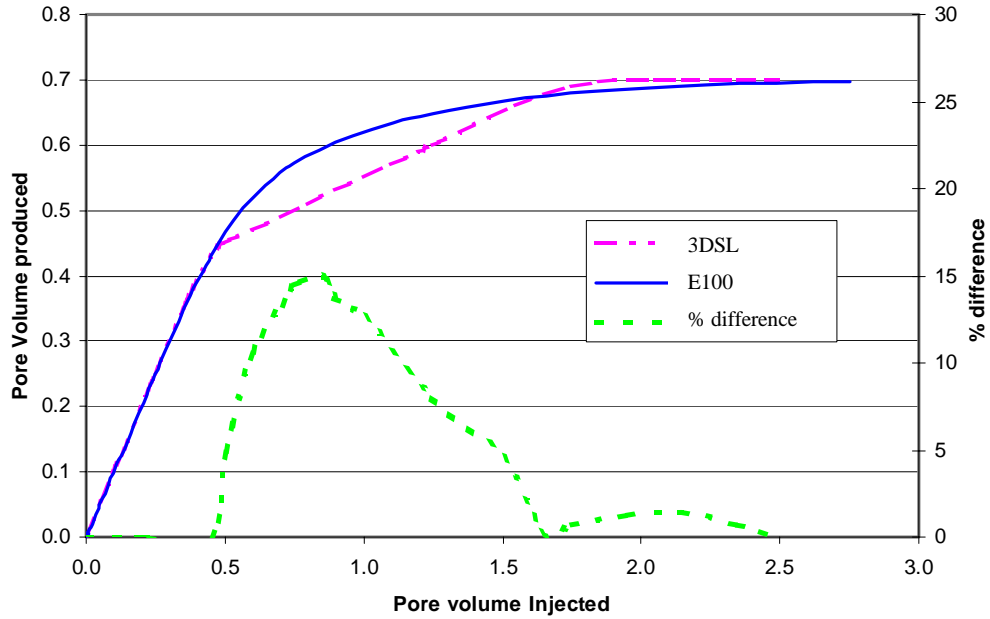


Fig. 5.72: Recovery curves/recovery difference for  $N_{cv} = 3$

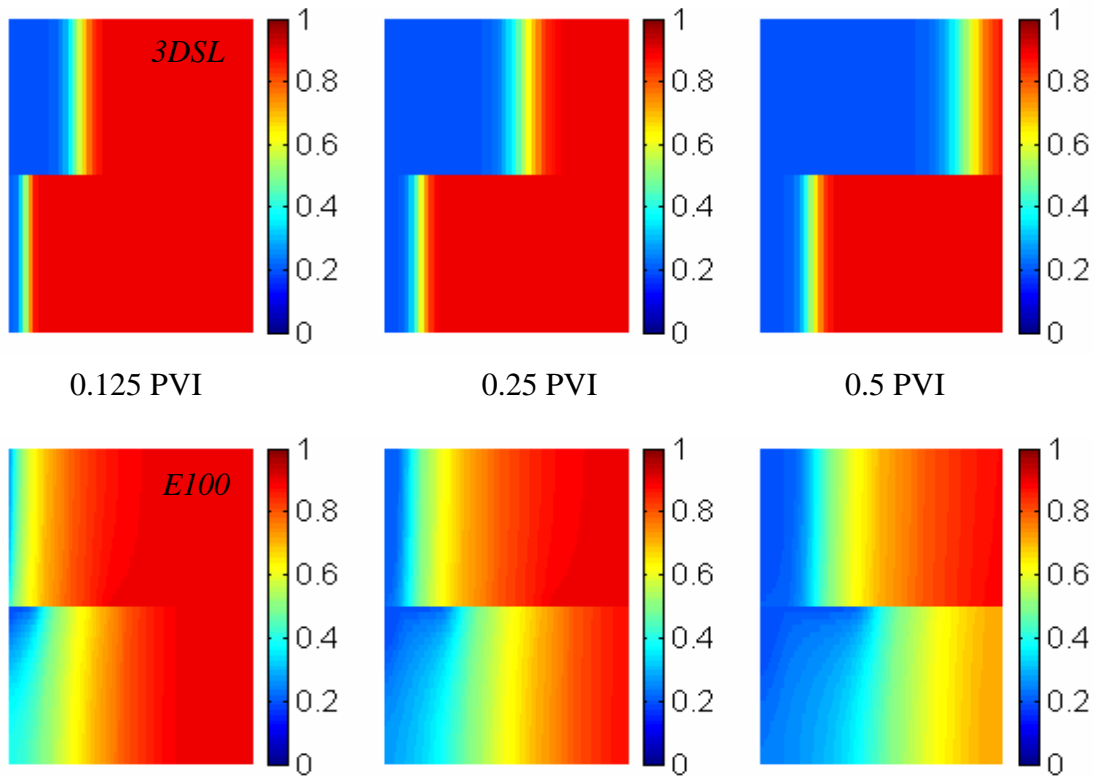


Fig. 5.73: Saturation maps for  $N_{cv} = 15$ ,  $N_{gv} = 0$ ,  $M = 1$ .

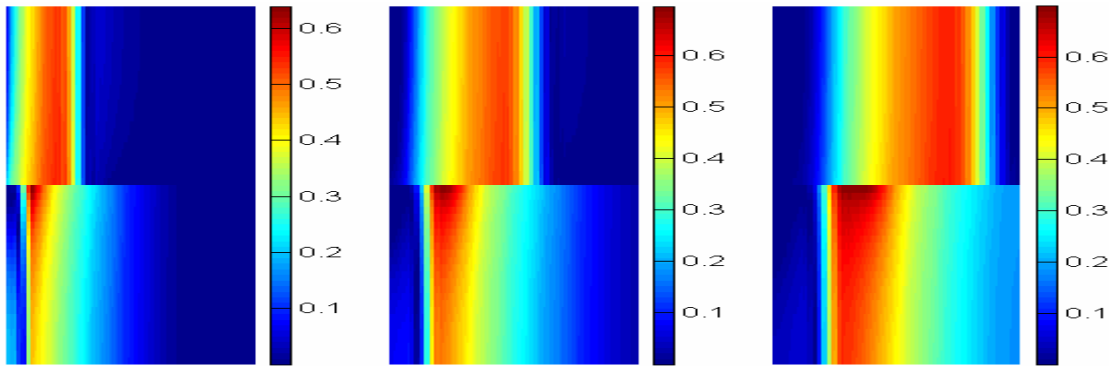


Fig. 5.74: Saturation difference for  $N_{cv} = 15$  at increasing pore volume injected.

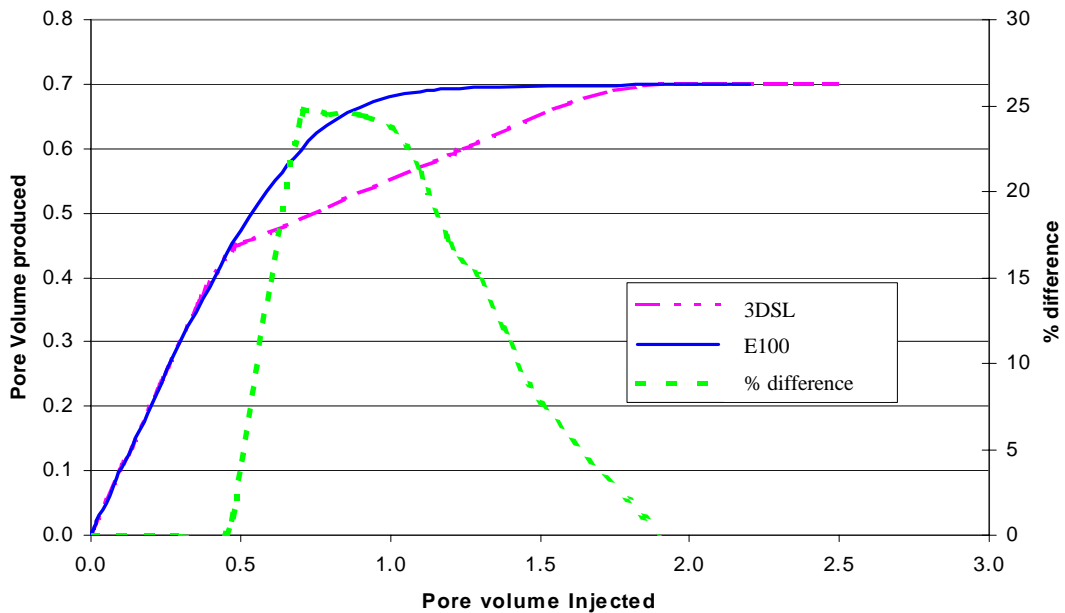


Fig. 5.75: Recovery curves/recovery for  $N_{cv}=15$ .

A careful look at the plots given above shows the increased saturation difference and high percentage difference in the recovery curves as the capillary-to-viscous ratio is increased. Clearly, the figures suggest that a displacement with average capillary-to-viscous ratio of 15 should not be modeled with a streamline simulator, unless some provision is made for representing the capillary forces (See Section 5.3).

To monitor the transition from good streamline simulation area to poor streamline simulation area, we compared the saturation profiles of displacements with increasing capillary number and mobility ratio, we noticed the strong dependence of the capillary effects on the mobility ratio. It was found that the higher the mobility ratio, the more significant the

effects of capillary pressure on the displacement at least for this homogeneous reservoir. Thus the limit of the use of streamline simulator for capillary dominated displacements will depend on the mobility ratio. The higher the mobility ratio, the lower the capillary number ( $N_{cv}$ ) displacement that the streamline based simulators can model without jeopardizing the accuracy of the simulation results.

Fig. 5.76 was generated with *Eclipse* just to show the increasing spatial effect of capillary forces. *3DSL* does not model capillary forces at all, and is on the first row. Fig. 5.77 shows the average error in the saturation as the capillary-to-viscous ratio increases. To get this plot, we took the absolute difference in the saturation data for the two simulators at each grid block. The sum of this difference in all the cells was taken, then averaged over the contributing cells. Because we have established that cross flow is localized at the fronts and the boundary between layers, this average saturation difference will be representative of crossflow effects.

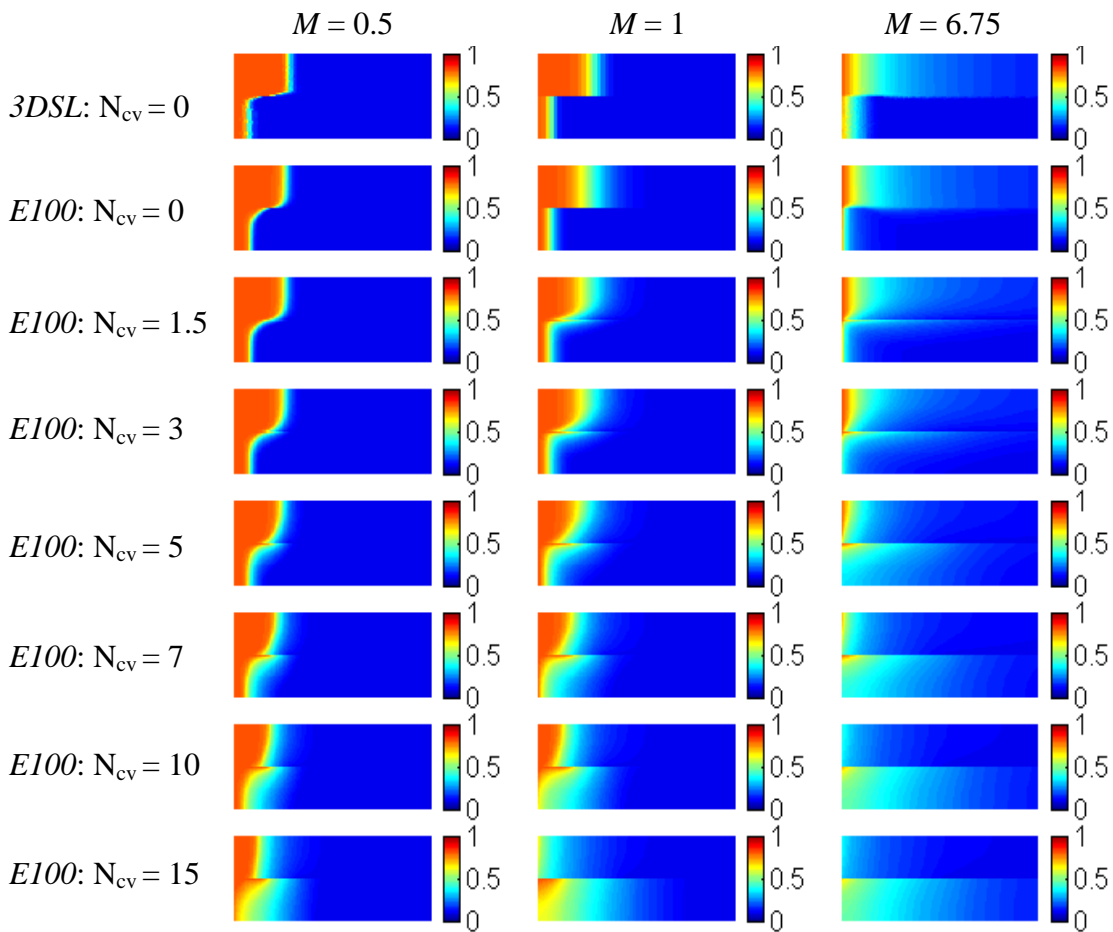


Fig. 5.76: Effects of mobility ratio on crossflow

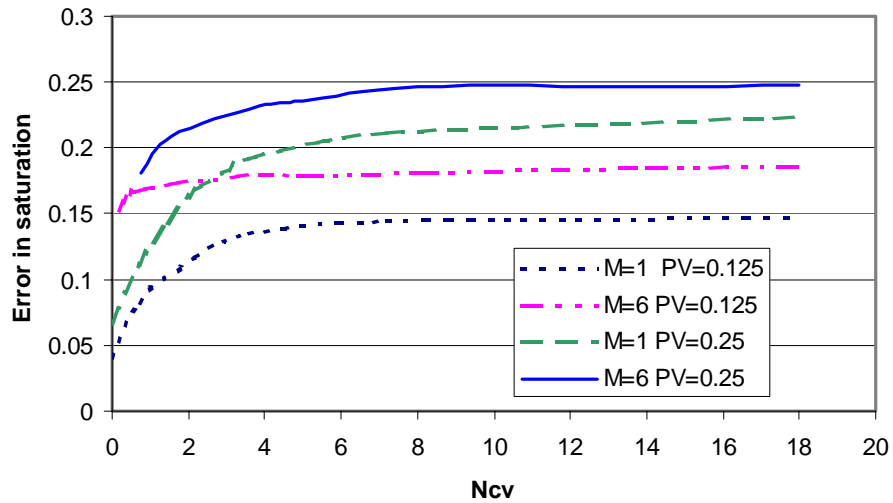


Fig. 5.77: Differences in predicted saturation

Fig. 5.76 suggests that the limit to the use of streamline simulator is around  $N_{cv} = 2$  for a unit mobility ratio. The saturation map was given more weight in this analysis, and the other comparison tools (recovery curve and the vector plots) were calibrated based on the results from the saturation profiles. The recovery difference plot was investigated at three different times during the displacements (breakthrough, 0.5 and 1 pore volume of injected fluid). Not much difference in recovery was noticed at early times, which is expected. The differences start showing from breakthrough up to a certain pore volume injected. Using the result ( $N_{cv} = 2$ ) from the saturation plots as basis, it corresponds to a tolerance factor of around 10-15% difference in recovery (Fig. 5.78). This seemingly high cutoff accounts for the about 7% difference in recovery between the two simulators due to numerical smearing rather than crossflow (see Fig. 5.65).

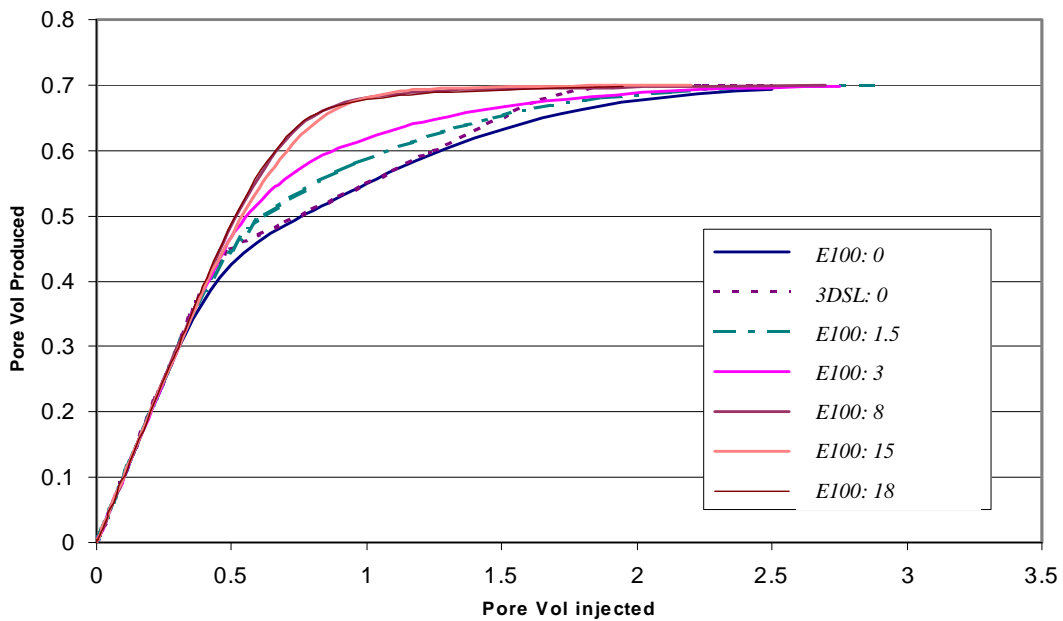


Fig. 5.78: Recovery curves for different capillary effects.  $M = 1$

Based on the cutoff listed above, we generated a chart summarizing the regions of applicability for the streamline simulators. For the good streamline area (A), the results of the simulations satisfy all the restrictions of the comparison tools namely below 10% difference in recovery and having a saturation profile that is not much different for both the *Eclipse* and *3DSL* simulators (the cutoff based on the saturation map was at  $N_{cv} = 2$ ). Region B covers the transition area where the effect of capillary forces is beginning to be significant. For Region C, the simulation results did not meet with all of the cutoffs of the saturation difference, recovery difference and the velocity ratio. For those points in region C, the saturation map showed the position of the flood front in the low permeability layer to be the same or faster than that in the high permeability layer. The points in chart represent the sample simulation runs. Points corresponding to  $M = 15$  and above are gas displacements simulation runs while the rest are from waterflood displacements.

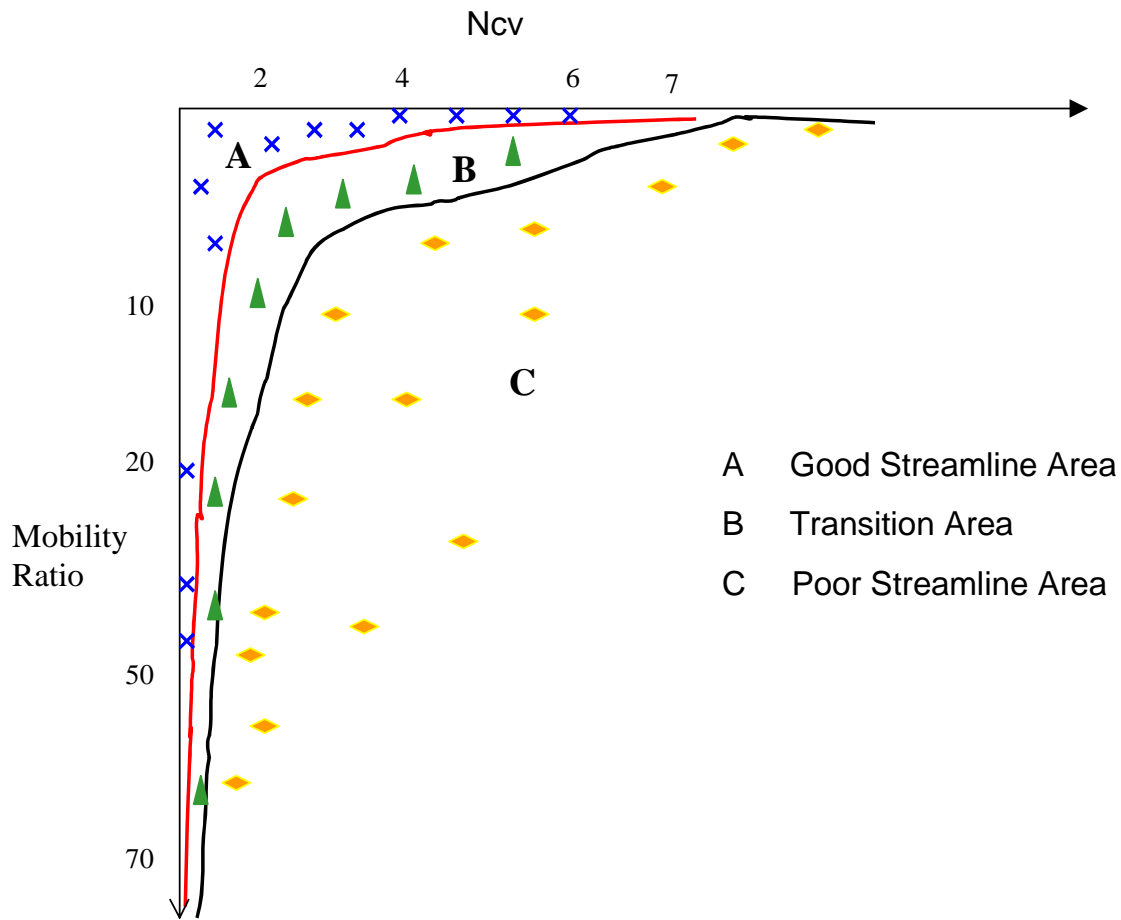


Fig. 5.79: Regions of capillary and mobility ratio for which streamline simulation approach should or should not be used.

Table 5-11: Simulator regions for unit mobility displacements

$N_{cv}$	Description
<2	Good Streamline Area
2-7	Transition Area
>7	Poor Streamline Area

### 5.2.4.2 Gravity effects

Gravity effects also alter the pressure field through time and hence the streamline paths. To model field scale displacement with the streamline model, gravity effects must be accounted for. The magnitude of the gravity force in a displacement is characterized by the time required for the fluids to segregate due to gravity forces relative to the time required for fluids to move across a domain due to viscous forces. Initially the streamline methods could not account for gravity effects since analytical solutions were mapped along streamlines. However, the application of operator splitting has allowed for representation of gravity effects in streamline simulation. Bratvedt (1996) gives a useful discussion on operator splitting and its implementation in streamline simulations.

In comparison with conventional simulation methods, the streamline method still retains some speed-ups but the magnitude of the speed-up depends on the number of streamline updates which in turn depends on the magnitude of the gravity number, the model size, and the type of displacement process. The gravity number  $N_{gv}$  was defined in section 5.1.

A series of calculations was performed for a layered system over a full range of gravity to viscous forces ( $N_{gv} = 0$ ,  $N_{gv} = 2.7$ ,  $N_{gv} = 9$ ,  $N_{gv} = 14$  and  $N_{gv} = 27$ ). The summary of the CPU requirements for the two simulators is given in Table 5-12.

Table 5-12: Pressure solves required to reach convergence ( $N_{cv} = 0$ )

$N_{gv}$	<i>3DSL</i>		<i>Eclipse</i>		Speed up Factor
	CPU (min)	Pressure Solves	CPU (min)	Pressure Solves	
0	0.8	1	5	182	7
2.7	1.5	20	8	501	6
9	3	20	15	1345	5
14	8	200	24	1652	3
27	15	1000	29	3945	1.7

The predictions of streamline approach and the finite difference approach are in excellent agreement provided sufficient care is taken to ensure an adequate frequency of pressure updates in the streamline approach. Fig. 5.80 and Fig. 5.81 report the predictions for  $N_{gv} = 27$ .

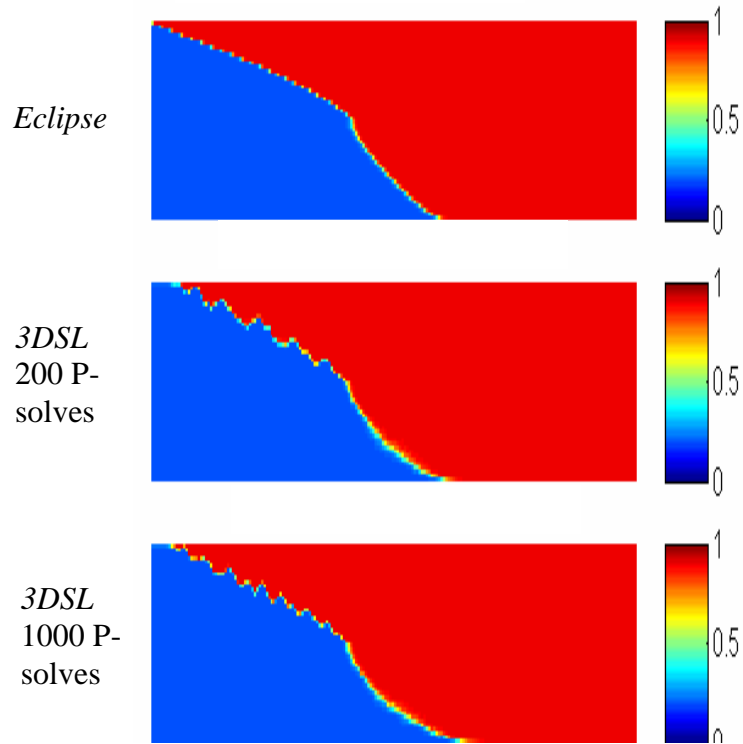


Fig. 5.80: Saturation map for  $N_{gv} = 27$  at 0.25 PVI

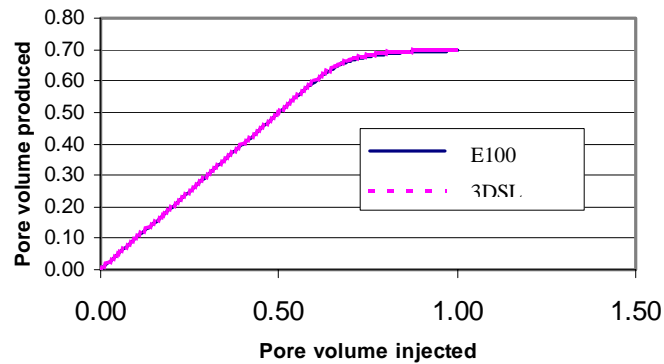


Fig. 5.81: Recovery curves for  $N_{gv} = 27$  at 0.25 pore volume

Clearly, a streamline method with operator splitting can account for gravity effects quite accurately. The issue of interest is rather on the number of pressure solves (thus time)

required to reach the degree of accuracy desired. In streamline simulation, the effects of gravity require more frequent pressure solves over a given time interval to reach a converged solution.

This study suggests that the practical range of gravity numbers that the streamline simulator can handle without losing the speed-up advantage is about 27. Displacements that are more dominated by gravity effects can with equal efficiency be solved by other simulation techniques.

### 5.2.5 Conclusions

Although a stratified model is the simplest form of reservoir heterogeneity, the approach used in this study and preliminary results obtained should provide a basis for analyzing fluid displacement in more complicated reservoir. The conclusion of this study will depend on the heterogeneity index (defined as permeability ratio of the layers) of the reservoir. The conclusions are:

1. Streamline simulators that do not include a representation of capillary crossflow, are not well suited for displacements with capillary number greater than 2 for a mobility ratio of one. In fact this number depends on the mobility ratio. Fig. 5.79 shows the regions of applicability of the streamline simulation technique. For a unit mobility displacement, the transition from good to poor agreement between streamline and conventional finite difference simulation is between  $N_{cv} = 2$  and  $N_{cv} = 7$ . Displacements with capillary to viscous number greater than 7 are best modeled with other simulation techniques or a streamline simulator that includes capillary crossflow (see Section 5.3).
2. Changes in mobility ratio significantly alter the effect of capillary pressure on displacement especially in the spatial distribution of the fluids. The greater the mobility ratio the more significant the effects of capillary pressure.
3. The operator splitting technique as implemented in streamline simulation method does an excellent job of capturing gravity effects, but the cost grows with the number of streamline updates required to achieve convergence. For any displacement where the gravity ratio is more than about 27, the effects of gravity are so significant that the speed-ups associated with streamline simulators are limited.

### 5.2.6 Nomenclature

M = mobility ratio  
 $N_{cv}$  = traverse capillary number  
 $N_{gv}$  = gravity number

### 5.3 Including capillary effects in streamline simulation

In the previous section the accuracy of the streamline approach was investigated for flow settings with varying degree of cross flow. The calculation examples suggest that traditional streamline simulation (without explicit representation capillary effects) is limited to flow settings where the capillary to viscous forces are low. In an attempt to expand the range of applicability of the streamline approach for immiscible displacement problems, Berenblyum *et al.*, (2003) proposed a method to include effect of capillary forces in streamline simulation. The introduction of capillary forces requires the modification of the pressure equation as well as the transport equation.

For two-phase immiscible displacements, the capillary effects can be introduced by recasting the pressure equation in terms of the wetting-phase pressure and the capillary pressure. The non-wetting phase pressure can subsequently be evaluated from the wetting-phase pressure and the capillary pressure given the saturation of the wetting (or non-wetting) phase.

The transport equation must also be modified to account for capillary effects. Along a given streamline the Buckley-Leveret (1949) equation must be replaced by the Rapaport-Leas (1953) equation to properly account for the longitudinal contribution of the capillary forces. The transverse effects of capillarity can subsequently be accounted for by an operator splitting technique on the pressure grid (Berenblyum *et al.*, 2003) in equivalence to the operator-splitting technique for gravitational forces discussed in Section 2.3.

With the above outlined modifications to the traditional streamline approach, the solution procedure for each time step is:

1. The modified pressure equation is solved implicitly on the finite difference grid
2. The Darcy velocity for is computed based on cell centered values of the modified pressure.
3. Streamlines are traced from injectors to producers based on the total velocity.
4. The saturation equation is solved explicitly along the streamlines
5. Saturation values are mapped back from the irregular grid (streamlined nodes) to the regular (finite difference) grid
6. Fluids are redistributed on the FD grid by a corrector (capillary) step

Fig. 5.82 demonstrates the accuracy of the modified streamline approach in handling flow settings where capillarity plays an important role in the fluid distribution within the porous medium. The reported example is for a unit mobility waterflood in a two-layer system with permeabilities 100 and 400 *mD*. The IFT for this displacement was 50 dynes/cm and hence expected to be strongly affected by capillary effects. All details on the displacement along with additional example calculation are available in Berenblyum *et al.* (2003). Fig. 5.82 also reports the simulation result from *Eclipse*. Excellent agreement is observed between the modified streamline simulator and the finite difference approach.

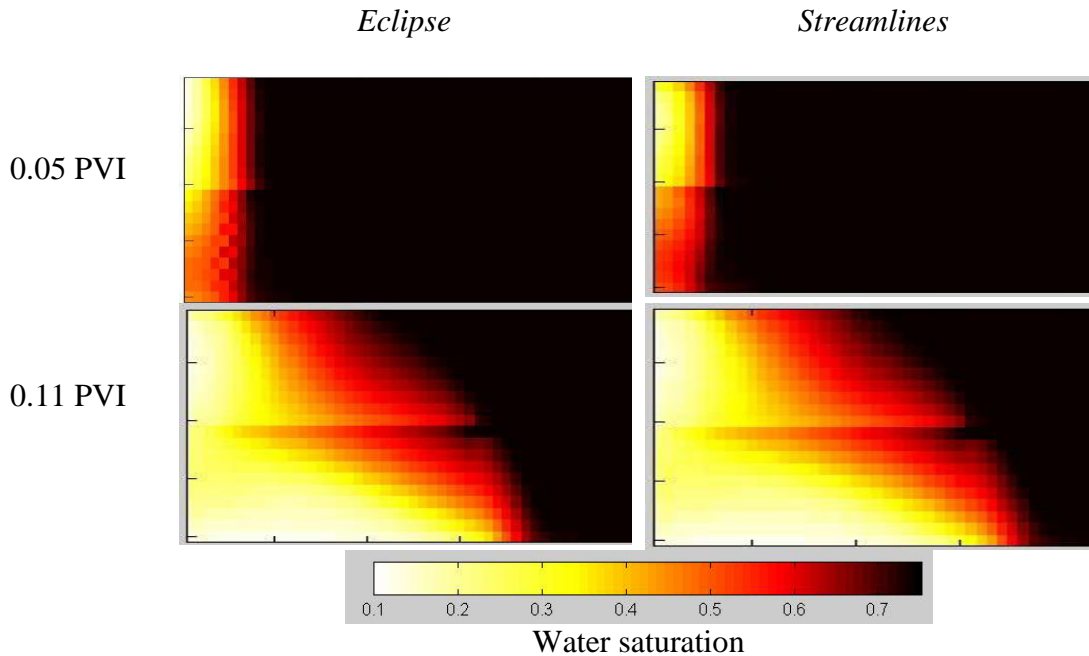


Fig. 5.82: Water saturations predicted by E100 and modified streamline approach

As pointed out in Section 5.2, representation of any non-convective mechanism in a streamline simulator is likely to reduce the overall efficiency of the approach as more frequent pressure updates are required to account for transverse flow. This fact was demonstrated for gravity effects in Sections 2.3 and 5.2. A similar trend is observed for the capillary operator-splitting approach. As a displacement process becomes increasingly dominated by capillary forces, an increasing amount of time is spent on redistributing fluids on the pressure grid essentially corresponding to running the streamline simulator in finite-difference mode. However, the modifications suggested by Berenblyum *et al.* (2003) extend the range of application of the streamline approach as compared to the standard streamline approach where only convective (and gravity) forces are included (see Section 5.2). Nevertheless, for displacements where capillary effects completely dominate the flow, finite difference based simulators with a fully implicit option materialize are the more appropriate approach.

#### 5.4 Effects of pressure gradients on displacement performance for miscible/near miscible gas floods

The analytical solutions presented in Chapter 2 were obtained using the assumption that the phase behavior can be evaluated at a constant pressure. In any real displacement, however, the local pressure will vary along the displacement length (See Fig. 5.83) from injector to producer ( $P_{inj} > MMP > P_{prod}$ ). This result in a pressure profile, which may mean that in the vicinity of a production well, the pressure may decline below the reservoir MMP. In this

section we investigate the accuracy of the assumption of constant pressure used in analytical solutions, and we examine the impact of the pressure gradient on displacement performance.

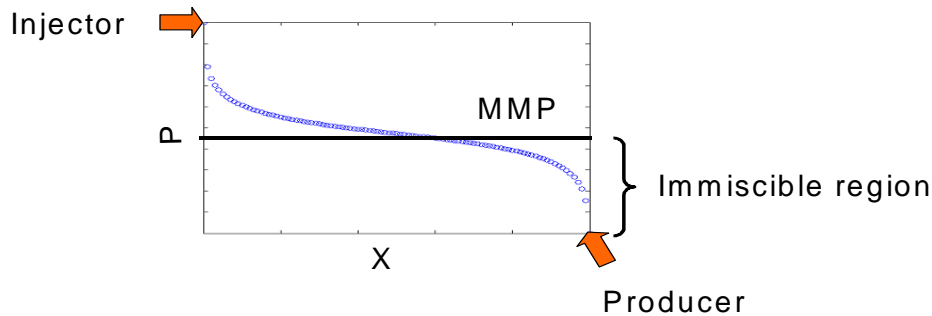


Fig. 5.83: Pressure distribution in a hypothetical reservoir.

### 5.4.1 1D displacements

To analyze the effect of this pressure gradient between injector and producer, displacement behavior of a gas/oil system was investigated with a 1D homogenous model. The impact of pressure gradients is analyzed by comparing available 1D solutions obtained by method of characteristics (MOC) with results of Eclipse-300 finite difference (FD) simulations. The analysis includes fluid displacements at miscible and near miscible conditions in terms of local displacement efficiency. To address the issue of pressure gradient effects on local displacement efficiency the following displacement was considered.

- 1D, homogenous, four-component system
- Initial oil : Methane ( $C_1$ , 0.3), n-Butane ( $C_4$ , 0.3), n-Decane ( $C_{10}$ , 0.4)
- Injection gas: Carbon dioxide, ( $CO_2$ , 0.5), Methane ( $C_1$ , 0.5)
- Minimum miscibility pressure (MMP) = 193 bar (2800 psi)
- 1000 grid blocks, Permeability ( $k$ ) = 500 md, Porosity ( $\phi$ ) = 0.25
- Initial reservoir Pressure = 180 bar, Temperature = 375 K
- FD simulator: Eclipse-300
- Brooks-Corey relative permeability curves with zero residual saturation

The following graph shows oil recovery as a function of pore volumes injected for different pressure gradients. The injection pressure was kept constant at 200 bar, which is just above system MMP (193 bar), and the production pressure was set at 178, 160, 140 and 120 bar. Fig. 5.84 shows the recovery curves for these simulations. The imposed pressure gradients (maximum, 60 bar) cause recovery to change, but only minimally. In this displacement, overall displacement performance, as measured by oil recovery, at least, is relatively insensitive to the pressure drawdown near the outlet.

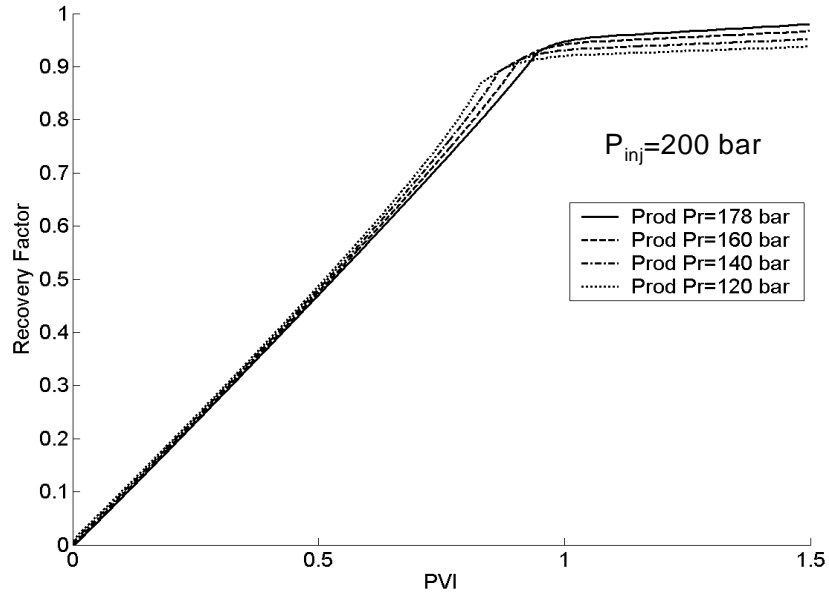


Fig. 5.84: Effect of pressure gradient on oil recovery in a multicontact miscible displacement.

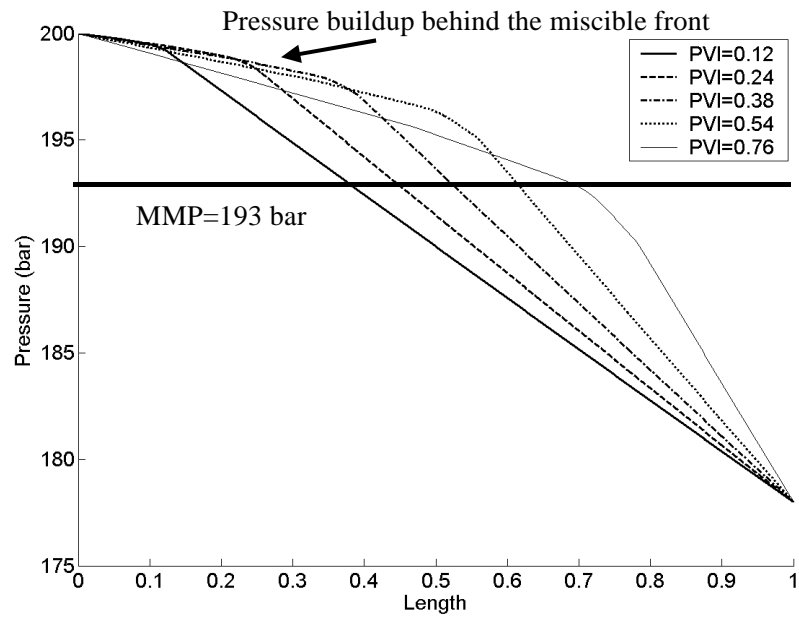


Fig. 5.85: Pressure profile at different times in 1D displacements.

The observed behavior is the result of evolution in the pressure profiles at different time steps, as is shown in Fig. 5.85. As oil is displaced by injected gas, there is a pressure buildup behind the miscible front. This occurs because of the low viscosity gas upstream of the front transfers high pressure downstream as the front moves from injector to producer, thereby maintaining relatively high pressure at the displacement front. Hence for much of the length of the reservoir the miscible front is above MMP, resulting in high displacement efficiency. When the pressure at the displacement front decreases below the MMP near the outlet, there is only small effect on oil recovery because the oil upstream has already been displaced, and formation of some residual oil in the zone near the outlet is a relatively small fraction of the total. At 178 *bar*, the displacement efficiency is still relatively high. What is surprising is that reducing the outlet pressure further to as much as 73 *bar* below the MMP, has such a small effect on recovery.

Next we consider the accuracy of the assumption of constant pressure for evaluation of phase behavior in the construction of analytical solutions. We do so by choosing various gas/oil models under different imposed pressure gradients. The following four step approach was adopted for the investigation:

1. Construct the analytical solution for the given system at the reservoir temperature and pressure, which are assumed to be constant by method of characteristics.
2. Compare the analytical solution with finite difference Eclipse-300 simulations by imposing a very small pressure gradient.
3. Impose a pressure gradient by increasing the pressure at the injector and reducing the pressure at the producer by the same magnitude (see Fig. 5.86)
4. Impose a pressure gradient by keeping the pressure at the injector constant and reducing the pressure at the producer (see Fig. 5.87).

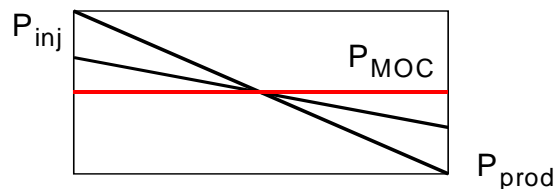


Fig. 5.86: Schematic for pressure distributions for step 3.

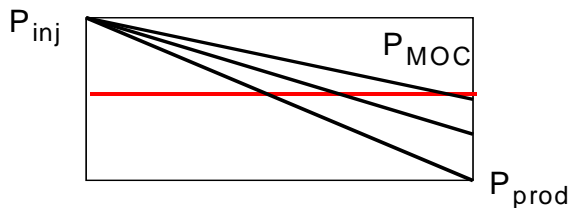


Fig. 5.87: Schematic for pressure distributions for step 4.

Simulations were performed for an immiscible (Displacement-1) and a nearly miscible system (Displacement-2). Both the displacements were for four component systems. The

finite difference computations were performed with 1000 grid blocks. The two displacement systems were:

Displacement-1: Immiscible:

- Initial oil: Methane ( $C_1$ , 0.1), n-Butane ( $nC_4$ , 0.2), n-Decane ( $n-C_{10}$ , 0.7)
- Injection gas: Nitrogen ( $N_2$ , 1.0)
- Initial reservoir  $P_r = 250 \text{ bar}$ ,  $T = 344 \text{ K}$

Displacement-2: Near miscible:

- Initial oil: Methane ( $C_1$ , 0.3), n-Butane ( $C_4$ , 0.3), n-Decane ( $C_{10}$ , 0.4)
- Injection gas: Carbon dioxide, ( $CO_2$ , 0.5), Methane ( $C_1$ , 0.5)
- Minimum miscibility pressure (MMP) =  $193 \text{ bar}$  (2800 psi)
- Initial reservoir  $P_r = 180 \text{ bar}$ ,  $T = 375 \text{ K}$

Various solutions were then compared for immiscible and near-miscible gas/oil systems by examining the gas saturation profiles at two times, 0.5 PVI and just prior to breakthrough of injected gas. For both the cases calculation of pore volumes was based on the fluid densities at the injection conditions.

Fig. 5.88 and Fig. 5.89 summarize the results of these tests at 0.5 PVI. Fig. 5.88(a) and Fig. 5.89(a) show that for both displacement systems, the numerical solution converges to the analytical solution as the number of grid blocks is increased. The rate of convergence is a bit lower for the near-miscible displacement, which is more sensitive to the effects of numerical dispersion than the immiscible displacement (Jessen *et al*, 2004). These results clearly show that the analytical solution obtained at the average pressure for a displacement agrees well with the numerical solution for small pressure drop.

Fig. 5.88(b) and Fig. 5.89(b) show the effect of larger total pressure drops, again for the analytical solution evaluated for a pressure midway between the inlet and the outlet. For the immiscible displacement, Fig. 5.88(b), the effect of larger pressure drop is minimal. Here again, use of analytical solution in streamline simulations is appropriate.

For the near-miscible system, Fig. 5.89 (b), the effect of pressure difference is larger, because the higher injection pressure are actually above MMP ( $193 \text{ bar}$ ). Even so, the saturation distributions at  $\pm 2$ ,  $\pm 20$ , and even  $\pm 40 \text{ bar}$  are similar to the analytical solution evaluated at the average pressure. Thus the use of an analytical solution with phase behavior evaluated at the average pressure is surprisingly accurate even for total pressure differences as large as 40% of the average pressure, at least for this system.

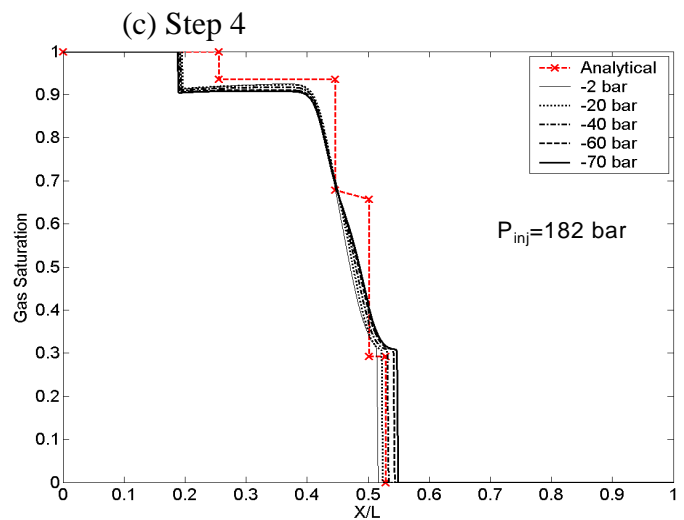
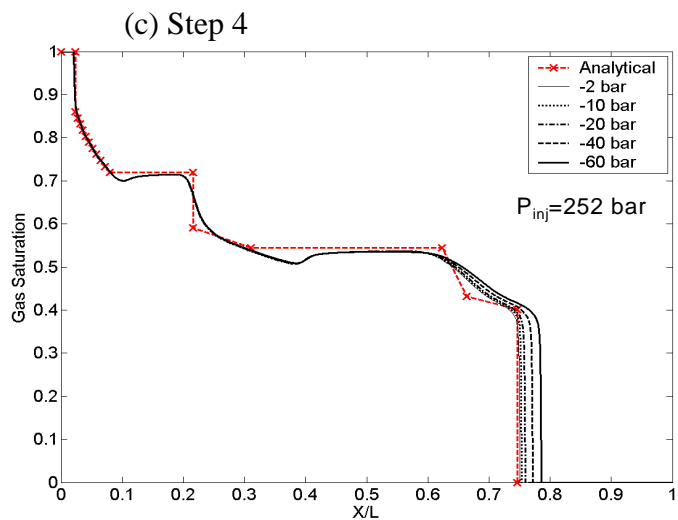
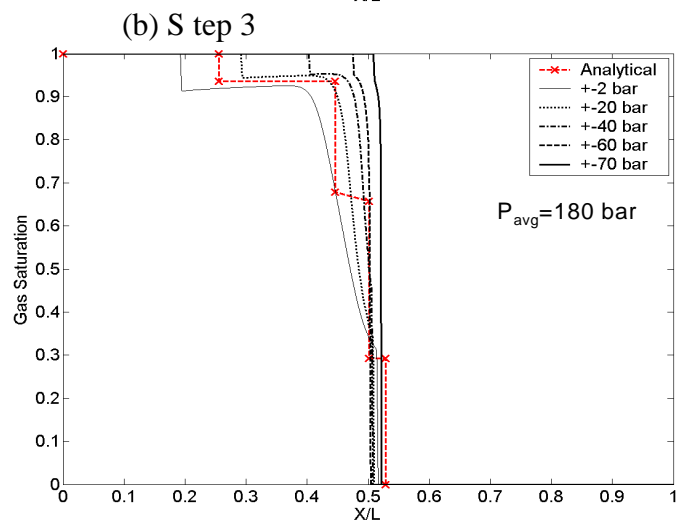
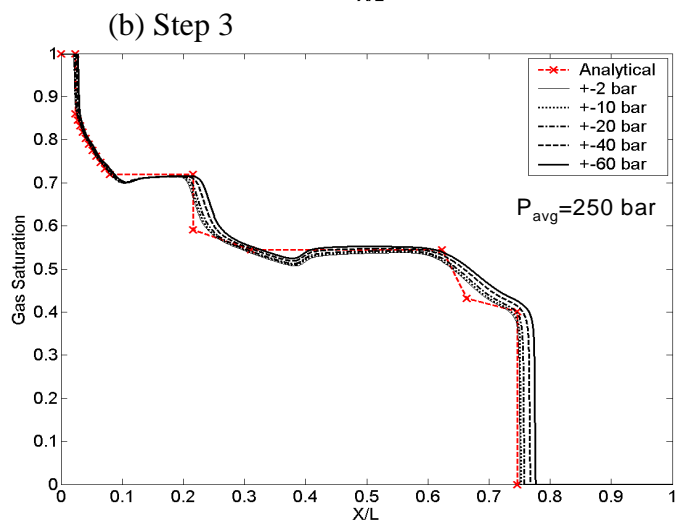
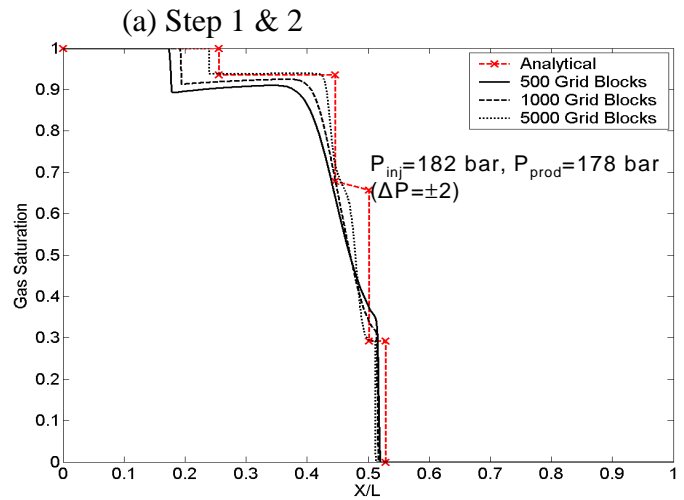
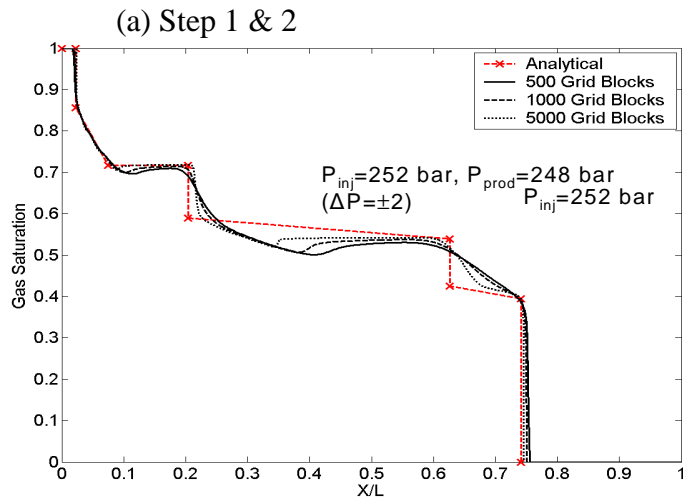


Fig. 5.88: Comparison of analytical solution with FD solutions for various total drops for Displacement-1 at 0.5 PVI

Fig. 5.89: Comparison of analytical solution with FD solutions for various total pressure drops for Displacement-2 at 0.5 PVI

Fig. 5.88 (c) and Fig. 5.89 (c) show the effect of holding the upstream pressure constant slightly above the initial pressure and reducing the outlet pressure. Fig. 5.89 demonstrates that immiscible displacement is insensitive again to this sort of pressure variation. Fig. 5.89(c) shows that even the near-miscible displacement is relatively insensitive to the downstream pressure reduction

Fig. 5.90 and Fig. 5.91 show the corresponding plots just prior to breakthrough of injected gas. As might be expected, the profiles show somewhat larger differences as the low pressure zone near the outlet is approached. Even so, comparison of Fig. 5.88 and Fig. 5.89 with Fig. 5.90 and Fig. 5.91 indicates that the differences between the solutions with significant lowering of outlet pressure are modest.

Fig. 5.90 and Fig. 5.91 clearly show that the effect of pressure gradient is enhanced as the front approaches the outlet. This is evident by the increasing separation between the curves for different pressure gradients. The deviation from the analytical solution is still small in the immiscible case, but it is larger in the near-miscible case, where the leading shocks are separated significantly.

Thus we conclude that there are many situations in which it is reasonable to use the analytical solutions to estimate reservoir displacement performance in streamline simulations. However, the deviation from the analytical solution increases as we approach breakthrough. The analysis presented shows that for most of the reservoir production history the analytical solution gives fairly close results as compared to the numerical results.

In the examples in Fig. 5.88 - Fig. 5.91, we have investigated the assumption of constant pressure by comparing the MOC solution evaluated at the initial average reservoir pressure with numerical solution for different pressure gradients.

Another indication of the potential impact of pressure differences on the phase behavior is given by the analytical (MOC) solutions evaluated at several pressures for immiscible and near-miscible gas/oil systems. The reservoir pressure will be bounded between the injection pressure and the production pressure, evaluation of MOC solution at these pressures will give an estimate of maximum variation in the solution.

Fig. 5.92 shows the MOC solutions for the immiscible displacement and Fig. 5.93 shows the MOC solutions for the near-miscible displacement. Fig. 5.92 shows that the immiscible system is rather insensitive to the pressure variation, but the near-miscible system is much more sensitive to the changes in pressure, especially at pressures near MMP. In the near-miscible case the solution changes significantly with the pressures. Thus, the greater sensitivity shown in Fig. 5.89 and Fig. 5.91 is consistent with the behavior of the analytical solution. Even in this example, however, use of an MOC solution evaluated at the average pressure gives a reasonable representation of the displacement behavior.

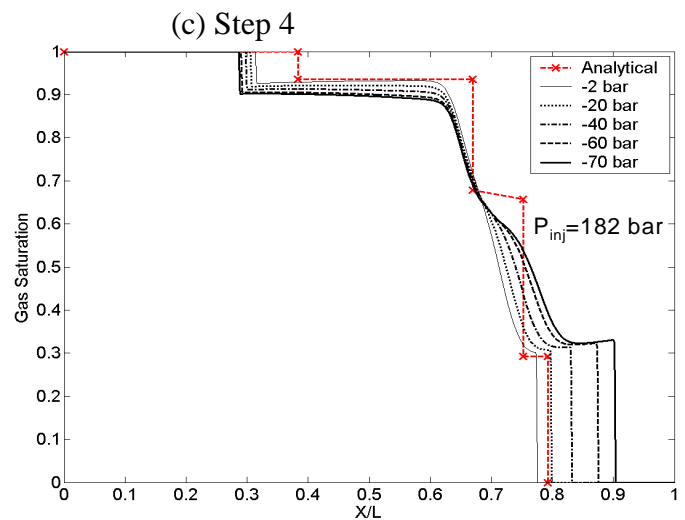
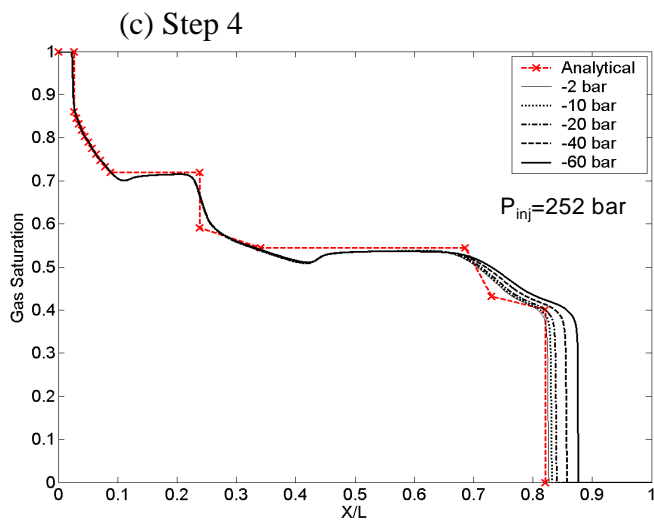
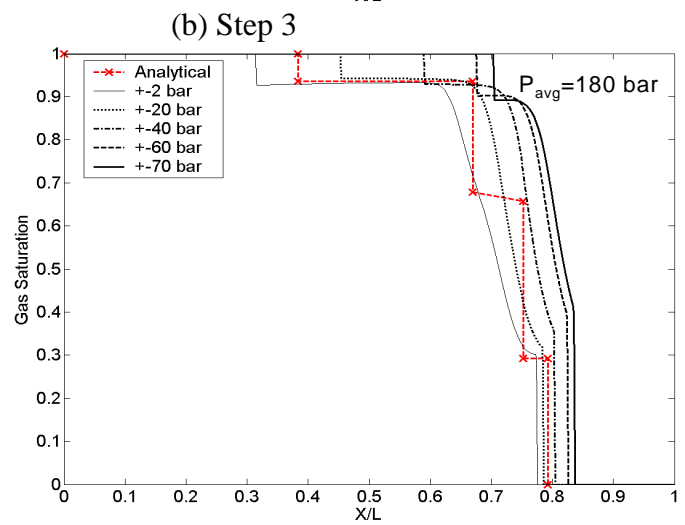
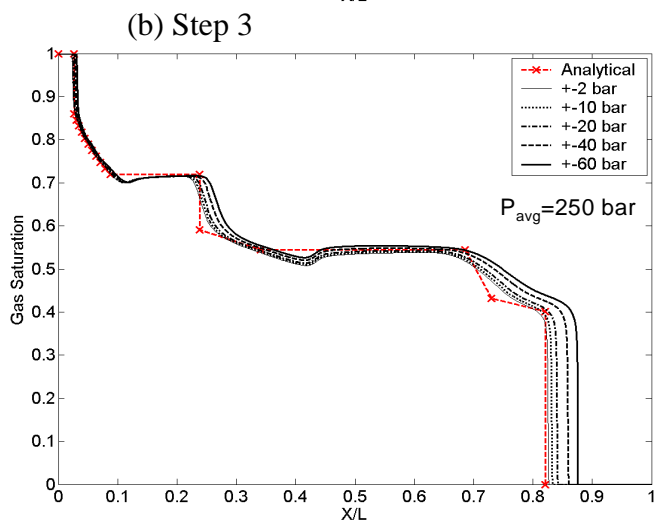
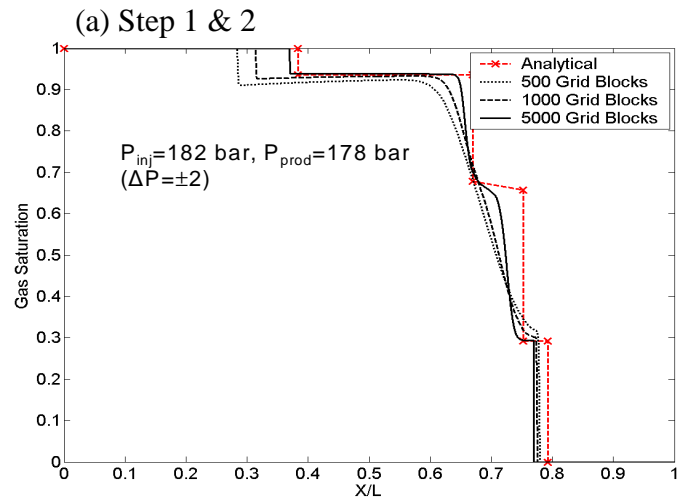
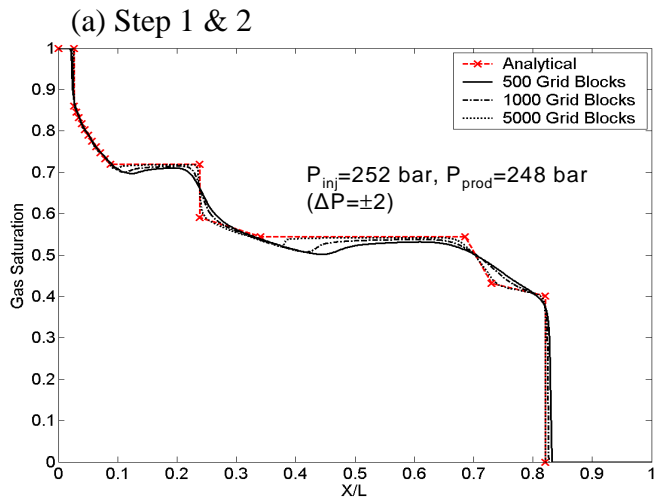


Fig. 5.90: Comparison of analytical solution with FD solutions for various total drops for Displacement-1 at 0.55 PVI

Fig. 5.91: Comparison of analytical solution with FD solutions for various total pressure drops for Displacement-2 at 0.75 PVI

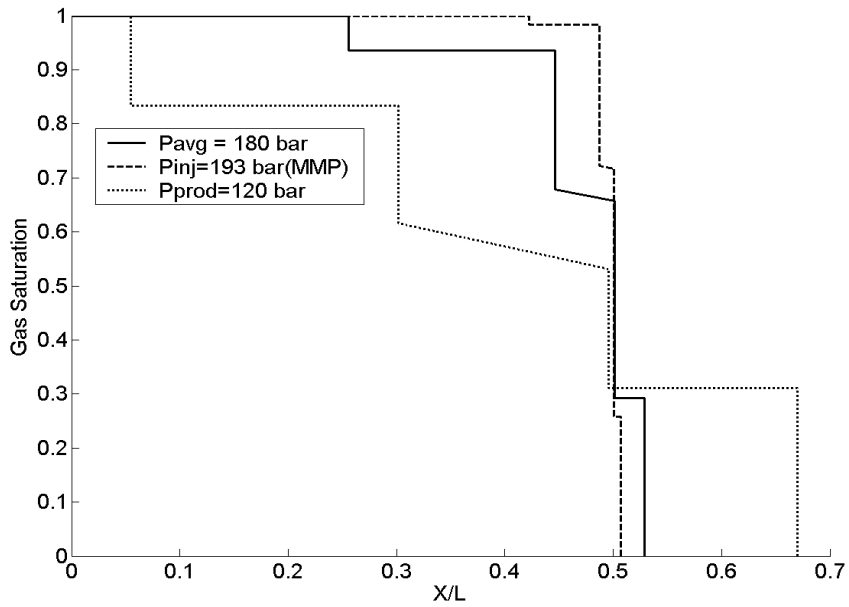


Fig. 5.92: Analytical solutions at 0.5 PVI for different pressures for the immiscible displacement

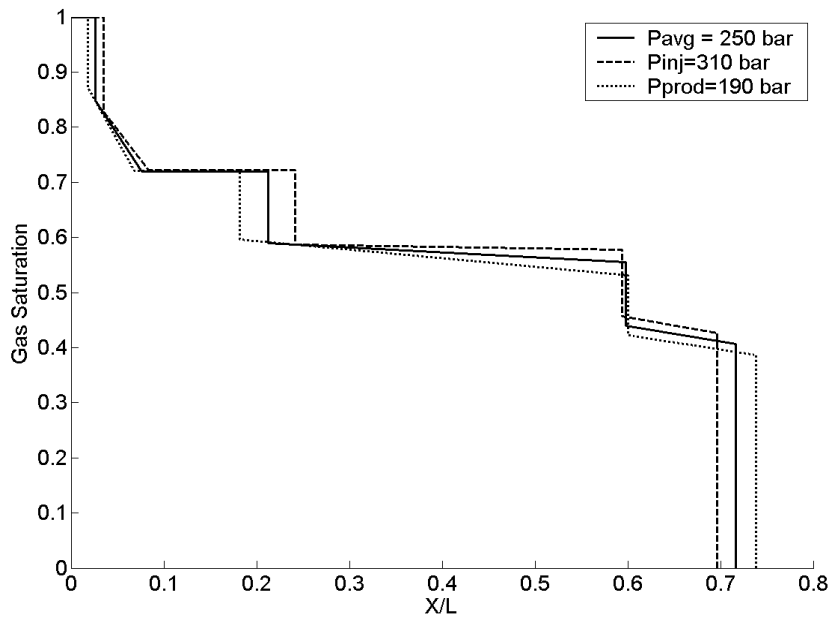


Fig. 5.93: Analytical solutions at 0.5 PVI for different pressures for the near-miscible displacement

### 5.4.2 2D displacements

To examine the effects of pressure gradients in 2D the following systems were considered

- A two layer model with permeability ratios of 1.5 and 5.0
- 2D fully heterogeneous model (SPE10 slice)

A simplified two-layer model is shown in Fig. 5.94, illustrates some of the effects of the pressure differences in heterogeneous porous media. The two layers are assumed to be non-communicating. The top layer is the high permeability layer ( $K_1$ ), and the bottom layer is the low permeability layer ( $K_2$ ). At any instant in time, the front location corresponds to point  $A_1$  in the high permeability layer and point  $B_1$  in the low permeability layer. At a later time the corresponding locations are  $A_2$  and  $B_2$  (Fig. 5.94). At a given flow rate, that the pressure drop in the low viscosity gas phase will be lower than the high viscosity oil phase. So, high permeability layer will have less pressure drop as compared to the low permeability layer at the front position, as shown in Fig. 5.94. This difference in pressure between two layers will cause crossflow. As the front advances, the difference in pressure between the two layers increases and will reach a maximum value just before breakthrough. Thus, differences in displacement performance as a result of pressure differences will be the result of changes in the phase behavior interacting with crossflow.

To analyze the effect of heterogeneity in a horizontal communicating two-layer system, the following gas/oil displacement was considered:

- Initial oil composition : Methane ( $C_1$ , 0.3), n-Butane ( $C_4$ , 0.3), n-Decane ( $C_{10}$ , 0.4)
- Injection gas composition: Carbon dioxide, ( $CO_2$ , 0.5), Methane ( $C_1$ , 0.5)
- Minimum miscibility pressure (MMP) = 193 *bar* (2800 *psi*)
- Initial reservoir  $P_r = 180$  *bar*,  $T = 375$  K
- Perm Contrast ( $K_1/K_2$ )= 1.5 & 5.0
- 100x100 grid blocks
- Wells perforated along the entire width
- Injection Pressure = 190 *bar*

For the two-layer model with  $K_1/K_2=1.5$ , injection pressure was kept constant at 190 *bar* and the production pressure was varied from 178 *bar* to 120 *bar*. Saturation maps shown in Fig. 5.95 are at 0.5 PVI and are very similar for various pressure gradients. To illustrate the extent of crossflow and front advancement, saturation difference maps are plotted as shown in Fig. 5.96. The saturation difference maps show the difference in the saturation map for an outlet pressure at 178 *bar* with the saturation map corresponding to the lower production pressure. Fig. 5.96 shows very limited crossflow and little front advancement as the pressure difference is increased from 12 *bar* to 70 *bar*.

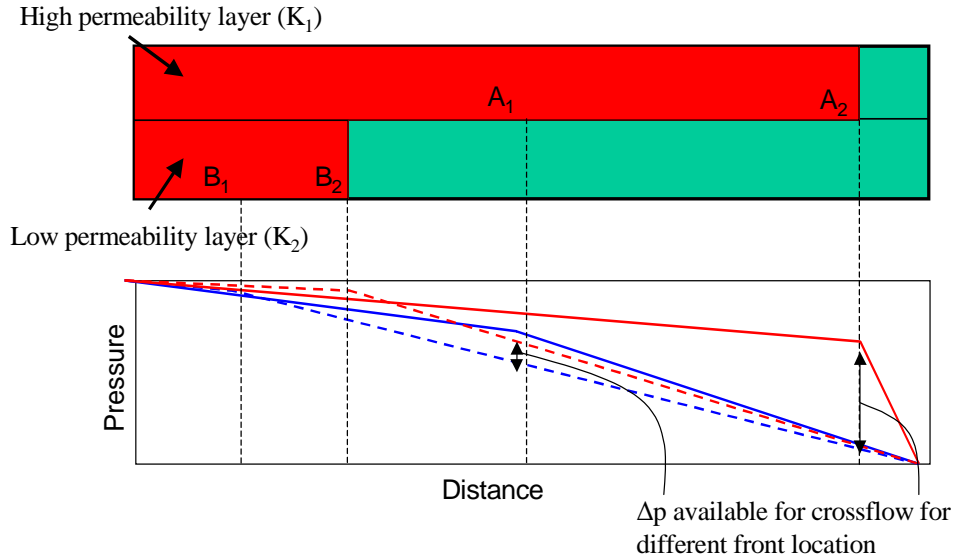


Fig. 5.94: A two-layer system showing pressure variation with front location.

Fig. 5.97 and Fig. 5.98 are the saturation plots and saturation difference plots for the model with a higher permeability contrast of 5.0 at 0.5 pore volumes injected. Again we observe that the extent of crossflow is small, but the front advancement is substantial. In this case significant front advancement is because the front is very close to the production boundary, which is at a lower pressure. As the gas front reaches the low pressure zone, it expands, causing earlier breakthrough with increasing pressure gradients. Increasing permeability contrast will accentuate pressure differences between layers, therefore Fig. 5.95 - Fig. 5.98 show, however, that the zone affected by crossflow is a relatively small fraction of the flow field.

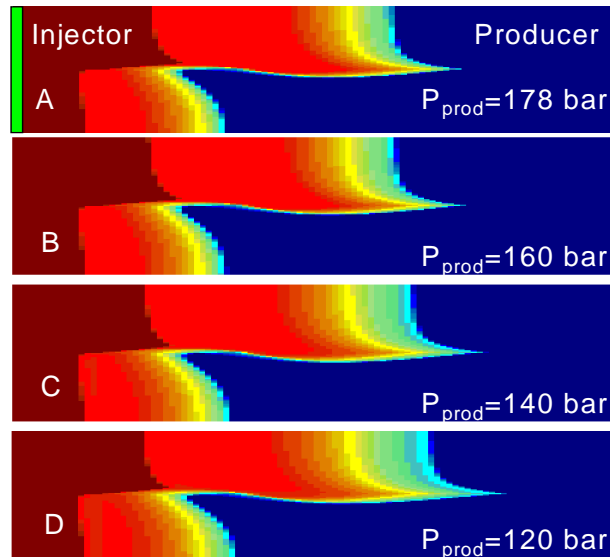


Fig. 5.95: Saturation plots of a two-layer system for permeability contrast of 1.5 at 0.5 PVI. Injection pressure is 190 bar.

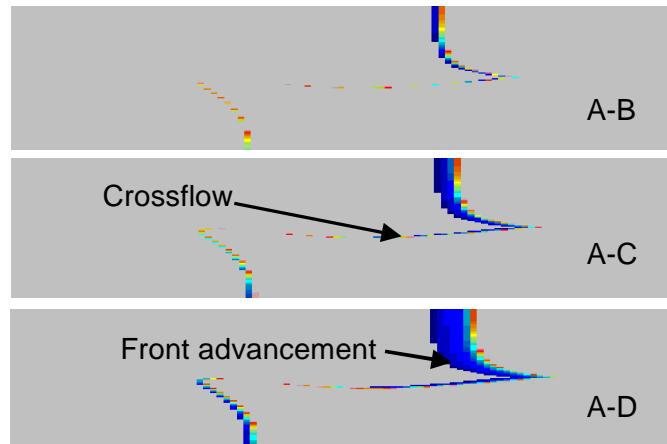


Fig. 5.96: Saturation difference plots of a two-layer system for permeability contrast of 1.5 at 0.5 PVI showing crossflow and front advancement.

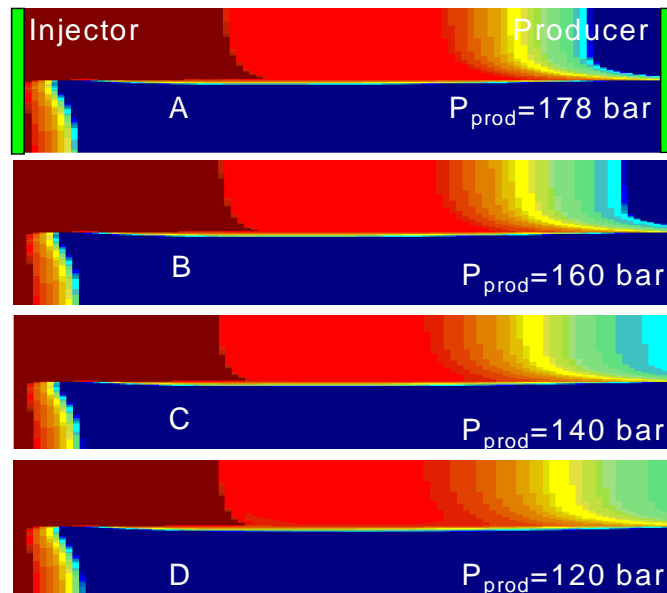


Fig. 5.97: Saturation plots of a two-layer system for permeability contrast of 5.0 at 0.5 PVI. Injection pressure is 190 bar.

Fig. 5.99 and Fig. 5.100 show recovery plots for the displacements in Fig. 5.95 - Fig. 5.97. Here again, there is marginal difference in the ultimate recovery for the two plots for permeability ratios of 1.5 and 5.0, but there is a small difference in the shape of the curve, especially in the region between breakthrough in the two layers. This difference is primarily because of the difference in gas expansion for the lower production pressures, which causes earlier breakthrough for lower production pressures.

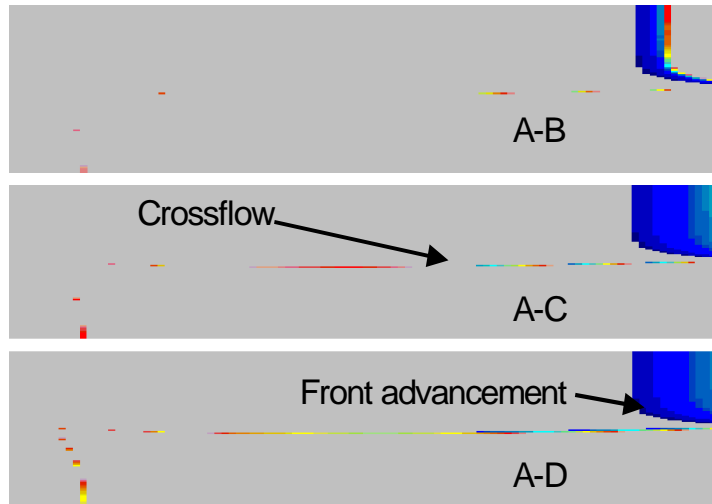


Fig. 5.98: Saturation plots of a two-layer system for permeability contrast of 5.0. Injection pressure is 190 bar.

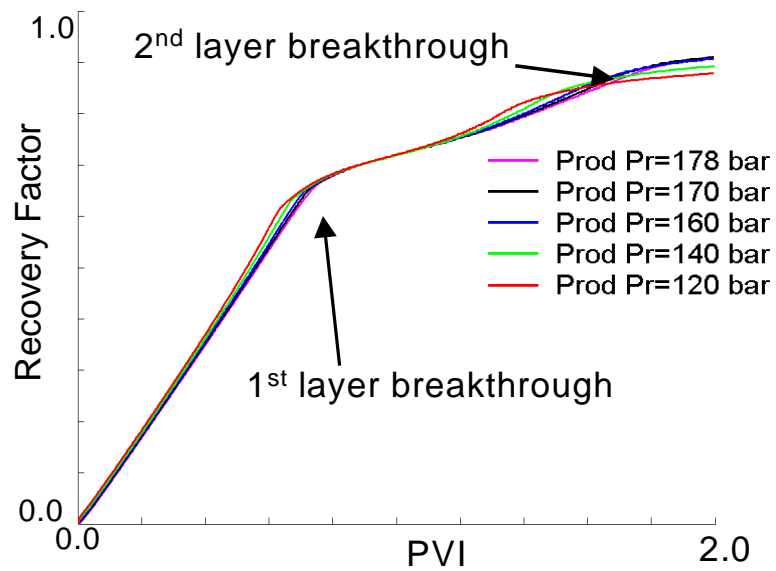


Fig. 5.99: Recovery curve of a two-layer system for permeability contrast of 1.5. Injection pressure is 190 bar .

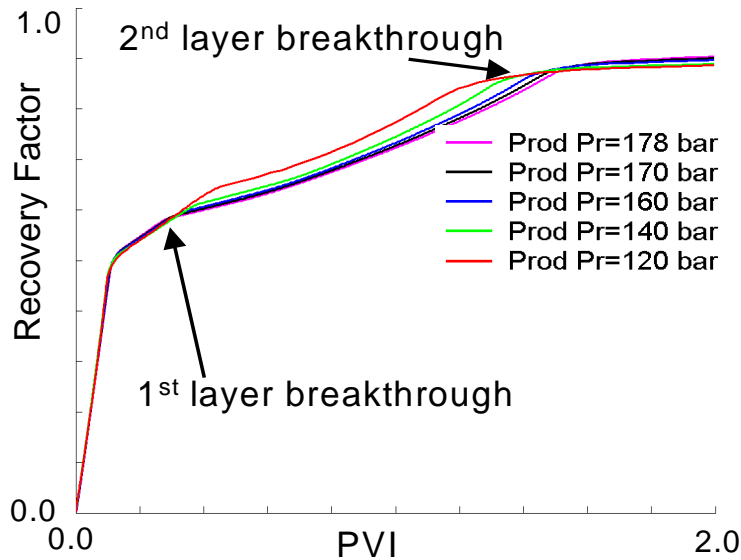


Fig. 5.100: Recovery curve of a two-layer system for permeability contrast of 1.5. Injection pressure is 190 *bar*.

The final example calculation is for a 10-component gas/oil system in a 2D heterogeneous reservoir. The porosity and permeability fields for this example were taken from SPE's 10'th comparative simulation study (Christie and Blunt, 2001). Following are the specification of the system:

- Initial reservoir Pr = 320 *bar*
- Temperature = 370 K
- 60x220 grid blocks
- Wells perforated along width
- Injection gas pressure = 330 *bar*

Thee 10-component fluid description is representative of an intermediate gravity crude oil. Detailed equation of state input can be found in Jessen *et al.* 2000. Initial oil and injection gas compositions are given in Table 5-13.

Fig. 5.101 represents the porosity and permeability field for the chosen 2D section. In this example, the injection pressure is held constant at 330 *bar*, and the production pressure was varied from 318 *bar* to 270 *bar*. Fig. 5.102 and Fig. 5.103 show the saturation and saturation difference maps at 0.5 pore volumes injected, respectively. We again observe the same trend as in the two-layer example. The saturation maps are quite similar and the saturation difference maps show marginal crossflow and little front advancement with increasing pressure gradient.

Table 5-13: Oil and injection gas composition for 2D heterogeneous displacements

Component	Injection Gas Comp (Mol fraction)	Initial Oil Comp (Mol fraction)
C1	0.4	0.4354
CO2	0.3	0.0034
C2	0.3	0.0383
C3	0.0	0.0148
C4	0.0	0.0182
C5	0.0	0.0152
C6	0.0	0.0192
C7-16	0.0	0.2722
C17-27	0.0	0.1162
C28-80	0.0	0.0672

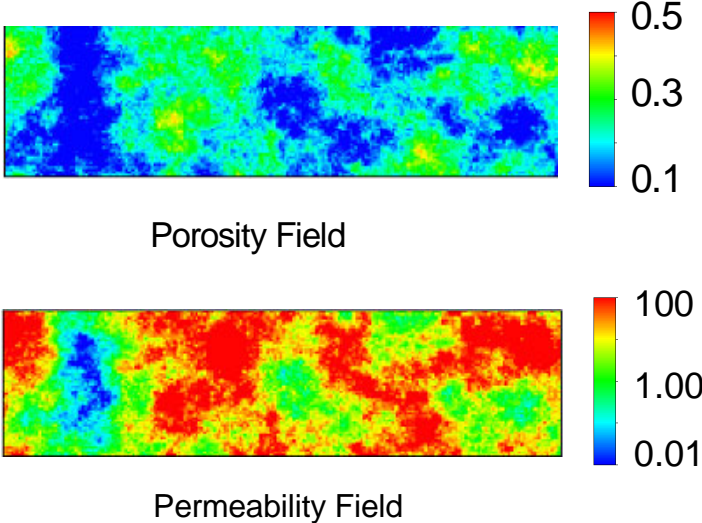


Fig. 5.101: Porosity and permeability field used in 2D heterogeneous displacements.

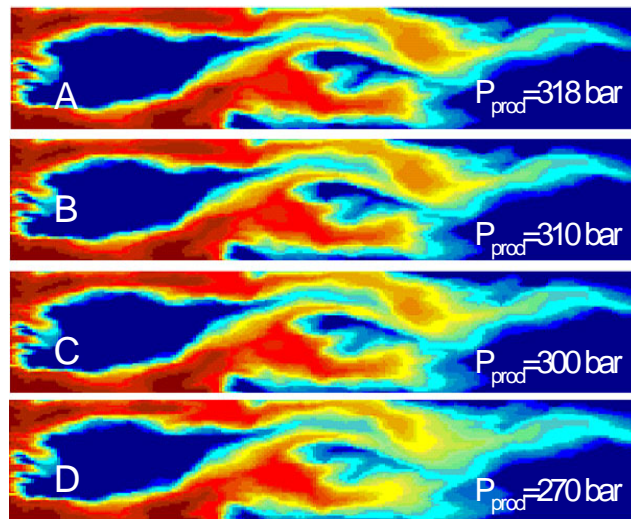


Fig. 5.102: Saturation plots of 10 component system at 0.5 pore volumes injected

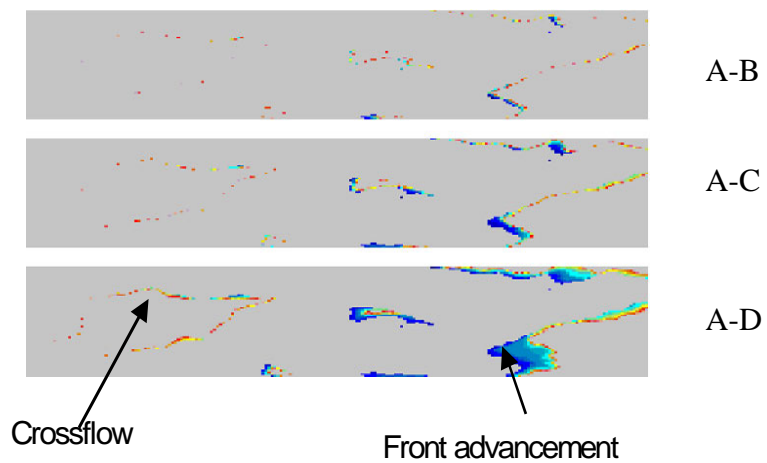


Fig. 5.103: Saturation difference plots of 10-component system at 0.5 pore volumes injected

Fig. 5.104 shows the effect of pressure gradient on the ultimate recovery. In this example, as well, reducing the pressure at the production end has quite small effect on overall displacement performance.

### 5.4.3 Conclusions

The examples presented in this section have considered an immiscible, a near-miscible and a 10-component displacement for both 1D and 2D systems. The effect of pressure gradients on various gas/oil systems was found to be small in all these examples. For most of the displacements the effect of crossflow was quite limited, but for some examples there was an effect of front advancement due to gas expansion, which was responsible for earlier gas breakthrough. Hence, at least for the systems studied the use of phase behavior calculations evaluated at an appropriate average pressure is a reasonable assumption.

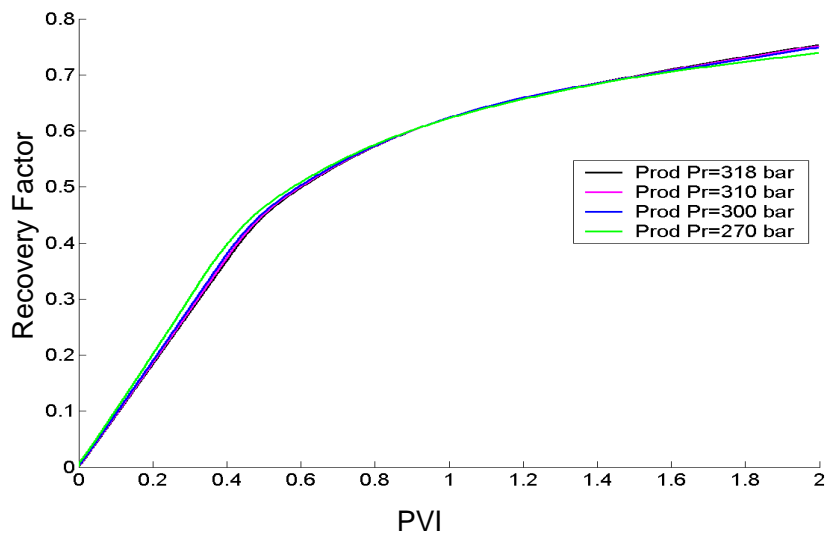


Fig. 5.104: Recovery curves for the 10-component system. Injection pressure is 330 *bar*

The results presented here also show that it is straightforward to test the impact of total pressure drop on the accuracy of streamline simulations using analytical solutions. 1D and 2D simulations, similar to those presented can be performed to evaluate whether use of analytical solutions in streamline sensitivity studies is reasonable if the total pressure difference can be estimated.

### 5.5 Summary

In this chapter a variety of investigations of the potential limitations of the streamline approach have been presented. The interplay of viscous, capillary, and gravity forces was examined in a set of experiments performed in two-layer glass bead packs. Those experiments illustrate the complexity of the scaling of these flows, even in the simple porous medium with simple fluid mixtures. The experimental results confirm the scaling arguments by various authors, and comparisons of the simulations with conventional simulation results indicates that it is reasonable to explore the relative importance of viscous, capillary, and gravity forces by conventional simulation.

A direct comparison of conventional simulation with streamline simulations that include the effects of gravity but not capillary forces was presented next. Those comparisons confirm that gravity effects are represented well by operator splitting techniques, but at the cost of slowing the streamline simulations. The range of capillary to viscous ratio for which basic streamline simulations are reasonably accurate was also explored. At values of  $N_{cv}$  less than about 2 for unit mobility displacements, the streamline approach gives good results. For higher values of  $N_{cv}$  another approach is appropriate. The value of  $N_{cv}$  at which the transition to capillary-influenced flow begins depends on mobility ratio, with the limiting value declining for adverse mobility displacements.

A demonstration that capillary effects can be represented in the streamline approach was also presented. That work was done by Roman Berenblyum, a PhD student at the Danish Technical University, in collaboration with this project. Here again, crossflow can be represented, but at the cost of increased computation time over the basic streamline approach. Thus, it is useful to test when the basic streamline approach can be used and when it must be augmented by representations of crossflow or replaced by another simulation approach.

Finally, the accuracy of the assumption made in Chapter 3 that it is reasonable to evaluate phase behavior at a single pressure was tested. That assumption makes possible the analytical solutions obtained in Chapter 3. As the results for condensate vaporization presented in Chapter 2 showed, the combination of the analytical solution with streamline simulation is orders of magnitude faster than conventional finite difference simulation. Nevertheless, the assumption is never strictly satisfied, because all displacements include some pressure drop over the displacement length, so it is important to test the inaccuracy that the assumption induces. The simulation results presented demonstrate that the assumption is a surprisingly good one. Even for near-miscible displacements, which should be the most sensitive to the effects of pressure changes, the analytical solutions obtained with the phase behavior evaluated at the average pressure of the displacement are quite reasonable. In addition, the pressure drop that occurs over a displacement length has only modest effect on crossflow, so that the use of streamline simulations is still reasonable for gas-oil displacements with significant pressure drop. These results suggest that there are many situations in which it is quite reasonable to use the analytical solutions of Chapter 3 for one-dimensional multicomponent flow combined with streamlines to represent the effects of heterogeneity. When that simulation approach is reasonable, it is orders of magnitude faster than conventional finite difference simulation, and compositional simulations on high-resolution grids is feasible. The analytical solutions are available only if injection and initial compositions are constant, a restriction that is often not satisfied. If so, the numerical approaches for solutions along streamlines described in Chapter 2 are the appropriate choice.

## 6 Summary

In this report we have considered how to predict the performance of gas injection processes at field scale. We have argued that accurate predictions of process performance will require high resolution representation of permeability variations, modeling of the compositional processes that control local displacement efficiency in high pressure gas injection processes, substantial reduction in the adverse computational effects of numerical dispersion over conventional finite-difference compositional simulation, and sufficient computation speed that large-scale problems can be considered. This report demonstrates that streamline methods are one option for meeting those requirements.

We have shown that when reservoir heterogeneity controls flow paths, and when effects of gravity segregation and capillary crossflow are small, compositional streamline simulations are appropriate, and they are orders of magnitude faster than conventional finite-difference compositional simulations. The example given in Chapter 2 of simulation of condensate recovery illustrates that point. In that example, a combination of an analytical solution for the condensate displacement process along a single streamline with a streamline representation of the effects of heterogeneity on the flow was used to perform simulations that were much less subject to the effects of numerical smearing than the corresponding finite difference simulations and much faster to perform. In that displacement, the locations of streamlines changed only slightly, as the result of changes in mobility as the injected gas replaced the fluid in place. Effects of reservoir heterogeneity were represented well by the streamlines, and the interaction of phase behavior and flow could be captured by the 1D analytical solution along each streamline.

The results presented in Chapter 3 indicate that it is now possible to construct analytical solutions for 1D flow of multicomponent gas/oil mixtures with an arbitrary number of components, with and without volume change, and for the full range of initial and injection compositions. Additional work by Juanes (2004) and by LaForce and Johns (2004) extends these ideas to systems that involve three-phase flow. These solutions will be particularly useful for comparison studies that examine the sensitivity of reservoir displacements to alternate well locations, to changes in injection gas composition, or to alternate reservoir descriptions. While these solutions are clearly an approximation, because the single analytical solution must be remapped along new streamline locations and because the phase behavior of the fluids is evaluated at a single displacement pressure, the speed advantage of the combination of streamlines and analytical solutions makes it an excellent choice for screening purposes and sensitivity studies. The results presented in Chapter 5, concerning the accuracy of the assumption of constant pressure for evaluation of phase equilibrium behavior, indicate that such calculations are surprisingly accurate.

There are, of course, many situations where effects of gravity are important. It is clearly possible to include the effects of gravity in streamline simulations, as the method proposed in Chapter 2 demonstrates. Work done by Berenblyum *et al.* (2003), in collaboration with this project indicates that the same statement can be made about capillary crossflow. These physical mechanisms can be represented by suitable operator splitting techniques. There is a

price to be paid, of course. Application of operator splitting requires that streamline locations be updated. If streamlines locations are very sensitive to gravity, for example, so that frequent pressure solves are required to locate streamlines, then much of the advantage of streamline computations is lost. There are definitely flow situations where streamlines are not the best choice, therefore. The scaling analysis and experimental verifications of the transitions from viscous to capillary to gravity dominated flow reported in Chapter 5 give some guidance as to the appropriateness of the use of streamline simulations. For displacements in which gravity segregation or capillary effects dominate, other simulation techniques should be considered. For flows dominated by heterogeneity, and for flows that involve some effects of gravity- and/or capillary-driven flow, streamline simulation with appropriate operator splitting, can still be substantially more efficient than conventional simulation approaches.

Accounting for the change in location of streamlines due to mobility changes or the use of operator splitting to account for gravity or capillary effects requires that streamline locations be remapped repeatedly. In addition, remapping streamlines makes it appropriate to solve the 1D compositional displacement problem along each streamline numerically (because the analytical solutions obtained so far apply only to displacements with constant initial compositions along a streamline). Accordingly, Chapter 2 includes a detailed discussion of ways to improve the accuracy of these calculations. Higher order methods for solving the 1D flow problem can be used to limit the adverse effects of numerical dispersion efficiently. The analysis of ways to reduce mapping errors indicates that considerable improvement in mass balance accuracy can be achieved at modest additional computation cost.

The experimental results presented in Chapter 4 also provide useful guidance concerning the fundamentals of three-phase flow in gas injection processes. They indicate that low interfacial tensions between oil and gas phases in the presence of water will cause an increase in the relative permeability to oil. That is, of course, exactly the objective of multicontact miscible gas injection processes, to increase the displacement efficiency of the oil. The observations suggest that mobility of the injected gas and oil will be higher in zones invaded by the gas in such displacements. As a result, streamlines along zones of fast flow (in high permeability regions of a reservoir) will be swept efficiently, providing flow paths that are still easier to invade. Thus, streamlines will bunch together in zones of high permeability that are swept early by gas, and they will be hard to move from those zones. Here again, these are situations that are appropriate for streamline simulation.

Taken together, the results presented here indicate that considerable progress has been made in the development of compositional streamline representations of gas injection processes. For many reservoir settings, streamline methods will offer the most accurate and most efficient simulation technique available. Streamline methods are fast enough that they can be applied to simulate compositional gas injection processes with much higher resolution and much less numerical dispersion that can be achieved with conventional finite difference approaches. Indeed, high resolution compositional reservoir simulations simply are not computationally feasible by any other technique. Thus, the research results reported here establish that compositional streamline simulation will play an important role in the toolkit of

reservoir simulation tools available for process prediction.

We emphasize, however, that there is still work to be done to make compositional streamline methods a fully functional reservoir simulation tool (just as the considerable success of conventional finite difference reservoir simulation methods is the result of decades of development). Research areas that have considerable potential for future improvements in the compositional streamline approach include: developing optimal methods for placement of streamlines, application of adaptive mesh refinement using error estimation, inclusion of the higher order methods developed here, further development of the mapping algorithms, and considering how streamlines should be calculated for flow in compressible systems. In addition, streamline approaches are especially appropriate for parallel computations, because the 1D solutions along individual streamlines can be done independently. The work presented here provides a substantial foundation for that research.

## 7 References

1. Adamson, A.W.: "Physical Chemistry of Surfaces", fifth edition, John Wiley & Sons, New York 1990.
2. Ahmed, G.: "An experimental study of recovery from a 2-D layered sand model.", MSc. Thesis, Stanford University, 1984.
3. Akin, S. and Demiral, B.: "Effect of Flow Rate on Imbibition Three-Phase Relative Permeabilities and Capillary Pressures," Paper SPE 38897, presented at the 1997 SPE ATCE, San Antonio, TX, 5-8 Oct.
4. Amaefule, J.O. and Handy, L.L.: "The Effect of Interfacial Tension on Relative Oil and Water Permeabilities of Consolidated Porous Media," SPEJ, 371-81, June 1982.
5. Amin, R. and Smith, T.N.: "Interfacial Tension and Spreading Coefficient under Reservoir Conditions," Fluid Phase Equilibria, 142, 1998, 231-241.
6. Asar, J. and Handy, L.L.: "Influence of Interfacial Tension on Gas/Oil relative permeability in a gas condensate system," SPE Reservoir Eng., Feb. 1983, 257.
7. Aziz, K., Settari, A.: "Petroleum Reservoir Simulation," Blitzprint Ltd., Calgary, AB (2002) 394.
8. Baker, L.E.: "Three-Phase Relative Permeability of Water-Wet, Intermediate-Wet, and Oil-Wet Sandstone," In Proc. of Seventh European Improved Oil Recovery Symp., Moscow, 1993.
9. Baker, R.O., Kuppe, F., Chugh, S., Bora, R., Stojanovic, S., Batycky, R. P.: "Full-Field Modeling using Streamline-Based Simulation: 4 Case Studies," SPE 66405 presented at the 2001 SPE Reservoir Simulation Symposium. Houston, TX. 11-14 February.
10. Baker R.O.: "Streamline Technology: Reservoir History matching and Forecasting - Its success, Limitations and Future". JCPT (April 2001).
11. Bardon, C. and Longeron, D.: "Influence of very low Interfacial Tensions on Relative Permeability," SPE 7609, presented at the 53rd Annual Tech Conference and Exhibition, Houston, TX, Oct 1-3 1978.
12. Batycky, R.P., Blunt M.J. and Thiele, M.R.: "A 3D Field Scale Streamline Simulator with Gravity and Changing Well Conditions", SPE 36726, ATCE, Denver, CO, 1996.

13. Batycky, R.P.: "A Three-Dimensional Two-Phase Field Scale Streamline Simulator," Ph.D. dissertation, Stanford University, Dept. of Petroleum Engineering. Stanford CA, January 1997.
14. Batycky, J.P. and McCaffery, F.G.: "Low Interfacial Tension Displacement Studies," Paper presented at the 1978 Annual Tech Meeting of the Pet. Soc. of CIM, Calgary, June 13-16.
15. Bear, J.: "Dynamics of Fluids in Porous Media," Dover Publications Inc, New York 1988.
16. Beliveau, D.: "Heterogeneity, Geostatistics, Horizontal Wells and Blackjack Poker," JPT (December 1995).
17. Berenblyum, R.A., Shapiro, A., Jessen, K., Stenby, E.H. and Orr, F.M., Jr.: "Black Oil Streamline Simulator with Capillary Effects," SPE 84037, SPE Annual Technical Conference and Exhibition, Denver, USA, 2003
18. Blunt, M.J., Lui, K. and Thiele, M.R.: "A Generalized Streamline Method to Predict Reservoir Flow," *Petroleum Geoscience* (1996) 2, p. 259-269.
19. Blunt, M.J.: "An Empirical Model for Three-Phase Relative Permeability," *SPE Journal*, 5 (4), p. 435, December 2000.
20. Bommer, M.P. and Schechter, R.S.: "Mathematical Modeling of In-Situ Uranium Leaching," *SPEJ* (Dec. 1979) 19, 393-400.
21. Bratvedt, F., Gimse, T., Tegnander, C.: "Streamline Computations for Porous Media Flow including Gravity," *Transport In Porous Media* (October 1996) 25, No. 1, 63-78.
22. Bratvedt, F., Bratvedt, K., Buchholz, C., Holden, L., Holden, H., and Risebro, N.H.: "A New Front-Tracking Method for Reservoir Simulation," *SPE Reservoir Engineering*, Feb. 1992, 107-116.
23. Buckley, S.E. and Leverett, M.C.: "Mechanisms of Fluid Displacement in Sands," *Trans. AIME* (1941) 249
24. Caudle, B.H., Slobod, R.L., and Brownscombe, E.R.: "Further Developments in the Laboratory Determination of Relative Permeability," *Trans. AIME*, 192, 145, 1951.
25. Cere', A. and Zanotti, F.: "Sharpening Behavior and Dispersion in Chemical Flooding," *Proc., Third European Meeting on Improved Oil Recovery, Rome* (1985).
26. Chen, W.H., Durlofsky, L.J., Engquist, B., Osher, S.: "Minimization of Grid Orientation Effects through use of Higher Order Finite Difference Methods," *SPE Advanced Technology Series*, 1: 43-52, July 1993.

27. Christie, M.A. and Blunt, M.J., "Tenth SPE Comparative Solution Project: A Comparison of Upscaling Techniques", SPEREE, August, 2001
28. Corey, A.T., Rathjens, C.H., Henderson, J.H., and Wyllie, M.R.J.: "Three-Phase Relative Permeability," Trans. AIME, 207, 3249, 1956.
29. Crane, M., Bratvedt, F., Bratvedt, K., Childs, P., Olufsen, R.: "A Fully Compositional Streamline Simulator," SPE 63156 presented at the 2000 SPE Annual Technical Conference and Exhibition. Dallas, TX, October 1-4, 2000.
30. Datta-Gupta, A.: "Streamline Simulation: A Technology Update," JPT (December 2000).
31. Datta-Gupta, A., S. Yoon, K. Nordaas and D.W. Vasco.: "Streamlines, Ray Tracing and Production Tomography: Generalization to Compressible Flow," Petroleum Geoscience, 7: S75-S86, 2001.
32. Datta-Gupta, A. and King, M.J.: "A Semi-Analytical Approach to Tracer Flow Modeling in Heterogeneous Permeable Media," Advances in Water Resources (1995) 18, p. 9-24.
33. Dawe, R. A., Wheat, M. R. and Bidner, M. S.: "Experimental Investigation of Capillary Pressure Effects on Immiscible Displacement in Lensed and Layered Porous Media," Transport in Porous Media, 7, 83-101 (1992).
34. Delclaud, J., Rochon, J. and Nectoux, A.: "Investigation of Gas/Oil Relative Permeabilities: High-Permeability Oil Reservoir Application," SPE 16999, presented at the 62rd Ann. Tech. Conf. and Exhib., Dallas, TX, 1987.
35. Delshad, M., Delshad M., Pope, G.A. and Lake, L. W.: "Two- and Three-Phase Relative Permeabilities of Micellar Fluids," SPE Formation Evaluation, September, 1987, 327-337.
36. Deutch, C.V., and Journel, A.G.: "GSLIB-Geostatistical Software Library and User's Guide," Oxford University Press, New York, NY (1998) 369.
37. DiCarlo, D.A., Sahni, A., and Blunt, M.J.: "Three-Phase Relative Permeability of Water-Wet, Oil-Wet, and Mixed-Wet Sandpacks," SPEJ, March 2000, 82.
38. Dindoruk, B.: "Analytical Theory of Multiphase, Multicomponent Displacement in Porous Media," Ph.D. thesis, Dept. of Petroleum Eng., Stanford University, Stanford, CA, 1992.
39. Dindoruk, B. Johns, R.T. and Orr, F.M., Jr.: "Analytical solutions for Four Component Gas Displacements with Volume Change on Mixing," ECMOR III, Delft, Holland, 1992b.

40. Dindoruk, B., Orr, F.M., Jr., and Johns, R.T.: "Theory of Multicontact Miscible Displacement with Nitrogen," SPEJ (September 1997) 268.
41. Donaldson, E.C. and Dean, G.W.: "Two- and Three-Phase Relative Permeability Studies," U.S. Bureau of Mines, Washington D.C. #6826, 1966.
42. Dria, D.E., Pope, G., and Sepehrnoori, K.: "Three-Phase Gas/Oil/Brine Relative Permeabilities Measured under CO<sub>2</sub> Flooding Conditions," SPE Reservoir Engineering, May 1993, 143.
43. Dumore, J.M., Hagoort, J. and Risseeuw, A.S.: "An Analytical Model for One-Dimensional Three Component Condensing and Vaporizing Gas Drives," Soc. Pet. Eng. J., 24:169-179, 1984.
44. Eleri, O.O., Grauge, A., and Skauge, A.: "Steady-State and Unsteady-State Two-Phase Relative Permeability Hysteresis and Measurements of Three-Phase Relative Permeability using Imaging Techniques," Paper SPE 30764 presented at the 1995 SPE Annual Technical Conference and Exhibition, Dallas, October 22-25.
45. Ermakov, P.: "Analytical Solutions for 1D Oil Displacements by Gas," M.Sc. Report, Department of Petroleum Engineering, Stanford University, Stanford, CA, 2000.
46. Fayers, F. J., and Lee, S. T.: "Crossflow Mechanisms in Oil Displacement by Gas Drive in Heterogeneous Reservoirs," SPE 24934 presented at the 67th Annual SPE Meeting, Washington D.C., Oct. 4-7, 1992.
47. Fulcher, R.A., Ertekin, T., and Stahl, C.D.: "Effect of Capillary Number and its Constituents on Two-Phase Relative Permeability," J. Pet. Tech., Feb. 1985, 249-60.
48. Goddin, C. S. *et al.*: "A Numerical Study of Waterflood Performance in a Stratified System with Crossflow," J. Pet. Tech., June 1966, 765-771.
49. Grader, A.S., and O'Meara, D.J.: "Dynamic Displacement Measurements of Three-Phase Relative Permeabilities using Three Immiscible Liquids," SPE 18293, presented at the SPE 63rd Ann. Tech. Conf. and Exhib., Houston, TX, Oct. 2-5, 1988.
50. Grinestaff, G. H., Caffrey, D. J.: "Waterflood Management: A Case Study of the Northwest Fault Block Area of Prudhoe Bay, Alaska, Using Streamline Simulation and Traditional Waterflood Analysis," SPE 63152 presented at the 2000 SPE Annual Technical Conference and Exhibition. Dallas, TX. October 1-4.
51. Godunov, S.K. Mat. Sb., 47:271, 1959.
52. Hamon, G. and Vidal, J.: "Scaling the Capillary Pressure from Laboratory Experiments on Homogeneous and Heterogeneous Samples," SPE 15852 presented at SPE European petroleum Conference, London, Oct. 20-22, 1986.

53. Harbert, L.W.: "Low Interfacial Tension Relative Permeability," SPE 12171, presented at the Annual Technical Conf. And Exhib., San Francisco, Oct. 5-8, 1983.
54. Helfferich, F.G.: "Theory of Multicomponent, Multiphase Displacement In Porous Media," SPEJ (February 1981) 51.
55. Harten, A., Engquist, B., Osher, S., and Chakravarthy, S.: "Uniformly High Order Accurate Essentially Non-Oscillatory Schemes III," J. Comput. Phys., 71: 231-303, 1987.
56. Helfferich, F.G.: "General Theory of Multicomponent, Multiphase Displacement in Porous Media," Soc. Pet. Eng. J., 21:51-62, 1981.
57. Hoier, L., and Whitson, C. H.: "Miscibility Variation In Compositionally Grading Reservoirs," SPE REE, February 2001.
58. Høier, L. 1997: "Miscibility Variations In Compositionally Grading Petroleum Reservoirs," Ph.D. dissertation, NTNU, Trondheim.
59. Ichiro, O., Datta-Gupta, A., and King, M.J.: "Time Step Selection During Streamline Simulation Via Transverse Flux Correction," SPE 79688 presented at the SPE Reservoir Simulation Symposium, Houston, TX, February 2003.
60. Ingsoy, P. and Skjaveland, S. M.: "Experimental Validation of New Method for Optimizing Miscible Flooding of Stratified Reservoirs," SPE 20241 presented at SPE/DOE 7th Symposium on Enhanced Oil Recovery, Tulsa, OK, April 22-25, 1990.
61. Ingebrigtsen, L., Bratvedt, F., and Berge, J.: "A Streamline Based Approach to Solution of Three-Phase Flow," SPE 51904 presented at the SPE Reservoir Simulation Symposium, Houston, TX, February 1999.
62. Jessen, K., Michelsen, M.L., and Stenby, E.H.: "Global Approach for Calculation of Minimum Miscibility Pressure," Fluid Phase Equilibria.153: 251, 1998.
63. Jessen, K.: "Fast, Approximate Solutions to 1D Multicomponent Gas Injection Problems," SPEJ, December 2001.
64. Jessen, K.: "Effective Algorithms for The Study of Miscible Gas Injection Problems," Ph.D. Thesis, IVC-SEP, Dept. of Chemical Engineering, Technical U. of Denmark, 2000.
65. Jessen, K., E.H. Stenby and F.M. Orr, Jr.: "Interplay of Phase Behavior And Numerical Dispersion in Finite Difference Compositional Simulation," SPE 75134 presented at the SPE/DOE 13th Symposium on Improved Oil Recovery, Tulsa, OK, April 2002.

66. Jessen, K., Orr, F. M. Jr.: "Compositional Streamline Simulation," SPE 77379 presented at the 2002 SPE Annual Technical Conference and Exhibition. San Antonio, TX., September 29 September October 2.
67. Jessen, K., Wang, Y., Ermakov, P., Zhu, J., and Orr, F.M., Jr.: "Fast, Analytical Solutions for 1D Multicomponent Gas Injection Problems," SPE 74700, SPEJ, December 2001.
68. Jiang, G.-S. and Shu, C.-W.: "Efficient Implementation of Weighted ENO Schemes," J. Comput. Phys., 126: 202-228, 1996.
69. Johansen, T., Dindoruk, B., and Orr, F.M., Jr.: "Global Triangular Structure in Four-Component Conservation Laws," Proc., Fourth European Conference on the Mathematics of Oil Recovery, Roros, Norway (1994).
70. Johns, R.T., and Orr, F.M., Jr.: "Miscible Gas Displacement of Multicomponent Oils," Soc. Pet. Eng. J., 1(1): 39-50, 1996.
71. Johns, R.T., Dindoruk, B., and Orr, F.M., Jr.: "Analytical Theory of Combined Condensing/Vaporizing Gas Drives," SPE Advanced Technology Series (1993) 2, 7.
72. Johnson, E.F., Bossler, D.P., and Naumann, V.O.: "Calculation of Relative Permeability from Displacement Experiments," AIME Trans. Vol. 216, p. 370, 1959.
73. Juanes, R., "Determination of the Wave Structure of the Three-Phase flow Riemann Problem", submitted to Transport in Porous Media, 2004.
74. King, M.J. and Datta-Gupta, A.: "Streamline Simulation: A Current Perspective," In Situ, 22(1): 91-140, 1998.
75. Knickerbocker, B.M., Peskeck, C.V., Davis, H.T., and Scriven, L.E.: "Patterns of Three-Liquid-Phase Behavior Illustrated by Alcohol-Hydrocarbon-Water-Salt Mixtures," J. Phys. Chem., 86, 393-400, 1982.
76. Kontogeorgis, G.M., Voutsas, E.C., Yakournis, I.V., and Tassios, D.P.: "An Equation of State for Associating Fluids," I&EC Res., 35, 4310, 1996.
77. LaForce, T. and Johns, R.T., "Analytical Theory for Three-Phase Partially Miscible Flow in Ternary Systems", SPE 89438, Proceedings SPE/DOE IOR, Tulsa, April 2004.
78. Lake, L.W.: "Enhanced Oil Recovery", Prentice Hall Publishers, New York City (1989), p. 29.
79. Lantz, R. B. "Quantitative Evaluation of Numerical Diffusion (Truncation Error)," SPEJ (September 1971).

80. LeVeque, R.J.: "Numerical Methods for Conservation Laws," Birkhauser Verlag, Basel, Switzerland, 1992.
81. Levy, D., Puppo, G., and Russo, G.: "Central WENO Schemes for Hyperbolic Systems of Conservation Laws, Mathematical Modeling And Numerical Analysis," 33(3): 547-571, 1999.
82. Lohrenz, J., Bray, B.G., and Clark, C.R.: "Calculating Viscosities of Reservoir Fluids from Their Compositions," JPT (October 1964) 1171.
83. Mahadevan, J., Lake, L.W., Johns, R.T.: "Estimation of True Dispersivity in Field Scale Permeable Media," SPE 75247 presented at the 2002 SPE/DOE Improved Oil Recovery Symposium. Tulsa, OK. 13-17 April.
84. Mallison, B.T., Gerritsen, M.G., Jessen, K., and F.M. Orr, Jr.: "High Order Schemes for Two-Phase Multicomponent Flow," SPE 79691 presented at the SPE Reservoir Simulation Symposium, Houston, TX, February 2003.
85. Manning, C.D. and Scriven, L.E.: "On Interfacial Tension Measurement with a Spinning Drop in Gyrostatic Equilibrium," Rev. Sci. Instrum., Vol. 48, No. 4, April 1977, 77.
86. McCain, W. D. Jr.: "Heavy Components Control Reservoir Fluid Behaviour," JPT (September 1994).
87. McDougall, S.R., Salino, P.A., and Sorbie, K. S.: "The Effect of Interfacial Tension Upon Gas-Oil Relative Permeability Measurements: Interpretation using Pore-Scale Models," SPE 38920, presented at the 1997 SPE Annual Technical Conf. and Exhib., San Antonio, TX, 5-8 Oct.
88. Melean, Y., Bureau, N., Brosets, D.: "Interfacial Effects in Gas-Condensate Recovery and Gas Injection Processes," SPE 71495 presented at the 2001 SPE Annual Technical Conference and Exhibition. New Orleans, LA. 30 September-3 October.
89. Michelsen M.L.: "Speeding Up The Two-Phase PT-Flash, with Application for Calculation of Miscible Displacements," Fluid Phase Equilibria, 1: 143, 1998.
90. Monroe, W.W. *et al.*: "Composition Paths in Four-Component Systems: Effect of Dissolved Methane on 1D CO<sub>2</sub> Flood Performance," SPERE (August 1990) 423.
91. Morrow, N.R. and McCaffery, F.G.: "Fluid Displacement Studies in Uniformly Wetted Porous Media. In Wetting, Spreading And Adhesion," Ed. J.F. Padday, Academic Press, N.Y., 1978, 289-319.

92. Morrow, N.R., Chatzis, I., and Taber, J.J.: "Entrapment and Mobilization of Residual Oil in Bead Packs," SPE 14423, SPE Reservoir Engineering, 927-935, August 1988.
93. Nesyaho, H. and Tadmor, E.: "Non-Oscillatory Central Differencing for Hyperbolic Conservation Laws," J. Comput. Phys., 87: 408-463, 1990.
94. Oak, M.J., Baker, L.E., and Thomas, D.C.: "Three-Phase Relative Permeability of Berea Sandstone," Journal of Petroleum Technology, August 1990, 1054.
95. Orr, F.M. Jr., "DOE Quarterly Report: High Resolution Prediction of Gas Injection Process Performance for Heterogeneous Reservoirs," Contract No. DE-FC26-00BC15319, Oct.-Dec., 2001.
96. Orr, F.M., Jr., Johns, R.T., and Dindoruk, B.: "Development of Miscibility in Four-Component CO<sub>2</sub> Floods," Soc. Pet. Res. Eng. 8(2): 135-142, 1993.
97. Orr, F.M., Jr., Silva, M.K., and Lien, C.L.: "Equilibrium Compositions of CO<sub>2</sub>-Crude Oil Mixtures: Comparison of Continuous Multiple Contact and Slim Tube Displacement Tests," Soc. Pet. Eng. J. 23, 281-291, 1983.
98. Pande, K.K., Orr, F.M. Jr.: "Interaction of Phase Behaviour, Reservoir Heterogeneity and Crossflow in CO<sub>2</sub> Floods," SPE 19668 presented at the 1989 SPE Annual Technical Conference and Exhibition. San Antonio, TX. 8-11 October.
99. Peddibhotla, S., Datta-Gupta, A. and Xue, G.: "Multiphase Streamline Modeling in Three Dimensions: Further Generalizations and a Field Application," SPE 38003 presented at the SPE Reservoir Simulation Symposium, Dallas, TX, June 1997.
100. Pejic, D. and Maini, B.B.: "Three-Phase Relative Permeability of Petroleum Reservoirs," Paper SPE81021, presented at the SPE Latin American and Caribbean Pet. Eng. Conf., Trinidad, April 27-30, 2003.
101. Peng, D.Y. and Robinson, D.B.: "A New Two-Constant Equation of State," Ind. Eng. Chem. Fund, 15: 59-64, 1976.
102. Pollock, D.W.: "Semi-analytical Computation of Path Lines for Finite Difference Models", Ground Water (Nov-Dec 1988) 26, No. 6, 743.
103. Pongpitak, S.: "Interaction Of Phase Behavior With Multiphase Flow In Porous Media," M.S. Thesis, New Mexico Inst. of Mining and Technology, Socorro, February, 1980.
104. Pozzi, A.L. and Blackwell, R.J.: "Design of Laboratory Models for study of Miscible Displacement," SPEJ 28-40 (March 1963).

105. Qiu, J. and Shu, C.-W.: "On the Construction, Comparison, and Local Characteristic Decomposition for High Order Central WENO Schemes," J. Comput. Phys., to appear.
106. Raal, J.D. and Muehlbauer, A.L.: "Phase Equilibria – Measurement And Computation," Taylor & Francis Publishers, Washington DC, p. 461, 1997,.
107. Rapoport, L.A. and Leas, W.J.: "Properties of Linear Waterfloods," AIME Trans. Vol. 198, p. 139, 1953.
108. Rubin, B. and Blunt, M.J.: "Higher Order Implicit Flux Limiting Schemes for Black Oil Simulation," SPE 21222 presented at the SPE Symposium on Reservoir Simulation, Anaheim, CA, February 1991.
109. Rubin, B. and Edwards, M.: "Extension of The TVD Midpoint Scheme to Higher-Order Accuracy in Time," SPE 25265 presented at the 12th Symposium on Reservoir Simulation, New Orleans, LA, 1993.
110. Sahni, A., Guzman, R. and Blunt, M.: "Theoretical Analysis of Three-Phase Flow Experiments in Porous Media," SPE 36664, presented at the SPE Ann. Tech. Conf. and Exhib., Denver, CO, Oct. 6-9, 1996.
111. Sahni, A., Burger, J.H. and Blunt, M.: "Measurement of Three Phase Relative Permeability During Gravity Drainage using CT Scanning," SPE 39655, presented at the SPE/DOE IOR Symposium, Tulsa, OK, Apr. 19-22, 1998.
112. Samier, P., Quettier, L., Thiele, M. "Applications of Streamline Simulations to Reservoir Studies," SPE 66362 presented at the 2001 SPE Reservoir Simulation Symposium. Houston, TX. 11-14 February.
113. Sam-Olibale, L. "Limitations of Streamline Simulation: A Crossflow Investigation," M.Sc. Report, Department of Petroleum Engineering, Stanford University. Stanford, CA (2002).
114. Saraf, D.N. and Fatt, I.: "Three-Phase Relative Permeability Measurement using a Nuclear Magnetic Resonance Technique for Estimating Fluid Saturation," SPE Journal, 9, 235, 1967.
115. Sarem, A.M.: "Three-Phase Relative Permeability Measurements by Unsteady-State Methods," SPE Journal, 9, 199, 1966.
116. Schechter, D.S., Zhou, D., and Orr, F.M., Jr.: "Low IFT Drainage and Imbibition," J. of Pet. Sci. and Eng., 11, 283-300, 1994.
117. Schneider, F.N. and Owens, W.W.: "Sandstone and Carbonate Two- and Three-Phase Relative Permeability Characteristics," SPE Journal, 3, 75, 1970.

118. Seto, C.J, Jessen, K. and Orr, F.M. Jr.: "Compositional Streamline Simulation of Field Scale Condensate Vaporization by Gas Injection," SPE 79690, SPE Reservoir Simulation Symposium, Houston, TX, February 3-5, 2003.
119. Shook, M., Li, D., and Lake, L.W.: "Scaling Immiscible Flow through Permeable Media by Inspectional Analysis," *In Situ*, 16(4), 311-349 (1992).
120. Siddiqui, S., Hicks, P.J., and Grader, A.S.: "Verification of Buckley-Leverett Three-Phase Theory using Computerized Tomography," *Journal of Petroleum Sci. and Eng.*, 15, 1-21, 1996.
121. Shu, C.-W. and S. Osher.: "Efficient Implementation of Essentially Non-Oscillatory Shock-Capturing Schemes," *J. Comput. Phys.*, 77: 439-471, 1988.
122. Skauge, A., Eleri, O.O., Graue, A., and Monstad, P.: "Influence of Connate Water on Oil Recovery by Gravity Drainage," Paper SPE 27817, presented at the 1994 SPE/DOE IOR Symp., Tulsa, OK, April 17-20.
123. Stalkup, F.I.: "Miscible Displacement, Monograph 8," Soc. Pet. Eng. of AIME, New York (1983).
124. Stalkup, F.I.: "Displacement Behavior of The Condensing/Vaporizing Gas Drive Process," SPE 16715, ATCE, Dallas, TX, 1987.
125. Sweby, P.K.: "High Resolution Schemes using Flux Limiters for Hyperbolic Conservation Laws," *SIAM J. Numerical Analysis*, 21: 995-1011, 1984.
126. Taber, J.J. and Meyer, W.K.: "Investigations of Miscible Displacements of Aqueous And Oleic Phases from Porous Media," *SPEJ*, 37-48, March 1964.
127. Talash, A.W.: "Experimental and Calculated Relative Permeability Data for a System Containing Tension Additives," SPE 5810, presented at the 1976 Improved Oil Recovery Symposium, Tulsa, OK, March, 22-24.
128. Tchelepi, H. and Orr, F.M. Jr.: "Integration of Viscous Fingering, Permeability Heterogeneity, and Gravity Segregation in Three Dimensions," *SPE Reservoir Engineering* (November 1994) 9, 266-271.
129. Tchelepi, H.: "Viscous Fingering, Gravity Segregation and Permeability Heterogeneity in Two Dimensional and Three Dimensional Flows," Ph.D. Dissertation. Stanford University, Stanford, 1994.
130. Tehrani, D.H., Henderson, G.D., Danesh, A., Al-Siyabi, Z., and Salino, P.A.: "Effect of Interfacial Tension on Gas and Oil Relative Permeability (Part I-Primary Drainage)," Paper P554 presented at the 59th EAGE Conf. And Tech. Exhib., Geneva, 1997.

131. Thiele, M.R.: "Modeling Multiphase Flow in Heterogeneous Media Using Streamtubes," Ph.D. dissertation, Department of Petroleum Engineering, Stanford University. Stanford, 1994.
132. Thiele, M.R., Blunt, M.J., and Orr, F.M., Jr., 1995a: "Modeling Flow in Heterogeneous Media using Streamtubes – I. Miscible and Immiscible Displacements" *In Situ* 19 (4), 299-339.
133. Thiele, M.R., Blunt, M.J., and Orr, F.M., Jr., 1995b: "Modeling Flow in Heterogeneous Media using Streamtubes – II. Compositional Displacements," *In Situ* 19 (4), 367-391.
134. Thiele, M.R., Rao, S.E. and Blunt, M.J.: "Quantifying Uncertainty In Reservoir Performance using Streamtubes", *Mathematical Geology* (Oct. 1996), 28, No. 7, 843-856.
135. Thiele, M.R., Batycky, R.P., Blunt, M.J., and Orr, F.M., Jr.: "Simulating Flow in Heterogeneous Media using Streamtubes And Streamlines," *SPE Reservoir Engineering*, 10(1), 5-12, 1996.
136. Thiele, M.R., Batycky, R.P., Blunt, M.J., Orr, F.M. Jr.: "A Streamline-Based 3D Field-Scale Compositional Reservoir Simulator." SPE 38889 presented at the 1997 SPE Annual Technical Conference and Exhibition. San Antonio, TX. 5-8 October.
137. Thiele, M.R., Batycky, R.P., Blunt, M.J. 1997: "A 3D Field Scale Streamline Simulator," SPE 38889, SPE Annual Technical. Conf., San Antonio, October.
138. Thiele, M.R. and Edwards, M.: "Physically Based Higher Order Godunov Schemes for Compositional Simulation," SPE 66403 presented at the SPE Reservoir Simulation Symposium, Houston, TX, February 2001.
139. Torabzadeh, S.J. and Handy, L.L.: "The Effect of Temperature and Interfacial Tension on Water/Oil Relative Permeabilities of Consolidated Sands," SPE 12689, presented at the SPE/DOE Symp. on EOR, Tulsa, OK, April 15-18.
140. Van Leer, B.: "Towards the Ultimate Conservative Finite Difference Scheme, V: A Second Order Sequel to Godunov's Method," *J. Comput. Phys.*, 32: 101-36, 1979.
141. Van Spronsen, E.: "Three-Phase Relative Permeability Measurements using the Centrifuge Method," SPE/DOE Symposium on Improved Oil Recovery, Tulsa, OK, 1982.
142. Virnovski, G.A.: "Determination of Relative Permeabilities in a Three-Phase Flow in Porous Medium.", Translated from *Izvestiya Akademii Nauk SSSR, Mekhanika Zhidkostii Gaza*, Sept. 1985, 5, 187-9

143. Vizika, O. and Lombard, J-M.: "Wettability and Spreading: Two Key Parameters in Oil Recovery with Three-Phase Gravity Drainage," SPE Reservoir Engineering, February 1996, 54.
144. Wang, Y. and F.M. Orr, Jr.: "Analytical Calculation of Minimum Miscibility Pressure," Fluid Phase Equilibria, 139:151-164, 1997.
145. Wang, Y.: "Analytical Calculation of Minimum Miscibility Pressure," Ph.D. Dissertation, Department of Petroleum Engineering, Stanford University, Stanford, 1998.
146. Wang, Y. and Orr, F.M., Jr.: "Calculation of Minimum Miscibility Pressure," J. Pet. Sci. Eng. (2000) 27, 151.
147. Welge, H.J.: "A Simplified Method for Computing Oil Recovery by Gas or Water Drive," AIME Trans. Vol. 195, p. 91, 1952.
148. Welge, H.J., Johnson, E.F., Ewing, S.P., and Brinkman, F.H.: "The Linear Displacement of Oil from Porous Media by Enriched Gas," J. Pet. Tech. (August) 787-796, 1961.
149. Yokoyama, Y., Lake, L.W.: "The Effects of Capillary Pressure on Immiscible Displacements in Stratified Porous Media," SPE 10109 presented at the 1981 SPE Annual Fall Technical Conference and Exhibition. San Antonio, TX, October 5-7.
150. Yuan, H. and Johns, R.T.: "Simplified Method for Calculation of Minimum Miscibility Pressure or Enrichment," SPE 77381, ATCE, San Antonio, Texas, September 29 – October 2, 2002.
151. Zanotti, F., De Notaristefani, C., and Gardini, L.: "Sharpening Behavior of Chemical Flooding," SPE 11809 available from SPE, Richardson, Texas (1983).
152. Zapata, V.J.: "The Effects of Viscous Crossflow on Sharp Front Displacement in Two-Layered Porous Media," MS Thesis, University of Texas at Austin.
153. Zick, A.A.: "A Combined Condensing/Vaporizing Mechanism in The Displacement of Oil by Enriched Gases," SPE15493, ATCE, New Orleans, LA, 1986.
154. Zhou, D., Fayers, F.J., Orr, F.M. Jr.: "Scaling of Multiphase Flow in Simple Heterogeneous Porous Media," SPE/DOE 27833 presented at the 1994 SPE/DOE Ninth Symposium on Improved Oil Recovery. Tulsa, OK. 17-20 April.